coatings

Special Issue Reprint

Ceramic Films and Coatings

Properties and Applications

Edited by
Qi Zhu

mdpi.com/journal/coatings

MDPI

Ceramic Films and Coatings: Properties and Applications

Ceramic Films and Coatings: Properties and Applications

Editor

Qi Zhu

MDPI

Basel • Beijing • Wuhan • Barcelona • Belgrade • Novi Sad • Cluj • Manchester

Editor
Qi Zhu
School of Materials Science
and Engineering
Northeastern University
Shenyang
China

Editorial Office
MDPI
St. Alban-Anlage 66
4052 Basel, Switzerland

This is a reprint of articles from the Special Issue published online in the open access journal *Coatings* (ISSN 2079-6412) (available at: https://www.mdpi.com/journal/coatings/special_issues/Ceram_film).

For citation purposes, cite each article independently as indicated on the article page online and as indicated below:

Lastname, A.A.; Lastname, B.B. Article Title. *Journal Name* **Year**, *Volume Number*, Page Range.

ISBN 978-3-7258-1027-7 (Hbk)
ISBN 978-3-7258-1028-4 (PDF)
doi.org/10.3390/books978-3-7258-1028-4

Contents

About the Editor

Qi Zhu

Qi Zhu received his Doctor's Engineering degree in Materials Science from Northeastern University, China, in 2012. He is now a Professor of Materials Science and Engineering at Northeastern University, China. He was a guest researcher at the National Institute for Materials Science (NIMS, Japan) in 2009–2011, and worked as a visiting researcher at NIMS in 2018–2019. His research interests include the design, syntheses, and application of functional inorganic materials and ceramic coatings. To date, he has published over 150 scientific papers on functional inorganic materials and ceramic coatings.

coatings

MDPI

Editorial

Ceramic Films and Coatings: Properties and Applications

Qi Zhu

Key Laboratory for Anisotropy and Texture of Materials (Ministry of Education), School of Materials Science and Engineering, Northeastern University, Shenyang 110819, China; zhuq@smm.neu.edu.cn

Ceramic films and coatings play an important role in the field of materials science. As such, various relevant technologies have been developing. The preparation of ceramic films is not a complicated process compared to bulk ceramics. In addition, ceramic films can be manufactured in a variety of shapes to meet both industrial and civil needs. They have recently become a research hotspot, with the aim to develop functional ceramic films and coatings for illumination, anticounterfeiting, anticorrosion, and wear resistance. Nevertheless, high-performance films and coatings are still a challenge to develop due to the fact that the preparation method, ingredients, microstructure, and densification have a significant influence on their properties and applications.

This Special Issue comprises 25 papers, mainly introducing surface coatings, ceramics, luminescence, anti-corrosion, and abrasion resistance. Among them, five papers are on protective coatings, exploring the effects of deposition behavior, additives, and other factors on the corrosion prevention of coatings. A new technique for the high-temperature deposition of low-permeability gas-tight silicon carbide protection coatings is proposed. This coating is effective in preventing the oxidation of SiC-C-Si and SiC-C-$MoSi_2$ ceramics, carbon–carbon composites, structural graphite, refractory metals, and alloys. The test results indicate that the coating has a relatively high thermal oxidation and shock stability, and good adhesion to the substrate [1]. Pyroxene glass–ceramic enamels prepared from blast furnace slag and additives were studied. The batch composition and process regimes of the enamels were elaborated for the production of high-temperature protective coatings for carbon steel. The prepared coatings can be used in corrosive environments and abrasive particles up to 1100 °C [2]. In order to obtain high-performance epoxy coatings for magnesium alloys, polyaniline (PANI) and graphene oxide (GO) composite powders with corrosion inhibition and barrier properties were chosen. In contrast to direct blending, the polymerized powder of polyaniline and graphene oxide can better exert the anti-corrosion and shielding effects of graphene oxide and polyaniline, and provide better protection for magnesium alloys [3]. Si_3N_4/TaC composite MAO coatings were prepared on Ti-6Al-4V (TC4) alloys via microarc oxidation (MAO). The effects of the number of Si_3N_4/TaC particles on the structure, composition, tribological behavior, and corrosion performance of the MAO coatings were studied. The findings show that Si_3N_4/TaC particles can be successfully doped into compound coatings, and the incorporation of Si_3N_4/TaC particles significantly decreases the pores of coatings, which improves the tribological and corrosion performance of complex MAO coatings [4]. WC-Co ceramic materials are widely used as protective coatings in various fields. The deposition behavior of single WC-17Co particles and the microstructure, hardness, toughness, and friction properties of WC-17Co coatings resulting from different spraying methods were studied. The findings indicate that the deposition behavior of single WC-17Co particles on Q235 steel substrate after deposition using varied spraying methods is distinctive [5].

In this Special Issue, five papers explore the impact of coating thickness, additives, and other factors on the wear resistance of coatings. A Si-doped CrN coating was prepared on the surface of W18Cr4V high-speed steel consisting of Si_3N_4 amorphous and CrN nanocrystals. The optimum wear resistance can be achieved by regulating the thickness

Citation: Zhu, Q. Ceramic Films and Coatings: Properties and Applications. *Coatings* **2024**, *14*, 483. https://doi.org/10.3390/coatings14040483

Received: 8 March 2024
Accepted: 10 April 2024
Published: 14 April 2024

of the coatings. In addition, the influence of toughness on abrasion resistance and the abrasion mechanism was studied [6]. An industrial-scale hot vapor deposition system was used to deposit TiN/Ti(C,N)/Al_2O_3 multilayer coatings. Two Al_2O_3 polycrystalline states were obtained by depositing specific bonding layers at the Al_2O_3/Ti(C,N) interface. The κ- Al_2O_3 multilayer-coated tools had the longest life that was twice as long as that of the CVD Al_2O_3 multilayer-coated ones. These findings can help increase tool properties for the machining of 24CrMoV5-1 steels by expanding the database of existing predictive models for tool wear and machined surface quality [7]. Three composite coatings, Inconel 718 nickel-based high-temperature alloy (IN718), IN718-50 wt.% WC prepared by adding WC particles, and IN718-50 wt.% WC prepared with the assistance of ultrasonic vibration, were prepared via laser cladding. The incorporation of WC increased the hardness and enhanced the tribological properties. Ultrasonic vibration significantly improved the solidification organization and reduced the aggregation of reinforcing particles [8]. TiN coatings were deposited on the surface of AISI 304 stainless steel via DC magnetron sputtering at four various nitrogen flux ratios to modify the structural features of the coatings. Furthermore, the structural characteristics of TiN coatings on AISI 304 stainless steel were modulated to improve mechanical and tribological performance [9]. Solid lubricated composite TiN coatings containing Pb additives were prepared on steel and titanium substrates using a split cathode-reactive magnetron sputtering process. The nanocomposite coatings have a high Pb content, good microhardness, low grain size, and excellent tribological properties [10].

This Special Issue includes two papers on phosphor particles, discussing the effects of the reaction conditions, dopant concentration, and other factors on the optical properties of phosphors. The $ZnGa_{2-x}(Mg/Si)_xO_4:Cr^{3+}$ nanoparticles were synthesized employing the sol-gel method. The sample emitted near-infrared radiation at 694 nm in the dominant band, which lasted more than 48 h after UV irradiation cessation [11]. The $RE_4O(OH)_9NO_3$ (RE = Y, Eu) crystalline microcrystals were successfully obtained using the hydrothermal method, and the surface modification of the microcrystalline surface was carried out via a reaction with vanadate ions. The red emission intensity of the microcrystals at 617 nm significantly improved due to the energy transfer of $VO^{3-} \rightarrow Eu^{3+}$ and the light harvesting ability of VO^{3-} [12]. In addition, three papers on luminescent films and coatings are included in this Special Issue. The YVO_4 thin films were hydrothermally prepared in 1 h at ~8 pH using layered yttrium hydroxide ($Y_2(OH)_5NO_3 \cdot nH_2O$) films as sacrificial precursors. The Eu^{3+}- and Dy^{3+}-doped YVO_4 films showed red and green emission, respectively [13]. The $GdAlO_3:Eu^{3+}$ transparent ceramic films were prepared by a two-dimensional interfacial reaction using rare-earth-derived layered gadolinium hydroxide exfoliated nanosheets. They have a high transmittance of more than 90% in the visible range and exhibit strong red emission under the UV excitation of 254 nm [14]. Moreover, a long-persistent luminescent coating using $SrAl_2O_4:Eu^{2+},Dy^{3+}$ phosphor was developed for luminescent road markings, offering safety and energy saving benefits. The addition of SiO_2 and $CaCO_3$ improved the dispersion and densification of the luminescent coating. The afterglow of the luminescent coating can be more than 5 hours after sunlight excitation [15].

Three papers in this Special Issue are concerned with transparent ceramics. The Yb:YAG transparent ceramics were prepared using the solid-state method and vacuum sintering technique. After a series of characterization and analysis, it was concluded that the properties of Yb:YAG ceramics were not related to the content of Yb [16]. A simple method for the preparation of ZrO_2-coated Y_2O_3 nano-powder from zirconium nitrate and industrial Y_2O_3 solutions is presented. The transformation process of the ZrO_2-coated layer during calcination was investigated, and the sample obtained showed a transmittance of 81.4% at 1100 nm [17]. Improving the phase domain uniformity and reducing the phase domain size are effective ways to increase the transmittance and mechanical hardness of nanocomposites. The Gd_2O_3-MgO nano-powders produced via the urea precipitation method have good transmittance and high Vickers hardness in the mid-infrared band of 3–6 μm, mainly attributed to the uniform distribution of phase

domains [18]. Moreover, the Special Issue includes two papers discussing microwave absorbing materials. $CoFe_2O_4$/SWCNTs composites with a necklace-like structure were produced using a simple solvent–thermal method, which is conducive to good impedance matching and results in excellent electromagnetic loss performance [19]. MnO-Co@C nanorods with a core shell structure were produced via in situ polymerization and high-temperature carbonization processes. The special composite structure formed resulted in better impedance matching and improved microwave absorption ability [20].

This Special Issue also includes three papers exploring the mechanical properties of materials by manipulating the content of additives. By controlling the addition quantity of $TiC_{0.7}N_{0.3}$ and hot-pressing sintering temperature, the influence on the microstructure, mechanical properties, particle size distribution, and relative density of Si_3N_4 ceramic cutting tools was explored, and finally the micro-nano Si_3N_4-based ceramic cutting tool materials with excellent toughness were successfully obtained [21]. WC-13Co composites with added Fe were produced via the pressureless sintering method, and the effects of Fe and C addition on the structural and mechanical performance in the W-Co-Fe-C system were investigated. With the addition of appropriate Fe and C, the hardness of the samples was improved, with an increase in fracture toughness [22]. WC-13Co cemented carbide was produced using the pressureless sintering method; the effects of the Mo and C content on its structure and properties were investigated, and the evolution mechanism of the eta phase during the sintering process was introduced in detail [23]. Finally, there two papers outline anti-corrosion coatings, including conductive and corrosion-resistant phosphate conversion coatings on an AZ91D magnesium alloy [24], and a self-healing microcapsule coating based on epoxy resin [25].

This Special Issue highlights the outstanding achievements in this field, which will help promote the future development of ceramic film and coating technology.

Funding: Fundamental Research Funds for the Central Universities (Grant N2302004) and National Natural Science Foundation of China (Grant 52371057).

Conflicts of Interest: The authors declare that they have no known competing financial interests or personal relationships that could have appeared to influence the work reported in this paper.

References

1. Shikunov, S.; Kaledin, A.; Shikunova, I.; Straumal, B.; Kurlov, V. Novel Method for Deposition of Gas-Tight SiC Coatings. *Coatings* **2023**, *13*, 354. [CrossRef]
2. Gorokhovsky, A.V.; Yurkov, G.Y.; Burmistrov, I.N.; Villalpando-Reyna, A.F.; Kuznetsov, D.V.; Gusev, A.A.; Khaidarov, B.B.; Konyukhov, Y.V.; Zakharova, O.V.; Kiselev, N.V. Glass-Ceramic Protective Coatings Based on Metallurgical Slag. *Coatings* **2023**, *13*, 269. [CrossRef]
3. Zhang, Y.; Xiao, S.; Wen, J.; Liu, X.; Dou, B.; Yang, L. Effect of Polyaniline and Graphene Oxide Composite Powders on the Protective Performance of Epoxy Coatings on Magnesium Alloy Surfaces. *Coatings* **2022**, *12*, 1849. [CrossRef]
4. Gao, W.; Wang, L.; Jin, Y.; Yao, Y.; Ding, Z.; Yang, W.; Liu, J. Effect of Si_3N_4/TaC Particles on the Structure and Properties of Microarc Oxidation Coatings on TC4 Alloy. *Coatings* **2022**, *12*, 1247. [CrossRef]
5. Chen, X.; Li, C.; Gao, Q.; Duan, X.; Liu, H. Comparison of Microstructure, Microhardness, Fracture Toughness, and Abrasive Wear of WC-17Co Coatings Formed in Various Spraying Ways. *Coatings* **2022**, *12*, 814. [CrossRef]
6. Cui, C.; Yang, C. Mechanical Properties and Wear Resistance of CrSiN Coating Fabricated by Magnetron Sputtering on W18Cr4V Steel. *Coatings* **2023**, *13*, 889. [CrossRef]
7. Zhu, M.; Achache, S.; Motta, M.P.; Delblouwe, A.; Pelaingre, C.; García-Wong, A.C.; Pierson, J.-F.; Sanchette, F. Characteristics and Cutting Performance of CVD Al_2O_3 Multilayer Coatings Deposited on Tungsten Carbide Cutting Inserts in Turning of 24CrMoV5-1 Steel. *Coatings* **2023**, *13*, 883. [CrossRef]
8. Wang, J.; Zhou, J.; Zhang, T.; Meng, X.; Li, P.; Huang, S.; Zhu, H. Ultrasonic-Induced Grain Refinement in Laser Cladding Nickel-Based Superalloy Reinforced by WC Particles. *Coatings* **2023**, *13*, 151. [CrossRef]
9. Fu, X.; Guo, S.; Wan, Y.; Li, Q.; Liu, B.; Zheng, H. Influence of the Nitrogen Flux Ratio on the Structural, Morphological and Tribological Properties of TiN Coatings. *Coatings* **2023**, *13*, 78. [CrossRef]
10. Lozovan, A.; Savushkina, S.; Lyakhovetsky, M.; Nikolaev, I.; Betsofen, S.; Kubatina, E. Investigation of Structural and Tribological Characteristics of TiN Composite Ceramic Coatings with Pb Additives. *Coatings* **2023**, *13*, 1463. [CrossRef]
11. Zhang, S.; Xiahou, J.; Sun, X.; Zhu, Q. Incorporation of Mg^{2+}/Si^{4+} in $ZnGa_2O_4$:Cr^{3+} to Generate Remarkably Improved Near-Infrared Persistent Luminescence. *Coatings* **2022**, *12*, 1239. [CrossRef]

12. Qu, J.; Liu, J.; Zhu, Q. Eroding the Surface of Rare Earth Microcrystals through Vanadate Ions for Considerable Improvement of Luminescence. *Coatings* **2022**, *12*, 230. [CrossRef]
13. Chen, T.; Zhang, H.; Luo, Z.; Liang, J.; Wu, X. Facile Preparation of YVO_4: RE Films and the Investigation of Photoluminescence. *Coatings* **2022**, *12*, 461. [CrossRef]
14. Zhang, T.; Chen, L.; Yao, J.; Zhu, Q. A Two-Dimensional Guidance Strategy to Fabricate Perovskite Gadolinium Aluminate Ceramic Film. *Coatings* **2022**, *12*, 1927. [CrossRef]
15. Zheng, M.; Li, X.; Bai, Y.; Tang, S.; Li, P.; Zhu, Q. Sunlight-Activated Long Persistent Luminescent Coating for Smart Highways. *Coatings* **2023**, *13*, 1050. [CrossRef]
16. Li, J.; Liu, X.; Wu, L.; Ji, H.; Dong, L.; Sun, X.; Qi, X. Fabrication of Yb:YAG Transparent Ceramic by Vacuum Sintering Using Monodispersed Spherical Y_2O_3 and Al_2O_3 Powders. *Coatings* **2022**, *12*, 1155. [CrossRef]
17. Fu, Z.; Wu, N.; Long, H.; Wang, J.; Zhang, J.; Hou, Z.; Li, X.; Sun, X. Fabrication of Highly Transparent Y_2O_3 Ceramics via Colloidal Processing Using ZrO_2-Coated Y_2O_3 Nanoparticles. *Coatings* **2022**, *12*, 1077. [CrossRef]
18. Wu, N.; Fu, Z.; Long, H.; Wang, J.; Zhang, J.; Hou, Z.; Li, X.; Sun, X. Synthesis of MgO Coating Gd_2O_3 Nanopowders for Consolidating Gd_2O_3-MgO Nanocomposite with Homogenous Phase Domain Distribution and High Mid-Infrared Transparency. *Coatings* **2022**, *12*, 1435. [CrossRef]
19. Hou, Z.; Liu, C.; Gong, J.; Wu, J.; Sun, S.; Zhang, M.; Sun, X. Micro-Structural Design of $CoFe_2O_4$/SWCNTs Composites for Enhanced Electromagnetic Properties. *Coatings* **2022**, *12*, 1532. [CrossRef]
20. Xin, Z.; Wu, J.; Sun, S.; Zhang, M.; Sun, X. Rational Design of Yolk Core-Shell Structure MnO-Co@C Nanospheres for High-Performance Microwave Absorption. *Coatings* **2022**, *12*, 1405. [CrossRef]
21. Guo, S.; Zhu, F.; Xiu, Z.; Zhang, M.; Sun, X. Enhanced Performance in Si_3N_4 Ceramics Cutting Tool Materials by Tailoring of Phase Composition and Hot-Pressing Temperature. *Coatings* **2023**, *13*, 475. [CrossRef]
22. Li, X.; Zhang, J.; Zhang, Q.; Zhang, X.; Ji, V.; Liu, J. Microstructure Evolution and Hardness Improvement of WC-Co Composites Sintered with Fe Substituting Part of Co Binder. *Coatings* **2023**, *13*, 116. [CrossRef]
23. Li, X.; Zhang, X.; Zhang, J.; Zhang, Q.; Ji, V.; Liu, J. Effect of Mo and C Additions on Eta Phase Evolution of WC-13Co Cemented Carbides. *Coatings* **2022**, *12*, 1993. [CrossRef]
24. Zhang, S.; Xu, Y.; Liu, L.; Lei, Q.; Dong, J.; Zhang, T. Preparation of Conductive and Corrosion Resistant Phosphate Conversion Coating on AZ91D Magnesium Alloy. *Coatings* **2023**, *13*, 1706. [CrossRef]
25. Zhang, S.; Liu, L.; Xu, Y.; Lei, Q.; Bing, J.; Zhang, T. Research on the corrosion resistance of an epoxy resin-based self-healing propylene glycol-loaded ethyl cellulose microcapsule coating. *Coatings* **2023**, *13*, 1514. [CrossRef]

coatings

MDPI

Article

Eroding the Surface of Rare Earth Microcrystals through Vanadate Ions for Considerable Improvement of Luminescence

Jiao Qu [1], Juanjuan Liu [2] and Qi Zhu [2,*]

[1] School of Mechanical Engineering and Automation, Shenyang Institute of Technology, Fushun 113122, China; qujiao0611@163.com

[2] Key Laboratory for Anisotropy and Texture of Materials (Ministry of Education), School of Materials Science and Engineering, Northeastern University, Shenyang 110819, China; ljjuan5409953@163.com

* Correspondence: zhuq@smm.neu.edu.cn; Tel.: +86-24-8369-1570

Abstract: Developing an efficient approach to improve the luminescence of the phosphors without heating processing is a challenge, but attracts much attention. In the present paper, prismatic microcrystals of $RE_4O(OH)_9NO_3$ (RE = Y, Eu) were synthesized by a hydrothermal reaction at 180 °C for 24 h. The reaction with VO_3^- did not change the crystal structure of the microcrystals and VO_3^- substituting for NO_3^- anions did not take place. However, it contributed to the formation of amorphous particles containing VO_3^- on the surface of a prism, which is similar to the surface corrosion of a metal, called "surface eroding". Therefore, surface modification was successfully achieved by eroding the surface of the microcrystals through the reaction with vanadate ions. As a result of $VO_3^- \rightarrow Eu^{3+}$ energy transfer and the light-harvesting ability of VO_3^-, the red emission intensity at 617 nm of the modified microcrystals greatly increased. Eroding the surface of rare earth microcrystals recommends a new paradigm for luminescence improvement of rare earth compounds.

Keywords: $Y_4O(OH)_9NO_3$; Eu^{3+}; eroding; rare earth compounds; microcrystals

Citation: Qu, J.; Liu, J.; Zhu, Q. Eroding the Surface of Rare Earth Microcrystals through Vanadate Ions for Considerable Improvement of Luminescence. *Coatings* **2022**, *12*, 230. https://doi.org/10.3390/coatings12020230

Academic Editor: Alina Pruna

Received: 29 December 2021
Accepted: 8 February 2022
Published: 10 February 2022

1. Introduction

Directly exciting RE^{3+} ions upon irradiation for luminescence is not an efficient method, because the f–f electronic transitions of the rare earth ions (RE^{3+}) are usually forbidden by the spin selection rules [1]. Therefore, doping RE^{3+} ions with a low concentration into an appropriate host lattice is widely used to produce solid-solution phosphor and obtain desirable luminescence [2]. In recent years, much attention has been paid to RE^{3+}-doped inorganic materials with a uniform size and specific morphology, because they allow for the attainment of functionalities, not only from the constituent substance but also from the special structure [3–6]. For rare earth oxide phosphors, calcining the precursors is widely used to obtain the phosphors with a variety of novel structures, since the precursors and their calcined products tend to exhibit generic relationships [3,7–11]. $RE_2(OH)_5NO_3 \cdot nH_2O$ layered rare earth hydroxide (LRH), $RE_4O(OH)_9NO_3$ oxy-hydroxyl nitrate, $RE(OH)_{2.94}(NO_3)_{0.06} \cdot nH_2O$ hydroxyl nitrate, and $RE(OH)_3$ hydroxide are the reported products synthesized from the hydrothermal reaction system [7–10], and their morphology and size could be easily regulated by varying the synthesis conditions, including the pH value, reaction temperature, and reaction time. Therefore, they are the desirable precursors for rare earth oxide phosphors. Therefore, there are a lot of investigations on these precursors. However, abundant water molecules or hydroxyls directly coordinate to the rare earth ions, which result in a serious luminescence quenching [8,9]. Thus, there is the question of how to enhance the emission intensity of the rare earth phosphors. Of course, the thermal decomposition of the precursors is an efficient method to synthesize rare earth oxides, and it could remove the water molecules/dehydroxyl and thus enhance the luminescence intensity [3]. However, morphological damage and crystal-structure collapse would take place during the annealing process, which may significantly affect

the final performance [12]. Therefore, developing an efficient approach to improve the luminescence of the phosphors without heating processing is a challenge, but attracts much attention.

Recently, it has been reported that an antenna effect could give rise to an enhanced photoluminescence upon light irradiation, because an effective intramolecular energy transfer from coordinated ligands to the activated RE^{3+} ions can enhance the absorption of the optical excitation. This antenna effect effectively promotes the energy transfer from coordinated ligands to the activated RE^{3+} ions, and thus enhances the emission intensity [13]. This light-harvesting ability was successfully applied onto the layered rare earth hydroxide nanosheets [14,15], hydroxyl nitrate square nanoplates [16], and rare earth nanoparticles [17,18], through the grafting of organic ligands, including picolinic acid and a rare earth complex, on the surface of the nanocrystals. Indeed, a considerable improvement of luminescence was observed for these rare earth crystals. However, the organic ligands were indirectly linked to the surface of the nanocrystals by hydrogen bonding, indicating that the hybrid phosphors grafted organic ligands were unstable. In addition, the hydrogen bonding connection made the energy transfer from the ligands to the activated RE^{3+} ions difficult [7,15], so it is not the most effective way for energy transfer, compared to the directly connecting coordination.

In the present work, prismatic microcrystals of $RE_4O(OH)_9NO_3$ (RE = Y, Eu) were synthesized by the hydrothermal reaction. The surface modification of the microcrystals was successfully achieved by eroding the surface of the microcrystals through vanadate ions. The main means of sample characterization are X-ray diffraction (XRD), transmission electron microscopy (TEM), selected area electron diffraction (SAED), scanning transmission electron microscopy (STEM), photoluminescence (PL)/photoluminescence excitation (PLE) spectroscopy, and fluorescence decay curve analysis. The reaction with VO_3^- contributed to the formation of amorphous particles containing VO_3^- on the surface of the prism, which lead to a great enhancement of luminescence. The usage of the energy transfer to the activated RE^{3+} ions through surface eroding processing, paves a new paradigm for luminescence improvement of the rare earth compounds.

2. Experimental Section

2.1. Synthesis

Preparation of oxy-hydroxyl nitrate microcrystals. The starting rare earth sources are rare earth oxides, which are Y_2O_3 and Eu_2O_3, all 99.99% pure products from Huizhou Ruier Rare-Chem, Hi-Tech, Co., Ltd. (Huizhou, China). Dissolving the rare earth oxide in hot nitric acid yielded a rare earth nitrate solution, which was then treated by evaporation at 90 °C to remove the excess acid. The synthesis of Y/Eu binary microcrystals (Y:Eu molar ratio of 0.95:0.05) was conducted via a hydrothermal reaction at 180 °C for 24 h with a pH value of 10–11, which was described in our previous work [3].

Erosion of the microcrystal surface. In typical processing, 2 mmol of $RE_4O(OH)_9NO_3$ microcrystals was dispersed in 60 mL of water containing a proper amount of NH_4VO_3 and NH_4OH with the pH value of 10–11. After being stirred for 30 min, the resultant suspension was transferred into a Teflon-lined stainless-steel autoclave of 100 mL capacity. The autoclave was tightly sealed and was put in an electric oven preheated to 200 °C. After a 12 h reaction, the autoclave was left to cool naturally to room temperature, and then the product was collected via centrifugation. The wet precipitate was washed with distilled water 3 times, rinsed with absolute ethanol, and was finally dried in air at 60 °C for a day. The oxy-hydroxyl nitrate microcrystals and the microcrystals eroded by VO_3^- are denoted as MC and MC-*R*V hereafter, with the *R*-fold VO_3^- in the reaction system.

2.2. Characterization Techniques

Phase identification was performed by X-ray diffraction (XRD, Model SmartLab, Rigaku, Tokyo, Japan), operating at 40 kV/40 mA using nickel-filtered Cu Kα radiation and a scanning speed of 6.0° 2θ/min. The product morphology was analyzed by field

emission scanning electron microscopy (FE-SEM, Model JSM-7001F, JEOL, Tokyo, Japan) and transmission electron microscopy (TEM, Model JEM-2000FX, JEOL, Tokyo, Japan). Elemental mapping was performed using scanning transmission electron microscopy (STEM, Model JEM-2000FX, JEOL, Tokyo, Japan). Fourier transform infrared spectroscopy experiments (FT-IR, Nicolet iS5, Thermal Fisher Scientific, NY, USA) were under taken using the standard KBr method. Photoluminescence (PL), photoluminescence excitation (PLE), and fluorescence decay were analyzed at room temperature using an FP-8600 fluorospectrophotometer (JASCO, Tokyo, Japan) equipped with a Φ60 mm integrating sphere and a 150-W Xe-lamp. The slit widths were 5 nm for both the excitation and emission sides. The spectral responses were corrected in the range 220–850 nm with a Rhodamine-B solution (5.5 g/L in ethylene glycol, for 220–600 nm range) and with a standard light source unit (ECS-333, JASCO, for 350–850 nm) as references. The external quantum efficiency (ε_{ex}, the total number of emitted photons divided by the total number of excitation photons) and the internal quantum efficiency (ε_{in}, the total number of emitted photons divided by the number of photons absorbed by the sample) of the phosphors are derived from the following equations [19], using the built-in analysis software:

$$\varepsilon_{ex} = \frac{\int \lambda P(\lambda) d\lambda}{\int \lambda E(\lambda) d\lambda} \quad (1)$$

$$\varepsilon_{in} = \frac{\int \lambda P(\lambda) d\lambda}{\int \lambda [E(\lambda) - R(\lambda)] d\lambda} \quad (2)$$

where $E(\lambda)/hv$, $R(\lambda)/hv$, and $P(\lambda)/hv$ are the number of photons in the excitation, reflectance, and emission spectra of the samples, respectively. The reflection spectrum of the spectral on diffusive white standards was used for calibration.

3. Results and Discussion

In the present study, the $RE_4O(OH)_9NO_3$ (RE = Y, Eu) microcrystals (termed as MC) was chosen as an example for surface modification. As reported in the literature [3], $Y_4O(OH)_9NO_3$ is a monoclinic crystal structure, which is a three-dimensional framework with one-dimensional channels containing NO_3^-. The NO_3^- is indirectly linked to Y^{3+} rather than forming a direct connection. There are 4 trivalent yttrium ions in the asymmetric unit, with 3 in a 7-coordinated environment with a capped trigonal prismatic geometry and 1 in a 9-coordinated environment with a tricapped trigonal prismatic geometry. The trivalent yttrium ions are linked through hydroxide anions forming the framework around the channels. In the channel, the nitrate ion is indirectly linked to Y^{3+} through the hydrogen bonding. As a result of the one-dimensional channels, $Y_4O(OH)_9NO_3$ always crystallizes into prismatic and wire-like crystallites [3]. Here, the incorporation of Eu^{3+} in $Y_4O(OH)_9NO_3$ does not significantly affect its crystal structure, because the diffractions of MC are indexed to the monoclinic $Y_4O(OH)_9NO_3$ (JCPDS File no. 79-1352), except for slight spectral shifts to the lower angle side (Figure 1c). The replacement of Y^{3+} with larger Eu^{3+} ions (for 8-fold coordination, $r_{Y^{3+}}$ = 0.1019 nm, $r_{Eu^{3+}}$ = 0.1066 nm) contributed to the lattice expansion, thus resulting in the diffraction shifts [20]. Figure 1d shows the FE-SEM image of MC, and pure hexagonal prisms with a diameter of ~0.3–0.5 μm and a length of ~1.5–2.5 μm are found in the observation.

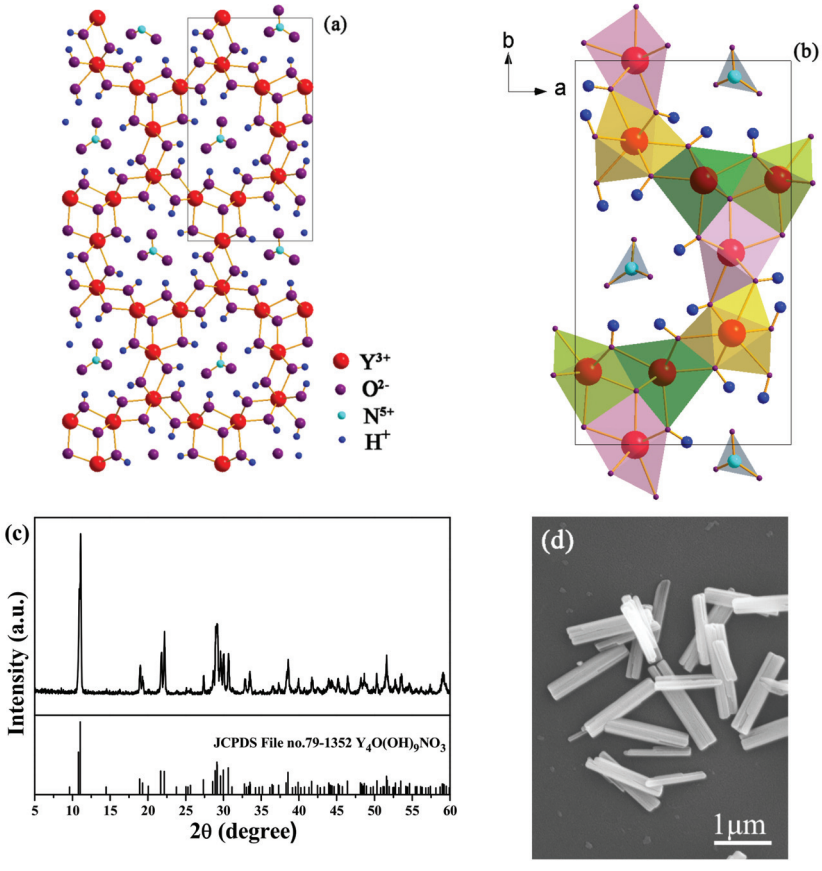

Figure 1. (**a**,**b**) Crystal structure of $Y_4O(OH)_9NO_3$, (**c**) XRD patterns, and (**d**) FE-SEM image of MC.

Figure 2 shows the XRD patterns of MC after the reaction with VO_3^-. Evidently, the reaction products are the same as MC, because all the diffractions are indexed to the monoclinic $Y_4O(OH)_9NO_3$ (JCPDS File no. 79-1352), indicating that the reaction with VO_3^- did not result in a phase transformation. Increasing the *R* value from 0 to 1.5 (*R*, the molar ratio of VO_3^- to MC) induced a small shift of the diffraction positions. Since VO_3^- is smaller than NO_3^- [21], VO_3^- substituting for NO_3^- anions may induce the diffraction shift to the higher angle side arising from the lattice contraction. Indeed, NO_3^- is indirectly coordinated in $Y_4O(OH)_9NO_3$ rather than the free anion, so it cannot be easily replaced by other anions through ion exchange. After the reaction with VO_3^-, the products mainly remain in the original morphology of MC (Figure 3). However, the surface of MC-*R*V (microcrystals reacted with VO_3^-, with *R*-fold VO_3^- in the reaction system) is not smooth, with nano-sized crystals on the prism surface. Increasing the *R* value from 0.25 to 1.5 contributed to a rougher particle surface for MC-*R*V. Since the above phenomenon is similar to that for the surface corrosion of metal, in the present paper, it is called "surface eroding" for the reaction with VO_3^-. However, there are not any other impurity phases in the XRD patterns, indicating that the nano-sized crystals are amorphous.

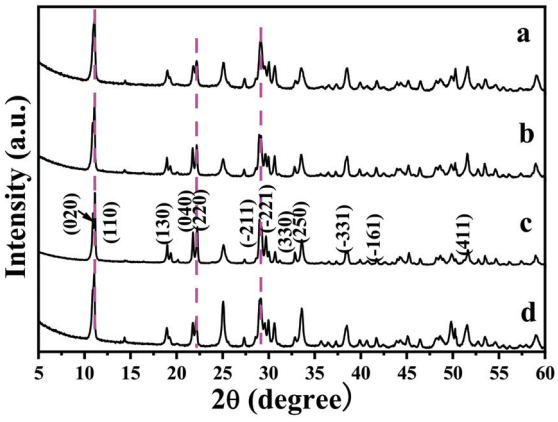

Figure 2. XRD patterns of MC-*RM*, with (**a**) *R* = 0.25, (**b**) *R* = 0.5, (**c**) *R* = 1.0, and (**d**) *R* =1.5.

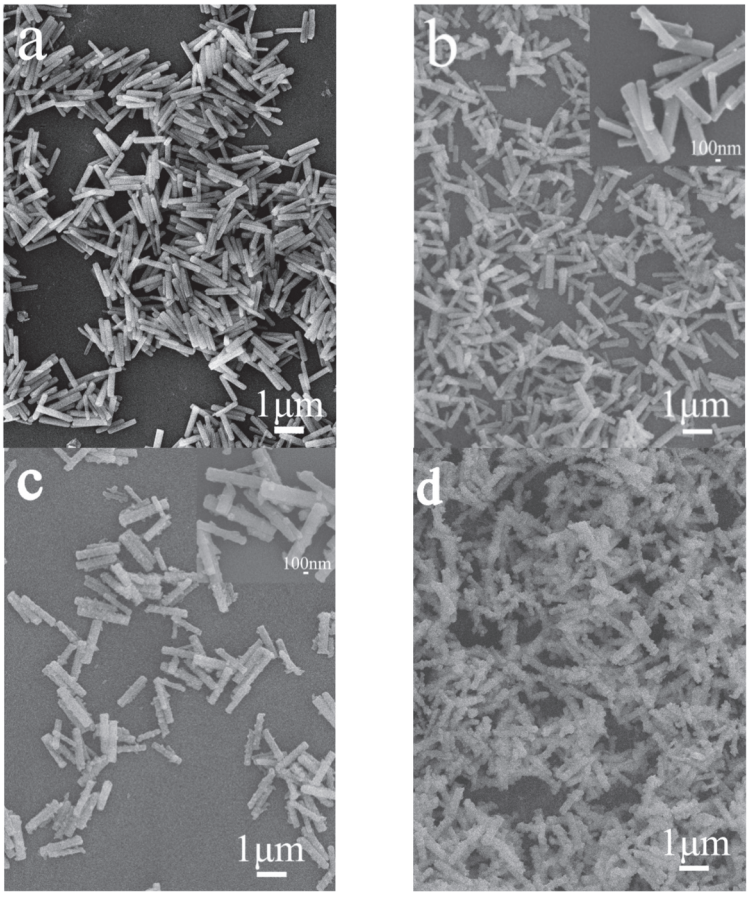

Figure 3. FE-SEM micrographs of MC (**a**) and MC-*RM* (**b**–**d**), with (**b**) *R* = 0.25, (**c**) *R* = 1.0, and (**d**) *R* =1.5.

Figure 4 shows the FT-IR spectra for the samples after the reaction with different VO_3^- contents. The MC exhibits splitting absorption peaks in the range of 3350–3750 cm^{-1},

with intense absorptions at 3401, 3487, and 3615 cm^{-1}, which arise from hydroxyl (OH^-) groups [22,23]. This is in compliance with the derived chemical formula of $RE_4O(OH)_9NO_3$. The absorption peaks around 1364 and 1407 cm^{-1} are assignable to the v_3 vibration mode of NO_3^- and the v_4 asymmetric stretch of O-NO_2, respectively [22,23]. It is clearly seen that the absorptions of NO_3^- in MC are different from those of the interlaye- free NO_3^- in layered rare earth hydroxide. After the reaction with VO_3^-, NO_3^- still exists in the FT-IR spectra and is not significantly affected by the reaction. However, the absorption for VO_3^- at 792 cm^{-1} appeared after the reaction with VO_3^- [22–24], and more intense absorption is found at a higher *R* value.

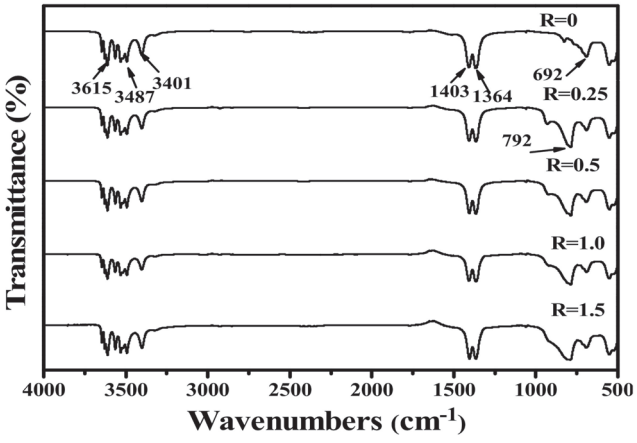

Figure 4. FT-IR spectra for MC (*R* = 0) and MC-*R*M after the reaction with VO_3^-.

Figure 5 shows the elemental mapping distribution of MC, and the results indicate that MC is a homogeneous solid solution, because all the elements of Y, Eu, and N are distributed among the particles. In addition, the close observation of MC through the TEM image found that MC is well crystallized, with sharp edges and corners, and the surface is smooth. Selected area electron diffraction (SAED) found that the MC is a single crystalline. The calculated planar spacings of ~0.352 nm and ~0.268 nm correspond well with the (230) and (-141) planes of $Y_4O(OH)_9NO_3$. After the reaction with VO_3^-, V is distributed among the particles, except for the original component elements of Y, Eu, and N (Figures 6 and 7). The TEM images of MC-*R*V confirmed that there are nano-sized crystals on the surface of the prisms, and they grow up and tend to dendritic growth. Evidently, the materials needed for growth are obtained from the dissolution of the MC surface, similar to the surface corrosion of metal. The diameter of the prisms became slimmer at a higher *R* value, further presenting direct evidence. Selected area electron diffraction (SAED) yields circular patterns, suggesting the MC-*R*V consists of polycrystalline (Figure 6). The calculated planar spacings of ~0.374 nm, ~0.301 nm, ~0.287 nm, and ~0.184 nm correspond well with the (140), (310), (320), and (500) planes of $Y_4O(OH)_9NO_3$, i.e., d(140) = 0.374026 nm, d(310) = 0.301376 nm, d(320) = 0.287141 nm, and d(500) = 0.183968 nm (JCPDS File no. 79-1352). Evidently, amorphous diffraction circular patterns were found in the SAED patterns, confirming the existence of amorphous particles on the surface of the prism. Collectively, the results from these analyses confirmed that the reaction with VO_3^- contributed to the formation of amorphous particles containing VO_3^- on the surface of the prism, which is similar to the surface corrosion of metal, called "surface eroding". Therefore, it can be said that the surface modification of MC was successfully achieved by eroding the surface of MC through vanadate ions.

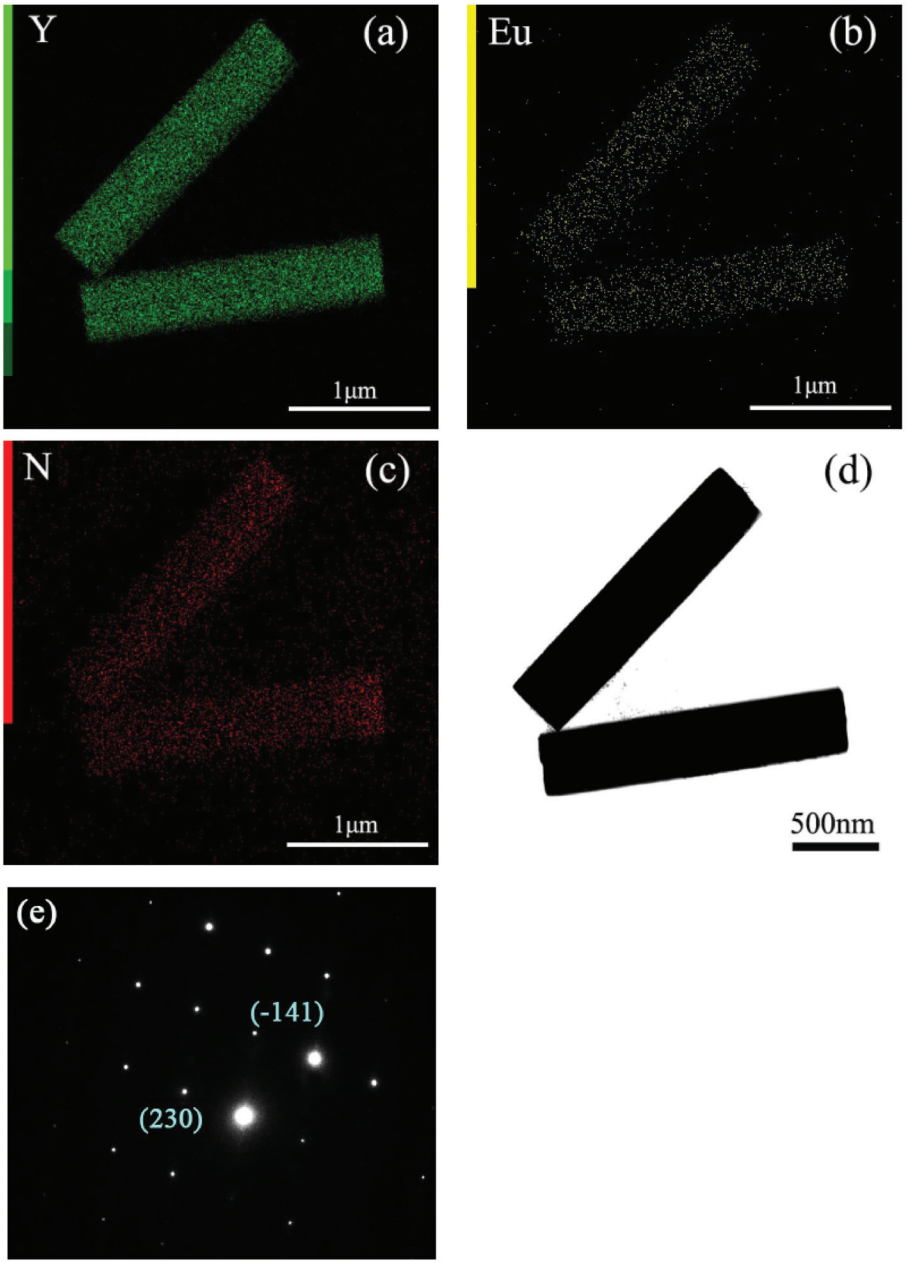

Figure 5. (**a**–**c**) Elemental mapping, (**d**) TEM image, and (**e**) SAED for MC.

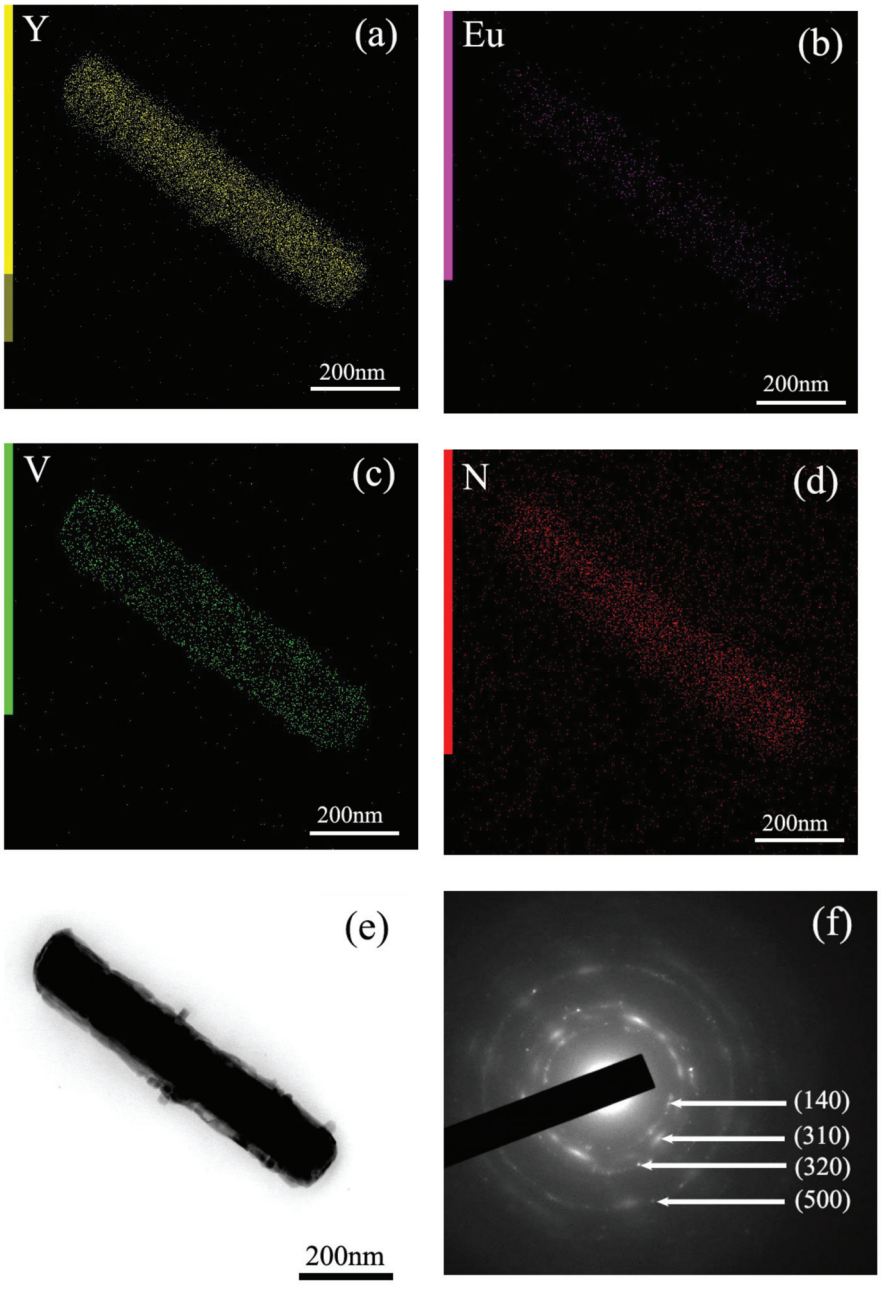

Figure 6. (**a**–**d**) Elemental mapping, (**e**) TEM image, and (**f**) SAED for MC-0.25V.

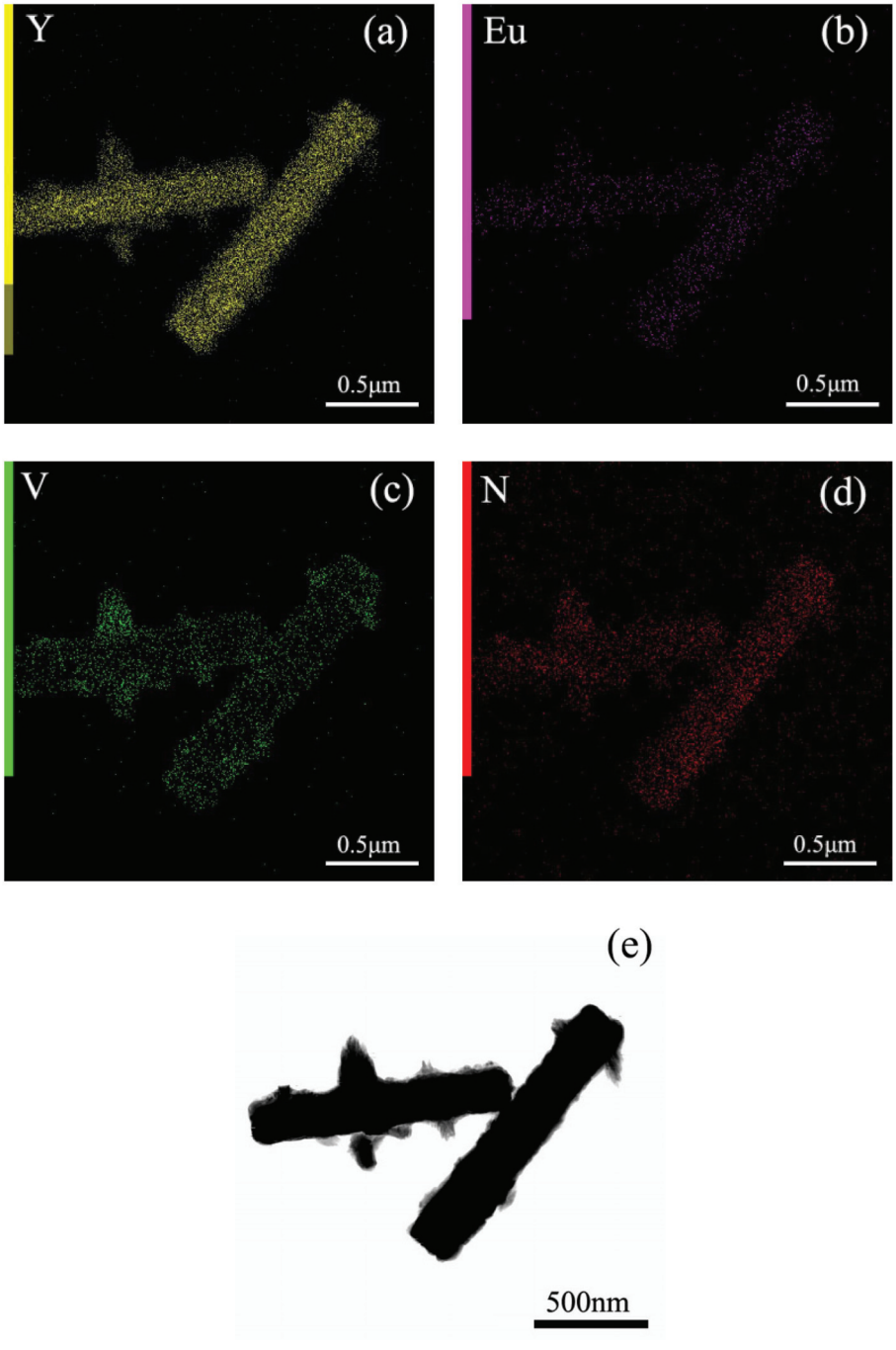

Figure 7. (**a**–**d**) Elemental mapping and (**e**) TEM image for MC-1.5V.

Figure 8 shows the PLE and PL spectra for MC. By monitoring the $^5D_0 \rightarrow {}^7F_2$ emission at 617 nm, a series of sharp lines in the PLE spectrum ranging from 300 nm to 500 nm can be ascribed to the transitions within the Eu^{3+} $4f^6$ electronic configuration. Different

from other rare earth hydroxide precursors, MC exhibited O^{2-}-Eu^{3+} charge transfer (CT) transitions at ~255 nm, as were commonly found for Eu^{3+}-activated Y_2O_3 [7–10]. Upon excitation at 395 nm (intra-$4f^6$ transition of Eu^{3+}), the PL spectrum displayed the typical $^5D_0 \rightarrow {}^7F_J$ (J = 0–4) transitions of Eu^{3+}. The relative intensities of the transitions to different J levels depended on the symmetry of the Eu^{3+} environment and can be described in terms of the Judd–Ofelt theory [7]. The Judd–Ofelt parity law predicts that the magnetic dipole $^5D_0 \rightarrow {}^7F_1$ transition is permitted while the electric dipole $^5D_0 \rightarrow {}^7F_2$ transition is forbidden, and the latter is allowed only on the condition that the Eu^{3+} ions occupy the asymmetric site [7–9]. The MC, having the composition of $(Y_{0.95}Eu_{0.05})_4O(OH)_9NO_3$, has a monoclinic structure and 2 kinds of Eu^{3+} ions, which are 7-coordinated Eu^{3+} ions in C_{2v} non-centrosymmetric sites and 9-coordinated Eu^{3+} ions in D_{3h} centrosymmetric sites [3]. Since the molar ratio of C_{2v} occupancy to that of D_{3h} is 3, most Eu^{3+} ions occupy the asymmetric site, and thus the $^5D_0 \rightarrow {}^7F_2$ transition at 617 nm is stronger than the $^5D_0 \rightarrow {}^7F_1$ transition at 595 nm [3]. However, the MC did not output a strong red light, mainly due to the fact that the hydroxyls directly coordinated to the rare earth ions Eu^{3+}, which resulted in serious luminescence quenching [24].

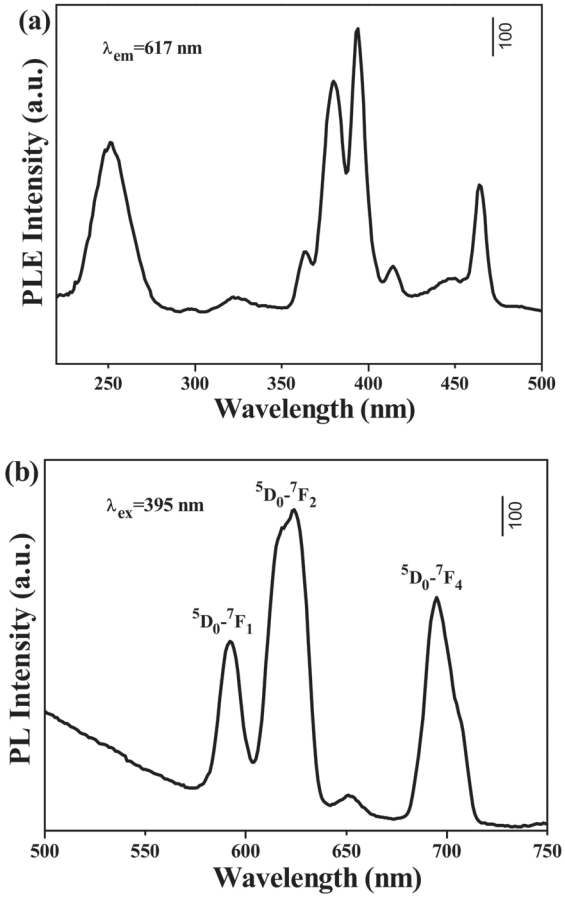

Figure 8. (**a**) PLE and (**b**) PL spectra for MC at room temperature.

Figure 9 shows the PLE and PL spectra for MC-*R*V, which was eroded by vanadate ions. The excitation spectrum consisted of a strong and broad absorption band ranging from 200 to 350 nm, which was assigned to the energy transfer from VO_3^- to Eu^{3+}. The

overlapped excitation was from 2 individual bands located at ~275 nm and ~323 nm, which corresponded to the transitions of $^1A_2(^1T_1)\rightarrow{}^1E\ (^1T_2)$ and $^1A_2(^1T_2)\rightarrow{}^1A_1\ (^1E)$ of V^{5+}, respectively [25,26]. The band at ~255 nm was the contribution of the O^{2-}-Eu^{3+} charge transfer [7–9], while the very weak transitions of $^7F_{0,1}\rightarrow{}^5L_6$ and $^7F_{0,1}\rightarrow{}^5D_2$ at 395 nm and 463 nm for Eu^{3+} were observed in the excitation spectra [7–9]. Since the strongest excitation was located at ~323 nm, the excitation wavelength was chosen as 323 nm ($^1A_2(^1T_2)\rightarrow{}^1A_1\ (^1E)$ transition of V^{5+}). Upon UV excitation at 323 nm, the PL spectra displayed strong emissions at 540 nm, 590 nm, 617 nm, 650 nm, and 702 nm, which were assigned to $^5D_1\rightarrow{}^7F_{0,1}$, $^5D_0\rightarrow{}^7F_1$, $^5D_0\rightarrow{}^7F_2$, $^5D_0\rightarrow{}^7F_3$, and $^5D_0\rightarrow{}^7F_4$ transitions of Eu^{3+}, respectively. The emission at 617 nm attained the dominate role. This further confirmed the existence of $VO_3{}^-\rightarrow Eu^{3+}$ energy transfer. Interestingly, the emission intensity at 617 nm was greatly enhanced by increasing the *R* value from 0 to 0.25, indicating that the $VO_3{}^-\rightarrow Eu^{3+}$ energy transfer contributed to the improved luminescence. The external/internal quantum efficiencies for *R* = 0 were 6 ± 1%/11 ± 1%, and the external/internal quantum efficiencies for *R* = 0.25 were 36 ± 1%/65 ± 1%, directly confirm the great enhancement of luminescence. However, a higher *R* value induced a rougher particle surface, which contributed to the light scattering and quenching of the luminescence. Therefore, increasing the *R* value further resulted in the luminescent decay. The external/internal quantum efficiencies for *R* = 0.5, *R* = 1.0, and *R* = 1.5 were 25 ± 1%/49 ± 2%, 18 ± 2%/43 ± 1%, and 10 ± 1%/37 ± 2%, respectively. However, the emission intensity for MC-*R*V is evidently stronger than that for MC on the whole, indicating that the erosion of the surface of rare earth microcrystals through vanadate ions can contribute to the considerable improvement to luminescence (Figure 10).

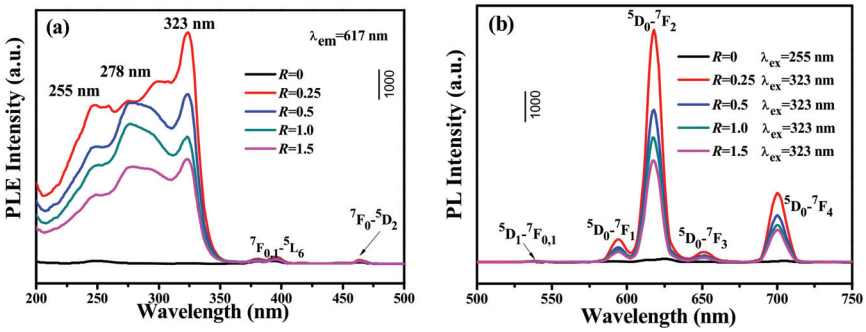

Figure 9. (**a**) PLE and (**b**) PL spectra for MC and MC-*R*V at room temperature.

The decay kinetics of the $^5D_0\rightarrow{}^7F_2$ transition at 617 nm for MC and MC-*R*Vre a investigated in Figure 11. All the fluorescence decay curves can be fitted to single exponentials. The average lifetimes of the MC, MC-0.25V, MC-0.50V, MC-1.0V, and MC-1.5V samples determined in this work are ~0.67 ms, ~1.38 ms, ~1.21 ms, ~1.14 ms, and ~1.12 ms, respectively. Evidently, the lifetime for MC-*R*V is longer than that for MC, since the energy transfer of $VO_3{}^-$ to Eu^{3+} is more time consuming.

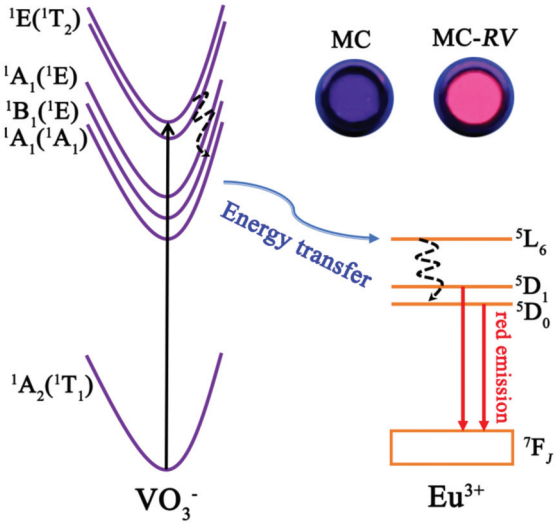

Figure 10. Schematic illustration of $VO_3^- \rightarrow Eu^{3+}$ energy transfer.

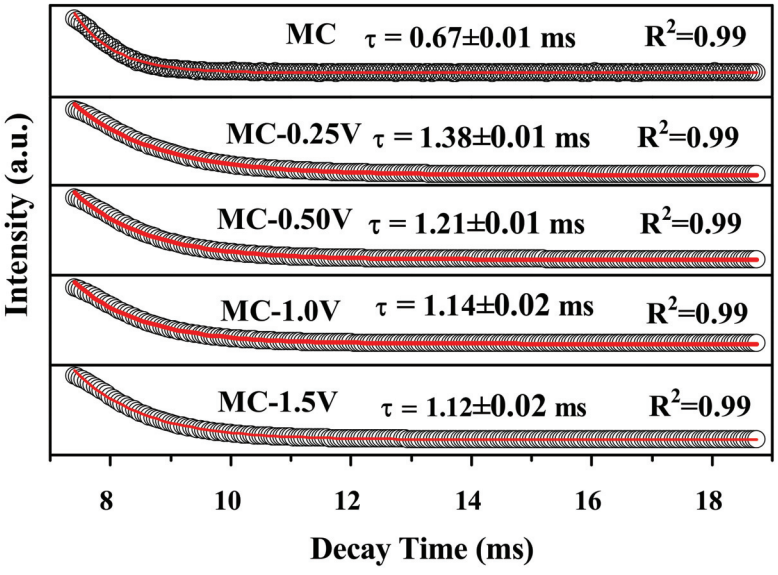

Figure 11. Fluorescence decay curves for the 617 nm emission of MC and MC-*RV*.

4. Conclusions

In the present study, prismatic microcrystals of $RE_4O(OH)_9NO_3$ (RE = Y, Eu) were synthesized by a hydrothermal reaction (180 °C for 24 h, pH = 10–11). The surface modification of the microcrystals was successfully achieved by eroding the surface of the microcrystals through vanadate ions. The main means of sample characterization were XRD, TEM, SAED, STEM, PLE/PL spectroscopy, and fluorescence decay curve analysis. The reaction with VO_3^- contributed to the formation of amorphous particles containing VO_3^- on the surface of the prism, which was similar to the surface corrosion of metal, called "surface eroding". Upon UV excitation at 323 nm ($^1A_2(^1T_2) \rightarrow {}^1A_1$ (^1E) transition of V^{5+}), the modified microcrystals displayed a strong red emission at 617 nm ($^5D_0 \rightarrow {}^7F_2$ transition of Eu^{3+}). As a

result of the $VO_3^- \rightarrow Eu^{3+}$ energy transfer, the emission intensity at 617 nm for the modified microcrystals increased greatly after modification by vanadate ions. Additionally, due to the $VO_3^- \rightarrow Eu^{3+}$ energy transfer, the modified microcrystals exhibited longer lifetimes. The usage of the energy transfer to the activated RE^{3+} ions through surface eroding processing for rare earth compounds recommends a new paradigm for luminescence improvement.

Author Contributions: Writing—original draft preparation, data curation, J.Q.; Formal analysis, investigation, J.L.; Conceptualization, writing—review and editing, visualization, Q.Z. All authors have read and agreed to the published version of the manuscript.

Funding: This research was founded by the Natural Science Foundation of Liaoning Province (Grant 2020-MS-081) and the National Natural Science Foundation of China (Grant 51302032).

Institutional Review Board Statement: Not applicable.

Informed Consent Statement: Not applicable.

Data Availability Statement: Data sharing is not applicable to this article.

Conflicts of Interest: The authors declare that they have no known competing financial interests or personal relationships that could have appeared to influence the work reported in this paper.

References

1. Blasse, G.; Grabmaier, B.C. *Luminescent Materials*; Springer: Berlin/Heidelberg, Germany, 1994.
2. Gai, S.L.; Li, C.X.; Yang, P.P.; Lin, J. Recent progress in rare earth micro/nanocrystals: Soft chemical synthesis, luminescent properties, and biomedical applications. *Chem. Rev.* **2014**, *114*, 2343–2389. [CrossRef] [PubMed]
3. Zhu, Q.; Li, J.-G.; Ma, R.; Sasaki, T.; Yang, X.; Li, X.D.; Sun, X.D.; Sakka, Y. Well-defined crystallites autoclaved from the nitrate/NH_4OH reaction system as the precursor for $(Y,Eu)_2O_3$ red phosphor: Crystallization mechanism, phase and morphology control, and luminescent property. *J. Solid State Chem.* **2012**, *192*, 229–237. [CrossRef]
4. Zhang, F.; Zhao, D.Y. Synthesis of uniform rare earth fluoride ($NaMF_4$) nanotubes by *in situ* ion-exchange from their hydroxide [$M(OH)_3$] parents. *ACS Nano* **2009**, *3*, 159–164. [CrossRef] [PubMed]
5. Xie, J.-H.; Wang, J.; Qiu, G.-H.; Li, X.-B.; Huang, W.-T.; Zhang, R.-R.; Lin, T.; Wang, L.-X.; Zhang, Q.-T. A strategy to achieve efficient green-emission dual-mode luminescence of Yb^{3+}, Er^{3+} doped $NaBiF_4$. *Rare Met.* **2021**, *40*, 2040–2048. [CrossRef]
6. Fu, R.; Hu, Y.-Y.; Qiao, H.-N.; Yang, C.-L.; Yin, H.; Qu, M.-G. Luminescence property and magnetic resonance imaging of Gd_2O_3:Tb^{3+} nanocrystals doped with Zn^{2+}, Li^+. *Rare Met.* **2021**, *40*, 2049–2058. [CrossRef]
7. Geng, F.X.; Ma, R.Z.; Sasaki, T. Anion-exchangeable layered materials based on rare-earth phosphors: Unique combination of rare-earth host and exchangeable anions. *Acc. Chem. Res.* **2010**, *43*, 1177–1185. [CrossRef]
8. Xu, Z.H.; Kang, X.J.; Li, C.X.; Hou, Z.Y.; Zhang, C.M.; Yang, D.M.; Li, G.G.; Lin, J. Ln^{3+} (Ln=Eu, Dy, Sm, and Er) ion-doped YVO_4 nano/microcrystals with multiform morphologies: Hydrothermal synthesis, growing mechanism, and luminescent properties. *Inorg. Chem.* **2010**, *49*, 6706–6715. [CrossRef]
9. Li, G.C.; Chao, K.; Peng, H.R.; Chen, K.Z. Hydrothermal synthesis and characterization of YVO_4 and YVO_4:Eu^{3+} nanobelts and polyhedral micron crystals. *J. Phys. Chem. C* **2008**, *112*, 6228–6231. [CrossRef]
10. Li, C.X.; Quan, Z.W.; Yang, J.; Yang, P.P.; Lin, J. Highly uniform and monodisperse β-$NaYF_4$:Ln^{3+} (Ln = Eu, Tb, Yb/Er, and Yb/Tm) hexagonal microprism crystals: Hydrothermal synthesisand luminescent properties. *Inorg. Chem.* **2007**, *46*, 6329–6337. [CrossRef]
11. Selvi, G.T.; Grace, A.N.; Jeong, S.K. Synthesis of rare earth hydroxycarbonate ($LaOHCO_3$) nanocrystals with tuneable morphology and luminescence properties. *Adv. Powder Technol.* **2020**, *31*, 2366–2378. [CrossRef]
12. Zhang, Y.; Wu, Z.; Geng, D.; Kang, X.; Shang, M.; Li, X.; Lian, H.; Cheng, Z.; Lin, J. Full color emission in $ZnGa_2O_4$: Simultaneous control of the spherical morphology, luminescent, and electric properties via hydrothermal approach. *Adv. Funct. Mater.* **2014**, *24*, 6581–6593. [CrossRef]
13. Allendorf, M.D.; Bauer, C.A.; Bhakta, R.K.; Houk, R.J.T. Luminescent metal-organic frameworks. *Chem. Soc. Rev.* **2009**, *38*, 1330–1352. [CrossRef] [PubMed]
14. Zhu, Q.; Li, S.Y.; Wang, Q.; Qi, Y.; Li, X.D.; Sun, X.D.; Li, J.-G. Grafting of terbium (III) complexes onto layered rare-earth hydroxide nanosheets to fabricate novel optical fiber temperature sensors. *Nanoscale* **2019**, *11*, 2795–2804. [CrossRef] [PubMed]
15. Zhu, Q.; Ding, S.N.; Xiahou, J.Q.; Li, S.Y.; Xu, X.D.; Li, J.-G. A groundbreaking strategy for fabricating YAG:Ce^{3+} transparent ceramic film via sintering of LRH nanosheets on sapphire. *Chem. Commun.* **2020**, *56*, 12761–12764. [CrossRef]
16. Zhu, Q.; Liu, J.J.; Li, X.D.; Li, J.-G. Grafting organic antenna onto rare earth hydroxynitrate nanosheets for excitation-dependent and greatly enhanced photoluminescence by multi-modal energy transfer. *Appl. Surf. Sci.* **2019**, *489*, 142–148. [CrossRef]
17. Zhu, Q.; Song, C.Y.; Tong, W.P.; Li, J.-G. Controllable phase/morphology tailoring of REF_3 and $NaREF_4$ (RE=La-Lu, Y), and insights into the up-conversion luminescence of GdF_3:Yb^{3+}/Tm^{3+} spheres. *Adv. Powder Technol.* **2020**, *31*, 2235–2243. [CrossRef]

18. Fan, X.F.; Gu, L.Q.; Hu, Y.L.; Zhu, Q. Wearing an organic "coat" on nanocrystals of LaF_3:Eu^{3+} to generate dynamic luminescence for optical anti-counterfeit. *Adv. Powder Technol.* **2021**, *32*, 2645–2653. [CrossRef]
19. Okubo, K.; Shigeta, T. Absolute fluorescent quantum efficiency of NBS phosphor standard sample. *J. Illum. Eng. Inst. Jpn.* **1999**, *83*, 87–93. [CrossRef]
20. Shannon, R.D. Revised effective ionic radii and systematic studies of interatomic distances in halides and chalcogenides. *Acta Cryst.* **1976**, *A32*, 751–767. [CrossRef]
21. Jeong, H.; Lee, B.-I.; Byeon, S.-H. Antenna effect on the organic spacer-modified Eu-doped layered gadolinium hydroxide for the detection of vanadate ions over a wide pH range. *ACS Appl. Mater. Interfaces* **2016**, *8*, 10946–10953. [CrossRef]
22. Nakamoto, K. *Infrared Spectra of Inorganic and Coordination Compounds*; John Wiley & Sons: New York, NY, USA, 1963.
23. Gadsden, J.A. *Infrared Spectra of Minerals and Related Inorganic Compounds*; Butterworths: London, UK, 1975.
24. Zhang, L.Z.; Wang, Z.H.; Huang, J.; Tang, F. Fabrication and photoluminescence properties of Eu^{3+} doped Y_2O_3 ceramic fiber with high aspect ratio. *Chin. J. Lumin.* **2021**, *4*, 1891–1899. [CrossRef]
25. Huang, S.; Wang, Z.H.; Zhu, Q.; Shi, X.F.; Wang, X.J.; Li, X.D.; Sun, X.D.; Li, J.-G. A new protocol for templated synthesis of YVO_4: Ln luminescent crystallites (Ln=Eu, Dy, Sm). *J. Alloys Compd.* **2019**, *776*, 773–781. [CrossRef]
26. Hsu, C.; Powell, R.C. Energy transfer in europium doped yttrium vanadate crystals. *J. Lumin.* **1975**, *10*, 273–293. [CrossRef]

coatings

MDPI

Article

Facile Preparation of YVO_4: RE Films and the Investigation of Photoluminescence

Taihui Chen [1,2], He Zhang [1,2], Zhihong Luo [1,2], Jun Liang [1,2,*] and Xiaoli Wu [1,2,3,*]

[1] Guangxi Key Laboratory of Optical and Electronic Materials and Devices, Guilin University of Technology, Guilin 541004, China; 15007805225@163.com (T.C.); zhang_xiao_he@126.com (H.Z.); luozhihong615@163.com (Z.L.)
[2] School of Materials Science and Engineering, Guilin University of Technology, Guilin 541000, China
[3] Collaborative Innovation Center for Exploration of Hidden Nonferrous Metal Deposits and Development of New Materials in Guangxi, Guilin University of Technology, Guilin 541004, China
* Correspondence: 1991005@glut.edu.cn (J.L.); wuxl-2008@163.com (X.W.)

Abstract: Facile preparation of YVO_4 films was hydrothermally achieved within 1 h by using layered yttrium hydroxide ($Y_2(OH)_5NO_3{\cdot}nH_2O$) films as the sacrificial precursor in the presence of excess $NaVO_3$ at pH~8, without subsequent heat treatment. Detailed structures and optical properties of the products were obtained by using a combination of XRD, FT-IR, FE-SEM, HR-TEM, and PLE/PL techniques. The phase and morphological evolution from $Y_2(OH)_5NO_3{\cdot}nH_2O$ to YVO_4 was unveiled by varying the reaction time. Photoluminescence spectra showed that the Eu^{3+} doped YVO_4 films exhibited the characteristic emission of Eu^{3+}, with the transition $^5D_0$–$^7F_2$ (614 nm, red) being the dominant; while Dy^{3+} activator doped YVO_4 films exhibited the characteristic emission of Dy^{3+}, with the transition $^4F_{9/2}$–$^6H_{13/2}$ (575 nm, green) being the most dominant.

Keywords: YVO_4 film; layered yttrium hydroxide film; sacrificial precursor; anion exchange; photoluminescence

Citation: Chen, T.; Zhang, H.; Luo, Z.; Liang, J.; Wu, X. Facile Preparation of YVO_4: RE Films and the Investigation of Photoluminescence. *Coatings* **2022**, *12*, 461. https://doi.org/10.3390/coatings12040461

Academic Editor: Alicia de Andrés

Received: 11 February 2022
Accepted: 24 March 2022
Published: 29 March 2022

1. Introduction

In recent years, lanthanide compounds have received widespread attention as excellent luminescent materials useful in the development of new lighting/visualization technologies [1,2]. Among them, the rare-earth orthovanadate (YVO_4: RE) is considered an attractive compound since it displays high quantum yield caused by the efficient energy transfer from the VO_4^{3-} ligand to RE^{3+}. Because of the continuous development of optoelectronic devices, the design and fabrication of luminescent films have become more and more important. In the present research, we proposed a methodology to produce red-emitting and green-emitting YVO_4: RE films, which may find wide applications in various lighting and display areas including fluorescent lamps, white LEDs, FEDs, PDPs, FDPs and CRTs, among others [3,4].

At present, a variety of techniques for the preparation of the vanadate films are available. They include the calcination of the MOF (metal-organic framework) precursor [5], pulsed-laser deposition [6], microwave-assisted chemical deposition [7] and sol-gel/electrospinning process [8], among others. The chemical deposition and pulsed-laser deposition are convenient when thin films are prepared from powder. However, these methods require expensive equipment. Calcination of the MOF (metal-organic framework) precursor and the sol-gel/electrospinning process require complex steps and/or high heat treatment temperatures, which may cause the film to crack. In the present work, a low-temperature method was used to synthesize YVO_4: RE films from Layered Yttrium Hydroxide (LYH) film as sacrificial template and $NaVO_3$ as an anion source. The phase and morphological evolution during the transformation of LYH to YVO_4 and photoluminescence properties of activated (Eu^{3+} and Dy^{3+}) doped YVO_4 films were investigated in detail.

The layered rare earth hydroxides (LRHs) are a new type of inorganic functional layered compounds, and the general formula of "251" typed LRH is $RE_2(OH)_5(A^{m-})_{1/m}{\cdot}nH_2O$ (RE = Rare-earth elements; A = Cl or NO_3). The structure of "251" typed LRH is constructed via alternative stacking of the hydroxide main layers composed of $[Ln(OH)_7H_2O]$ and $[Ln(OH)_8H_2O]$ coordination polyhedral and interlayer NO_3^- free anions along the *c*-axis ([001] direction) [9,10]. Because of their special layered structure and properties of rare-earth elements, the "251" typed LRHs have attracted extensive attention since they were first reported in 2006 [11]. In the past several years, different aspects of the "251" typed LRHs have been studied including the interlayer anion exchange capacity [10–15], catalytic performance of intercalated products [11,14,15], exfoliation of bulk crystals into nanosheets [16–18], photoluminescence [9,10,19–21], enhancement of luminescence [22–29], and the self-assembly of functional films [29–34]. Also, because of their composition and structure, a significant amount of research has been performed to study, photoluminescence properties of the "251" typed LRH. However, poor photoluminescence has been observed [9,10,19–21]. This low performance can be attributed to the presence of hydroxyl, crystal water, and nitrate groups in the LRH structure, that provide channels for nonradiative relaxation. The most common method used to achieve photoluminescence optimization, consists of inserting inorganic [21] or organic anions [25,26] via interlayer anion exchange to sensitize activators in the host layer. However, this method presents some limitations because the quenching groups are still present in the structure. Another way to enhance photoluminescence by doping the LYH and LGdH matrix with subsequent calcination to remove the quenching groups and form cubic Y_2O_3:RE/Gd_2O_3:RE [16,19,22–24,31,32]. The heat treatment also requires high temperatures (>550 °C). Thus, in this optimization method, production of a flat film without cracks is still a challenge. In 2016, $(Y_{1-x}Eu_x)PO_4$ was successfully synthesized by using $(Y_{1-x}Eu_x)_2(OH)_5NO_3{\cdot}nH_2O$ as the sacrificial template and NaH_2PO_4 as an anion source [35]. However, high temperatures (600–1000 °C) were also required to produce the target $(Y_{1-x}Eu_x)_2PO_4$ phase. Still, it provides a theoretical basis for the design and preparation of various rare-earth materials. To the best of our knowledge, electrodeposited "251" typed LRH films have not been utilized as a precursor template to synthesize $REVO_4$ films at low temperatures, and without the need of further heat treatment. We believe that this strategy may attract wide research interest and result in the practical application of "251" typed LRHs.

2. Experiment

Materials: The rare-earth source of $Y(NO_3)_3{\cdot}6H_2O$ (99.5% pure), $Eu(NO_3)_3{\cdot}6H_2O$ (99.9% pure), $Dy(NO_3)_3{\cdot}6H_2O$ (99.9% pure) and Sodium metavanadate ($NaVO_3$, 99.9% pure) were purchased from Shanghai Macklin Biochemical Co., Ltd., Shanghai, China. The indium tin oxide (ITO) glass (sheet resistance: $\leq$5 Ω) were obtained from Xiang Cheng Technology Ltd., Shenzhen, China. The platinum electrode and Ag/AgCl/saturated KCl electrode were purchased from Tianjin Ida Technology Co. Ltd., Tianjin, China.

Synthesis: The three-electrode cell system was used to prepare the $Y_2(OH)_5NO_3{\cdot}nH_2O$ film, in which the rare-earth nitrate solution as electrodeposition solution, ITO glass, platinum foil, and Ag/AgCl/saturated KCl were used as the working, counter, and reference electrodes, respectively. After the deposition, all films were cleaned with deionized water and dried at 60 °C for 30 min. For the synthesis of the activator doped system $(Y_{1-x}RrepeatingH)_5NO_3{\cdot}nH_2O$ (RE = Eu and Dy), the RE/(Y + RE) atomic ratio was tuned according to the doping amounts of activators, and then repeat the electrodeposition process. For the synthesis of YVO_4 films, 0.5 mol/L of $NaVO_3$ solution with pH value of 8 was prepared; then the LYH films were placed in the $NaVO_3$ solution, and the mixture was subjected to hydrothermal reaction at 100 °C. Afterward, the prepared films were naturally cooled, washed several times with distilled water and ethanol, and then dried at 60 °C for 30 min.

Characterization techniques: Phase identification was made via X-ray diffractometry (XRD, Model X'Pert PRO, PANalytical B.V., Almelo, The Netherlands) operated at 40 kV/40 mA nickel filtered using Cu-Kα radiation (λ = 0.15406 nm) and a scanning speed of 15.0° 2θ per minute. Fourier transform infrared spectroscopy (FT-IR, Model Spectrum RXI, Perkin-Elmer, Shelton, Connecticut) was conducted via the standard KBr method. The morphology and microstructure of the products were analyzed by field emission scanning electron microscopy (FE-SEM, Model JSM6380-LV, JEOL, Tokyo, Japan) and transmission electron microscopy (TEM, FEM-3000F, JEOL, Tokyo, Japan). The photoluminescence properties were measured on a FluoroMax-4 fluorescence spectrophotometer (HORIBA, Kyoto, Japan) using a 150 W Xe-lamp as the excitation source at room temperature.

3. Results and Discussion

3.1. Characterization of $Y_2(OH)_5NO_3{\cdot}nH_2O$ (LYH) Film and YVO_4 Film

Figure 1a shows the XRD patterns of the precursor film and the anion-exchange film, respectively. The precursor film presents a series of (00*l*) and (220) diffraction patterns characteristic of $Y_2(OH)_5NO_3{\cdot}nH_2O$ compounds [10,12,13], In addition, the diffraction peaks of the anion-exchange film can be assigned to pure tetragonal YVO_4 (PDF No.17-0341) [36]. Figure 1b shows the FT-IR spectra of the precursor and the anion-exchange films. In the precursor film spectrum, the absorption peak at ~1384 cm^{-1} corresponds to uncoordinated NO_3^- (v_3) stretching [19–21,23,24], while the absorption band at ~3600 cm^{-1} indicates OH^- vibration [19–21,23,24]. Additionally, the absorption bands at ~3438 and ~1634 cm^{-1} are attributable to the O-H stretching (v_1 and v_3) and H-O-H bending (v_2) vibrations of hydration water, respectively [19–21,23,24]. The FT-IR analysis confirmed the existence of all the functional groups present in LYH. In the case of the anion-exchange film, the vibration peak of NO_3^- and hydroxyl disappeared, while a strong absorption peak at 820 cm^{-1} appeared. This peak can be assigned to stretch vibration (v_3) originating from the V-O stretching vibration in VO_4^{3-} [8,37]. However, the absorptions of H_2O were still observable at 3412 cm^{-1} and 1640 cm^{-1}, which indicated the presence of some hydration or surface-absorbed water molecules in the anion-exchange film rather than the coordinated H_2O from the precursor LYH film [36]. These results demonstrated that the YVO_4 film was successfully synthesized by using $Y_2(OH)_5NO_3{\cdot}nH_2O$ film as a precursor template and $NaVO_3$ as an anion source.

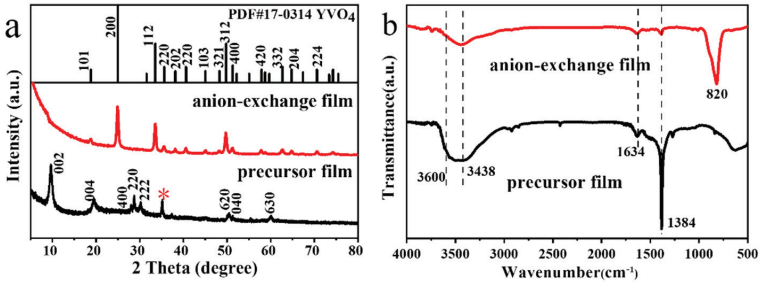

Figure 1. XRD patterns (**a**), FT-IR spectra (**b**) of the precursor film and anion-exchange film. The diffraction peaks of ITO glass were marked with *.

As shown in Figure 2a, the FE-SEM image indicated that the LYH precursor film crystallized as flower-like aggregates, which were assembled in nanosheets with different lateral and vertical arrangements and angles. As observed from the FE-SEM image in Figure 2b and the TEM image in Figure 2c, the YVO_4 film crystallized in structures like rice grains, which were totally different from those observed in the precursor template. Selected area electron diffraction (SAED, the inset of Figure 2c) yielded diffraction spots that correspond to the (200), (301) and (202) planes of tetragonal structured YVO_4, indicating that the anion exchange film under observation is a well-crystallized single crystal. The iden-

tified (200), (301) and (202) diffractions displayed values of d_{200} = 3.559 Å, d_{301} = 2.220 Å and d_{202} = 2.357 Å, respectively. These results were close to the values of d_{200} = 3.574 Å, d_{301} = 2.228 Å and d_{202} = 2.361 Å calculated from the XRD results, respectively. The (202) and (200) planes observed in the SAED pattern presented a dihedral angle of ~48.7°, which was also close to the calculated value of ~48.5°. High-resolution TEM (HR-TEM) analysis clearly resolved the lattice fringes of the LRH crystal, and a spacing of 0.354 nm properly corresponded to the (200) plane of the host layer (Figure 2d).

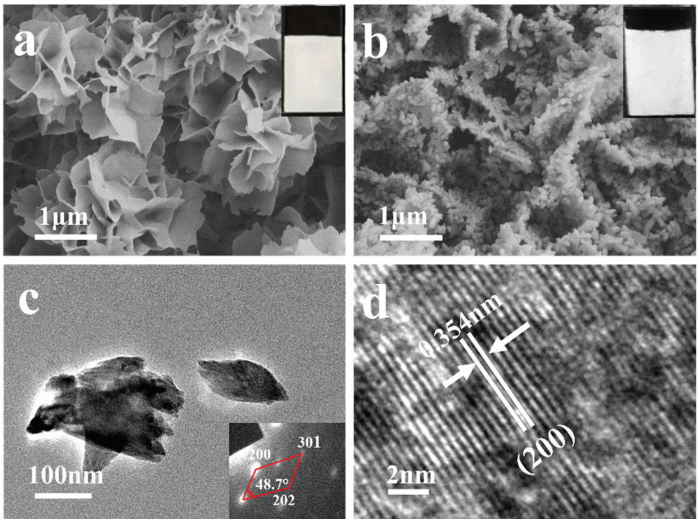

Figure 2. FE-SEM image of the $Y_2(OH)_5NO_3{\cdot}nH_2O$ film (**a**), FE-SEM image (**b**), TEM image (**c**), and HR-TEM image (**d**) of the YVO_4 film. The inset in (**a**) is the digital photograph of the $Y_2(OH)_5NO_3{\cdot}nH_2O$ film, The inset in (**b**) is the digital photograph of the YVO_4 film and the inset in (**c**) is the selected area electron.

3.2. Evolution of Phase and Morphology from LYH to YVO_4 upon Anion Exchange

Through a series of exploratory experiments, it was found that the concentration of $NaVO_3$ in the solution is the key factor affecting the phase and morphology of the exchanged products, and high concentrations of the anion source facilitated the reaction. To determine the phase and morphological evolution during the transformation from LYH to YVO_4, different hydrothermal reactions were performed. For this purpose, we used 0.05 M $NaVO_3$ (with a fixed volume of 50 mL) as the anion source and LYH film as the precursor template. In addition, different reaction times were tested at pH of ~7.3. Figure 3a compares the XRD patterns of the original LYH template and anion-exchange films at different reaction times. Data indicated that at a reaction time of 5 min, a mixture of phases was present. Herein, the peaks at 9.95°and 29.25° correspond to the characteristic diffraction of the (220) plane present in the LYH template. In addition, the diffraction peaks at 24.46°, 35.69° and 50.24° were well correlated with the (200), (112) and (312) planes of the YVO_4 phase, respectively. Obviously, LYH phase is the main phase in the mixture product. FT-IR (Figure 3b) showed that the absorption of uncoordinated NO_3^- at 1384 cm^{-1} and the absorption of VO_4^{3-} at 820 cm^{-1} were simultaneously observed when the reaction time was 5 min. With the increase in reaction time, the diffraction peaks of LYH became weaker, and the final YVO_4 anion exchange product was obtained until the reaction time reached 1h. The corresponding FT-IR spectra of the exchanged products showed the weakened absorptions of hydroxyl and NO_3^-, and enhanced absorptions of VO_4^{3-}. Until the reaction time reached 1 h, the absorptions of hydroxyls and NO_3^- disappeared. According to the synthesis used in the present research, the phase conversion process from

LYH to YVO_4 may be described as follows: $VO_3^-(aq) + 2OH^-(aq) \rightarrow VO_4^{3-}(aq) + H_2O(aq)$. Subsequently, the coordinated hydroxyl and water present in $[Y_2(OH)_5(H_2O)_n]^+$ host layer were completely exchanged by VO_4^{3-}.

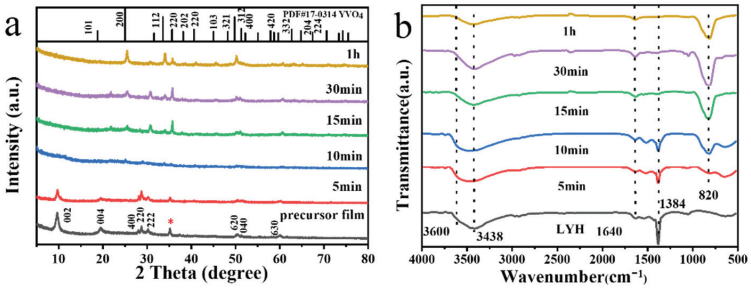

Figure 3. XRD patterns (**a**) and FT-IR spectra (**b**) of anion exchange films prepared with different reaction time. The diffraction peaks of ITO glass were marked with *.

The morphological evolution from LYH to YVO_4 can be observed in Figure 4. The sample with the reaction time of 5 min largely retained the LYH nanoplate-like morphology, among which some YVO_4 particles were found. The FE-SEM data showed that, with increasing reaction time, more LYH nanosheets were converted into YVO_4 spindle-shaped particles. When the reaction proceeded for 1 h, all the LYH nanosheets were completely transformed into YVO_4 spindle-shaped particles. This indicated that phase transition occurred a dissolution–reprecipitation mechanism.

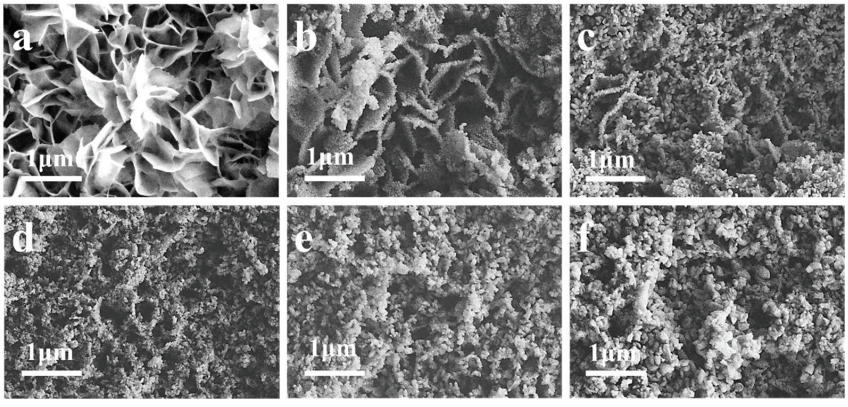

Figure 4. FE-SEM images of anion-exchange films prepared with different reaction times: 0 min (**a**), 5 min (**b**), 10 min (**c**), 15 min (**d**), 30 min (**e**) and 1 h (**f**).

3.3. Structure Characterization and Photoluminescence of Activators Doped YVO_4 Films

In the present research, two types of activated ion doped YVO_4 films (Eu^{3+} doped and Dy^{3+} doped) were prepared. Figure 5a shows the XRD results of the films obtained when reactions proceeded with different molar contents of Eu^{3+}. Data indicated that all the diffraction peaks can be well indexed to the tetragonal YVO_4 (PDF No.17-0341). As shown in Figure 5b, the body-centered tetragonal unit cell of YVO_4 consists of four units, where two sets of oxygen atoms, differing in the Y-O bond length, are coordinated to Y^{3+} to form the YO_8 dodecahedron. The derived cell parameters are summarized in Table 1. Compared with the standard YVO_4 film, the YVO_4: Eu film presented a larger cell volume, which was ascribed to the increase in the RE-O bond length. This resulted from the replacement of smaller ionic radius of Y^{3+} with the larger Eu^{3+} (eight-fold coordination, 0.1019 nm

for Y^{3+}, 0.1066 nm for Eu^{3+}) and caused the direct crystallization of solid solution. The crystallite size assayed from the Scherrer equation via profile broadening analysis of the (200) diffraction, and the calculated values of the crystallite size are summarized in Table 1. Data shows that the crystalline size of YVO_4: Eu nanoparticles gradually decreased with the increased doping amount of RE^{3+} ions.

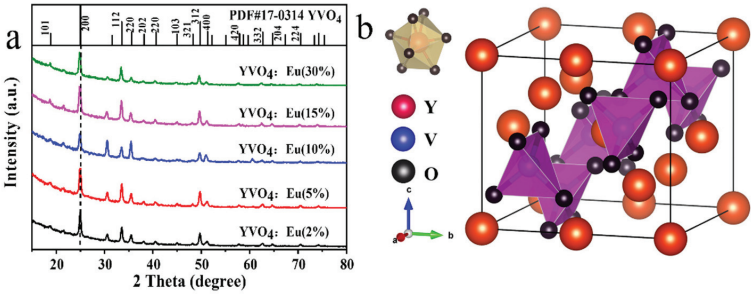

Figure 5. XRD patterns of the YVO_4:Eu films with different molar doping concentration (**a**) and the schematic crystal structure of tetragonal $REVO_4$ (**b**). The Y^{3+} ligands of YVO_4 crystal structure are shown in the insets.

Table 1. The results of structure refinement and the crystalline sizes for YVO_4:Eu^{3+}.

Samples	A = b (Å)	c (Å)	V (Å^3)	Crystalline Sizes (nm)
YVO_4: Eu (2%)	7.100	6.259	315.516	24.51
YVO_4: Eu (5%)	7.121	6.288	318.856	23.20
YVO_4: Eu (10%)	7.137	6.304	321.105	21.73
YVO_4: Eu (15%)	7.160	6.295	322.717	21.01
YVO4: Eu (30%)	7.163	6.315	324.014	20.46

The photoluminescence excitation (PLE) spectra of the YVO_4: Eu^{3+} films observed by monitoring the red emission of Eu^{3+} at 614 nm consisted of a strong and broad excitation band ranging from ~280 to 320 nm (Figure 6a), which was attributed to the energy transfer from VO_4^{3-} to Eu^{3+} [38]. The molecular orbital theory suggests that the absorption band was overlapped by the charge electron transitions of VO_4^{3-} ion from the $^1A_2(^1T_1)$ ground state to the $^1E(^1T_2)$ excited state at 290 nm and $^1A_1(^1E)$ excited state at 308 nm [36]. Negligible peaks located at 396 nm and 466 nm were observed, which resulted from the general $^7F_{0,1}$–$^5L_6$ and $^7F_{0,1}$–$^5D_2$ transitions of Eu^{3+}, respectively. Upon UV excitation at 290 nm, the photoluminescence (PL) spectra of the YVO_4: Eu^{3+} films (Figure 6b) exhibited transitions from the $^5D_0$ excited state to the ^7F_J (J = 1, 2, and 3) ground states of Eu^{3+} ranging from 500 to 650 nm, with the transition $^5D_0$–$^7F_2$ (614 nm, red emission) being the most dominant [39,40]. According to the Judd-Ofelt parity rule [41,42], the relative intensity of emission peaks is closely related to the transition of excited electrons to different energy levels and the coordination environment of Eu^{3+}. The intensity of the $^5D_0 \rightarrow {}^7F_2$ electric dipole transition is greater than that of the $^5D_0 \rightarrow {}^7F_1$ magnetic dipole transition, indicating the activator Eu^{3+} occupies a low-symmetry site in the lattice. As shown in Figure 6b, the optimal concentration of doped Eu^{3+} was 10 mol (%); over-doping led to the concentration quenching of luminescence via cross-relaxation mechanism. Figure 6c,d show the excitation and emission spectra of YVO_4: Dy^{3+}, respectively. By monitoring the emission of Dy^{3+} at 573 nm, it was observed that the PLE spectra of the YVO_4: Dy^{3+} films exhibited a strong and broad band ranging from 280-310 nm, which was also associated with the efficient energy transfer from VO_4^{3-} to Dy^{3+}. Moreover, the peaks located at 350–500 nm were attributed to the $^4F_{9/2}$–$^6H_{15/2}$ and $^4F_{9/2}$–$^6H_{13/2}$ intra-transitions of Dy^{3+} (Figure 6c). Upon the excitation at 290 nm, the emission spectra of the YVO_4: Dy^{3+} films were composed of two bands centered at ~483 nm (blue emission) and 573 nm (green emission, dominant),

which corresponded to the $^4F_{9/2}$–$^6H_{15/2}$ and $^4F_{9/2}$–$^6H_{13/2}$ intra-transitions of Dy^{3+}, respectively. Data in Figure 6d indicated that the optimal doped Dy^{3+} concentration was 5 mol (%). Additionally, the $(Y_{0.90}Eu_{0.05})VO_4$ and $(Y_{0.95}Dy_{0.05})VO_4$ films exhibited vivid red and bright green emissions under UV excitation at 254 nm.

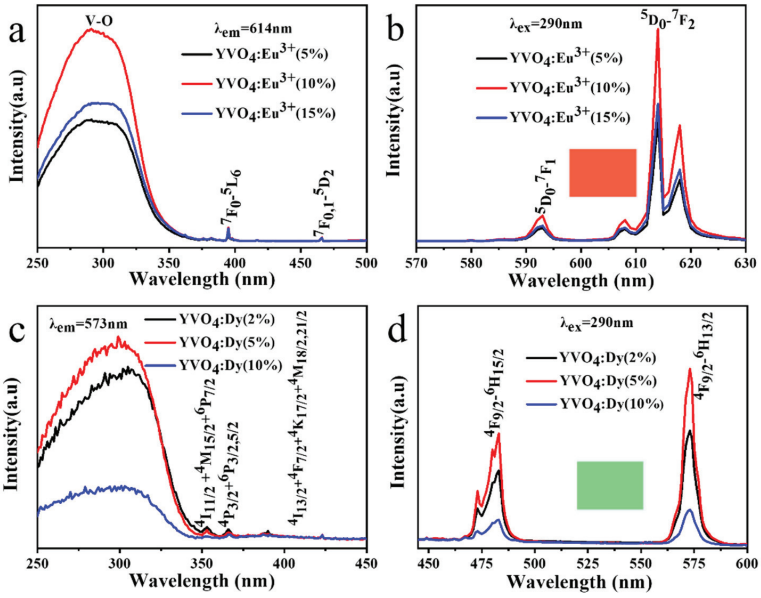

Figure 6. The excitation spectra (**a**) and emission spectra (**b**) of $Y_{1-x}Eu_xVO_4$ films prepared for 1 h, excitation spectra (**c**) and emission spectra (**d**) of $Y_{1-x}Dy_xVO_4$ films prepared for 1 h. Insets in (**b**,**d**) show red emission and green emission of the $(Y_{0.90}Eu_{0.10})VO_4$ film and $(Y_{0.95}Dy_{0.05})VO_4$ film under the UV excitation at 254 nm, respectively.

4. Conclusions

The rapid preparation of YVO_4 films was successfully performed via anion exchange reaction by using the electrodeposited LYH films as a precursor template and $NaVO_3$ as anion source at pH ~7.3, without further heat treatment. The phase evolution from LYH to YVO_4 was systematically studied, and the morphological evolution from flower-like LYH nanosheets to YVO_4 spindle-shaped particles indicated that a dissolution-reprecipitation mechanism occurred. Photoluminescence showed that YVO_4:Eu^{3+} films and YVO_4:Dy^{3+} films exhibited characteristic emissions depending on the RE^{3+}. In addition, the optimal concentrations of doped Eu^{3+} and Dy^{3+} were determined as 10 mol (%) and 5 mol (%), respectively. Moreover, the $(Y_{0.90}Eu_{0.10})VO_4$ and $(Y_{0.95}Dy_{0.05})VO_4$ film exhibit vivid red color and bright green color under UV excitation at 254 nm.

Author Contributions: Conceptualization, T.C. and H.Z.; methodology, X.W.; software, T.C.; validation, Z.L. and J.L.; formal analysis, X.W.; investigation, T.C.; resources, X.W.; data curation, Z.L.; writing-original draft preparation, T.C.; writing—review and editing, X.W.; visualization, X.W.; supervision, X.W.; project administration, X.W.; funding acquisition, X.W. and J.L. All authors have read and agreed to the published version of the manuscript.

Funding: This work was financially supported by the Natural Science Foundation of China (No. 52062011, 51402059) and Natural Science Foundation of Guangxi Province (No. 2018GXNSFAA050011).

Institutional Review Board Statement: Not applicable.

Informed Consent Statement: Not applicable.

Data Availability Statement: Not applicable.

Conflicts of Interest: The authors declare no conflict of interest.

References

1. Dunlap-Shohl, W.A.; Zhou, Y.; Padture, N.P.; Mitzi, D.B. Synthetic Approaches for Halide Perovskite Thin Films. *Chem. Rev.* **2019**, *119*, 3193–3295. [CrossRef] [PubMed]
2. Liang, K.; Li, L.; Yang, Y. Inorganic Porous Films for Renewable Energy Storage. *ACS Energy Lett.* **2017**, *2*, 373–390. [CrossRef]
3. Liu, L.; Wang, S.; Zhao, B.; Pei, P.; Fan, Y.; Li, X.; Zhang, F. Er^{3+} Sensitized 1530 nm to 1180 nm Second Near-Infrared Window Upconversion Nanocrystals for In Vivo Biosensing. *Angew. Chem. Int. Ed.* **2018**, *57*, 7518–7522. [CrossRef] [PubMed]
4. Mashford, B.S.; Nguyen, T.L.; Wilson, G.J.; Mulvaney, P. All-inorganic quantum-dot light-emitting devices formed via low-cost, wet-chemical processing. *J. Mater. Chem. A* **2010**, *20*, 167–172. [CrossRef]
5. Vadivel, S.; Paul, B.; Kumaravel, M.; Hariganesh, S.; Rajendran, S.; Mantilaka, M.M.M.G.P.G.; Mamba, G.; Puviarasu, P. Facile synthesis of $YbVO_4$, and YVO_4 nanostructures through MOF route for photocatalytic applications. *Inorganic Chem. Commun.* **2020**, *115*, 107855. [CrossRef]
6. Yi, S.; Bae, J.S.; Shim, K.S.; Moon, B.K.; Jeong, J.H.; Chung, S.T.; Kim, J.H. Luminescence characteristics of Eu-doped $GdVO_4$ thin films grown by pulsed-laser deposition. *J. Vac. Sci. Technol. A* **2005**, *23*, 1124–1127. [CrossRef]
7. Xu, H.; Wang, H.; Jin, T.; Yan, H. Rapid fabrication of luminescent Eu: YVO_4 films by microwave-assisted chemical solution deposition. *Nanotechnology* **2005**, *16*, 65–69. [CrossRef]
8. Hou, Z.; Yang, P.; Li, C.; Wang, L.; Lian, H.; Quan, Z.; Lin, J. Preparation and Luminescence Properties of YVO_4:Ln and Y(V, P)O_4:Ln (Ln) Eu^{3+}, Sm^{3+}, Dy^{3+}) Nanofibers and Microbelts by Sol-Gel/Electrospinning Process. *Chem. Mater.* **2008**, *20*, 6686–6696. [CrossRef]
9. Geng, F.; Matsushita, Y.; Ma, R.; Xin, H.; Tanaka, M.; Izumi, F.; Iyi, N.; Sasaki, T. General synthesis and structural evolution of a layered family of $Ln_8(OH)_{20}Cl_4{\cdot}nH_2O$ (Ln = Nd, Sm, Eu, Gd, Tb, Dy, Ho, Er, Tm, and Y). *J. Am. Chem. Soc.* **2008**, *130*, 16344–16350. [CrossRef]
10. Geng, F.; Xin, H.; Matsushita, Y.; Ma, R.; Tanaka, M.; Izumi, F.; Iyi, N.; Sasaki, T. New layered rare-earth hydroxides with anion-exchange properties. *Chem. Eur. J.* **2008**, *14*, 9255–9260. [CrossRef]
11. Gandara, F.; Perles, J.; Snejko, N.; Iglesias, M.; Gomez-Lor, B.; Gutierrez-Puebla, E.; Monge, M.A. Layered rare-earth hydroxides: A class of pillared crystalline compounds for intercalation chemistry. *Agnew. Chem. Int. Ed.* **2006**, *45*, 7998–8001. [CrossRef] [PubMed]
12. McIntyre, L.J.; Jackson, L.K.; Fogg, A.M. $Ln_2(OH)_5NO_3 \cdot xH_2O$ (Ln = Y, Gd-Lu): A Novel Family of Anion Exchange Intercalation Hosts. *Chem. Mater.* **2008**, *20*, 335–340. [CrossRef]
13. Hindocha, S.A.; McIntyre, L.J.; Fogg, A.M. Precipitation synthesis of lanthanide hydroxy nitrate anion exchange materials, $Ln_2(OH)_5NO_3{\cdot}H_2O$ (Ln =Y, Eu-Er). *J. Solid State Chem.* **2009**, *182*, 1070–1074. [CrossRef]
14. Gandara, F.; Puebla, E.G.; Iglesias, M.; Proserpio, D.M.; Snejko, N.; Monge, M.A. Controlling the structure of Arenedisulfonates toward Catalytically Active Materials. *Chem. Mater.* **2009**, *21*, 655–661. [CrossRef]
15. Sokolov, M.R.; Enakieva, Y.Y.; Yapryntsev, A.D.; Shiryaev, A.A.; Zvyagina, A.I.; Kalinina, M.A. Intercalation of Porphyrin-Based SURMOF in Layered Eu (III) Hydroxide: An Approach Toward Symbimetic Hybrid Materials. *Adv. Funct. Mater.* **2020**, *30*, 2000681. [CrossRef]
16. Lee, K.H.; Lee, B.I.; You, J.; Byeon, S.H. Transparent Gd_2O_3: Eu phosphor layer derived from exfoliated layered gadolinium hydroxide nanosheets. *Chem. Commun.* **2010**, *46*, 1461–1463. [CrossRef]
17. Zhao, Y.; Li, J.; Guo, M.; Yang, X. Structural and photoluminescent investigation of LTbH/LEuH nanosheets and their color-tunable colloidal hybrids. *J. Mater. Chem. C* **2013**, *1*, 3584–3592. [CrossRef]
18. Hu, L.; Ma, R.; Ozawa, T.C.; Sasaki, T. Exfoliation of layered europium hydroxide into unilamellar nanosheets. *Chem. Asian J.* **2010**, *5*, 248–251. [CrossRef]
19. Zhu, Q.; Li, J.; Zhi, C.; Li, X.; Sun, X.; Sakka, Y.; Golberg, D.; Bando, Y. Layered Rare-Earth Hydroxides (LRHs) of $(Y_{1-x}Eu_x)_2(OH)_5NO_3{\cdot}nH_2O$ (x = 0–1): Structural Variations by Eu^{3+} Doping, Phase Conversion to Oxides, and the Correlation of Photoluminescence Behaviors. *Chem. Mater.* **2010**, *22*, 4204–4213. [CrossRef]
20. Wu, X.; Li, J.; Zhu, Q.; Li, J.; Ma, R.Z.; Sasaki, T.; Li, X.; Sun, X.; Sakka, Y. The effects of Gd^{3+} substitution on the crystal structure, site symmetry, and photoluminescence of Y/Eu layered rare-earth hydroxide (LRH) nanoplates. *Dalton Trans.* **2012**, *41*, 1854–1861. [CrossRef]
21. Wu, X.; Li, J.; Zhu, Q.; Liu, W.; Li, J.; Li, X.; Sun, X.; Sakka, Y. One-step freezing temperature crystallization of layered rare-earth hydroxide ($Ln_2(OH)_5NO_3{\cdot}nH2O$) nanosheets for a wide spectrum of Ln (Ln = Pr-Er, and Y), anion exchange with fluorine and sulfate, and microscopic coordination probed via photoluminescence. *J. Mater. Chem. C* **2015**, *3*, 3428–3437. [CrossRef]
22. Hu, L.; Ma, R.; Ozawa, T.C.; Sasaki, T. Oriented Monolayer Film of Gd_2O_3:0.05Eu Crystallites: Quasi-Topotactic Transformation of the Hydroxide Film and Drastic Enhancement of Photoluminescence Properties. *Agnew. Chem. Int. Ed.* **2009**, *48*, 3846–3849. [CrossRef] [PubMed]

23. Zhu, Q.; Li, J.; Zhi, C.; Ma, R.; Sasaki, T.; Xu, J.; Liu, C.; Li, X.; Sun, X.; Sakka, Y. Nanometer-thin layered hydroxide platelets of $(Y_{0.95}Eu_{0.05})_2(OH)_5NO_3{\cdot}xH_2O$: Exfoliation-free synthesis, self-assembly, and the derivation of dense oriented oxide films of high transparency and greatly enhanced luminescence. *J. Mater. Chem.* **2011**, *21*, 6903–6908. [CrossRef]
24. Huang, J.; Zhang, T.; Ren, K.; Zhang, R.; Wu, X.; Li, J. Fabrication of oriented oxide films from exfoliated yttrium hydroxide layers: Enhanced photoluminescence and unexplored behavior of energy transfer. *J. Alloys Compd.* **2018**, *763*, 815–821. [CrossRef]
25. Chu, N.; Sun, Y.; Zhao, Y.; Li, X.; Sun, G.; Ma, S.; Yang, X. Intercalation of organic sensitisers into layered europium hydroxide and enhanced luminescence property. *Dalton Trans.* **2012**, *41*, 7409–7414. [CrossRef]
26. Sun, Y.; Chu, N.; Gu, Q.; Pan, G.; Sun, G.; Ma, S.; Yang, X. Hybrid of Europium-Doped Layered Yttrium Hydroxide and Organic-Sensitizer Effect of Solvent on Structure and Luminescence Behavior. *Eur. J. Inorg. Chem.* **2013**, 32–38. [CrossRef]
27. Wu, X.; Li, J.; Li, J.; Zhu, Q.; Li, X.; Sun, X.; Sakka, Y. Layered rare-earth hydroxide (LRH) and oxide nanoplates of the Y/Tb/Eu system: Phase controlled processing, structure characterization, and color-tunable photoluminescence via selective excitation and efficient energy transfer. *Sci. Technol. Adv. Mater.* **2013**, *14*, 015006. [CrossRef]
28. Wu, X.; Li, J.; Ping, D.; Li, J.; Zhu, Q.; Li, X.; Sun, X.; Sakka, Y. Structure Characterization and Photoluminescence Properties of $(Y_{0.95-x}Gd_xEu_{0.05})_2O_3$ Red phosphors Converted from Layered Rare-Earth Hydroxide (LRH) nanoflake precursors. *J. Alloys Compd.* **2013**, *559*, 188–195. [CrossRef]
29. Liu, S.; Li, J.; Liu, W.; Cui, H.; Liu, M.; Chen, J.; Zhu, H.; Li, X.; Sun, X. A novel method for improving particle growth and photoluminescence through F- substituting for gallery NO_3- in layered Y./Eu hydroxides. *Chem. Eng. J.* **2020**, *380*, 122618. [CrossRef]
30. Zhu, Q.; Li, J.; Li, X.; Sun, X.; Yang, Q.; Zhu, M.; Sakka, Y. Tens of micron-sized unilamellar nanosheets of Y/Eu layered rare-earth hydroxide: Efficient exfoliation via fast anion exchange and their self-assembly into oriented oxide film with enhanced photoluminescence. *Sci. Technol. Adv. Mater.* **2014**, *15*, 506–512. [CrossRef]
31. Hu, L.; Ma, R.Z.; Ozawa, T.C.; Geng, F.; Lyi, N.B.; Sasaki, T. Oriented films of layered rare-earth hydroxide crystallites self-assembled at the hexane/water interface. *Chem. Commun.* **2008**, *40*, 4897–4899. [CrossRef] [PubMed]
32. Yoon, Y.S.; Byeon, S.H.; Lee, I.S. Unexplored thermal transformation behavior of two-dimensionally bound gadolinium hydroxide layers: Fabrication of oriented crystalline films of gadolinium oxychloride nanosheets suitable for the multicolor luminescence with color tunability. *Adv. Mater.* **2010**, *22*, 3272–3276. [CrossRef] [PubMed]
33. Lee, B.I.; Lee, E.S.; Byeon, S.H. Assembly of layered rare-earth hydroxide nanosheets and SiO_2 nanoparticles to fabricate multifunctional transparent films capable of combinatorial color generation. *Adv. Funct. Mater.* **2012**, *22*, 3562–3569. [CrossRef]
34. Zhu, Q.; Li, S.; Wang, Q.; Qi, Y.; Li, X.; Sun, X.; Li, J. Grafting of terbium(iii) complexes onto layered rare-earth hydroxide nanosheets to fabricate novel optical fiber temperature sensors. *Nanoscale* **2019**, *11*, 2795. [CrossRef]
35. Liu, L.; Yu, M.; Zhang, J.; Wang, B.; Liu, W.; Tang, Y. Facile fabrication of color-tunable and white light emitting nano-composite films based on layered rare-earth hydroxides. *J. Mater. Chem. C* **2015**, *3*, 2326–2333. [CrossRef]
36. Wang, Z.; Li, J.; Zhu, Q.; Li, X.; Sun, X. Sacrificial conversion of layered rare-earth hydroxide (LRH) nanosheets into $(Y_{1-x}Eu_x)PO_4$ nanophosphors and investigation of photoluminescence. *Dalton Trans.* **2016**, *45*, 5290–5299. [CrossRef]
37. Huang, S.; Wang, Z.; Zhu, Q.; Shi, X.; Wang, X.; Li, X.; Sun, X.; Li, J. A new protocol for templated synthesis of YVO_4: Ln luminescent crystallites (Ln = Eu, Dy, Sm). *J. Alloys Compd.* **2019**, *776*, 773–781. [CrossRef]
38. Xu, W.; Wang, Y.; Bai, X. Controllable synthesis and size-dependent luminescent properties of YVO_4:Eu^{3+} nanospheres and microspheres. *J. Phys. Chem. C* **2010**, *114*, 14018–14024. [CrossRef]
39. Yang, X.; Zhang, Y.; Xu, L.; Zhai, Z.; Li, M.; Li, M.; Liu, X.; Hou, W. Surfactant-free sacrificial template synthesis of submicrometer-sized YVO_4:Eu^{3+} hierarchical hollow spheres with tunable textual parameters and luminescent properties. *Dalton Trans.* **2013**, *42*, 3986–3993. [CrossRef]
40. Jia, G.; Song, Y.; Yang, M. Uniform YVO_4:Ln^{3+} (Ln = Eu, Dy, and Sm) nanocrystals: Solvothermal synthesis and luminescence properties. *Opt. Mater.* **2009**, *31*, 1032–1037. [CrossRef]
41. Judd, B.R. Optical absorption intensities of rare-earth ions. *Phys. Rev.* **1962**, *127*, 750. [CrossRef]
42. Ofelt, G.S. Intensities of crystal spectra of rare-earth ions. *J. Chem. Phys.* **1962**, *37*, 511–520. [CrossRef]

coatings

MDPI

Article

Comparison of Microstructure, Microhardness, Fracture Toughness, and Abrasive Wear of WC-17Co Coatings Formed in Various Spraying Ways

Xiao Chen, Chengdi Li *, Qinqin Gao, Xixi Duan and Hao Liu *

Xinyu Key Laboratory of Materials Technology and Application for Intelligent Manufacturing, School of Mechanical and Electrical Engineering, Xinyu University, Xinyu 338004, China; chenxiaoxyxy@126.com (X.C.); qinqingao_2000@126.com (Q.G.); xixiduan_2001@126.com (X.D.)

* Correspondence: cdl1988_xyxy@126.com (C.L.); haol_xyxy@126.com (H.L.); Tel.: +86-790-666-6108 (C.L. & H.L.)

Abstract: WC-Co cermet materials serving as protective coatings are widely used in many fields. Conventional WC-17Co coatings were formed in high-velocity oxygen-fuel (HVOF), warm spraying (WS), and cold spraying (CS), respectively. Deposition behavior of a single WC-17Co particle, as well as the microstructure, microhardness, fracture toughness, and abrasive wear of WC-17Co coatings formed in various spraying ways were investigated. The results show that the deposition behavior of a single WC-17Co particle was different after it was deposited onto a Q235 steel substrate in various spraying ways. The WC-17Co splat deposited by HVOF showed a center hump and some molten areas, as well as some radial splashes presented at the edge of the splat. The WC-17Co splat deposited by WS presented a flattened morphology with no molten areas. However, the WC-17Co splat deposited by CS remained nearly spherical in shape and embedded into the substrate to a certain depth. All the WC-17Co coatings had the same phase compositions with that of feedstock. The microstructure of all the WC-17Co coatings was dense with no cracks or abscission phenomena between the coatings and substrate. Moreover, fine WC particles were formed in the coatings due to the fracture of coarse WC particles, and the content of fine WC particles in the cold-sprayed coating was significantly more than the other coatings. A stripe structure was formed by the slippage of fine WC particles with a plastic flow of Co binder in the warm-sprayed and cold-sprayed coatings. More fine WC particles, as well as the stripe structure, in the coatings were conducive to improve the microhardness and fracture toughness of the coating. The microhardness and fracture toughness of the cold-sprayed WC-17Co coating were the highest among the coatings. The main wear mechanism of all coatings was the groove and some peel-offs. The cold-sprayed WC-17Co coating with the lowest wear loss presented the highest wear resistance among the coatings.

Keywords: WC-17Co coating; high-velocity oxygen-fuel; warm spray; cold spray; microstructure; microhardness; fracture toughness; abrasive wear

Citation: Chen, X.; Li, C.; Gao, Q.; Duan, X.; Liu, H. Comparison of Microstructure, Microhardness, Fracture Toughness, and Abrasive Wear of WC-17Co Coatings Formed in Various Spraying Ways. *Coatings* **2022**, *12*, 814. https://doi.org/10.3390/coatings12060814

Academic Editor: Diego Martinez-Martinez

Received: 18 May 2022
Accepted: 7 June 2022
Published: 10 June 2022

1. Introduction

WC-Co cermet materials, due to their exceptional comprehensive properties, are widely used as protective coatings of wear-resistant parts in many fields (e.g., aerospace, automobile, petrochemical, equipment manufacturing) [1–5]. Therefore, WC-Co coatings were prepared by many researchers using various spraying technologies. Thermal spraying processes, such as high-velocity oxygen-fuel (HVOF) and plasma spray, are the most frequently used technology to fabricate WC-Co cermet coatings. The microstructure and properties (e.g., mechanical, wear behavior, erosion behavior) of WC-Co coatings prepared by plasma spraying were investigated [6–10]. Studies showed that WC-Co coatings could improve the properties of the substrate, especially the coatings with a dense microstructure. However, due to the high temperature effect of plasma spraying, the decarburization and decomposition phenomena of WC ceramic phase always occurred in the as-sprayed

coatings, resulting in the formation of W, W_2C, Co_3W_3C, or Co_6W_6C phases [6–10]. Due to the low flame temperature and short residence time of particles in flame flow, the HVOF process is a favorable and feasible method to fabricate cermet coatings with excellent properties (e.g., high microhardness, low porosity, high bonding strength, and good wear resistance), especially suitable for preparing carbide cermet coatings [11,12]. Therefore, researchers have conducted a significant amount of research on the microstructure and properties of HVOF-sprayed WC-Co coatings with different WC size (e.g., conventional, fine, nanostructured, bimodal, and multimodal) and/or Co content (e.g., 10Co, 12Co, 17Co, and 25Co) [13–22]. Shipway et al. [15] reported that, due to the higher decomposition of nanostructured WC, the wear rate of conventional WC-12Co coating was lower than that of nanostructured WC-12Co coating. Cho et al. [16] also reported that, due to the denser microstructure and lower decomposition of micron WC-Co coating, the hardness and friction coefficient of micron WC-Co coating were higher than of nano WC-Co coating. Guilemany et al. [17] reported that, due to the more decarburization phenomena in the nanostructured WC-12Co coatings, the microhardness of the nanostructured WC-12Co coating was higher in comparison to bimodal and conventional WC-12Co coatings. Meanwhile, the bimodal WC-12Co coating showed a lower friction coefficient and better wear resistance than other coatings. Baumann et al. [18] reported that the fine WC-12Co coating showed the highest microhardness and wear resistance in comparison to nanostructured and conventional WC-12Co coatings. Ding et al. [3] showed that the multimodal WC-12Co coating with denser microstructure exhibited higher microhardness and better erosion resistance than submicron and conventional WC-12Co coatings. Although the WC-Co coatings could improve microhardness and wear/erosion resistance, W, W_2C, Co_3W_3C, or Co_6W_6C phases also always occurred in the HVOF-sprayed coatings [3,13–19].

A warm spraying (WS) process, as a new kind of thermal spraying technology, has been used to prepare metal (e.g., Al, Cu, and Ti etc) [21–23], Ti6Al4V [24], hydroxyapatite (HA) [25], HA/Ti [26], Ti-Al-based intermetallic coatings [27]. Meanwhile, due to the high particle temperature, which is nevertheless lower than the melting point characteristic of standard WS processes, WC-based cermet coatings were successfully deposited by warm spraying [28–32]. Chivavibul et al. [28,29] have studied the microstructure, mechanical properties, and wear resistance of WC-Co coatings with various Co contents determined by WS and HVOF processes. The results showed that the fracture toughness of warm-sprayed WC-Co coatings increased was the Co content increased, and the wear resistance of warm-sprayed WC-Co coatings was better than those of HVOF-sprayed coatings [29]. Watanabe et al. [31,32] reported that WC-Co/Cu and WC-Co/Al multilayer coatings were successfully fabricated by warm spraying. The results showed that, due to higher volume fraction of copper in WC-Co/Cu coating, the work of the fractured WC-Co/Cu coatings was higher than the monolithic WC-Co coatings, as well as the bending strength was moderately better [31]. The durability of WC-Co/Al multilayer coatings was enhanced by ductile aluminum [32]. At present, there are few reports on the research of warm-sprayed WC-Co coatings, but it can be found from existing reports that the phase compositions of WC-Co coatings prepared by warm spraying were the same as that of those powders.

Cold spraying is a kind of technology in which high velocity solid-state particles impacted into substrates to form coatings [33]. Therefore, extensive research has been done into WC-based coatings with different WC size (e.g., conventional [34–37], such as nanostructured [37–39], bimodal [40], and multimodal [41,42]) coatings fabricated by cold spraying. Couto et al. [34] reported that cold-sprayed WC-12Co and WC-17Co coatings retained the same composition phases with the original powder, and the coatings with dense microstructure showed excellent tribological and electrochemical properties. Yin et al. [35] reported that WC-Co-Ni coatings with different WC mass fractions were successfully fabricated by cold spraying, and the coating formation mechanism and tribological performance were investigated. The results showed that metallic bonding between the WC-Co and Ni particles was a possibility that occurred due to the Co phase in the WC-Co powders, and then the fine WC-17Co pieces caused by high-velocity impacting remained

in the WC-Co-Ni coating. In addition, the tribological performance of WC-Co-Ni coatings improved as the WC content increased. Li et al. [38] studied the deposition behavior of single nanostructured WC-12Co particle. The results showed that the dense nanostructured WC-12Co coating presented high microhardness (1800 $Hv_{0.3}$), and post-annealing treatment was beneficial to improve the bonding between deposited nanostructured WC-12Co particles and the toughness of the coatings. Yang et al. [40] reported that cold-sprayed WC-(nanoWC-Co) coatings showed higher microhardness and toughness, as well as much higher wear resistance by comparing with HVOF-sprayed conventional WC-Co coatings. In addition, the post-spray annealing treatment could improve the toughness of the coating, especially the wear resistance. Ji et al. [42] reported that the mechanical and abrasive wear properties were influenced by the content of nano WC-17Co particles in the multimodal WC-17Co feedstocks. And the abrasive wear mechanism of multimodal WC-17Co was also investigated.

In recent years, there are few reports on the preparation of WC-Co coatings by various spraying ways. Hence, in order to investigate the effects of various spraying methods on the deposition behavior of a single WC-17Co particle, as well as the microstructure, mechanical, and abrasive wear properties of the coatings, WC-17Co coatings were fabricated by HVOF, WS, and CS technologies in this study. The main innovations of this study are as follows: (1) contrastive analysis is applied to the deposition behavior of a single WC-17Co particle across various spraying methods; (2) the warm-spraying technology is applied to fabricate WC-17Co coating; (3) the decomposition and decarburization of WC are restrained by controlling the HVOF processing parameters; (4) the contrastive analysis on the microstructure, microhardness, fracture toughness, and abrasive wear properties of WC-Co coatings prepared by various spraying methods is investigated.

2. Materials and Methods

2.1. Materials

Raw materials used in this study were commercially available conventional WC-17Co powders with WC size of 0.2–2 μm (Ganzhou Zhangyuan Tungsten Advance Material Co., Ltd., Ganzhou, China). An agglomeration sintering method was used to manufacture these powders. The surface and cross-section morphologies of WC-17Co powders were shown in Figure 1. The size distribution of WC-17Co powders analyzed by a laser diffraction meter (GSL-1020, Liaoning Instrument Research Institute Co., Ltd., Liaoning, China) was shown in Figure 2. The size distribution (D10, D50, and D90) of powders was 19.5 μm, 29.6 μm, and 44.6 μm, respectively. Q235 steel with dimensions of 50 mm × 25 mm × 3 mm was used as a substrate for depositing single WC-17Co coatings. Prior to spraying, Q235 steel substrate was pre-cleaned by acetone for 10 min in ultrasonic cleaner, and then grit blasted by aluminum oxide of 700 μm to achieve a roughened surface for improving the bonding strength between the coating and substrate.

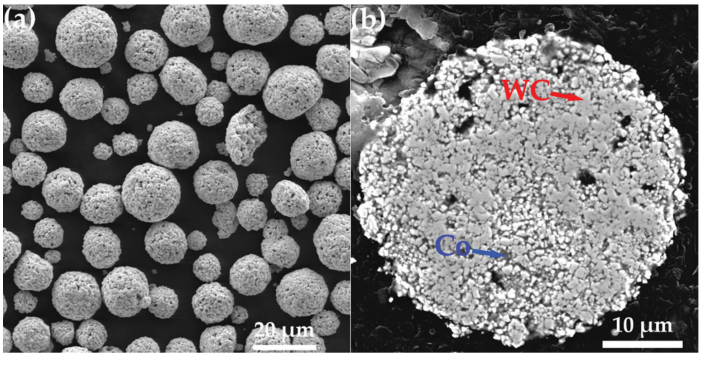

Figure 1. The morphologies of WC-17Co powder (**a**) surface, 2000×, (**b**) cross-section, 5000×.

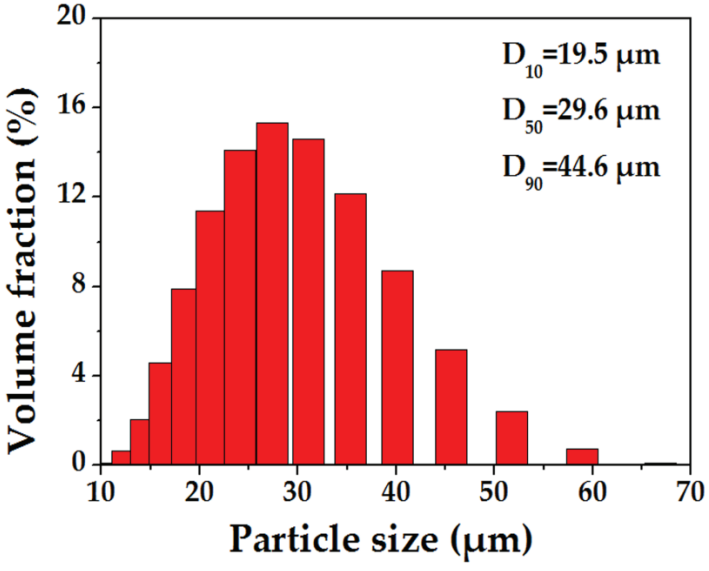

Figure 2. The particle size distribution of WC-17Co powders.

2.2. Coating Preparation

HVOF, WS, and CS equipment adopted a home-made high-velocity oxygen fuel spray system (CH-2000, Xi'an Jiaotong University, Shanxi, China), a modified high-velocity oxygen fuel spray system (CH-2000, Xi'an Jiaotong University, Shanxi, China), and a home-made cold-spray system (CS-2000, Xi'an Jiaotong University, Shanxi, China), respectively. Nitrogen gas was used as an auxiliary gas to adjust the flame temperature for warm spraying in this study. A schematic diagram of HVOF and WS spray systems is illustrated in Figure 3, and a schematic diagram of CS spraying system is illustrated in Figure 4. The detail parameters of as-sprayed WC-17Co coatings are listed in Table 1. Spraying powder feeding adopted a scraper powder feeder (Guangzhou Sanxin Metal S & T Co., Ltd., Guangzhou, China).

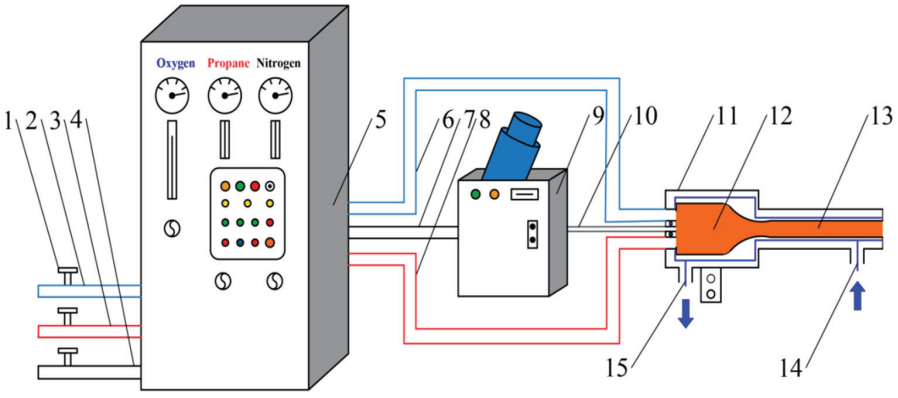

Figure 3. Schematic diagram of HVOF and WS spray system: (1) valve, (2,6) oxygen pipe, (3,8) propane pipe, (4,7) nitrogen pipe, (5) console cabinet, (9) powder feeder, (10) powder feeding pipe, (11) spray gun, (12) flame chamber, (13) spraying tube, (14) cold water inlet, and (15) cold water outlet.

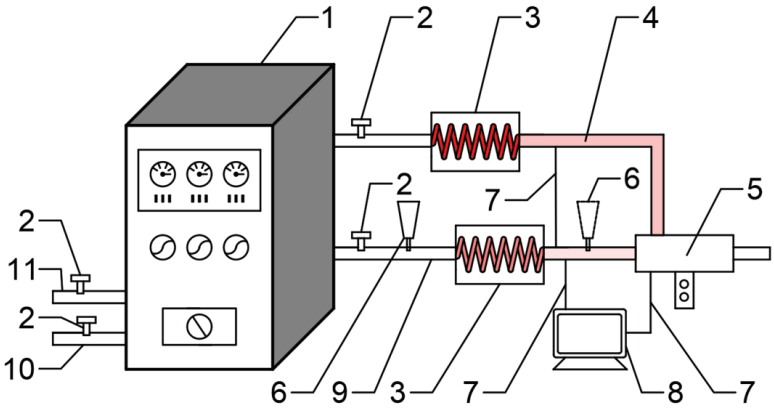

Figure 4. Schematic diagram of cold-spray system: (1) console cabinet, (2) Valve, (3) gas heater, (4) accelerating gas pipe, (5) spray gun, (6) powder feeder, (7) thermal couples, (8) display panel, (9) carrier gas, (10) powder feeder gas inlet, (11) accelerating gas inlet.

Table 1. The detail spraying parameters of as-sprayed WC-17Co coatings.

HVOF Spray	Value	Warm Spray	Value	Cold Spray	Value
Pressure of O_2 /MPa	0.55	Pressure of O_2 /MPa	0.55	Accelerating gas pressure/MPa	2.4
Flow rate of O_2 /L·min^{-1}	543	Flow rate of O_2 /L·min^{-1}	543	Powder-feeding gas pressure/MPa	2.6
Pressure of C_3H_8 /MPa	0.4	Pressure of C_3H_8 /MPa	0.4	Gas temperature in gun chamber/°C	750 ± 30
Flow rate of C_3H_8 /L·min^{-1}	24	Flow rate of C_3H_8 /L·min^{-1}	24		
Pressure of N_2 /MPa	0.6	Pressure of N_2 /MPa	0.6		
Flow rate of N_2 /L·min^{-1}	45	Flow rate of N_2 /L·min^{-1}	450		
Transverse speed of gun/mm·s^{-1}	150	Transverse speed of gun/mm·s^{-1}	100	Transverse speed of gun/mm·s^{-1}	10
Spray distance/mm	200	Spray distance/mm	200	Spray distance/mm	20
Rotation rate/r·min^{-1}	50	Rotation rate/r·min^{-1}	50	Rotation rate/r·min^{-1}	50
coats of powder	20	coats of powder	20	coats of powder	20
Substrate	Q235 steel	Substrate	Q235 steel	Substrate	Q235 steel

2.3. Microhardness, Fracture Toughness and Abrasive Wear

Vickers microhardness tests were performed on the polished cross-section of as-sprayed WC-17Co coatings, and the equipment used included a digital microhardness tester (HXD-1000 TM/LCD, ShanghaiPrecision Instruments Co., Ltd., Shanghai, China) under a load of 2.94 N for a dwell time of 20 s. The average value of ten random measurements was used as the final microhardness. A Vickers indentation technique was used to evaluate the plain strain fracture toughness (i.e., K_{IC}) of as-sprayed WC-17Co coatings at 5 kgf load and 20 s dwell time. Fracture toughness (K_{IC}) was calculated by applying the following equation proposed by Niihara [43]:

$$K_{IC} = 0.0193(H_v d)\left(\frac{E}{H_v}\right)^{2/5}(a)^{-1/2} \quad (1)$$

where, K_{IC} is the fracture toughness, H_v is the Vickers hardness, d is the half-diagonal of the Vickers indentation, E is the elastic modulus, and a is the indentation crack length.

The elastic modulus of the coatings was determined according to the following formula as established in [44]:

$$(\frac{b'}{a'}) = (\frac{b}{a}) - \alpha(\frac{H_v}{E}) \quad (2)$$

where, a and b are the diagonal dimensions of Knoop indenter, a' and b' are the long and short diagonal dimensions measured on residual Knoop indentation impression, α is a constant equal to 0.45, H_v is the Vickers hardness.

The abrasive wear test was carried out by a pin-on-disk method. The detail of the preparation for wear specimens can be found in the literature, namely [45]. The schematic diagram of abrasive wear test was shown in Figure 5. The wear parameters of as-sprayed WC-17Co are listed in Table 2.

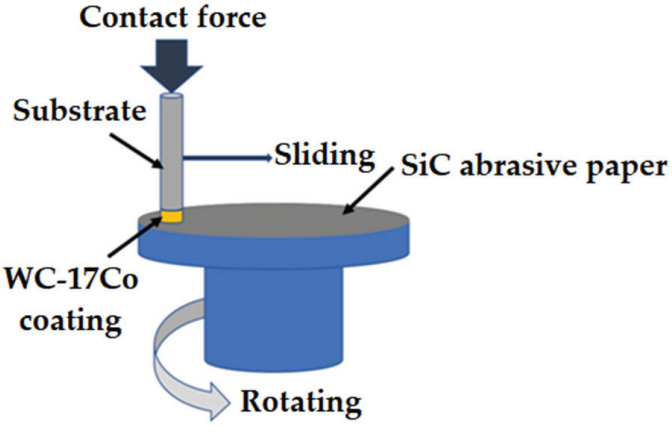

Figure 5. Schematic diagram of abrasive wear test.

Table 2. The wear parameters of as-sprayedWC-17Co coatings.

Wear Parameters	Values
Load/N	10
Rotation speed of the disk/r·min^{-1}	60
Radial feed rate of the pin/mm·r^{-1}	4
Wear distance/m	16
SiC abrasive paper	300 grit size

2.4. Microstructure Characterization of Powders and Coatings

A test involving a scanning electron microscope (SEM; VEGA II-LSU, TESCAN, Brno, Czech Republic) was performed on the samples to characterize the morphologies of feedstock powders, deposited splats, coatings cross-section, and worn surface in backscattering electron (BSE) model. The elemental composition of single WC-17Co splat was analyzed by electron dispersive x-ray spectroscopy (EDS;VEGA II-LSU, TESCAN, Brno, Czech Republic). X-ray diffraction (XRD; Bruker D8 Advance, Karlsruhe, Germany) was conducted for the phase compositions of feedstock powders and as-sprayed coatings with Cu-Kα radiation (λ = 1.5418 Å, 35 kV, and 35 mA) for the scanning range (2θ) of 20–90° with a step of 0.02° and a scanning speed of 10 °/min. Figure 6 shows the XRD patterns of conventional WC-17Co powders. The average porosity and thickness of conventional WC-17Co coatings were calculated by the image-analysis method (Software Image J, vesion 1, National Institutes of Health, Bethesda, MD, USA) with ten SEM micrographs from cross-section morphologies and backscattered electron (BSE) microscopies.

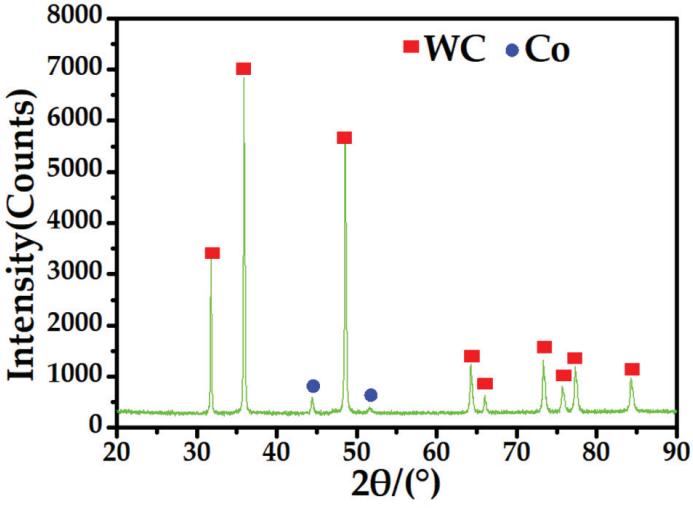

Figure 6. The X-ray diffraction (XRD) patterns of conventional WC-17Co powders.

3. Results and Discussion

3.1. Deposition Behavior of WC-17Co Splats

Figure 7 shows the surface morphologies of the WC-17Co splats deposited in various spraying methods. It can be seen that a WC-17Co splat deposited by HVOF showed a center hump (marked in cyan dot circle in Figure 7a), and some radial splashes (as indicated by the green arrow in Figure 7a) presented at the edge of the splat. Meanwhile, there were also observed some molten areas (as indicated by the yellow arrow in Figure 7a) in the WC-17Co splat, while the WC-17Co splat deposited by WS presented a typical pie shape morphology with no molten areas. However, due to the plastic deformation of the WC-17Co splat, some cracks (as indicated by the black arrow in Figure 7b) occurred on the surface of the splat, and an obvious ripple (as indicated by the orange arrow in Figure 7b) appeared around the splat, contributing to the cooperative deformation of the substrate. The morphology of the WC-17Co splat deposited by CS still remained nearly spherical in shape, which was the same as that of the original feedstock powders. Due to the high-velocity impacting effect of cold-sprayed splat, some cracks (as indicated by the black arrow in Figure 7c) also appeared on the surface of the large cold-sprayed WC-17Co splat. In addition, compared to the analysis results of the warm-sprayed WC-17Co splat, the plastic deformation of the substrate was more severe after cold spraying, more ripple (as indicated by the orange arrow in Figure 7c) and revers (as indicated by the purple arrow in Figure 7c) phenomena appeared around the splat. Moreover, there appeared gaps (as indicated by green arrow in Figure 7c) between the splat and the substrate. Meanwhile, it can be further observed that the embedding depth of the small splat into Q235 steel substrate was deeper than that of the large splat (as shown in Figure 8).

3.2. XRD Patterns of As-Sprayed WC-17Co Coatings

Figure 9 shows the XRD patterns of WC-17Co coatings as-sprayed in various spraying ways. It can be found that, although there was a small amount of W_2C phase in HVOF-sprayed coating, the main phase compositions of all WC-17Co coatings were WC and Co phases. This illustrates that, the decomposition and decarburization of WC could be effectively inhibited by controlling HVOF process parameters; however, the W_2C phase also formed at a certain high-spraying temperature of HVOF. Meanwhile, due to the low temperature effect of WS and CS, the phase compositions of WC-17Co powders were transplanted into warm-sprayed and cold-sprayed coatings [46]. When comparing the warm-sprayed and cold-sprayed coatings to HVOF-sprayed WC-17Co coatings, it also

can be further found that the diffraction peaks of WC and Co of warm-sprayed and cold-sprayed WC-17Co coatings were broader. Lima et al. [47] reported that residual stresses and grain refinement are the main factors that induce the peak broadening, and the residual stress is often caused by high temperatures during spraying. Ji et al. [41] also reported that, in the cold spraying process, grain refinement is the main reason for the peak broadening of WC, and the effect of residual stress is negligible. Therefore, due to the control of the HVOF process parameters for reducing the flame temperature in this study, residual stress had little influence on the WC-17Co coating. Figure 10 shows the full widths at half maximums (FWHMs) of WC and Co diffraction peaks of WC-17Co coatings formed in various spraying ways. It can be found that the FWHMs of WC and Co diffraction peaks of warm-sprayed and cold-sprayed WC-17Co coatings were larger than those of HVOF-sprayed coatings; in addition, those of cold-sprayed WC-17Co coatings were the largest. This illustrates that plastic deformation degree of incident WC-17Co particles with lower spraying temperature, such as warm spraying and cold spraying, was larger than that of WC-17Co particles deposited by HVOF. In addition, due to the high-velocity characteristic of cold spraying, the incident WC-17Co particles could be fragmented to more fine particles after impacting onto Q235 steel substrate or pre-deposited layer. Therefore, the diffraction peaks of WC and Co of cold-sprayed WC-17Co coatings were more broadened than those of warm-sprayed WC-17Co coatings.

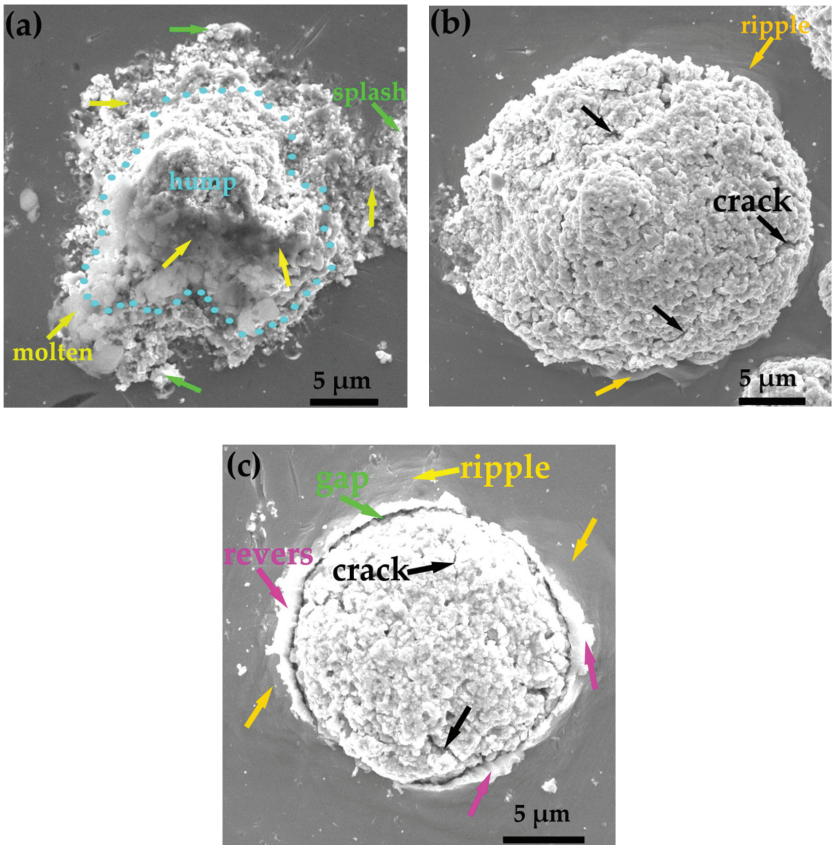

Figure 7. Surface morphologies of WC-17Co splats deposited by various spraying methods (**a**) HVOF, (**b**) WS, (**c**) CS.

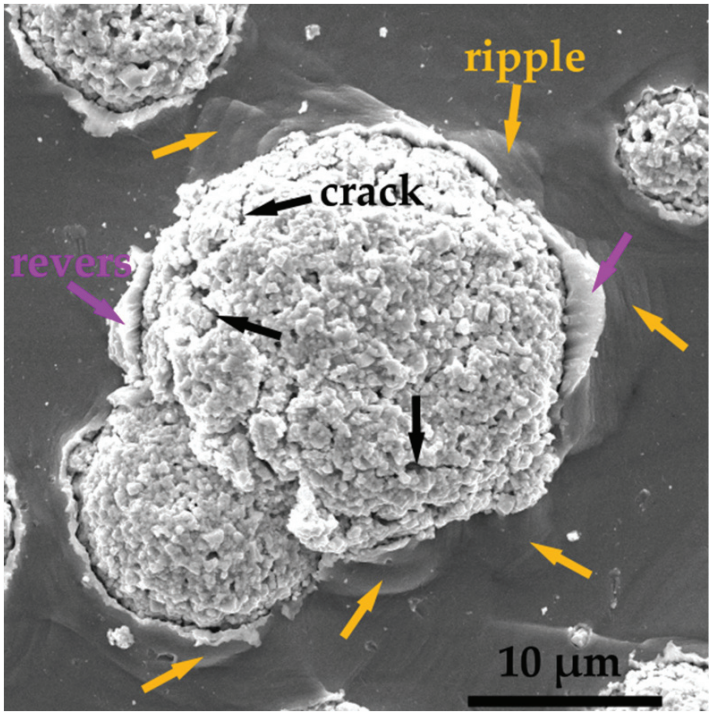

Figure 8. Surface morphologies of different size WC-17Co splats deposited by cold spraying.

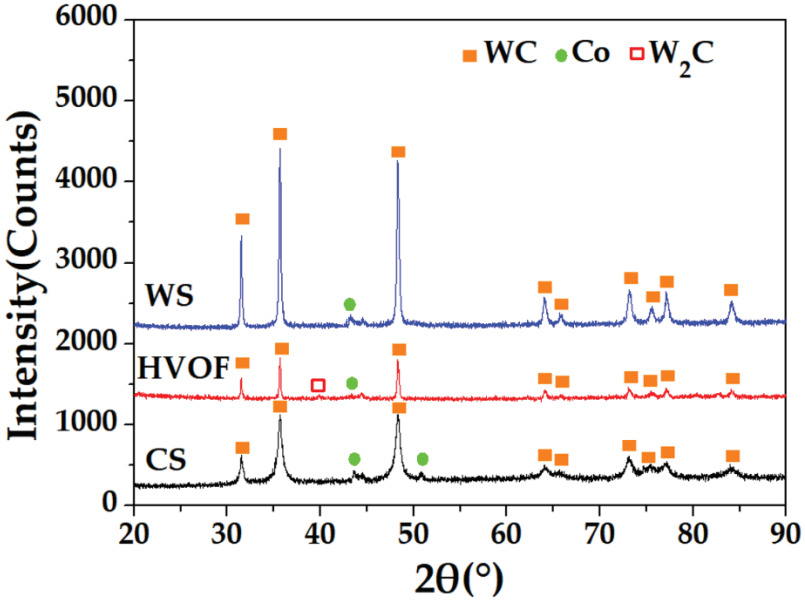

Figure 9. XRD patterns of WC-17Co coatings formed in various spraying ways.

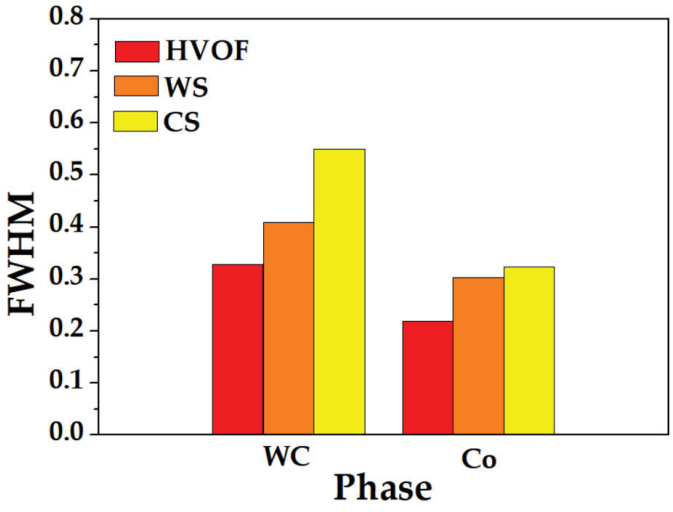

Figure 10. Full widths at half maximum (FWHMs) of WC and Co in WC-17Co coatings formed in various spraying ways.

3.3. Microstructure of As-Sprayed WC-17Co Coatings

Figure 11 shows the cross-section morphologies of WC-17Co coatings formed by various spraying methods. It can be seen that there were no cracks or abscission phenomenons occurred between the coating and substrate (as shown in Figure 11b,d,f). Further analysis of the morphologies of WC-17Co coatings (as shown in Figure 11a,c,e) found that the interface between WC and Co in all WC-17Co coatings was well-bonded. Meanwhile, the content of fine WC particles (as indicated by the red arrow in Figure 11a,c,e) in the cold-sprayed coating was significantly more than the other coatings. The size range of fine WC particles formed in HVOF, WS, and CS was about 0.11–0.16 μm, 0.10–0.13 μm, 0.09–0.12 μm, respectively. It was also further indicated that more fragmented phenomenon of coarse WC particles occurred in the cold-sprayed WC-17Co coatings. These phenomena are consistent with the phase compositions analysis and results of WC-17Co coatings. By measuring the mean porosity and thickness of WC-17Co coatings formed in various spraying ways, it was found that the mean porosity of WC-17Co coatings formed in HVOF, WS, and CS was 1.57%, 0.89%, and 0.058%, respectively (as shown in Figure 12). In general, the microstructure of all coatings is dense; however, the porosity of warm-sprayed and cold-sprayed WC-17Co coatings was lower than that of HVOF-sprayed coating, and the porosity of cold-sprayed coating was the lowest. The main reasons for this phenomenon were attributed to solid-state particles' continuous impact and compaction on the warm-sprayed or cold-sprayed WC-17Co coatings at the lower spraying temperature. Meanwhile, stripe structure (as indicated by the yellow arrow in Figure 11c,e) formed by the slippage of fine WC particles with a plastic flow of Co binder could fill the pores in the warm-sprayed or cold-sprayed WC-17Co coatings [41]. Therefore, due to the cold spraying high-velocity characteristic and more stripe structure in the cold-sprayed coating, the porosity of cold-sprayed WC-17Co coating was the lowest among all the coatings. The mean thickness of WC-17Co coatings formed in HVOF, WS, and CS was 544.33 ± 4.81 μm, 528.75 ± 5.98 μm, and 207.61 ± 9.64 μm, respectively (as shown in Figure 13). Figure 14 shows the morphologies of WC-17Co particles deposited onto Q235 steel substrate surface in various spraying ways. It can be found that craters were formed as the incident particles rebounding from the Q235 steel substrate surface (as indicated by white arrow in Figure 14). The ratio of WC-17Co splats (as indicated by black arrow in Figure 14) adhered on the Q235 steel substrate surface in HVOF, WS, and CS was 54.66%, 50.18%, and 30.12%, respectively. This illustrates that decreasing the spraying temperature resulted in more content of the craters caused by

particles rebounding from the substrate surface. Therefore, this result also revealed that, although the porosity of cold-sprayed WC-17Co coating was the lowest in this study, more rebounding-particles phenomena presented during cold spraying process led to the lowest thickness of the cold-spraying coating among all the coatings.

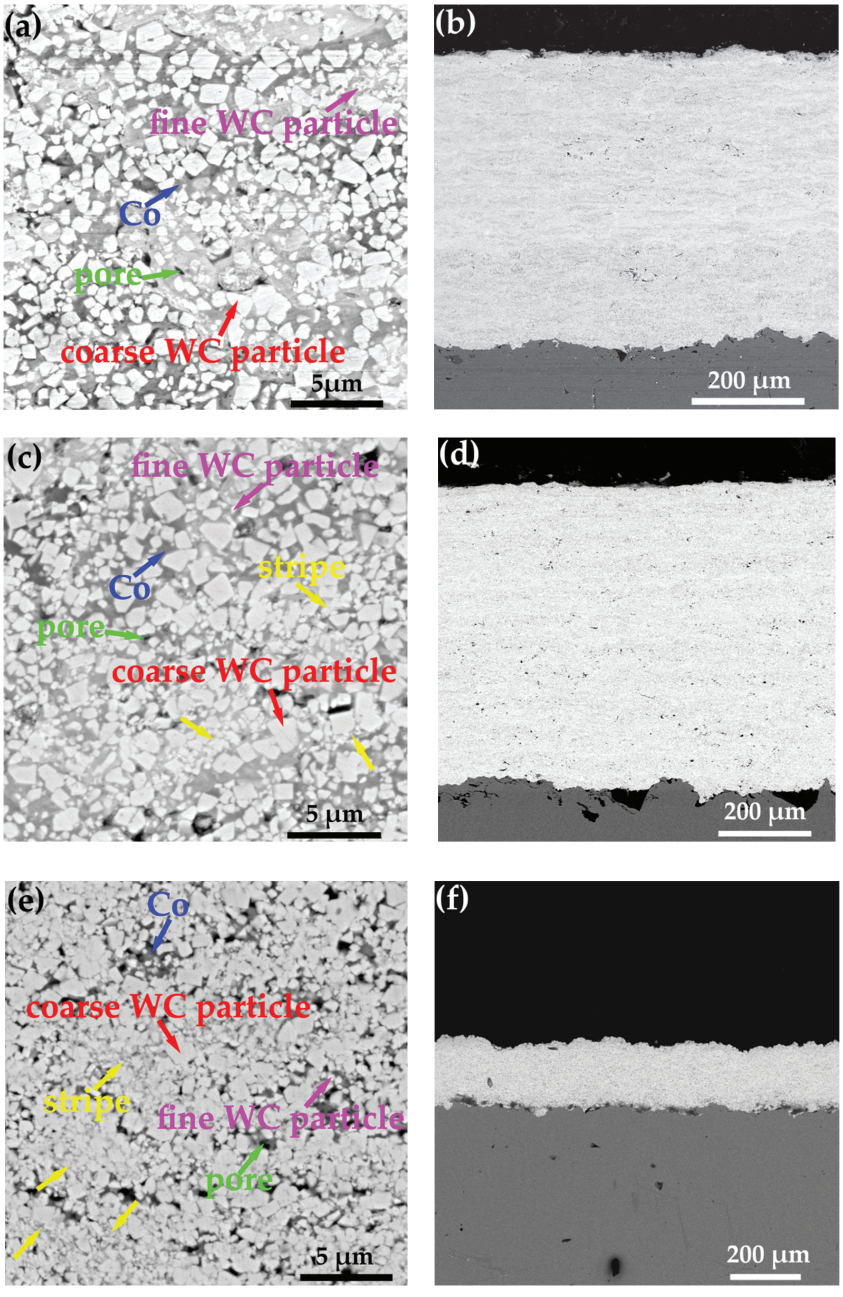

Figure 11. Cross-section morphologies of WC-17Co coatings formed by various spraying methods (**a**,**b**) HVOF, (**c**,**d**) WS, (**e**,**f**) CS.

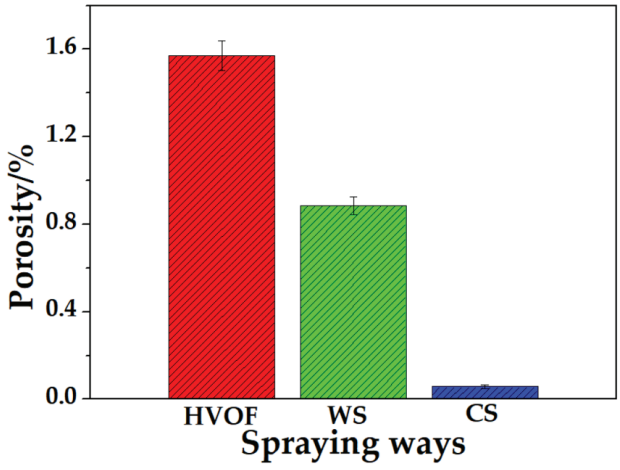

Figure 12. Porosity of WC-17Co coatings formed by various spraying methods.

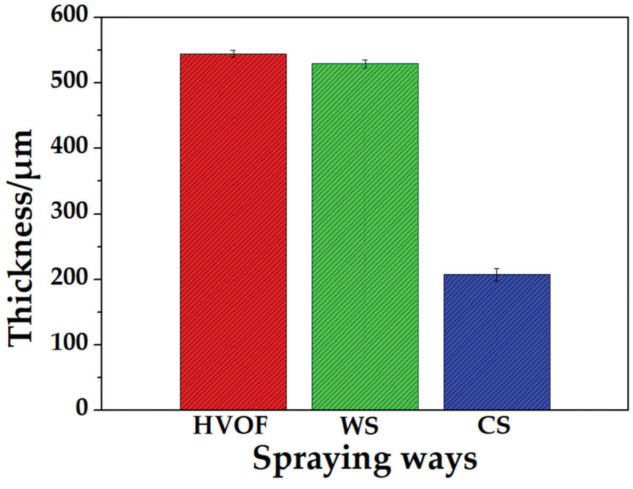

Figure 13. Thickness of WC-17Co coatings formed by various spraying methods.

3.4. Microhardness and Fracture Toughness of As-Sprayed WC-17Co Coatings

The average microhardness of WC-17Co coatings formed in HVOF, WS, and CS was 980.0 ± 17.6 $HV_{0.3}$, 1034.8 ± 57.5 $HV_{0.3}$, and 1136 ± 26.8 $HV_{0.3}$, respectively (as shown in Figure 15). It can be found that the average microhardness of the cold-sprayed WC-17Co coating was the highest among all the coatings. Although the W_2C phase in the coating could affect the hardness significantly [29], the content of W_2C phase was very low in the HVOF-sprayed WC-17Co coating in this study. Hence, the influence of W_2C phase on the hardness in this study was slight. Ji et al. [41] reported that stripe microstructure could enhance the spreading or flattening of WC-Co particles and improve the microstructure and microhardness of the coatings. Wang et al. [42] also reported that high content of nano WC and high density could increase the microhardness of cold-sprayed multimodal WC-12Co coatings. Therefore, combined with the microstructure analysis results of warm-sprayed or cold-sprayed WC-17Co coatings in this study, fine WC particles were formed based on the combined action of particles impacting on the substrate or pre-deposited layer and continuous impacting of incident particles. Meanwhile, a stripe structure was

formed by the slippage of fine WC particles with a plastic flow of Co binder; in particular, a stripe structure was more prevalent in cold-sprayed coatings. Therefore, the average microhardness of cold-sprayed WC-17Co coating was the highest. The average fracture toughness of WC-17Co coatings formed in HVOF, WS, and CS was 8.88 ± 0.31, 10.42 ± 0.28, and 13.18 ± 0.49 MPa·m$^{-1/2}$, respectively (as shown in Figure 16). The Vickers indentation cracks of as-sprayed WC-17Co coatings were shown in Figure 17. Lee et al. [48] reported that decreasing powder size or the mixing ratio of the coarse WC particles could increase the fracture toughness of the coatings. Chen et al. [49] reported that W_2C phase could decrease the fracture toughness of the coating. Therefore, the fracture toughness of cold-sprayed WC-17Co coating was the highest among all the coatings in this study. This also illustrates that the fracture toughness increased with increasing the content of fine WC particles and stripe structure.

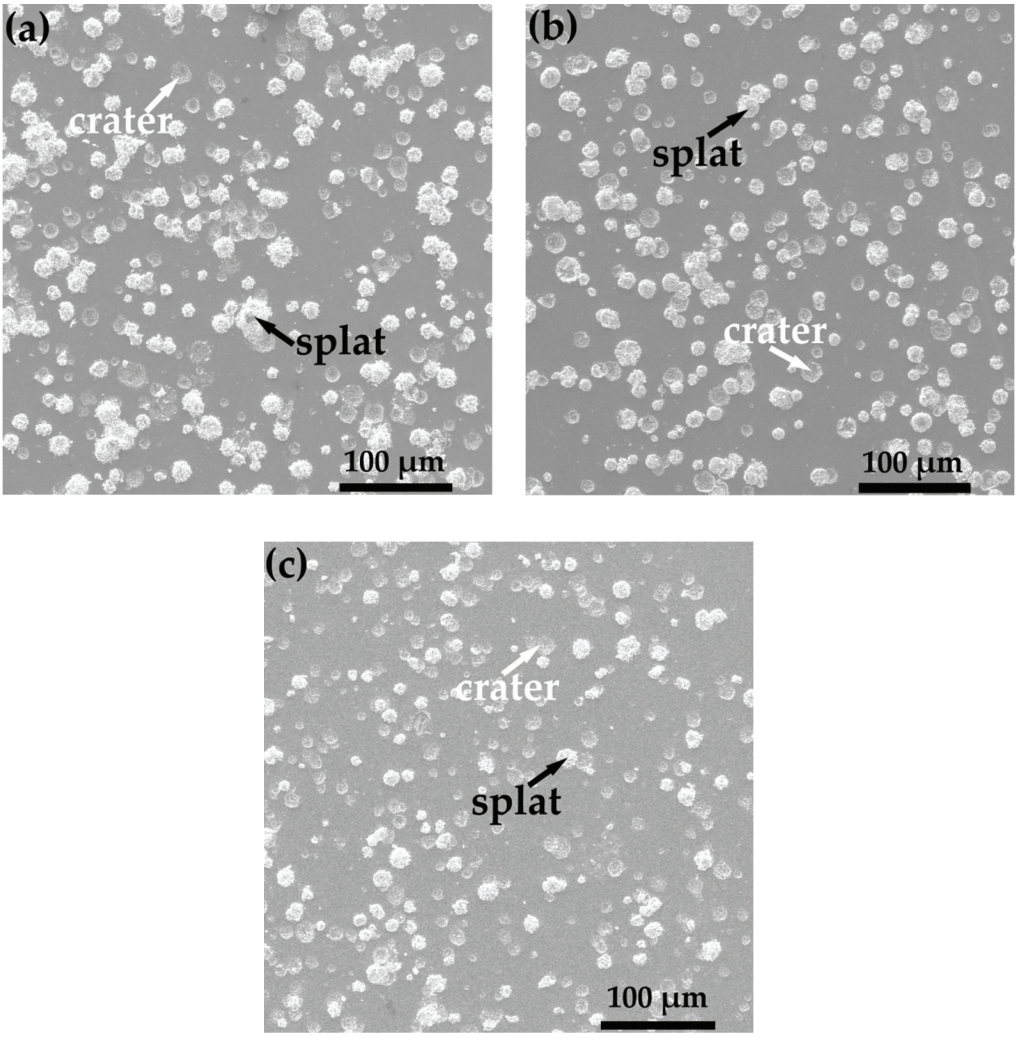

Figure 14. Morphologies of WC-17Co particles deposited onto Q235 steel substrate in various spraying ways (**a**) HVOF, (**b**) WS, (**c**) CS.

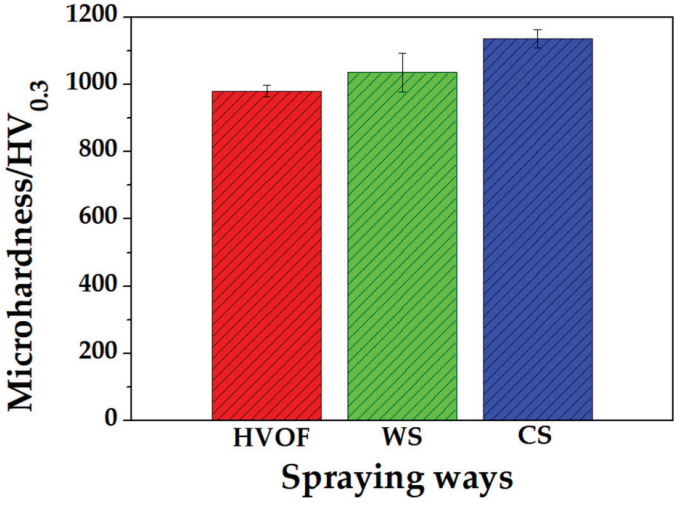

Figure 15. Microhardness of WC-17Co coatings formed by various spraying methods.

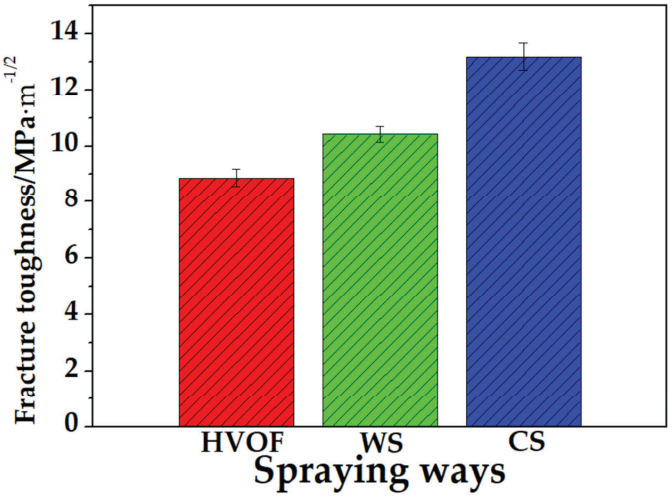

Figure 16. Fracture toughness of WC-17 coatings formed by various spraying methods.

3.5. Abrasive Wear of As-Sprayed WC-17Co Coatings and Q235 Steel

The worn surface morphologies of WC-17Co coatings formed in various spraying ways and Q235 steel substrate were shown in Figure 18. It can be seen that the main wear mechanism of all coatings was the groove (as indicated by the cyan arrow in Figure 18a,c,e) and some peel-offs (as indicated by the white arrow in Figure 18a,c,e), but the worn surface of Q235 steel was only wide and deep groove (as indicated by the cyan arrow in Figure 18g). The main reasons for the peel-off phenomenon in this study were that the crack formation (as indicated by the black arrow in Figure 18a) caused by the fracture of coarse WC particles resulted in WC particles pulled-out from the worn surface, or the exposed WC particles peeled off due to the poor bonding between WC particle and Co binder after the removal of soft Co matrix. Furthermore, in contrast to HVOF sprayed and warm-sprayed WC-17Co coatings, the grooves of cold-sprayed coating were smoother and shallower (as shown in Figure 18f). The reason for this phenomenon was that, according to the microstructure

analysis of the cold-sprayed WC-17Co coating (as shown in Figure 11e), more fine WC particles and stripe structures presented in cold-sprayed WC-17Co coatings; fine WC particles uniformly distributed into the Co binder phase, resulting in an increase in the wear resistance of the coating. Figure 19 shows the average weight loss of WC-17 coatings formed in various spraying ways and Q235 steel substrate. The average weight loss of WC-17Co coatings formed in HVOF, WS, and CS was 8.15 ± 0.31 mg, 5.31 ± 0.32 mg, and 4.05 ± 0.41 mg, respectively. This also illustrates that combining with the results analysis of the microstructure, mechanical properties, and worn surface morphologies of the coatings, the cold-sprayed WC-17Co coating presented the lowest wear loss among all the coatings. However, the average weight loss of Q235 steel substrate was 21.77 ± 0.25 mg, which was more than 5 times that of the cold-sprayed WC-17Co coating.

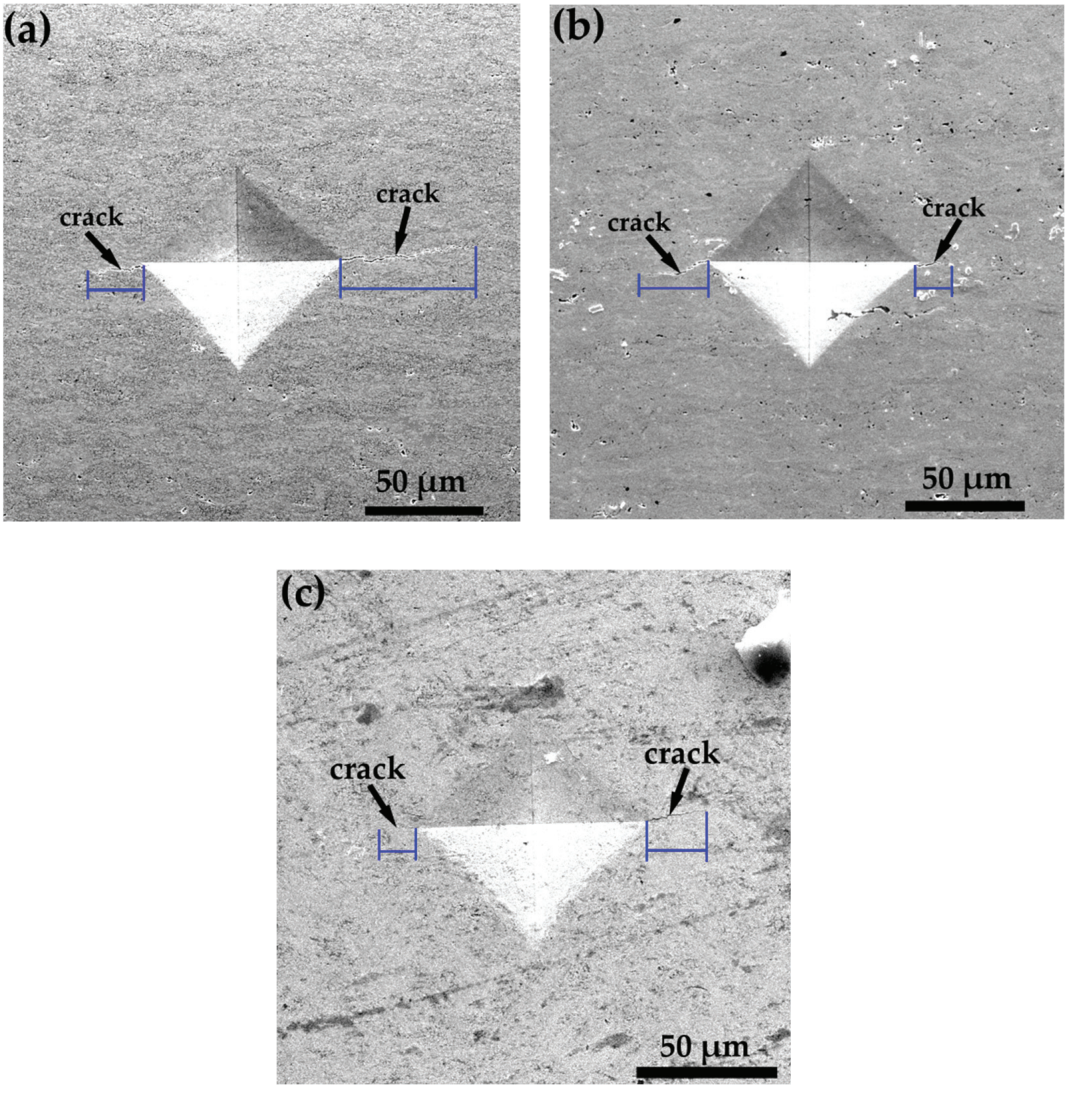

Figure 17. Vickers indentation morphologies of WC-17 coatings formed in various spraying ways (**a**) HVOF, (**b**) WS, (**c**) CS.

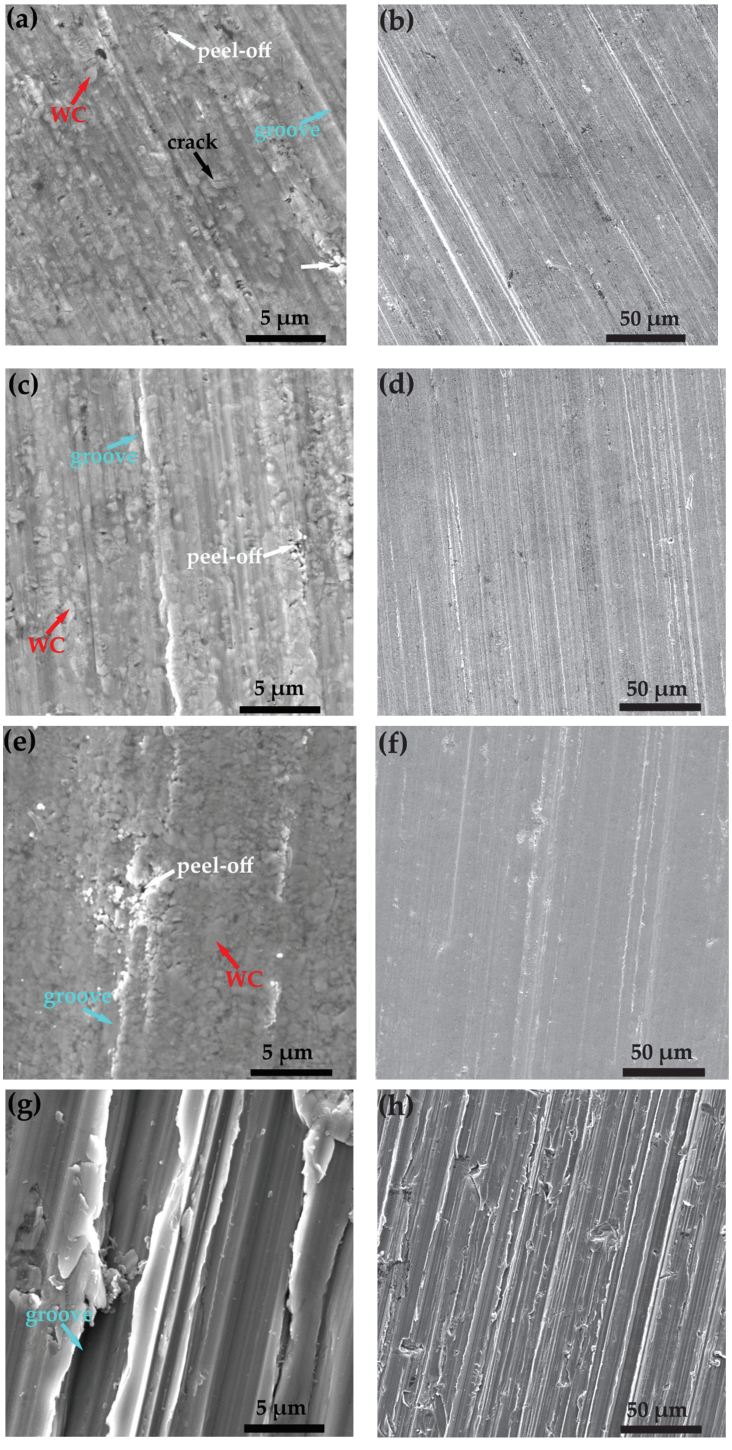

Figure 18. Worn surface morphologies of WC-17 coatings formed by various spraying methods and Q235 steel substrate (**a**,**b**) HVOF, (**c**,**d**) WS, (**e**,**f**) CS, (**g**,**h**) Q235 steel substrate.

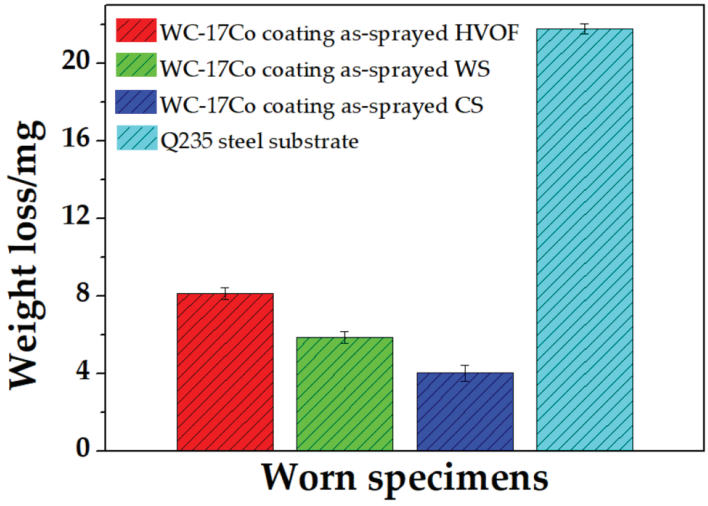

Figure 19. Weight loss of WC-17 coatings formed by various spraying methods and Q235 steel substrate.

4. Conclusions

Conventional WC-17Co powder was deposited onto Q235 steel substrate by various spraying methods to form different WC-17Co coatings. The deposition behavior of single WC-17Co particles, as well as the comparison of microstructure, microhardness, fracture toughness and abrasive wear of as-sprayed WC-17Co coatings, were investigated in this study. The main conclusions are as follows:

I. In comparison to the WC-17Co splat deposited by HVOF and WS, the WC-17Co splat deposited by CS remained nearly spherical shape, and the embedding depth of the small particle into Q235 steel substrate was deeper than that of large splat. Due to the high-velocity impacting effect of cold-sprayed splat, the plastic deformation of the substrate was severe with more ripple and revers.

II. Although there was a small amount of W_2C phase in HVOF-sprayed coating, the main phase compositions of all the WC-17Co coatings were WC and Co phases. By comparing with HVOF-sprayed WC-17Co coating, the diffraction peaks of WC and Co of warm-sprayed and cold-sprayed WC-17Co coatings were broadened. By measuring the full widths at half maximums (FWHMs) of WC and Co diffraction peaks of WC-17Co coatings formed in various spraying ways, the FWHMs of WC and Co diffraction peaks of warm-sprayed and cold-sprayed WC-17Co coatings were larger than those of HVOF-sprayed coatings; moreover, those of the cold-sprayed WC-17Co coatings were the largest.

III. Due to the fragment of coarse WC particles, fine WC particles were observed in the coatings; in particular, the content of fine WC particles in the cold-sprayed coating was the highest. The size range of fine WC particles formed in HVOF, WS, and CS was about 0.110.16 μm, 0.10–0.13 μm, 0.09–0.12 μm, respectively. Due to the cold spraying high-velocity characteristic and more stripe structures in the cold-sprayed coating, the microstructure of the cold-sprayed coating was denser than the other coatings. The mean porosity of WC-17Co coatings formed in HVOF, WS, and CS was 1.57%, 0.89%, and 0.058%, respectively. The mean thickness of the WC-17Co coatings formed in HVOF, WS, and CS was 544.33 ± 4.81 μm, 528.75 ± 5.98 μm, and 207.61 ± 9.64 μm, respectively.

IV. The average microhardness of the WC-17Co coatings formed in HVOF, WS, and CS was 980.0 ± 17.6 $HV_{0.3}$, 1034.8 ± 57.5 $HV_{0.3}$, and 1136 ± 26.8 $HV_{0.3}$, respectively. The

average fracture toughness of WC-17Co coatings formed in HVOF, WS, and CS was 8.88 ± 0.31, 10.42 ± 0.28, and 13.18 ± 0.49 MPa·m$^{-1/2}$, respectively.

V. The main wear mechanism of all coatings was the groove and some peel-offs. The average weight loss of the WC-17Co coatings formed in HVOF, WS, and CS was 8.15 ± 0.31 mg, 5.31 ± 0.32 mg, and 4.05 ± 0.41 mg, respectively. However, the average weight loss of Q235 steel was 21.77 ± 0.25 mg, which was more than 5 times that of the cold-sprayed WC-17Co coating.

Author Contributions: Conceptualization, X.C.; Methodology, X.C. and C.L.; Software, Q.G.; Validation, X.C. and X.D.; Formal Analysis, X.C.; Investigation, H.L.; Resources, X.C.; Data Curation, X.C. and H.L.; Writing—Original Draft Preparation, X.C.; Writing—Review and Editing, C.L.; Visualization, Q.G.; Supervision, X.D.; Project Administration, X.C.; Funding Acquisition, X.C. All authors have read and agreed to the published version of the manuscript.

Funding: This research was funded by National Science Foundation of China, grant number 52161018, the Science and Technology Project of Jiangxi Educational Bureau, grant number GJJ191068, GJJ212304, GJJ212307, and the Science Technology Project of Jiujiang City, grant number [2015] No.64.

Institutional Review Board Statement: Not applicable.

Informed Consent Statement: Not applicable.

Data Availability Statement: Not applicable.

Conflicts of Interest: The authors declare no conflict of interest.

References

1. Magnani, M.; Suegama, P.H.; Espallargas, N. Influence of HVOF parameters on the corrosion and wear resistance of WC-Co coatings sprayed on AA7050 T7. *Surf. Coat. Technol.* **2008**, *202*, 4746–4757. [CrossRef]
2. Katiyar, P.K.; Singh, P.K.; Singh, R.; Kumar, A. Modes of failure of cemented tungsten carbide tool bits (WC/Co): A study of wear parts. *Int. J. Refract. Met. Hard Mater.* **2016**, *54*, 27–38. [CrossRef]
3. Ding, Z.; Chen, W.; Wang, C. Resistance of cavitation erosion of multimodal WC-12Co coatings sprayed by HVOF. *Trans. Nonferrous Met. Soc. China* **2011**, *21*, 2231–2236. [CrossRef]
4. Ma, N.; Cheng, Z.X.; Wu, H.T.; Ye, F.X. Effects of structure of feedstock powders on the microstructure and properties of HVOF sprayed WC-Co coatings. *Rare Met. Mat. Eng.* **2015**, *44*, 3219–3223.
5. Sahraoui, T.; Fenineche, N.E.; Montavon, G.; Coddet, C. Alternative to chromium: Characteristics and wear behavior of HVOF coatings for gas turbine shafts repair (heavy-duty). *J. Mater. Process. Technol.* **2004**, *152*, 43–55. [CrossRef]
6. Ghadami, F.; Sohi, M.H.; Ghadami, S. Effect of TIG surface melting on structure and wear properties of air plasma-sprayed WC-Co coatings. *Surf. Coat. Technol.* **2015**, *261*, 108–113. [CrossRef]
7. Balamurugan, G.M.; Duraiselvam, M.; Anandakrishnan, V. Comparison of high temperature wear behaviour of plasma sprayed WC-Co coated and hard chromium plated AISI 304 austenitic stainless steel. *Mater. Des.* **2012**, *35*, 640–646. [CrossRef]
8. Bonache, V.; Salvador, M.D.; García, J.C.; Sánchez, E.; Bannier, E. Influence of plasma intensity on wear and erosion resistance of conventional and nanometric WC-Co coatings deposited by APS. *J. Therm. Spray Technol.* **2011**, *20*, 549–559. [CrossRef]
9. Chen, H.; Gou, G.Q.; Tu, M.J.; Liu, Y. Research on the friction and wear behavior at elevated temperature of plasma-sprayed nanostructured WC-Co coatings. *J. Mater. Eng. Perform.* **2010**, *19*, 1–6. [CrossRef]
10. Zhan, Q.; Yu, L.G.; Ye, F.X.; Xue, Q.J.; Li, H. Quantitative evaluation of the decarburization and microstructure evolution of WC-Co during plasma spraying. *Surf. Coat. Technol.* **2012**, *206*, 4068–4074. [CrossRef]
11. Wood, R.J.K. Tribology of thermal sprayed WC-Co coatings. In special issue: Tribology of Hard Coatings. *Int. J. Refract. Met. Hard Mater.* **2009**, *28*, 82–94. [CrossRef]
12. Fedrizzi, L.; Valentinelli, L.; Rossi, S.; Segna, S. Tribocorrosion behaviour of HVOF cermet coatings. *Corros. Sci.* **2007**, *49*, 2781–2799. [CrossRef]
13. Ding, X.; Ke, D.; Yuan, C.Q.; Ding, Z.X.; Cheng, X.D. Microstructure and cavitation erosion resistance of HVOF deposited WC-Co coatings with different size WC. *Coatings* **2018**, *8*, 307. [CrossRef]
14. Mi, P.B.; Zhao, H.J.; Wang, T.; Ye, F.X. Sliding wear behavior of HVOF sprayed WC-(nano-WC-Co) coating at elevated temperatures. *Mater. Chem. Phys.* **2018**, *206*, 1–6. [CrossRef]
15. Shipway, P.H.; McCartney, D.G.; Sudaprasert, T. Sliding wear behaviour of conventional and nanostructured HVOF sprayed WC-Co coatings. *Wear* **2005**, *259*, 820–827. [CrossRef]
16. Cho, T.Y.; Yoon, J.H.; Kim, K.S.; Song, K.O.; Joo, Y.K.; Fang, W.; Zhang, S.H.; Youn, S.J.; Chun, H.G.; Hwang, S.Y. A study on HVOF coatings of micron and nano WC-Co powders. *Surf. Coat. Technol.* **2008**, *202*, 5556–5559. [CrossRef]

17. Guilemany, J.M.; Dosta, S.; Miguel, J.R. The enhancement of the properties of WC-Co HVOF coatings through the use of nanostructured and microstructured feedstock powders. *Surf. Coat. Technol.* **2006**, *201*, 1180–1190. [CrossRef]
18. Baumann, I.; Hagen, L.; Tillmann, W.; Hollingsworth, P.; Stangier, D.; Schmidtmann, G.; Tolan, M.; Paulus, M.; Sternemann, C. Process characteristics, particle behavior and coating properties during HVOF spraying of conventional, fine and nanostructured WC-12Co powders. *Surf. Coat. Technol.* **2021**, *405*, 126716. [CrossRef]
19. Mi, P.B.; Ye, F.X. Structure and wear performance of the atmospheric heat-treated HVOF sprayed bimodal WC-Co coating. *Int. J. Refract. Met. Hard Mater.* **2018**, *76*, 185–191. [CrossRef]
20. Ribu, D.C.; Rajesh, R.; Thirumalaikumarasamy, D.; Kaladgi, R.A.; Saleel, A.C.; Nisar, S.K.; Shaik, S.; Afzal, A. Experimental investigation of erosion corrosion performance and slurry erosion mechanism of HVOF sprayed WC-10Co coatings using design of experiment approach. *J. Mater. Res. Technol.* **2022**, *18*, 293–314. [CrossRef]
21. Kuroda, S.; Watanabe, M.; Kim, K.; Katanoda, H. Current status and future prospects of warm spray technology. *J. Therm. Spray Technol.* **2011**, *20*, 653–676. [CrossRef]
22. Watanabe, M.; Brauns, C.; Komatsu, M.; Kuroda, S.; Gärtner, F.; Klassen, T.; Katanoda, H. Effect of nitrogen flow rate on microstructures and mechanical properties of metallic coatings by warm spray deposition. *Surf. Coat. Technol.* **2013**, *232*, 587–599. [CrossRef]
23. Kawakita, J.; Kuroda, S.; Fukushima, T.; Katanoda, H.; Matsuo, K.; Fukanuma, H. Dense titanium coatings by modified HVOF spraying. *Surf. Coat. Technol.* **2006**, *201*, 1250–1255. [CrossRef]
24. He, D.; Kusano, M.; Watanabe, M. Detecting the defects of warm-sprayed Ti-6Al-4V coating using Eddy current testing method. *NDT E Int.* **2022**, *125*, 102565. [CrossRef]
25. Yao, H.L.; Ji, G.C.; Chen, Q.Y.; Bai, X.B.; Zou, Y.L.; Wang, H.T. Microstructures and properties of warm-sprayed carbonated hydroxyapatite coatings. *J. Therm. Spray Technol.* **2018**, *27*, 924–937. [CrossRef]
26. Ji, G.C.; Zou, Y.L.; Chen, Q.Y.; Yao, H.L.; Bai, X.B.; Yang, C.; Wang, H.T.; Wang, F. Mechanical properties of warm sprayed HATi bio-ceramic composite coatings. *Ceram. Int.* **2020**, *46*, 27021–27030. [CrossRef]
27. Sienkiewicz, J.; Kuroda, S.; Murakami, H.; Araki, H.; Giżyński, M.; Kurzydłowski, K.J. Fabrication and oxidation resistance of TiAl matrix coatings reinforced with silicide precipitates produced by heat treatment of warm sprayed coatings. *J. Therm. Spray Technol.* **2018**, *27*, 1165–1176. [CrossRef]
28. Chivavibul, P.; Watanabe, M.; Kuroda, S.; Kawakita, J.; Komatsu, M.; Sato, K.; Kitamura, J. Effect of powder characteristics on properties of warm-sprayed WC-Co coatings. *J. Therm. Spray Technol.* **2010**, *19*, 81–88. [CrossRef]
29. Chivavibul, P.; Watanabe, M.; Kuroda, S.; Kawakita, J.; Komatsu, M.; Sato, K.; Kitamura, J. Development of WC-Co coatings deposited by warm spray process. *J. Therm. Spray Technol.* **2008**, *17*, 750–756. [CrossRef]
30. Wesmann, J.A.R.; Espallargas, N. Elucidating the complex role of surface oxides formed during sliding of self-mated warm sprayed WC-CoCr in different environments. *Tribol. Int.* **2016**, *94*, 360–372. [CrossRef]
31. Watanabe, M.; Komatsu, M.; Kuroda, S. Multilayered WC-Co/Cu coatings by warm spray deposition. *Surf. Coat. Technol.* **2011**, *205*, 5358–5368. [CrossRef]
32. Watanabe, M.; Komatsu, M.; Kuroda, S. WC-Co/Al multilayer coatings by warm spray deposition. *J. Therm. Spray Technol.* **2012**, *21*, 597–608. [CrossRef]
33. Li, W.Y.; Cao, C.C.; Yin, S. Solid-state cold spraying of Ti and its alloys: A literature review. *Prog. Mater. Sci.* **2020**, *110*, 100633. [CrossRef]
34. Couto, M.; Dosta, S.; Torrell, M.; Fernández, J.; Guilemany, J.M. Cold spray deposition of WC-17 and 12Co cermets onto aluminum. *Surf. Coat. Technol.* **2013**, *235*, 54–61. [CrossRef]
35. Yin, S.; Ekoi, E.J.; Lupton, T.L.; Dowling, D.P.; Lupoi, R. Cold spraying of WC-Co-Ni coatings using porous WC-17Co powders: Formation mechanism, microstructure characterization and tribological performance. *Mater. Des.* **2017**, *126*, 305–313. [CrossRef]
36. Suo, X.; Yin, S.; Li, H.; Lupoi, R. Numerical and experimental investigation on bonding behavior of cold sprayed porous WC-17Co particles onto different substrates. *Coatings* **2018**, *8*, 367. [CrossRef]
37. Ang, A.S.M.; Berndt, C.C.; Cheang, P. Deposition effects of WC particle size on cold sprayed WC-Co coatings. *Surf. Coat. Technol.* **2011**, *205*, 3260–3267. [CrossRef]
38. Li, C.J.; Yang, G.J.; Gao, P.H.; Ma, J.; Wang, Y.Y.; Li, C.X. Characterization of nanostructured WC-Co deposited by cold spraying. *J. Therm. Spray Technol.* **2007**, *16*, 1011–1020. [CrossRef]
39. Gao, P.H.; Li, C.J.; Yang, G.J.; Li, Y.G.; Li, C.X. Influence of substrate hardness transition on built-up of nanostructured WC-12Co by cold spraying. *Appl. Surf. Sci.* **2010**, *256*, 2263–2268. [CrossRef]
40. Yang, G.J.; Gao, P.H.; Li, C.X.; Li, C.J. Mechanical property and wear performance dependence on processing condition for cold-sprayed WC-(nanoWC-Co). *Appl. Surf. Sci.* **2015**, *332*, 80–88. [CrossRef]
41. Ji, G.C.; Wang, H.T.; Chen, X.; Bai, X.B.; Dong, Z.X.; Yang, F.G. Characterization of cold-sprayed multimodal WC-12Co coating. *Surf. Coat. Technol.* **2013**, *235*, 536–543. [CrossRef]
42. Wang, H.T.; Chen, X.; Bai, X.B.; Ji, G.C.; Dong, Z.X.; Yi, D.L. Microstructure and properties of cold sprayed multimodal WC-17Co deposits. *Int. J. Refract. Met. Hard Mater.* **2014**, *45*, 196–203. [CrossRef]
43. Niihara, K.; Morena, R.; Hasselman, D.P.H. Evaluation of K_{IC} of brittle solids by the indentation method with low crack-to-indent ratios. *J. Mater. Sci. Lett.* **1982**, *1*, 13–16. [CrossRef]

44. Marshall, D.B.; Noma, T.; Evans, A.G. A simple method for determining elastic-modulus-to-hardness ratios using Knoop indentation measurements. *J. Am. Ceram. Soc.* **1982**, *65*, 175–176. [CrossRef]
45. Chen, X.; Wang, H.T.; Ji, G.C.; Bai, X.B.; Fu, W. Microstructure and properties of TiB_2-Ni coatings with different binder phase contents deposited by HVOF spray process. *Rare Met.* **2015**, *41*, 1385–1393. [CrossRef]
46. Li, W.Y.; Jiang, R.R.; Huang, C.J.; Zhang, Z.H.; Feng, Y. Effect of cold sprayed Al coating on mechanical property and corrosion behavior of friction stir welded AA2024-T351 joint. *Mater. Des.* **2015**, *65*, 757–761. [CrossRef]
47. Lima, R.S.; Karthikeyan, J.; Kay, C.M.; Lindemann, J.; Berndt, C.C. Microstrucrural characteristics of cold-sprayed nanostructured WC-Co coatings. *Thin Solid Films.* **2002**, *416*, 129–135. [CrossRef]
48. Lee, C.W.; Han, J.H.; Yoon, J.; Shin, M.C.; Kwun, S.I. A study on powder mixing for high fracture toughness and wear resistance of WC-Co-Cr coatings sprayed by HVOF. *Surf. Coat. Technol.* **2010**, *204*, 2223–2229. [CrossRef]
49. Chen, C.; Guo, Z.X.; Li, S.H.; Xiao, Y.; Chai, B.B.; Liu, J.B. Microstructure and properties of WC-17Co cermets prepared using different processing routes. *Ceram. Int.* **2019**, *45*, 9203–9210. [CrossRef]

coatings

MDPI

Article

Fabrication of Highly Transparent Y_2O_3 Ceramics via Colloidal Processing Using ZrO_2-Coated Y_2O_3 Nanoparticles

Zhongchao Fu [1,*], Nan Wu [1], Haibo Long [1], Jianming Wang [2], Jun Zhang [3], Zhaoxia Hou [1], Xiaodong Li [4] and Xudong Sun [4]

[1] Liaoning Province Key Laboratory of Micro-Nano Materials Research and Development, School of Mechanical Engineering, Shenyang University, Shenyang 110044, China; wunan20102010@163.com (N.W.); flydragon0109@163.com (H.L.); luckyxia2007@126.com (Z.H.)
[2] Liaoning Key Laboratory of Advanced Materials Preparation Technology, School of Mechanical Engineering, Shenyang University, Shenyang 110044, China; wjmlucky1979@163.com
[3] Key Laboratory of Research and Application of Multiple Hard Films, College of Mechanical Engineering, Shenyang University, Shenyang 110044, China; zhjun88@126.com
[4] Key Laboratory for Anisotropy and Texture of Materials (Ministry of Education), Northeastern University, Shenyang 110819, China; xdli@mail.neu.edu.cn (X.L.); xdsun@mail.neu.edu.cn (X.S.)
* Correspondence: zhongchaofu@syu.edu.cn; Tel.: +86-024-6226-9467

Abstract: An easy approach is described for the preparation of ZrO_2-coated Y_2O_3 nanopowder from a solution of zirconium nitrate with commercial Y_2O_3 nanopowder. The evolution process of the ZrO_2 coating layer upon calcination, such as the phase and microstructure of the particles' surface, was studied. Calcination of the powder at 700 °C resulted in ZrO_2-coated Y_2O_3 nanopowder. The rheological properties of the suspensions of ZrO_2-coated Y_2O_3 powders were studied. A well-dispersed suspension with a solid loading of 35.0 vol% using ZrO_2-coated Y_2O_3 nanopowder was obtained. The consolidated green body obtained by the centrifugal casting method showed improved homogeneity with a relative density of 50.2%. Transparent ceramic with high transparency and an average grain size of 1.7 μm was obtained by presintering at 1500 °C for 16 h in air, followed by post-HIP at 1550 °C for 2 h under 200 MPa pressure. The in-line transmittance at the wavelength of 1100 nm (1.0 mm thick) reached 81.4%, close to the theoretical transmittance of Y_2O_3 crystal.

Keywords: Y_2O_3; ZrO_2; transparent ceramics; colloidal processing; nanopowders

Citation: Fu, Z.; Wu, N.; Long, H.; Wang, J.; Zhang, J.; Hou, Z.; Li, X.; Sun, X. Fabrication of Highly Transparent Y_2O_3 Ceramics via Colloidal Processing Using ZrO_2-Coated Y_2O_3 Nanoparticles. *Coatings* **2022**, *12*, 1077. https://doi.org/10.3390/coatings12081077

Academic Editor: Csaba Balázsi

Received: 1 July 2022
Accepted: 28 July 2022
Published: 30 July 2022

1. Introduction

Transparent yttria (Y_2O_3) is one of the most promising materials for application in high-power lasers [1], heat-resistive transparent windows [2], high-temperature refractories, and semiconductor devices [3], owing to its broad wavelength range of transparency (0.2–8.0 μm), high corrosion resistance, high melting point (2430 °C), high thermal conductivity, low phonon energy, and easy doping of rare-earth activator ions with a band gap energy of 6.3 eV [4]. To achieve fully densified ceramics with desired optical properties, fabrication of polycrystalline Y_2O_3 ceramics requires careful control of each step of ceramic processing, including powder synthesis, consolidation, and sintering. Simultaneously, each step has a direct impact on the following step.

By utilization of Y_2O_3 powder produced via established synthesis routes or directly using commercial powder, sintering methods and mechanisms have been mostly studied by researchers recently [5–9]. Typically, transparent Y_2O_3 ceramics can be sintered by pressure-assisted sintering processes such as spark plasma sintering (SPS) [5], hot pressing (HP) [6], and hot isostatic pressing (HIP) [7]. Pressureless sintering methods, such as vacuum sintering [10] and hydrogen atmosphere sintering [11], are also effective. Moreover, the HIP sintering method utilizes three-dimensional gas pressure to presintered bodies that are in the final stage of sintering, which is much more effective to eliminate pores compared

to other sintering methods. Presintering in air followed by HIP treatment possesses more advantages than traditional vacuum presintering plus HIP treatment, including energy-saving, low cost, and efficient process without annealing [12]. On the other hand, fully dense Y_2O_3 ceramics can be obtained using ZrO_2 as sintering additives, which can decrease the grain boundary mobility, leading to Y_2O_3 ceramics with a fully dense fine microstructure and high optical properties [13]. According to the published literature, fabrication of highly transparent ceramics has mainly been achieved by vacuum presintering plus HIP treatment, which requires high-cost equipment and a long annealing process. Compared with vacuum presintering, presintering in air is a low-cost and efficient process without annealing. In 2015, Wang et al. [7] fabricated transparent Y_2O_3 ceramics through air presintering at 1550 °C plus HIPing at 1600 °C for 3 h. The in-line transmittance of the ceramic was 81.7% at 1064 nm, and the thickness of the sample was 1.0 mm. In 2016, Liu et al. [8] also reported transparent Y_2O_3 ceramics by air presintering plus HIPing. However, the sample only showed an IR transmittance of 83.0% in the 3.0 to 5.0 μm wavelength region

It is well known that colloidal processing has exhibited advantages over traditional dry pressing by producing green compacts with a homogenous microstructure, high relative density, and more versatile geometrical options [14–16]. There are, however, to the best of our knowledge, relatively few studies devoted to the colloidal processing of Y_2O_3 green bodies. Y_2O_3 powders are highly reactive in aqueous medium. Dissolving ions, including Y^{3+}, $Y(OH)^{2+}$, and $Y_2(OH)_2^{4+}$, which can suppress the electrical double layer, is the most critical challenge in preparing long-term well-dispersed suspensions with high solids loading [17–20]. In order to inhibit the hydrolysis issue of Y_2O_3 during colloidal processing, in 2014, Sun et al. [20] coated Y_2O_3 powder by a nucleophilic addition reaction between polyurethane and tetraethylene pentamine. In 2017, Xu et al. [21] prepared Y_2O_3 suspensions using alcohol as the dispersion medium. However, the boiling point of ethanol was as low as 78 °C, and the consolidated green compacts were easy to crack during the drying process. Until now, the solid loading of Y_2O_3 suspensions reported in previous literature has generally been in the range of 20 vol%–30.0 vol%, which is much lower than other oxide materials [19,21,22]. It has been found that coating is an effective method to alter the surface properties of the particles and is feasible to improve the stability and dispersity of the core material during colloidal processing [23,24]. Notably, several studies have shown that ZrO_2 possesses much higher inertness in aqueous suspension compared to Y_2O_3 [25,26]. In our previous research [10], particles consisting of a Y_2O_3 core coated with ZrO_2 were developed via the precipitation method by taking dual advantages of ZrO_2 as particle surface passivator and sintering aid, and high-transparency ZrO_2 doped Y_2O_3 ceramic was fabricated. Nevertheless, the coating process is complicated, and sintering still involves vacuum sintering.

In this work, a simple method to obtain ZrO_2-coated Y_2O_3 nanoparticles by thermal decomposition of zirconium nitrate was described to improve the dispersion of Y_2O_3 in aqueous suspensions. Highly transparent Y_2O_3 ceramics were prepared by a simple shaping approach. followed by air presintering plus HIPing without annealing. The effect of coating on the dispersity and stability of the Y_2O_3 suspensions during colloidal processing was investigated in comparison with uncoated powder.

2. Materials and Methods

2.1. Starting Materials

High-purity commercial Y_2O_3 nanopowder (99.99% pure; Huizhou Ruier Rare Chemical Hi-Tech Co., Ltd., Huizhou, China) was adopted as the starting material. Zirconium nitrate ($Zr(NO_3)_4 \cdot 5H_2O$, analytical reagent, Sinopharm chemical reagent, Shanghai, China) was adopted to prepare a 0.2 mol/L solution. Triammonium citrate (TAC) (Sinopharm Chemical Reagent Co., Ltd., Shanghai, China) was used as dispersant. The pH value of the suspensions was adjusted by HCl or KOH solution.

2.2. Coating Procedure and Suspension Preparation

Y_2O_3 powder was dispersed in ethyl alcohol with 2.0 wt.% dispersant added. After milling with ZrO_2 balls for 12 h, the suspension was then dried at 90 °C in an oven. The dried powder was sieved through a 200-mesh nylon screen. The powders were then calcinated at 1100 °C for 4 h, which was named starting powder (S.P.).

The S.P. was dispersed into ethyl alcohol, followed by the addition of a corresponding ratio of 5.0 at% Zr^{4+} zirconium nitrate solution, and then the suspension was milled for 24 h. Subsequently, the suspension was dried at 80 °C for 12 h. The dried hygroscopic powder (D.P.) consisting of a complex hydrate of dried metal nitrate salt was consecutively calcined at 600, 700, and 800 °C for 4 h in a furnace to obtain ZrO_2-coated Y_2O_3 nanopowder. The mass ratio of TAC for different solid loadings of suspensions was 1.5 wt.%.

2.3. Consolidation and Sintering

The centrifugal slip-casting method was adopted using a laboratory centrifuge at 3000 rpm for 40 min. The green compacts were left at room temperature for 24 h, followed by drying at 80 °C for 12 h in an oven. The compacted samples were then presintered at 1500 °C for 16 h in air to reach the final stage of sintering. Finally, the presintered samples were post-HIPed at 1550 °C for 2 h under 200 MPa in argon atmosphere. Figure 1 shows a flowchart of the experimental procedure.

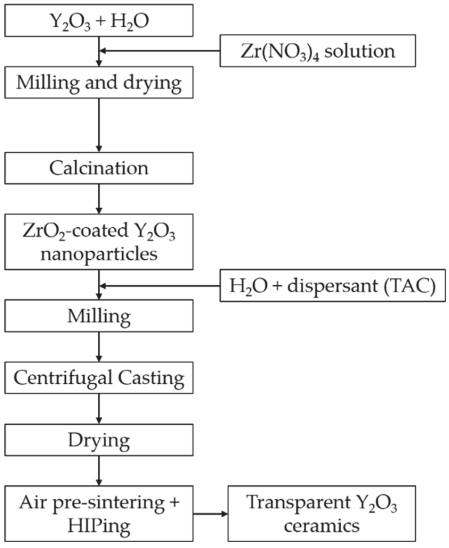

Figure 1. Flowchart for preparation of transparent Y_2O_3 ceramics.

2.4. Characterization

The crystal phase was identified by XRD (*X'pert* PROMPD, PANalytical, Almelo, the Netherlands) using nickel-filtered CuKα radiation. The morphologies of the powders were observed by transmission electron microscopy (TEM, Model JEM-2100F, JEOL, Tokyo, Japan). Zeta potential measurements were adopted to analyze the charged state of the particles' surface (DT-1202, Dispersion Technology Inc., New York, NY, USA). The rheological properties of the suspensions were tested by a cone-plate viscometer (Brookfield DV-II+Pro, Brookfield Engineering Laboratories, Middleboro, MA, USA). The relative densities of the green compact and sintered bodies were measured by the Archimedes method with regard to the theoretical density of Y_2O_3 (5.03 g/cm^3). The morphologies of the sintered bodies were observed by FE-SEM using a Hitachi scanning electron microscope (S-4800, Tokyo, Japan). The samples after polishing on both surfaces were used to measure the in-line

transmittance by using an ultraviolet/visible/near-infrared spectrophotometer (Model Lambda 750S, PerkinElmer, Waltham, MA, USA).

3. Results and Discussion

3.1. Coating Y_2O_3 Particle with Zirconium Nitrate via Thermal Decomposition Method

XRD patterns of the S.P., D.P., and powder after calcination at different temperatures are shown in Figure 2. All the peaks match the standard cubic Y_2O_3 phase (JCPDS card, No. 43-1036), and no ZrO_2 phase was detected. Compared with the S.P., the diffraction peak intensity of the D.P. was weakened, indicating the presence of zirconium nitrate crystal on the surface of the Y_2O_3 particle. The radius of Zr^{4+} ions (r = 0.72 Å) is smaller than Y^{3+} ions (r = 0.89 Å), which will shift the diffraction peaks to larger angles [27]. The diffraction peaks of the powders shift to larger angles after 600 °C calcination, indicating the dissolution of Zr^{4+} within the Y_2O_3 lattice gradually with the decomposition of $Zr(NO_3)_4$. With a further increase in the calcination temperatures from 600 to 800 °C, the diffraction peaks of Y_2O_3 continuously shift towards larger angles (Figure 2b), which leads us to conclude that the increased dissolution of ZrO_2 within the Y_2O_3 lattice coincides with the increase in calcination temperature.

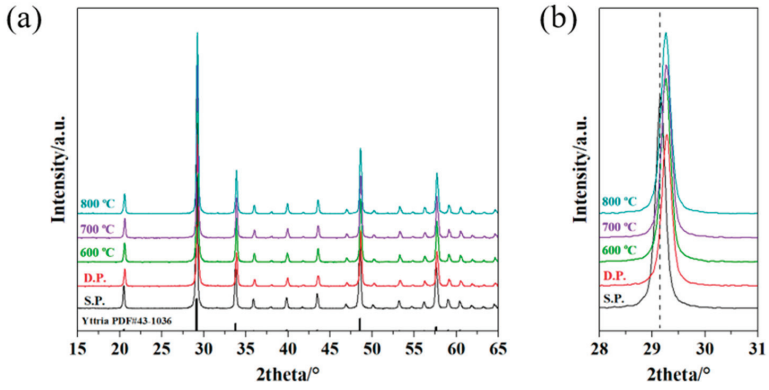

Figure 2. X-ray diffraction patterns of starting powder, dried powder, and ZrO_2-coated powders calcined at varied temperatures, (**a**) XRD patterns in the 2θ range of 15–65°, (**b**) Magnification of XRD patterns in the 2θ range of 28°–30°.

In order to deeply investigate the evolution during the coating procedure, the morphological characteristics of the powders were analyzed by transmission electron microscopy, as shown in Figure 3. The particles for the S.P. possess high crystallinity with flat and clear edges. The average size of the particles is ~100.0 nm (Figure 3a). In contrast, the D.P. exhibits rough surfaces with loosely packed tiny particles of zirconium nitrate crystal, as shown in Figure 3b. On account of that, the S.P. was already calcined at 1100 °C before the coating process, and there was no significant change in the morphology of the core particle after different temperature calcination. However, it is worth noting that with the increasing calcination temperature, the tiny particles consisting of the coating layer gradually decreased and disappeared (Figure 3c,d,f). As we can see from Figure 3d,e, after calcination at 700 °C, a coating layer with a thickness of 5–10 nm could be observed. On the one hand, the d-spacing of the coating layer of 2.94 Å could be indexed to the ZrO_2 (tetragonal) structure of the (011) crystal plane. On the other hand, the d-spacing of 5.29 Å is the (200) plane for the Y_2O_3 (cubic) structure. With the further increase in calcination temperature to 800 °C (Figure 3f), the coating layer nearly disappeared, indicating that ZrO_2 gradually dissolved into the Y_2O_3 lattice with the increase in calcination temperature.

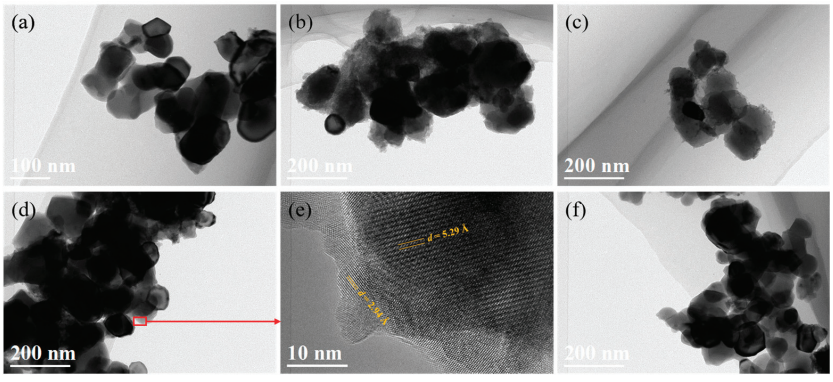

Figure 3. TEM images and corresponding HRTEM images of starting powders, (**a**), dried powders (**b**), and powder with ZrO_2 coating layer calcined at different temperatures of 600 °C (**c**), 700 °C (**d**,**e**), and 800 °C (**f**).

During calcination, $Zr(NO_3)_4$ decomposed and adhered onto the surfaces of Y_2O_3 particles. ZrO_2 dissolved into the Y_2O_3 lattice with the increase in calcination temperature. The diffusion depth of Zr^{4+} into Y_2O_3 lattice for the sample calcinated at 700 °C for 4 h was evaluated using the following equations [28]:

$$D_{\text{lattice}} = \exp(-423\ (\text{kJ/mol})\ /\ RT)\ \text{m}^2\text{s}^{-1} \quad (1)$$

where D_{lattice} is the diffusion coefficient, and T is temperature. According to Boniecki's research, the diffusion coefficient of Zr^{4+} in the Y_2O_3 lattice at 1600 °C was 7.04×10^{-22} m^2s^{-1}; hence, we can calculate the diffusion coefficient of Zr^{4+} in the Y_2O_3 lattice at 700 °C as follows [29]:

$$D_{\text{lattice}}^{700} = \frac{\exp(-423\ (\text{kJ/mol})\ /\ \text{Rg}927)\ \text{m}^2\text{s}^{-1}}{\exp(-423\ (\text{kJ/mol})\ /\ \text{Rg}1827)\ \text{m}^2\text{s}^{-1}} \times 7.04\ \times\ 10^{-22} \quad (2)$$

where Rg is the ideal gas content, and 927 and 1827 are the absolute temperatures of 700 and 1600 °C. As the holding time of calcination was 4 h, the diffusion area was achieved as follows:

$$\text{S} = D_{\text{lattice}}^{700} \times 4\ \times\ 3600\ \approx\ 9.30\ \text{nm}^2 \quad (3)$$

where S is the diffusion area. The diffusion depth could then be evaluated as 3.44 nm, which was far below the radius of the raw particles (100 nm). On the basis of our findings, one can conclude that powder after 700 °C calcination consisted of surface-coated ZrO_2 and Zr^{4+} solid solution outside of the Y_2O_3 lattice, which was beneficial to the inhibition of hydrolysis issue.

3.2. Dispersion Properties of ZrO_2-Coated Y_2O_3 Powders

Figure 4 shows the rheological behaviors of suspensions for the S.P. and coated powders with a solid loading of 10.0 vol% at pH = 10.1 with TAC added. The viscosity of the suspension with S.P. (S-suspension) decreases as the shear rate increases, showing a shear-thinning behavior. For the suspension with coated powder calcinated at different temperatures, there was a significant decrease in the viscosity, which exhibits a relatively constant viscosity corresponding to Newtonian. The lowest viscosity occurred when the calcination temperature was 700 °C. According to the above analysis, suspensions formulated with powders calcined at 700 °C (C-suspension) were adopted to be a better choice for the following steps to fabricate transparent ceramics.

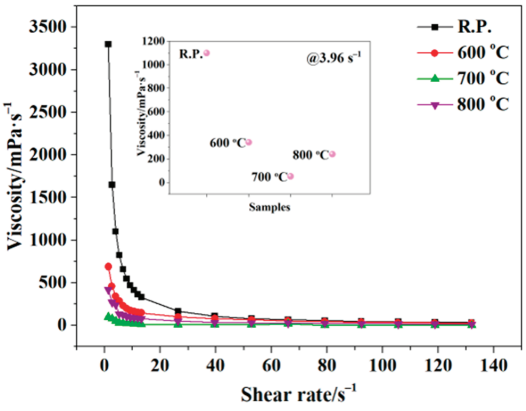

Figure 4. Viscosity for 10.0 vol% suspensions of powders calcinated at different temperatures, inset picture: viscosity for suspensions @3.96 s^{-1}.

The zeta potential of the ZrO_2-coated Y_2O_3 powders calcined at 700 °C for 4 h calcination, the S.P., and the synthesized ZrO_2 powder treated under identical conditions are shown in Figure 5. The isoelectric point (IEP) of the S.P. and synthesized ZrO_2 powder are 10.1 and 8.0, respectively. The IEP for ZrO_2-coated Y_2O_3 powders showed between the S.P. and synthesized ZrO_2 powder. The coating of ZrO_2 reduced the IEP of Y_2O_3 particles from 10.1 to 9.3. The negatively charged groups of TAC were absorbed on the surfaces of ZrO_2-coated yttria nanoparticles. As observed from this figure, the addition of TAC shifted the IEP value from 10.1 to 5.6. Moreover, the absolute zeta potential of particles in suspensions increases with the increase in pH, and it reaches 49 mV at the pH of 11. The good dispersion of coated Y_2O_3 powder in aqueous suspension is favorable for the preparation of well-dispersed and high solids loading solution in an easy method.

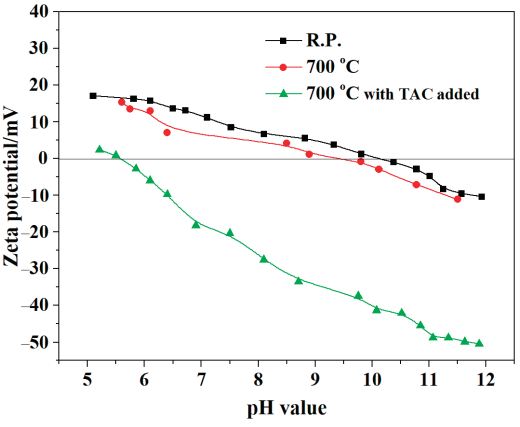

Figure 5. Zeta potential versus pH for 10.0 wt.% suspensions with different powders and TAC added.

3.3. Consolidation and Sintering of Y_2O_3 Transparent Ceramics

Figure 6 shows the SEM images of the green bodies consolidated from two suspensions with a solid loading of 35.0 vol%. Larger micron-scale pores can be observed for the sample consolidated using S-suspensions (Figure 6a), which are difficult to eliminate during the sintering process. In sharp contrast, the green bodies of the C-suspension yielded a more homogeneous and compact microstructure (Figure 6b). Only nanosized pores can be seen, and the particles are in close contact with each other. The relative densities of the green bodies are 50.2% and 29.2% for the C-suspension and S-suspension, respectively.

As we all know, green compacts with smaller pore size distribution and a homogeneous microstructure show high sinterability and were easy to densify at lower temperatures.

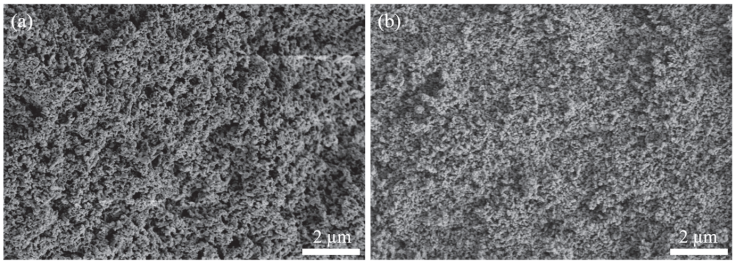

Figure 6. SEM micrographs of the fracture surfaces of the green compacts were obtained from (**a**) S-suspension and (**b**) C-suspension.

Figure 7 shows SEM images of the Y_2O_3 ceramics sintered at 1500 °C for 16 h in air. For the sample prepared from the S-suspension, a porous structure with the presence of open pore channels is shown in Figure 7a. The relative density of the sample is 86.4%, which is the typical feature of intermediate-stage sintering [30]. In comparison, for the sample prepared from the C-suspension (Figure 7b), the number of pores is much less than that in the S-suspension one. Moreover, it can also be noticed that the sample has a much smaller average pore size. The relative density of the sample reaches 96.4%, and there are no open pores found in the sample, suggesting that it is already at the final stage of sintering [27]. From the results we obtained, one can conclude that the higher relative density and more homogeneous microstructure improved the sinterability.

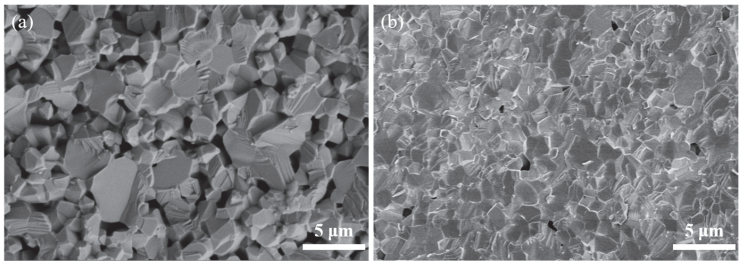

Figure 7. SEM micrographs of sintered bodies for 16 h at 1500 °C obtained from (**a**) S-suspension and (**b**) C-suspension.

The in-line transmittance curves of the samples are shown in Figure 8. The transmittance of the sample prepared by the S.P. is lower than its theoretical value. The relative density of the sample is 95.5%. In contrast, the sample prepared with coated powder after 700 °C calcination has a remarkable improvement in transmittance observed. The relative density of the sample is 99.9%. The in-line transparency (ILT) at 1100 nm is 81.4%. At the wavelength of 2000 nm, the ILT approaches 82.6%, which is very close to the theoretical value of Y_2O_3 crystal. The inset photograph shows the optical images of the as-obtained Y_2O_3 ceramic prepared with coated powder after polishing, and the characters below the ceramic sample can be seen very clearly.

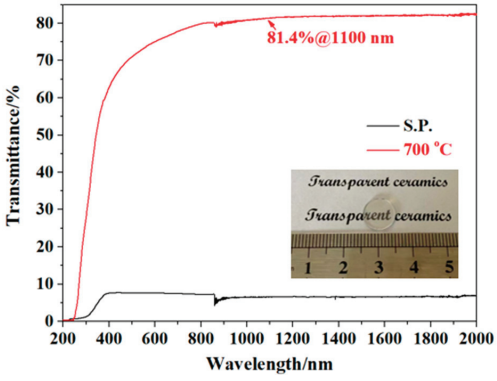

Figure 8. In-line transmittance of HIPed Y_2O_3 ceramics at 1550 °C (thickness = 1.0 mm), inset photograph: ceramic prepared with coated powder after polishing.

It is worth mentioning that the absorption edge shifts to the slong wavelength of the sample prepared by the S.P. at the wavelength of 250–350 nm range could be observed. The addition of Zr^{4+} to Y_2O_3 will produce oxygen interstitial of O_i'' during the sintering process and inhibit the grain boundary mobility to promote the densification of Y_2O_3 ceramics. Herein, the shift of the undoped sample could be due to the change of band gap energy and the oxygen vacancies [31] formed during the sintering process. Moreover, the very tiny little residual pores in the sintered body could also be an important issue for the decrease in the transmittance at short wavelengths.

Figure 9 shows the microstructure of the fracture surfaces for the HIPed samples. Compared with the sample prepared by the C-suspension, the sample prepared by the S-suspension (shown in Figure 9a) exhibited an exaggerated grain size and lots of intergranular pores and intragranular pores act as light scattering centers in transparent ceramics, resulting in a decrease in transmittance. The average grain size of the sample obtained from the S.P. is 3.3 μm. However, fully densified and no pores are observed in the sample prepared by ZrO_2-coated powder (Figure 9b,c), which helps to explain their higher optical quality. The typical grain size distribution is shown in Figure 9d. The mean grain size is 1.7 μm, indicating that ZrO_2 effectively promoted the densification and inhibited the grain growth of the sintered body.

Compared with Wang and Liu's results [7,8], we achieved highly transparent Y_2O_3 ceramic with fine grain size, and the ILT was ~80.0% in the visible wavelength range by air presintering plus HIPing at a lower temperature. Herein, we proposed a new method to synthesize ZrO_2-coated Y_2O_3 powder for colloidal processing. By adopting ZrO_2-coated Y_2O_3 powder, a well-dispersed suspension with high solid loading (35.0 vol%) was achieved. After consolidation, the green compacts were sintered in an energy-saving and effective method, which is low-temperature air presintering plus HIPing without annealing. Moreover, the sintered body was fully densified, and the average grain size is less than 2.0 μm, which may make it a promising fabrication method in the preparation of sesquioxide transparent ceramics. We point out that this is the most effective and simple method to fabricate highly transparent ceramics with fine grain size.

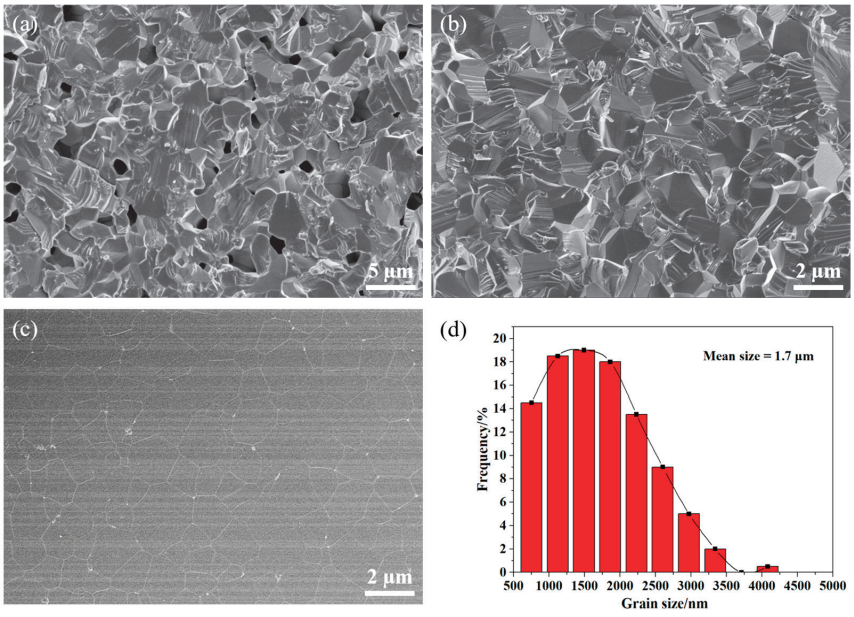

Figure 9. SEM micrographs of the fracture surfaces of HIPed Y_2O_3 ceramics obtained from (**a**) S.P. and (**b**) ZrO_2 coated powder after 700 °C calcination, (**c**) thermally etched surfaces of sample obtained from ZrO_2 coated powder after 700 °C calcination and (**d**) grain size distribution of the sample.

4. Conclusions

In summary, the coating of Y_2O_3 particles with a thin ZrO_2 layer via an easy method was reported, and it was found to be an effective method to inhibit hydrolysis issues during suspension preparation. Consequently, a homogeneous green body with a relative density of 50.2% was obtained, which is beneficial for fabrication of highly transparent Y_2O_3 ceramics with fine grain size via low-temperature air presintering plus HIPing treatment. The Y_2O_3 ceramic presintered at 1500 °C × 16 h and post-HIPed at 1550 °C × 2 h showed a grain size of 1.7 μm and high in-line transmittance (81.4% at 1100 nm, thickness: ~1.0 mm), very close to the theoretical value of Y_2O_3. This is the most effective and simple method to fabricate highly transparent ceramics with fine grain size.

Author Contributions: Writing—original draft preparation, data curation, formal analysis, and investigation, Z.F.; data curation, H.L. writing—review and editing, X.L. supervision, N.W., J.W., J.Z., Z.H. and X.S. All authors have read and agreed to the published version of the manuscript.

Funding: This research was funded by the postdoctoral research start-up funding of Shenyang University (No. 1220502052022010215).

Institutional Review Board Statement: Not applicable.

Informed Consent Statement: Not applicable.

Data Availability Statement: Data sharing is not applicable to this article.

Conflicts of Interest: The authors declare that they have no known competing financial interests or personal relationships that could have appeared to influence the work reported in this paper.

References

1. Li, Q.; Wang, J.; Ma, J.; Ni, M.; Yang, F.; Liu, P.; Lee, K.Y.; Hsiang, H.; Shen, D.; Tang, D. Fabrication of, high-efficiency Yb:Y_2O_3 laser ceramics without photodarkening. *J. Am. Ceram. Soc.* **2022**, *105*, 3375–3381. [CrossRef]
2. Xiao, Z.; Yu, S.; Li, Y.; Ruan, S.; Kong, L.B.; Huang, Q.; Huang, Z.; Zhou, K.; Su, H.; Yao, Z.; et al. Materials development and potential applications of transparent ceramics: A review. *Mater. Sci. Eng. R* **2020**, *139*, 14–19. [CrossRef]

3. Iwasawa, J.; Nishimizu, R.; Tokita, M. Plasma-resistant dense yttrium oxide film prepared by aerosol deposition process. *J. Am. Ceram. Soc.* **2007**, *90*, 2327–2332. [CrossRef]
4. Kirm, M.; Feldbach, E.; Kink, R.; Lushchik, A.; Lushchik, C.; Maaroos, A.; Martinson, I. Mechanisms of intrinsic and impurity luminescence excitation by synchrotron radiation in wide-gap oxides. *J. Electron Spectros. Relat. Phenom.* **1996**, *79*, 91–94. [CrossRef]
5. Furuse, H.; Nakasawa, S.; Yoshida, H.; Morita, K.; Suzuki, T.S.; Kim, B.-N.; Sakka, Y.; Hiraga, K. Transparent ultrafine Yb^{3+}:Y_2O_3 laser ceramics fabricated by spark plasma sintering. *J. Am. Ceram. Soc.* **2018**, *101*, 694–702. [CrossRef]
6. Gan, L.; Park, Y.-J.; Park, M.-J.; Kim, H.; Kim, J.-M.; Ko, J.-W.; Lee, J.-W. Facile fabrication of highly transparent yttria ceramics with fine microstructures by a hot-pressing method. *J. Am. Ceram. Soc.* **2015**, *989*, 2002–2004. [CrossRef]
7. Wang, Z.Y.; Zhang, L.; Yang, H.; Zhang, J.; Wang, L.X.; Zhang, Q.T. High optical quality Y_2O_3 transparent ceramics with fine grain size fabricated by low temperature air pre-sintering and post-HIP treatment. *Ceram. Int.* **2016**, *42*, 4238–4245. [CrossRef]
8. Zhang, L.; Ben, Y.; Chen, H.; Tang, D.; Fu, X.; Sun, R.; Song, B.; Wong, C. Low temperature-sintering and microstructure of highly transparent yttria ceramics. *J. Alloys Compd.* **2017**, *695*, 2580–2586. [CrossRef]
9. Liu, L.K.; Zhu, Q.H.; Zhu, Q.Q.; Jiang, B.X.; Feng, M.H.; Zhang, L. Fabrication of fine-grained undoped Y_2O_3 transparent ceramic using nitrate pyrogenation synthesized nanopowders. *Ceram. Int.* **2019**, *45*, 5339–5345. [CrossRef]
10. Fu, Z.C.; Li, X.D.; Ren, Y.; Zhang, M.; Geng, X.T.; Zhu, Q.; Li, J.-G.; Sun, X.D. Coating Y_2O_3 nano-particles with ZrO_2-additive via precipitation method for colloidal processing of highly transparent Y_2O_3 ceramics. *J. Eur. Ceram. Soc.* **2019**, *39*, 4996–5004. [CrossRef]
11. Zhang, J.; An, L.-Q.; Liu, M.; Shimai, S.; Wang, S.-W. Sintering of Yb^{3+}:Y_2O_3 transparent ceramics in hydrogen atmosphere. *J. Eur. Ceram. Soc.* **2009**, *29*, 305–309. [CrossRef]
12. Fu, Z.C.; Li, X.D.; Zhang, M.; Zhu, Q.; Li, J.-G.; He, J.; Wang, X.-A.; Sun, X.D. Achieving fabrication of highly transparent Y_2O_3 ceramics via air pre-sintering by deionization treatment of suspension. *J. Am. Ceram. Soc.* **2021**, *104*, 2689–2701. [CrossRef]
13. Ning, K.J.; Wang, J.; Ma, J.; Dong, Z.L.; Kong, L.B.; Tang, D.Y. Fabrication of laser grade Yb: Y_2O_3 transparent ceramics with ZrO2 additive through hot isostatic pressing. *Mater. Today Commun.* **2020**, *24*, 2352–4928. [CrossRef]
14. Lange, F.F. Powder processing science and technology for increased reliability. *J. Am. Ceram. Soc.* **1989**, *72*, 3–15. [CrossRef]
15. Olhero, S.M.; Ganesh, I.; Torres, P.M.C.; Alves, F.J.; Ferreira, J.M.F. Aqueous colloidal processing of ZTA composites. *J. Am. Ceram. Soc.* **2009**, *92*, 9–16. [CrossRef]
16. Lewis, J.A. Colloidal processing of ceramics. *J. Am. Ceram. Soc.* **2000**, *83*, 2341–2359. [CrossRef]
17. Yasrebi, M.; Zimek-Moroz, M.; Kemp, W.; Sturgis, D.H. Role of particle dissolution in stability of binary yttria–silica colloidal suspensions. *J. Am. Ceram. Soc.* **1996**, *79*, 1223–1227. [CrossRef]
18. Kuroda, Y.; Hamano, H.; Mori, T.; Yoshikawa, Y.; Nagao, M. Specific adsorption behavior of water on a Y_2O_3 surface. *Langmuir* **2000**, *16*, 6937–6947. [CrossRef]
19. Jin, L.L.; Mao, X.J.; Wang, S.W.; Dong, M.J. Optimization of the rheological properties of yttria suspensions. *Ceram. Int.* **2009**, *35*, 925–927. [CrossRef]
20. Sun, Z.Q.; Zhu, X.W.; Li, M.S.; Zhou, Y.C.; Sakka, Y. Hydrolysis and dispersion properties of aqueous $Y_2Si_2O_7$ suspensions. *J. Am. Ceram. Soc.* **2009**, *92*, 54–61. [CrossRef]
21. Xu, Y.Y.; Mao, X.J.; Fan, J.T.; Li, X.K.; Feng, M.H.; Jiang, B.X.; Leia, F.; Zhang, L. Fabrication of transparent yttria ceramics by alcoholic slip-casting. *Ceram. Int.* **2017**, *43*, 8839–8844. [CrossRef]
22. Sun, Y.; Shimai, S.Z.; Peng, X.; Zhou, G.H.; Kamiya, H.; Wang, S.W. Fabrication of transparent Y_2O_3 ceramics via aqueous gelcasting. *Ceram. Int.* **2014**, *40*, 8841–8845. [CrossRef]
23. Arshad, M.; Amer, M.; Hayat, Q.; Janik, V.; Zhang, X.; Moradi, M.; Bai, M. High-Entropy Coatings (HEC) for High-Temperature Applications: Materials, Processing, and Properties. *Coatings* **2022**, *12*, 691. [CrossRef]
24. Aiken, B.; Matijević, E. Preparation and properties of uniform coated inorganic colloidal particles. IV. Yttrium basic carbonate and yttrium oxide on hematite. *J. Colloid. Interface Sci.* **1988**, *126*, 645–649. [CrossRef]
25. Shojai, F.; Pettersson, A.B.A.; Mäntylä, T.; Rosenholm, J.B. Electrostatic and electrosteric stabilization of aqueous slips of 3Y–ZrO_2 powder. *J. Eur. Ceram. Soc.* **2000**, *20*, 277–283. [CrossRef]
26. Yasrebi, M.; Springgate, M.E.; Nikolas, D.G.; Kemp, W.; Sturgis, D.H. Colloidal stability of zirconia-doped yttria–silica binary aqueous suspensions. *J. Am. Ceram. Soc.* **1997**, *80*, 1615–1618. [CrossRef]
27. Crocombette, J.P.; Jollet, F. Site selectivity in ZrO_2-doped Y_2O_3 evidenced by X-ray absorption spectra calculations. *J. Phys. Condens. Matter.* **1994**, *6*, 8341–8348. [CrossRef]
28. Wakai, F.; Sakaguchi, S.; Matsuno, Y. Superplasticity of yttria-stabilized tetragonal ZrO_2 polycrystals. *Adv. Ceram. Mater.* **1986**, *1*, 259–263. [CrossRef]
29. Boniecki, M.; Natanzon, Y.; Łodziana, Z. Effect of cation doping on lattice and grain boundary diffusion in superplastic yttria-stabilized tetragonal zirconia. *J. Eur. Ceram. Soc.* **2010**, *30*, 657–668. [CrossRef]
30. Coble, R.L. Sintering crystalline solids I. Intermediate and final state diffusion models. *J. Appl. Phys.* **1961**, *32*, 787–792. [CrossRef]
31. Lushchik, A.; Feldbach, E.; Kotomin, E.A.; Kudryavtseva, I.; Kuzovkov, V.N.; Popov, A.I.; Seeman, V.; Shablonin, E. Distinctive features of diffusion-controlled radiation defect recombination in stoichiometric magnesium aluminate spinel single crystals and transparent polycrystalline ceramics. *Sci. Rep.* **2020**, *10*, 7810. [CrossRef]

coatings

MDPI

Article

Fabrication of Yb:YAG Transparent Ceramic by Vacuum Sintering Using Monodispersed Spherical Y_2O_3 and Al_2O_3 Powders

Jinsheng Li [1,2,*], Xin Liu [2], Lei Wu [2], Haipeng Ji [3], Liang Dong [2], Xudong Sun [1,*] and Xiwei Qi [2,4,*]

[1] Institute of Ceramics and Powder Metallurgy, School of Materials Science and Engineering, Northeastern University, Shenyang 110819, China
[2] Key Laboratory of Dielectric and Electrolyte Functional Materials Hebei Province, School of Resources and Materials, Northeastern University at Qinhuangdao, Qinhuangdao 066004, China
[3] Key Laboratory of Advanced Energy Catalytic and Functional Material Preparation of Zhengzhou City, School of Materials Science and Engineering, Zhengzhou University, Zhengzhou 450001, China
[4] College of Metallurgy and Energy, North China of Science and Technology, Tangshan 063210, China
* Correspondence: jinsheng1986@163.com (J.L.); xdsun@mail.neu.edu.cn (X.S.); qxw@mail.neuq.edu.cn (X.Q.)

Abstract: In the present work, Yb:YAG (yttrium aluminum garnet) transparent ceramics were fabricated using monodispersed spherical Y_2O_3, Al_2O_3 powders and commercial Yb_2O_3 nano-powder as raw materials, adding 0.5 wt% tetraethyl orthosilicae (TEOS) through the solid-state method and vacuum sintering technology. The prepared monodispersed Y_2O_3 and Al_2O_3 powders adopted by homogeneous co-precipitation showed improved mixing uniformity and lead to the reduced defect of the YAG powders. After sintering in vacuum at 1700 °C for 10 h, the $(Y_{1-x}Yb_x)AG$ (x = 0, 0.01, 0.10) ceramics with high transparency were obtained. Analysis of the densification rate, micromorphology, and optical properties of the ceramics suggests that the performance of the Yb:YAG ceramics is independent of the doping amount of Yb. Moreover, when the Y_2O_3, Al_2O_3, and Yb_2O_3 mixtures were laid aside for some time in the air after milling and drying, the performances of the as-prepared Yb:YAG ceramics would be affected distinctively. It is likely because the Y_2O_3 is easily hydrolyzed to $Y(OH)_3$, $Y(OH)^{2+}$ and $Y_2(OH)_2^{4+}$, which impinged the sintering activity of the powder mixture.

Keywords: Yb:YAG; transparent ceramics; vacuum sintering

Citation: Li, J.; Liu, X.; Wu, L.; Ji, H.; Dong, L.; Sun, X.; Qi, X. Fabrication of Yb:YAG Transparent Ceramic by Vacuum Sintering Using Monodispersed Spherical Y_2O_3 and Al_2O_3 Powders. *Coatings* **2022**, *12*, 1155. https://doi.org/10.3390/coatings12081155

Academic Editor: Aivaras Kareiva

Received: 30 June 2022
Accepted: 8 August 2022
Published: 10 August 2022

1. Introduction

Yttrium aluminum garnet (YAG) belongs to the cubic crystal system and has excellent optical, mechanical properties and chemical stability. Among the solid laser materials, YAG crystal has the best comprehensive performances [1–6]. YAG doped with (Ce^{3+}, Eu^{3+}) can be widely used in the fields of scintillation and luminescent materials [7]. YAG doped with other rare earth ions (Nd^{3+}, Yb^{3+}) can be widely used as laser crystal in the fields of laser, medical instruments, and military defense. Compared with Nd:YAG, the Yb:YAG shows significant advantages, such as no concentration quenching effect of Yb doping and high quantum efficiency. As the central absorption wavelength of Yb^{3+} is about 940 nm, which perfectly matches with the InGaAs diode, Yb:YAG has become the preferred solid laser gain medium with high efficiency [8,9].

Traditionally, YAG single crystal laser was grown by the Czochralski method. There are many limitations such as low growth rate, high cost and the difficulty of obtaining a large size. As the YAG transparent ceramics have similar physical, chemical and laser properties with single crystal, it is preferred to prepare YAG ceramics with low cost and a high doping concentration of rare earth ions [10,11]. Since Ikesue prepared high-quality Nd:YAG transparent ceramics and used laser diode (LD) pumping to obtain laser output in 1995, YAG transparent ceramics have developed rapidly [12].

The solid-state method and wet-chemical method were conventionally used to fabricate YAG transparent ceramics [13–21]. The wet-chemical method includes the sol–gel method, combustion synthesis method, hydroxide co-precipitation method, homogeneous precipitation method, glycol thermal treatment, spray-pyrolysis method and so on. The precursor powders contain surface water and structural water. Due to the adsorption of water, it is difficult to eliminate the hard agglomeration of the powder caused by surface tension and hydrogen bonding. Moreover, the difference in the precipitation solubility and sedimentation rate of the precursor cations in the precipitation method makes it difficult to obtain an accurate stoichiometric ratio and uniform composition of YAG powders. The solid-state method is the traditional method to prepare YAG powders during which the well-mixed high-purity oxide powders were sintered at high temperatures. This method is low cost and easy to operate and scale up. However, agglomeration could be observed in the commercial Y_2O_3 powders, and the particle size is usually inhomogeneous. Furthermore, the mismatch of powder particle sizes between the Y_2O_3 and Al_2O_3 powders results in poor uniform mixing. In this case, higher activation energy is required for sufficient ion diffusion, and higher calcination temperature and longer sintering period were required to obtain a YAG single phase [22,23].

In this study, Yb:YAG transparent ceramics were prepared using monodispersed spherical Y_2O_3 and Al_2O_3 powders through homogeneous coprecipitation and commercial Yb_2O_3 nano-powders as raw materials by solid-state process and vacuum sintering. The optical properties and micro-morphology of the YAG ceramics doped with different concentrations of Yb were analyzed. In addition, it is found that the sintering activity of the Y_2O_3, Al_2O_3 and Yb_2O_3 mixing powders would be greatly affected after being placed for some time after ball milling. The phase formation, micro-morphology and sintering activity of the laying aside precursor powders were also analyzed in depth.

2. Experimental Procedures

2.1. Materials

Y_2O_3 (99.99% purity, Huizhou Ruier Rare-Chem. Hi-Tech. Co., Ltd., Huizhou, China), Yb_2O_3 (99.99% purity, Huizhou Ruier Rare-Chem. Hi-Tech. Co., Ltd., Huizhou, China), $Al(NO_3)_3{\cdot}9H_2O$ (purity > 99%; Zhenxin Chemical Reagent Factory, Shanghai, China), nitric acid (analytical grade, Sinapharm, Shanghai, China), urea (analytical grade, Sinapharm, Shanghai, China) and tetraethoxysilane (TEOS, >99.99%, AlfaAesar) were used as the raw materials.

2.2. Preparation of Spherical Y_2O_3 and Al_2O_3 Powders

Homogeneous precipitation was used to prepare the monodispersed spherical Y_2O_3 powders. Firstly, Y_2O_3 powders were dissolved into heated HNO_3 at 90 °C to obtain the $Y(NO_3)_3$ solution. Then, 0.15 M Y^{3+} and 0.5 M urea were mixed into 500 mL of solution and stirred equably at 90 °C for 2 h. After the reaction, the precipitate was collected via centrifugation, washed with deionized water and ethanol three times, and then dried at 80 °C for 24 h in an oven to obtain soft and white precursor powder. Y_2O_3 powders were obtained by grinding and sieving the precursor powder and then calcination in a muffle furnace at 900 °C for 4 h. The main chemical reactions for the preparation of Y_2O_3 are as follows:

$$yY^{3+} + x{NH_4}^+ + z{OH}^- + m{CO_3}^{2-} + nH_2O \leftrightarrow (NH_4)_xY_y(OH)_z(CO_3)_m{\cdot}nH_2O \quad (1)$$

$$(NH_4)_xY_y(OH)_z(CO_3)_m{\cdot}nH_2O \leftrightarrow xNH_3 + 0.5yY_2O_3 + mCO_2 + nH_2O \quad (2)$$

The process to obtain the monodispersed spherical Al_2O_3 is similar to that of Y_2O_3. Firstly, $Al(NO_3)_3{\cdot}9H_2O$ is dissolved in water to obtain a certain concentration of $Al(NO_3)_3$ solution. Then, 0.006 M $Al(NO_3)_3$ and 0.005 M $(NH_4)_2SO_4$ and 0.12 M urea were mixed to form 500 mL solution and stirred equably at 90 °C for 1.5 h. After that, the precipitate was collected via centrifugation, washed with deionized water and ethanol, and then dried at

80 °C for 24 h in an oven to obtain soft and white precursor powder. Al_2O_3 powders were obtained by grinding, sieving and calcinating the precursor powder in a muffle furnace at 1000 °C for 4 h. The main chemical reactions for the preparation of Al_2O_3 are as follows:

$$yAl^{3+} + xNH_4^+ + zOH^- + mCO_3^{2-} + nH_2O \leftrightarrow (NH_4)_xAl_y(OH)_z(CO_3)_m \cdot nH_2O \quad (3)$$

$$(NH_4)_xAl_y(OH)_z(CO_3)_m \cdot nH_2O \leftrightarrow xNH_3 + 0.5yAl_2O_3 + mCO_2 + nH_2O \quad (4)$$

2.3. Preparation of Yb:YAG Transparent Ceramics

The Yb:YAG transparent ceramics were prepared by the solid-state reaction method and vacuum sintering technique. The prepared monodispersed spherical Y_2O_3, Al_2O_3 powders, and commercial Yb_2O_3 nano-powders were weighed according to the stoichiometric ratio. The Yb doping concentrations were 0%, 1 at % and 10 at%, respectively. Tetraethyl orthosilicate (TEOS, 0.5 wt%) was used as the sintering aids. Ball milling was then used to mix the powders uniformly. Absolute ethyl alcohol was used as the ball-milling media, and the ratio of solid and liquid was 1:4. The mixture was milled with corundum grinding ball for 16 h and dried in an oven at 80 °C for 24 h. The mixture powder was calcined in air for 1200 °C, 1300 °C, 1400 °C and 1500 °C to analyze the formation of the YAG phase.

$(Y_{1-x}Yb_x)$AG powders prepared were formed by the bidirectional pressing of a steel mold and cold isostatic pressing at 200 MPa to obtain green products with a thickness of 5 mm and a diameter of 13 mm. The green products were then sintered at 1600–1700 °C in a vacuum furnace with the heating and cooling rates of 5 °C/min and 10 °C/min, respectively. Then, the ceramic products after sintering were annealed in the air at 1300 °C to eliminate the oxygen vacancies. Finally, the ceramic products were polished to measure the transmittance and observe the microstructure.

2.4. Characterization

Phase composition analysis of the samples was performed by X-ray diffraction (XRD, Model PW3040/60; PANALYTICAL B.V, Amsterdam, The Netherlands) under 40 kV/40 mA using nickel-filtered Cu Kα radiation at a scanning speed of 4.0°·2θ/min and a step size of 0.02°. The morphologies were observed using field emission scanning electron microscopy (Model JSM-7001F; JEOL, Tokyo, Japan) with an acceleration voltage of 10 kV. The densification behaviors of YAG powder compacts in flowing O_2 were analyzed through dilatometry by a thermal mechanical analyzer (SETSYS Evolution 1750; Setaram, Lyons, France) at a constant heating rate of 10 °C/min and a cooling rate of 15 °C/min. The in-line transmission of the ceramic samples was measured by an ultraviolet-visible spectrometer (PerkinElmer Lambda750S, Waltham, MA, USA).

3. Results and Discussion

Figure 1a,b show the morphologies of the as-prepared Y_2O_3 precursor and that calcined at 900 °C. Both precursor powders were monodispersed and uniform. The average particle size of precursor was about 400 nm, and that of calcined powders was approximately 200 nm. Figure 1c shows the morphology of the commercial Yb_2O_3 nano-powder. The average particle size was about 40 nm.

Figure 2 shows the morphologies of as-prepared Al_2O_3 precursor and that calcined at 1000 °C. Both were monodispersed and homogeneous. Shrinkage of the precursor powder was obvious, as the size decreased from 700 nm to about 400 nm. This is due to the volatility of NH_4^+, CO_3^{2-} and OH^- in the precursor during calcination.

Figure 3 exhibits the XRD patterns of the products of the YAG precursor sintered at different temperatures. The powders calcined at 1200 °C contain phases of YAG ($Y_3Al_5O_{12}$, JCPDS card No. 33-0040), YAP ($YAlO_3$, JCPDS card No. 70-1677), YAM ($Y_4Al_2O_9$, JCPDS card No. 14-0475), and α-Al_2O_3. The dominant phase was YAP. When calcined at 1300 °C, the YAM phase was completely transformed into the YAP phase. At 1400 °C, only a small amount of YAP existed as the impurity phase, and the major phase was YAG. At 1500 °C,

only the YAG phase remained. The phase evolution is quite similar to that previously reported [24]. After calculation, the lattice parameter of the $(Y_{1-x}Yb_x)AG$ (x = 0, 0.01, 0.10) crystals calcined at 1500 °C are 1.2002 nm, 1.1986 nm and 1.1964 nm, respectively, because the ionic radius of Yb is smaller than that of the Y ionic radius. After Yb entered the YAG lattice, it will lead to lattice contraction. So, the lattice constant decreased with the increase in Yb doping.

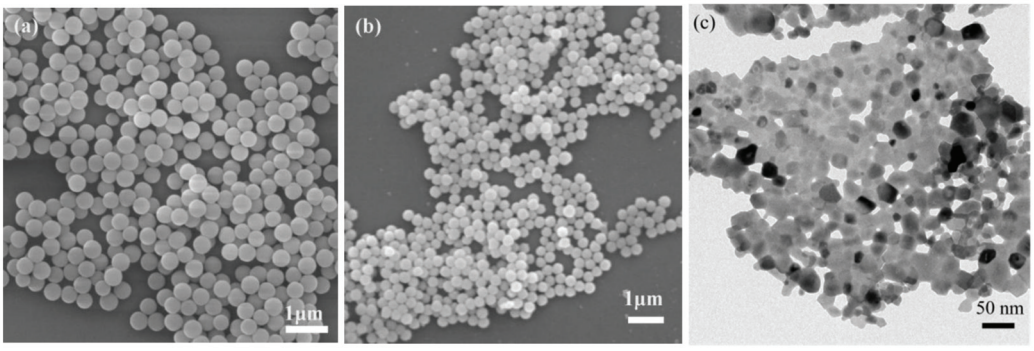

Figure 1. Micrographs showing particle morphologies of the Y_2O_3 precursor (**a**) and calcined at 900 °C (**b**) and commercial Yb_2O_3 nano-powder (**c**).

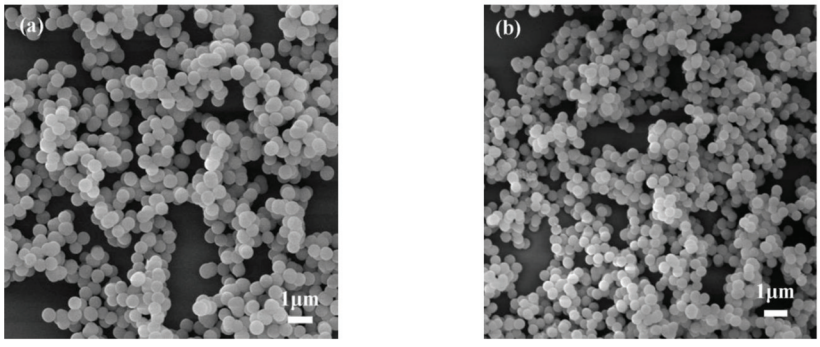

Figure 2. Micrographs showing morphologies of the Al_2O_3 precursor (**a**) and calcined at 1000 °C (**b**).

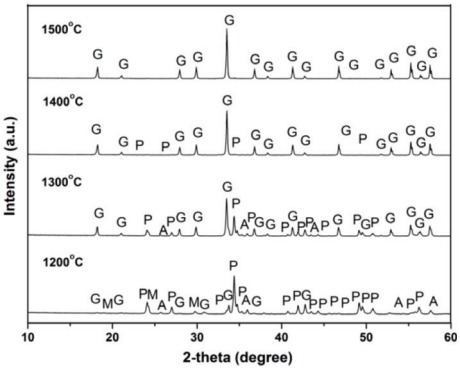

Figure 3. XRD patterns of the products calcined at various temperatures. G represents YAG garnet, P represents YAP phase, M represents YAM phase, and A represents Al_2O_3 phase.

For the formation of the YAG phase, the diffusion of ions during the solid-state reaction needs to overcome the energy barrier. The relation between the diffusion coefficient (D) and temperature (T) can be expressed by Equation (5) [25]:

$$D = D_0 \exp(\frac{-Q}{RT}) \quad (5)$$

where D is the self-diffusion coefficient, D_0 is the pre-exponential factor, Q refers to the self-diffusion activation energy, R is the Boltzmann constant, and T is the thermodynamic temperature. The exponential term ($-Q/RT$) is the probability that an atom overcomes the energy barrier transition.

According to Equation (5), the atomic diffusion coefficient is exponentially related to temperature. When the temperature rises, the diffusion coefficient increases as well. Thus, high temperature is required to enhance atomic diffusion and obtain the YAG phase.

In addition, particle size is a vital parameter that influences the reaction rate in a solid-state reaction. The particle size can change the reaction interface, diffusion cross-section and particle surface structure. Equation (6) was used to describe the relationship between the rate constant and particle size of reactants in a solid-state reaction [26].

$$K_f = \frac{2DC_0}{r^2} \quad (6)$$

where K_f is the reaction rate constant, C_0 is the concentration of the reactant, D is the atomic diffusion coefficient, and r refers to the particle radius of the reactant.

As shown in Equation (6), the rate of solid reaction increased with the reduction in particle radius. The smaller the particle size, the larger the specific surface, the larger the reaction cross-section, the flatter the distribution curvature of bond strength, the larger the proportion of weak bonds, and the greater the reaction and diffusion ability. The temperature required for the YAG phase formation starting from the monodispersed Al_2O_3 spherical powders was higher than that using the Al_2O_3 nano-powders in the previous work under the same conditions, which was mainly due to the low activity and slow diffusion rate of large spherical Al_2O_3 particle size in the present work [27].

The mixing uniformity of oxide powders also matters. When the raw materials failed to be mixed thoroughly, diffusion would be difficult because of a long distance between cations. Therefore, a higher temperature was needed to eliminate the transient phase. Meanwhile, when hard agglomeration appeared in a raw mixture, the activity of the powders would be poor, which would lead to an uneven mixture. In this experiment, monodispersed spherical Y_2O_3 and Al_2O_3 powders improved the mixing uniformity, which then greatly reduced the defect of final ceramics.

Figure 4 exhibits the shrinkage and shrinkage rate curves during sintering of the $(Y_{1-x}Yb_x)AG$ (x = 0, 0.01, 0.10) products at a constant heating rate (10 °C/min). The expansion phenomenon can be observed in the samples from 400 to 1200 °C, which can be explained by the phenomenon of expansion on heating and contraction on cooling. Linear shrinkage and linear shrinkage rate were similar, which are independent on the doping concentration of Yb. The shrinkage was about 8%, and the maximum shrinkage rate was about 0.8 %/min.

Sharp contraction can be observed around 1250 °C, which can be attributed to the difference in density that came from the YAM to YAP transformation process. The result is consistent with the XRD analysis. Furthermore, the densification process is another reason for the contraction. The expansion phenomenon can be observed when the temperature reached about 1450 °C, which was mainly due to the YAP to YAG transformation process. However, the densification rate was lower than the expansion rate coming from the phase transition. When the temperature was higher than 1500 °C, the densification led to a constant sample volume shrinking.

Figure 5 shows the thermally etched surface morphologies of $(Y_{1-x}Yb_x)AG$ ceramic samples sintered at 1600 °C. Similar surface morphologies and the average particle size of

the samples can be observed. The particle size was about 1.2 μm, and the relative density of the Yb:YAG ceramic sample was about 97.5%. The pore distribution was uniform and the pores were basically distributed at particle boundaries. There were no large pores, which was beneficial for the late stage of sintering. At the evaluated sintering temperature, the small pores could be easily eliminated along grain boundaries with the grain growth.

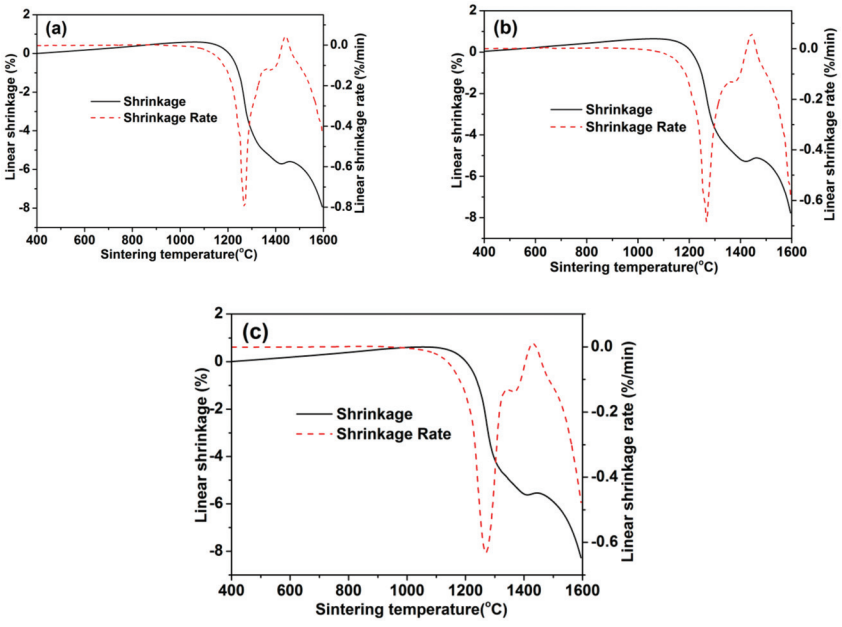

Figure 4. Shrinkage and shrinkage rate during constant heating rate (10 °C/min) sintering of the $(Y_{1-x}Yb_x)AG$ (x = 0, 0.01, 0.10) compacts, (**a**) x = 0, (**b**) x = 0.01, (**c**) x = 0.1.

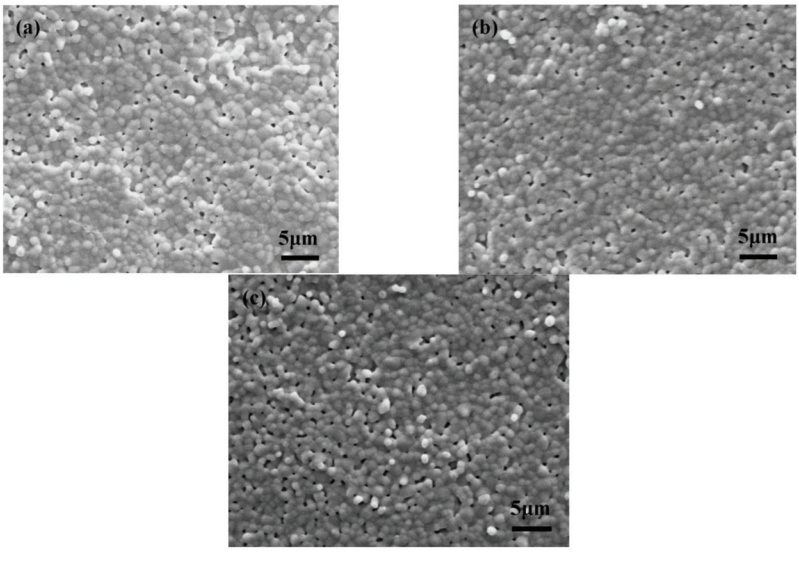

Figure 5. Thermally etched surface morphologies of $(Y_{1-x}Yb_x)AG$ ceramic samples sintered at 1600 °C, (**a**) x = 0, (**b**) x = 0.01, (**c**) x = 0.1.

Figure 6 shows the thermally etched surface morphologies of the Yb:YAG transparent ceramics sintered at 1700 °C. Compared with those sintered at 1600 °C, the grain size increased distinctly, and almost all pores were removed. Grain boundary diffusion and volume diffusion were the main mechanisms when sintered at 1700 °C. In the later stage of sintering, pores were completely isolated. Then, a sum effect of grain growth, hole coarsening, and volume shrinkage finally resulted in an actual density of the ceramic that was close to the theoretical density. The average particle size of the ceramic under the vacuum sintering at 1700 °C was about 5.5 μm using the Win Roof statistics. The relative density of the Yb:YAG ceramic sample was about 99.8%.

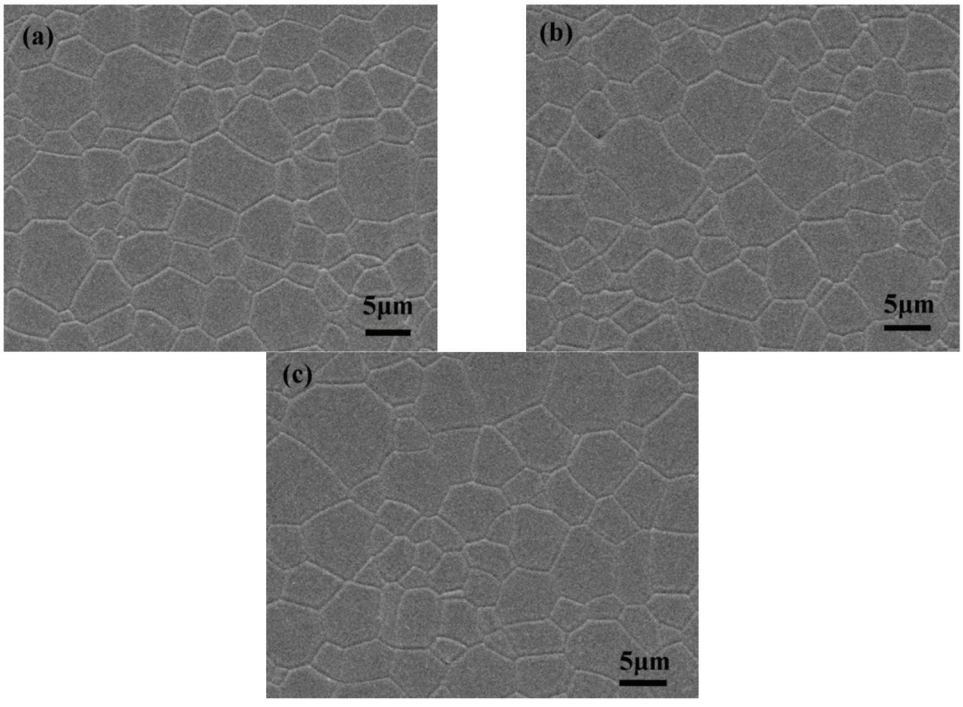

Figure 6. Thermally etched surface morphologies of $(Y_{1-x}Yb_x)AG$ transparent ceramics sintered at 1700 °C, (**a**) $x = 0$, (**b**) $x = 0.01$, (**c**) $x = 0.1$.

As mentioned above, in spite of the change of the Yb^{3+} content, the densification rate and surface microscopic morphologies of the Yb:YAG ceramics were similar, which is consistent with previous study [27]. It is thus proved that the doping of Yb had little influence on the pores discharge, grain growth and densification of ceramics.

Figure 7 shows the EDX analysis of the $(Y_{0.94}Yb_{0.06})AG$ transparent ceramic sintered at 1700 °C. The Y, Yb, Al, Si and O elements were uniformly distributed, and there was no concentration gradient and segregation. When sintered at high temperatures, the addition of Si formed the Y-Si-O liquid phase. The existence of the liquid phase made the YAG ceramics more conducive to particle rearrangement, dissolution–precipitation, and densification in the middle and late stages of sintering. The solubility of SiO_2 on the surface of the YAG particles was restricted. When the liquid phase exceeds the solubility on the particle surface, a Si-rich glass phase is easily formed [28]. The addition of Si content was 0.5 wt % in our study, which was less than its solubility on the YAG grain surface. Such a small amount of Si doping will promote densification but will not become enriched along the grain boundaries.

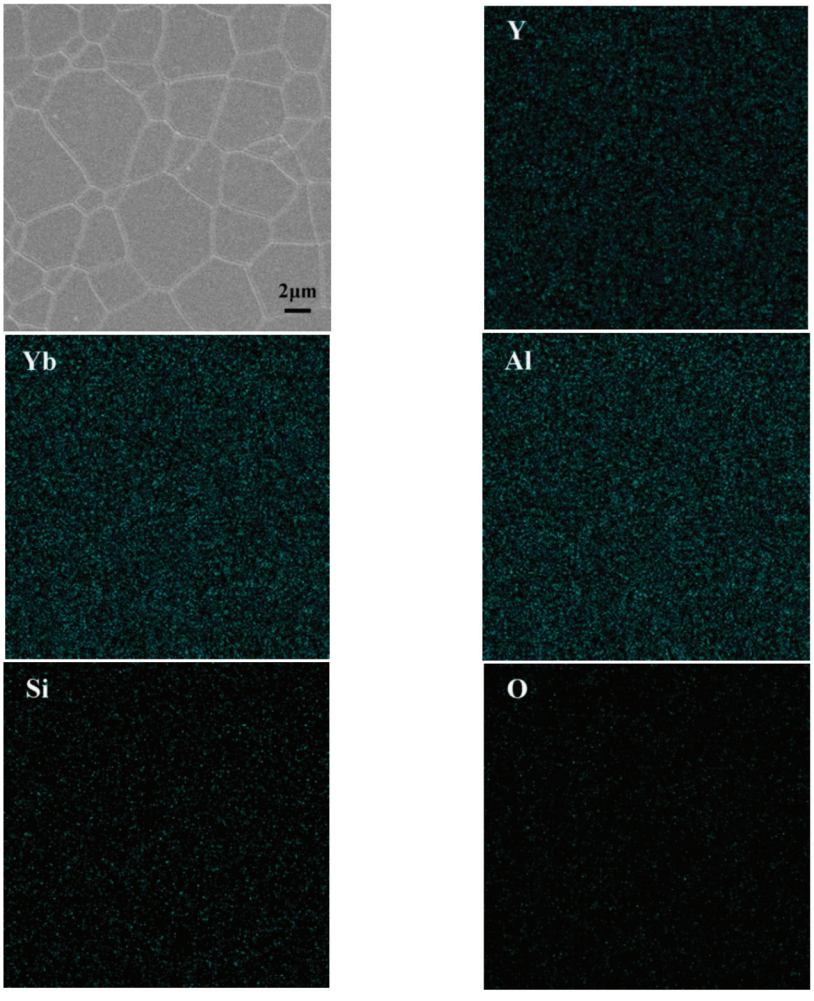

Figure 7. EDX spectra analysis of the composition distributions of the $(Y_{0.94}Yb_{0.06})AG$ transparent ceramic sintered at 1700 °C.

Unlike Nd^{3+}, the ionic radius of Yb^{3+} was small, and it is thus easier for Yb^{3+} to enter the YAG lattice. In addition, because of the low segregation coefficient of Yb^{3+} (0.18), there is a limited lattice drag effect when Yb^{3+} was doped in YAG. The doping of Yb did not promote or inhibit the densification process of the YAG transparent ceramics [29–33].

$(Y_{1-x}Yb_x)AG$ transparent ceramics were obtained by dry pressing and isostatic pressing, which were sintered in vacuum at 1700 °C for 10 h. Figure 8 shows the $(Y_{1-x}Yb_x)AG$ transparent ceramics (1.2 mm thick, both sides polished) with different doping contents of Yb (from left to right: x = 0, 0.01 and 0.10, before annealing and x = 0, 0.01 and 0.10, after annealing). All the samples were observed to have fine optical transmittance.

Figure 9 shows the optical transmittance of the Yb:YAG transparent ceramics. There were four absorption peaks at 250 nm, 300 nm, 380 nm and 640 nm before annealing. The ytterbium mainly existed in the form of Yb^{2+} in the reduction atmosphere. The absorption peaks at 250 nm and 300 nm are due to the defects (oxygen vacancies) produced by fast neutrons ion irradiation via elastic collision, and they form F and F^+ center. The absorption peak at 300 nm is weak. The optical absorption spectrum increases with fluence up to

saturation level. So, sometimes, the 300 nm absorption peak does not appear [34]. The absorption peak at 380 nm was attributed to the absorption of Yb^{2+} ions, and the peak at 640 nm was due to the oxygen vacancies that existed in the ceramics sintered in vacuum. The ceramics had a slightly higher linear transmittance after annealing due to the removal of oxygen vacancies and color centers after annealing.

Figure 8. Photos of $(Y_{1-x}Yb_x)AG$ transparent ceramics (1.2 mm thick), from left to right: x = 0, 0.01 and 0.1, before annealing and x = 0, 0.01 and 0.1, after annealing.

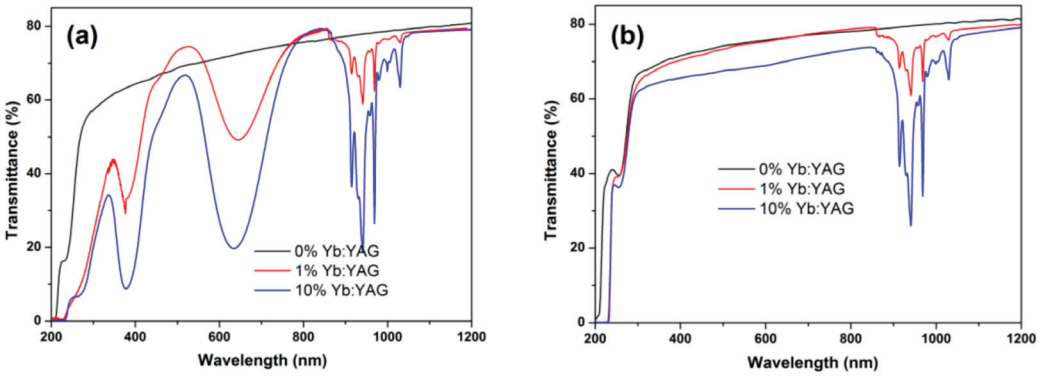

Figure 9. Optical transmittance of $(Y_{1-x}Yb_x)AG$ (x = 0, 0.01 and 0.1) transparent ceramics, (**a**) before annealing, and (**b**) after annealing.

The optical transmittance of the samples after annealing were 81.43%, 79.93% and 79.15%, respectively, at 1200 nm with the increasing of Yb contents. The in-line transmission of the sintered Yb:YAG samples had high transmission and was comparable to YAG single crystal grown by the Czochralski method (about 84% transmission). The minimum optical transmittance can be seen at 916 nm, 941 nm and 968 nm, which can be explained by the absorption of light in Yb:YAG ceramics. This matches with the transition of Yb^{3+} from the $^2F_{7/2}$ ground state to the $^2F_{5/2}$ excited state.

According to the mathematical expression of Beer–Lambert law, A = lg(1/T) = Kbc. T is the transmission ratio (light transmittance), and B is the absorption layer thickness. Obviously, as with Er:YAG transparent ceramic, the absorption band of Yb:YAG transparent ceramic does not satisfy Beer's law. The factors affecting the transmittance of YAG ceramic include pores, impurities, defects and grain boundaries, which have nothing to do with the ceramic thickness.

It is worth mentioning that the sintering activity of the Y_2O_3 and Al_2O_3 powders was apparently influenced if the precursor powders were laid aside for a period in the air after milling and drying. The precursor powders and ceramic sample performances were studied using monodispersed spherical Y_2O_3, commercial Al_2O_3 and Yb_2O_3 powders through the solid-state method and the vacuum-sintering technique.

Figure 10 shows the morphologies of the $(Y_{0.94}Yb_{0.06})AG$ precursor calcined at 1100 °C. It can be seen that agglomeration can be observed in $(Y_{0.94}Yb_{0.06})AG$ precursor after laying aside for a month, which was unfavorable as the raw materials for preparing transparent ceramics. Powder agglomeration has always been an obstacle for transparent ceramics sintering. This is because during the sintering process, the agglomerated grains would grow abnormally, and the pores would be retained in the grains.

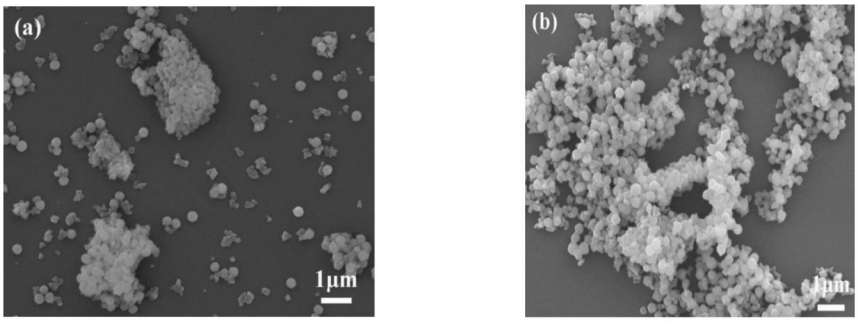

Figure 10. Micrographs showing particle morphologies of the precursor of $(Y_{0.94}Yb_{0.06})AG$ powders laying aside a month (**a**) and the precursor calcined at 1100 °C (**b**).

Figure 11 exhibits the ceramics obtained with different precursor powders via vacuum sintering at 1700 °C for 5 h. It can be seen that the ceramics obtained using fresh precursor were transparent and the relative density was 99.98% after calculation. In comparison, the ceramic obtained with the precursor placed in air for a month was opaque, and the relative density was only 97.87%.

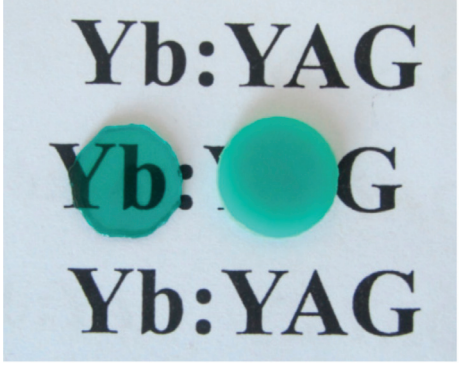

Figure 11. Photos of $(Y_{0.94}Yb_{0.06})AG$ transparent ceramics calcined at 1700 °C, 5 h, the left: the ceramic of the precursor directly sintering; the right: the ceramic of the precursor laying aside a month and sintering at the same condition.

Figure 12 shows the thermally etched surface morphologies of $(Y_{1-x}Yb_x)AG$ ceramics sintered at 1700 °C. The surface of the ceramics shown in Figure 12a was clean, and there were no pores using the fresh precursor powders. Meanwhile, as observed in Figure 12b, there were large poles on the surface of ceramics when using the precursor powder after laying aside for a month. Poles acted as the scattering centers of light and thus had a remarkable influence on the optical properties of the ceramics. According to Greskovich's report, as the enclosed pores rose from 0.25% to 0.85%, the optical transmittance decreased by 33% [35].

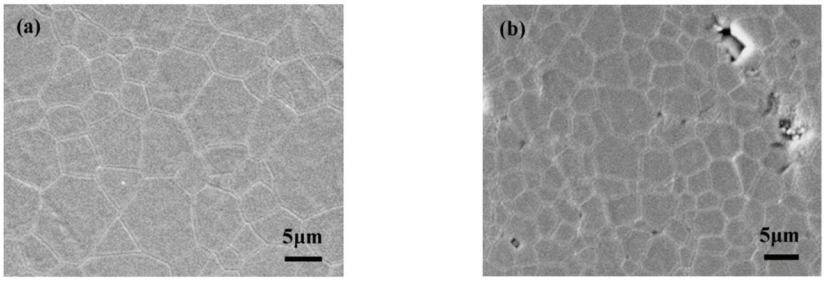

Figure 12. Thermally etched surface morphologies of $(Y_{0.94}Yb_{0.06})AG$ ceramics sintered at 1700 °C, (**a**) the precursor not laying aside, (**b**) the precursor laying aside a month.

Figure 13 shows the XRD patterns of the ceramics after vacuum sintering at 1700 °C. It can be observed that both ceramics consist of a single YAG phase. Thus, the main reason for the decreased transmittance for the Yb:YAG ceramic obtained from the stale precursor is the relatively high porosity rather than the influence of the second phase. The only difference between the two types of precursor powders was the storage time in air. The results were closely related to the agglomeration of precursor powders. The sintering activity of stale precursor powders became lower and impacted the optical transmittance of YAG ceramics.

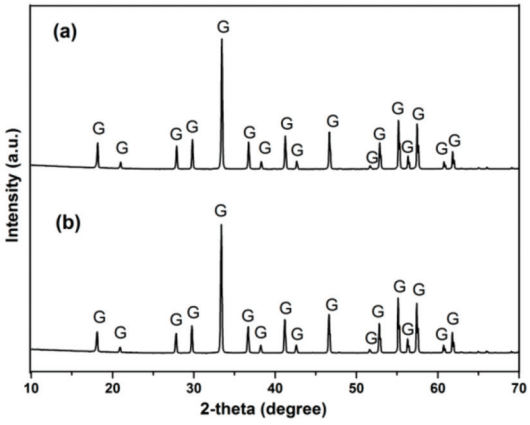

Figure 13. XRD patterns of the ceramics after vacuum sintering: (**a**) the precursor laying aside a month, compaction and sintering, (**b**) the precursor powers immediately compaction and sintering.

Based on the previous studies [36–41], the main dissolved ions of Y_2O_3 are not only Y^{3+} but also $Y(OH)^{2+}$ and $Y_2(OH)_2{}^{4+}$, which are positive polyvalent ions and easily adsorbed to the surface of negatively charged materials. In addition, the Y_2O_3 powders were easy to absorb H_2O and CO_2 in the air, which changes the surface activity of powders. The reaction process can be expressed as follows:

$$Y_2O_3 + H_2O \rightarrow Y_2O_3{\cdot}H_2O \rightarrow Y(OH)_3 \rightarrow Y^{3+} + 3OH^- \quad (7)$$

$$CO_2 + 2OH^- = CO_3{}^{2-} + H_2O \quad (8)$$

$$2Y^{3+} + 3CO_3{}^{2-} + nH_2O = (Y_2CO_3)_3{\cdot}nH_2O \quad (9)$$

The XRD pattern of the precursor leftover after a month is shown in Figure 14. In addition to the diffraction peaks of Y_2O_3 and Al_2O_3, there were also impurity peaks of $C_3H_3O_6Y{\cdot}2H_2O$ (i.e, $Y(HCOO)_3{\cdot}2H_2O$) induced by the interaction between the precursor powders, the added organic active agent, H_2O, and CO_2 in the air.

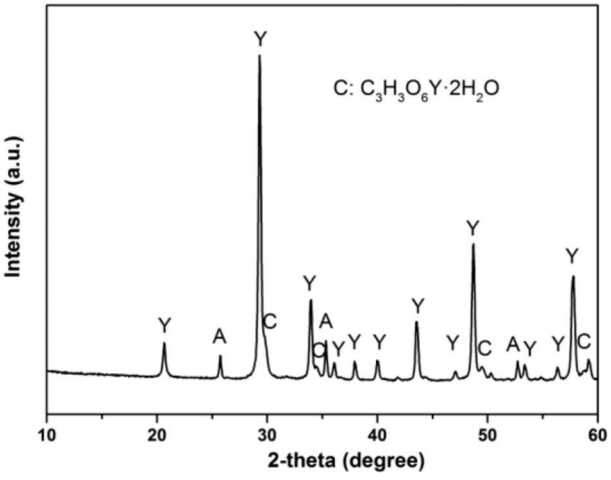

Figure 14. XRD pattern of the precursor powders after a month.

The precursor agglomeration was mainly due to the high specific surface area of the raw materials and the weak physical force of the powders, which includes the van der Waals' force, electrostatic interaction, capillary tension and magnetic force. The action range of van der Waals force is less than 100 μm, and the van der Waals force has a strong effect on the powder particles whose size is less than 0.05 μm. During calcination, a sintering bond occurred among small particles and led to the powder agglomeration. Another reason for powders agglomeration was that the vapor pressure of the grain surface is high. When leftover in the air, the surface of the powder would be wetted by air, which was related to the humidity of air and the curvature of the particles. At the contact point of the powder particles, capillary bridging was built by wetting solution, and the particles became agglomerated. The attraction force (F) among the particles has little relationship with the wetting solution but is mainly influenced by gas–liquid interface energy γ_{LV} and particle diameter D. The relational expression of these factors is shown in Equation (10) [42]:

$$F = 5\gamma_{LV}D \tag{10}$$

The mass of the particle depends on the size of the particle. So, the ratio of the aggregate force to the mass is large for small particles. The agglomeration intensity σ can be expressed by Equation (11):

$$\sigma = \frac{7S\gamma_{LV}(1-\theta)}{D\theta} \tag{11}$$

where S is saturation of the wetting liquid, θ is the degree of porosity and D refers to particle diameter. As shown in Equation (11), capillary tension has an obvious effect on the powder particle size under 100 μm.

According to the investigation above, after milling, sieving, and laying aside in the air for a period, Y_2O_3 powders can easily react with the addition of an active agent and H_2O and CO_2 in the air. Therefore, the powder surface characteristics had been influenced. After calcination, Y_2O_3 powders were partly agglomerated, which impacted the course of reaction with Al_2O_3 powders. During the high-temperature vacuum sintering, as the surface energy of the agglomeration powders is small, the aggregated powders were preferential sintered. The densification rates of the different parts of the sintered body were different. Therefore, it was difficult for pores to exclude along grain boundaries. The existence of pores in the gain particles made the ceramics opaque.

4. Conclusions

Yb:YAG transparent ceramics were fabricated using commercial Yb_2O_3 nano-powders and the prepared monodispersed spherical Y_2O_3 and Al_2O_3 powders as raw materials by vacuum sintering.

(1) The homogeneous co-precipitation method was adopted for the preparation of spherical Y_2O_3 and Al_2O_3 powders, and the average particle size was about 200 nm and 400 nm, respectively. The prepared spherical powders improved the mixing uniformity and greatly reduced the defect in the solid-state method of preparing YAG ceramics.

(2) Yb:YAG transparent ceramics were fabricated using vacuum sintering at 1700 °C for 10 h. The optical transmittance of the ceramics can achieve up to 80% at 1200 nm. From the analysis of densification rate, micromorphology and optical properties of the ceramics, it was found that the performances of the Yb:YAG ceramics are independent of the doping amount of Yb.

(3) The Y_2O_3, Al_2O_3 and Yb_2O_3 mixing precursors were laid aside for a period of time in the air after milling and drying, and the sintering activity of the powders and the obtained Yb:YAG ceramic products would be influenced significantly due to the fact that the yttrium oxide was easily hydrolyzed and it was facile to react with the active agent and air.

Author Contributions: Methodology, X.S.; validation, X.Q., J.L. and X.S.; formal analysis, X.L., L.D., H.J. and L.W.; data curation, L.W.; writing—original draft preparation, J.L.; writing—review and editing, J.L. All authors have read and agreed to the published version of the manuscript.

Funding: This work was supported by the S&T Program of Hebei (22567627H) and the Natural Science Foundation of Hebei Province (Grant No. E2018501042 and E2021501017) and the Young Talents Program of Hebei Province (Grant No. BJ2020202) and the Hebei Key Laboratory of Dielectric and Electrolyte Functional Material, Northeastern University at Qinhuangdao (HKDEFM2021301).

Institutional Review Board Statement: Not applicable.

Informed Consent Statement: Not applicable.

Data Availability Statement: Not applicable.

Conflicts of Interest: The authors declare no conflict of interest.

References

1. Yu, S.Q.; Jing, W.; Tang, M.J.; Xu, T.; Yin, W.L.; Kang, B. Fabrication, microstructure and optional properties of large-sized Nd:YAG and composite Yb:YAG transparent ceramics slabs, Ceram. *Ceram. Int.* **2019**, *45*, 19340–19344. [CrossRef]
2. Huang, C.C.; Weng, T.H.; Lin, C.L.; Su, Y.K. Light output, thermal properties, and reliability of using glass phosphors in WLED packages. *Coatings* **2021**, *11*, 239. [CrossRef]
3. Malyavin, F.; Tarala, V.; Kuznetsov, S.; Kravtsov, A.; Chikulina, I.; Shama, M.; Medyanik, E.; Ziryanov, V.; Evtushenko, E.; Vakalov, D.; et al. Influence of the ceramic powder morphology and forming conditions on the optical transmittance of YAG:Yb ceramics. *Ceram. Int.* **2019**, *45*, 4418–4423. [CrossRef]
4. Katz, A.; Barraud, E.; Lemonnier, S.; Sorrel, E.; Eichhorn, M.; D'Astorg, S.; Leriche, A. Role of LiF additive on spark plasma sintered transparent YAG ceramics. *Ceram. Int.* **2017**, *43*, 15626–15634. [CrossRef]
5. Yu, S.; Jing, W.; Tang, M.; Xu, T.; Yin, W.; Kang, B. Fabrication of Nd:YAG transparent ceramics using powders synthesized by citrate sol-gel method. *J. Alloy. Compd.* **2019**, *772*, 751–759. [CrossRef]
6. Wang, Q.Q.; Shi, Y.; Feng, Y.G.; Liu, X.; Chen, H.H.; Xie, T.F.; Li, J. Fabrication and Laser Parameters of Yb:YAG Transparent Ceramics with High Optical Quality. *J. Inorg. Mater.* **2020**, *35*, 205–210.
7. Polisadova, E.; Valiev, D.; Vaganov, V.; Oleshko, V.; Han, T.; Zhang, C.; Burachenko, A.; Popov, A. Time-resolved cathodoluminescence spectroscopy of YAG and YAG:Ce3+ phosphors. *Opt. Mater.* **2019**, *96*, 109289. [CrossRef]
8. Hu, Q.-Q.; Li, S.; Yuan, Q.; Zhang, H.; Wang, L. Transparent YAG:Ce ceramic with designed low light scattering for high-power blue LED and LD applications. *J. Eur. Ceram. Soc.* **2020**, *41*, 735–740. [CrossRef]
9. Brundage, R.T.; Yen, W.M. Energy transfer amongYb3+ions in a silicate glass. *Phys. Rev. B* **1986**, *34*, 8810–8814. [CrossRef]
10. Lu, J.; Lu, J.; Murai, T.; Takaichi, K.; Uematsu, T.; Ueda, K.; Yagi, H.; Yanagitani, T.; Akiyama, Y.; Kaminskii, A.A. Development of Nd:YAG ceramic lasers. *Adv. Solid State Lasers Proc.* **2002**, *68*, 507–517.

11. Qadri, S.; Kim, W.; Bayya, S.; Shaw, L.; Qadri, S.; Kolis, J.; Stadelman, B.; Sanghera, J. Epitaxial Growth of Single Crystal YAG for Optical Devices. *Coatings* **2021**, *11*, 644. [CrossRef]
12. Ikesue, A.; Kinoshita, T.; Kamata, K.; Yoshida, K. Fabrication and Optical Properties of High-Performance Polycrystalline Nd:YAG Ceramics for Solid-State Lasers. *J. Am. Ceram. Soc.* **1995**, *78*, 1033–1040. [CrossRef]
13. Xu, X.J.; Sun, X.D.; Liu, H.; Li, J.-G.; Li, X.D.; Huo, D.; Liu, S.H. Systhesis of monodispersed spherical yttrium aluminum garnet (YAG) powders by a homogeneous precipitation method. *J. Am. Ceram. Soc.* **2014**, *95*, 3821–3826. [CrossRef]
14. Li, J.; Chen, F.; Liu, W.; Zhang, W.; Wang, L.; Ba, X.; Zhu, Y.; Pan, Y.; Guo, J. Co-precipitation synthesis route to yttrium aluminum garnet (YAG) transparent ceramics. *J. Eur. Ceram. Soc.* **2012**, *32*, 2971–2979. [CrossRef]
15. Ikesue, A.; Furusato, I.; Kamata, K. Fabrication of polycrystalline, transparent YAG ceramics by a solid state reaction method. *J. Am. Ceram. Soc.* **1995**, *78*, 225–228. [CrossRef]
16. Li, J.; Sun, X.; Liu, S.; Li, X.; Li, J.-G.; Huo, D. A homogeneous co-precipitation method to synthesize highly sinterability YAG powders for transparent ceramics. *Ceram. Int.* **2015**, *41*, 3283–3287. [CrossRef]
17. Li, J.; Sun, X.; Liu, S.; Li, X.; Huo, D.; Li, J.-G.; Zhu, Q.; Zhang, M.; Sang, Y.; Liu, H. A novel stearate melting method for synthesizing highly reactive YAG nanopowders. *J. Alloys Compd.* **2013**, *585*, 48–53. [CrossRef]
18. Li, J.; Liu, Z.; Wu, L.; Han, X.; Qi, X.; Sun, X. Influence of ammonium sulfate on YAG nanopowders and Yb:YAG ceramics synthesized by a novel homogeneous co-precipitation method. *J. Rare Earths* **2018**, *36*, 981–985. [CrossRef]
19. Wang, J.Q.; Zhang, S.H.; Ze, R. Microwave synthesis of homogeneous YAG nanopowder leading to a transparent ceramic. *J. Am. Ceram. Soc.* **2009**, *92*, 1217–1223. [CrossRef]
20. Zhang, Z.Y.; Yang, K.; Rong, J.; Zhuang, Y.; Ai, Y.Z.T.; Zhong, X.H.; Sheng, J.; Yang, H.F.; Ding, C.X. Study on process optimization of sprayable powders and deposition performance of amorphous Al_2O_3-YAG coatings. *Coatings* **2020**, *10*, 1158. [CrossRef]
21. Karipbayev, Z.; Lisitsyn, V.; Mussakhanov, D.; Alpyssova, G.; Popov, A.; Polisadova, E.; Elsts, E.; Akilbekov, A.; Kukenova, A.; Kemere, M.; et al. Time-resolved luminescence of YAG:Ce and YAGG:Ce ceramics prepared by electron beam assisted synthesis. *Nucl. Instrum. Methods Phys. Res. Sect. B Beam Interact. Mater. Atoms* **2020**, *479*, 222–228. [CrossRef]
22. Nien, Y.-T.; Lu, T.-H.; Bandi, V.R.; Chen, I.-G. Microstructure and Photoluminescence Characterizations of Y3Al5O12:Ce Phosphor Ceramics Sintered with Silica. *J. Am. Ceram. Soc.* **2012**, *95*, 1378–1382. [CrossRef]
23. Yang, H.; Zhu, G.; Yuan, L.; Zhang, C.; Li, F.; Xu, H.; Yu, A. Characterization and Luminescence Properties of YAG:Ce^{3+} Phosphors by Molten Salt Synthesis. *J. Am. Ceram. Soc.* **2012**, *95*, 49–51. [CrossRef]
24. Glushkova, V.B.; Krzhizhanovskaya, V.A.; Egorova, O.N.; Udalov, Y.P.; Kachalova, L.P. Interaction of yttrium and aluminum oxides. *J. Inorg. Mater.* **1983**, *19*, 80–84.
25. Kingery, W.D.; Bowen, H.K.; Uhlmann, D.R. *Introduction to Ceramic*; A Wiley Interscience Press: New York, NY, USA, 1975.
26. Wen, L. Preparation of Y_2O_3 and YAG Transparent Ceramics. Ph.D. Thesis, Northeastern University, Shenyang, China, 2003.
27. Li, J.; Guan, Q.; Wu, L.; Yue, J.; Li, X.; Sun, X.; Qi, X. Influence of Yb and Si on the fabrication of Yb:YAG transparent ceramics using spherical Y_2O_3 powders. *Ceram. Int.* **2019**, *45*, 17354–17362. [CrossRef]
28. Li, J.; Liu, J.; Liu, B.; Liu, W.; Zeng, Y.; Ba, X.; Xie, T.; Jiang, B.; Liu, Q.; Pan, Y.; et al. Influence of heat treatment of powder mixture on the microstructure and optical transmission of Nd:YAG transparent ceramics. *J. Eur. Ceram. Soc.* **2014**, *34*, 2497–2507. [CrossRef]
29. Kochawattana, S.; Stevenson, A.; Lee, S.-H.; Ramirez, M.; Gopalan, V.; Dumm, J.; Castillo, V.K.; Quarles, G.J.; Messing, G.L. Sintering and grain growth in SiO_2 doped Nd:YAG. *J. Eur. Ceram. Soc.* **2008**, *28*, 1527–1534. [CrossRef]
30. Boulesteix, R.; Maître, A.; Baumard, J.-F.; Rabinovitch, Y.; Sallé, C.; Weber, S.; Kilo, M. The effect of silica doping on neodymium diffusion in yttrium aluminum garnet ceramics: Implications for sintering mechanisms. *J. Eur. Ceram. Soc.* **2009**, *29*, 2517–2526. [CrossRef]
31. Epicier, T.; Boulon, G.; Zhao, W.; Guzik, M.; Jiang, B.; Ikesue, A.; Esposito, L. Spatial distribution of the Yb^{3+} rare earth ions in $Y_3Al_5O_{12}$ and Y_2O_3 optical ceramics as analyzed by TEM. *J. Mater. Chem.* **2012**, *22*, 18221–18229. [CrossRef]
32. Hostaša, J.; Esposito, L.; Piancastelli, A. Influence of Yb and Si content on the sintering and phase changes of Yb:YAG laser ceramics. *J. Eur. Ceram. Soc.* **2012**, *32*, 2949–2956. [CrossRef]
33. Esposito, L.; Epicier, T.; Serantoni, M.; Piancastelli, A.; Alderighi, D.; Pirri, A.; Toci, G.; Vannini, M.; Anghel, S.; Boulon, G. Integrated analysis of non-linear loss mechanisms in Yb:YAG ceramics for laser applications. *J. Eur. Ceram. Soc.* **2012**, *32*, 2273–2281. [CrossRef]
34. Izerrouken, M.; Meftah, A.; Nekkab, M. Radiation damage induced by swift heavy ions and reactor neutrons in $Y_3Al_5O_{12}$ single crystals. *Nucl. Instrum. Methods Phys. Res. Sect. B Beam Interact. Mater. At.* **2007**, *258*, 395–402. [CrossRef]
35. Greskovich, C.; Woods, K.N. Fabrication of transparent ThO_2-doped Y_2O_3. *Am. Ceram. Soc. Bull.* **1973**, *52*, 473–478.
36. Zhang, L.; Yang, J.; Yu, H.; Pan, W. High performance of La-doped Y_2O_3 transparent ceramics. *J. Adv. Ceram.* **2020**, *9*, 493–502. [CrossRef]
37. Sun, Y.; Shimai, S.; Peng, X.; Zhou, G.H.; Kamiya, H.; Wang, S.W. Fabrication of transparent Y_2O_3 ceramics via aqueous gel casting. *Ceram. Int.* **2014**, *40*, 8841–8845. [CrossRef]
38. Liu, W.; Jin, L.; Wang, S. Preparation of transparent Y_2O_3 ceramic via gel casting: Realization of high solid volume via surface modification. *J. Am. Ceram. Soc.* **2019**, *102*, 6414–6421. [CrossRef]

39. Fu, Z.; Li, X.; Ren, Y.; Zhang, M.; Geng, X.; Zhu, Q.; Li, J.-G.; Sun, X. Coating Y_2O_3 nano-particles with ZrO_2-additive via precipitation method for colloidal processing of highly transparent Y_2O_3 ceramics. *J. Eur. Ceram. Soc.* **2019**, *39*, 4996–5004. [CrossRef]
40. Sun, Z.Q.; Zhu, X.W.; Li, M.S.; Zhou, Y.C.; Sakka, Y. Hydrolysis and dispersion properties of aqueous $Y_2Si_2O_7$ suspensions. *J. Am. Ceram. Soc.* **2009**, *92*, 54–61. [CrossRef]
41. Nowicki, W.; Nowicka, G. Verification of the Schulze-Hardy Rule: A Colloid Chemistry Experiment. *J. Chem. Educ.* **1994**, *71*. [CrossRef]
42. Ruan, J.M.; Huang, P.Y. *Powder Metallurgy Principle*; China Machine Press: Beijing, China, 2012; pp. 140–141.

coatings

MDPI

Article

Incorporation of Mg^{2+}/Si^{4+} in $ZnGa_2O_4:Cr^{3+}$ to Generate Remarkably Improved Near-Infrared Persistent Luminescence

Shimeng Zhang, Junqing Xiahou, Xudong Sun and Qi Zhu *

Key Laboratory for Anisotropy and Texture of Materials (Ministry of Education), School of Materials Science and Engineering, Northeastern University, Shenyang 110819, China
* Correspondence: zhuq@smm.neu.edu.cn; Tel.: +86-024-8367-2700

Abstract: Near-infrared emitting nano-sized particles of $ZnGa_{2-x}(Mg/Si)_xO_4:Cr^{3+}$ (x = 0–0.15, termed as ZGMSO:Cr^{3+}) with persistent luminescence were prepared by sol-gel processing followed by calcination. The samples were tested by XRD, TEM, STEM, SAED, Raman, XPS, UV-Vis-NIR, TL, PLE/PL spectroscopy, and persistent luminescence decay analysis. Equimolar incorporation of Mg^{2+} and Si^{4+} ions did not change the spindle structure of $ZnGa_2O_4$ seriously. Most Mg^{2+} ions are more likely to occupy the sites in octahedron, but Si^{4+} ions are more likely to occupy the sites in tetrahedron in priority. A broader bandgap, up shift of conduction band minimum, and more anti-defects were found at a higher Mg^{2+}/Si^{4+} doping concentration. ZGMSO:Cr^{3+} outputs near-infrared emission with a dominated band at 694 nm ($^2E \rightarrow {}^4A_2$ transition of Cr^{3+}), which can last longer than 48 h after the stoppage of UV irradiation. Mg^{2+}/Si^{4+} doping contributes to a better near-infrared persistent luminescence, and the strongest and the longest NIR afterglow was observed at x = 0.05, owing to that the x = 0.05 sample has the deepest defects. The synthesized nanoparticles of ZGMSO:Cr^{3+} not only output intense NIR afterglow but also can be recharged by the red light of LED several times, indicating that they are the potential nano probes for bio imaging in living animals.

Keywords: anti-defects; afterglow; bandgap; persistent luminescence; $ZnGa_2O_4$; Cr^{3+}

Citation: Zhang, S.; Xiahou, J.; Sun, X.; Zhu, Q. Incorporation of Mg^{2+}/Si^{4+} in $ZnGa_2O_4:Cr^{3+}$ to Generate Remarkably Improved Near-Infrared Persistent Luminescence. *Coatings* **2022**, *12*, 1239. https://doi.org/10.3390/coatings12091239

Academic Editor: Michelina Catauro

Received: 3 August 2022
Accepted: 22 August 2022
Published: 25 August 2022

1. Introduction

Cr^{3+}-activated zinc gallate ($ZnGa_2O_4:Cr^{3+}$) [1] and Cr^{3+}-doped zinc gallogermanate ($Zn_3Ga_2GeO_8:Cr^{3+}$) [2,3] spinel phosphors are the new favorites in persistent luminescence materials and attract tremendous attention, mainly due to their near-infrared (NIR) emissions at ~700 nm (the spin forbidden $^2E \rightarrow {}^4A_2$ transition of Cr^{3+}) and ~650–1600 nm (the spin-allowed $^4T_2 \rightarrow {}^4A_2$ transition of Cr^{3+}), that would last for a long time with several or dozens of hours after removing the light source. Recently, functionalized NIR-emitting persistent luminescent nanoparticles of $ZnGa_2O_4:Cr^{3+}$ and $Zn_3Ga_2GeO_8:Cr^{3+}$ with long lasting afterglow have been successfully synthesized for bio-imaging in living animals [4–14], mainly due to their two advantages: (1) the long-lasting afterglow feature permits detection without external illumination, which can eliminate the noise from the background because of in situ excitation; (2) the NIR emission is beneficial for whole body imaging of living animals because its ratio of signal to noise is high and the penetration is deep. However, for practical applications of the NIR persistent phosphors, the effective afterglow signal rather than the very weak luminescence signal may last for several hours, and the optical materials need to be effectively activated by visible light. Therefore, increased attention has been paid to the improvement of NIR persistent luminescence of spinel phosphors through compositional modification [15–20].

It has been predicted that any combination of ions including alkaline earth, lanthanide or Li^+ ions in $ZnGa_2O_4:Cr^{3+}$ and $Zn_3Ga_2GeO_8:Cr^{3+}$ may possibly produce materials with remarkable NIR persistent luminescence, because the incorporation of foreign ions would increase the efficient electron traps [2,21–23]. More recently, Sn^{4+}-doped $ZnGa_2O_4:Cr^{3+}$ [24],

Pr^{3+} [5], Bi^{3+} [25], Eu^{3+} [26], Yb^{3+}/Er^{3+} [27] doped zinc gallogermanate persistent luminescent materials were synthesized, and the improved NIR persistent luminescence is attributed to distorted octahedral sites arising from foreign ions occupying six-coordinated Ga site [28]. However, the reports on incorporation of two different valence ions in $ZnGa_2O_4:Cr^{3+}$ at the same time are rather limited because of their complex occupation on Zn site (four-coordinated) or Ga site (six-coordinated). But it has ability to potentially regulate the effective defects which are beneficial to the improvement of NIR persistent luminescence. In this work, equimolar Mg^{2+} and Si^{4+} ions were introduced in $ZnGa_2O_4:Cr^{3+}$ through occupying both the four- and six- coordinated sites, which increase the efficient electron traps by local microstructure regulation, thus generating remarkable improved near-infrared persistent luminescence. The local structure and the near-infrared persistent luminescence of $ZnGa_{2-x}(Mg/Si)_xO_4:Cr^{3+}$ (x = 0–0.15, termed as ZGMSO:Cr^{3+}) were investigated via detailed characterizations of X-ray diffractometry (XRD), transmission electron microscopy (TEM), STEM, SAED, Raman, X-ray photoelectron spectrometer (XPS), UV-Vis-NIR, Thermoluminescence (TL), PLE/PL spectroscopy, and persistent luminescence decay analysis. The results of this work may have wide implications on other optical materials with persistent luminescence.

2. Experimental Section

2.1. Synthesis

The starting materials of $Zn(NO_3)_3{\cdot}6H_2O$, $Mg(NO_3)_2{\cdot}6H_2O$, $Cr(NO_3)_3{\cdot}9H_2O$, SiO_2, and Ga_2O_3, were purchased from Sinopharm (Shanghai, China) with the purity of 99.99%. Ga_2O_3 was dissolved in nitric acid solution. ZGMSO:Cr^{3+} samples were prepared by sol-gel processing in the presence of trimethylaminomethane (THAM), followed by calcinations at 1000 °C. The molar ratio of THAM to total cationic ions is maintained at 2:1, and the Cr^{3+} content is fixed at 0.5 at.%, substituting for Ga^{3+}.

2.2. Characterization Techniques

X-ray diffractometry (XRD, Model SmartLab, Rigaku, Tokyo, Japan) was used for phase identification, which was performed by operating at 40 kV/40 mA using nickel filtered Cu Kα radiation and a scanning speed of 6.0° 2θ/min. A Raman microscope (Model R-XploRA Plus, Horiba, Kyoto, Japan) was used for Raman scattering measurements, using the with a 532 nm He-Ne laser as the excitation source. At the sample, the laser power was fixed at 49.1 mW. An X-ray photoelectron spectrometer (Model Axis Supra, Kratos Analytical Ltd., Manchester, UK) was used for the data of X-ray photoelectron spectroscopy (XPS) using the monochromatized Al Kα X-ray radiation. At room temperature, the measurements were performed using an ultrahigh vacuum chamber with a base pressure below 3×10^{-9} Torr. C 1 s (284.8 eV) of carbon impurities was used as reference to calibrate binding energies. Transmission electron microscopy (TEM, Model JEM-2000FX, JEOL, Tokyo, Japan) was used to test the morphologies of the products. The composition of the product was analyzed by inductively coupled plasma (ICP) spectroscopy (Model Optima 8300 and Optima 4300, Perkin Elmer, Shelton, CT, USA) with a detection limit of 0.01 wt.%. UV-Vis-NIR spectrophotometer (UV-3600 Plus, Shimadzu, Kyoto, Japan) was used for diffuse reflectance spectra of the samples at room temperature. A spectrometer (Model FJ427A TL, Beijing Nuclear Instrument Factory, Beijing, China) was used to test the glow curves of the samples with a heating rate of 1 °C·s^{-1} on after exposure to UV light for 5 min at room temperature. FP-8600 fluorospectrophotometer (Jasco, Tokyo, Japan) was used to analyze the photoluminescence of the phosphors, and Horiba JY FL3-21 (Horiba, Kyoto, Japan) was used to detect the persistent luminescence signals.

For Rietveld refinement, the data were collected through a step-scan mode over the 2θ range of 15°–120°, using a step interval of 0.02° and a counting time of 1 s per step. TOPAS 4.2 software was carried out for the Rietveld refinement of the XRD patterns.

3. Results and Discussion

3.1. Synthesis, Morphology and Local Structure

XRD pattern of the prepared ZGMSO:Cr^{3+} (x = 0–0.20) calcined at 1000 °C are displayed in Figure 1. The diffractions of the samples with x = 0–0.15 are well-indexed to spinel structured $ZnGa_2O_4$ (JCPDS No. 38–1240). There are two kinds of sites for cationic ions in the crystal structure, which are A site for Zn^{2+} in a tetrahedron surrounded by four oxygen anions, and B site for Ga^{3+} in an octahedron surrounded by six oxygen anions, respectively [28]. Appearance of a small trace of another phase corresponding to Zn_2SiO_4 (JCPDS No. 85–0453) takes place with the x value reaching 0.20, along with main phase of $ZnGa_2O_4$. The results indicates that the incorporation threshold of Mg^{2+} and Si^{4+} in $ZnGa_2O_4$ is 15% (x = 0.15). Inductively coupled plasma (ICP) spectroscopy was employed to analyze the composition of the product, and the results of chemical analysis for ZGMSO:Cr^{3+} (x = 0.01, 0.05, 0.15) are shown in Table 1. Elemental analysis identified $ZnGa_{2\cdot08}(Mg^{2+}/Si^{4+})_{0.0095}O_{4.14}$:0.0048$Cr^{3+}$ for x = 0.01 sample, $ZnGa_{2.05}(Mg^{2+}/Si^{4+})_{0.046}O_{4.15}$:0.0049$Cr^{3+}$ for x = 0.05 sample, and $ZnGa_{1.97}(Mg^{2+}/Si^{4+})_{0.154}O_{4.19}$:0.0047$Cr^{3+}$ for x = 0.15 sample, respectively. The results indicate that the composition of the prepared samples is very close to the stated objective one. Figure 2a shows the typical Rietveld structure refinements of x = 0.05 sample, using the standard $ZnGa_2O_4$ as initial model of crystal structure. Comparing the calculated and the experimental data finds that all the diffraction peaks are well matching, in absence of other impurity in the sample. The calculated values of residual factor are R_{wp} = 10.63%, R_p = 6.66%, R_{exp} = 5.92% and x^2 = 1.80. The acceptable reliability factors further confirmed that the sample is a single phase, which crystallizes in a spinel structure (cubic) with the space group of Fd-3m. Figure 2b shows Morphology of x = 0.05 sample under TEM observation, that indicates that the sample entirely consist of nanoparticles, with the sizes ranging from ~20 to ~100 nm. The SAED analysis (Figure 2c) suggested that the nanoparticles are single crystalline and exhibit excellent crystallinity. The calculated plain spacings from SAED pattern are assigned to the (220) and (422) plains of $ZnGa_2O_4$ (JCPDS No. 38–1240), indicating the formation of spinel structured solid solution. Elemental mapping results are shown in Figure 3, finding that all cationic elements are distributed among the particles, and all the elements outline the particle morphology consistent with that in Figure 2b, suggesting that the nanoparticles are homogeneous solid solutions.

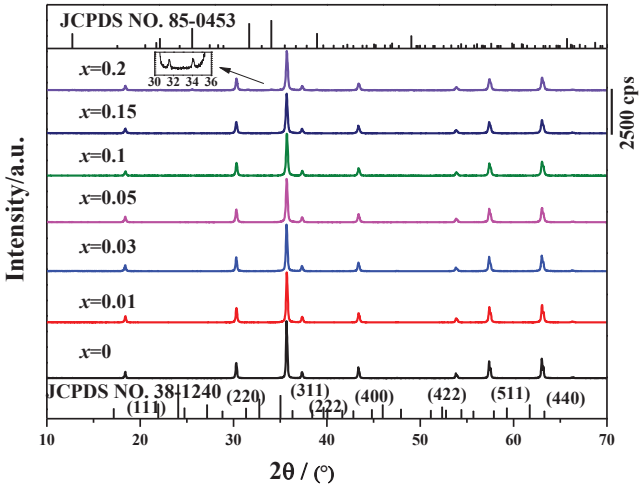

Figure 1. XRD pattern for the prepared ZGMSO:Cr^{3+} (x = 0–0.20) calcined at 1000 °C.

Table 1. Results of chemical analysis for ZGMSO:Cr^{3+} (x = 0.01, 0.05, 0.15).

x	Chemical Analysis (wt.%)					Chemical Formula
	Zn	Ga	Mg	Si	Cr	
0.01	23.4	51.9	0.04	0.05	0.09	$ZnGa_{2.08}(Mg^{2+}/Si^{4+})_{0.0095}O_{4.14}$:0.0048$Cr^{3+}$
0.05	23.3	51.1	0.22	0.21	0.09	$ZnGa_{2.05}(Mg^{2+}/Si^{4+})_{0.046}O_{4.15}$:0.0049$Cr^{3+}$
0.15	24.2	49.2	0.66	0.80	0.09	$ZnGa_{1.97}(Mg^{2+}/Si^{4+})_{0.154}O_{4.19}$:0.0047$Cr^{3+}$

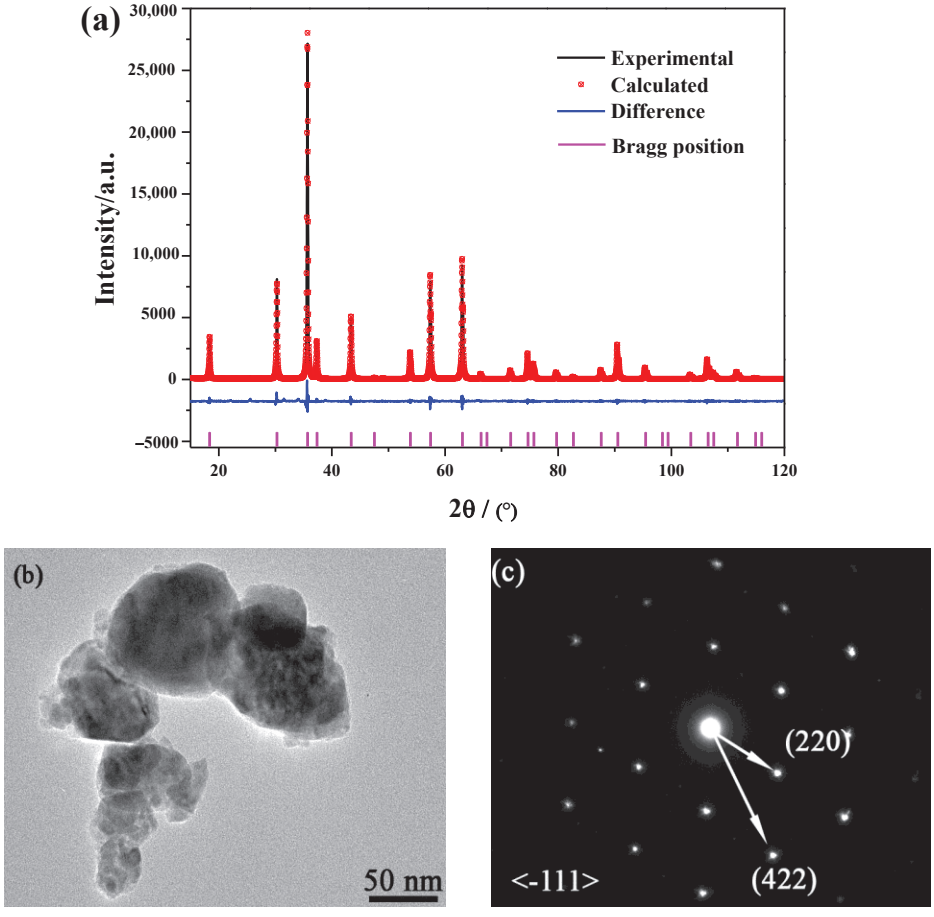

Figure 2. (**a**) Rietveld refinements, (**b**) TEM image, and (**c**) SAED patterns of ZGMSO:Cr^{3+} (x = 0.05 sample).

Figure 4a presents the X-ray photoelectron spectroscopy (XPS) survey spectra (Figure 4a). The results match well to the elemental mapping results, because other elements were not detected except for the original components and contaminating carbon. High-resolution XPS spectra of Zn $2p_{3/2}$, Ga $2p_{3/2}$, Mg 1s, Si 2p core levels for ZGMSO:Cr^{3+} (x = 0–0.15) were analyzed in Figure 4b–e, which reveals the effect of incorporation of Mg^{2+}/Si^{4+} on the microstructure. Due to a few of tetrahedral Ga and octahedral Zn sites arising from anti-defects appear in spinel-structured zinc gallate [1], a small amount of anti-site Zn^{2+} and Ga^{3+} contribute to the asymmetric XPS spectra, which may be fitted using a bi-Gaussian function (Figure 4b,c). Due to the binding energy of cationic ions in the tetrahedral sites is

smaller than that in the octahedral sites, the fitting binding energy at higher is assigned to the cationic ions occupying octahedral while the lower value is assigned to the cationic ions occupying tetrahedral sites [29]. Although Zn^{2+} ions in tetrahedron and Ga^{3+} in octahedron takes the dominate role, increasing the doping content of Mg^{2+}/Si^{4+} (x value) induces more Zn^{2+} ions being in octahedron while more Ga^{3+} ions being in tetrahedron (Tables S1 and S2), indicating more anti-defects appear. Since most Mg^{2+} ions are in octahedron, the fitted area ratio of the peak at the higher energy (~1304 eV) takes the dominate role (Figure 4d and Table S3). When the x increases from 0.01 to 0.15 (Table S3), the fitted area ratio of the peak at the lower value of ~1300 eV increases and then takes the dominate role, indicating more Mg^{2+} ions occupying tetrahedral sites at a higher Mg^{2+}/Si^{4+} doping content. However, most Si^{4+} ions are in tetrahedron, because the fitted area ratio of the peak at the lower value of ~105 eV is larger (Figure 4e and Table S4). Since the ionic radii of Si^{4+} (0.026 nm for four coordination and 0.040 nm for six coordination) is much smaller than that of Zn^{2+} (0.060 nm for four coordination) and that of Ga^{3+} (0.062 nm for six coordination) [30], Si^{4+} ions are indeed in both the tetrahedron (Zn sites) and octahedron (Ga sites). Increasing the x value did not significantly affect the occupation ratio of Si^{4+} in tetrahedral and octahedral sites. The above results suggest: (1) Si^{4+} ions occupy the tetrahedral sites in $ZnGa_2O_4$ in priority and their occupation exhibits an independence on the Mg^{2+}/Si^{4+} doping content (x value); (2) more incorporation of Mg^{2+}/Si^{4+} would induce more anti-defects appear.

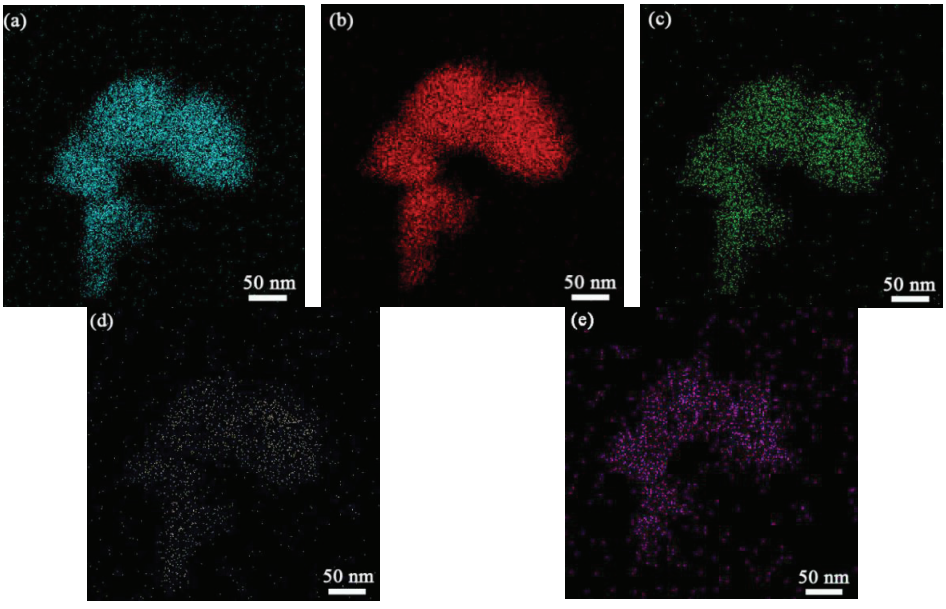

Figure 3. Element distribution of ZGMSO:Cr^{3+} (x = 0.05 sample), with (**a**) Zn, (**b**) Ga, (**c**) Mg, (**d**) Si, (**e**) Cr.

Raman spectra of ZGMSO:Cr^{3+} (x = 0–0.15) are exhibited in Figure 5. For the spinel structure, group theory predicts the following phonon modes, $\Gamma = A_{1g} + E_g + T_{1g} + 3T_{2g} + 2A_{2u} + 2E_u + 5T_{1u} + 2T_{2u}$ [31]. Gorkom et al. [32] reported that the Raman peak at ~714 cm^{-1} is assigned to A_{1g} Raman-active modes (k = 0), while the peak at ~610 cm^{-1} is assigned to T_{2g} Raman-active modes (k = 0). In this work, the Raman peaks at ~610 and ~714 cm^{-1} are clearly observed for $ZnGa_2O_4$ (x = 0 sample), which indicates there are a large amount of ZnO_4 groups with symmetric stretching vibrations [32,33]. However, the intensity of Raman peaks at ~610 and ~714 cm^{-1} weakens with increasing the x up to 0.15. More Mg^{2+}/Si^{4+} doping (larger x value) would induce more Si^{4+} and Mg^{2+} ions occupying

tetrahedral sites, along with more anti-defects of Ga^{3+} ions in tetrahedral sites, so a few of ZnO_4 groups in symmetric status transformed into ZnO_4 groups in distorted status, which contributes to the weakened Raman peaks.

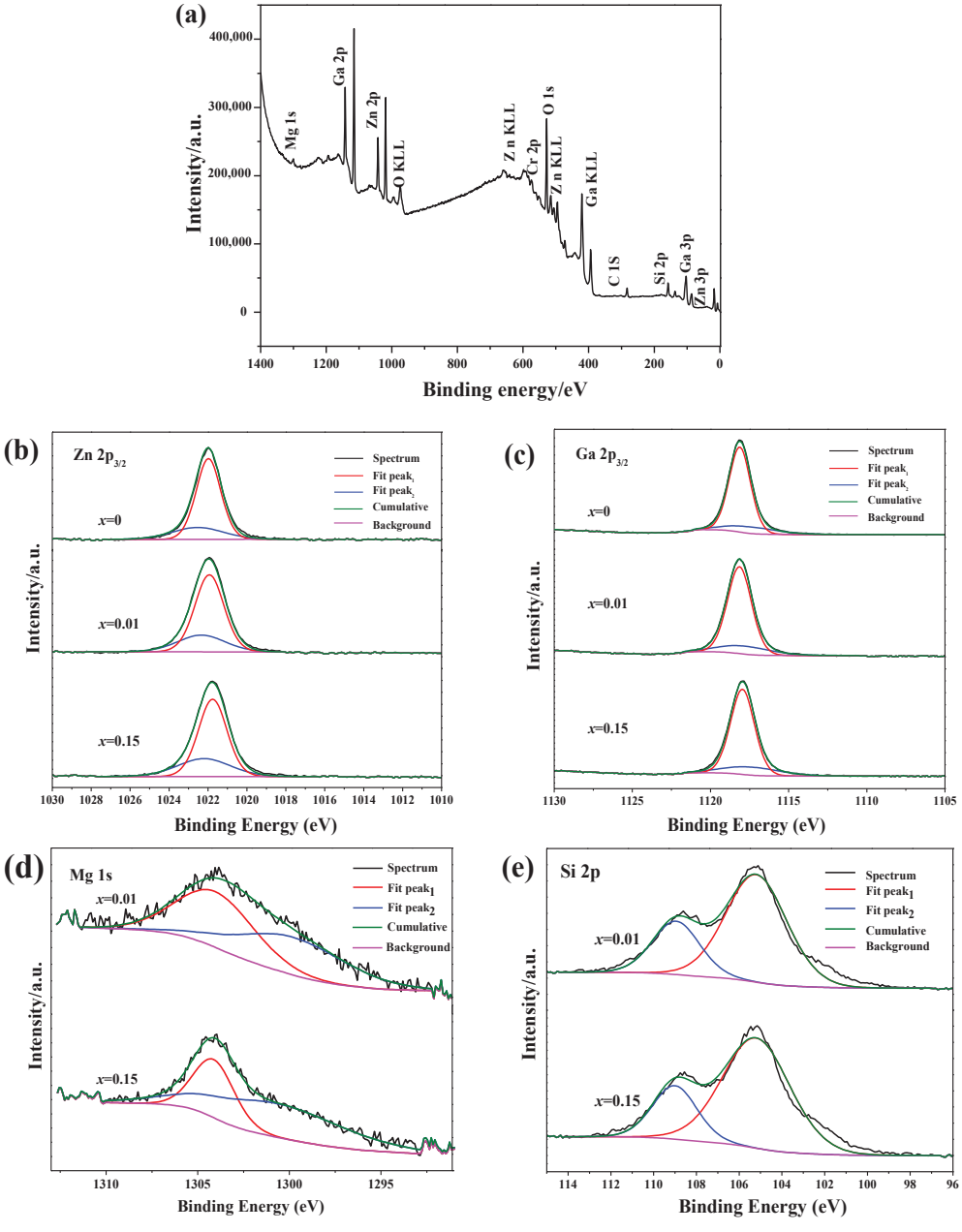

Figure 4. (**a**) XPS survey spectrum of ZGMSO:Cr^{3+} (x = 0.05 sample) and (**b**–**e**) high-resolution XPS spectra of ZGMSO:Cr^{3+} (x = 0–0.15): (**b**) Zn $2p_{3/2}$, (**c**) Ga $2p_{3/2}$, (**d**) Mg 1s, (**e**) Si 2p.

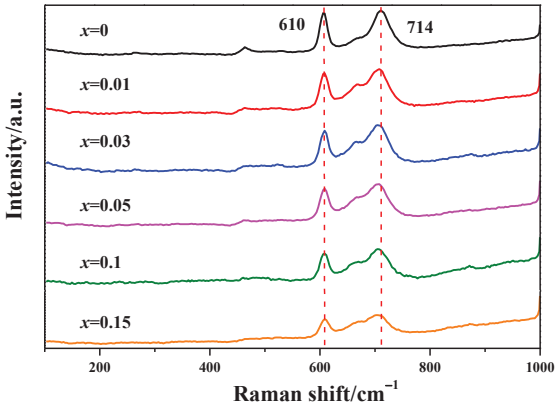

Figure 5. Raman spectra of the prepared ZGMSO:Cr^{3+} (x = 0–0.15) calcined at 1000 °C.

3.2. Photoluminescence and NIR Persistent Luminescence of ZGMSO:Cr^{3+}

Figure 6a displays the photoluminescence excitation (PLE) and emission (PL) spectra of $ZnGa_2O_4$:Cr^{3+} and ZGMSO:Cr^{3+} (taking x = 0.05 sample as an example) at room temperature. In the PLE spectra, three excitation bands are found by being monitored at a near-infrared (NIR) wavelength of 694 nm. The strongest excitation bands at the wavelength range from 220 to 320 nm, are arising from the overlap of VB → CB transition and $^4A_2 \rightarrow {}^4T_1$ (^4P) transition of Cr^{3+} [1,2]. While the excitation peaks at 410 and 565 nm are assigned to $^4A_2 \rightarrow {}^4T_1$ (^4F) transition and $^4A_2 \rightarrow {}^4T_2$ transition of Cr^{3+}, respectively [1,2,14], indicating the samples can be excited by visible light, such as blue and orange red light, except for the UV irradiation. Under the 265 nm UV excitation, the samples exhibit a near-infrared (NIR) emission with the maximum at 694 nm, which is arising from the $^2E \rightarrow {}^4A_2$ transition of Cr^{3+}, this is mainly due to Cr^{3+} ions occupying the distorted octahedrons. It is interesting to find that incorporation of Mg^{2+}/Si^{4+} ions, leads to the NIR emission intensity at 694 nm increasing by ~23% and the maximum peak of the strongest UV excitation band shifting from 256 to 265 nm, through comparing with the excitation and emission spectra of $ZnGa_2O_4$:Cr^{3+} and ZGMSO:Cr^{3+} (Figure 6a). The NIR persistent-luminescence decay curves of $ZnGa_2O_4$:Cr^{3+} and ZGMSO:Cr^{3+} are compared in Figure 6b, which were monitored at 694 nm after UV light irradiation for 300 s at room temperature. Both of $ZnGa_2O_4$:Cr^{3+} and ZGMSO:Cr^{3+} could output strong NIR afterglow that lasting more than 7200 s, but ZGMSO:Cr^{3+} exhibits much more intense NIR afterglow than that of $ZnGa_2O_4$:Cr^{3+} and thus having a longer afterglow time, which indicates that Mg^{2+}/Si^{4+} doping contributes to an improved NIR persistent luminescence. The persistent luminescence spectra of ZGMSO:Cr^{3+} with various durations confirmed that the NIR signal of afterglow can still be detected after removing the UV light source at 48 h (2880 min, Figure 6c). The appearance of NIR afterglow in Figure 6e directly shows that intense afterglow of ZGMSO:Cr^{3+} can last longer than 240 min, which is much stronger than that of $ZnGa_2O_4$:Cr^{3+}. Since ZGMSO:Cr^{3+} can also be excited by visible light, it was second in situ excited under a red-light lamp for 120 s, and repeated signal of NIR afterglow was observed after removing the excitation. The persistent luminescence spectra of ZGMSO:Cr^{3+} with various durations indicate that the repeated signal of afterglow can last more than three hours (Figure 6d), while the appearances of NIR afterglow in Figure 6e directly show that the repeated signal of afterglow can last more than four hours and exhibit priority to that of $ZnGa_2O_4$:Cr^{3+}. Therefore, it can be inferred that ZGMSO:Cr^{3+} sample possesses an excellent NIR persistent luminescence property and can be repeatedly recharge by red LED light. Since incorporation of Mg^{2+}/Si^{4+} ions in $ZnGa_2O_4$:Cr^{3+} contributes to the electrons traps which can store UV and visible light [14,24], the prepared samples exhibited rechargeable

ability for UV light and red LED light. In the following section, the influence of Mg^{2+}/Si^{4+} doping on the NIR persistent luminescence would be investigated in detail.

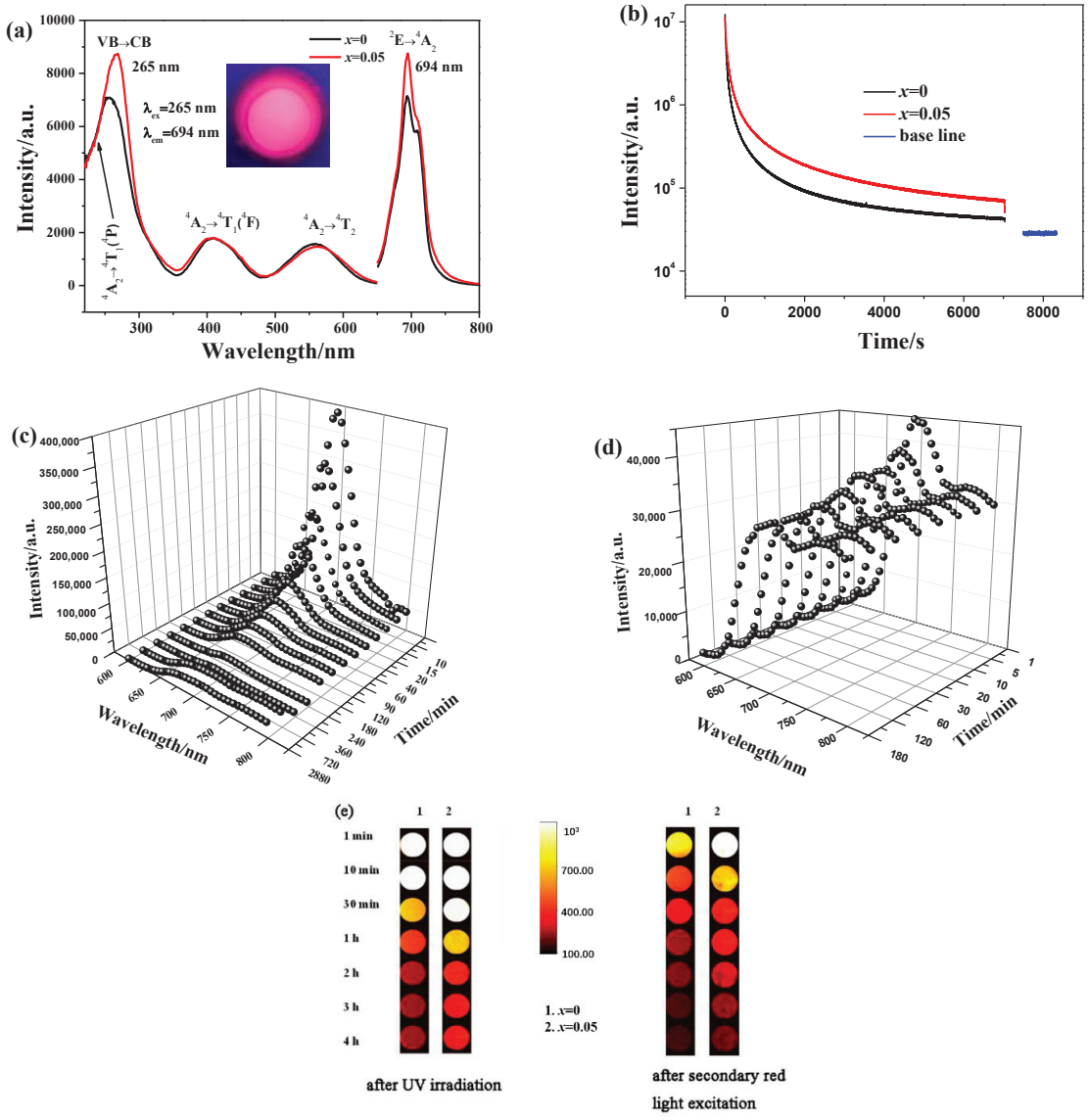

Figure 6. (**a**) PLE/PL spectra and (**b**) NIR persistent luminescence decay curves (monitored at 694 nm, 5-min excitation at 254-nm UV light illumination) of $x = 0$ and $x = 0.05$ samples. (**c**,**d**) are persistent luminescence spectra of $x = 0.05$ sample with various durations after stopping UV light and secondary excitation with a red light from a LED lamp. (**e**) is appearance of NIR afterglow of $x = 0.05$ sample with various durations obtained by a Kodak In Vivo Imaging System FX Pro at different times after removing UV irradiation for 5 min and the appearance of recharging NIR afterglow thought a secondary excitation of red light.

3.3. Effects of Mg^{2+}/Si^{4+} Doping on the NIR Persistent Luminescence and Mechanism

Figure 7a estimates the bandgap energies of ZGMSO (the host of ZGMSO:Cr^{3+}) with various x values, which were determined by a UV-Vis-NIR spectrophotometer. The absorption coefficient (α) and incident photon energy ($h\nu$) follows the relationship as $\alpha = B_d(h\nu\text{-}E_g)^{1/2}$, where B_d is the absorption constant and E_g is the bandgap energy [34]. Figure 7a shows the relationship of $(Ah\nu)^2$ versus $h\nu$ based on the spectral data. Bandgaps of 4.65 eV for x = 0, 4.70 eV for x = 0.05, and 4.77 eV for x = 0.15 are obtained by extrapolating the linear parts of the curves, which indicates that a higher x value induces a broader bandgap. Figure 7b presents the valence-band XPS spectra, which finds that all the samples have the almost the same edges of the maximum energy at about 2.88 eV. Therefore, the conduction band minimum (CBM) can be calculated from the data of bandgap and valence-band maximum (VBM), and the results are −1.78 eV for x = 0, −1.82 eV for x = 0.05, and −1.89 eV for x = 0.15, respectively. Figure 7c shows TL glow curves of ZGMSO:Cr^{3+} with various x values, and only one main peak ranging from 25 °C (298 K) to 300 °C (573 K) was observed. The main peak temperature of the TL glow curves are summarized in Table 2. Increasing the x value from 0 to 0.05 results in the temperature of peak maximum increasing from 105 °C (378 K) to 128 °C (401 K). Further increasing the x value from 0.05 to 0.15 only yields a slightly decrease with the maximum of the peak being 127 °C (400 K) and 124 °C (397 K) for x = 0.10 and x = 0.15, respectively. The electron-trap depths of ZGMSO:Cr^{3+} samples can be estimated from the following equation as E = Tm/500 [14], where Tm is the peak maximum in TL curves. The electron-trap depth calculated from the TL peaks increases from 0.756 to 0.802 eV with elevating the x value from 0 to 0.05. While the electron-trap depths exhibit a very small reduction by further elevating the x value up to 0.15.

Through the combination of the above results, a schematic illustration of the energy level was constructed in Figure 8. Since the $^4T_1$ (^4P) level of Cr^{3+} is broad and it locates partly in the bandgap and partly in the conduction band (CB), the excitation bands arising from the VB → CB transition and the $^4A_2 \rightarrow {}^4T_1$ (^4P) transition of Cr^{3+} overlap, which thus contributes to the strongest excitation band at the wavelength ranging from 220 to 320 nm (Figure 6a). More Mg^{2+}/Si^{4+} incorporation (larger x value) induces the up shift of CBM, so more parts of the $^4T_1$ (^4P) level appear in the bandgap that are near the CBM (Figure 8). The separation of CB and $^4T_1$ (^4P) level contributes to the red shift of the maximum peak of the strongest UV excitation band. Additionally, due to more part of $^4T_1$ (^4P) level breaks away from CB, more excited electrons leap into the $^4T_1$ (^4P) level rather than the CB, which results in more excited electrons going from $^4T_1$ (^4P) level to ^2E level through nonradiative transition and thus contributing to the enhanced emission intensity at 694 nm ($^2E \rightarrow {}^4A_2$ transition of Cr^{3+}, Figure 6a). Since traps with deep trap depth are not easy to be emptied at room temperature, the sample having deeper traps usually exhibit more intense and longer afterglow. Therefore, x = 0.05 sample exhibits the most intense and the longest persistent luminescence, owing to its deepest defects. Since the x = 0.10 sample and x = 0.15 sample have the trap depth close to that of x = 0.05 sample, they exhibit the similar persistent luminescence to that of x = 0.05 sample (Figure 9). Previous literatures reported that anti-defects play the role as the electron traps that can capture the excited electrons, so they would contribute to the improved persistent luminescence [35–37]. Here, more incorporation of Mg^{2+}/Si^{4+} resulted in more anti-defects, which thus contributed to the improved NIR persistent luminescence. However, Si^{4+} ions occupy the tetrahedral sites (Zn sites) in $ZnGa_2O_4$ in priority, which leads to the appearance of Ga vacancy with three negative charges and Si^{4+} in Zn sites with two positive charges. These defects contribute to the electron traps with a deeper depth more than ~1.0 eV [28,38,39], where the captured electrons cannot easily escape at room temperature and thus contributes to the worse NIR persistent luminescence. Therefore, the most intense and the longest persistent luminescence was observed for x = 0.05 sample, which are the comprehensive outcome from the anti-defects and the defects arising from Si^{4+} ions occupying the tetrahedral sites.

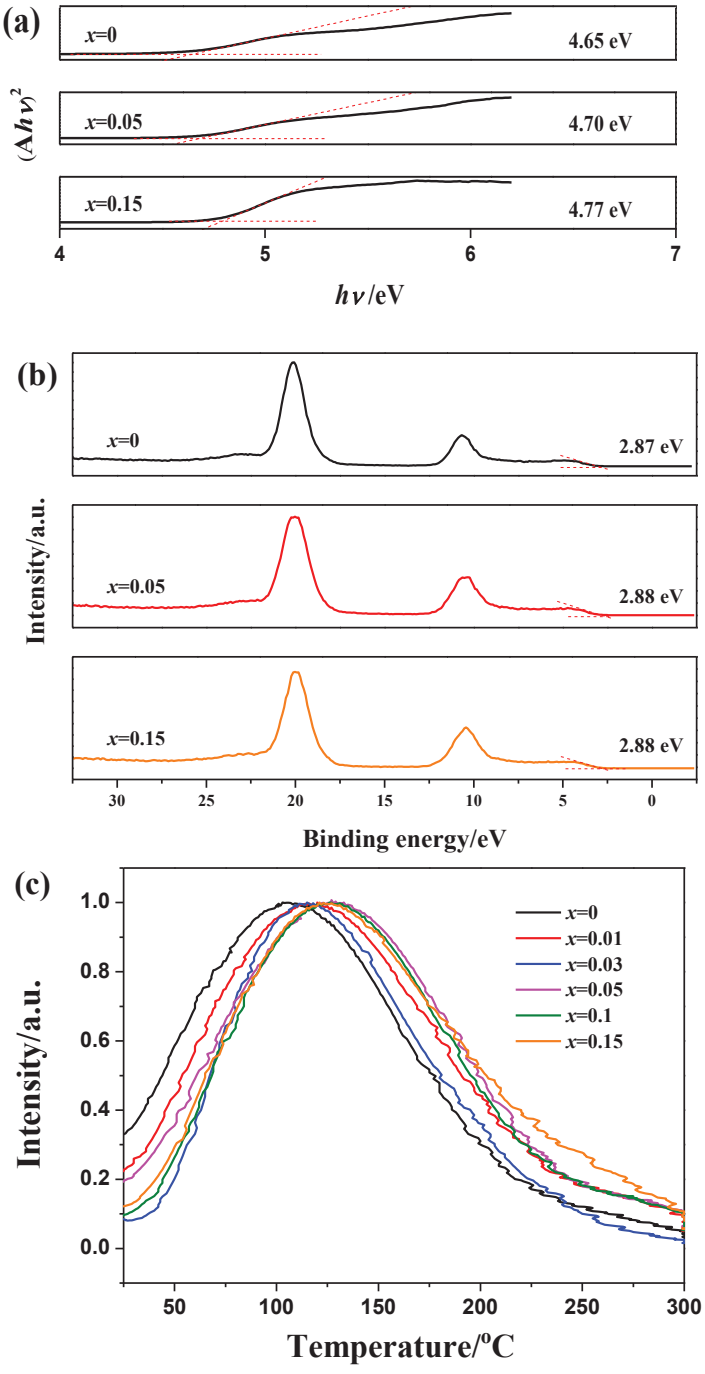

Figure 7. (**a**) Determination of bandgap energies, (**b**) Valence-band XPS spectra, and (**c**) TL glow curves of ZGMSO:Cr^{3+} (x = 0–0.15).

Table 2. Main peak temperatures of the TL glow curves and estimated trap depths.

x	Peak Temperature (°C)	Trap Depth (eV)
0	105	0.756
0.01	114	0.774
0.03	117	0.780
0.05	128	0.802
0.10	127	0.800
0.15	124	0.794

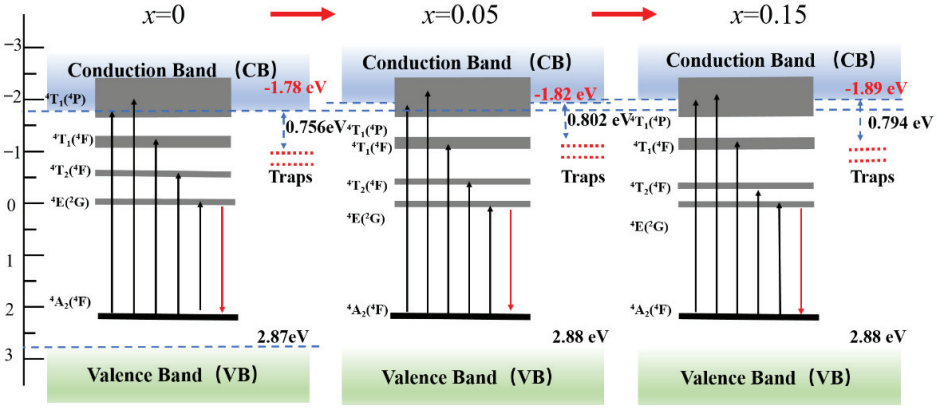

Figure 8. Schematic illustration of energy level diagram.

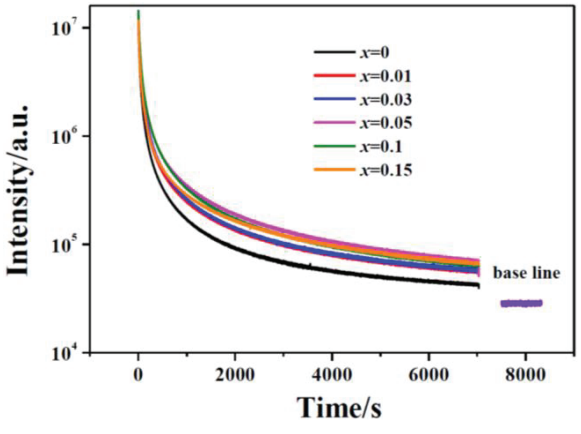

Figure 9. NIR persistent luminescence decay curves of ZGMSO:Cr^{3+} (x = 0–0.15).

4. Conclusions

In this work, nano-sized particles of $ZnGa_{2-x}(Mg/Si)_xO_4:Cr^{3+}$ (x = 0–0.15, termed as ZGMSO:Cr^{3+}) were prepared by sol-gel processing, which were then calcined at 1000 °C. The nanoparticles are single crystalline and well crystallized. Incorporation of equimolar Mg^{2+} and Si^{4+} ions did not significantly affect the spindle structure of $ZnGa_2O_4$. Most Mg^{2+} ions occupy the octahedral sites, but more Mg^{2+} ions occupying tetrahedral sites at a higher Mg^{2+}/Si^{4+} doping content. Si^{4+} ions occupy the tetrahedral sites in priority, which are independent on the Mg^{2+}/Si^{4+} doping content. More incorporation of Mg^{2+}/Si^{4+}

contributes to broader bandgap, up shift of conduction band minimum, and increased anti-defects. Under the UV excitation, ZGMSO:Cr^{3+} exhibits a near-infrared (NIR) emission with the maximum at 694 nm, which is arising from the $^2E \rightarrow {}^4A_2$ transition of Cr^{3+}, because Cr^{3+} ions are in the distorted octahedrons. Mg^{2+}/Si^{4+} doping contributes to an improved NIR persistent luminescence, and the most intense and the longest NIR afterglow was observed for $x = 0.05$ sample, owing to its deepest defects. The best sample possesses an excellent NIR long-lasting luminescence with intense NIR signal of afterglow more than 48 h and can be rechargeable by a red light of LED lamp. The prepared persistent-luminescence phosphors are suitable for applications in long-term in vivo imaging, and they imaging signal can be repeated in vivo through in situ recharge with external excitation of a red LED lamp.

Supplementary Materials: The following supporting information can be downloaded at: https://www.mdpi.com/article/10.3390/coatings12091239/s1, Table S1: The binding energies of the Zn 2p3/2 core-levels of ZGMSO:Cr^{3+}, Table S2: The binding energies of the Ga $2p_{3/2}$ core-levels of ZGMSO:Cr^{3+}, Table S3: The binding energies of the Mg 1s core-levels of ZGMSO:Cr^{3+}, Table S4: The binding energies of the Si 2p core-levels of ZGMSO:Cr^{3+}.

Author Contributions: S.Z.: data curation, formal analysis, writing—original draft. J.X.: data curation, formal analysis. X.S.: data curation, formal analysis. Q.Z.: resources, supervision, conceptualization, writing—review and editing, conceptualization. All authors have read and agreed to the published version of the manuscript.

Funding: Natural Science Foundation of Liaoning Province (Grant No. 2020-MS-081) and the National Natural Science Foundation of China (Grant No. 51302032).

Institutional Review Board Statement: Not applicable.

Informed Consent Statement: Not applicable.

Data Availability Statement: Data available on request from the authors.

Conflicts of Interest: The authors declare no conflict of interest.

References

1. Maldiney, T.; Bessière, A.; Seguin, J.; Teston, E.; Sharma, S.K.; Viana, B.; Adrie, J.J.B.; Pieter, D.; Michel, B.; Didier, G.; et al. The in vivo Activation of Persistent Nanophosphors for Optical Imaging of Vascularization, Tumours and Grafted Cells. *Nat. Mater.* **2014**, *13*, 418–426. [CrossRef]
2. Pan, Z.W.; Lu, Y.Y.; Liu, F. Sunlight-activated Long-persistent Luminescence in the Near-infrared from Cr^{3+}-doped Zinc Gallogermanates. *Nat. Mater.* **2012**, *11*, 58–63. [CrossRef]
3. Hu, Z.F.; Ye, D.H.; Lan, X.J.; Zhang, W.; Luo, L.; Wang, X.H. Influence of Co-doping Si Ions on Persistent Luminescence of $ZnGa_2O_4$:Cr^{3+} Red Phosphors. *Opt. Mater. Express* **2016**, *6*, 1329. [CrossRef]
4. Lu, T. Micro and Nanoscale Characterization of Three Dimensional Surfaces. In *Basics and Applications*; Napoca Star Publishing House: Cluj-Napoca, Romania, 2015; pp. 21–27.
5. Abdukayum, A.; Chen, J.T.; Zhao, Q.; Yan, X.P. Functional Near Infrared-emitting Cr^{3+}/Pr^{3+} Co-doped Zinc Gallogermanate Persistent Luminescent Nanoparticles with Superlong Afterglow for in vivo Targeted Bioimaging. *J. Am. Chem. Soc.* **2013**, *135*, 14125–14133. [CrossRef]
6. Shi, J.P.; Sun, X.; Li, J.L.; Man, H.Z.; Shen, J.S.; Yu, Y.K.; Zhang, H.W. Multifunctional Near Infrared-Emitting Long-Persistence Luminescent Nanoprobes for Drug Delivery and Targeted Tumor Imaging. *Biomaterials* **2015**, *37*, 260–270. [CrossRef]
7. Zou, R.; Gong, S.M.; Shi, J.P.; Jiao, J.; Wong, K.A.; Zhang, H.W.; Wang, J.; Su, Q. Magnetic-NIR Persistent Luminescent Dual-modal ZGOCS@MSNs@Gd_2O_3 Core-shell Nanoprobes for in vivo Imaging. *Chem. Mater.* **2017**, *29*, 3938–3946. [CrossRef]
8. Zou, R.; Huang, J.J.; Shi, J.P.; Huang, L.; Zhang, X.J.; Wong, K.L.; Zhang, H.W.; Jin, D.Y.; Wang, J.; Su, J. Silica Shell-assisted Synthetic Route for Mono-disperse Persistent Nanophosphors with Enhanced in vivo Recharged Near-infrared Persistent Luminescence. *Nano. Res.* **2017**, *10*, 2070–2082. [CrossRef]
9. Li, Z.J.; Zhang, Y.W.; Wu, X.; Huang, L.; Li, D.S.; Fan, W.; Han, G. Direct Aqueous-Phase Synthesis of Sub-10 nm "Luminous Pearls" with Enhanced in vivo Renewable Near-Infrared Persistent Luminescence. *J. Am. Chem. Soc.* **2015**, *137*, 5304–5307. [CrossRef]
10. Lu, Y.C.; Yang, C.X.; Yan, X.P. Radiopaque Tantalum Oxide Coated Persistent Luminescent Nanoparticles as Multimodal Probes for in vivo Near-infrared Luminescence and Computed Tomography. *Nanoscale* **2017**, *7*, 17929–17937. [CrossRef]

11. Wu, Y.L.; Li, Y.; Qin, X.X.; Qiu, J.R. A Multi-Functional Biomaterial with NIR Long Persistent Phosphorescence, Photo-Thermal Response and Magnetism. *Chem. Asian. J.* **2016**, *11*, 2537–2541. [CrossRef]
12. Li, Y.; Chen, R.C.; Li, Y.Y.; Sharafudeen, K.; Liu, S.J.; Wu, D.K.; Wu, Y.L.; Qin, X.X.; Qin, J.R. Folic Acid-Conjugated Chromium (III) Doped Nanoparticles Consisting of Mixed Oxides of Zinc, Gallium and Tin, and Possessing Near-infrared and Long Persistent Phosphorescence for Targeted Imaging of Cancer Cells. *Microchim. Acta.* **2015**, *182*, 1827–1834. [CrossRef]
13. Lv, Y.; Ding, D.D.; Zhuang, Y.X.; Feng, Y.S.; Shi, J.P.; Zhang, H.W.; Zhou, T.L.; Chen, H.M.; Xie, R.J. Chromium-Doped Zinc Gallogermanate@zeolitic Imidazolate Framework-8: A Multifunctional Nanoplatform for Rechargeable in vivo Persistent Luminescence Imaging and pH-Responsive Drug Release. *ACS. Appl. Mater. Interfaces* **2019**, *11*, 1907–1916. [CrossRef] [PubMed]
14. Zhu, Q.; Xiahou, J.Q.; Guo, Y.; Guo, Y.; Li, H.L.; Ding, C.; Wang, J.; Li, X.D.; Sun, X.D.; Li, J.G. $Zn_3Ga_2Ge_2O_{10}$:Cr^{3+} Uniform Microspheres: Template-Free Synthesis, Tunable Bandgap/Trap-Depth, and in vivo Rechargeable Near-Infrared Persistent Luminescence. *ACS. Appl. Bio. Mater.* **2019**, *2*, 577–587. [CrossRef] [PubMed]
15. Li, Y.; Zhou, S.F.; Li, Y.Y.; Sharafudeen, K.; Ma, Z.J.; Dong, G.P.; Peng, M.Y.; Qiu, J.R. Long Persistent and Photo-Stimulated Luminescence in Cr^{3+}-doped Zn-Ga-Sn-O Phosphors for Deep and Reproducible Tissue Imaging. *J. Mater. Chem. C* **2014**, *2*, 2657–2663. [CrossRef]
16. Zhao, H.X.; Yang, C.X.; Yan, X.P. Fabrication and Bioconjugation of B^{III} and Cr^{III} Co-Doped $ZnGa_2O_4$ Persistent Luminescent Nanoparticles for Dual-Targeted Cancer Bioimaging. *Nanoscale* **2016**, *8*, 18987–18994. [CrossRef]
17. Duan, X.L.; Liu, J.; Wu, Y.C.; Yu, F.P.; Wang, X.Q. Structure and Luminescent Properties of Co^{2+}/Cr^{3+} Co-doped $ZnGa_2O_4$ Nanoparticles. *J. Lumin.* **2014**, *153*, 361–368. [CrossRef]
18. Li, P.F.; Zhang, X.Y.; Zhang, J.R.; Qi, X.W.; Liu, X. Investigations of Thermal Stability and Spectroscopic Features of Sm^{3+} Doped Strontium Aluminate Glasses. *Coatings* **2022**, *12*, 3. [CrossRef]
19. Gai, C.L.; He, D.W.; Wang, Y.S.; Wang, J.G.; Li, J.M. Engineering of Halide Cation in All-Inorganic Perovskite with Full-Color Luminescence. *Coatings* **2021**, *11*, 330. [CrossRef]
20. Fang, J.; Liu, W.T.; Zhou, W.Y.; Zhu, C.; Ni, Y.R.; Fang, L.; Lu, C.H. Down-Conversion Polymer Composite Coatings with Multipeak Absorption and Emission. *Coatings* **2021**, *11*, 282. [CrossRef]
21. Patel, N.P.; Srinivas, M.; Modi, D.; Verma, V.; Venkata, K.; Murthy, R. Optimization of Luminescence Properties of Tb^{3+}-Doped α-$Sr_2P_2O_7$ Phosphor Synthesized by Combustion Method. *Rare Met.* **2018**, *37*, 587–593. [CrossRef]
22. Sheoran, S.; Singh, K.; Tanwar, V.; Singh, S.; Samantilleke, A.; Singh, D. Synthesis and Spectroscopic Investigations of Trivalent Europium-doped $Z_2Si_3O_8$ (Z = Mg, Ca and Sr) Nanophosphors for Display Applications. *Rare Metals* **2021**, *40*, 2610–2617. [CrossRef]
23. Xie, J.H.; Wang, J.; Qiu, G.H.; Li, X.B.; Huang, W.T.; Zhang, R.R.; Lin, T.; Wang, L.X.; Zhang, Q.T. A Strategy to Achieve Efficent Green-Emission Dual-Mode Luminescence of Yb^{3+}, Eu^{3+} Doped $NaBiF_4$. *Rare Metals* **2021**, *40*, 2040–2048. [CrossRef]
24. Allix, M.; Chenu, S.; Véron, E.; Poumeyrol, T.; Kouadri-Boudjelthia, E.A.; Alahraché, S.; Porcher, F.; Massiot, D.; Fayon, F. Considerable Improvement of Long-Persistent Luminescence in Germanium and Tin Substituted $ZnGa_2O_4$. *Chem. Mater.* **2013**, *25*, 1600–1606. [CrossRef]
25. Zhuang, Y.X.; Ueda, J.; Tanabe, S. Tunable Trap Depth in $Zn(Ga_{1-x}Al_x)_2O_4$: Cr, Bi Red Persistent Phosphors: Considerations of High-Temperature Persistent Luminescence and Photostimulated Persistent Luminescence. *J. Mater. Chem. C* **2013**, *1*, 7849–7855. [CrossRef]
26. Wang, Q.Q.; Zhang, S.Y.; Li, Z.W.; Zhu, Q. Near Infrared-Emitting Cr^{3+}/Eu^{3+} Co-doped Zinc Gallogermanate Persistence Luminescent Nanoparticles for Cell Imaging. *Nanoscale Res. Lett.* **2018**, *13*, 64. [CrossRef]
27. Liu, F.; Liang, Y.J.; Pan, Z.W. Detection of Up-converted Persistent Luminescence in the Near Infrared Emitted by the $Zn_3Ga_2GeO_8$:Cr^{3+}, Yb^{3+}, Er^{3+} Phosphor. *Phys. Rev. Lett.* **2014**, *113*, 177401. [CrossRef]
28. Li, Y.; Gecevicius, M.; Qiu, J.R. Long Persistent Phosphors-from Fundamentals to Applications. *Chem. Soc. Rev.* **2016**, *45*, 2090–2136. [CrossRef] [PubMed]
29. Gong, Z.; Liu, Y.X.; Yang, J.; Yan, D.T.; Zhu, H.C.; Liu, C.G.; Xu, C.S.; Zhang, H. A Pr^{3+} Doping Strategy for Simultaneously Optimizing the Size and Near Infrared Persistent Luminescence of ZGGO:Cr^{3+} Nanoparticles for Potential Bio-imaging. *Phys. Chem. Chem. Phys.* **2017**, *19*, 24513–24521. [CrossRef]
30. Shannon, R.D. Revised Effective Ionic Radii and Systematic Studies of Interatomic Distances in Halides and Chaleogenides. *Acta. Cryst. A* **1976**, *32*, 751–767. [CrossRef]
31. Kang, H.I.; Kim, J.S.; Lee, M.; Bahng, J.H.; Choi, J.C.; Park, J.K.; Kim, G.C.; Kim, T.W.; Hwang, Y.H.; Mho, S.I.; et al. Tunable Color Emission of $ZnGa_2O_4$:Si^{4+} Phosphors with Enhanced Brightness Due to Donor Formation. *Solid State Commun.* **2002**, *122*, 633–636. [CrossRef]
32. Gorkom, G.; Haanstra, J.; Boom, H. Infrared and Raman Spectra of the Spinel $ZnGa_2O_4$. *J. Raman. Spectrosc.* **1973**, *1*, 513–519. [CrossRef]
33. López, S.; Romero, A. First-Principles Study of the High-Pressure Phase Tansition in $ZnAl_2O_4$ and $ZnGa_2O_4$: From Cubic Spinel to Orthorhombic Post-Spinel Structures. *Phys. Rev. B* **2009**, *79*, 214103. [CrossRef]
34. Wu, Y.L.; Li, Y.; Qin, X.X.; Chen, R.C.; Wu, D.K.; Liu, S.J.; Qin, J.R. Near-Infrared Long-Persistent Phosphor of $Zn_3Ga_2Ge_2O_{10}$:Cr^{3+} Sintered in Different Atmosphere. *Spectrochim. Acta A Mol. Biomol. Spectrosc.* **2015**, *151*, 385–389. [CrossRef]
35. Zhu, Q.; Xiahou, J.Q.; Li, X.D.; Sun, X.D.; Li, J.G. Defect Cluster Engineering in $ZnGa_{2-x}(Mg/Ge)_xO_4$:Cr^{3+} Nanoparticles for Remarkably Improved NIR Persistent Luminescence. *J. Am. Ceram. Soc.* **2021**, *104*, 4594–4605. [CrossRef]

36. Xiahou, J.Q.; Zhu, Q.; Zhu, L.; Li, S.Y.; Li, J.G. Local Structure Regulation in Near-Infrared Persistent Phosphor of $ZnGa_2O_4:Cr^{3+}$ to Fabricate Natural-Light Rechargeable Optical Thermometer. *ACS. Appl. Electron. Mater.* **2021**, *3*, 3789–3803. [CrossRef]
37. Xiahou, J.Q.; Zhu, Q.; Zhu, L.; Huang, S.; Zhang, T.; Sun, X.D.; Li, J.G. Lattice-Site Engineering in $ZnGa_2O_4:Cr^{3+}$ through Li^+ Doping for Dynamic Luminescence and Advanced Optical Anti-Counterfeiting. *J. Mater. Chem. C* **2022**, *10*, 7935. [CrossRef]
38. Lin, X.H.; Zhang, R.L.; Tian, X.M.; Li, Y.; Du, B.U.; Nie, J.M.; Li, Z.Z.; Chen, L.; Ren, J.J.; Qiu, J.R.; et al. Coordination Geometry-dependent Multi-Band Emission and Atypically Deep-Trap-Dominated NIR Persistent Luminescence from Chromium-Doped Aluminates. *Adv. Optical Mater.* **2018**, *6*, 1701161. [CrossRef]
39. Gupta, P.; Kumar, M.; Nagarajan, R. Interplay Between Defects and Cation Nonstoichiometry in Lithium-Substituted $CdGa_2O_4$ Leading to Multifunctional Behavior. *J. Phys. Chem. C* **2018**, *122*, 22094–22105. [CrossRef]

coatings

MDPI

Article

Effect of Si_3N_4/TaC Particles on the Structure and Properties of Microarc Oxidation Coatings on TC4 Alloy

Wei Gao [1], Liqun Wang [2], Yaohua Jin [1], Yuhong Yao [1], Zhisong Ding [1], Wei Yang [1,*] and Jiangnan Liu [1,*]

[1] School of Materials Science and Chemical Engineering, Xi'an Technological University, Xi'an 710032, China
[2] School of Physics, Xi'an Jiaotong University, Xi'an 710049, China
* Correspondence: yangwei_smx@163.com (W.Y.); liujiangnan@xpu.edu.cn (J.L.); Tel.: +86-029-8617-3369 (W.Y.); +86-029-8617-3324 (J.L.)

Abstract: Si_3N_4/TaC composite MAO coatings were fabricated by microarc oxidation (MAO) on a Ti–6Al–4V (TC4) alloy in a phosphate-based electrolyte containing Si_3N_4/TaC mixed particles. The influence of the amount of Si_3N_4/TaC particles on the microstructure, composition, tribological behavior, and corrosion properties of the MAO coatings has been investigated. Morphological research of the MAO coatings was carried out using scanning electron microscopy (SEM), with the surface porosity analyzed by ImageJ software. X-ray diffraction (XRD) was used for the detection of the phase characteristic of the MAO coatings, and an abrasive wear test and electrochemical measurements were conducted in the artificial seawater solution by the ball-on-disc friction tester and the electrochemical workstation, respectively. The results showed that Si_3N_4/TaC particles could be successfully incorporated into the composite coatings, and the addition of Si_3N_4/TaC particles greatly reduced the porosity of the coatings, thus improving both tribological and corrosion properties of the composite MAO coatings. The composite MAO coating with the addition of 1 g/L Si_3N_4 + 0.5 g/L TaC particles showed the best tribological property and the optimum corrosion properties.

Keywords: microarc oxidation; TC4 alloy; Si_3N_4/TaC particles; porosity; tribological property; electrochemical corrosion

Citation: Gao, W.; Wang, L.; Jin, Y.; Yao, Y.; Ding, Z.; Yang, W.; Liu, J. Effect of Si_3N_4/TaC Particles on the Structure and Properties of Microarc Oxidation Coatings on TC4 Alloy. *Coatings* **2022**, *12*, 1247. https://doi.org/10.3390/coatings12091247

Academic Editor: Francesco Marra

Received: 23 July 2022
Accepted: 23 August 2022
Published: 26 August 2022

1. Introduction

Titanium alloys are widely used in aerospace, marine, and biomedical fields due to their low density, high specific strength, low thermal expansion coefficient, and excellent biocompatibility [1–4]. However, their low hardness, poor tribological properties, and high electrode potential give rise to the problems such as surface abrasion, contact corrosion, and marine biofouling, thus limiting the extensive applications in the complicated marine environment [5]. At present, some surface modification methods, such as anodizing [6,7], vapor deposition [8], magnetron sputtering [9], microarc oxidation (MAO) [10,11], etc., [12–15] are used to improve the corrosion resistance and wear resistance of the aluminum, magnesium, and titanium alloys. Moreover, as an in situ growth technique for preparing ceramic coatings, MAO has some attractive characteristics such as easy operation, high production efficiency, and environmental friendliness, thus being widely used in the surface modification of titanium alloys [16]. It is well known that the high temperature and high pressure used in the process of MAO lead to coatings that contain a high density of pores. Thus, many studies have focused on improving the microstructures and properties of the coatings via optimizing the electrical conditions, such as the applied voltage/current magnitude, mode, frequency, and duty cycle via modifying the electrolyte compositions [16–23]. Recently, some functional particles such as Al_2O_3, ZrO_2, CeO_2, MoS_2, etc. [24–30], have been successfully introduced to the electrolyte to enhance the functional properties of titanium alloys. Wang et al. [27] confirmed that the composite ceramic coating containing Al_2O_3 on a Ti–6Al–4V (TC4) alloy exhibited better wear resistance at 300 °C due to the dense surface structure and higher volume fraction of Al_2TiO_5. Mu et al. [28] added

MoS_2 to the electrolyte to greatly reduce the friction coefficient of the MAO coatings on TC4 alloy. Chen et al. [29] also introduced MoS_2 particles into the electrolyte and proved that MoS_2 was able to retard the formation of micropores during the processing of MAO and thus significantly improving the corrosion resistance of the MAO coating, which would expand the application of TC4 alloy in the marine environment. Ao et al. [30] fabricated the TiO_2/hBN composite coating on the surface of Ti–6Al–4V alloy via microarc oxidation and found that the composite coating consisting of rutile TiO_2, anatase TiO_2, and an hBN phase was less porous than the particle-free coating and that the presence of hBN particles in the MAO coating could improve its anti-friction property.

Silicon nitride (Si_3N_4) ceramics that have a low thermal expansion coefficient, good mechanical properties at high temperatures, high thermal shock resistance and high resistance to chemical attack, and good tribological properties are widely used in manufacturing the Si_3N_4-based composite used in high-temperature applications. Some works have been conducted to prepare Si_3N_4 composite MAO coatings on magnesium alloys, pure Ti, and TC4 alloy [31–34]. Lou et al. [31] revealed that the addition of 2 g/L Si_3N_4 to the electrolyte made the MAO coatings on AZ31 Mg alloy have optimal corrosion resistance, a low friction coefficient, and good adhesion strength. However, Lu et al. [32] found that Si_3N_4 particles were difficult to incorporate into the coating due to their high melting point and that large Si_3N_4 particles had a negative effect on the coating thickness. As a result, the addition of Si_3N_4 particles did not enhance the corrosion resistance [32]. Aliofkhazraei et al. [33] successfully fabricated Si_3N_4/TiO_2 nanocomposite coatings by MAO on commercially pure titanium samples in a suspension with fine Si_3N_4 nanoparticles and found the coatings have high hardness and good wear resistance. In addition, our previous work [34] also demonstrated that the Si_3N_4 composite MAO coatings on a TC4 alloy fabricated by the addition of 1 g/L and 3 g/L Si_3N_4 had the best antibacterial property and wear resistance, respectively.

Tantalum carbide (TaC) is one of the common metal carbides with excellent physical and chemical properties such as high hardness (20 GPa), high melting point (3880 °C), excellent wear resistance, chemical stability, and so on [35]. Ding et al. [36] successfully prepared the TaC composite coatings by MAO on TC4 alloy and found that the coatings, when prepared with the addition of 5 g/L TaC, had the best wear resistance and corrosion resistance in seawater.

Based on previous research [34,36], the present study aims to take full advantage of the high hardness and excellent wear resistance of both TaC and Si_3N_4 particles as well as the good lubrication of Si_3N_4 particles to prepare the Si_3N_4/TaC composite MAO coatings on the surface of the TC4 alloy. Therefore, Si_3N_4 and TaC mixed particles were introduced into the phosphate-based electrolyte. The microstructure, wear resistance, and corrosion properties of the Si_3N_4/TaC composite MAO coatings were investigated to provide technical support for the applications of titanium alloy in marine environments.

2. Materials and Methods

2.1. Materials

Ti–6Al–4V alloy with 6.6% Al, 4.3% V, 0.1% Fe, and balance Ti (in wt. %) was used as the substrate material. The plate specimens, with the dimensions of φ20 mm × 5 mm, were sequentially ground with alumina waterproof abrasive paper up to 1200 grit and ultrasonically degreased in acetone for 10 min, followed by rinsing with distilled water and then dried in warm air.

2.2. MAO Treatment

MAO is a plasma-chemical and electrochemical process that combines electrochemical oxidation with a high voltage spark treatment in an aqueous electrolyte, leading to the formation of a physically protective oxide film or a ceramic-like coating on the metal surface to improve wear and corrosion resistance. The specimens were treated using the microarc oxidation equipment (JHMAO–60, XAUT, Xi'an, China) with a pulse power un-

der the following conditions: a constant voltage of 450 V, a frequency of 750 Hz, and a duty cycle of 3% for 10 min in the base electrolyte solution containing 20.0 g/L $(NaPO_3)_6$, 3.0 g/L Na_2WO_4, 3.0 g/L KF, 3.0 g/L KOH, and 5.0 g/L $CuSO_4$. For the lower porosity of the MAO coating with the addition of 4 g/L Si_3N_4 or 2 g/L TaC to the electrolyte solution obtained in the preliminary experimental results, a certain proportional concentration of Si_3N_4 nanoparticles (about 50 nm) and TaC microparticles (1–2 μm), i.e., 1 g/L Si_3N_4 + 0.5 g/L TaC, 2 g/L Si_3N_4 + 1 g/L TaC, 4 g/L Si_3N_4 + 2 g/L TaC, were added into the base electrolyte. The coated specimens prepared with the addition of 0 g/L, 1 g/L Si_3N_4 + 0.5 g/L TaC, 2 g/L Si_3N_4 + 1 g/L TaC, 4 g/L Si_3N_4 + 2 g/L TaC are simplistically denoted as 0 g/L, 1 g/L + 0.5 g/L 2 g/L + 1 g/L, and 4 g/L + 2 g/L Ta, respectively. The MAO process of the TC4 alloy is shown schematically in Figure 1, where the TC4 substrate was connected to the anode, and a 316 L stainless steel container was connected to the cathode. During the MAO process, the stainless steel barrel was put into the circulation cooling water tank to maintain the temperature of the electrolyte solution below 30 °C. The electrolyte was continuously stirred by both an electric stirrer with a speed of 300 r/min and an air stirrer with a displacement of 10 L/min to maintain the uniform distribution of the particles in the electrolyte. After the MAO process, the samples were rinsed in distilled water and then dried in warm air.

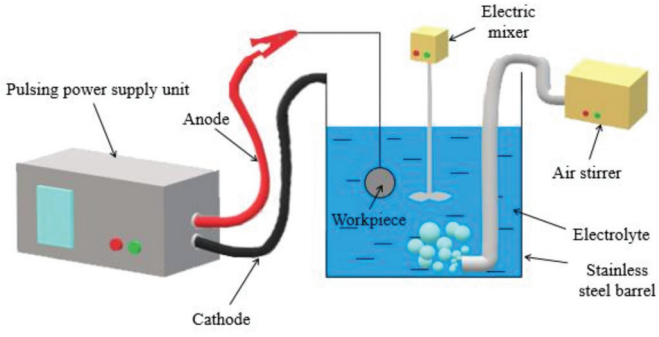

Figure 1. Schematic diagram of MAO process for TC4 alloy.

2.3. Surface Morphologies

The surface morphologies and element distribution of the MAO coatings were characterized by a scanning electron microscope (SEM, VEGA3–SBH, TESCAN, Brno, Czech Republic) operating in the secondary electron mode with an accelerating voltage of 30 kV and Oxford Inca X–Max energy dispersive spectrometry (EDS, Oxford Instruments plc, Oxford, UK), respectively. The surface porosity and the number of both the microholes and Si_3N_4 or TaC particles in the MAO coatings were quantified using ImageJ v1.48u software (NIH, Bethesda, Rockville, MD, USA, version 1,48u). Moreover, the thickness of the MAO coatings was measured using a TT260 eddy current thickness meter (Beijing TIME, Beijing, China) with an accuracy of 0.1 μm. Six measurements were conducted for each sample.

2.4. Phase Composition

The phase constituents of the coatings were detected at room temperature by an X-ray diffractometer (XRD, Bruker D8 DISCOVER A25, Bruker, Billerica, MA, USA) with Cu K_α (λ = 0.15405 nm) radiation at 30 kV and 40 mA. The XRD patterns were obtained in the 2θ ranging from 20° to 100° at a scanning speed of 2°/min.

2.5. Electrochemical Research

The corrosion properties of the coatings were evaluated by the electrochemical workstation (CHI 660C) attached to a typical three-electrode cell setup consisting of a specimen as the working electrode and a saturated calomel as the reference electrode (SCE), and a platinum sheet as the counter electrode. The electrochemical polarization measurements were carried out with a scan rate of 5 mV/s in the artificial seawater solution (Table 1). Before every measurement, the artificial seawater solution was deaerated by bubbling purified nitrogen gas for 1 h to eliminate the effect of the dissolved oxygen, and then the open current potential (OCP) was firstly recorded for 15 min to yield a state potential. The potentiodynamic polarization curves were plotted after the specimen was corroded freely for about 30 min to reach a quasi-stationary value of OCP. The corrosion potential (E_{corr}) and the corrosion current density (I_{corr}) of both TC4 alloy and the MAO coatings were calculated by fitting Tafel polarization curves with corrView software (version 3.1.0).

Table 1. Composition of the artificial seawater solution.

Chemical Reagents	Concentration, g/L
NaCl	24.53
$MgCl_2 \cdot 6H_2O$	11.11
Na_2SO_4	4.09
$CaCl_2$	1.16
KCl	0.70
$NaHCO_3$	0.20
KBr	0.10

2.6. Friction Tests

The tribological performance of both the TC4 alloy and the MAO coatings was evaluated at room temperature in the artificial seawater solution (Table 1) using a ball-on-disc friction tester (HT–1000 TRIBOLAB, ZKKH Co., Ltd., Lanzhou, China). The coatings or TC4 alloy served as the discs, and a GCr15 steel ball with a diameter of 5 mm served as the loading medium. A 5 N load was applied downward through the steel ball against the TC4 substrate and the MAO coatings at a constant sliding rate of 0.1 m/s. Each wear test lasted for 30 min. After the friction test, the morphologies and element distribution of the wear scars were also observed by SEM with Oxford Inca X–Max energy dispersive spectrometry (Oxford Instruments plc, Oxford, UK).

3. Results

3.1. Composition and Microstructure

The surface morphologies of both the ground TC4 and the MAO coatings with different concentrations of Si_3N_4/TaC particles are shown in Figure 2. As shown in Figure 2, there were some scratches and small pores of 1–2 μm on the surface of the ground TC4 alloy (Figure 2a); regardless of the Si_3N_4/TaC particles, there were many crater-like holes of different sizes in the coatings formed by the spark discharge and gas bubbles throughout the discharge channels during the MAO process, where the melted materials were expelled by the discharge and could not flow back to fill the discharge channels before their solidification [37,38]. Moreover, some significant changes could also be observed on the surface of the MAO coatings with the addition of the Si_3N_4/TaC particles (Figure 2c–e). For example, there were some microcracks in the MAO coatings with the Si_3N_4/TaC particles, which may be attributed to the fact that the particle additions block the flow of the melted metal, thus leading to the formation of the microcracks. On the other hand, it was found that some bright particles adhered to the surfaces of the coatings and that both the number and the size of the bright particles increased with the increasing Si_3N_4/TaC particle concentration (Figure 2c–e), indicating that the Si_3N_4 or TaC particles might be involved in the reaction of the MAO process. To further reveal the effect of the addition of the Si_3N_4/TaC particles on the MAO coatings, the number density and the size of microholes, the number

density of the bright particles, and the thickness of the MAO coatings were quantified. The results are given in Figure 3 and Table 2, showing that the thickness of the composite MAO coatings gradually increased with the increment of the concentration of Si_3N_4/TaC particles (Figure 3), which probably resulted from the inert or partly reactive incorporation of Si_3N_4/TaC particles into the oxide layer [21,27,29,30]. Compared with the MAO coating without Si_3N_4/TaC particles, the addition of Si_3N_4/TaC particles made the porosity significantly decrease. However, further increasing the concentration of Si_3N_4/TaC particles gave rise to a slight increment in the porosity (Figure 3). The previous studies also reported that the addition of the ceramic particles to the electrolyte reduced the porosity and average size of the micropores in the MAO coatings [25,27,30–33]. With increasing the concentration of Si_3N_4/TaC particles, the microarc discharge was more intense and allowed the particles to sinter together, which was evident by the observation of the larger bright particles in the coating with a higher concentration of Si_3N_4/TaC particles (Figure 2e). Meanwhile, a high concentration of Si_3N_4/TaC particles caused the ability of the particles to fill the microholes weaken during the MAO process and thus a slightly higher porosity, number density, and average size of the microholes were observed in the MAO coating with a high concentration of Si_3N_4/TaC particles. This well explained why the coatings with 1 g/L Si_3N_4 + 0.5 g/L TaC particles had the relevantly flat surface with the lowest porosity, the smallest average size, and number density of the microholes. Ding et al. [36] reported that the addition of TaC particles was beneficial to fill the micropores formed by the spark discharge during MAO process to make the surface become flat. Similar results were also reported in the MAO coatings incorporated by some hard particles (Cr_2O_3, Al_2O_3, etc.) [26,27,39].

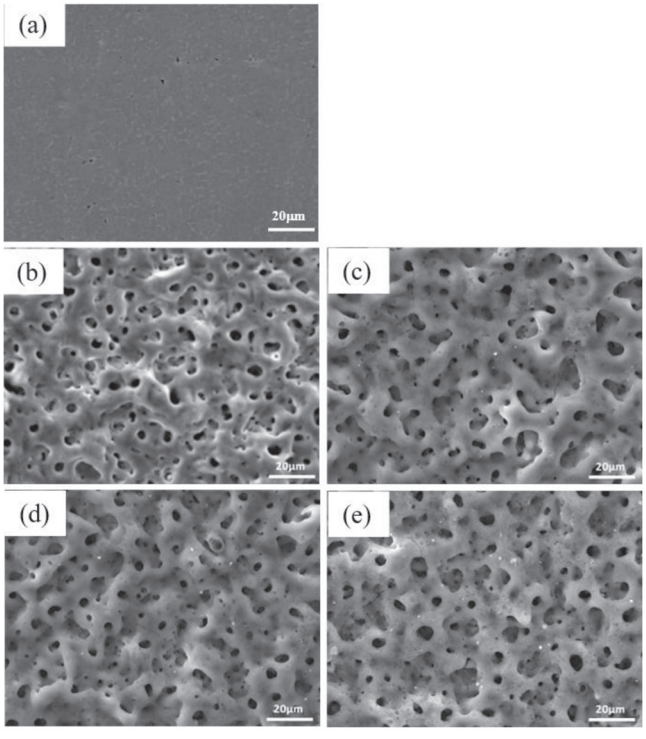

Figure 2. Surface morphologies of the ground TC4 alloy and the MAO coatings with different concentration of Si_3N_4/TaC particles: (**a**) TC4; (**b**) 0 g/L; (**c**) 1 g/L Si_3N_4 + 0.5 g/L TaC; (**d**) 2 g/L Si_3N_4 + 1 g/L TaC; (**e**) 4 g/L Si_3N_4 + 2 g/L TaC.

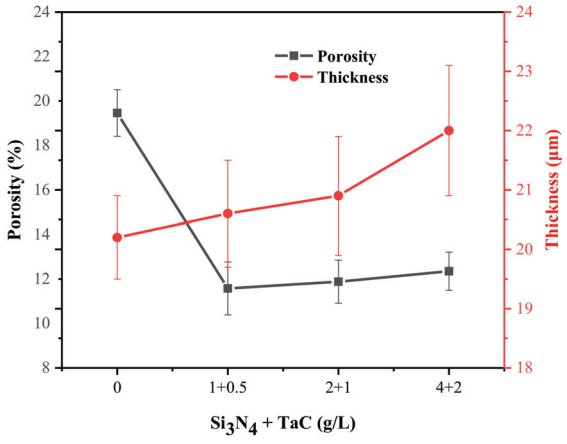

Figure 3. Surface porosity and thickness of the composite MAO coating with different concentration of Si_3N_4/TaC particles.

Table 2. Surface characteristic of the MAO coatings with different concentration of Si_3N_4/TaC particles.

Specimen	Surface Density of the Microholes, Number/mm^2	Average Diameter of the Microholes, μm	Surface Density of the Bright Particles, Number/mm^2
0 g/L	25,316 ± 1751	1.835 ± 1.275	0
1 g/L + 0.5 g/L	16,652 ± 1335	1.740 ± 1.226	2005 ± 151
2 g/L + 1 g/L	17,426 ± 1811	1.771 ± 0.861	3828 ± 202
4 g/L + 2 g/L	17,543 ± 2002	1.794 ± 1.136	5845 ± 346

The EDS mappings of the MAO coatings in Figure 4, especially in the enlarged image in Figure 4d, confirm that the bright particles were enriched with Ta and Si, which supported the incorporation of some Si_3N_4/TaC particles in the composite coatings that caused the number of the holes to decrease and the surface flatten. Table 3 shows the average compositions of the surfaces of the MAO coatings with different concentrations of Si_3N_4/TaC particles. Table 4 presents the EDS results of regions A (bright particle 1), B (bright particle 2), and C in the MAO coatings with the addition of 4 g/L Si_3N_4 + 2 g/L TaC particles, showing that some bright particles were enriched in Si, while others were enriched in Ta. As the plasma temperature during the MAO process was lower than the melt temperature of Si_3N_4 (1900 °C) and TaC (3880 °C), Si_3N_4 or TaC particles might be inertly absorbed onto or sintered to the MAO coatings. However, the size of the Si-rich particle in region A in Figure 4d was about 800 nm, which was much larger than the average size of the Si_3N_4 particles (about 50 nm). This suggested that the Si_3N_4 particles were very likely melted during the MAO process. In fact, it was reported that the melting point of the nano-sized particles decreased with the decreasing particle size [40,41]. It was likely that the nano-sized Si_3N_4 particles were reactively incorporated into the MAO coatings.

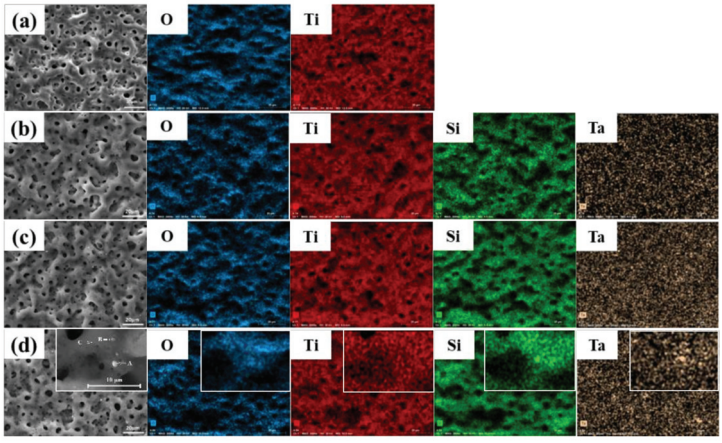

Figure 4. EDS mappings of the MAO coatings with different concentration of Si_3N_4/TaC particles: (**a**) 0 g/L; (**b**) 1 g/L Si_3N_4 + 0.5 g/L TaC; (**c**) 2 g/L Si_3N_4 + 1 g/L TaC; (**d**) 4 g/L Si_3N_4 + 2 g/L TaC.

Table 3. Percentage of elements in the MAO coatings with different concentration of Si_3N_4/TaC particles (at. %).

Specimen	O	Ti	Si	Ta
0 g/L	69.3	20.5	-	-
1 g/L + 0.5 g/L	68.5	19.6	3.2	0.2
2 g/L + 1 g/L	67.5	19.0	5.6	0.6
4 g/L + 2 g/L	66.8	15.8	11.6	1.0

Table 4. EDS results of region A, B, and C in the enlarged image in Figure 4d (at. %).

Region	O	Ti	Si	Ta
A	42.0	23.4	25.3	3.5
B	60.1	13.5	11.0	8.5
C	55.5	20.2	17.0	1.0

The phase constituents of the MAO coatings with different contents of Si_3N_4/TaC particles were investigated by XRD. The results are illustrated in Figure 5, and they show that the MAO coatings formed in the absence of Si_3N_4/TaC particles were mainly composed of anatase-type TiO_2 and rutile-type TiO_2, while both the TaC phase and Si_3N_4 phases could be detected in the coatings with the addition of the Si_3N_4/TaC particles. Moreover, by increasing the concentration of Si_3N_4/TaC particles, the peak intensity of rutile TiO_2 and TaC gradually increased, which was confirmed by the SEM results, i.e., the amounts of the Si-rich or Ta-rich bright particles increased with the increasing concentration of the Si_3N_4/TaC particles (Figure 2c–e). The formation of $Al_4Ti_2SiO_{12}$ may be associated with high temperature and high pressure during the MAO process. Wang et al. [27] found that Al_2TiO_5 in the Si_3N_4/Al_2O_3 composite coatings formed on TC4 alloy by MAO in the electrolyte with Al_2O_3 particles. The occurrence of $Al_4Ti_2SiO_{12}$ and the decrease in the metastable anatase-TiO_2 suggested that Al_2TiO_5 might react with Si_3N_4 to form $Al_4Ti_2SiO_{12}$ during localized high temperature and high pressure in the process of MAO. Aliofkhazraei et al. [33] fabricated Si_3N_4/TiO_2 nanocomposite coatings on commercially pure Ti and found the existence of $Si_4Al_2O_2N_6$ in the composite coatings.

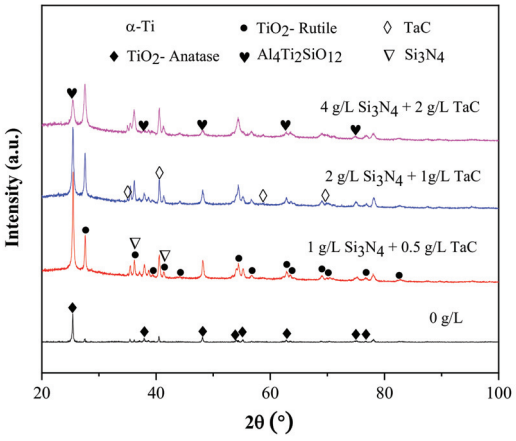

Figure 5. XRD patterns of the MAO coatings with different concentration of Si_3N_4/TaC particles.

This indicated that the Si_3N_4 particles were partially reactively incorporated into the composite MAO coatings, which was inconsistent with the results from Lu et al. [32]. Figure 3 shows that with an increasing Si_3N_4/TaC concentration, the thickness of the coatings increased slightly from 20.2 μm for the coating without Si_3N_4/TaC particles to 22.0 μm for the coating with the addition of 4 g/L Si_3N_4 + 2 g/L TaC particles, which contributed to the incorporation of the Si_3N_4 and TaC particles into the composite coatings during the process of MAO. Similar results were also reported in some studies [26,27,30], i.e., the excessive addition of the particles produced a large number of particles in the composite coatings and a thicker coating.

3.2. Tribological Properties

Figure 6 presents the friction coefficient of both the TC4 alloy and the composite MAO coatings with different concentrations of Si_3N_4/TaC particles against the GCr15 steel ball in the artificial seawater, which showed that the friction coefficient of the TC4 alloy fluctuated significantly and reached about 0.5 after nearly 5 min. The friction coefficients of the MAO coatings with different concentrations of Si_3N_4/TaC particles all first increased due to the high initial surface roughness and then decreased due to the improvement of the surface contact condition between the protrusions and the GCr15 steel ball with the sliding time [27,30]. For the high hardness of the MAO coatings, their friction coefficients were lower and experienced less fluctuation compared to the TC4 alloy. It was also observed from Figure 6 that the MAO coatings, without the addition of the Si_3N_4/TaC particles, had the lowest friction coefficient of about 0.15, and the friction coefficient of the composite MAO coatings slightly increased with the concentration of Si_3N_4/TaC particles. Previous research [34] revealed that Si_3N_4 addition could improve the wear resistance of the MAO coatings and significantly reduce the friction coefficient, which was attributed to Si_3N_4 having excellent lubrication. Thus, the friction coefficient of the composite MAO coatings was a little higher than that of the MAO coatings in the absence of Si_3N_4/TaC particles, which may be associated with the addition of hard TaC particles. In order to reveal wear damages to the coatings, SEM was used to examine the worn surfaces. The morphologies of their worn surfaces are illustrated in Figure 7, showing that the TC4 alloy had the widest wear scar of 787.8 μm with a lot of furrows along the wear direction. This was ascribed to the fact that the TC4 alloy has a much lower hardness than the MAO coatings [42,43]. The wear width of the MAO coatings ranged from 358.2 to 445.3 μm, which is significantly lower than the wear width of the TC4 alloy. This indicated that the MAO coatings greatly improved the tribological properties of the TC4 alloy, regardless of the addition of Si_3N_4/TaC particles.

The wear width of the composite MAO coatings was lower than that of the particle-free coatings and slightly increased with the concentration of Si_3N_4/TaC particles.

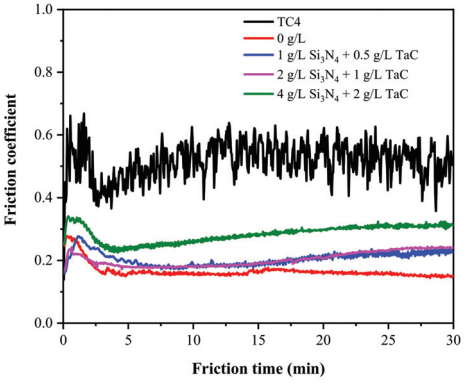

Figure 6. Friction coefficient of both the TC4 alloy and the composite MAO coatings with different concentration of Si_3N_4/TaC particles.

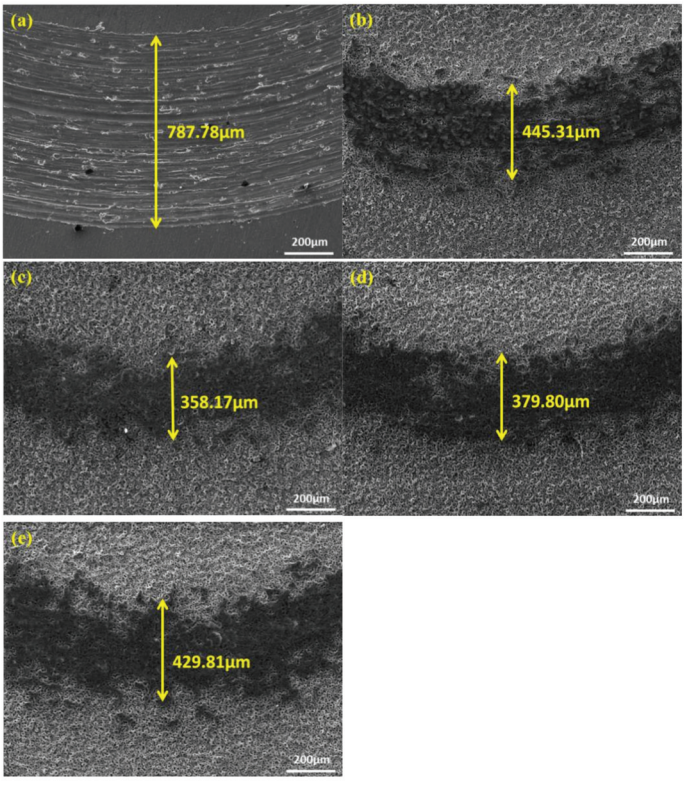

Figure 7. SEM image of the wear scar of both the TC4 alloy and the composite MAO coatings with different concentration of Si3N4/TaC particles: (**a**) TC4; (**b**) 0 g/L; (**c**) 1 g/L Si_3N_4 + 0.5 g/L TaC; (**d**) 2 g/L Si_3N_4 + 1 g/L TaC; (**e**) 4 g/L Si_3N_4 + 2 g/L TaC.

3.3. Corrosion Resistance

The potentiodynamic polarization curves of the TC4 alloy and the composite MAO coatings with the different concentrations of Si_3N_4/TaC particles in the artificial seawater were plotted in Figures 8 and 9, respectively. The relevant electrochemical data are listed in Table 5. It could be easily found from Figures 8 and 9 and Table 5 that the addition of Si_3N_4/TaC particles caused the corrosion potential (E_{corr}) of the composite coatings to move to a positive direction and the current densities decrease by about three orders of magnitude, indicating that the corrosion resistance of the composite coatings was significantly improved compared with the TC4 alloy substrate. Moreover, as can be seen from Figures 8 and 9 and Table 5, the corrosion potential of the particle-free MAO coatings reached −0.176 V_{SCE}, which was significantly higher than that of the TC4 alloy substrate, with a minimum corrosion potential of −1.229 $V_{SCE.}$ The corrosion current densities (I_{corr}) of the particle-free coatings were a little bit higher than that of the TC4 alloy substrate, which was attributed to the fact that the particle-free coatings have high porosity (19.5%) (Figure 4). In general, the corrosion resistance of the MAO coatings mainly depends on the porosity, thickness, and composition of the coating. Chen et al. [29] investigated the corrosion resistance of the MoS_2-modified MAO coatings on the titanium alloy with different MoS_2 concentrations of 0, 2, 4, 6, and 8 g/L in a 3.5 wt. % NaCl solution and the results showed that the addition of MoS_2 could significantly improve the corrosion resistance of the MAO coating and that the MoS_2-modified MAO coating with an additional amount of 4 g/L possessed the minimum porosity and average pore size and hence showed the best corrosion resistance. Therefore, it was easily understood that for the minimum porosity of 11.5%, the composite MAO coatings incorporated with the concentration of 1 g/L Si_3N_4 + 0.5 g/L TaC particles had the optimal corrosion properties in the artificial seawater.

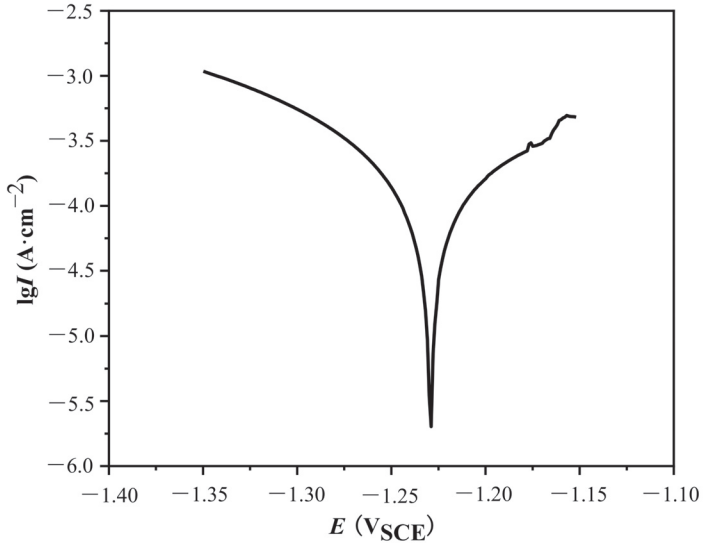

Figure 8. Potentiodynamic polarization curves of TC4 alloy in the artificial seawater.

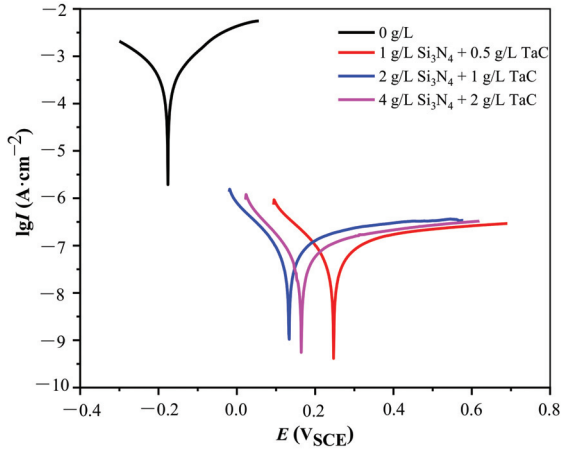

Figure 9. Potentiodynamic polarization curves of the MAO coatings with different concentration of Si_3N_4/TaC particles in the artificial seawater.

Table 5. Potentials and current densities of both the TC4 alloy and the composite MAO coatings with different concentration of Si_3N_4/TaC particles.

Specimen	TC4	0 g/L	1 g/L + 0.5 g/L	2 g/L + 1 g/L	4 g/L + 2 g/L
E_{corr}, V_{SCE}	−1.229	−0.176	0.246	0.135	0.165
I_{corr}, A·cm^{-2}	8.47×10^{-5}	2.67×10^{-4}	4.23×10^{-8}	6.43×10^{-8}	4.15×10^{-8}

4. Discussions

Figure 6 shows that the TC4 alloy suffered excessive abrasive wear and that the MAO coatings with different concentrations of Si_3N_4/TaC particles were slightly worn during the friction test. To investigate the effect of the Si_3N_4/TaC particles on the tribological behaviors of both the TC4 alloy and the composite MAO coatings with different concentrations of Si_3N_4/TaC particles against the GCr15 steel ball in the artificial seawater, EDS mapping was used to reveal the distribution of the Si_3N_4/TaC particles in the wear scars (Figure 10). The EDS results showed that only 0.1 wt. % Fe was distributed in the wear scar of the TC4 alloy, whereas 2–3 wt. % Fe existed in the wear scar of the composite MAO coatings (Table 6), which indicated that the composite coatings had an excellent anti-wear effect. In addition, only about 0.3 wt. % V and 1.6 wt. % Al was detected in the wear scar of the composite MAO coatings, revealing that the coatings were not destroyed during the friction test. The low hardness TC4 alloy substrate was directly exposed to the artificial seawater and was easily worn by the high hardness GCr15 grinding ball; thus an abrasive wear scar, with deep and wide furrows, was observed (Figure 7a). It was well established that due to the ceramic-like characteristics with relatively thick and dense structures, the MAO coatings that possessed the characteristics with relatively thick and dense structures had excellent hardness properties and better tribological performance. Lan et al. [44] revealed that the wear failure mechanisms of the MAO coatings in the artificial seawater were abrasive wear and adhesive wear. It was well known that when a certain number of the Si_3N_4/TaC particles were embedded into the micropores of the MAO coatings by means of inert or reactive incorporation, those particles could play an important role in micro-lubrication and micro-cutting [45], which greatly reduced the friction coefficient of the composite MAO coatings. As shown in Figure 2c–e, the bright particles were distributed not only in the microholes but also on the flat surface to form the micro-bulges. During the friction process, these micro-bulges or micro-bumps became the main contact points to bear the normal and shear force against the GCr15 grinding ball. Thus, during the friction test, a lot of wear

debris was plowed by the micro bumps in the MAO coatings from the GCr15 grinding ball surface to fill into the micropores of the coatings or adhere to the surface of the coating. Meanwhile, the hard Si_3N_4 or TaC particles in the MAO coating adhered to the surface of the GCr15 grinding ball. Furthermore, the Si_3N_4/TaC particles dispersed throughout the composite MAO coatings, thus improving the strength of the MAO coating and further reducing the width of the wear scar during the friction process. This was evident by the fact that the MAO coating with Si_3N_4/TaC particles showed a narrower wear scar compared to the MAO coating without Si_3N_4/TaC particles (Figure 7). Particularly, the composite MAO coating fabricated with the addition of 1 g/L Si_3N_4 + 0.5 g/L TaC particles possessed a uniform distribution of Si_3N_4/TaC particles (Figure 10c), showing the narrowest wear scar (Figure 7), thus appearing to have the best tribological properties.

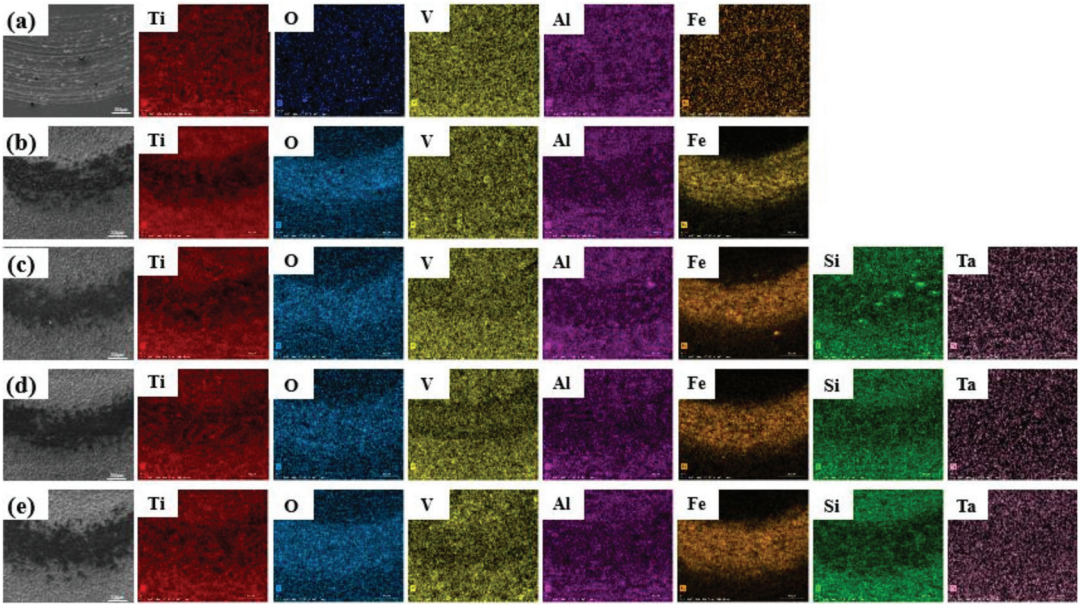

Figure 10. EDS mapping of the wear scar of both the TC4 alloy and the composite MAO coatings with different concentration of Si_3N_4/TaC particles: (**a**) TC4; (**b**) 0 g/L; (**c**) 1 g/L Si_3N_4 + 0.5 g/L TaC; (**d**) 2 g/L Si_3N_4 + 1 g/L TaC; (**e**) 4 g/L Si_3N_4 + 2 g/L TaC.

Table 6. Percentage of elements of the wear scar of both the TC4 alloy and the composite MAO coatings with different concentration of Si_3N_4/TaC particles (wt. %).

Specimen	O	Ti	V	Al	Si	Ta	Fe
TC4	19.4	71.7	3.1	6.3	-	-	0.1
0 g/L	72.3	17.7	0.3	1.6	-	-	3.0
1 g/L + 0.5 g/L	72.5	16.6	0.3	1.6	2.7	0.2	2.1
2 g/L + 1 g/L	71.8	15.0	0.3	1.6	4.5	0.5	2.3
4 g/L + 2 g/L	71.5	12.4	0.3	1.5	8.9	0.7	2.4

The corrosion properties of the MAO coatings mainly depended on the porosity, composition, and thickness of the coatings [16,44]. When the artificial seawater solution was used as the electrolyte, the MAO coating substrate and the inside of the microholes acted as the cathode and the anode, respectively. Galvanic corrosion could occur in the inside of the microholes as the anode coupled with the coating substrate caused the microholes to penetrate through the coatings and thus finally caused the corrosion of the TC4 alloy.

Figure 11 schematically shows the corrosion resistance mechanism of the MAO coatings with the different concentrations of the effect of the Si_3N_4/TaC particles. It was well reported that the coating defects, e.g., the surface porosity, deep cracks, and coating thickness, could affect the corrosion resistance of the MAO coatings [25,46–48]. As seen in Figure 3 and Table 2, the addition of Si_3N_4/TaC particles not only increases the coating thickness of the MAO coatings but also reduces the surface porosity, size, and the number of microholes in the MAO coatings. It was easy to understand that the coatings with the thicker coating and the lower surface porosity caused the corrosion electrolyte to be difficult to penetrate into the substrate. However, the open voids and channels in the coatings provide shortcuts for the corrosive electrolyte to penetrate into the substrate, thus weakening protection for the substrate. The MAO coatings with the addition of 1 g/L Si_3N_4 + 0.5 g/L TaC particles, whose surface porosity and thickness were 11.85% and 20.6 μm, respectively, had better corrosion properties than that of the MAO coatings with the addition of 4 g/L Si_3N_4 + 2 g/L TaC particles, whose surface porosity and thickness were 12.35% and 22.0 μm, respectively, indicating that surface porosity might be a more important influence factor than the thickness on the corrosion properties of the MAO coatings.

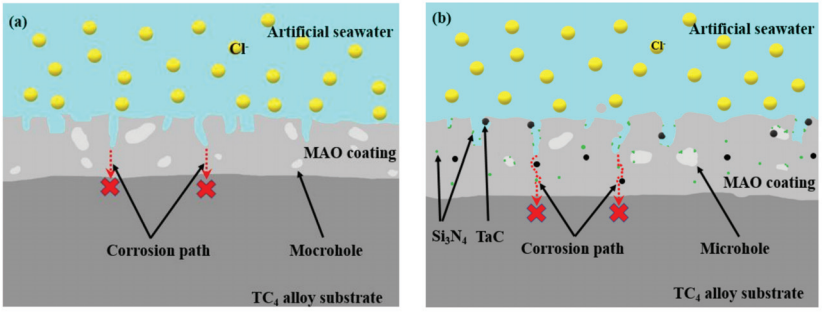

Figure 11. Corrosion resistance mechanism of the MAO coatings with and without Si_3N_4/TaC particles: (**a**) MAO coating without Si_3N_4/TaC particles; (**b**) MAO coating with Si_3N_4/TaC particles.

5. Conclusions

(1) The phase constituents of the composite MAO coatings with different contents of Si_3N_4/TaC particles were mainly composed of anatase TiO_2, rutile TiO_2, TaC, Si_3N_4, and $Al_4Ti_2SiO_{12}$. By increasing the concentration of the Si_3N_4/TaC particles, the peak intensity of rutile TiO_2 and TaC gradually increased, and the content of the metastable anatase-TiO_2 decreased.

(2) For the inert or partly-reactive incorporation of Si_3N_4/TaC particles during the MAO process, the thickness of the composite MAO coatings gradually increased with the increment of the concentration of Si_3N_4/TaC particles. The porosity of the MAO coatings first decreased and then increased with the increasing concentration of Si_3N_4/TaC particles.

(3) The MAO coatings greatly improved the tribological properties of the TC4 alloy in the artificial seawater solution, regardless of the addition of the Si_3N_4/TaC particles. The composite MAO coatings with 1 g/L Si_3N_4 + 0.5 g/L TaC particles presented a relatively lower friction coefficient and the narrowest wear scar, thus showing the best tribological properties.

(4) The addition of Si_3N_4/TaC particles could enhance the corrosion resistance of the MAO coatings. The composite MAO coatings with 1 g/L Si_3N_4 + 0.5 g/L TaC particles exhibited the highest corrosion potential and the lower current density, i.e., the optimal corrosion resistance in the artificial seawater solution. This could be attributed to the fact that the coating had the lowest surface porosity.

Author Contributions: Conceptualization, W.Y. and J.L.; methodology, W.G.; software, L.W.; validation, Y.J., Y.Y. and L.W.; formal analysis, W.G. and Z.D.; investigation, W.Y.; resources, J.L.; data curation, Z.D.; writing—original draft preparation, W.G. and Z.D.; writing—review and editing, Y.J. and Y.Y.; visualization, Y.J. and Z.D.; supervision, Y.Y.; project administration, W.Y. All authors have read and agreed to the published version of the manuscript.

Funding: This research was funded by the National Natural Science Foundation of China (52071252), Key Research and Development Program of Shaanxi Province (2021ZDLSF03-11, 2021GY-208, 2022GY-407).

Institutional Review Board Statement: Not applicable.

Informed Consent Statement: Not applicable.

Data Availability Statement: Not applicable.

Conflicts of Interest: The authors declare no conflict of interest.

References

1. Jha, A.K.; Singh, S.K.; Kiranmayee, M.S.; Sreekumar, K.; Sinha, P.P. Failure analysis of titanium alloy (Ti6Al4V) fastener used in aerospace application. *Eng. Fail. Anal.* **2010**, *17*, 1457–1465. [CrossRef]
2. Ding, R.; Guo, Z.X.; Wilson, A. Microstructural evolution of a Ti–6Al–4V alloy during thermomechanical processing. *Mater. Sci. Eng. A* **2002**, *327*, 233–245. [CrossRef]
3. Rack, H.J.; Qazi, J.I. Titanium alloys for biomedical applications. *Mater. Sci. Eng. C* **2006**, *26*, 1269–1277. [CrossRef]
4. Yang, W.; Gao, Y.; Guo, P.; Xu, D.P.; Wang, A.Y. Adhesion, biological corrosion resistance and biotribological properties of carbon films deposited on MAO coated Ti substrates. *J. Mech. Behav. Biomed.* **2020**, *101*, 103448. [CrossRef] [PubMed]
5. Xie, R.; Lin, N.; Peng, Z.; Zou, J.; Han, P.; Wang, Z.; Tang, B. Surface damage mitigation of TC4 alloy via micro arc oxidation for oil and gas exploitation application: Characterizations of microstructure and evaluations on surface performance. *Appl. Surf. Sci.* **2018**, *436*, 467–476. [CrossRef]
6. Mousavi-Semnani, S.Z.; Yousefpour, M.; Zareidoost, A. Enhancing the biocompatibility of ZrO_2 thin film on Zr–2.5Nb alloy by anodizing treatment using an electrolyte containing biofunctional groups. *Thin Solid Films* **2022**, *753*, 139279. [CrossRef]
7. Deng, H.Y.; Xu, K.X.; Liu, S.G.; Zhang, C.F.; Zhu, X.W.; Zhou, H.R.; Xia, C.Q.; Shi, C.B. Impact of engineering surface treatment on surface properties of biomedical TC4 Alloys under an artificial human environment. *Coatings* **2022**, *12*, 157. [CrossRef]
8. Huang, J.; Ma, J.; Wu, L.; Wei, J.; Li, H. Microstructure and wear resistance of WS_2/W composite coating on TC4 titanium alloy surface. *J. Phys. Conf. Ser.* **2021**, *1885*, 032046. [CrossRef]
9. Salman, S.H.; Shihab, A.A.; Kh.Elttayef, A.H. Design and construction of nanostructure TiO_2 thin film gas sensor prepared by R.F magnetron sputtering technique. *Energy Procedia* **2019**, *157*, 283–289. [CrossRef]
10. Wu, S.K.; Yang, W.; Gao, W.; Yao, Y.H.; Zhang, Y.; Chen, J. Characterization of MAO + Cu composite coatings on aluminum alloy. *Coatings* **2021**, *11*, 1172. [CrossRef]
11. Da Silva Rodrigues, J.; Antonini, L.M.; da Cunha Bastos, A.A.; Zhou, J.; de Fraga Malfatti, C. Corrosion resistance and tribological behavior of ZK30 magnesium alloy coated by plasma electrolytic oxidation. *Surf. Coat. Technol.* **2021**, *410*, 126983. [CrossRef]
12. Gao, J.; Zheng, K.; Yu, S.W.; Hei, H.J.; Wu, Y.X.; Gong, H.R.; Ma, Y. Characterization of quasi-static/dynamic contact mechanical properties of Mo surface-modified TC4. *Coatings* **2002**, *12*, 123. [CrossRef]
13. Chen, C.A.; Jian, S.Y.; Lu, C.H.; Lee, C.Y.; Aktuğ, S.L.; Ger, M.D. Evaluation of microstructural effects on corrosion behavior of AZ31B magnesium alloy with a MAO coating and electroless Ni–P plating. *J. Mater. Res. Technol.* **2020**, *9*, 13902–13913. [CrossRef]
14. Asl, V.Z.; Chini, S.F.; Zhao, J.; Palizdar, Y.; Shaker, M.; Sadeghi, A. Corrosion properties and surface free energy of the ZnAl LDH/rGO coating on MAO pretreated AZ31 magnesium alloy. *Surf. Coat. Technol.* **2021**, *426*, 127764.
15. Song, Y.; Wang, H.; Liu, Q.; Li, G.; Wang, S.; Zhu, X. Sodium dodecyl sulfate (SDS) intercalated MgAl layered double hydroxides film to enhance the corrosion resistance of AZ31 magnesium alloy. *Surf. Coat. Technol.* **2021**, *422*, 127524. [CrossRef]
16. Wang, Y.M.; Jiang, B.L.; Lei, T.Q.; Guo, L.X. Dependence of growth features of microarc oxidation coatings of titanium alloy on control modes of alternate pulse. *Mater. Lett.* **2004**, *58*, 1907–1911. [CrossRef]
17. Wang, Y.M.; Jia, D.C.; Guo, L.X.; Lei, T.Q.; Liang, B.L. Effect of discharge pulsating on microarc oxidation coatings formed on Ti6Al4V alloy. *Mater. Chem. Phys.* **2005**, *90*, 128–133. [CrossRef]
18. Xue, W.B.; Wang, C.; Deng, Z.W.; Chen, R.Y.; Zhang, T.H. Influence of electrolytes on the microstructure of microarc oxidation coatings on Ti–6Al–4V alloy. *J. Mater. Sci. Technol.* **2002**, *18*, 37–39.
19. Yang, W.; Xu, D.P.; Guo, Q.Q.; Chen, T.; Chen, J. Influence of electrolyte composition on microstructure and properties of coatings formed on pure Ti substrate by micro arc oxidation. *Surf. Coat. Technol.* **2018**, *349*, 522–528. [CrossRef]
20. Yao, Z.P.; Xu, Y.J.; Jiang, Z.H.; Wang, F.P. Effects of cathode pulse at low frequency on the structure and composition of plasma electrolytic oxidation ceramic coatings. *J. Alloys Compd.* **2009**, *488*, 273–278. [CrossRef]
21. Gao, W.; Liu, J.N.; Wei, J.P.; Yao, Y.H.; Ma, X.Q.; Yang, W. Enhanced properties of micro arc oxidation coating with Cu addition on TC4 alloy in marine environment. *Coatings* **2021**, *11*, 1168. [CrossRef]

22. Zhang, Y.; Yang, W.; Yu, S.; Wang, L.Q.; Ma, X.Q.; Gao, W.; Lan, N.; Shao, W.T. Microstructure and properties in artificial seawater of copper-doped micro-arc coatings on TC4 alloy. *Coatings* **2022**, *12*, 883. [CrossRef]
23. Rafieerad, A.R.; Ashra, M.R.; Mahmoodian, R.; Bushroa, A.R. Surface characterization and corrosion behavior of calcium phosphate-base composite layer on titanium and its alloys via plasma electrolytic oxidation: A review paper. *Mater. Sci. Eng. C* **2015**, *57*, 307–413. [CrossRef] [PubMed]
24. Muhaffffel, F.; Kaba, M.; Cempura, G.; Derin, B.; Kruk, A.; Atar, E.; Cimenoglu, H. Influence of alumina and zirconia incorporations on the structure and wear resistance of titania-based MAO coatings. *Surf. Coat. Technol.* **2019**, *377*, 124900. [CrossRef]
25. Lu, X.P.; Mohedano, M.; Blawert, C.; Matykina, E.; Arrabal, R.; Kainer, K.U.; Zheludkevich, M.L. Plasma electrolytic oxidation coatings with particle additions—A review. *Surf. Coat. Technol.* **2016**, *307*, 1165–1182. [CrossRef]
26. Wang, C.; Hao, J.M.; Xin, Y.Z.; Guo, C.F.; Chen, H. High temperature oxidation behavior of TiO_2 + ZrO_2 composite ceramic coatings prepared by microarc oxidation on Ti6Al4V alloy. *Surf. Coat. Technol.* **2015**, *215*, 201–207. [CrossRef]
27. Wang, S.X.; Zhao, Q.; Liu, D.X.; Du, N. Microstructure and elevated temperature tribological behavior of TiO_2/Al_2O_3 composite ceramic coating formed by microarc oxidation of Ti6Al4V alloy. *Surf. Coat. Technol.* **2015**, *272*, 343–349. [CrossRef]
28. Mu, M.; Liang, J.; Zhou, X.; Xiao, Q. One-step preparation of TiO_2/MoS_2 composite coating on Ti6Al4V alloy by plasma electrolytic oxidation and its tribological properties. *Surf. Coat. Technol.* **2013**, *214*, 124–130. [CrossRef]
29. Chen, X.W.; Li, M.L.; Zhang, D.F.; Cai, L.P.; Ren, P.; Hu, J.; Liao, D.D. Corrosion resistance of MoS_2-modified titanium alloy micro-arc oxidation coating. *Surf. Coat. Technol.* **2022**, *433*, 128127. [CrossRef]
30. Ao, N.; Liu, D.X.; Wang, S.X.; Zhao, Q.; Zhang, X.H.; Zhang, M.M. Microstructure and tribological behavior of a TiO_2/hBN composite ceramic coating formed via micro-arc oxidation of Ti–6Al–4V alloy. *J. Mater. Sci. Technol.* **2016**, *32*, 1071–1076. [CrossRef]
31. Lou, B.S.; Lin, Y.Y.; Tseng, C.M.; Lu, Y.C.; Duh, J.G.; Lee, J.W. Plasma electrolytic oxidation coatings on AZ31 magnesium alloys with Si_3N_4 nanoparticle additives. *Surf. Coat. Technol.* **2017**, *332*, 358–367. [CrossRef]
32. Lu, X.P.; Blawert, C.; Scharnagl, N.; Kainer, K.N. Influence of incorporating Si_3N_4 particles into the oxide layer produced by plasma electrolytic oxidation on AM50 Mg alloy on coating morphology and corrosion properties. *J. Magnes. Alloy* **2013**, *1*, 267–274. [CrossRef]
33. Aliofkhazraei, M.; Sabour Rouhaghdam, A.; Shahrabi, T. Abrasive wear behavior of Si_3N_4/TiO_2 nanocomposite coatings fabricated by plasma electrolytic oxidation. *Surf. Coat. Technol.* **2010**, *205*, S41–S46. [CrossRef]
34. Gao, W.; Liu, J.N.; Ding, Z.S.; Zhang, Y.; Yao, Y.H.; Yang, W. Influence of Si_3N_4 nanoparticles on microstructure and properties of microarc oxidation coatings on TC4 alloy. *Rare Metal Mater. Eng.* **2022**, *51*, 1537–1542.
35. Zhang, X.H.; Hilmas, G.E.; Fahrenholtz, W.G. Densification and mechanical properties of TaC-based ceramics. *Mater. Sci. Eng. C* **2009**, *501*, 37–43. [CrossRef]
36. Ding, Z.S.; Gao, W.; Wei, J.P.; Jin, Y.H.; Zhao, C.; Yang, W. Effects of TaC microparticles on structure and properties of micro-arc oxidation coating on Ti–6Al–4V alloy. *Acta Phys. Sin.* **2022**, *71*, 028102. [CrossRef]
37. Wang, F.; Wang, X.H.; Xie, W.E.; Wang, F.; Gan, Q.; Ping, S.; Wei, J.; Li, F.Q.; Wang, Z.M. Simultaneous incorporation of gallium oxide and tantalum microparticles into micro-arc oxidation coating of titanium possessing antibacterial effect and stimulating cellular response. *Biomater. Adv.* **2022**, *135*, 212736. [CrossRef]
38. Zhang, S.L.; Zou, X.R.; Liu, N.; Wang, H.R.; Xia, C.Q.; Liang, C.Y. In situ preparation of a novel Ta_2O_5/MAO composite coating on magnesium for anti-corrosion protection. *Surf. Coat. Technol.* **2022**, *430*, 128003. [CrossRef]
39. Du, N.; Wang, S.X.; Zhao, Q.; Zhu, W.H. Microstructure and tribological properties of microarc oxidation composite coating containing Cr_2O_3 particles on TC4 titanium alloy. *Rare Metal Mater. Eng.* **2013**, *42*, 621–624.
40. Gleiter, H. Nanostructured materials: Basic concepts and microstructure. *Acta Mater.* **2000**, *48*, 1–29. [CrossRef]
41. Qi, W.H.; Wang, M.P. Size and shape dependent melting temperature of metallic nanoparticles. *Mater. Chem. Phys.* **2004**, *88*, 280–284. [CrossRef]
42. Xue, W.B.; Wang, C.; Chen, R.Y.; Deng, Z.W. Structure and properties characterization of ceramic coatings produced on Ti–6Al–4V alloy by microarc oxidation in aluminate solution. *Mater. Lett.* **2002**, *52*, 435–441. [CrossRef]
43. Wang, Y.M.; Jiang, B.L.; Lei, T.Q.; Guo, L.X. Microarc oxidation coatings formed on Ti6Al4V in Na_2SiO_3 system solution: Microstructure, mechanical and tribological properties. *Surf. Coat. Technol.* **2006**, *201*, 82–89. [CrossRef]
44. Lan, N.; Yang, W.; Gao, W.; Guo, P.; Zhao, C.; Chen, J. Characteristic of ta–C film on micro arc oxidation coated titanium all in artificial seawater. *Diam. Relat. Mater.* **2021**, *117*, 108483. [CrossRef]
45. Jin, F.Y.; Chu, P.K.; Tong, H.H.; Zhao, J. Improvement of surface porosity and properties of alumina films by incorporation of Fe micrograins in micro-arc oxidation. *Appl. Surf. Sci.* **2006**, *253*, 863–868. [CrossRef]
46. Muhaffel, F.; Cimenoglu, H. Development of corrosion and wear resistant micro-arc oxidation coating on a magnesium alloy. *Surf. Coat. Technol.* **2019**, *357*, 822–832. [CrossRef]
47. Lou, B.S.; Lee, J.W.; Tseng, C.M.; Lin, Y.Y.; Yen, C.A. Mechanical property and corrosion resistance evaluation of AZ31 magnesium alloys by plasma electrolytic oxidation treatment: Effect of MoS_2 particle addition. *Surf. Coat. Technol.* **2018**, *350*, 813–822. [CrossRef]
48. Laleh, M.; Rouhaghdam, A.S.; Shahrabi, T.; Shanghi, A. Effect of alumina sol addition to micro-arc oxidation electrolyte on the properties of MAO coatings formed on magnesium alloy AZ91D. *J. Alloys Compd.* **2010**, *496*, 548–552. [CrossRef]

coatings

MDPI

Article

Rational Design of Yolk Core-Shell Structure MnO-Co@C Nanospheres for High-Performance Microwave Absorption

Zhen Xin [1,2,3], Junjie Wu [4], Shuchen Sun [5,*], Mu Zhang [1,2,3,*] and Xudong Sun [1,2,3,*]

[1] Key Laboratory for Anisotropy and Texture of Materials (Ministry of Education), Northeastern University, Shenyang 110819, China
[2] School of Materials Science and Engineering, Northeastern University, Shenyang 110819, China
[3] Foshan Graduate School of Innovation, Northeastern University, Foshan 528311, China
[4] Sinosteel Engineering & Technology (Inner Mongolia) Co., Ltd., Baotou 014000, China
[5] School of Metallurgy, Northeastern University, Shenyang 110819, China
* Correspondence: sunsc@smm.neu.edu.cn (S.S.); zhangm@mail.neu.edu.cn (M.Z.); xdsun@mail.neu.edu.cn (X.S.)

Abstract: MnO-Co@C nanospheres were fabricated by in situ polymerizing and high-temperature carbonizing processes. This unique synthesis method does not require any template or reducing gas. The synthesized multicore-shell structure has a shell of about 500 nm and multiple nuclei of several tens of nanometers. Subsequently, extensive experiments were conducted to adjust the material composition of the nanospheres by adjusting the amount of resorcinol and formaldehyde. The results showed that the obtained material performed best when resorcinol and formaldehyde were added to 0.2 g $MnCo_2O_4$ at 0.3 g and 0.42 mL, respectively. The efficient absorption bandwidth (EAB) value reaches 3.3 GHz when the absorber thickness is 3 mm. The reflection loss (RL) is up to −23.8 dB when the frequency is at 8.6 GHz. The unique yolk core-shell structure gives the material a heterogeneous interface, and the enhanced interfacial polarization loss causes the enhanced dielectric loss. The carbon layer with microporosity also causes conduction loss and multiple reflections. The composite structure formed by metallic Co, MnO, and carbon has better impedance matching and improved microwave absorption capability.

Keywords: MnO-Co@C nanospheres; yolk core-shell; microwave absorption

Citation: Xin, Z.; Wu, J.; Sun, S.; Zhang, M.; Sun, X. Rational Design of Yolk Core-Shell Structure MnO-Co@C Nanospheres for High-Performance Microwave Absorption. *Coatings* **2022**, *12*, 1405. https://doi.org/10.3390/coatings12101405

Academic Editor: Rafael L. Quirino

Received: 24 August 2022
Accepted: 5 September 2022
Published: 27 September 2022

1. Introduction

At present, microwave absorbing materials (MAMs) are widely used in military and civil fields, such as stealth defense systems of aircraft, electromagnetic interference prevention, etc. [1–3]. Simple methods to manufacture high-performance MAMs have been a hot subject for decades. Studies have shown that a material's microwave absorbing performance (MAP) can be boosted by combining materials with dissipation and magnetic loss properties [4,5]. Researchers have identified a variety of microwave absorbing materials with good single loss mechanisms, such as single metals, alloys, carbon materials, conductive polymers with good properties, etc. However, these materials have a few drawbacks, including high density, complicated production processes, poor thermostability, and ease of oxidizing in air, and these drawbacks limit their applications. [6]. Among a variety of magnetic MAMs, Co has a more excellent absorption capability due to its large anisotropic field, high saturating strength of magnetization strength, and high-frequency Snoek's limit, but the absorption bandwidth is narrow due to eddy current loss, impedance mismatch, and lack of dielectric loss. Additionally, in the past few years, manganese oxides have been widely studied in several fields due to their low cost and abundant resources [7], such as Fe/MnO@C composites [8] and Co/MnO composites [9], which show excellent electromagnetic MAPs due to the extended electromagnetic microwave path and polarization loss.

In order to obtain outstanding MAPs, two or more composite materials can be used together to regulate electromagnetic parameters and impedance matching. For example, carbon-containing materials (carbon fibers, porous carbon nanospheres, carbon-based nanotubes etc.) [10–12] have been used in combination with other metal cations. For example, Zhou et al. prepared metal-organic framework (MOF)-derived porous metal/C composites (rod-like Co/ZnO/C composites) [13]. Such methods can achieve better electromagnetic MAPs. Multi-component absorbers consistently exhibit a wider range of microwave absorption spectra and stronger reflection loss (RL) than single-type absorbers [14]. In addition to the inter-matching between magnetic and dielectric elements, microstructure greatly influences the MAPs of composites. The core-shell structure of MAMs has recently received much attention. Such unique multilayer microstructures not only provide a significant benefit to microwave absorption due to their multilayer polarization, multiple reflections with microporous interfaces, and cooperative behavior, but also produce a high degree of chemical homogeneity by preventing the agglomeration of metal particles, making composite materials much more effective than single-component absorbers [15,16]. Liu et al. [17] successfully prepared core-shell Fe_3O_4@C. They found that a metal oxide surface coated with a carbon layer could improve the complex dielectric constant and the characteristic impedance matching, which significantly enhancing microwave absorption. Therefore, we infer that the yolk-shell microspheres combining dielectric carbon shells and magnetic MnO-Co cores can produce multiple reflective losses. This is due to the effective gap between magnetic and dielectric elements, and the impedance match allows the complex permittivity and permeability of the materials to be elevated.

Herein, we introduce a facile one-pot method to produce yolk core-shell structure MnO-Co@C nanospheres via in-situ reduction. The thickness of the carbon shell could be managed by regulating the volume of resorcinol and formaldehyde. The research revealed that the carbon shell can inhibit the agglomeration of MnO-Co nanospheres and adjust the complex dielectric constant of the material so that MnO-Co@C nanospheres have a stronger magnetic loss capability. The resistance matching of the material is improved, and the MAPs of the material are enhanced. These results may provide new ideas for improving conventional MAMs.

2. Experimental Section

2.1. Chemicals

All chemicals are for straight use (analytical grade drugs). Manganese acetate tetrahydrate ($Mn(CH_3COO)_2{\cdot}4H_2O$), cobalt acetate tetrahydrate ($Co(CH_3COO)_2{\cdot}4H_2O$), polyvinylpyrrolidone (PVP), ethylene glycol ($(CH_2OH)_2$), resorcinol, ethanol (C_2H_6OH), formaldehyde (37%) and ammonia ($NH_3{\cdot}H_2O$, 26%) were purchased from Sinopharm Chemical Reagent, Co., Ltd. (Shenyang, Liaoning, China). The water used throughout the experiment was deionized water.

2.2. The Preparation of $MnCo_2O_4$ Nanospheres

The preparation process of $MnCo_2O_4$ nanospheres is described in [18]. Briefly, 3.0 g of PVP was dissolved in 250 mL of $(CH_2OH)_2$ and agitated for one hour. Next, 2.5 mmol of $Mn(CH_3COO)_2{\cdot}4H_2O$ and 5.0 mmol of $Co(CH_3COO)_2{\cdot}4H_2O$ were dissolved in the solution and stirred for one hour. The mixed solution was then transferred to a 500 mL round bottom flask, heated at 160 °C for 5 h, and naturally chilled to room temperature. Then, the reaction was centrifuged (8000 rpm), cleaned with ethanol, and dried in an oven at 80 °C for 12 h. The reaction was heated to 400 °C at 0.5 °C/min and held for 2 h to obtain $MnCo_2O_4$ nanospheres.

2.3. The Preparation of Core-Shell MnO-Co@C Nanospheres

Core-shell MnO-Co@C nanospheres were generated by a classical in situ polymerization and high-temperature carbonization method [19,20]. In short, 0.3 g of synthesized $MnCo_2O_4$ material was dispersed in a mixing solution that included 32 mL C_2H_6OH, 80 mL

deionized water, and 0.4 mL $NH_3 \cdot H_2O$. This solution was sonicated for 30 min and then magnetic stirred for 15 min. Resorcinol was added, the solution was stirred for 30 min, and then the formaldehyde was added. Next, the solution was agitated at room condition for 12 h, washed with deionized water and ethanol, and dried to obtain $MnCo_2O_4$@phenolic resin, which was transferred to a tube furnace and held for 3 h under argon protective gas using 1 °C/min ramp to 750 °C. Three samples were produced in this way, using different amounts of resorcinol and formaldehyde. The samples were labeled MnO-Co@C-0.2, MnO-Co@C-0.3, and MnO-Co@C-0.4, and the addition amounts of resorcinol and formaldehyde for the three samples were 0.2 and 0.28, 0.3 and 0.42, and 0.4 and 0.56, respectively.

2.4. Characterization

A characterization of the constituent phases and the crystal structure of the samples was carried out by X-ray powder diffraction (XRD; smartlab9, Rigaku, Tokyo, Japan, Cu-Kα source (40 kV, 200 mA)). The surface appearance and dimensional information of the material were assessed by scanning electron microscopy (SEM; JSM-7001F, JEOL, Tokyo, Japan). The element distribution inside the material and the internal morphology was observed by transmission electron microscopy (TEM; JEM-2100F, JEOL, Tokyo, Japan). X-ray photoelectron spectroscopy (XPS) was used to analyze the chemical bonding states of the elements on the material surfaces, using an Axis Supra with an Al Kα X-ray source. A vector network analysis (VNA; ENA-E5080B, Keysight, Colorado Springs, CO, USA) was used to measure the related factors of the absorbing material in the frequency series 2–18 GHz and used to calculate the reflection loss magnitude. The product was homogeneously mixed with paraffin wax in a mass ratio of 3:7 and pressed into a ring sample with an outside diameter of 7 mm, an inside diameter of 3 mm, and a depth of roughly 3 mm.

3. Results and Discission

The composition procedure of the core-shell MnO-Co@C nanospheres is shown in Figure 1. Mesoporous $MnCo_2O_4$ nanospheres with a mean diameter of approximately 500 nm were synthesized by a polyvinylpyrrolidone (PVP)-assisted solvothermal method. Then resorcinol and formaldehyde were used to form a layer of phenolic resin developed on the interface of $MnCo_2O_4$. Finally, the precursor material is carbonized and reverted in a high-temperature shielding atmosphere to obtain multinuclear yolk-shell MnO-Co@C structures.

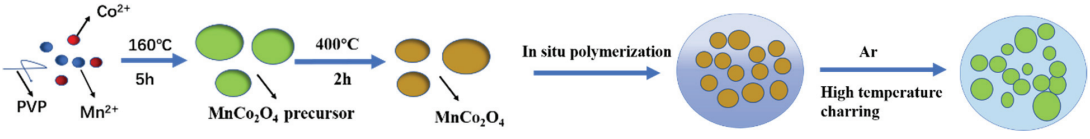

Figure 1. Schematic illustration of the composite process for core-shell MnO-Co@C nanospheres.

Figure 2 shows the morphology of $MnCo_2O_4$ nanospheres and MnO-Co@C nanospheres. Figure 3a shows that the average size of the diameter of the prepared $MnCo_2O_4$ nanospheres is about 500 nm, and the shrinkage shape of the nanoparticles becomes irregularly wrapped inside the carbon layer after in situ polymerization and calcination at 750 °C. Combined with the XRD figure, it can be known that the internal nanoparticles were reduced to MnO-Co, and a small agglomeration of MnO-Co@C nanospheres occurred with the increase of the carbon amount. The TEM shows that the small metal nanoparticles are amorphously distributed inside the carbon layer, and the carbon layer is uneven and microporous, thus increasing the multiple reflections of the material and providing reflection channels.

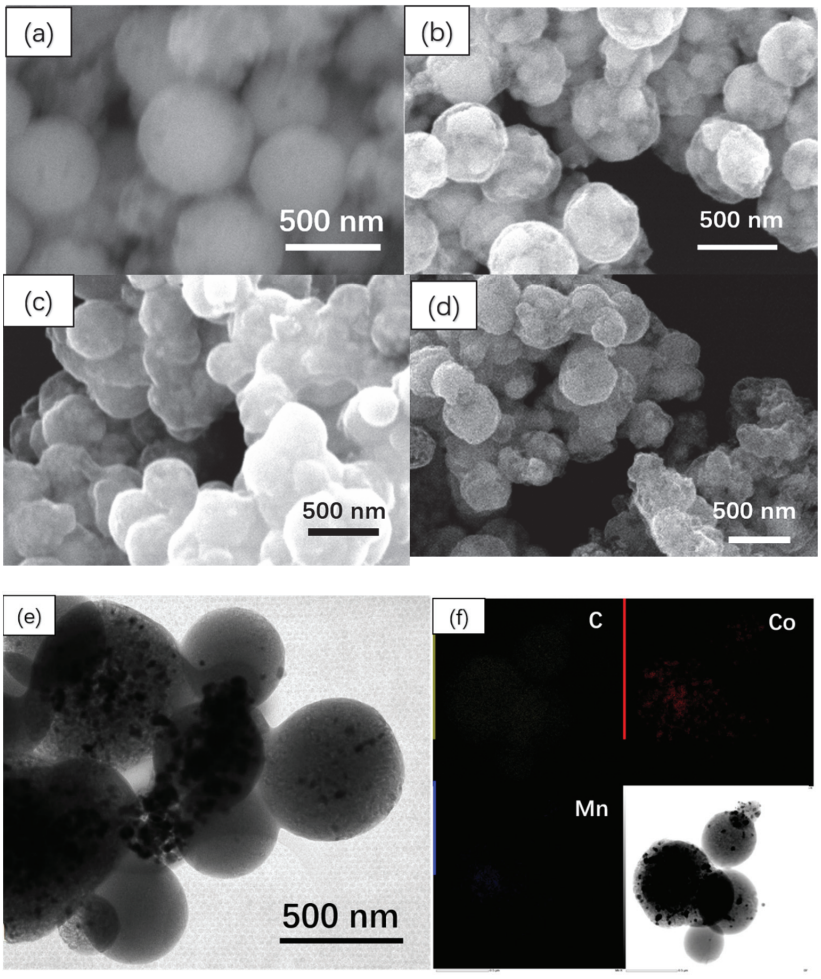

Figure 2. SEM images of $MnCo_2O_4$ (**a**), MnO-Co@C-0.2 (**b**), MnO-Co@C-0.3 (**c**), and MnO-Co@C-0.4 (**d**). TEM images of MnO-Co@C-0.3 (**e**), and elemental mapping distribution of MnO-Co@C-0.3 (**f**).

Figure 3a shows the XRD results of MnO-Co@C-0.2, MnO-Co@C-0.3 and MnO-Co@C-0.4. The diffraction peaks at 44.2°, 51.5°, and 75.8° for all the samples matches the (111), (200) and (220) planes of fcc Co (JCPDS 15-0806). The diffraction peaks at 35°, 40.7°, 58.9°, 70.4°, and 74° all match the (111), (200), (220), (311), (222) planes of MnO (JCPDS 75-0626). It was demonstrated that carbonizing at 750 °C is sufficient to help the carbon to fully reduce the cobalt metal, while the MnO was not reduced [7,21]. It can be seen from the intensity of the peaks that the content of Co is higher than that of MnO. As we can see, with the increase of carbon content, the intensity of peaks of Co and MnO do not show significant differences. In the sense, we assume that the metallic Co can be easily reduced leaving the MnO dispersed around the Co and carbon shell, giving rise to the formation of multiple interfaces within this unique core-shell structure. Consequently, the presence of metallic Co and MnO increases the interfacial species of the core-shell structure. No significant characteristic peaks of impurities were found in all XRD plots, indicating the high purity of the prepared samples.

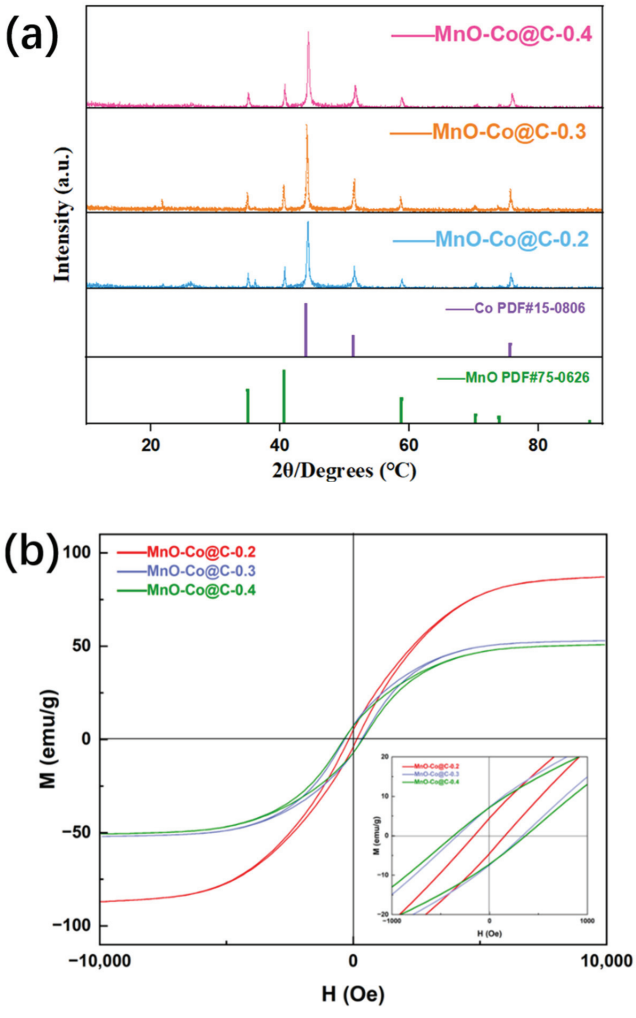

Figure 3. (**a**) The XRD pattern of MnO-Co@C-0.2, MnO-Co@C-0.3, and MnO-Co@C-0.4, (**b**) hysteresis loops of MnO-Co@C-0.2, MnO-Co@C-0.3, and MnO-Co@C-0.4.

The hysteresis lines of MnO-Co@C-0.2, MnO-Co@C-0.3, and MnO-Co@C-0.4 are shown in Figure 3b. According to these M-H curves, we can see that the saturation magnetization strength of the samples are 87.113 emu/g, 52.487 emu/g, and 50.746 emu/g, respectively. As you may observe from the graph, the material's saturation magnetization strength decreases steadily with the addition of carbon content. For ferromagnetic MAMs, the initial magnetic permeability (μ_i) can be expressed as [22]:

$$\mu_i = \frac{M_s^2}{akH_cM_s + b\lambda\xi} \quad (1)$$

where a and b are two constants determined by the material composition, M_s is the saturation magnetization strength, H_c is the coercivity, λ is the magnetostriction constant, and ξ is the elastic strain parameter of the crystal. An increase in the magnetic powder μ_i usually implies an increase in the magnetic loss potential, and the high M_s and low H_c also favor an increase in the magnetic loss potential.

The surface chemical composition and valence states of MnO-Co@C ternary nanocomposites were detected by X-ray photoelectron spectroscopy (XPS), and we can observe from Figure 4 that MnO-Co@C-0.3 has four characteristic peaks belonging to C 1s, O 1s, Co 2p, and Mn 2p, respectively. The characteristic peaks can be seen in the high-resolution spectra of C 1s at 283.8eV, 285eV, and 288.4eV, respectively, attributable to C=C, C-O, and O=C-C [23,24]. Co 2p can be adapted to 6 different feature peaks. The characteristic peaks at 779.2 eV and 794.6 eV belong to metallic Co, the feature peaks at 780.6 and 796.3 eV match the Co-O bond, and the remaining feature peaks at 786.8 eV and 803 eV can correspond to the satellite peaks [24]. Mn 2p can be fitted as 2 distinct feature peaks at 652.5 eV and 640.5 eV belonging to Mn^{2+} [25].

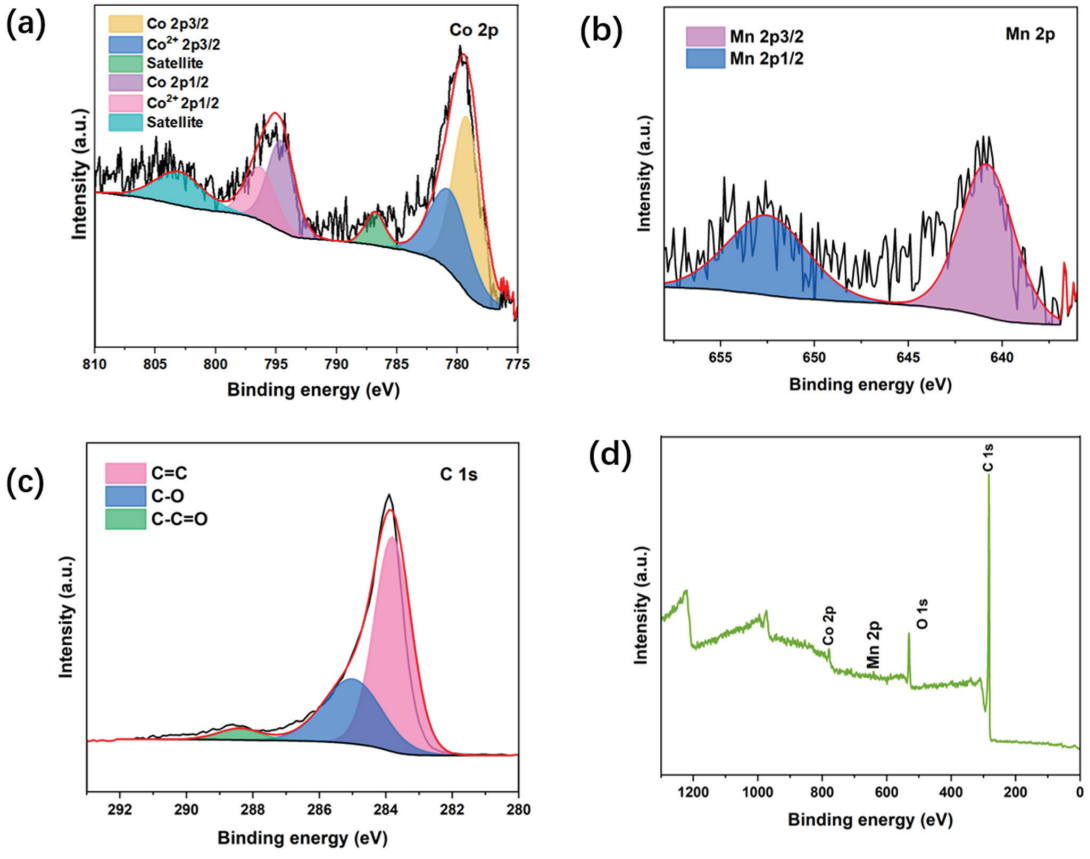

Figure 4. (**a**–**c**) high-resolution spectra Co 2p, Mn 2p, and C 1s, (**d**) Full scan XPS spectra of MnO-Co@C-0.3.

The reflection loss (RL) associated with the complex permittivity ($\varepsilon_r = \varepsilon' - j\varepsilon''$) and permeability ($\mu_r = \mu' - j\mu''$) was measured in the range of 2–18 GHz to evaluate the MAPs of the composite, based on the transmission line theory [26]:

$$Z_{in} = Z_0\sqrt{\mu_r/\varepsilon_r}\tan\ h\left|j\left(\frac{2\pi fd}{c}\right)\sqrt{\varepsilon_r\mu_r}\right| \quad (2)$$

$$RL(dB) = 20\log\left|\frac{Z_{in} - Z_0}{Z_{in} + Z_0}\right| \quad (3)$$

where Z_{in} is the input resistance of the absorbers, Z_0 is the free space resistance, c is the velocity of light, and d is the thickening of the absorbers. The real part (ε', μ') indicates the storage capacity of microwave energy, and the imaginary part (ε'', μ'') indicates the ability to dissipate electromagnetic microwaves.

Figure 5a displays ε' values of MnO-Co@C-0.2, MnO-Co@C-0.3, and MnO-Co@C-0.4 in the frequency range of 2–18 GHz. We can observe that the value of MnO-Co@C-0.3 and MnO-Co@C-0.4 are relatively close and fall slightly in the range of 2–16 GHz. The ε' value of MnO-Co@C-0.2 is approximately 5.5 and remains almost unchanged. On the ground of free electron theory, it is proposed that the imaginary part of the complex permittivity can be redefined as $\varepsilon'' \approx 1/2\pi\rho f\varepsilon_0$ [27], where ρ is the resistivity and ε_0 is the free space permittivity. It is known that the value of ε'' is influenced by the conductivity, and the larger the conductivity, the larger the value of ε''. The gradual increase in the ε'' values of the samples may be owing to the high cobalt metal content, and the graphitization of the material with the addition of resorcinol and formaldehyde. The dielectric tangent loss factor ($\tan\delta_\varepsilon = \varepsilon''/\varepsilon'$) [28] is used to express the dielectric loss capability of the material. We can find that the value of $\tan\delta_\varepsilon$ for MnO-Co@C-0.3 and MnO-Co@C-0.4 increases relative to the value of MnO-Co@C-0.2, fluctuating around 0.4, indicating that the dielectric loss capability of MnO-Co@C-0.3 and MnO-Co@C-0.4 is more significant than that of MnO-Co@C-0.2. We can observe from Figure 5c,d that the values of μ' and μ'' of all the three samples do not vary much, and the values are close to each other, with the value of μ' fluctuating around 1 and μ'' around 0. Similarly, the $\tan\delta_\mu = \mu''/\mu'$ [28] does not show much difference. It is possible to assume that the magnetic properties of the samples are not strong. The magnetic loss comes from the hysteresis, category wall resonance, ferromagnetic resonance, and eddy currents effects [29]. Hysteresis losses are insignificant in weaker electric fields, and domain wall resonance losses usually occur in lower frequencies (MHz) [30]. Therefore, the natural ferromagnetic resonance and eddy currents effects are commonly considered the major loss mechanisms of ferromagnetic absorbers at higher frequencies (GHz). The eddy current losses can be stated as [31]:

$$\mu'' = 2\pi\mu_0(\mu')^2\sigma d2f/3 \quad (4)$$

where σ is the electrical conductivity and μ_0 is the magnetic conductivity in the presence of vacuum. The reflection loss is caused by the eddy current effect. $C_0 = \mu''(\mu')^{-2}f^{-1}$ When the frequency changes, C_0 is a constant, indicating the existence of eddy current loss in the material [32].

The ability of a material to dissipate electromagnetic energy can be quantified by the attenuation coefficient α, expressed by the formula [21]:

$$\alpha = \left(\frac{\sqrt{2}\pi f}{c}\right)\sqrt{\mu_r''\varepsilon_r'' - \mu_r'\varepsilon_r'} + \sqrt{(\mu_r''\varepsilon_r'' - \mu_r'\varepsilon_r')^2 + (\mu_r''\varepsilon_r' - \mu_r'\varepsilon_r'')^2} \quad (5)$$

From Figure 5h, it can be obtained that the α values of MnO-Co@C-0.2, MnO-Co@C-0.3, and MnO-Co@C-0.4 increase with the growth of frequency, and the values of Mno-Co@C-0.3 and MnO-Co@C-0.4 are higher than MnO-Co@C-0.2. It indicates that the electromagnetic dissipation capability of MnO-Co@C-0.3 and MnO-Co@C-0.4 is higher in the region of 2–18 GHz.

According to Equations (2) and (3), the correlation between the thickness of the relevant EMW absorbing material and the reflection loss (RL) in the spectrum of frequencies from 2–18 GHz can be calculated. Figure 6 illustrates the reflection loss of MnO-Co@C-0.2, MnO-Co@C-0.3, and MnO-Co@C-0.4 corresponding to the frequency and thickness in the spectrum of frequencies region of 2–18 GHz. We can obtain from the Figure 6a that the MnO-Co@C-0.2 absorption effect is inferior. When the absorber's thickness is 1–5 mm, and the microwave frequency is 2–18 GHz, no RL value reaches the effective value of −10 dB (absorption of 90% of electromagnetic microwaves). As the amount of resorcinol

and formaldehyde increases, the carbon layer becomes thicker and has a good reduction effect on the alloy. The MAPs of MnO-Co@C-0.3 and MnO-Co@C-0.4 are much better than MnO-Co@C-0.2. For MnO-Co@C-0.3, when the absorber thickness is about 3 mm, the EAB_{max} value reaches 3.3 GHz and the RL_{min} is −23.8 dB. The addition of resorcinol and formaldehyde further increases the absorbing effect of the materials. Thus, we reasoned that MnO-Co@C-0.3 has the best ratio. We can infer that as the carbon content increases, the amount of Co being reduced gradually increases, the non-homogeneous MnO-Co@C interface gradually increases, and the interfacial polarization is enhanced. As the carbon layer has a large number of dipoles, polarization loss is generated, which increases the dielectric loss of the material. The exchange resonance leads to an increase in magnetic loss, which promotes a good impedance match and increases the overall MAPs of the material. However, further increases of carbon content will not help much, as MnO-Co@C-0.4 did not perform better. The above results show that the spherical yolk core-shell MnO-Co@C material with a reasonable carbon content ratio can achieve broadband EMW absorption with good overall performance. This excellent microwave absorption performance originates from the impedance matching of the composite; the cooperation between dielectric losses and magnetic losses.

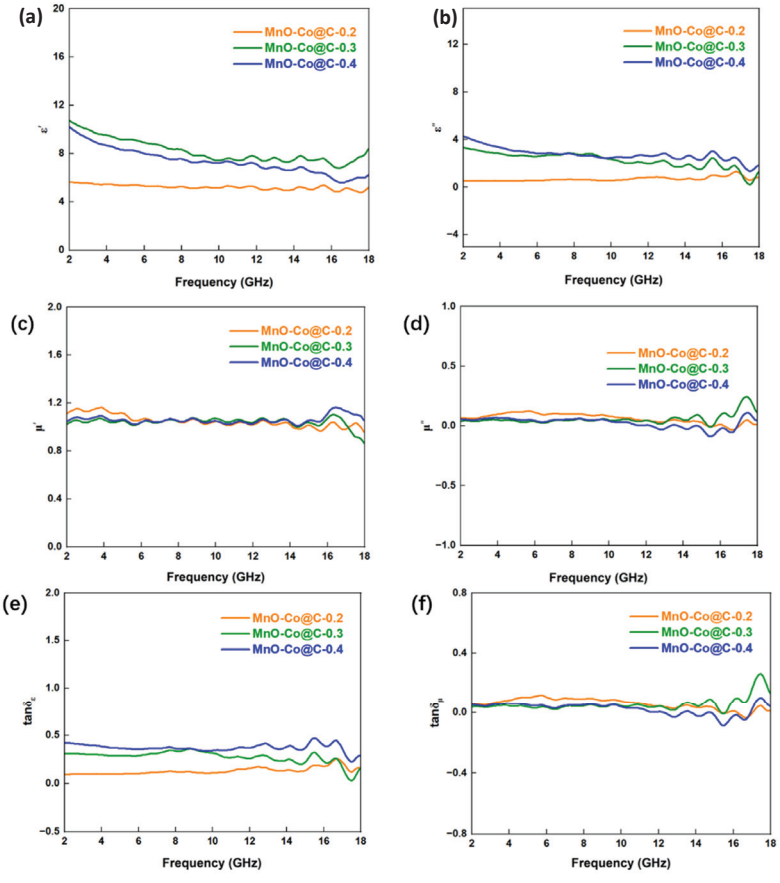

Figure 5. *Cont.*

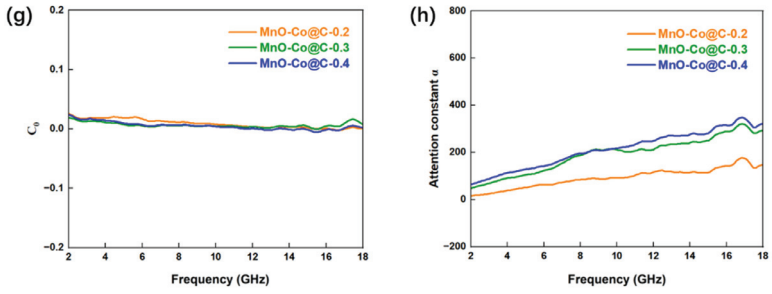

Figure 5. Electromagnetic parameters of MnO-Co@C-0.2, MnO-Co@C-0.3, and MnO-Co@C-0.4: (**a**) ε', (**b**) ε'', (**c**) μ' (**d**) μ'', (**e**) the dielectric loss tangent factor $\tan\delta_\varepsilon$, (**f**) the magnetic loss tangent factor $\tan\delta_\mu$, (**g**) C_0, (**h**) attention constant α.

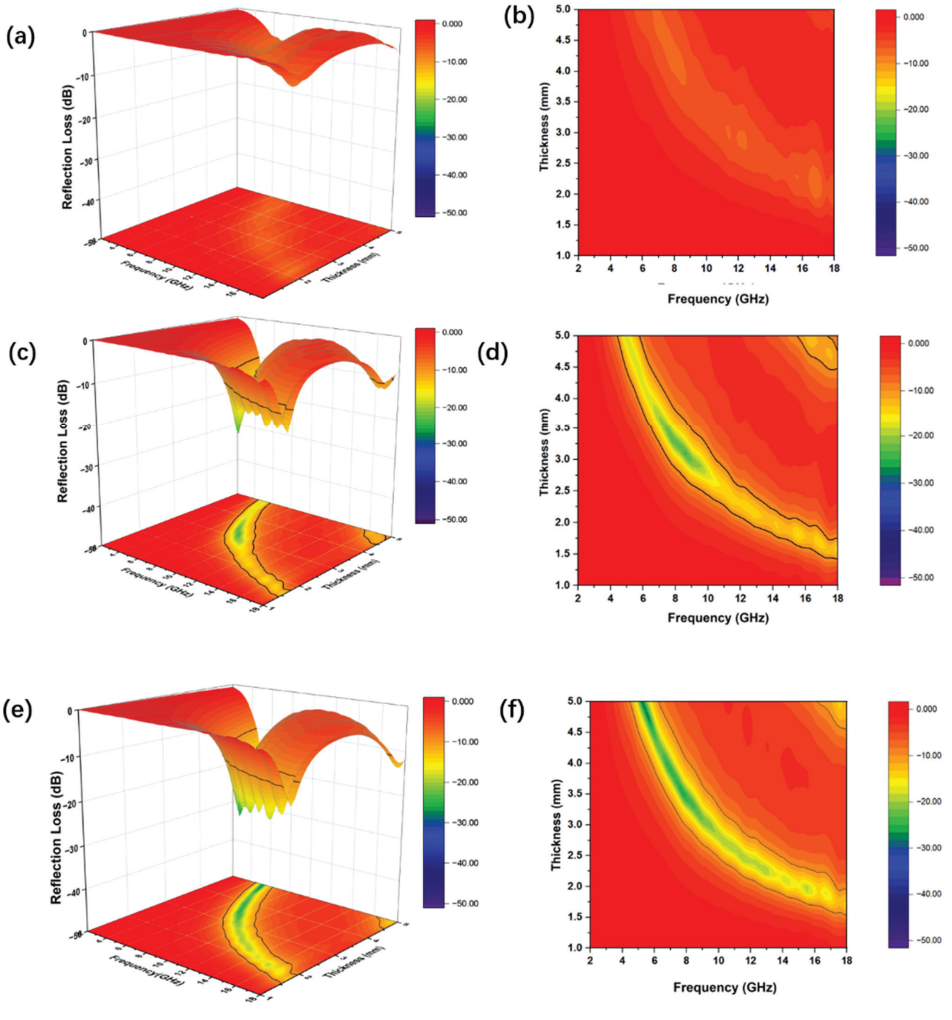

Figure 6. Reflection loss values in the frequency of 2–18 GHz for (**a**,**b**) MnO-Co@C-0.2; (**c**,**d**) MnO-Co@C-0.3; (**e**,**f**) MnO-Co@C-0.4.

4. Conclusions

In conclusion, a novel metal-metal oxide-carbon material interface was designed to form a special yolk core-shell structure. The spherical yolk core-shell MnO-Co@C material exhibits good EMW absorption performance and achieves the best reflection loss value of −23.8 dB and the EAB_{max} reaches 3.3 GHz when the surface thickness is 3 mm. Both of the dielectric and magnetic losses, and the unique yolk core-shell structure, all contribute significantly to the material's excellent microwave absorption. Core-shell MnO-Co@C nanospheres have the advantages of a simple preparation method, enhanced wave absorption performance, wide absorption bandwidth, and low density, making them a great application prospect in microwave absorption.

Author Contributions: Conceptualization, M.Z. and X.S.; methodology, S.S.; software, Z.X.; validation, J.W., S.S. and M.Z.; formal analysis, M.Z.; investigation, Z.X.; resources, S.S.; data curation, X.S.; writing—original draft preparation, Z.X.; writing—review and editing, M.Z.; visualization, M.Z.; supervision, M.Z.; project administration, J.W.; funding acquisition, M.Z. All authors have read and agreed to the published version of the manuscript.

Funding: This research was funded by National Natural Science Foundation of China (52072063), Research start-up fund of Foshan Graduate School of Northeastern University.

Institutional Review Board Statement: Not applicable.

Informed Consent Statement: Not applicable.

Data Availability Statement: Not applicable.

Conflicts of Interest: The authors declare no conflict of interest.

References

1. Micheli, D.; Vricella, A.; Pastore, R.; Marchetti, M. Synthesis and electromagnetic characterization of frequency selective radar absorbing materials using carbon nanopowders. *Carbon* **2014**, *77*, 756–774. [CrossRef]
2. Shahzad, F.; Alhabeb, M.; Hatter, C.B.; Anasori, B.; Hong, S.M.; Koo, C.M.; Gogotsi, Y. Electromagnetic interference shielding with 2D transition metal carbides (MXenes). *Science* **2016**, *353*, 1137–1140. [CrossRef]
3. Giannakopoulou, T.; Kompotiatis, L.; Kontogeorgakos, A.; Kordas, G. Microwave behavior of ferrites prepared via sol-gel method. *J. Magn. Magn. Mater.* **2002**, *246*, 360–365. [CrossRef]
4. Wang, J.; Liu, L.; Jiao, S.; Ma, K.; Lv, J.; Yang, J. Hierarchical Carbon Fiber@MXene@MoS_2 Core-sheath Synergistic Microstructure for Tunable and Efficient Microwave Absorption. *Adv. Funct. Mater.* **2020**, *30*, 2002595. [CrossRef]
5. Zhang, D.; Liu, T.; Cheng, J.; Cao, Q.; Zheng, G.; Liang, S.; Wang, H.; Cao, M.S. Lightweight and High-Performance Microwave Absorber Based on 2D WS2-RGO Heterostructures. *Nano-Micro Lett.* **2019**, *11*, 38. [CrossRef]
6. Ma, R.-T.; Shang, H.-Y.; Wang, X.; Jiang, D. Dielectric, magnetic and microwave absorbing properties of polyaniline-$Co_{0.7}Cr_{0.1}Zn_{0.2}Fe_2O_4$ composites. *Rare Met.* **2017**, *36*, 118–122. [CrossRef]
7. Qiu, Y.; Wen, B.; Yang, H.; Lin, Y.; Cheng, Y.; Jin, L. MOFs derived Co@C@MnO nanorods with enhanced interfacial polarization for boosting the electromagnetic wave absorption. *J. Colloid Interface Sci.* **2021**, *602*, 242–250. [CrossRef]
8. He, G.; Duan, Y.; Pang, H. Microwave Absorption of Crystalline Fe/MnO@C Nanocapsules Embedded in Amorphous Carbon. *Nano-Micro Lett.* **2020**, *12*, 57. [CrossRef]
9. Xu, D.; Qiao, J.; Wu, N.; Liu, W.; Wang, F.; Lv, L.; Pan, J.; Dong, Y.; Liu, J. Facile Synthesis of Three-Dimensional Porous Co/MnO Composites Derived from Bimetal Oxides for Highly Efficient Electromagnetic Wave Absorption. *ACS Sustain. Chem. Eng.* **2019**, *7*, 8687–8695. [CrossRef]
10. Shu, R.; Li, W.; Zhou, X.; Tian, D.; Zhang, G.; Gan, Y.; Shi, J.; He, J. Facile preparation and microwave absorption properties of RGO/MWCNTs/$ZnFe_2O_4$ hybrid nanocomposites. *J. Alloys Compd.* **2018**, *743*, 163–174. [CrossRef]
11. Liu, P.-B.; Huang, Y.; Sun, X. Excellent Electromagnetic Absorption Properties of Poly(3,4-ethylenedioxythiophene)-Reduced Graphene Oxide-Co_3O_4 Composites Prepared by a Hydrothermal Method. *ACS Appl. Mater. Interfaces* **2013**, *5*, 12355–12360. [CrossRef] [PubMed]
12. Li, X.; Feng, J.; Du, Y.; Bai, J.; Fan, H.; Zhang, H.; Peng, Y.; Li, F. One-pot synthesis of $CoFe_2O_4$/graphene oxide hybrids and their conversion into FeCo/graphene hybrids for lightweight and highly efficient microwave absorber. *J. Mater. Chem. A* **2015**, *3*, 5535–5546. [CrossRef]
13. Liao, Q.; He, M.; Zhou, Y.; Nie, S.; Wang, Y.; Hu, S.; Yang, H.; Li, H.; Tong, Y. Highly Cuboid-Shaped Heterobimetallic Metal-Organic Frameworks Derived from Porous Co/ZnO/C Microrods with Improved Electromagnetic Wave Absorption Capabilities. *ACS Appl. Mater. Interfaces* **2018**, *10*, 29136–29144. [CrossRef]

14. Yu, M.; Liang, C.; Liu, M.; Liu, X.; Yuan, K.; Cao, H.; Che, R. Yolk–shell Fe_3O_4@ZrO_2 prepared by a tunable polymer surfactant assisted sol–gel method for high temperature stable microwave absorption. *J. Mater. Chem. C* **2014**, *2*, 7275–7283. [CrossRef]
15. Tian, C.; Du, Y.; Xu, P.; Qiang, R.; Wang, Y.; Ding, D.; Xue, J.; Ma, J.; Zhao, H.; Han, X. Constructing Uniform Core-Shell PPy@PANI Composites with Tunable Shell Thickness toward Enhancement in Microwave Absorption. *ACS Appl. Mater. Interfaces* **2015**, *7*, 20090–20099. [CrossRef]
16. Liu, X.G.; Li, B.; Geng, D.Y.; Cui, W.B.; Yang, F.; Xie, Z.G.; Kang, D.J.; Zhang, Z.D. (Fe, Ni)/C nanocapsules for electromagnetic-wave-absorber in the whole Ku-band. *Carbon* **2009**, *47*, 470–474. [CrossRef]
17. Liu, X.; Cui, X.; Chen, Y.; Zhang, X.-J.; Yu, R.; Wang, G.-S.; Ma, H. Modulation of electromagnetic wave absorption by carbon shell thickness in carbon encapsulated magnetite nanospindles-poly (vinylidene fluoride) composites. *Carbon* **2015**, *95*, 870–878. [CrossRef]
18. Zhou, S.; Luo, X.; Chen, L.; Xu, C.; Yan, D. $MnCo_2O_4$ nanospheres for improved lithium storage performance. *Ceram. Int.* **2018**, *44*, 17858–17863. [CrossRef]
19. Qiao, Z.-A.; Guo, B.; Binder, A.J.; Chen, J.; Veith, G.M.; Dai, S. Controlled Synthesis of Mesoporous Carbon Nanostructures via a "Silica-Assisted" Strategy. *Nano Lett.* **2013**, *13*, 207–212. [CrossRef]
20. Meng, X.; Liu, Y.; Han, G.; Yang, W.; Yu, Y. Three-dimensional (Fe_3O_4/ZnO)@C Double-core@shell porous nanocomposites with enhanced broadband microwave absorption. *Carbon* **2020**, *162*, 356–364. [CrossRef]
21. Ding, D.; Wang, Y.; Li, X.; Qiang, R.; Xu, P.; Chu, W.; Han, X.; Du, Y. Rational design of core-shell Co@C microspheres for high-performance microwave absorption. *Carbon* **2017**, *111*, 722–732. [CrossRef]
22. Saini, P.; Choudhary, V.; Vijayan, N.; Kotnala, R.K. Improved Electromagnetic Interference Shielding Response of Poly(aniline)-Coated Fabrics Containing Dielectric and Magnetic Nanoparticles. *J. Phys. Chem. C* **2012**, *116*, 13403–13412. [CrossRef]
23. Wu, Y.; Shu, R.; Zhang, J.; Wan, Z.; Shi, J.; Liu, Y.; Zhao, G.; Zheng, M. Oxygen vacancies regulated microwave absorption properties of reduced graphene oxide/multi-walled carbon nanotubes/cerium oxide ternary nanocomposite. *J. Alloys Compd.* **2020**, *819*, 152944. [CrossRef]
24. Wang, J.; Jia, Z.; Liu, X.; Dou, J.; Xu, B.; Wang, B.; Wu, G. Construction of 1D Heterostructure NiCo@C/ZnO Nanorod with Enhanced Microwave Absorption. *Nano-Micro Lett.* **2021**, *13*, 175. [CrossRef] [PubMed]
25. Samanta, A.; Barman, B.K.; Mallick, S.; Raj, C.R. Three-Dimensional Nitrogen-Doped Graphitic Carbon-Encapsulated MnO-Co Heterostructure: A Bifunctional Energy Storage Material for Zn-Ion and Zn–Air Batteries. *ACS Appl. Energy Mater.* **2020**, *3*, 10108–10118. [CrossRef]
26. Kuchi, R.; Sharma, M.; Lee, S.W.; Kim, D.; Jung, N.; Jeong, J.-R. Rational design of carbon shell-encapsulated cobalt nanospheres to enhance microwave absorption performance. *Prog. Nat. Sci. Mater. Int.* **2019**, *29*, 88–93. [CrossRef]
27. Ren, F.; Yu, H.; Wang, L.; Saleem, M.; Tian, Z.; Ren, P. Current progress on the modification of carbon nanotubes and their application in electromagnetic wave absorption. *RSC Adv.* **2014**, *4*, 14419–14431. [CrossRef]
28. Panwar, R.; Puthucheri, S.; Singh, D.; Agarwala, V.; Lee, J.-R. Microwave absorption properties of FSS-impacted composites as a broadband microwave absorber. *Adv. Compos. Mater.* **2017**, *26*, 99–113. [CrossRef]
29. Wen, B.; Cao, M.-S.; Hou, Z.-L.; Song, W.-L.; Zhang, L.; Lu, M.-M.; Jin, H.-B.; Fang, X.-Y.; Wang, W.-Z.; Yuan, J. Temperature dependent microwave attenuation behavior for carbon-nanotube/silica composites. *Carbon* **2013**, *65*, 124–139. [CrossRef]
30. Wu, M.; Zhang, Y.D.; Hui, S.; Xiao, T.D.; Ge, S.; Hines, W.A.; Budnick, J.I.; Taylor, G.W. Microwave magnetic properties of $Co_{50}/(SiO_2)_{50}$ nanoparticles. *Appl. Phys. Lett.* **2002**, *80*, 4404–4406. [CrossRef]
31. Zhu, J.; Wei, S.; Haldolaarachchige, N.; Young, D.P.; Guo, Z. Electromagnetic Field Shielding Polyurethane Nanocomposites Reinforced with Core-Shell Fe-Silica Nanoparticles. *J. Phys. Chem. C* **2011**, *115*, 15304–15310. [CrossRef]
32. Jian, X.; Wu, B.; Wei, Y.; Dou, S.X.; Wang, X.; He, W.; Mahmood, N. Facile Synthesis of Fe_3O_4/GCs Composites and Their Enhanced Microwave Absorption Properties. *ACS Appl. Mater. Interfaces* **2016**, *8*, 6101–6109. [CrossRef] [PubMed]

coatings

MDPI

Article

Synthesis of MgO Coating Gd_2O_3 Nanopowders for Consolidating Gd_2O_3-MgO Nanocomposite with Homogenous Phase Domain Distribution and High Mid-Infrared Transparency

Nan Wu [1,*], Zhongchao Fu [1], Haibo Long [1], Jianming Wang [2], Jun Zhang [3], Zhaoxia Hou [1], Xiaodong Li [4] and Xudong Sun [4]

[1] Liaoning Province Key Laboratory of Micro-Nano Materials Research and Development, School of Mechanical Engineering, Shenyang University, Shenyang 110044, China
[2] Key Laboratory of Advanced Materials & Preparation Technology of Liaoning Province, Shenyang University, Shenyang 110044, China
[3] Key Laboratory of Research and Application of Multiple Hard Films, College of Mechanical Engineering, Shenyang University, Shenyang 110044, China
[4] Key Laboratory for Anisotropy and Texture of Materials (Ministry of Education), Northeastern University, Shenyang 110819, China
* Correspondence: wunan20102010@163.com; Tel.: +86-024-6226-9802

Abstract: Improved optical and mechanical properties are required for future infrared windows working in harsher mechanical and thermal environments than today. Ameliorating the homogeneity of the phase domain and reducing the size of the phase domain are effective approaches for enhancing the optical transmittance and mechanical hardness of a nanocomposite. In this work, we reported that the Gd_2O_3-MgO nanopowders were prepared by two different processes. The core–shell nanopowders synthesized by urea precipitation have a much lower agglomeration than the nanopowders prepared by sol–gel. Excellent transmittance (70.0%–84.1%) at 3–6 μm mid-infrared wave range and a high Vickers hardness value (10.3 ± 0.6 GPa) were maintained using the nanopowders synthesized by urea precipitation mainly due to its homogenous phase domain distribution.

Keywords: Gd_2O_3-MgO; core–shell; urea precipitation; nanocomposite; homogenous phase domain distribution

Citation: Wu, N.; Fu, Z.; Long, H.; Wang, J.; Zhang, J.; Hou, Z.; Li, X.; Sun, X. Synthesis of MgO Coating Gd_2O_3 Nanopowders for Consolidating Gd_2O_3-MgO Nanocomposite with Homogenous Phase Domain Distribution and High Mid-Infrared Transparency. *Coatings* **2022**, *12*, 1435. https://doi.org/10.3390/coatings12101435

Academic Editors: Emerson Coy and Luca Valentini

Received: 10 August 2022
Accepted: 26 September 2022
Published: 29 September 2022

1. Introduction

Transparent polycrystalline ceramics have attracted widespread attention due to their wide range of applications such as laser hosts, infrared windows/domes, and transparent armors, instead of their single-crystal counterparts, mainly due to their processing flexibility and low cost for fabricating items with large sizes and complex shapes [1–3]. In particular, transparent polycrystalline ceramics have great potential in the application of infrared windows because of their excellent optical and mechanical properties [4–6]. With the increasingly harsh service environment of infrared windows, higher requirements are being suggested for the optical and mechanical properties of infrared windows in extreme environments [7,8]. Although traditional single-phase infrared transparent ceramics such as Y_2O_3, MgF_2, and $MgAl_2O_4$ have high infrared transmittance, the inevitable grain coarsening during the preparation process results in deteriorated mechanical properties, thus limiting their widespread application [5,9,10].

One way to improve the mechanical properties of the infrared transparent ceramic is to introduce a second ceramic phase to forming composites. Composites including fiber-reinforced composites [11], sandwich planet composites [12–14], composite ceramics [15], and polymers [16] are being applied in many fields. For example, in the field of mid-infrared windows, second-phase MgO is being introduced into Y_2O_3 to fabricate the

Y_2O_3-MgO nanocomposite with better optical and mechanical properties than any single-phase polycrystalline ceramics [17]. Y_2O_3 and MgO (based on the volume ratio of 50:50) were evenly mixed in order to mitigate grain growth during consolidation due to the fact that the grains of each phase pin the boundary in the other phase, thus restraining the grain boundary migration and grain coarsening. The reduced grain size will not only increase the infrared transmittance of the nanocomposite owing to the reduction in light scattering but also improve the mechanical strength according to Hall–Petch behavior [18]. Another example is via the introduction of MgO to consolidate Gd_2O_3–MgO nanocomposites with varied crystallographic modifications of the Gd_2O_3 constituent, and the nanocomposite has excellent optical and mechanical properties for mid-infrared window applications in our previous works [19,20].

The successful fabrication of nanocomposites with homogeneous phase domain distribution, fine grain sizes, and phase domain sizes is particularly challenging. Muoto et al. reported that the particle size and phase domain homogeneity of the initial nanocomposite powders directly determine the grain size and phase domain uniformity of the sintered nanocomposite ceramics, thus influencing their optical and mechanical properties [18]. Therefore, it is significant to synthesize nanocomposite powders with good dispersion and homogenous constituent phase distribution. Among the varied methods for producing nanopowders, such as spray pyrolysis [21,22], glycine–nitrate process [23,24], sol–gel combustion [24], and hydrothermal method [25], the sol–gel combustion method has always been favored, mainly due to its reduced synthesis temperature and the atomic-level mixing of starting reactants [8,17,26]. However, the properties of nanocomposite powders prepared by sol–gel combustion method such as particle size and dispersion are influenced by various factors such as starting reactants, fuel type, and equivalence ratio Φ. Additionally, the sol–gel process has long powder preparation cycles which are not conductive to batch production. Urea precipitation is a powder synthesis method with a simple operation, uniform system, and controllable precipitation process [27,28]. The introduction of Gd_2O_3 nanoparticles as the core can induce the Mg^{2+} precursor to precipitate on the surface of the nanoparticles via heterogeneous formation, thereby forming Gd_2O_3-MgO core–shell nanopowders. This can not only inhibit the grain overgrowth during the nanocomposite sintering process, but also solve the difficult problem of the complex and difficult-to-control precipitation variables of double cations.

In this work, to achieve the nanocomposites with homogeneous phase domain distribution, urea precipitation and sol–gel were used to synthesize Gd_2O_3-MgO nanopowders. We show that the core–shell nanocomposite powder with good dispersion can be obtained via the urea precipitation method, and the nanocomposites with homogenous distribution of constituent phases, higher optical transmittance, and a hardness value can be obtained after hot-press sintering. The underlying influence mechanism of the nanopowders with different morphologies on the microstructure of the nanocomposites was discussed.

2. Material and Methods

2.1. Preparation of the Gd_2O_3-MgO Core–Shell Nanopowders by Urea Precipitation

MgO coating Gd_2O_3 core–shell nanopowders were synthesized by urea precipitation. The raw materials were gadolinium oxide nanopowders (5N), urea, and magnesium nitrate hexahydrate ($Mg(NO_3)_2{\cdot}6H_2O$). All the raw materials were of analytical grade (Sinopharm Chemical Reagent, Shanghai, China). First, the 74.78 mmol $Mg(NO_3)_2$ and stoichiometric urea were dissolved in deionized water into a three-necked flask to form a mixed solution. Then, 6.99 g Gd_2O_3 was weighted with a volume ratio of 50:50 to MgO (monoclinic-Gd_2O_3:cubic-MgO) into the container via sufficient stirring and dispersing. After that, the dispersed Gd_2O_3 was put into the above solution in the three-necked flask. Additionally, then, the solution in the three-necked flask was heated and stirred at 90 °C for 3 h to obtain the turbid solution. After that, the resulting suspension was obtained by filtration and then the suspension was put into a 90 °C oven for drying, thus obtaining the dried precursors. Then, the dried precursors were calcined at 850 °C to prepare the core–shell nanopowders.

The nanopowders were ball-milled with Al_2O_3 balls in a roller ball mill (100 r/min). The slurry was placed into an 80 °C oven for drying. Finally, the nanocomposite powders were sieved by a 200-mesh screen.

2.2. Synthesis of the Gd_2O_3-MgO Nanopowders by Sol–Gel Combustion

Nanopowders of Gadolinium oxide–magnesium oxide were synthesized by sol–gel combustion technique. Commercial $Gd(NO_3)_3{\cdot}6H_2O$, $Mg(NO_3)_2{\cdot}6H_2O$, $C_6H_{10}O_8$, and ethylene glycol were used as raw reactants (Sinopharm, Shanghai, China). In a typical synthesis procedure, firstly, distilled deionized water, citric acid, and glycol were mixed to form an aqueous solution. Secondly, the 0.03854 mol $Gd(NO_3)_3$ and 0.07478 mol $Mg(NO_3)_2$ solutions were added into the above aqueous solution to prepare a clear sol. The sol was placed into an oven at 90 °C to obtain the precursor. Then, the precursors were calcined at 600 °C to obtain the nanopowders. The nanopowders were also obtained via a series of ball milling, drying, and screening processes consistent with Section 2.1.

2.3. Sintering of the Gd_2O_3-MgO Nanocomposite

The treated (calcined, ball-milled, and screened) Gd_2O_3-MgO nanopowders synthesized by two methods were dry-pressed at 100 MPa in a steel-mold (Φ_{diam} = 25 mm) to obtain the green bodies, and then the green bodies were sintered via hot pressing at 1350 °C for 0.5 h. The load was applied at the temperature of 600 °C, and gradually increased to 50 MPa at 1000 °C. Post-sinter annealing was carried out at 1000 °C for 20 h in air. Both surfaces of the samples were polished, and then thermally etched for the property characterization.

2.4. Investigation for the Nanocomposite Powders and Sintered Ceramics

Simultaneous thermogravimetric and differential scanning calorimetry analyses of the precursor synthesized by two different processes were carried out on a TGA-DSC apparatus (STA449F3, Netzsch, Selb, Germany). The precursor to be analyzed was heated at 10 °C/min in flowing air. The XRD analysis was conducted to identify the structures of the nanopowders and nanocomposites by X-ray diffraction (X'pert, PANalytical, Almelo, The Netherlands) using Cukα radiation. The crystal size of the nanocomposite powders can be calculated by Scherrer's formula:

$$D_{XRD} = (K\lambda)/(\beta cos\theta) \quad (1)$$

where K belongs to a constant, taking 0.89; λ represents the wavelength of Cukα wavelength; the width at half height for diffraction peak of the measured sample is represented by β; θ is the Bragg diffraction angle; and D_{hkl} means the crystal size of the nanopowders. The specific surface area of the nanocomposite powders was determined using a gas sorption analyzer by the Brunauer–Emmett–Teller (Tri-Star II 3020, Norcross, GA, USA) method. The mean particle size of the nanopowders was calculated via Formula (2):

$$D_{BET} = 6000/(\rho S_{BET}) \quad (2)$$

where S_{BET} denotes the specific surface area of the nanopowders; ρ stands for the theoretical density of the nanopowders; and D_{BET} represents the mean particle size. The ratio of D_{BET}/D_{XRD} was adopted to evaluate the agglomeration factor of the nanocomposite powders synthesized by a different method. Transmission electron microscopy (JEM-2100F, JEOL, Tokyo, Japan) determined the morphologies of the nanopowders prepared by different techniques. The structures and morphologies of the sintered nanocomposite ceramics were evaluated via scanning electron microscopy (JSM-7001F, JEOL, Tokyo, Japan). The statistics of the mean grain size for nanocomposite ceramics were obtained by measuring at least 200 grains on the BSE images using the line-intercept method. The infrared in-line transmittance of the nanocomposite was measured using a Fourier transform infrared spectrometer (Nicolet iS5, Thermo Scientific, Waltham, MA, USA). The test for the Vickers

hardness was performed via a tester (401 MVD, Wolpert, Norwood, MO, USA), the load was 500 g, the dwell time was 10 s, and the average of 10 measurements was taken as the final hardness value of the specimen [29].

3. Results and Discussion

3.1. The Thermal Behaviors of the Precursors Synthesized by Two Processes

Figure 1 shows the simultaneous thermal behaviors of the precursors synthesized by the two methods. For the precursor synthesized by urea precipitation (shown in Figure 1a), based on previous research results [30], in the process from room temperature to 1000 °C, the total mass loss is 41.7%, which is divided into four steps. The first stage is from room temperature to 196 °C, with a mass loss of 9.6%, and an endothermic peak at 170 °C is ascribed to the evaporation of absorbed water and the release of bound water. The mass loss in the second stage is 2.2%, which occurs in the temperature range between 196 and 281 °C. The exothermic peak at 271 °C on the DSC curve is mainly due to the decomposition and oxidation of nitrate. The third period is from 281 to 624 °C, and the mass loss is 18.3%; the endothermic peaks are located at 437, 466, and 614 °C, and are related to the decomposition of hydroxides and carbonates. The 11.6% mass loss occurs in the fourth step, and there is an exothermic peak at 629 °C which is attributed to the crystallization of oxides. No obvious weight loss was observed after 850 °C, indicating that MgO-coated Gd_2O_3 nanopowders can be obtained at 850 °C. Figure 2a shows that the precursor calcined at 850 °C is composed of Gd_2O_3 and MgO phases.

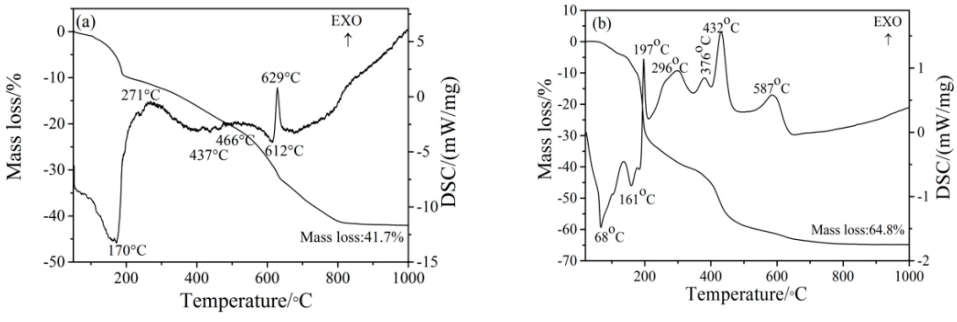

(**a**) (**b**)

Figure 1. Plot of the differential thermal analysis and thermogravimetry data obtained at a heating rate of 10 °C/min from the precursors synthesized by different methods: (**a**) urea precipitation; and (**b**) sol–gel.

For the precursor synthesized by sol–gel (shown in Figure 1b), it can be clearly seen that four-period weight loss occurred. The first weight loss period over the temperature ranging from room temperature to 178 °C is assigned to residual water volatilization. The DSC curve has two remarkable endothermic peaks at 68 and 161 °C. A sudden drop was observed in the second period weight loss, which was from 178 to 222 °C. In this period, there was a sharp exothermic peak at 197 °C, since the precursor was ignited. This is because there is a redox reaction between nitrate and citrate, thus generating intermediate products and releasing carbon oxide and nitrogen oxide gases [31,32]. The third period occurred between 222 and 510 °C and there are three exothermic peaks (296, 376, and 432 °C) being caused by the decomposition of the intermediate products. An exothermic peak at 587 °C emerged in the fourth period, which is ascribed to the decomposition of the remaining organics and the oxide crystallization. The XRD result in Figure 2a proves that the precursor heated at 600 °C consists of Gd_2O_3 and MgO. The thermal decomposition process of the precursor is consistent with our previous results [20].

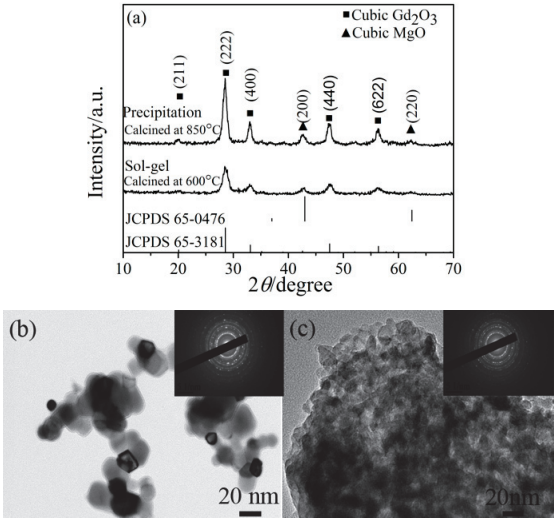

Figure 2. (**a**) XRD patterns of the nanocomposite powders preparation via different methods. TEM images of the calcined nanopowders synthesized by different methods; (**b**) urea precipitation; and (**c**) sol–gel. The insets are the SADPs of the calcined nanopowders synthesized by different methods.

3.2. Effects of Preparation Process on the Performances of Nanocomposite Powders

Figure 2a shows the XRD patterns of the nanopowders synthesized from a different method. Obviously, the composite nanopowders were cubic Gd_2O_3 and MgO phases, regardless of the synthesis methods. The diffraction peaks of the sample synthesized by urea precipitation are much more intense and sharper than that of the sample synthesized by sol–gel. Table 1 shows the particle size (D_{BET}), crystal size (D_{XRD}), and agglomeration factor calculated. Although the crystal sizes of the nanocomposite powders synthesized by sol–gel are finer than that of the nanopowders synthesized by urea precipitation, the agglomeration factor has an obvious increase. TEM results further verified the conjecture for the morphologies for the two nanocomposite powders synthesized by different methods. The sample synthesized by urea precipitation has a larger particle size and better dispersion than those synthesized by sol–gel. The diffuse amorphous rings in the insets selected area diffraction patterns (SADPs) are consistent with the XRD data (shown in Figure 2a) which indicate that the nanopowders synthesized by urea precipitation have better crystallinity. In addition, the sample shown in Figure 2b exhibits a clear interface between core and shell, indicating that the Gd_2O_3, as a core, is successfully cladded with MgO as a shell.

Table 1. Characterization of the Gd_2O_3-MgO nanocomposite powders synthesized from different methods.

Experiment Method	D_{BET} (nm)	D_{XRD} (nm)	Agglomeration Factor
Precipitation	59.8	32.3	1.9
Sol–gel	29.7	9.1	3.3

Clearly, the above results demonstrate that the properties of the composite nanopowders are greatly affected by the synthesis method. With the variation of the synthesis method, the crystal size and the agglomeration state for nanocomposite powders varied remarkably. The discrepancies can be related to the thermal decomposition processes of the precursors exhibited in the TG-DSC curves. For sol–gel process, the sharp exothermic peak of 197 °C in the DSC data and the sudden weight loss on the TG indicate that the decomposition process is instantaneous. The rapid reaction rate can restrict particle growth and

eventually form extremely fine crystallite sizes [18,24,33]. In the sol–gel reaction system, excessive fuel will generate a lot of heat in the later decomposition process, leading to the agglomeration of nanocomposite powder. Therefore, although the crystallite size of nano powders synthesized by sol–gel method is much finer, the agglomeration of nanopowders is more serious. In addition, Figure 1b shows that the peaks at 296, 376, and 432 °C in the DSC data also verified that the reaction at the later stage was very intense. Such a result is similar to our previous study [20]. For urea precipitation, the entire reaction process is gentle without violent decomposition and abrupt weight loss, since no extra heat is required for nanopowder agglomeration. Therefore, the nanopowder synthesized by urea precipitation has a lower agglomeration state.

3.3. Effects of Synthesis Process on the Phase, Microstructure, Optical, and Mechanical Properties of Nanocomposites

Figure 3 shows the structures of the Gd_2O_3-MgO nanocomposite ceramics. The characteristic monoclinic Gd_2O_3 and cubic MgO peaks emerged without any detectable impurity phase, irrespective of the two synthesis methods. It is worth noting that the Gd_2O_3 powders exhibited a cubic phase (shown in Figure 2a), but it turned into a monoclinic phase after sintering at 1350 °C. It is reported that Gd_2O_3 undergoes a cubic to monoclinic transformation above 1250 °C [34]. It is worth noting that the high-temperature monoclinic Gd_2O_3 is unstable in thermodynamics. However, the two samples are still retained in a monoclinic Gd_2O_3 phase at room temperature. The reason for the absence of the monoclinic-cubic reverse transition can be attributed to the slow atom spread dynamics and rapid cooling after hot pressing [35,36].

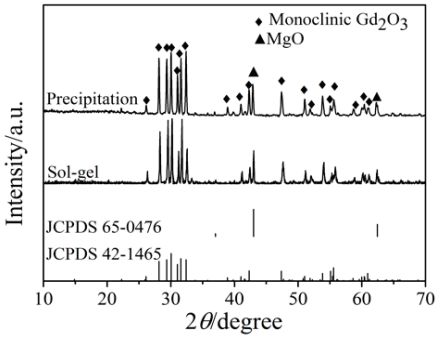

Figure 3. XRD patterns of the sintered nanocomposite ceramics with nanocomposite powders from different methods.

The effect of nanocomposite powders synthesized by different methods on the microstructure of the hot-pressed nanocomposites was characterized via BSE images. Figure 4 shows the representative BSE images. There is no significant difference in the grain size of the two samples; however, the structure and distribution of the phase domain are quite different. For the nanocomposite sintered using the urea precipitation nanopowders (shown in Figure 4a), the grain sizes of Gd_2O_3 (bright phase) and MgO (dark phase) are 160 and 120 nm, respectively, and the sample has a very even microstructure and a homogenous two-phase distribution. For the nanocomposite sintered using the sol–gel nanopowders, the grain sizes of Gd_2O_3 and MgO become slightly finer—140 and 130 nm. However, the clusters in each phase are large, which leads to a large-sized phase domain and inhomogeneous phase domain distribution.

One of the major goals of improving the phase domain homogeneity in synthesized nanopowder is to suppress the grain coarsening during the subsequent sintering processing of the nanopowders. It can be seen from Figures 2 and 4 and Table 1 that the agglomeration state of the initial nanopowders has a significant effect on the microstructure of the sintered

nanocomposite. The speculative schematic diagrams of the microstructure evolution process of the nanopowders prepared by two different processes during the sintering process are shown in Figure 5. For the nanopowders synthesized by urea precipitation, Gd_2O_3 as a core is effectively coated by MgO as shell, and the Gd_2O_3 grains are pinned by the MgO grains; thus, due to the core–shell structure constrains and the effective pinning effect, the microstructure will be stable until the coarsening of the one-phase domain can occur. However, the severe agglomeration of nanopowders prepared by sol–gel may cause each phase domain in the powder to contain multiple homophase particles. During the sintering process, the homophase particles in each phase domain will rapidly combine and grow. The reason for this phenomenon is that the agglomerated homophase particles only need to cross the homophase grain boundary, so the grains only undergo a short-distance rearrangement of atomic positions; eventually, resulting in large grain and phase domain sizes and inhomogeneous phase domain distribution.

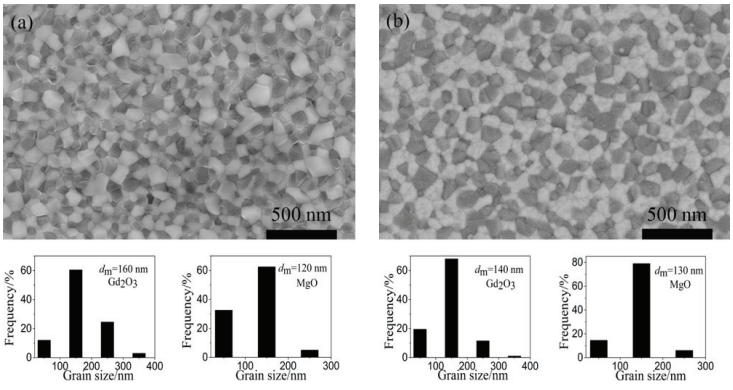

Figure 4. BSE images and grain size distributions of the sintered nanocomposite ceramics with nanocomposite powders with two methods: (**a**) urea precipitation; and (**b**) sol–gel.

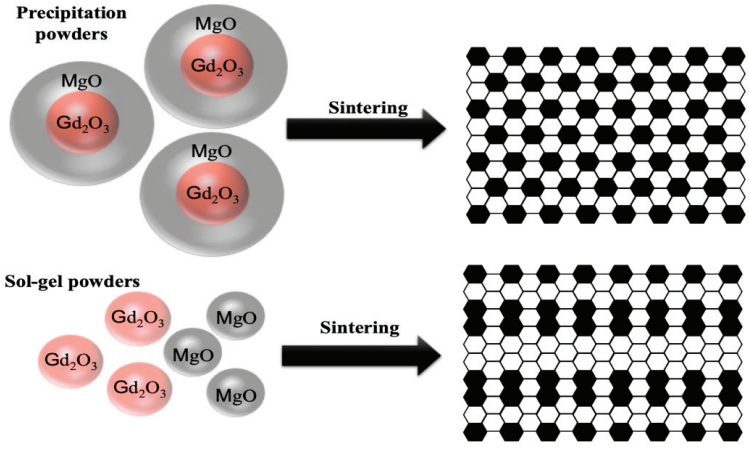

Figure 5. Diagrammatic sketch of the phase domain and grain size evolution during the sintering of composite materials using different nanopowders.

As can be seen from the above analysis, initial nanocomposite powders with slight agglomeration, fine phase domain size, and homogenous phase domain distribution are conductive to exert pinning effect and restrain grain growth in the subsequent sintering process. This hypothetical microstructure evolution was well verified in this work. The

agglomeration state of the core–shell nanopowders synthesized by urea precipitation is slighter than that of the nanopowders synthesized by sol–gel (as shown in Figure 2 and Table 1). After hot pressing, the homogeneity of the phase domain of the former is obviously superior to that of the latter. This phenomenon of the agglomeration state of nanocomposite powder affecting the phase domain uniformity of the nanocomposite after sintering was observed in the previous fabrication of Y_2O_3-MgO and MgO-ZrO_2 nanocomposites [18,33,37].

Figure 6 shows the optical transmittance in the infrared band of the Gd_2O_3-MgO nanocomposites sintered using the nanopowders synthesized by two methods. The microstructure, such as the porosity, grain size, size, and homogeneity of the phase domain greatly affects the infrared transmittance of the sample. On the one hand, the porosity is the main factor affecting the transmittance when the ceramic bulk is at a low relative density, because light scattering from a large number of pores will seriously deteriorate the light transmission because of the different refractive index of MgO, Gd_2O_3, and air. Additionally, the infrared transmittance also degrades when the relative density of the sample is high due to grain overgrowth and uneven phase domain distribution. As shown in Figure 4, there is no significant difference in the grain size between the two samples, and there are no obvious pores. Therefore, the distribution and uniformity of the phase domain play a dominant role in affecting the infrared transmittance in this work. As expected, the sample sintered using the core–shell nanopowders showed excellent transmittance (70.0%–84.1%) at 3–6 μm mid-infrared thanks to the more homogeneous phase domain distribution. Moreover, the two specimens have several absorption peaks at approximately 7 μm due to the asymmetrical and symmetrical stretching vibrations of the carboxylate groups, forming in the starting powders or subsequent sintering process because of the remaining carbon-containing groups. This is detrimental to the optical performance of a nanocomposite in the infrared wavelength range [38]. Therefore, the production of carbon-free nanocomposite powders with good dispersion and a uniform phase domain is key to further improving the infrared transmittance performance of nanocomposites. The detailed results will be described in the subsequent paper.

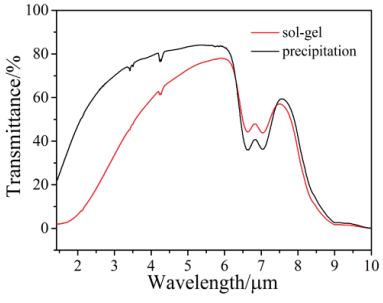

Figure 6. IR transmission spectra of the sintered nanocomposite ceramics with nanocomposite powders with two methods (the thickness of the sample is 2.0 mm).

The mechanical hardness of the sintered Gd_2O_3-MgO nanocomposites using nanopowders with different methods were measured. As Figure 7 shows, the Vickers hardness of the sample sintered using the core–shell nanopowders synthesized by urea precipitation is higher than that of the sample sintered using the nanopowders prepared by sol–gel due to a more homogeneous phase domain distribution. The hardness value of 10.3 ± 0.6 GPa is significantly higher than that of pure dense MgO and Y_2O_3 ceramics (5–7 GPa) [39,40], and the hardness value is similar to that of Y_2O_3-MgO reported by Xu et al. (10.0 ± 0.1 GPa) [7] or Ma et al. (10.6 ± 0.2 GPa) [24]. In addition, the optical and mechanical properties will be further improved for adapting to a much harsher environment in the future when the microstructure is further optimized. There is still room to homogenize the phase domain

distribution and reduce the grain size via the optimization of the nanopowders' preparation and sintering process.

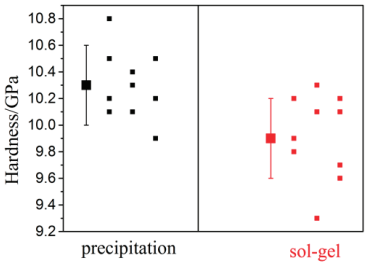

Figure 7. Vickers hardness of the sintered Gd_2O_3-MgO nanocomposites using nanopowders with different methods.

4. Conclusions

The Gd_2O_3-MgO nanopowders with different morphologies were synthesized by urea precipitation and citric sol–gel, respectively. The thermal behaviors of the precursors prepared by two processing methods influenced the agglomeration state of the nanopowders. The Gd_2O_3-MgO nanopowders with a core–shell structure have lower agglomeration, and are make it easy to obtain nanocomposites with a homogeneous phase domain distribution after hot-press sintering. For the Gd_2O_3-MgO nanocomposite sintered at 1350 °C and 50 MPa using the core–shell nanopowders, the average sizes of Gd_2O_3 and MgO are 160 and 120 nm, respectively. The nanocomposite with even two-phase distribution exhibits an outstanding transmission (70.0%–84.1%) in the mid-infrared range and a high hardness value (10.3 ± 0.6 GPa). The results indicate that core–shell nanopowder is conductive to restraining the growth of the phase domain size and the formation of an inhomogeneous phase domain for nanocomposites.

Author Contributions: Writing—original draft preparation, data curation, formal analysis, and investigation, N.W.; Data Curation, H.L. Writing—review and editing, X.L. Supervision, Z.F., J.W., J.Z., Z.H. and X.S. All authors have read and agreed to the published version of the manuscript.

Funding: This research was funded by postdoctoral research start-up funding (No. 1220502052022010216).

Institutional Review Board Statement: Not applicable.

Informed Consent Statement: Not applicable.

Data Availability Statement: Data sharing is not applicable to this article.

Conflicts of Interest: The authors declare that they have no known competing financial interest or personal relationships that could have appeared to influence the work reported in this paper.

References

1. Li, Q.; Wang, J.; Ma, J.; Ni, M.; Yang, F.; Liu, P.; Lee, K.Y.; Hsiang, H.-I.; Shen, D.; Tang, D. Fabrication of, high-efficiency Yb:Y_2O_3 laser ceramics without photodarkening. *J. Am. Ceram. Soc.* **2022**, *105*, 3375–3381. [CrossRef]
2. Reza, P.; Hassanzadeh-Tabrizi, S.A.; Reza, E.; Amir, A.; Amir, A.N. Polycrystalline infrared-transparent MgO fabricated by spark plasma sintering. *Ceram. Inter.* **2019**, *45*, 18943–18950. [CrossRef]
3. Hao, Y.; Wang, S.; Zhang, Y.B. Effect of Cr^{3+} on the microstructure and photoluminescence of $MgAl_2O_4$ transparent ceramic. *J. Lumin.* **2022**, *242*, 11852. [CrossRef]
4. Alhaji, A.; Taherian, M.H.; Ghorbani, S.; Sharifnia, S.A. Development of synthesis and granulation process of $MgAl_2O_4$ powder for the fabrication of transparent ceramic. *Opt. Mater.* **2019**, *98*, 10944. [CrossRef]
5. Gan, L.; Park, Y.-J.; Kim, H.; Kim, J.-M.; Ko, J.-W.; Lee, J.-W. Fabrication of submicron-grained IR-transparent Y_2O_3 ceramics from commerical nano-raw powders. *Ceram. Inter.* **2015**, *41*, 11992–11998. [CrossRef]
6. Jiang, N.; Xie, R.-J.; Liu, Q.; Li, J. Fabrication of sub-micrometer MgO transparent ceramics by spark plasma sintering. *J. Eur. Ceram. Soc.* **2017**, *37*, 4947–4953. [CrossRef]

7. Xu, S.Q.; Li, J.; Li, C.Y.; Pan, Y.B.; Guo, J.K. Infrared-transparent Y_2O_3-MgO nanocomposites fabricated by the glucose sol-gel combustion and hot-pressing technique. *J. Am. Ceram. Soc.* **2015**, *98*, 2796–2802. [CrossRef]
8. Liu, L.H.; Morita, K.; Suzuki, T.S.; Kim, B.N. Evolution of microstructure, mechanical, and optical properties of Y_2O_3-MgO nanocomposites fabricated by high pressure spark plasma sintering. *J. Eur. Ceram. Soc.* **2020**, *40*, 4547–4555. [CrossRef]
9. Chang, C.S.; Hon, M.H.; Yang, S.J. The optical properties of hot-pressed magnesium fluoride and single-crystal magnesium fluoride in the 0.1 to 9.0 μm. *J. Mater. Sci.* **1991**, *26*, 1627–1630. [CrossRef]
10. Mroz, T.; Goldman, L.M.; Gledhill, A.D.; Li, D.S.; Padture, N.P. Nanostructured, infrared-transparent magnesium-aluminate spinel with superior mechanical properties. *Int. J. Appl. Ceram. Technol.* **2012**, *9*, 83–90. [CrossRef]
11. Al-Furjan, M.S.H.; Shan, L.; Shen, X.; Zarei, M.S.; Hajmohammad, M.H.; Kolahchi, R. A review on fabrication techniques and tensile properties of glass, carbon, and Kevlar fiber reinforced rolymer composites. *J. Mater. Res. Technol.* **2022**, *19*, 2930–2959. [CrossRef]
12. Al-Furjan, M.S.H.; Xu, M.X.; Farrokhian, A.; Jafari, G.S.; Shen, X.; Kolahchi, R. On wave propagation in piezoelectric-auxetic honeycomb-2D-FGM micro-sandwich beams based on modified couple stress and refined zigzag. *Waves Random Complex Media* **2022**, 2030499. [CrossRef]
13. Al-Furjan, M.S.H.; Shan, L.; Shen, X.; Kolahchi, R.; Rajak, D.K. Combination of FEM-DOM for nonlinear mechanics of porous GPL-reinforced sandwich nanoplates based on various theories. *Thin. Wall. Struct.* **2022**, *178*, 109495. [CrossRef]
14. Al-Furjan, M.S.H.; Yin, C.; Shen, X.; Kolahchi, R.; Zarei, M.S.; Hajmohammad, M.H. Energy absorption and vibration of smart auxetic FG porous curved conical panels resting on the frictional viscoelastic torsional substrate. *Mech. Syst. Signal. Pract.* **2022**, *178*, 109269. [CrossRef]
15. Fujioka, K.; Yagasaki, K.; Sawada, T.; Minemoto, H.; Fuji, H.; Yamamoto, K. AlN-Ce-doped yttrium aluminum garnet composite ceramic phosphor for high-power laser lighting. *Opt. Mater.* **2021**, *121*, 111507. [CrossRef]
16. Zhang, Q.; Wang, Q.; Huang, S.; Jiang, Y.; Chen, Z. Preparation and electrochemical study of PVDF-HFP/LATP/g-C_3N_4 composite polymer electrolyte membrane. *Inorg. Chem. Commun.* **2021**, *131*, 108793. [CrossRef]
17. Liu, L.H.; Morita, K.; Suzuki, T.S.; Kim, B.N. Effect of volume ratio on optical and mechanical properties of Y_2O_3-MgO composites fabricated by spark-plasma-sintering process. *J. Eur. Ceram. Soc.* **2021**, *41*, 2096–2105. [CrossRef]
18. Muoto, C.K.; Jordan, E.H.; Gell, M.; Aindow, M. Phase homogeneity in Y_2O_3-MgO nanocomposites synthesized by thermal decomposition of nitrate precursors with ammonium acetate additions. *J. Am. Ceram. Soc.* **2011**, *94*, 4207–4217. [CrossRef]
19. Wu, N.; Li, X.D.; Li, J.-G.; Zhu, Q.; Sun, X.D. Fabrication of Gd_2O_3-MgO nanocomposite optical ceramics with varied crystallographic modifications of Gd_2O_3 constituent. *J. Am. Ceram. Soc.* **2018**, *101*, 4887–4891. [CrossRef]
20. Wu, N.; Li, X.D.; Zhang, M.; Ren, Y.; Zhu, Q.; Peng, H.J.; Ru, H.Q.; Sun, X. Synthesis of nanopowders with low agglomeration by elaborating Φ values for producing Gd_2O_3-MgO nanocomposites with extremely fine grain sizes and high mid-infrared transparency. *J. Eur. Ceram. Soc.* **2021**, *41*, 2898–2907. [CrossRef]
21. Wafula, H.; Juma, A.; Sakwa, T.; Musembi, R.; Simiyu, J. A surface photovoltage study of surface defects on Co-doped TiO_2 thin films deposited by spray pyrolysis. *Coatings* **2016**, *6*, 30. [CrossRef]
22. Jiang, D.; Mukherjee, A.K. Spark plasma sintering of an infrared-transparent Y_2O_3-MgO nanocomposite. *J. Am. Ceram. Soc.* **2010**, *93*, 769–773. [CrossRef]
23. Bedekar, V.; Chavan, S.V.; Tyagi, A.K. Highly sinter-active nanocrystalline RE_2O_3 (RE = Gd, Eu, Dy) by a combustion process, and role of oxidant-to-fuel ratio in preparing their different crystallographic modifications. *J. Mater. Res.* **2007**, *22*, 587–594. [CrossRef]
24. Ma, H.J.; Jung, W.K.; Baek, C.Y.; Kim, D.K. Influence of microstructure control on optical and mechanical properties of infrared transparent Y_2O_3-MgO nanocomposite. *J. Eur. Ceram. Soc.* **2017**, *37*, 4902–4911. [CrossRef]
25. Svetlana, R.E.; Aliya, N.M.; Oksana, V.N.; Zhang, Y.Q.; Skibina, J.D.; Lamberov, A.A. Formation of phases and porous system in the product of hydrothermal treatment of x-Al_2O_3. *Coatings* **2018**, *8*, 30. [CrossRef]
26. Xu, S.Q.; Li, J.; Li, C.Y.; Pan, Y.B.; Guo, J.K. Hot pressing of infrared-transparent of Y_2O_3-MgO nanocomposites using sol-gel combustion synthesized powders. *J. Am. Ceram. Soc.* **2015**, *98*, 1019–1026. [CrossRef]
27. Ma, C.; Li, X.D.; Zhang, M.; Liu, S.H.; Li, J.-G.; Sun, X.D. Synthesis of equal-sized Y_2O_3:Bi,Eu mono-spheres and their color-tunable photoluminescence and thermal quenching properties. *Ceram. Inter.* **2018**, *44*, 18462–18470. [CrossRef]
28. Ma, C.; Li, X.D.; Liu, S.H.; Zhu, Q.; Huo, D.; Li, J.-G.; Sun, X. Fabrication of Lu_2O_3:Eu transparent ceramics using powder consisting of mono-dispersed spheres. *Ceram. Inter.* **2015**, *41*, 9577–9584. [CrossRef]
29. Man, X.; Wu, N.; Zhang, M.; He, H.L.; Sun, X.D.; Li, X.D. Lu_2O_3-MgO nano-powder: Synthesis and fabrication of composite infrared transparent ceramics. *J. Inorg. Mater.* **2021**, *36*, 1263–1269. [CrossRef]
30. Jiang, H.T.; Qin, H.M.; Feng, S.W.; Chen, H.B.; Jiang, J. Y_2O_3-MgO composite nano-ceramics prepared from core-shell nano-powders. *Chin. J. Lumin.* **2021**, *42*, 997–1006. [CrossRef]
31. Roy, S.; Sharma, A.D.; Roy, S.N.; Maiti, H.S. Synthesis of $YB_2Cu_3O_{7-x}$ powder by autoignition of citrate-nitrate gel. *J. Mater. Res.* **1993**, *8*, 2761–2766. [CrossRef]
32. Chakrabort, A.; Devi, P.S.; Roy, S.; Maiti, H.S. Low-temperature synthesis of ultrafine $La_{0.84}Sr_{0.16}MnO_3$ powder by an autoignition process. *J. Mater. Res.* **1994**, *9*, 986–991. [CrossRef]
33. Muoto, C.K.; Jordan, E.H.; Gell, M.; Aindow, M. Effect of precursor chemistry on the structural characteristics of Y_2O_3-MgO nanocomposites synthesized by a combined sol-gel/thermal decomposition route. *J. Am. Ceram. Soc.* **2011**, *94*, 372–381. [CrossRef]

34. Liu, C.; Liu, J.; Dou, K. Judd-Ofelt intensity parameters and spectral properties of $Gd_2O_3:Eu^{3+}$ nanocrystals. *J. Phys. Chem. B* **2006**, *110*, 20277–20281. [CrossRef] [PubMed]
35. Awin, E.W.; Sridar, S.; Shabadi, R.; Kumar, R. Structural, functional and mechanical properties of spark plasma sintered gadolinia (Gd_2O_3). *Ceram. Inter.* **2016**, *42*, 1384–1391. [CrossRef]
36. Portnoi, K.I.; Fadeeva, V.I.; Timofeeva, N.I. The polymorphism of some rare earth oxides and their reaction with water. *Sov. At. Energy* **1964**, *14*, 582–585. [CrossRef]
37. Muoto, C.K.; Jordan, E.H.; Gell, M.; Aindow, M. Phase homogeneity in MgO-ZrO_2 nanocomposites synthesized by a combined sol-gel/thermal decomposition route. *J. Am. Ceram. Soc.* **2010**, *93*, 3102–3109. [CrossRef]
38. Shen, Z.Y.; Zhu, Q.Q.; Feng, T.; Qian, K.C.; Xie, J.X.; Liu, L.K.; Zhang, G.; Wang, W.; Yuan, Q.; Feng, M.; et al. Fabrication of infrared-transparent Y_2O_3-MgO composites using nanopowders synthesized via thermal decomposition. *Ceram. Inter.* **2021**, *47*, 13007–13014. [CrossRef]
39. Wang, J.W.; Zhang, L.C.; Chen, D.Y.; Jordan, E.H.; Gell, M. Y_2O_3-MgO-ZrO_2 infrared transparent ceramic nanocomposites. *J. Am. Ceram. Soc.* **2012**, *95*, 1033–1037. [CrossRef]
40. Iyer, A.; Jacquelynn, K.M.; Reutenaur, J.; Suib, S.L.; Aindow, M.; Gell, M.; Jordan, E.H. A sucrose-mediated sol-gel technique for the synthesis of MgO-Y_2O_3 nanocomposites. *J. Am. Ceram. Soc.* **2013**, *96*, 346–350. [CrossRef]

coatings

MDPI

Article

Micro-Structural Design of $CoFe_2O_4$/SWCNTs Composites for Enhanced Electromagnetic Properties

Zaoxia Hou [1,2,3], Chenyang Liu [1,2,3], Jialuo Gong [1,2,3], Junjie Wu [4], Shuchen Sun [5,*], Mu Zhang [1,2,3,*] and Xudong Sun [1,2,3,*]

[1] Key Laboratory for Anisotropy and Texture of Materials (Ministry of Education), Northeastern University, Shenyang 110819, China
[2] School of Materials Science and Engineering, Northeastern University, Shenyang 110819, China
[3] Foshan Graduate School of Innovation, Northeastern University, Foshan 528311, China
[4] Sinosteel Engineering & Technology (Inner Mongolia) Co., Ltd., Baotou 014000, China
[5] School of Metallurgy, Northeastern University, Shenyang 110819, China
* Correspondence: sunsc@smm.neu.edu.cn (S.S.); zhangm@mail.neu.edu.cn (M.Z.); xdsun@mail.neu.edu.cn (X.S.)

Abstract: In order to prepare microwave-absorbing materials with low density and high wave absorption performance, $CoFe_2O_4$/SWCNTs composites with well-designed necklace-like structures were successfully prepared in this paper by a simple solvothermal method. $CoFe_2O_4$/SWCNTs composites with different cobalt salt contents were synthesized by adjusting the experimental parameters. The results of the relative complex permeability and relative permittivity of the samples, which were investigated by vector network analysis in the frequency range of 2 to 18 GHz, are collected to support the study of the microwave absorption characteristics of the samples. Different microsphere densities and different cobalt salt contents have obvious differences in the electromagnetic absorption properties of the composites. When the additions of $FeCl_3 \cdot 6H_2O$, $Co(Ac)_2 \cdot 4H_2O$, and NH_4Ac were 0.432, 0.200, and 0.400 g, respectively, the best reflection loss reached −42.07 dB, and the effective absorption frequency (RL < −10 dB) ranges from 3.2 to 18 GHz. Therefore, this is a preparation strategy of $CoFe_2O_4$/SWCNTs composites with necklace structure, which has the advantages of simple process, environmental friendliness, low cost, and high stability. The unique necklace-like structure design makes the carbon nanotubes partially exposed, which is more beneficial to achieve good impedance matching and giving the $CoFe_2O_4$/SWCNTs composite excellent electromagnetic loss capability.

Keywords: $CoFe_2O_4$/SWCNTs composites; microwave absorption; necklace-like structure; double loss mechanism; impedance matching

Citation: Hou, Z.; Liu, C.; Gong, J.; Wu, J.; Sun, S.; Zhang, M.; Sun, X. Micro-Structural Design of $CoFe_2O_4$/SWCNTs Composites for Enhanced Electromagnetic Properties. *Coatings* **2022**, *12*, 1532. https://doi.org/10.3390/coatings12101532

Academic Editor: Stefan Ioan Voicu

Received: 24 August 2022
Accepted: 29 September 2022
Published: 13 October 2022

1. Introduction

Nowadays, with the rapid development and broad application of electronic devices and wireless communication technologies, electromagnetic radiation poses a serious threat to human health and the regular operation of electronic devices and has become another major problem after air, water, and noise pollution [1–4]. To solve the problem of electromagnetic radiation pollution, absorbing materials that can absorb and attenuate incident electromagnetic waves and convert the incident electromagnetic energy into heat-based energy to be consumed are attracting much attention [5]. There are many materials for radiation protection, such as glasses based on TeO_2-WO_3-Bi_2O_3-MoO_3-SiO [6], while this paper focuses on carbon nanotube-based microwave-absorbing composites. Therefore, the research and development of high-performance absorbing materials to solve the electromagnetic pollution problem are urgent [7]. According to the research progress of absorbing materials, using the excellent properties of composite absorbing materials with different components to make materials with both magnetic loss and electrical loss will become the future requirements and development direction of absorbing materials.

Carbon materials have been recognized and widely used in the microwave absorption field [8–10]. It is well known that carbon nanotubes are one of the significant carbon materials in the field of electromagnetic absorption [11,12] and one of the crucial materials in the field of military wave-absorbing stealth technology and civil electromagnetic protection [13]. Wu et al. [14] synthesized three-dimensional porous CuS@rGO composite aerogels with MA properties and IR stealth capability by hydrothermal and ascorbic acid thermal reduction methods and subsequent freeze-drying techniques. Peymanfar et al. [15,16] dissected carbon-based biomass-derived materials used as microwave-absorbing structures and provided a new idea of immobilizing oxygen-containing functional groups in carbon-based structures. Carbon nanotubes (CNTs) have attracted extensive attention as microwave absorbers due to their low density and good electrical conductivity [17,18]. However, because carbon nanotubes have strong electrical conductivity [19], large complex dielectric constant [20–22], small permeability, and low magnetic loss, they mainly attenuate electromagnetic waves through dielectric loss, which is difficult to match with free space, resulting in poor impedance matching characteristics and less than ideal electromagnetic absorption performance [23,24]. To improve impedance matching and microwave absorption performance, the preparation of carbon nanotubes compounded with other materials is an effective method. However, the disadvantage of ferric oxide (Fe_3O_4) is that the high-frequency band absorption effect is not ideal, the density is larger [25–27], so it is not good enough to achieve the "thin, light, wide, strong" requirements of the new absorbing material. Spinel-type cobalt ferrite is a kind of spinel-type ferrite with excellent performance, which has medium saturation magnetization strength, excellent chemical stability, high coercivity, strong wear anisotropy, high mechanical strength, and large magnet crystal anisotropy constant, so it has a wide range of applications in rechargeable batteries, high-density magnetic recording, biomedicine and other fields [28]. At the same time, cobalt ferrate is also a good electromagnetic wave-absorbing material, which enhances the effect on electromagnetic waves due to its many pores, and has received wide attention from scholars in the field of microwave absorption [29,30]. Fu et al. [31] prepared a new $CoFe_2O_4$ hollow sphere/graphene composite using a facile vapor diffusion method in combination with calcination at 550 °C. The composite achieved a minimum reflection loss value of −18.58 dB at 12.9 GHz and effective absorption bandwidth of 3.7 GHz when the thickness is 2 mm. Luo et al. [32] successfully prepared layered $CoFe_2O_4$/CNTs/WPU composite aerogels using a facile directional freeze-drying method. The best microwave absorption performance of the heterogeneous aerogel reached −45.8 dB at 11.68 GHz when the matched thickness was 6.8 mm. Zhang et al. [33] used a vapor diffusion method in combination with calcination to synthesize olive sphere-shaped $CoFe_2O_4$ particles assembled from nanoparticle layers showing a porous structure, and the minimum RL value of $CoFe_2O_4$ olive spheres with a thickness of 2.5 mm reached −34.1 dB and an effective absorption bandwidth of 2.6 GHz. Wu et al. [34] synthesized core/shell structured nanocomposites with carbon nanotubes (CNTs) as the core and $CoFe_2O_4$ nanoparticles as the shell by a one-step hydrothermal method, matching the min RL value is −49.96 dB when a thickness dm value is 3.18 mm and the best absorption bandwidth of 4.40 GHz when the dm value is 1.64 mm. In summary, the composite material of cobalt ferrite and carbon material is one of the most popular electromagnetic wave-absorbing materials at present. However, there are still some problems, including the complicated preparation method and the poor matching thickness of the material. Therefore, we design a composite wave-absorbing material of $CoFe_2O_4$ and carbon nanotubes with simple preparation and a unique necklace-like structure.

Morphology, phase, and defects also play a significant role in microwave absorption. Peymanfar et al. [35] investigate the microwave absorption properties of graphitic carbon nitride based on structure and defects. Chen et al. [36] found a competitive and cooperative relationship between conduction loss, interfaces, and defects. The solvothermal method of preparation is characterized by particle formation through the dissolution and crystallization process, which is characterized by high purity, good dispersion, complete

grain development, and controllable size. Because of these advantages of the solvothermal method, it is better to control the microstructure of the sample and thus adjust the electromagnetic parameters of the microwave absorber.

In order to meet the requirements of lightweight and thin thickness, a simple solvothermal method is chosen to prepare $CoFe_2O_4$/SWCNTs composites in this paper, and necklace-like $CoFe_2O_4$/SWCNTs composites with dual dielectric and magnetic losses are successfully prepared. Due to the synergistic effect of the magnetic loss capacity of $CoFe_2O_4$ and the dielectric loss capacity of SWCNTs, as well as the multiple scattering attenuation effects of the 3D lattice necklace-like structure on electromagnetic waves, the composites exhibit good wave absorption performance. The minimum RL value reaches −42.07 dB, the EABD reaches 3.8 GHz, and the thickness range is 1–5 mm. This method is simple and easy to implement and provides an effective way to develop high-performance MAM.

2. Materials and Methods

2.1. Chemicals

All reagents applied in this experiment were analytical grade. Ferric chloride ($FeCl_3 \cdot 6H_2O$, 99.0%) hexahydrate, cobalt acetate ($Co(Ac)_2 \cdot 4H_2O$, 99.5%) tetrahydrate, ammonium acetate (NH_4Ac), and ethylene glycol were from Shanghai Sinopharm Group Chemical Reagent Co. The carbon nanotubes used to prepare the necklace structured $CoFe_2O_4$/SWCNTs composites were from Nanjing Xianfeng Nanomaterial Technology Co. Ltd. (Nanjing, China). The deionized water used in all experiments was from Milli-Q system (Millipore, Bedford, MA, USA).

2.2. Functionalization of Single-Walled Carbon Nanotubes

After acid treatment, the number of functional groups on the surface of carbon nanotubes increases, making them more suitable for accepting other nanoparticles on their surface growth. A typical acidification process is as follows, 200 mg of carbon nanotubes are added to a three-necked flask containing a mixture of concentrated nitric acid and concentrated sulfuric acid (volume ratio: 3:1). The above mixture was dispersed by continuous strong sonication for 3 h. When the carbon nanotubes were completely dispersed, the three-neck flask was placed in an oil bath, heated to 80 °C, and maintained at that constant temperature for 1 h. Then the acidified carbon nanotubes were cooled to room temperature and left to stand in deionized water for 12 h. The rested carbon nanotubes were rinsed to neutral (PH ≈ 7) by filtration with a large amount of deionized water and dried at 60 °C in an oven for 8 h. The functionalized carbon nanotubes are ready for subsequent use.

2.3. Preparation of $CoFe_2O_4$/SWCNTs Necklace-like Structure

0.54 g $FeCl_3 \cdot 6H_2O$, 0.25 g $Co(Ac)_2 \cdot 4H_2O$, and 0.50 g NH_4Ac were dissolved in 60 mL EG. After the solution was completely dissolved, different contents of functionalized SWCNTs were weighed and added to the light yellow solution, then sonicated continuously for 3 h. After the SWCNTs were well dispersed, small magnets were added and stirred for 30 min. Then the solution was poured into a 100 mL Teflon-lined stainless autoclave and held in an oven at 200 °C for 24 h. The samples were removed and washed with deionized water and ethanol 3 times, respectively. Vacuum drying was conducted at 60 °C for 8 h.

The experimental parameters (cobalt salt gradient (0.2 g, 0.25 g, 0.3 g, 0.35 g as Co-1, Co-2, Co-3, Co-4) where carbon nanotubes were 4 mg) were adjusted to achieve the modulation of the microstructure of spinel ferrites, to investigate the effect of micro-structural changes on the absorbing properties of the samples. The cobalt and iron salts were varied together, and they were added in multiples of 0.8, 1, 1.2, and 1.4 based on 0.25 g of cobalt salt and 0.54 g of iron salt as a reference. Finally, the stoichiometry of the cobalt salt was chosen as the standard to differentiate the four samples. The ratio of cobalt salt to iron salt did not change; what changed was the amount added. By adjusting the ratio of cobalt salts, it is the amount of cobalt and iron salts added that adjusts the microstructure of the material

2.4. Characterization

The crystal structure and phase composition of $CoFe_2O_4$/SWCNTs composites were characterized by an X-ray diffractometer (XRD, Model Smartlab 9, Tokyo, Japan) with a Cu Kα source (40 KV, 200 mA). Scanning electron microscopy (SEM, JSM-7001F, Tokyo, Japan) and transmission electron microscopy (TEM, JEM-2100F, Tokyo, Japan) were used to analyze the morphology and structure of the $CoFe_2O_4$/SWCNTs nanomaterials. The composition and distribution of chemical elements on the surface of the samples were investigated by X-ray photoelectron spectroscopy (XPS, Kratos, Manchester, U.K.). The magnetic hysteresis loops were measured by a vibrating sample magnetometer (VSM, Lake Shore Cryotronics, Westerville, OH, USA) at room temperature.

2.5. Characterization of Absorption Properties

The relative complex permeability and relative permittivity of the samples were tested by vector network analysis (VNA, Agilent N5234A, California, CA, USA) in the frequency range of 2 to 18 GHz. The sample powder was miscible with paraffin wax in the mass ratio of 3:7 at 80 °C. The miscible material is quickly poured into a hollow cylindrical mold with an outer diameter of 7 mm, an inner diameter of 3 mm, and a thickness was about 3 mm.

3. Results and Discussion

We successfully synthesized necklace-like $CoFe_2O_4$/SWCNTs composite heterostructures by a simple solvothermal method using functionalized carbon nanotubes as raw materials, and the schematic illustration of the synthesis strategy of $CoFe_2O_4$/SWCNTs composites is shown in Figure 1.

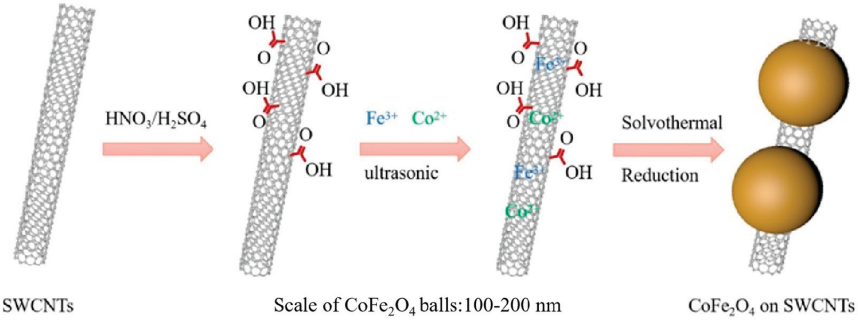

Figure 1. Schematic illustration of synthesis strategy for $CoFe_2O_4$/SWCNTs composites.

First, when CNTs were treated with acid, some negatively charged oxygen-containing functional groups were produced, which provide sites for the growth of $CoFe_2O_4$ grains. Then, the oxygen-containing functional groups were used as nucleation centers, which are firmly bonded with carbon nanotubes to form a necklace-like composite structure. The specific process in the solvent heat is that when the carbon nanotubes are completely dispersed in the EG solution, Co^{2+} and Fe^{3+} in the solution can be fixed on the surface of single-walled carbon nanotubes by electrostatic adsorption. During the solvothermal process, EG can be dehydrated to generate H_2O in a sealed autoclave under high temperature and pressure. Then an alkaline environment is created by hydrolysis of NH_4AC. Finally, cobalt and iron salts react with OH^- to form cobalt ferrite ($Co^{2+} + 2Fe^{3+} + 8OH^- \rightarrow CoFe_2O_4 + 4H_2O$) [37,38]. Thus, necklace-like $CoFe_2O_4$/SWCNTs composites are formed, with $CoFe_2O_4$ nanoparticles passing through and immobilizing on the CNTs surface.

The phase composition and structure of the necklace-like $CoFe_2O_4$/SWCNTs composites were investigated by XRD, as shown in Figure 2. All the diffraction peaks obtained were in accordance with the $CoFe_2O_4$ standard card (JCPDS No. 22-1086). The diffraction peaks were clear and intense, and no obvious impurity peaks were observed, which indicated that the $CoFe_2O_4$/SWCNTs composite has good crystallization and high purity. In

addition, the diffraction peaks of $CoFe_2O_4$/SWCNTs composites are almost consistent with the $CoFe_2O_4$ standard card, which indicates that it is an amorphous structure with little SWCNTs content.

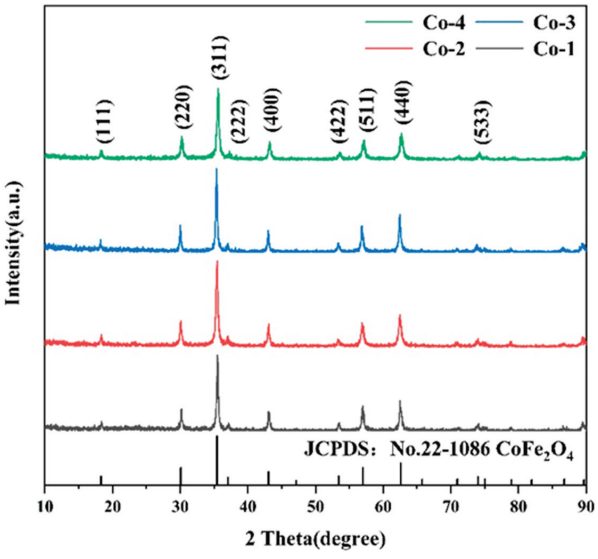

Figure 2. XRD patterns of $CoFe_2O_4$/SWCNTs composites prepared under different experimental parameters.

The microscopic morphology of the $CoFe_2O_4$/SWCNTs composites was characterized using SEM, and the morphology of the sample under the cobalt salt gradient is shown in Figure 3. The sample is composed of spherical nanoclusters and cylindrical carbon nanotubes, and the nanospheres wrap around the carbon nanotubes to form a necklace-like structure. SEM of Figure 3a–d clearly shows that the number and distribution density of spherical $CoFe_2O_4$ clusters obtained by adding different amounts of cobalt salts are significantly different at a carbon nanotube content of 4 mg. With the gradual increase in the cobalt salt content, the number of $CoFe_2O_4$ microspheres increases, and the spheres become more uniform in size but with little change in size. It is not difficult to understand that the increase in cobalt salt concentration will produce more $CoFe_2O_4$ microsphere nanocrystals and increase the loading capacity of $CoFe_2O_4$ microspheres on the surface of single-walled carbon nanotubes, the interface in the material increases, and the necklace-like structures pile up with each other to form a network. It provides the conditions for improving wave absorption performance.

The morphology and structure of the $CoFe_2O_4$/SWCNTs composites were further characterized by TEM, and the results are shown in Figure 4. As can be observed from Figure 4a, the $CoFe_2O_4$ microspheres with diameters of about 100–200 nm are uniformly anchored on SWCNTs, and the necklace-like structure of the composite is consistent with the SEM image. In addition, the HRTEM image of Figure 4b shows a lattice spacing of about 0.25 nm and 0.17 nm, which is attributed to the (311) and (422) crystal plane of spinel cobalt ferrite, further confirming the presence of $CoFe_2O_4$. The SAED pattern of Figure 4c reveals the polycrystalline structure of the $CoFe_2O_4$/SWCNTs composite.

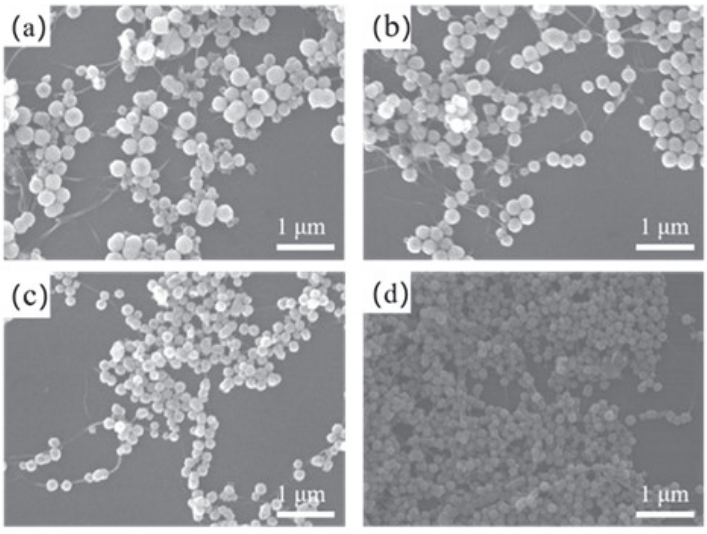

Figure 3. SEM images of $CoFe_2O_4$/SWCNTs composites under Co salt gradient: (**a**) Co-1, (**b**) Co-2, (**c**) Co-3, (**d**) Co-4.

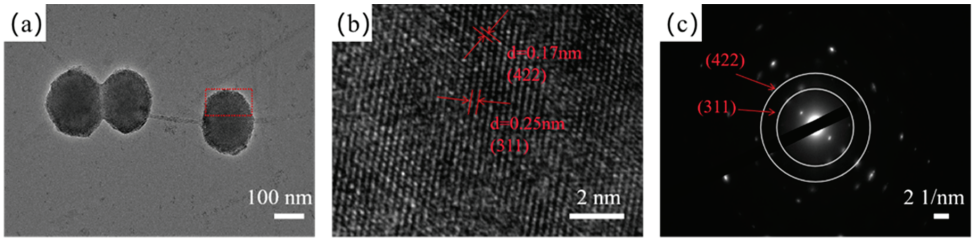

Figure 4. (**a**) TEM image of $CoFe_2O_4$/SWCNTs, (**b**) HRTEM image of $CoFe_2O_4$/SWCNTs and (**c**) selected area electron diffraction (SAED) image of $CoFe_2O_4$/SWCNTs.

To further investigate the chemical composition and bonding of the $CoFe_2O_4$/SWCNTs composites, XPS characterization was performed, as shown in Figure 5. All binding energies were normalized concerning C 1s at 284.8 eV. It can be clearly observed from the full spectrum in Figure 5a that there are four elements present, Co, Fe, O, and C, respectively. Figure 5b demonstrates the high-resolution Co 2p spectra, where the peaks at 781.2 eV and 796.8 eV are attributed to the Co^{2+} $2p_{3/2}$ and Co^{2+} $2p_{1/2}$ spectra, respectively [39,40]. The double-peaked signals at about 786.3 eV and 803.2 eV are assigned to the two oscillating satellites. Thus, the high-resolution XPS spectra of Co 2p indicate the presence of Co^{2+} ions. The Fe 2p spectra of the $CoFe_2O_4$/SWCNTs composites are shown in Figure 5c. The peaks at 724.4 and 711.2 eV correspond to the binding energies of Fe^{3+} $2p_{1/2}$ and Fe^{3+} $2p_{3/2}$, respectively, with the oscillating satellites located at 714.8 eV [41]. The detected Co 2p and Fe 2p photoelectron peaks are consistent with the reported peaks of Co^{2+} and Fe^{3+} in $CoFe_2O_4$. In Figure 5d, the O 1s spectrum is divided into three parts. The peak at 533.0 eV can be attributed to the adsorbed water. The two peaks located at 531.5 and 530.4 eV are consistent with oxygen in the defect and metal-oxygen bonds, respectively [42].

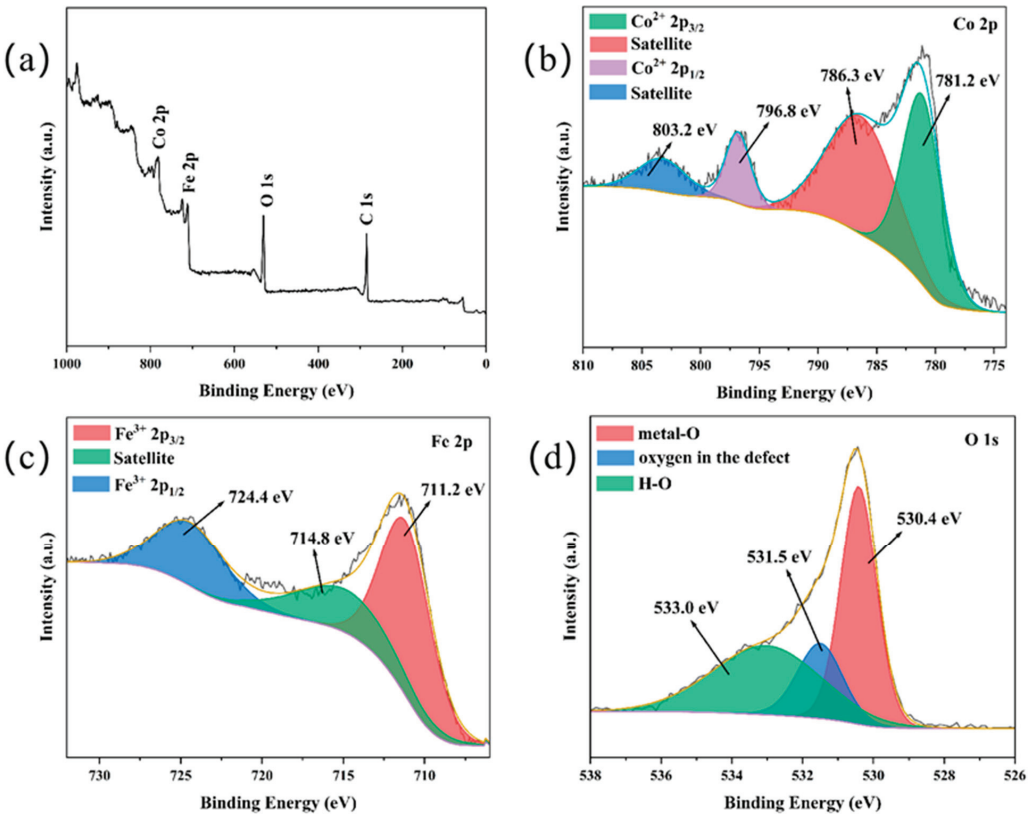

Figure 5. XPS spectra of $CoFe_2O_4$/SWCNTs composites: (**a**) full spectrum, (**b**) Co 2p, (**c**) Fe 2p, and (**d**) O 1s.

With the above analysis, we believe that the necklace-like $CoFe_2O_4$/SWCNTs nanocomposites have been successfully prepared. Next, we compared and analyzed the wave absorption properties of $CoFe_2O_4$/SWCNTs composites with different experimental parameters. The wave absorption properties of electromagnetic wave-absorbing materials are mainly determined by the complex permittivity ($\varepsilon_r = \varepsilon' - j\varepsilon''$) and complex permeability ($\mu_r = \mu' - j\mu''$), with the real part ε' and μ' are related to the ability of the material to store electric field energy and magnetic field energy, respectively, and ε'' and μ'' are related to the ability of the material to lose electric field energy and magnetic field energy, respectively [43]. Figure 6a–b shows the real and imaginary parts of the dielectric constants of the prepared $CoFe_2O_4$/SWCNTs nanocomposites at cobalt salt gradients in the range of 2–18 GHz. The ε' and ε'' values of the four samples showed a trend of increasing and then gradually decreasing as the content of added cobalt salts increased, indicating that the ε' and ε'' values did not keep getting larger as the content of cobalt salts increased. The higher ε' of the Co-2 sample indicates that the sample has better electromagnetic wave storage and polarization ability. The dielectric tangential loss factor ($\tan\delta_\varepsilon = \varepsilon''/\varepsilon'$) indicates the dielectric loss capacity of MAM. The $\tan\delta_\varepsilon$ of Co-1 gradually increases from 0.21 to 0.6 at 10.4–12.3 GHz. The $\tan\delta_\varepsilon$ of Co-4 varied around 0.3. The values of Co-2 reach a maximum peak of 0.73 at 15.4 GHz, and the values of Co-3 reach a maximum peak of 0.65 at 6 GHz. It is proved that the dielectric loss capacity of Co-2 and Co-3 is stronger than that of Co-4 in the frequency range of 2–18 GHz (Figure 6c). In terms of complex permeability, the real part of Co-1 and Co-4 varies around 1.1, and the real part of Co-2 and Co-3 varies around 1.3 (Figure 6d). For the imaginary part of magnetic permeability, Co-2 and Co-3 show a

decrease followed by an increase in the range of 4–8 GHz, while Co-4 shows a regular change around 0.1and Co-1 decreases from 0.02 to −0.26 at 10.4–12.3 GHz (Figure 6e). The values of the magnetic loss tangent factor ($\tan\delta_\mu = \mu'' / \mu'$) of all four samples in Figure 6f are below 0.25, and the small values indicate that the magnetic storage capacity and magnetic loss capacity are not strong. Taken together, it shows that the $CoFe_2O_4$/SWCNTs necklace composite has dielectric and magnetic losses, mainly dielectric losses.

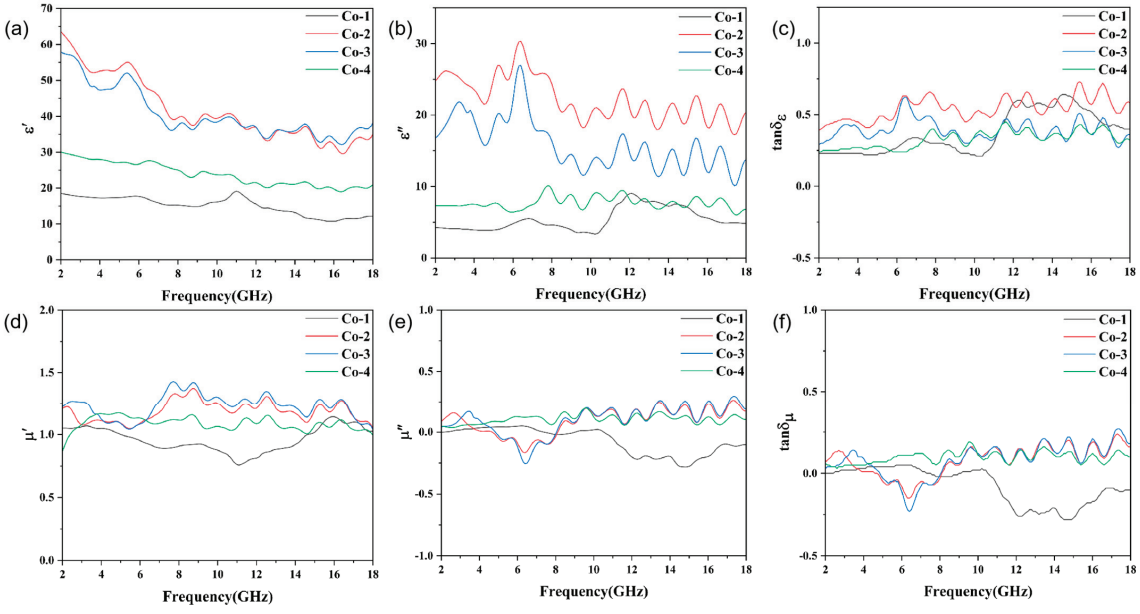

Figure 6. Electromagnetic parameters of Co-1, Co-2, Co-3, Co-4: (**a**) ε', (**b**) ε'', (**c**) dielectric loss angle tangent factor $\tan\delta_\varepsilon$, (**d**) μ', (**e**) μ'', (**f**) magnetic loss angle tangent factor $\tan\delta_\mu$.

According to the Debye theory, ε' and ε'' follow Equation (1) [44], where ε_∞ and ε_s represent the relative permittivity and static permittivity at the high-frequency limit, respectively.

$$(\varepsilon' - \frac{\varepsilon_s + \varepsilon_\infty}{2})^2 + (\varepsilon'')^2 = (\frac{\varepsilon_s - \varepsilon_\infty}{2})^2 \quad (1)$$

Theoretically, one Cole-Cole semicircle corresponds to one Debye relaxation polarization process. As can be seen from Figure 7, the number of Cole-Cole semicircles for the sample with the least amount of cobalt and iron salt addition in the figure is significantly higher than the rest of the samples, probably due to the higher number of $CoFe_2O_4$ clusters in both samples, which provide more heterogeneous interfaces.

To further explore the absorption performance, we calculated the reflection loss (RL) for different thicknesses in the frequency range from 2 to 18 GHz according to Equations (2) and (3), where Z_{in} is the input impedance of the absorbing material, Z_0 is the impedance in free space, ε_r is the complex permittivity, μ_r is the complex permeability, f is the frequency of electromagnetic waves in free space, d is the thickness of the absorber, and c is the speed of light in free space [45].

$$Z_{in} = Z_0\sqrt{\mu_r/\varepsilon_r}\tan h\left[j\left(\frac{2\pi f d}{c}\right)\sqrt{\mu_r\varepsilon_r}\right] \quad (2)$$

$$RL(dB) = 20\,log\left|\frac{Z_{in} - Z_0}{Z_{in} + Z_0}\right| \quad (3)$$

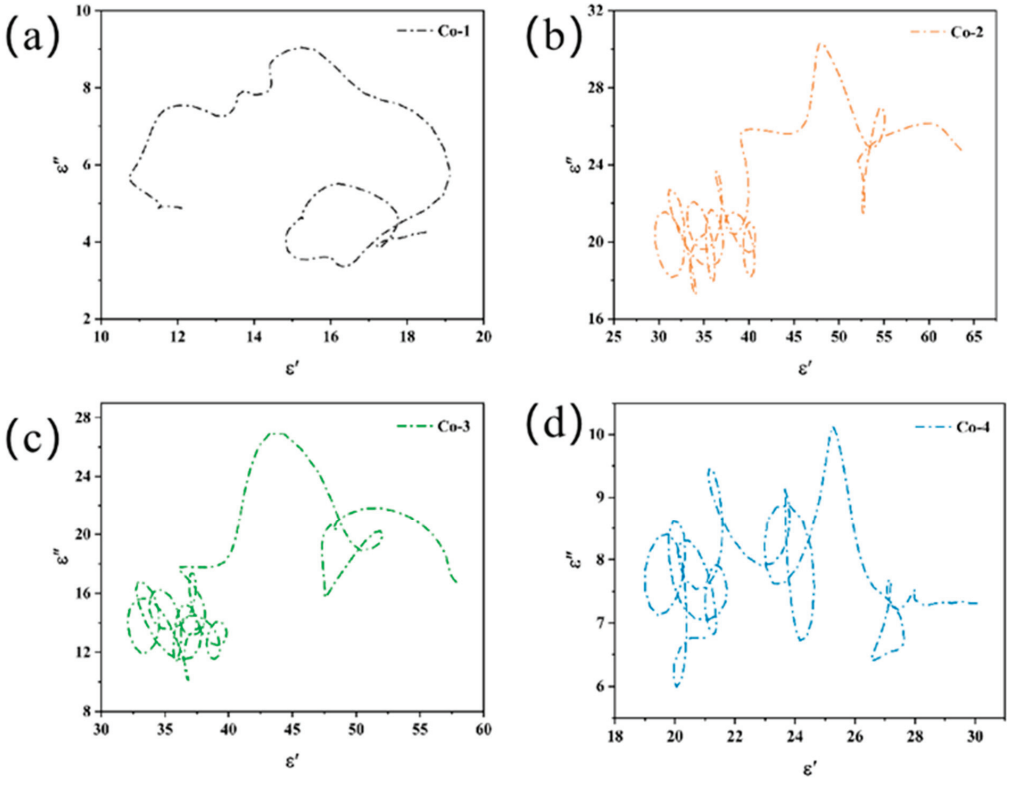

Figure 7. Cole-Cole curves of (**a**) Co-1, (**b**) Co-2, (**c**) Co-3, (**d**) Co-4.

The data of the four samples were calculated, and a 1.5 mm coating thickness was selected to carry out. The reflection loss (RL) and impedance matching change with frequency was drawn, as shown in Figure 8.

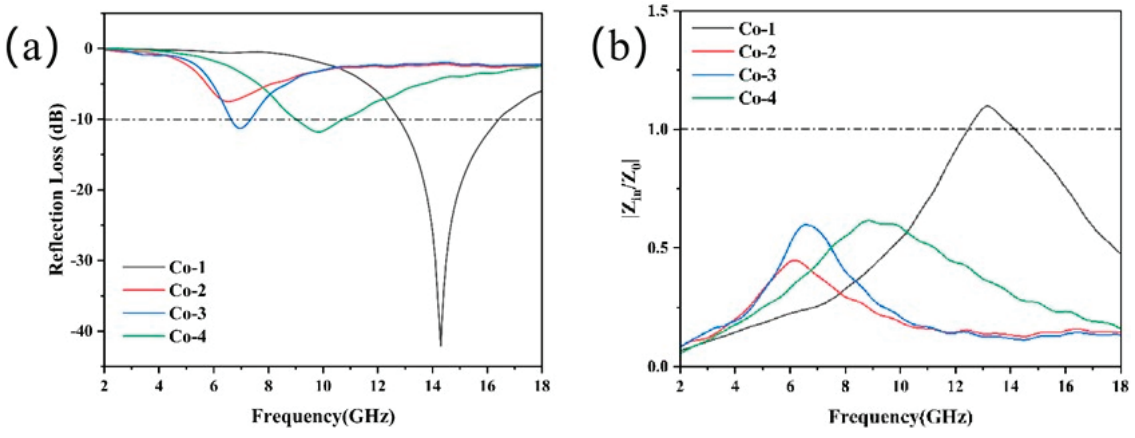

Figure 8. Reflection loss diagram (**a**) and impedance matching (**b**) of $CoFe_2O_4$/SWCNTs heterostructures with different cobalt salt additions at a thickness of 1.5 mm.

From Figure 8a, we can see that with a coating thickness of 1.5 mm, the absorption effect of the Co-1 sample is better, and the peak value of reflection loss reaches −42.07 dB at near 14 GHz. With the increase in cobalt salt addition, the value of reflection loss is −42.07 dB, −7.50 dB, −11.27 dB, and −11.81 dB, and the absorption performance appears to decrease at first and then increase. With the increase in $CoFe_2O_4$ content, the effective absorption band of the samples shifted to low frequencies, then to high frequencies, when the Co-2 sample reached the lowest frequencies. The results indicate that the $CoFe_2O_4$/SWCNTs composites can exhibit excellent microwave absorption performance only when the component ratio is appropriate. The closer the impedance matching Z is to 1, the more the incident wave propagates in the absorbing medium and the better the absorption performance. As can be seen in Figure 8b, Co-1 is closest to 1, so it has the best wave absorption performance.

To further visualize the comparative observation of the absorption capacity of the four samples, three-dimensional plots and contour plots of the relationship between reflection loss, frequency, and sample thickness were drawn, as shown in Figure 9.

As we can see from Figure 9b,f, the Co-2 samples do not exhibit significant microwave absorption properties. None of the RL values reach −10 dB (absorbing 90% of electromagnetic waves) when the range of the thickness of the absorber is 1–5 mm, and the range of frequency of the microwave is 2–18 GHz. When d is 2.09 mm, and f is 4.6 GHz, the minimum RL value of Co-2 is −8.3 dB. As can be seen from Figure 6a–f, Co-2 and Co-3 have extremely similar variations in the parameters of dielectric constant, permeability, dielectric loss factor, and magnetic loss factor. However, since the dielectric constant of Co-3 is lower than that of Co-2, the material impedance matching is improved, and the wave absorption performance is improved. The minimum RL value of Co-3 is −10.52 dB when d is 2.08 mm, and f is 4.9 GHz. The performance of this weak absorption property is consistent with its poorer values of dielectric and magnetic loss factors. In contrast, both Co-1 and Co-4 have good absorption properties. The minimum RL value reaches −42.07 dB (at 14.3 GHz) and EAB of 3.8 GHz (from 12.8 GHz to 16.6 GHz) when the d of Co-1 is 1.50 mm, while when the d of Co-4 is 4.00 mm, the minimum RL value is −19.37 dB and EAB of 0.7 GHz (from 3 GHz to 3.7 GHz). According to Figure 11, the necklace-like $CoFe_2O_4$/SWCNTs composites have good absorption capability and low absorption thickness compared with other reported $CoFe_2O_4$/CNT composites, but the effective absorption bandwidth is narrow, which limits their practical application capability. However, considering the potential of low-density $CoFe_2O_4$/SWCNTs composites in the field of microwave-absorbing materials, this simple and controlled solvothermal method can be extended to composite carbon nanotubes with other ferrites to prepare ferrite/carbon nanotube composites with better microwave absorption properties.

In general, materials with high microwave absorption performance are required to possess low absorber thickness, light mass, wide effective absorption bandwidth, and strong absorption capability. As the requirements for absorbing materials increase, it is clear that a single material cannot meet the requirements for high efficiency, lightweight, and wide efficient absorption bandwidth. In this paper, the samples prepared by simple solvent heat consist of carbon nanotubes as dielectric material and $CoFe_2O_4$ nanoparticles as magnetic material. Figure 10 shows the magnetization properties of the cobalt salt gradient samples characterized by VSM at room temperature with a magnetic field of −10,000 Oe: magnetic hysteresis loops of Co-1, Co-2, Co-3, and Co-4. The saturation magnetization (Ms) of Co-1, Co-2, Co-3, and Co-4 were 70.0, 58.1, 63.4 and 73.5 emu/g, respectively. By increasing the addition of cobalt and iron salts, differences in the degree of crystallization of cobalt ferrate particles and changes in intra-grain defects are produced, causing fluctuations in saturation magnetization. As can be seen from the Co-1 and Co-4 samples in Figure 10, Ms can be enhanced by increasing the magnetic phase. From Figure 10, it was found that the Ms of the samples appeared to decrease and then increase with the increase in the cobalt salt addition ratio, but the difference in the value change was not large. From Figure 3, it can be seen that the size of $CoFe_2O_4$ microspheres does not vary much, which is in accordance

with the literature expression [46], and the Ms, residual magnetization (Mr), and coercivity (Hc) of nanocrystals are only determined by the size.

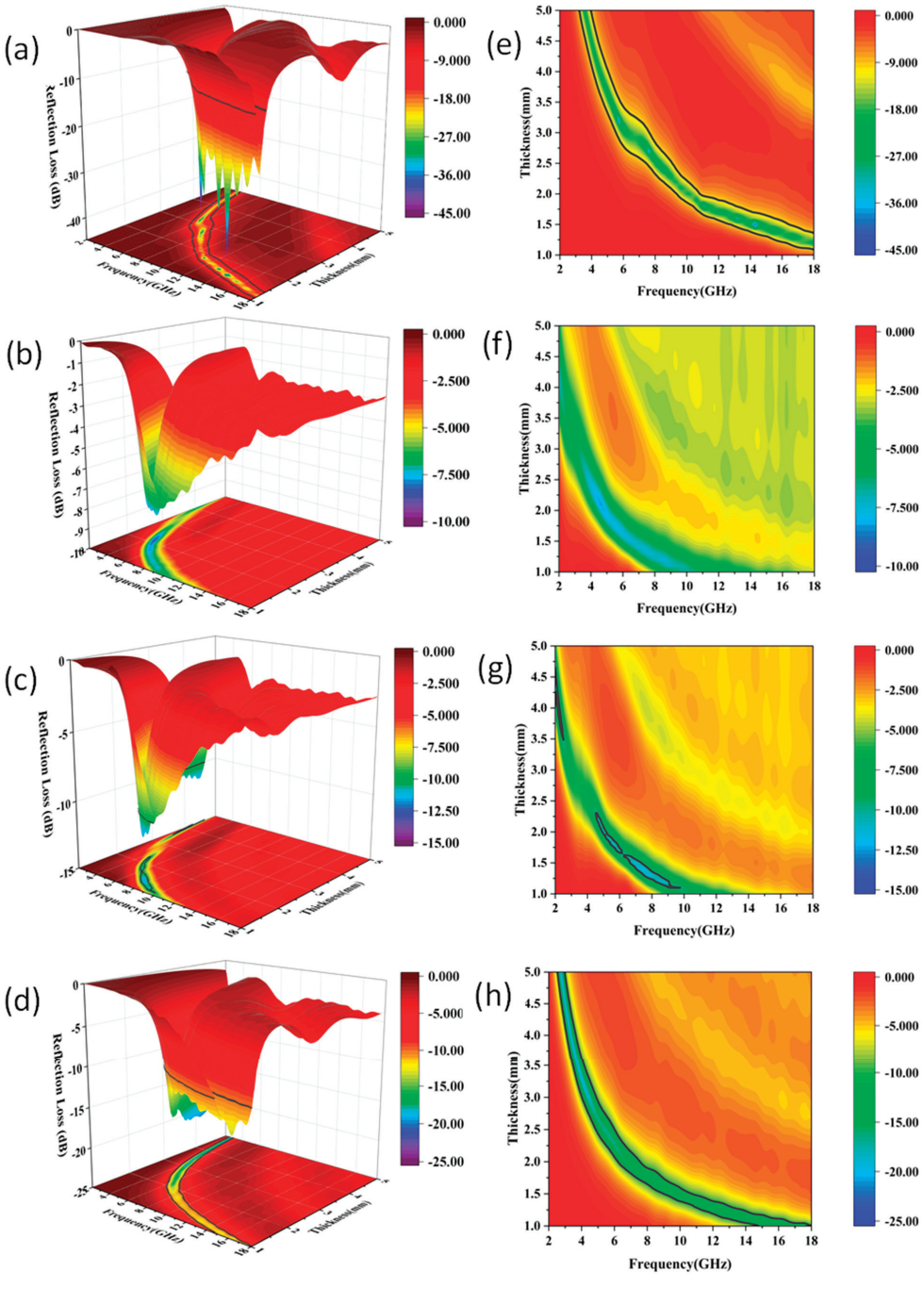

Figure 9. Three-dimensional and contour plots of the RL values of $CoFe_2O_4$/SWCNTs composites with different cobalt salt contents: (**a**,**e**) Co-1, (**b**,**f**) Co-2, (**c**,**g**) Co-3, and (**d**,**h**) Co-4.

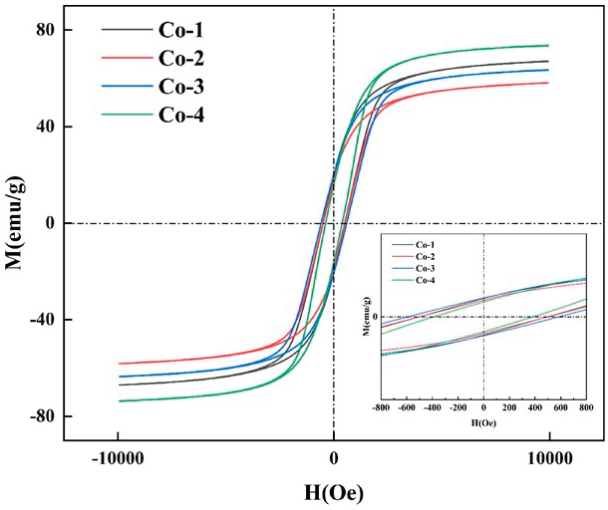

Figure 10. Magnetic hysteresis loops of Co-1, Co-2, Co-3, and Co-4.

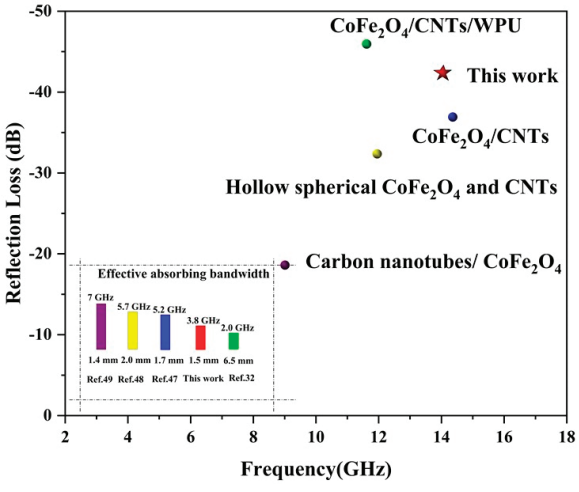

Figure 11. Comparison of the electromagnetic wave absorption capacity of this part of work with some composites of $CoFe_2O_4$/carbon [32,47–49].

The microwave absorption performance of $CoFe_2O_4$/SWCNTs composites can be attributed to the unique necklace-like structure and the composite loss mechanism of carbon nanotubes and $CoFe_2O_4$ particles. For pure carbon nanotubes, only dielectric losses contribute to the energy loss of electromagnetic waves, while for pure $CoFe_2O_4$ particles, the effect of magnetic losses exceeds the dielectric losses. This means that in both cases, the magnetic and dielectric losses are not balanced, which leads to poor wave absorption performance. However, for $CoFe_2O_4$/SWCNTs nanocomposites, the microwave absorption is improved due to the combination of paramagnetic CNTs and magnetic $CoFe_2O_4$ with a better match between dielectric and magnetic losses. Moreover, in addition to defect polarization, dipole polarization, and interfacial polarization, the high impedance matching, and 3D lattice structure allow more electromagnetic waves to enter the absorber (Figure 12), and the $CoFe_2O_4$/SWCNTs composites show a large number of nanoparticles anchored on the surface of carbon nanotubes (Figure 3a–d), which provide multiple reflections

in the conductive network with a structure that can effectively dissipate the incident electromagnetic waves. All these play an important role in improving electromagnetic absorption performance.

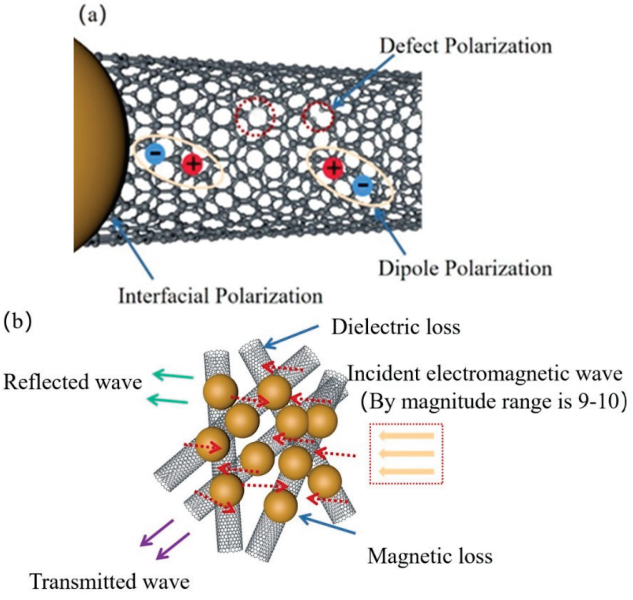

Figure 12. Schematic illustration of EM wave absorption mechanisms for $CoFe_2O_4$/SWCNTs composites: (**a**) relaxation loss; (**b**) absorbing mechanism.

4. Conclusions

In summary, in this work, necklace-like $CoFe_2O_4$/SWCNTs nanocomposites were prepared by the solvothermal method. This special structural design not only effectively solves the problem of poor impedance matching between a single carbon material and a single ferrite material but also can combine dielectric loss and magnetic loss, which can reflect and scatter electromagnetic waves many times to achieve electromagnetic wave energy dissipation, and as long as good impedance matching is achieved when the component ratio is appropriate. The $CoFe_2O_4$/SWCNTs nanocomposites exhibit excellent absorption performance: when the additions of $FeCl_3 \cdot 6H_2O$, $Co(Ac)_2 \cdot 4H_2O$, and NH_4Ac are 0.432 g, 0.200 g, and 0.400 g, respectively, the samples obtained at this time, the best reflection loss reaches −42.07 dB. This simple microstructure design scheme provides a new idea for the preparation of new wave-absorbing materials.

Author Contributions: Conceptualization, M.Z. and X.S.; methodology, S.S.; software, J.W.; validation, M.Z., X.S. and S.S.; formal analysis, M.Z.; investigation, Z.H.; resources, C.L.; data curation, J.G.; writing—original draft preparation, Z.H.; writing—review and editing, M.Z.; visualization, J.G.; supervision, M.Z.; project administration, C.L.; funding acquisition, M.Z. All authors have read and agreed to the published version of the manuscript.

Funding: This research was funded by the National Natural Science Foundation of China (Grant No. 52072063) and the research start-up fund of Foshan Graduate School of Northeastern University.

Institutional Review Board Statement: Not applicable.

Informed Consent Statement: Not applicable.

Data Availability Statement: Not applicable.

Conflicts of Interest: The authors declare no conflict of interest.

References

1. Kong, L.-B.; Li, Z.-W.; Liu, L.; Huang, R.; Abshinova, M.; Yang, Z.-H.; Tang, C.-B.; Tan, P.-K.; Deng, C.-R.; Matitsine, S. Recent progress in some composite materials and structures for specific electromagnetic applications. *Int. Mater. Rev.* **2013**, *58*, 203–259. [CrossRef]
2. Pan, H.-S.; Cheng, X.-Q.; Zhang, C.-H.; Gong, C.-H.; Yu, L.-G.; Zhang, J.; Zhang, Z. Preparation of Fe_2Ni_2N/SiO_2 nanocomposite via a two-step route and investigation of its electromagnetic properties. *Appl. Phys. Lett.* **2013**, *102*, 012410. [CrossRef]
3. Wang, B.-L.; Wu, Q.; Fu, Y.-G.; Liu, T. A review on carbon/magnetic metal composites for microwave absorption. *J. Mater. Sci. Technol.* **2021**, *86*, 91–109. [CrossRef]
4. Yin, P.-F.; Zhang, L.-M.; Feng, X.; Wang, J.; Dai, J.; Tang, Y. Recent Progress in Ferrite Microwave Absorbing Composites. *Integr. Ferroelectr.* **2020**, *211*, 82–101. [CrossRef]
5. Wang, G.-H.; Ong, S.J.H.; Zhao, Y.; Xu, Z.C.J.; Ji, G.-B. Integrated multifunctional macrostructures for electromagnetic wave absorption and shielding. *J. Mater. Chem. A* **2020**, *8*, 24368–24387. [CrossRef]
6. Kozlovskiy, A.; Shlimas, D.-I.; Zdorovets, M.-V.; Popova, E.; Elsts, E.; Popov, A.-I. Investigation of the Efficiency of Shielding Gamma and Electron Radiation Using Glasses Based on TeO_2-WO_3-Bi_2O_3-MoO_3-SiO to Protect Electronic Circuits from the Negative Effects of Ionizing Radiation. *Materials* **2022**, *14*, 6071. [CrossRef]
7. Singh, S.; Kumar, A.; Singh, D. Enhanced Microwave Absorption Performance of SWCNT/SiC Composites. *J. Electron. Mater.* **2020**, *49*, 7279–7291. [CrossRef]
8. Jian, H.; Du, Q.-R.; Men, Q.-Q.; Guan, L.; Li, R.-S.; Fan, B.-B.; Zhang, X.; Guo, X.-Q.; Zhao, B.; Zhang, R. Structure-dependent electromagnetic wave absorbing properties of bowl-like and honeycomb TiO_2/CNT composites. *J. Mater. Sci. Technol.* **2022**, *109*, 105–113. [CrossRef]
9. Liao, Q.; He, M.; Zhou, Y.; Nie, S.; Wang, Y.; Hu, S.; Yang, H.; Li, H.; Tong, Y. Highly Cuboid-Shaped Heterobimetallic Metal-Organic Frameworks Derived from Porous Co/ZnO/C Microrods with Improved Electromagnetic Wave Absorption Capabilities. *ACS Appl. Mater. Interfaces* **2018**, *10*, 29136–29144. [CrossRef]
10. Zhang, F.; Jia, Z.-R.; Wang, Z.; Zhang, C.-H.; Wang, B.-B.; Xu, B.-H.; Liu, X.-H.; Wu, G.-L. Tailoring nanoparticles composites derived from metal-organic framework as electromagnetic wave absorber. *Mater. Today Phys.* **2021**, *20*, 100475.
11. Cao, M.-S.; Yang, J.; Song, W.-L.; Zhang, D.-Q.; Wen, B.; Jin, H.-B.; Hou, Z.-L.; Yuan, J. Ferroferric oxide/multiwalled carbon nanotube vs polyaniline/ferroferric oxide/multiwalled carbon nanotube multiheterostructures for highly effective microwave absorption. *ACS Appl. Mater. Interfaces* **2012**, *4*, 6949–6956. [CrossRef]
12. Zhao, D.-L.; Shen, Z.-M. Preparation and microwave absorbing properties of microwave absorbing materials containing carbon nanotubes. *J. Inorg. Mater.* **2005**, *20*, 608–612.
13. Huo, J.; Wang, L.; Yu, H. Polymeric nanocomposites for electromagnetic wave absorption. *J. Mater. Sci.* **2009**, *44*, 3917–3927. [CrossRef]
14. Wu, Y.; Zhao, Y.; Zhou, M.; Tan, S.-J.; Peymanfar, R.; Aslibeiki, B.; Ji, G.-B. Ultrabroad Microwave Absorption Ability and Infrared Stealth Property of Nano-Micro CuS@rGO Lightweight Aerogels. *Nanomicro. Lett.* **2022**, *14*, 171. [CrossRef] [PubMed]
15. Peymanfar, R.; Mirkhan, A. Biomass-derived materials: Promising, affordable, capable, simple, and lightweight microwave absorbing structures. *Chem. Eng. J.* **2022**, *446*, 136903. [CrossRef]
16. Peymanfar, R.; Moradi, F. Functionalized carbon microfibers (biomass-derived) ornamented by Bi2S3 nanoparticles: An investigation on their microwave, magnetic, and optical characteristics. *Nanotechnology* **2020**, *32*, 065201. [CrossRef]
17. Odom, T.W.; Huang, J.L.; Kim, P.; Lieber, C.K. Atomic structure and electronic properties of single-walled carbon nanotubes. *Nature* **1998**, *391*, 62–64. [CrossRef]
18. Thomassin, J.M.; Jérôme, C.; Pardoen, T.; Bailly, C.; Huynen, I.; Detrembleur, C. Polymer/carbon based composites as electromagnetic interference (EMI) shielding materials. *Mater. Sci. Eng. R Rep.* **2013**, *74*, 211–232. [CrossRef]
19. Chen, S.-H.; Kuo, W.-S.; Yang, R.-B. Microwave absorbing properties of a radar absorbing structure composed of carbon nanotube papers/glass fabric composites. *Int. J. Appl. Ceram. Technol.* **2019**, *16*, 2065–2072. [CrossRef]
20. Li, Q.; Xue, Q.-Z.; Zheng, Q.-B.; Hao, L.-Z.; Gao, X.-L. Large dielectric constant of the chemically purified carbon nanotube/polymer composites. *Mater. Lett.* **2008**, *62*, 4229–4231. [CrossRef]
21. Tang, P.; Zhang, R.; Chen, Z.-Q.; Hu, Y.-P.; Gong, Z.-Z. Dielectric properties of carbon nanotubes-polyethylene composites. *J. Funct.Polym.* **2016**, *29*, 290–295.
22. Wang, L.; Dang, Z.-M. Carbon nanotube composites with high dielectric constant at low percolation threshold. *Appl. Phys. Lett.* **2005**, *87*, 042903. [CrossRef]
23. Lv, H.-L.; Ji, G.-B.; Zhang, H.-Q.; Du, Y.-W. Facile synthesis of a CNT@Fe@SiO_2 ternary composite with enhanced microwave absorption performance. *RSC Adv.* **2015**, *5*, 76836–76843. [CrossRef]
24. Xiang, C.-S.; Pan, Y.-B.; Liu, X.-J.; Sun, X.-W.; Shi, X.-M.; Guo, J.-K. Microwave attenuation of multiwalled carbon nanotube-fused silica composites. *Appl. Phys. Lett.* **2005**, *87*, 123103. [CrossRef]
25. Li, J.-S.; Xie, Y.-Z.; Lu, W.-B.; Chou, T.-W. Flexible electromagnetic wave absorbing composite based on 3D rGO-CNT-Fe_3O_4 ternary films. *Carbon* **2018**, *129*, 76–84. [CrossRef]
26. Wu, G.; He, Y.; Zhan, H.; Shi, Q.-Q.; Wang, J.-N. A novel Fe_3O_4/carbon nanotube composite film with a cratered surface structure for effective microwave absorption. *J. Mater. Sci. Mater. Electron.* **2020**, *31*, 11508–11519. [CrossRef]

27. Zhang, M.; Song, S.-N.; Liu, Y.-M.; Hou, Z.-X.; Tang, W.-Y.; Li, S.-N. Microstructural Design of Necklace-Like Fe_3O_4/Multiwall Carbon Nanotube (MWCNT) Composites with Enhanced Microwave Absorption Performance. *Materials* **2021**, *14*, 4783. [CrossRef]
28. Sharifianjazi, F.; Moradi, M.; Parvin, N.; Nemati, A.; Rad, A.J.; Sheysi, N.; Abouchenari, A.; Mohammadi, A.; Karbasi, S.; Ahmadi, Z.; et al. Magnetic $CoFe_2O_4$ nanoparticles doped with metal ions: A review. *Ceram. Int.* **2020**, *46*, 18391–18412. [CrossRef]
29. Klym, H.; Karbovnyk, I.; Luchechko, A.; Kostiv, Y.; Pankratova, V.; Popov, A.-I. Evolution of Free Volumes in Polycrystalline $BaGa_2O_4$ Ceramics Doped with Eu^{3+} Ions. *Crystals* **2022**, *11*, 1515. [CrossRef]
30. Zhao, D.; Wu, X.; Guan, H.; Han, E. Study on supercritical hydrothermal synthesis of $CoFe_2O_4$ nanoparticles. *J. Supercrit. Fluids* **2007**, *42*, 226–233. [CrossRef]
31. Fu, M.; Jiao, Q.-Z.; Zhao, Y.; Li, H.-S. Vapor diffusion synthesis of $CoFe_2O_4$ hollow sphere/graphene composites as absorbing materials. *J. Mater. Chem. A* **2014**, *2*, 735–744. [CrossRef]
32. Luo, J.-W.; Wang, Y.; Qu, Z.-J.; Wang, W.; Yu, D. Lightweight and robust cobalt ferrite/carbon nanotubes/waterborne polyurethane hybrid aerogels for efficient microwave absorption and thermal insulation. *J. Mater. Chem. C* **2021**, *9*, 12201–12212. [CrossRef]
33. Zhang, S.-L.; Jiao, Q.-Z.; Zhao, Y.; Li, H.-S.; Wu, Q. Preparation of rugby-shaped $CoFe_2O_4$ particles and their microwave absorbing properties. *J. Mater. Chem. A* **2014**, *2*, 18033–18039. [CrossRef]
34. Wu, M.; Darboe, A.K.; Qi, X.-S.; Xie, R.; Qin, S.-J.; Deng, C.-Y.; Wu, G.-L.; Zhong, W. Optimization, selective and efficient production of CNTs/$Co_xFe_{3-x}O_4$ core/shell nanocomposites as outstanding microwave absorbers. *J. Mater. Chem. C* **2020**, *8*, 11936–11949. [CrossRef]
35. Peymanfar, R.; Selseleh-Zakerin, E.; Ahmadi, A. Tailoring energy band gap and microwave absorbing features of graphite-like carbon nitride (g-C3N4). *J. Alloys Compd.* **2021**, *867*, 159039. [CrossRef]
36. Chen, G.; Zhang, L.-M.; Luo, B.-C.; Wu, H.-J. Optimal control of the compositions, interfaces, and defects of hollow sulfide for electromagnetic wave absorption. *J. Colloid Interf. Sci.* **2021**, *607*, 24–33. [CrossRef]
37. Chen, T.; Du, P.; Jiang, W.; Liu, J.; Hao, G.-Z.; Gao, H.; Xiao, L.; Ke, X.; Zhao, F.-Q.; Xuan, C.-L. A facile one-pot solvothermal synthesis of $CoFe_2O_4$/RGO and its excellent catalytic activity on thermal decomposition of ammonium perchlorate. *RSC Adv.* **2016**, *6*, 83838–83847. [CrossRef]
38. Yu, M.; Feng, Z.-H.; Huang, Y.; Wang, K.; Liu, L. $CoFe_2O_4$ nanoparticles directly grown on carbon nanotube with coralline structure as anodes for lithium ion battery. *J. Mater. Sci. Mater. Electron.* **2019**, *30*, 4174–4183. [CrossRef]
39. Wang, C.-X.; Wang, B.-B.; Cao, X.; Zhao, J.-W.; Chen, L.; Shan, L.-G.; Wang, H.-N.; Wu, G.-L. 3D flower-like Co-based oxide composites with excellent wideband electromagnetic microwave absorption. *Compos. B. Eng.* **2021**, *205*, 108529. [CrossRef]
40. Zhou, C.-H.; Wu, C.; Yan, M. Hierarchical FeCo@MoS_2 Nanoflowers with Strong Electromagnetic Wave Absorption and Broad Bandwidth. *ACS Appl. Nano Mater.* **2018**, *1*, 5179–5187. [CrossRef]
41. Guo, D.-G.; Kang, H.-Z.; Wei, P.-K.; Yang, Y.; Hao, Z.-W.; Zhang, Q.-X.; Liu, L. A high-performance bimetallic cobalt iron oxide catalyst for the oxygen evolution reaction. *CrystEngComm* **2020**, *22*, 4317–4323. [CrossRef]
42. Sun, X.; Zhu, X.-Y.; Yang, X.-F.; Sun, J.; Xia, Y.-Z.; Yang, D.-J. $CoFe_2O_4$/carbon nanotube aerogels as high performance anodes for lithium ion batteries. *Green Energy Environ.* **2017**, *2*, 160–167. [CrossRef]
43. Hasar, U.C. A New Microwave Method Based on Transmission Scattering Parameter Measurements for Simultaneous Broadband and Stable Permittivity and Permeability Determination. *Electromagn. Waves* **2009**, *93*, 161–176. [CrossRef]
44. Han, M.-Y.; Zhou, M.; Wu, Y.; Zhao, Y.; Cao, J.-M.; Tang, S.-L.; Zou, Z.-Q.; Ji, G.-B. Constructing angular conical FeSiAl/SiO_2 composites with corrosion resistance for ultra-broadband microwave absorption. *J. Alloys Compd.* **2022**, *902*, 163792. [CrossRef]
45. Wang, S.-S.; Zhu, H.-H.; Jiao, Q.-Z.; Jiao, X.-G.; Feng, C.-H.; Li, H.-S.; Shi, D.-X.; Wu, Q.; Zhao, Y. Controllable synthesis of multi-shelled SiO_2@C@$NiCo_2O_4$ yolk–shell composites for enhancing microwave absorbing properties. *New J. Chem.* **2021**, *45*, 20928–20936. [CrossRef]
46. Song, Q.; Zhang, Z.-J. Shape Control and Associated Magnetic Properties of Spinel Cobalt Ferrite Nanocrystals. *J. Am. Chem. Soc.* **2004**, *126*, 6164–6168. [CrossRef]
47. Yuan, Y.; Wei, S.-C.; Liang, Y.; Wang, B.; Wang, Y.-J.; Xin, W.; Wang, X.-L.; Zhang, Y. Solvothermal assisted synthesis of $CoFe_2O_4$/CNTs nanocomposite and their enhanced microwave absorbing properties. *J. Alloys Compd.* **2021**, *867*, 159040. [CrossRef]
48. Zhang, S.-L.; Qi, Z.-W.; Zhao, Y.; Jiao, Q.-Z.; Ni, X.; Wang, Y.-J.; Chang, Y.; Ding, C. Core/shell structured composites of hollow spherical $CoFe_2O_4$ and CNTs as absorbing materials. *J. Alloys Compd.* **2017**, *694*, 309–312. [CrossRef]
49. Che, R.-C.; Zhi, C.-Y.; Liang, C.-Y.; Zhou, X.-G. Fabrication and microwave absorption of carbon nanotubes/$CoFe_2O_4$ spinel nanocomposite. *Appl. Phys. Lett.* **2006**, *88*, 033105. [CrossRef]

coatings

MDPI

Article

Effect of Polyaniline and Graphene Oxide Composite Powders on the Protective Performance of Epoxy Coatings on Magnesium Alloy Surfaces

Yingjun Zhang [1,2,*], Shuai Xiao [1], Jie Wen [3], Xinyu Liu [1], Baojie Dou [1] and Liu Yang [4]

[1] College of Materials Science and Engineering, Sichuan University of Science and Engineering, Zigong 643000, China
[2] Material Corrosion and Protection Key Laboratory of Sichuan Province, Sichuan University of Science and Engineering, Zigong 643000, China
[3] Chengdu LEPS Technology Co., Ltd., Chengdu 610023, China
[4] Chengdu Hongrun Paint Co., Ltd., Chengdu 610000, China
* Correspondence: zhangyingjun@hrbeu.edu.cn

Abstract: Composite fillers are often used to improve the protective properties of coatings. To obtain a high protective performance of epoxy coatings for magnesium alloys, polyaniline (PANI) and graphene oxide (GO) composite powders were selected because of their corrosion inhibition and barrier performance, respectively. The paper mainly focuses on the effect of the preparation methods of the composite powders on the protective performance. PANI and GO composite powders were prepared by in situ polymerization and blending, respectively. First, the composite powder was characterized by X-ray diffractometer, Fourier transform infrared spectroscopy, and scanning electron microscopy. Then, the different composite powders and pure PANI powder were dispersed uniformly in epoxy resin, and the coating was prepared on the surface of the AZ91D magnesium alloy and studied by an electrochemical impedance test, adhesion strength test and physical properties test. The results show that the impedance value of the coating with the added PANI and GO composite powders by in situ polymerization was 4×10^9 Ω·cm^2 and higher than that with the added pure PANI (4×10^9 Ω·cm^2) and PANI and GO mixed powders (1×10^9 Ω·cm^2) after 2400 h immersion in a 3.5% NaCl solution; the former also had better flexibility, ss impact resistance, and adhesion strength. Compared with the direct blending method, the PANI and GO polymerization powders can exert the shielding effect of GO and PANI corrosion inhibition better and achieve a better protective effect on the magnesium alloy.

Keywords: magnesium alloy; polyaniline; graphene oxide; corrosion protection

Citation: Zhang, Y.; Xiao, S.; Wen, J.; Liu, X.; Dou, B.; Yang, L. Effect of Polyaniline and Graphene Oxide Composite Powders on the Protective Performance of Epoxy Coatings on Magnesium Alloy Surfaces. *Coatings* **2022**, *12*, 1849. https://doi.org/10.3390/coatings12121849

Academic Editor: Alessandro Latini

Received: 31 October 2022
Accepted: 23 November 2022
Published: 29 November 2022

1. Introduction

As the lightest metal material (65% of aluminum's density and 25% of iron's density) in engineering applications at present, magnesium alloys have the advantages of high specific strength, specific stiffness, and strong electromagnetic shielding ability. They also have broad application prospects in aerospace and other fields. However, their relatively high corrosion susceptibility and low potential (−2.37 V vs. SHE) limit their application in many transport applications [1–4]. Some surface treatments, such as anodizing, microarc oxidation, and chemical conversion film, are used to improve the corrosion resistance of magnesium alloys successfully [5–7]. However, the thickness or compactness is limited because the protection performance of the film is still dissatisfying.

Organic coating is a commonly used method in most metal protection methods because of its simple process, convenient construction, and excellent protection performance [8]. However, the long-term protection of magnesium alloys is difficult to achieve because of their high activity. One of the most common ways is to add different functional fillers to

increase the protective properties of the coating. The fillers can be divided into three main categories according to their mechanism of action. (1) Increased barrier performance of coating. Generally, some layered materials, such as montmorillonite [9], hydrotalcites [10], glass [11], and graphene [12], have attracted intense research interest because their lamellar elements increase the lengths of the diffusion pathways of oxygen, water, and aggressive ions [13]. In recent years, two-dimensional graphene oxide (GO) has attracted extensive attention because of its high specific surface area, nanosheet layer, and excellent barrier ability [14,15]. (2) Corrosion inhibition effect. The adding of some corrosion inhibition functional fillers into the coating is an approach. However, the high activity of magnesium alloys causes the selectivity of the fillers to be insufficient. Polyaniline (PANI) has been studied most widely because of its good stability, low cost, and unique doping mechanism [16–18]. In our previous works, the PANI coating achieved better protection against magnesium alloys because of its unique corrosion mechanism [19]. (3) Sacrificial anode protection. Some low-potential metals, such as Zn and Al, are used as sacrificial anodic protective fillers. However, it is difficult for the magnesium alloy matrix because of its lower potential.

In order to obtain the protective coating with an excellent comprehensive performance, composite fillers with the different functions mentioned above are added at the same time. In this paper, GO and PANI were added into the coating at the same time to improve the corrosion resistance for magnesium alloys by a combined effect. Some research found that the synthesized PANI/GO composite powders could improve the corrosion protection performance of coatings for steel [15,16,20], but there is not as much research on composite powder blending. Meanwhile, studies on magnesium alloys are limited. Therefore, this paper focuses on the effect of the coating prepared by added in situ polymerization and the direct blending compounding of PANI and GO on the protective properties of magnesium alloys.

2. Materials and Methods

2.1. Experimental Materials

Ammonium persulfate, aniline, sodium dodecylbenzene sulfonate, hydrochloric acid, and acetone were all analytically pure. The epoxy resin was E44 (purchased from Nantong Star Synthetic Materials Co., Ltd., Nantong, China), the curing agent was Cardolite LITE3100 (purchased from Caderai Chemical Co., Ltd., Zhuhai, China), and the commercial GO powder was produced by Suzhou Tanfeng Graphene Technology (Suzhou, China) Co., Ltd. The selected metal substrate was AZ91D magnesium alloy (with a chemical composition of Al 9.14%, Zn 0.86%, Mn 0.30%, Cu 0.09%, Si 0.08%, Fe 0.01%, and Ni 0.01%, and the rest was Mg, Dongguan Jiejin Metal Materials Co., Ltd, Dongguan, China). The magnesium alloy was surface-treated with 200 and 400 sandpapers in turn, washed with deionized water and acetone, and dried for later use.

2.2. Preparation of Composite Powder

A total of 0.1 g of sodium dodecylbenzene sulfonate was dissolved in 20 g deionized water in a three-necked flask by stirring. Then, we added 1 g of GO, dispersed at a high speed of 800 r/min for 1 h, named GO slurry. In addition, 10 g aniline was weighed into a three-necked flask, and hydrochloric acid was added dropwise at a speed of 400 r/min to control the pH within the range of 1 to 1.5 and stirred for 1 h. The dispersed GO slurry was added to a three-necked flask, and stirring continued for 1 h. After the stirring was completed, 24.5 g ammonium persulfate solution was added dropwise. After reacting for 12 h, the solution was washed with deionized water, filtered with suction until the filtrate was colorless, and dried to obtain PAGO. At the same time, pure PANI was prepared by the same synthesis process without GO, and PMGO also was prepared by blending PANI and GO directly according to the same ratio (PANI:GO = 10:1).

2.3. Preparation of Coating

The PANI, PAGO, and PMGO powders were added to the epoxy resin at 6% of the mass of the epoxy resin and dispersed at a high speed of 2000 r/min for 2 h. Then, the curing agent was added according to the mass ratio of 1:1.3 (epoxy: curing agent), stirred evenly, and then we coated it on the surface of the treated magnesium alloy. The cured thickness of the coating was (120 ± 15) μm, and a free film was prepared on the silica gel plate simultaneously.

2.4. Powder Characterization

The four kinds of powders were sputtered with gold before determined via scanning electron microscopy (SEM, VEGA3SBU, Tesken, Brno, The Czech Republic). Frontier near-infrared spectrometer (FT-IR, FT 9700, PerkinElmer, Waltham, Mass, USA) was used to identify whether the synthesized powder was indeed PANI and to find out the difference of the different compound powder at 400~4000 wavenumber region. The KBr pellet method was used to prepare FT-IR samples. X-ray Diffractometer (Bruker/D2 PHASER, XRD, Bruker, Karlsruhe, Germany) was conducted with a copper Kα X-ray source.

2.5. Performance Test of Coating

Adhesion test was carried out using the BGD500 digital display pull-off adhesion tester produced by Biuged Laboratory Instruments (Guangzhou, China) Co., Ltd.

Autolab electrochemical workstation was used to test the performance of the coating in 3.5 wt.% NaCl solution. The 1 cm^2 platinum sheet and Ag/AgCl (saturated KCl, Huayu Instrument Co.,Ltd., Shanghai, China) were the counter and reference electrodes, respectively. The coated magnesium alloy sample was a working electrode with a test area of 9 cm^2. The test frequency was 10^{-2} to 10^5 Hz, and the disturbance signal was a 30 mV sine wave.

According to the requirements of the ISO or Chinese standards (Table 1), the hardness, impact resistance, and flexibility of the coating were tested. All the test instruments were produced by Shanghai Modern Environmental Engineering Technology (Shanghai, China) Co., Ltd.

Table 1. Test standards and instructions of the physical properties of the coating.

Test Property \ Description	Standards	Instructions	Instruments
Film hardness	ISO 15184 [21]	Pencil test	PPH-1 pencil hardness tester
Flexibility	GB/T 1731-93 [22]	Bend test	QTX film flexibility tester
Impact resistance	GB/T 1732-93 [23]	Falling-weight test	QCJ impact tester

3. Results

3.1. Analytical Characterization of Powder

Figure 1 shows the micromorphology of the synthesized PANI, GO, PAGO, and PMGO powders. PANI is an irregular globular and large agglomeration (Figure 1a). GO is distributed with an irregular flaky structure, and its surface is smooth. The accumulated lamellae may be due to the strong interaction between the surfactant groups after long-term storage (Figure 1b). Compared with GO, PAGO shows a smaller and thicker lamellar structure, and the GO sheet is surrounded by PANI particles (Figure 1c). The PANI particles are deposited uniformly on the GO surface. The particle size of PANI-deposited GO is smaller than that of pure PANI. With the adsorption and polymerization of aniline, GO was exfoliated into sheets and in steady state. Figure 1d shows the GO and PANI randomly scattered in the PMGO powder.

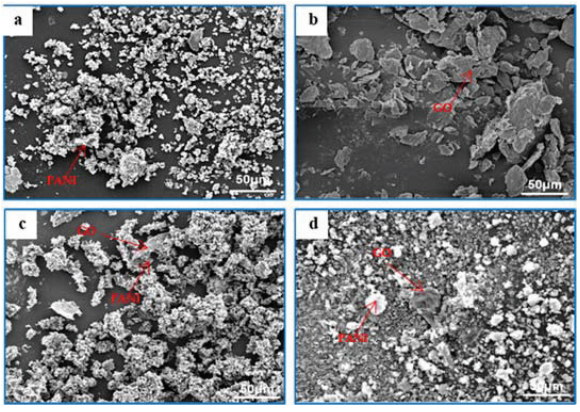

Figure 1. SEM of (**a**) PANI, (**b**) GO, (**c**) PAGO, and (**d**) PMGO powders.

Figure 2 shows the infrared test results of the PANI, GO, and PAGO powders. According to the literature [24–27], the characteristic absorption peaks that appear at 1572 and 1465 cm^{-1} in the infrared spectrum of PANI are the C=C bending vibration of the quinone ring and the C=C bending vibration of the benzene ring, respectively. The peaks at 1298 cm^{-1} correspond to the C–N stretching of a secondary aromatic amine; the peaks at 1104 cm^{-1} are assigned to vibrations associated with the C–H of the quinone ring. For GO, the characteristic absorption peaks at 1043, 1224, and 1718 cm^{-1} are the C–O–C stretching vibration of the GO surface, the C–O stretching vibration of the carboxyl group, and the C=O stretching vibration of the carboxylic acid, respectively [28]. The characteristic absorption peaks of the PMGO powders included PANI and GO and did not significantly change, which indicated that there was no reaction between them. However, compared with PANI and GO, all the characteristic absorption peaks of PANI appeared in the infrared spectrum of the synthesized PAGO powder, but some characteristic absorption peaks of GO, such as the C=O stretching vibration of the carboxylic acid (1718 cm^{-1}), disappeared owing to a partial peak overlap and coverage, indicating that PANI was successfully polymerized on the GO surface.

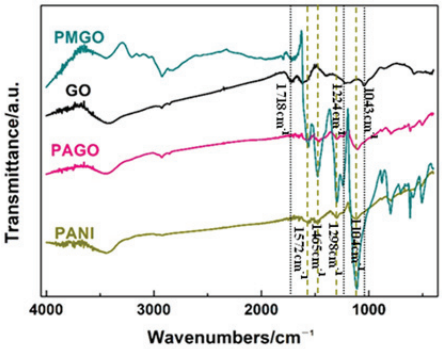

Figure 2. Infrared spectrum of synthetic powder.

Figure 3 shows the XRD test results of the PANI, GO, PAGO, and PMGO powders. The PANI synthesized in the figure has characteristic diffraction peaks at 2θ of 20.3° and 25.0°, and its diffraction peaks are relatively broad, indicating that the state is partially crystalline [29]. GO has a strong diffraction peak at 2θ of 11.0°, indicating an increased degree of oxidation and disorder of the graphite sheet [30]. The characteristic diffraction peaks that appeared in the synthesized PAGO are consistent with those of PANI, and the

diffraction peak that corresponded to GO almost disappears, suggesting that GO is completely surrounded by PANI. However, the XRD pattern of the PMGO powder contained the diffraction peaks of PANI and GO, indicating the separate situation between the PANI and GO powders. But compare to the strong diffraction peak of GO, the diffraction peak of PANI is inconspicuous. In addition, these results confirm that PANI was successfully polymerized on the GO surface.

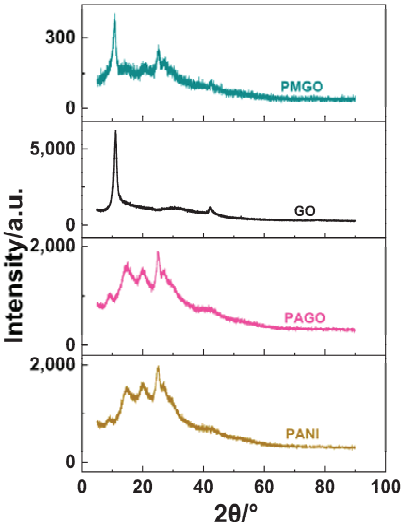

Figure 3. XRD of the synthesized powders.

3.2. Coating Performance Analysis

3.2.1. Analysis of the Physical Properties of Coatings

Table 2 shows the test results of the physical properties of the PANI, PAGO, and PMGO coatings. Compared with the PANI coating, the hardness, flexibility, and impact resistance of the PMGO coating are improved when GO is added through blending, whereas the impact resistance is further improved and the flexibility is also enhanced for the PAGO coating when GO is introduced by polymerization, because the GO lamellar structure can disperse the stress applied on the coating. When PANI is blended with GO, granular PANI and lamellar GO are randomly distributed in the coating. When PANI and GO are polymerized in situ, PANI is uniformly distributed in the coating after PANI is deposited on the GO surface (Figure 1c). Thus, it can play a more effective role in toughening graphene.

Table 2. Test results of the physical properties of the coating.

Property / Coating	Hardness	Flexibility	Impact Resistance (1 kg)
PANI	3H	Diameter Φ4 mm	24 cm
PAGO	4H	Radius of curvature 0.5 ± 0.1 mm	35 cm
PMGO	4H	Radius of curvature 1.5 ± 0.1 mm	28 cm

Figure 4 shows the water absorption (marked as Q) of PANI, PAGO, and PMGO free film. Q can be determined using the following formula.

$$Q = \frac{w_t - w_0}{w_0},$$

where w_t (g) is the amount of absorbed water at t (s) time, and w_0 (g) is the initial weight before immersion. Changes in Q of different coatings are roughly similar in Figure 4. That is, they all rise rapidly at the beginning and reach a stable state with the increase in time, and the saturated water absorption (Q-saturation) of the three kinds of coatings are all maintained at a low level, of which the Q-saturation of the PANI coating is the highest at 1.48%, whereas that of the PAGO coating is the lowest at 1.12%. The GO lamellar structure can disperse the shrinkage stress during the curing period, which is helpful for forming a denser coating. Therefore, the defects of the coating are reduced, and the Q-saturation of the coating is low.

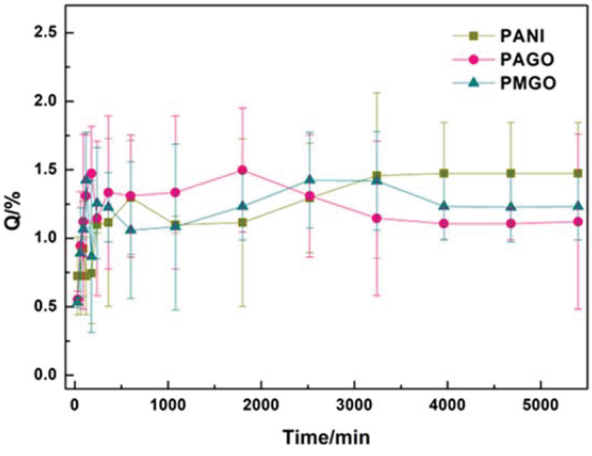

Figure 4. Variation curve of water absorption rate of different coatings.

3.2.2. Analysis of Adhesion Strength of Coatings

Figure 5 shows the adhesion strength value and surface morphologies of the dry and wet adhesions of different coatings (gray column chart shows the test results of the wet adhesion strength of different coatings after 1200 h immersion). The dry adhesion strength of the PANI, PAGO, and PMGO coatings are 9.6, 11.5, and 10.7 MPa, respectively. After the test, only part of the metal matrix observed all three kinds of coatings, which also indicates high adhesion strength. Compared with the pure PANI coating, the adhesion strength of the PAGO and PMGO coatings was enhanced by the addition of GO. The main reason may be that the lamellar structure of GO can reduce the stress concentration of the coating. The adhesion strength of the PAGO coating is higher than that of the PMGO coating because GO was dispersed better by in situ polymerization than by direct mixing, and GO can play a better role.

Meanwhile, the PANI, PMGO, and PAGO coatings could also be defined as composite material, epoxy resin as the matrix (continuous phase), and different kinds of fillers as the reinforced (dispersed) phase. Therefore, the fracture of the coating during the adhesion test could refer to the idea of the mechanics of composite materials. Some novel and strong models, such as the "Tsai-Wu"and "Checkerboard" models, have been recently proposed to estimate the strength of epoxy-reinforced glass or graphene specimens. According to the literature, a very little volume of graphene nanoplatelets would double the critical buckling load of the transverse-oriented fiber composite by calculation, which can be attributed to the significant increment of the matrix modulus of elasticity [31,32].

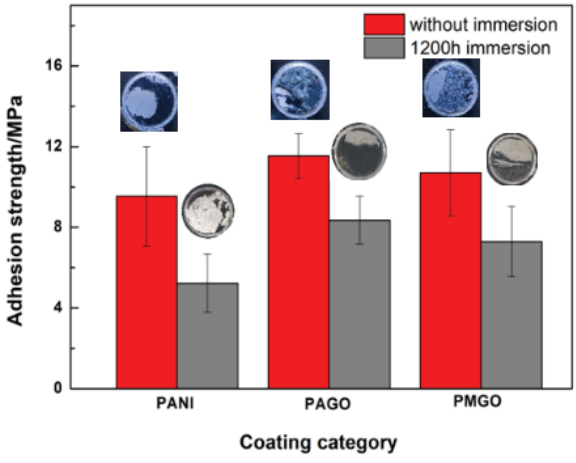

Figure 5. Dry and wet adhesions of the three kinds of coatings.

The wet adhesion strength of the PANI coating is 5.2 MPa, and almost all of the coatings are stripped, and some gray product film is formed. The wet adhesion of the PAGO coating is 8.4 MPa, and only a small portion of the coating was removed. The wet adhesion of the PMGO coating is 7.3 MPa, and about half of the coating was stripped. The wet adhesion strength of the PMGO and PAGO coatings is higher than that of the PANI coating, because the labyrinth effect caused by the GO lamellar structure delays the infiltration of the corrosion medium. Thus, the adhesion strength is enhanced. Compared with the PMGO coating, the wet adhesion strength is higher, and the stripping area of the PAGO coating is smaller because the dispersion effect of GO by in situ polymerization is better than that by direct mixing, and the shielding effect is stronger.

3.2.3. Analysis of Coating Protection Performance

Figure 6 presents the Nyquist and Bode diagrams of the EIS of the PANI, PAGO, and PMGO coatings in different time periods. The low-frequency impedance modulus of the coating can be used to characterize the protective performance of the coating. In this study, the impedance value of the coating was taken when the frequency was 0.01 Hz. Figure 7 shows that the three kinds of coatings all show a rapid decrease at first and then a relatively stable state. The reason is that at the initial stage of immersion, with the increase in time and the penetration of the solution, the shielding property of the coating decreases rapidly when the water absorption reaches saturation. The performance of the coating tends to be stable. The high modulus of the PAGO coating in the early stage of immersion is due to the lamellar shielding effect of GO. In addition, in the process of soaking for 2400 h, the values of the three kinds of coatings are all higher than $10^8 \Omega \cdot cm^2$, indicating that the coatings have a protective effect on the magnesium alloy, and the values of the coatings with the PAGO powder coating are higher than those of the others, indicating that the coatings have a better protective performance.

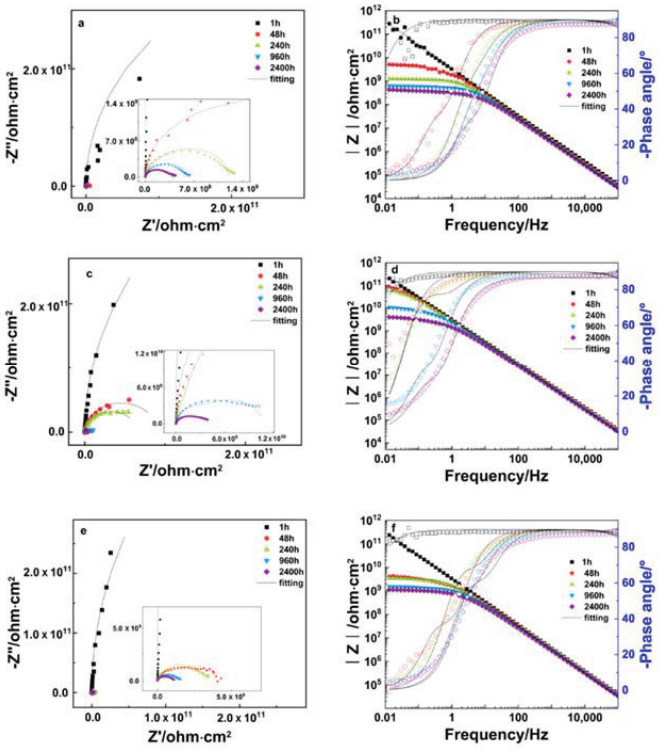

Figure 6. EIS spectra of three kinds of coatings. (**a**,**b**)—PANI; (**c**,**d**)—PAGO; and (**e**,**f**)—PMGO.

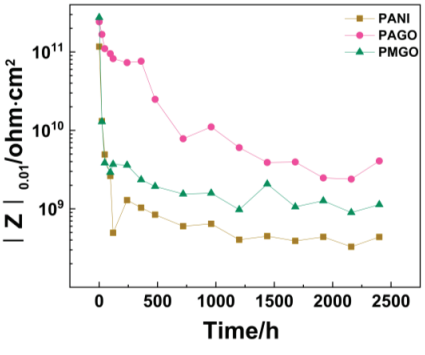

Figure 7. Low-frequency impedance value of the three coatings versus time.

The equivalent circuit diagram of Figure 8 was selected to fit the data. Figure 8a was selected for data fitting during the immersion process, when there is a time constant in the impedance spectrum of the coating; that is, there is only one capacitive arc in the Nyquist diagram, and there is no platform in the Bode curve in the low-frequency region. This indicates that the corrosive species penetrated into the coating but did not reach the coating/substrate interface. Meanwhile, Figure 8b was selected for data fitting when the platform appears in the low-frequency region, suggesting that the corrosive agent has penetrated the coating and reached the coating/substrate interface. R_s represents the solution resistance; Q_c represents the coating capacitance; $R_{coating}$ represents the coating resistance; Q_{dl} represents the electric double layer capacitance at the coating–metal interface,

and R_t represents the charge transfer resistance. The red solid line in Figure 6 is the result of data fitting.

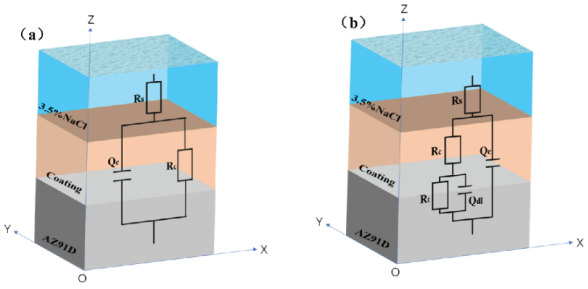

Figure 8. Equivalent circuits of coating/magnesium alloy systems (Models A and B).

3.2.4. Analysis of Coating Protection Mechanism

(1) Shielding Effect of the Coating

Figure 9 shows the variation curve of the coating resistance ($R_{coating}$ of the PANI coating, PAGO coating, and PMGO coating during 2400 h immersion after equivalent circuit fitting. $R_{coating}$ reflects the barrier property of the coating [33], which is an important factor for characterizing the protective performance of the coating. The $R_{coating}$ values of the three coatings decreased rapidly at first and then tended to be stable with the increase in immersion time. The rapid decrease in the early stage was mainly caused by water absorption in the process of coating soaking, and the later stage tended to be stable because the water absorption reached the saturation state. The PAGO coating and the PMGO coating were higher than the PANI coating because the GO coating had better shielding performance, whereas the PAGO and PMGO coatings had a larger difference because of their different dispersion degrees in the coating, which affected the compactness of the coating. At the same time, the compatibility between the powder and coating in the PMGO coating was poor, thereby resulting in the lower $R_{coating}$ value of the PMGO coating than that of the PAGO coating. Such a result is consistent with the Q-saturation of the coating (Figure 4). The results show that the coating with PAGO powder had better resistance to solution penetration. Thus, the PAGO coating had a better protective effect on the AZ91D magnesium alloy than other coatings.

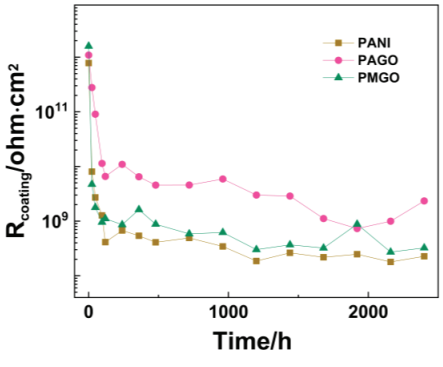

Figure 9. Variation curve of coating resistance with immersion time.

(2) Corrosion inhibition effect of coating

Figure 10 shows the variation curve of the R_t values of the PANI, PAGO, and PMGO coatings during 2400 h immersion. The higher the R_t value is, the smaller the corrosion rate of the metal substrate will be [34]. Therefore, R_t is inversely proportional to the corrosion

rate of the metal. During the whole immersion process of the coating, the R_t values of the PANI, PAGO, and PMGO coatings showed a fluctuation of decrease-increase-decrease, which is the result of the joint action of corrosion of the magnesium alloy and the corrosion inhibition of PANI. Among them, the R_t value of PAGO and PMGO coating is higher than that of the PANI coating, which is mainly due to the shielding effect of GO, which ensures that PANI can inhibit the corrosion of the magnesium alloy effectively. The R_t value of the PAGO coating is higher than that of the PMGO coating because the coating has better shielding properties (Figure 9). Therefore, compared with the other coatings, the addition of the PAGO powder coating has a better protective effect on the AZ91D magnesium alloy.

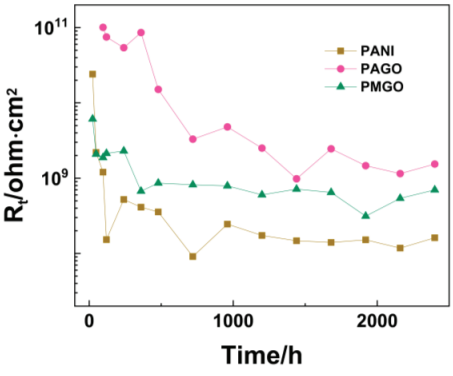

Figure 10. Change curve of charge transfer resistance with immersion time.

(3) Protection mechanism of coatings

Figure 11 shows the protection mechanism of different coatings. For the PANI coating, some defects were formed during hardening because of the solvent's volatility, PANI particle agglomeration, and shrinkage stress. These defects provide the initial channel for solution penetration. With the increase in soaking time, some new diffusion channels formed because of water polarization and osmosis. When the aqueous solution reached the magnesium alloy surface, the oxidation-reduction action of PANI formed a protective product film [19]. For the PAGO coating, shrinkage stress would be reduced because of the excellent flexibility of the GO sheets, and the PAGO particles would be dispersed more uniformly, thereby making coatings with fewer defects on the diffusion channel. Therefore, the PAGO coating had an excellent shielding performance. Similarly, PANI formed a protective product film when the aqueous solution reached the magnesium alloy surface. For the PAGO coating, shrinkage stress would be reduced because of the excellent flexibility of the GO sheets, and the PAGO particles would be more uniformly dispersed, therefore making a coating with fewer defects on the diffusion channel. Therefore, the PAGO coating had an excellent shielding performance. Similarly, PANI formed a protective product film when the aqueous solution reached the magnesium alloy surface. For the PMGO coating, the PANI particles and GO sheets dispersed unevenly in the coating, which would influence the shielding performance of the coating, though shrinkage stress would be reduced because of the excellent flexibility of the GO sheets.

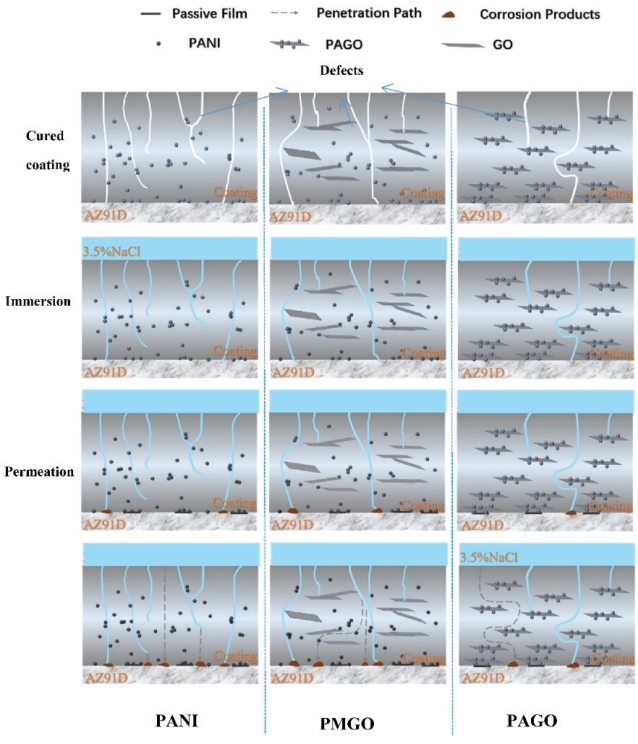

Figure 11. Schematic of the protection mechanism of different coatings.

4. Conclusions

In this study, the physical and corrosion protective performances of epoxy coatings containing three kinds of fillers (PANI, PMGO, and PAGO) were compared. GO/PANI were prepared and applied on mild steel. The results of various tests show that (1) the composite powder containing GO could improve the performance of the PANI coating whether it was prepared by blending or the polymerization method; (2) compared with the blending method, the composite powder prepared by the polymerization method had a better physical performance and corrosion protective effect on the magnesium alloy; (3) the PAGO coating had a better shielding performance because of its fewer defects, and it was more uniformly dispersed. Similarly, PANI formed a protective product film when the aqueous solution reached the magnesium alloy surface.

The EIS results indicate that the PAGO coating had outstanding corrosion protective performance for the magnesium alloy after 2400 h. This was an exciting result because it is difficult to protect magnesium alloys from corrosion. However, the influence of the type and ratio of PANI and GO on the properties of the coatings will be discussed further.

Author Contributions: Y.Z.: Conceptualization, Writing—original draft, Writing—review and editing, and Supervision. S.X.: Resources and Investigation. J.W.: Methodology. X.L.: Resources. B.D.: Data curation and Writing—review and editing. L.Y.: Investigation. All authors have read and agreed to the published version of the manuscript.

Funding: This work was supported by the National Natural Science Foundation of China (No. U21A2045 and No.51801131), Sichuan Science and Technology Program (No.2022NSFSC0300 and No.2022ZHCG0076).

Institutional Review Board Statement: Not applicable.

Informed Consent Statement: Not applicable.

Data Availability Statement: Not applicable.

Conflicts of Interest: The authors declare no conflict of interest.

References

1. Liu, S.; Guo, H. A review of SLMed magnesium alloys: Processing, properties, alloying elements and postprocessing. *Metals* **2020**, *10*, 1073. [CrossRef]
2. Liu, L.; Chen, X.; Pan, F. A review on electromagnetic shielding magnesium alloys. *J. Magnes. Alloys* **2021**, *9*, 1906–1921. [CrossRef]
3. Umoren, S.A.; Abdullahi, M.T.; Moses, M.S. An overview on the use of corrosion inhibitors for the corrosion control of Mg and its alloys in diverse. *J. Mater Res. Technol.* **2022**, *20*, 2060–2093. [CrossRef]
4. Tan, J.; Ramakrishna, S. Applications of magnesium and its alloys: A review. *Appl. Sci.* **2021**, *11*, 6861. [CrossRef]
5. Dai, X.; Wu, L.; Xia, Y.; Chen, Y.; Zhang, Y.; Jiang, B.; Xie, Z.; Ci, W.; Zhang, G.; Pan, F. Intercalation of Y in Mg-Al layered double hydroxide films on anodized AZ31 and Mg-Y alloys to influence corrosion protective performance. *Appl. Surface. Sci.* **2021**, *551*, 149432. [CrossRef]
6. Huang, J.; Dun, Y.; Wan, Q.; Wu, Z.; Zhao, X.; Tang, Y.; Zhang, X.; Zuo, Y. Improved corrosion resistance of MAO coating on Mg-Li alloy by RGO modified silanization. *J. Alloys Compd.* **2022**, *929*, 167283. [CrossRef]
7. Chang, L.-R.; Cao, F.H.; Cai, J.-S.; Liu, W.-J.; Zhang, Z.; Zhang, J.-Q. Influence of electric parameters on MAO of AZ91D magnesium alloy using alternative square-wave power source. *Elsevier* **2011**, *21*, 307–316. [CrossRef]
8. Li, B.; Zhang, Z.; Liu, T.; Qiu, Z.; Su, Y.; Zhang, J.; Lin, C.; Wang, L. Recent progress in functionalized coatings for corrosion protection of magnesium alloys-a review. *Materials* **2022**, *15*, 3912. [CrossRef]
9. Zhang, Y.; Shao, Y.; Shi, Q.; Wang, Y.; Meng, G.; Li, P. Effect of polyaniline/montmorillonite content on the corrosion protection of epoxy coating. *Anti-Corros. Method. M.* **2017**, *64*, 75–82. [CrossRef]
10. Chen, J.; Kang, K.; Song, Y.; Han, E.-H.; Ma, S.; Ao, J. Corrosion behavior of hydrotalcite film on AZ31 alloy in simulated body fluid. *Coatings* **2019**, *9*, 113. [CrossRef]
11. Zhao, X.; Qi, Y.; Zhang, Z.; Li, K. The influence of glass flake and micaceous iron oxide on electrochemical corrosion performance of waterborne silicate coatings in 3.5% NaCl solution. *Coatings* **2019**, *9*, 833–847. [CrossRef]
12. Cui, G.; Bi, Z.; Zhang, R.; Liu, J.; Yu, X.; Li, Z. A comprehensive review on graphene-based anti-corrosive coatings. *Chem. Eng. J.* **2019**, *373*, 104–121. [CrossRef]
13. Mu, J.; Gao, F.; Cui, G.; Wang, S.; Tang, S.; Li, Z. A comprehensive review of anticorrosive graphene-composite coatings. *Prog. Org. Coat.* **2021**, *157*, 1063. [CrossRef]
14. Zhu, X.; Ni, Z.; Dong, L.; Yang, Z.; Cheng, L.; Zhou, X.; Xing, Y.; Wen, J.; Chen, M. In-situ modulation of interactions between polyaniline and graphene oxide films to develop waterborne epoxy anticorrosion coatings. *Prog. Org. Coat.* **2019**, *133*, 106–116. [CrossRef]
15. Ramezanzadeh, B.; Bahlakeh, G.; Ramezanzadeh, M. Polyaniline-cerium oxide (PAni-CeO_2) coated graphene oxide for enhancement of epoxy coating corrosion protection performance on mild steel. *Corros. Sci.* **2018**, *137*, 111–126. [CrossRef]
16. Gao, F.; Luo, Y.; Xu, J.; Du, X.; Wang, H.; Cheng, X.; Du, Z. Preparation of graphene oxide-based polyaniline composites with synergistic anticorrosion effect for waterborne polyurethane anticorrosive coatings. *Prog. Org. Coat.* **2021**, *156*, 106233. [CrossRef]
17. DeBerry, D.W. Modification of the electrochemical and corrosion behavior of stainless steels with an electroactive coating. *J. Electrochem. Soc.* **1985**, *132*, 1022–1026. [CrossRef]
18. Chiang, J.C.; MacDiarmid, A.G. 'Polyaniline': Protonic acid doping of the emeraldine form to the metallic regime. *Elsevier* **1986**, *13*, 193–205. [CrossRef]
19. Zhang, Y.; Shao, Y.; Zhang, T.; Meng, G.; Wang, F. The effect of epoxy coating containing emeraldine base and hydrofluoric acid doped polyaniline on the corrosion protection of AZ91D magnesium alloy. *Corros. Sci.* **2011**, *53*, 3747–3755. [CrossRef]
20. Li, Z.; Yan, S.; He, Y.; Zhang, C.; Li, H.; Xie, P.; He, Z.; Fan, Y. Synthesis of graphene oxide functionalized by polyaniline coated alpha-zirconium phosphate to enhance corrosion resistance of waterborne epoxy coating. *Colloid. Surface. A.* **2021**, *629*, 127427. [CrossRef]
21. ISO 15184:2012(E); Paints and Varnishes-Determinationof Film Hardness by Pencil Test. Available online: https://webstore.ansi.org/standards/iso/iso151842012#:~{}:text=Paints%20and%20varnishes%20-%20Determination%20of%20film%20hardness,on%20the%20upper%20layer%20of%20a%20multi-coat%20system (accessed on 30 October 2022).
22. GB/T 1731-93; Determination of Flexibility of Films. Available online: https://webstore.ansi.org/standards/spc/gb17311993 (accessed on 30 October 2022).
23. GB/T 1732-93; Determination of Impact Resistance of Film. Available online: https://www.standardsofchina.com/standard/GBT1732-1993 (accessed on 30 October 2022).
24. Sathiyanarayanan, S.; Azim, S.S.; Venkatachari, G. A new corrosion protection coating with polyaniline-TiO2 composite for steel. *Electrochim. Acta* **2007**, *52*, 2068–2074. [CrossRef]
25. Parsa, A.; Ab Ghani, S. The improvement of free-radical scavenging capacity of the phosphate medium electrosynthesized polyaniline. *Electrochim. Acta* **2008**, *54*, 2856–2860. [CrossRef]
26. Han, Y.; Liu, Z.; Wang, S.; Wang, W.; Wang, C.; Gao, C. Highly dispersed polyaniline/graphene oxide composites for corrosion protection of polyvinyl chloride/epoxy powder coatings on steel. *J. Mater. Sci.* **2021**, *56*, 12486–12505. [CrossRef]

27. Yu, H.; Zhang, B.; Bulin, C.; Li, R.; Xing, R. High-efficient synthesis of graphene oxide based on improved hummers method. *Sci. Rep.* **2016**, *6*, 36143. [CrossRef]
28. Wang, H.; Li, R.; Wu, Q.; Fei, G.; Li, Y.; Zou, M.; Sun, L. Gemini surfactant-assisted fabrication of graphene oxide/polyaniline towards high-performance waterborne anti-corrosive coating. *Appl. Surf. Sci.* **2021**, *565*, 150581. [CrossRef]
29. Zhou, Q.; Wei, T.; Yue, J.; Sheng, L.; Fan, Z. Polyaniline nanofibers confined into graphene oxide architecture for high-performance supercapacitors. *Electrochim. Acta* **2018**, *291*, 234–241. [CrossRef]
30. Ding, J.-H.; Zhao, H.-R.; Zheng, Y.; Zhao, X.; Yu, H.-B. A long-term anticorrsive coating through graphene passivation. *Carbon* **2018**, *138*, 197–206. [CrossRef]
31. Chen, X.; Sun, X.; Chen, P.; Wang, B.; Gu, J.; Wang, W.; Chai, Y.; Zhao, Y. Rationalized improvement of Tsai-Wu failure criterion considering different failure modes of composite materials. *Compos. Struct* **2021**, *256*, 113120. [CrossRef]
32. Kabir, H.; Aghdam, M.M. A robust Bézier based solution for nonlinear vibration and post-buckling of random checkerboard graphene nano-platelets reinforced composite beams. *Compos. Struct.* **2019**, *212*, 184–198. [CrossRef]
33. Liu, X.; Xiong, J.; Lv, Y.; Zuo, Y. Study on corrosion electrochemical behavior of several different coating systems by EIS. *Prog. Org. Coat.* **2009**, *64*, 497–503. [CrossRef]
34. Hassan, H.H.; Abdelghani, E.; Amin, M.A. Inhibition of mild steel corrosion in hydrochloric acid solution by triazole derivatives. *Electrochim. Acta* **2007**, *52*, 6359–6366. [CrossRef]

coatings

MDPI

Article

A Two-Dimensional Guidance Strategy to Fabricate Perovskite Gadolinium Aluminate Ceramic Film

Tao Zhang [1], Lu Chen [2], Jing Yao [2] and Qi Zhu [2,*]

[1] Shenyang National Laboratory for Materials Science, Northeastern University, 3-11 Wenhua Road, Shenyang 110819, China
[2] Key Laboratory for Anisotropy and Texture of Materials (Ministry of Education), School of Materials Science and Engineering, Northeastern University, Shenyang 110819, China
* Correspondence: zhuq@smm.neu.edu.cn; Tel.: +86-24-8367-2700

Abstract: Gadolinium aluminate is an effective host for doping with various ions, and it can emit various colors. However, it is not easy to prepare transparent ceramics of gadolinium aluminate using traditional methods, although transparent ceramics are very suitable for solid lighting. In this work, a two-dimensional guidance strategy has been successfully carried out for perovskite-structured aluminate ceramic film. Through the two-dimensional interfacial reaction, $GdAlO_3:Eu^{3+}$ ($GAP:Eu^{3+}$) transparent ceramic films were successfully fabricated using nanosheets exfoliated from layered gadolinium hydroxide, a rare earth source. The final films were tested by characterization techniques, including XRD, SEM, TEM, FT-IR, PLE/PL spectroscopy, temperature-dependent PL spectroscopy, and luminescence decay analysis. The perovskite film of transparent ceramics can be obtained by calcining LRH nanosheets on the substrate of amorphous alumina at 1550 °C in air with a reaction time of 2 h. During the interface reaction, temperature-dependent element diffusion takes the dominant role, and increased reactants take in the reaction with increasing calcination temperature. The grain for ceramic film is only 2–5 μm, which is much smaller than that for bulk ceramic. This is mainly due to the lower temperature and the interface diffusion. Ceramic film has a high transmittance larger than 90% at the visible range. Upon UV excitation at 254 nm, the film exhibits intense emission at the red wavelength range. The outcomes described in this work may have wide implications for transparent ceramics and layered rare-earth hydroxides.

Keywords: transparent ceramics; gadolinium aluminate; ceramic film; layered rare-earth hydroxide

Citation: Zhang, T.; Chen, L.; Yao, J.; Zhu, Q. A Two-Dimensional Guidance Strategy to Fabricate Perovskite Gadolinium Aluminate Ceramic Film. *Coatings* **2022**, *12*, 1927. https://doi.org/10.3390/coatings12121927

Academic Editor: Alicia de Andrés

Received: 6 November 2022
Accepted: 2 December 2022
Published: 8 December 2022

1. Introduction

Recently, light-emitting diodes (LEDs) have attracted increased attention because of their high luminous efficiency, low energy costs and environmentally friendly nature [1,2]. Traditionally, LEDs were fabricated by combining an LED chip (such as InGaN) and phosphor powders. Taking the white LED as an example, the blue LED chip and the yellow garnet phosphor of $Y_3Al_5O_{12}:Ce^{3+}$ ($YAG:Ce^{3+}$) are the two most important components. However, the glue used for the phosphor powders in LED chips is sensitive to high temperatures and varied humidity, so the mixture of glue and phosphor will age and peel off as time goes by [3–5]. Now, transparent ceramic is widely accepted as the preferred luminophore for LEDs because of its stability and high transparency [6]. Because transparent ceramics have high transmittance and can easily be prepared into bulk ceramics with various shapes, they are suitable for application in high-power and high-density devices, except for light-emitting devices [6]. Transparent ceramics can be used in optical components, scintillators, transparent armor, solid-state lasers, and solid-state lighting. Except for the transparent ceramics of garnet rare earth aluminates, such as $Y_3Al_5O_{12}$ and $Lu_3Al_5O_{12}$, perovskite rare-earth aluminate is another system for transparent ceramics [7–9]. The investigations of perovskite rare-earth aluminate mainly focus on the three systems of $GdAlO_3$, $LaAlO_3$ and $YAlO_3$, because in the 4*f* sublayer of Gd^{3+}, La^{3+}, and Y^{3+}, the electrons are half, fully, or not

filled [7,8]. Therefore, they are suitable hosts that can be doped with various activators and emit various emissions.

By comparison, there are a lot of investigations into $YAlO_3$ and $LaAlO_3$, while the studies on $GdAlO_3$ are rather limited. $GdAlO_3$ (GAP) has a tetrahedron unit cell structure with a = 5.305 Å, b = 7.448 Å, c = 5.254 Å, and the unit cell belongs to the orthogonal perovskite structure of ABO_3. However, $GdAlO_3$ is not a perfect perovskite; it is a distorted perovskite [9]. In the ideal perovskite, Gd^{3+} has various coordinations with oxygen atoms, changing from 12 to 8, while Al^{3+} only has one kind of 6 coordination with oxygen atoms. The structure has the space group of *Pbnm*, deviating from the cubic space group *Pm*3*m*, which is due to distortion from the octahedron of $[BO_6]$. The octahedral cluster of $[AlO_6]$ is arranged along the *c* axis, and the polyhedron of $[GdO_8]$ connects with the octahedron of $[AlO_6]$ in a collinear or coplanar manner [9]. Because of its special crystal structure, it is possible to optimize or realize the varied luminescence through a modification of crystal structure and composition. Up to now, the doping ions employed for $GdAlO_3$ hosts are mainly Eu^{3+} (red) and Ce^{3+} (yellow), and a small number of other ions, including Yb^{3+} (yellow), Tb^{3+} (blue and green), Pr^{3+} (blue and red), Er^{3+} (green), $Er^{3+}/Yb^{3+}/Tm^{3+}$ (white), and Cr^{3+} and Mn^{4+} (near infrared) [10–18]. In addition, previous studies have focused on the optical properties of $GdAlO_3$ nanocrystals and phosphor powders, and the reports on $GdAlO_3$ transparent ceramics and ceramic films are rather limited.

More recently, we proposed a novel strategy to fabricate transparent ceramic film of garnet-structured $Y_3Al_5O_{12}$ (YAG) through an interface reaction using the exfoliated nanosheets of layered rare-earth hydroxides (LRHs) as the rare-earth source [6,19]. The outcomes pave a two-dimensional guidance strategy for transparent ceramic film, and they may have a demonstrative effect on other systems, including the perovskite system. LRHs can be exfoliated into nanosheets with single- or several-layer thickness, which are the building units for the fabrication of films with multifunctions owing to 2D morphologies [20]. It is not easy for larger rare earths to form LRHs, and Gd might be the boundary, so most layered rare-earth hydroxides are formed for the rare earths with smaller ionic radii, such as Eu, Tb, Sm, Ho, and Y [21]. However, most rare-earth aluminates are garnet-structured with the composition of $RE_3Al_5O_{12}$ for the smaller rare earths, while they are perovskite-structured for the larger rare earths with the composition of $REAlO_3$ [22]. Therefore, layered rare-earth hydroxides with larger rare-earth ionic radii are the possible candidates to fabricate perovskite-structured rare-earth aluminates films. On this basis, layered gadolinium hydroxides are the best choice to fabricate perovskite-structured aluminates films, because gadolinium is almost the largest element for layered rare-earth hydroxides in the processing window.

In this work, a two-dimensional guidance strategy has been successfully carried out for perovskite-structured aluminate ceramic film. Through the interfacial reaction, $GdAlO_3$:Eu^{3+} (GAP:Eu^{3+}) films of transparent ceramic were fabricated using the exfoliated layered gadolinium hydroxide nanosheets as the rare-earth source. The final films were tested by characterization techniques, including XRD, SEM, TEM, FT-IR, PLE/PL spectroscopy, temperature-dependent PL spectroscopy, and luminescence decay analysis. The transparent film exhibits intense emission at the red wavelength range. In the following section, the synthesis and properties of the ceramic films are investigated in detail.

2. Experimental Section

2.1. Materials and Synthesis

The raw materials are rare-earth oxides of Gd_2O_3 and Eu_2O_3 with 99.99% purity (Huizhou Ruier Rare-Chem. Hi-Tech. Co., Ltd., Huizhou, China), and are the rare-earth source. Ammonia hydroxide (NH_4OH, 25 wt %), nitric acid (HNO_3, 67 wt %), and anhydrous ethanol (C_2H_5OH, 99.7%) were purchased from Sinopharm Chemical Reagent Co., Ltd. (Shanghai, China) The aqueous solutions of rare-earth nitrates were made by dissolving the powder of rare-earth oxides in hot nitric acid.

Synthesis of LRH crystals and exfoliation of LRH nanosheets. First, 2 mmol rare-earth nitrate solution of $Gd(NO_3)_3$ and $Eu(NO_3)_2$ (Gd:Eu molar ratio of 95:5) was prepared by stirring the mixed solution at room temperature. After adding a proper NH_4OH, the colloidal suspension was adjusted with a pH value around 7. After that, the white mixed suspension was moved to a 100 mL Teflon-lined autoclave. After the hydrothermal reaction, the products were collected through centrifugation. The LRH crystals were exfoliated into nanosheets by hydrothermal anion exchange followed by mechanical agitation in formamide, according to our previous work [20]. The dodecyl sulfate (DS^-, $C_{12}H_{25}OSO_3^-$)-intercalated LRH was obtained like the first preparation [23]. The products after ion exchange are called LRH-DS in the later text.

Film fabrication of GAP transparent ceramic. Exfoliated nanosheets were spin-coated on a substrate of amorphous alumina and then calcined at selected temperatures with the reaction time of 2 h. Through an interfacial reaction, films of $GdAlO_3$ (GAP) transparent ceramic were grown on the substrate.

2.2. Characterization

Phase identification was performed by X-ray diffractometry (XRD, Model SmartLab, Rigaku, Tokyo, Japan) under 40 kV/40 mA, using nickel-filtered Cu-Kα radiation (λ = 0.15406 nm). The scanning speed was 6.0°/2θ per minute and the scanning range was 5°–60°. The FT-IR spectra were performed by Fourier transform infrared spectroscopy (FT-IR, Model Nicolet iS5, Thermo Fisher Scientific, Madison, WI, USA) using the standard KBr method. The morphology and microstructure of the products were analyzed by field emission scanning electron microscopy (FE-SEM, Model JSM-7001F, JEOL, Tokyo, Japan) and transmission electron microscopy (TEM, Model JEM-2000FX, JEOL, Tokyo, Japan). A fluorescence spectrophotometer (Model FP-8600, JASCO, Tokyo, Japan) was used for luminescence analysis. It was equipped with a 150 W Xe-lamp and an integrating sphere (Model ISF-513, JASCO, Tokyo, Japan).

3. Results and Discussion

3.1. Synthesis of LRH Crystals and Exfoliation of Nanosheets

The XRD patterns of LRH are shown in Figure 1a. The synthesized product is layered rare-earth hydroxide, since the diffraction peaks match well to the reported diffraction data. The diffraction peaks of (002) and (004) confirm the unique layered structure, while the appearance of (220) confirms that the compounds have a well-developed layered structure [20,21]. It is interesting to find that the (00*l*) reflections shift strongly to the lower-angle side, whereas the (*hk*0) reflections remain at the same position after the anion exchange with DS^-. This phenomenon can be well understood by the layer distance increase in LRH-DS, which results in a significant change in the crystal plane perpendicular to the host layer without affecting other planes [24,25]. There are no other impurities, implying that the products have a single phase of LRH. Therefore, the incorporation of Eu^{3+} did not affect the XRD diffraction peaks of LRH (Figure 1a). Through the anion exchange with DS^-, the LRH-DS still remains the layered characteristic, but the layer distance becomes significantly larger than that for the original LRH (Figure 1a). Close observation of the small-angle XRD in Figure 1b shows that the 2θ value of LRH-DS shifts to the side of the smaller angle, so the interlayer distance increases from ~0.84 nm for the original LRH to ~2.61 nm for the ion-exchanged LRH-DS. Figure 1c shows FT-IR spectra for the original LRH and ion-exchanged LRH-DS, which further confirms the completed reaction of ion exchange. The absorption peak at a wavenumber larger than 3500 cm^{-1} indicates the existence of o hydroxyl (OH^-), and the absorption peaks at a wavenumber range larger than 3000 cm^{-1} but smaller than 3500 cm^{-1} indicate the existence of H_2O. At the same time, the shoulder peak at ~1634 cm^{-1} also indicates the existence of H_2O. The above results confirm that there is molecular water in the compounds. For the LRH sample, there is a sharp absorption peak at ~1389 cm^{-1}, which confirms the existence of free NO_3^- [26–28]. However, the vibration of free NO_3^- disappears for ion-exchanged LRH-DS. Instead, new

absorption peaks at ~1050 cm^{-1}, ~1173 cm^{-1}, ~1466 cm^{-1}, ~2845 cm^{-1}, ~2915 cm^{-1}, and ~2962 cm^{-1} are found through anion-exchange processing, which are assigned to the vibrations of OSO_3^-, -CH_2, and -CH_3, respectively, indicating that $C_{12}H_{25}SO_4^-$ (DS^-) has replaced the NO_3^- of LRH via anion exchange [26,27]. The FE-SEM images of LRH are shown in Figure 2a. The products are platelets with a lateral size of 1–2 μm, and the surface is smooth. However, they are irregular platelets rather than hexagon platelets, which are usually observed for LRHs [20,21]. After anion exchange, the thickness of LRH crystals significantly increases, and the interlayers are found to be obviously loose for the LEH-DS sample (Figure 2b). Dispersing the LRH-DS in formamide yielded the transparent suspension containing exfoliated nanosheets (Figure 2c,d). Under laser beam irradiation, the suspension exhibited a clear observable Tyndall effect (Figure 2e). The TEM observation finds that the exfoliated nanosheets are rather thin, but the surface is not smooth, with flocculent molecules on the nanosheets, which may be the residual DS^-. The nanosheets exfoliated from LRH are the important reaction source of rare earth for the fabrication of ceramic films.

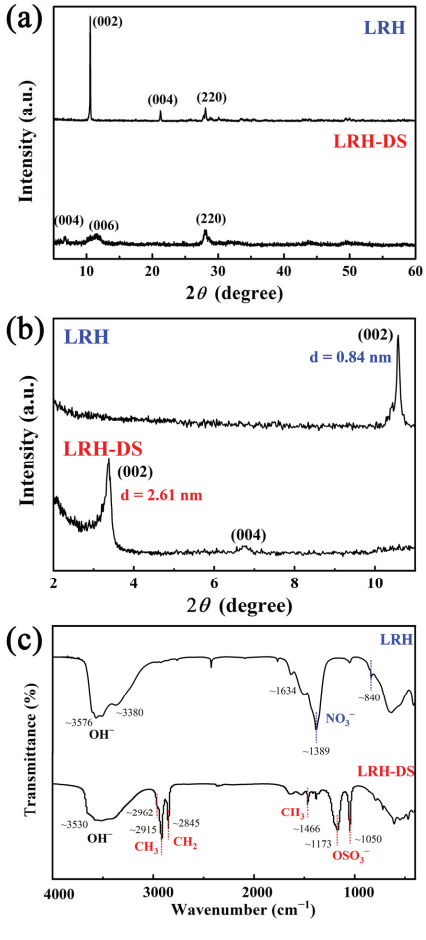

Figure 1. (**a**,**b**) XRD patterns and (**c**) FT-IR spectra for layered rare-earth hydroxide (LRH) and anion-exchanged product LRH-DS.

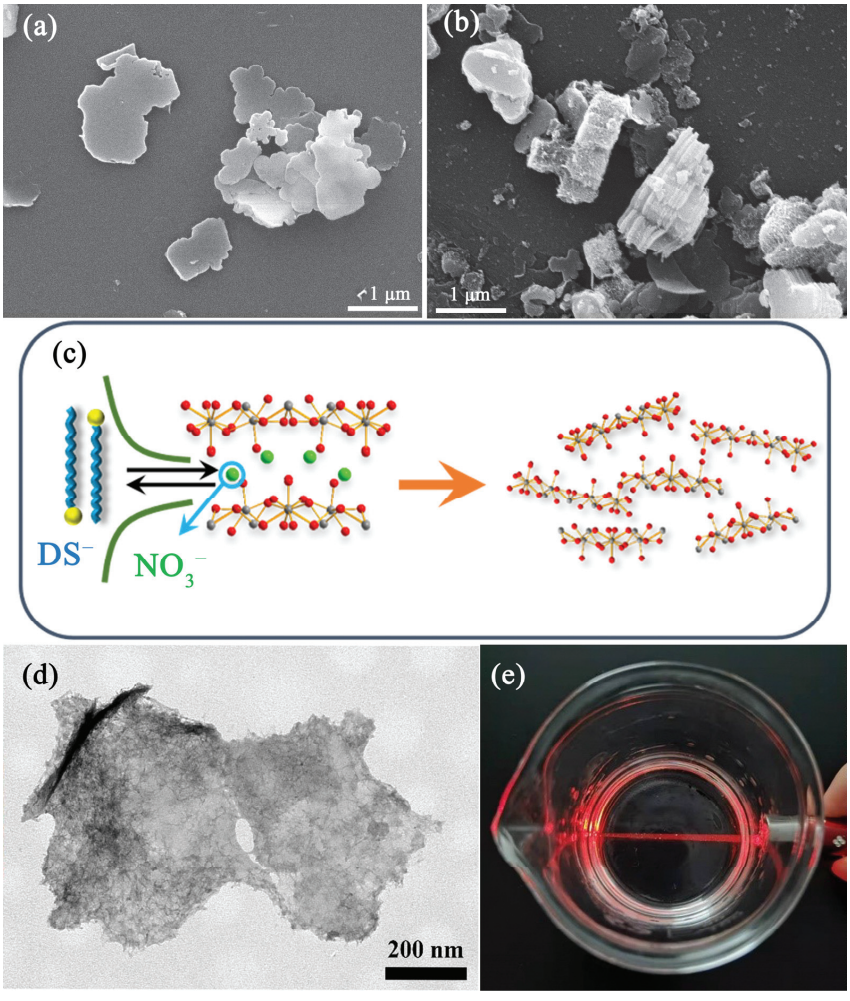

Figure 2. FE-SEM images of (**a**) layered rare-earth hydroxide and (**b**) anion-exchanged product. (**c**) Schematic illustration for nanosheet exfoliation. (**d**,**e**) TEM image of exfoliated nanosheets and colloidal suspension containing the exfoliated nanosheets.

3.2. Preparation and Characterization of GAP Ceramic Film

Figure 3 shows the schematic illustration for fabricating ceramic film of GAP and the formation mechanism. The exfoliated LRH nanosheets were directly prepared on the substrate of Al_2O_3 and calcined at selected temperatures for 120 min. The XRD patterns of prepared films at different temperatures are shown in Figure 4. After calcination at 800 °C, only cubic-structured Gd_2O_3 is found, which is converted from the exfoliated LRH nanosheets on Al_2O_3 substrate (Figure 4). Elevating the temperature from 800 °C to 1000 °C yields a small trace of $Gd_4Al_2O_9$ (GAM) along with the main Gd_2O_3, indicating that Al_2O_3 begins to react with Gd_2O_3 at the interface. When the temperature reaches 1300 °C, the main phase for the ceramic film is $GdAlO_3$, along with a small amount of $Gd_3Al_5O_{12}$ (GAG), $Gd_4Al_2O_9$ and crystalline Al_2O_3. Further increasing the temperature up to 1550 °C finally yields $GdAlO_3$ (GAP). The above results indicate that GAP is formed at a temperature higher than 1300 °C. Because the LRH nanosheets react with the amorphous alumina substrate at the interface, the temperature-dependent element diffusion takes the

dominant role, and more reactants participate in the reaction with increasing calcination temperature. At the low temperature of 800 °C, the LRH transforms into Gd_2O_3 and Al_2O_3 does not react with Gd_2O_3, because element diffusion does not happen. However, at a temperature of 1000 °C, some element diffusion takes place from Gd_2O_3 and Al_2O_3, which leads to the appearance of a small amount of $Gd_4Al_2O_9$ along with the main-phase Gd_2O_3. The element diffusion becomes stronger at the higher temperature of 1300 °C, and the reaction between Gd_2O_3, Al_2O_3, and $Gd_4Al_2O_9$ is more thorough, which finally contributes to the main $GdAlO_3$ and a small amount of $Gd_3Al_5O_{12}$ and $Gd_4Al_2O_9$. Because the thicknesses of the films are not uniform, the amount of Gd_2O_3 that participates in the reaction is not the same, and the resultant phases are not the same at different areas of the ceramic film. However, the almost uniform film that makes the dominant phase is $GdAlO_3$. At a temperature of 1300 °C, the crystallization of the amorphous alumina takes place, so some crystalline Al_2O_3 appears in the films. However, the Al_2O_3 for the interface reaction is completely in excess (Figure S1), so all the Gd_2O_3 reacts with Al_2O_3 to form $GdAlO_3$ at a temperature of 1550 °C. All crystalline Al_2O_3 at the interface participates in the reaction, so there is no crystalline Al_2O_3 in the film or a small trace of crystalline Al_2O_3 under the film that is undetectable.

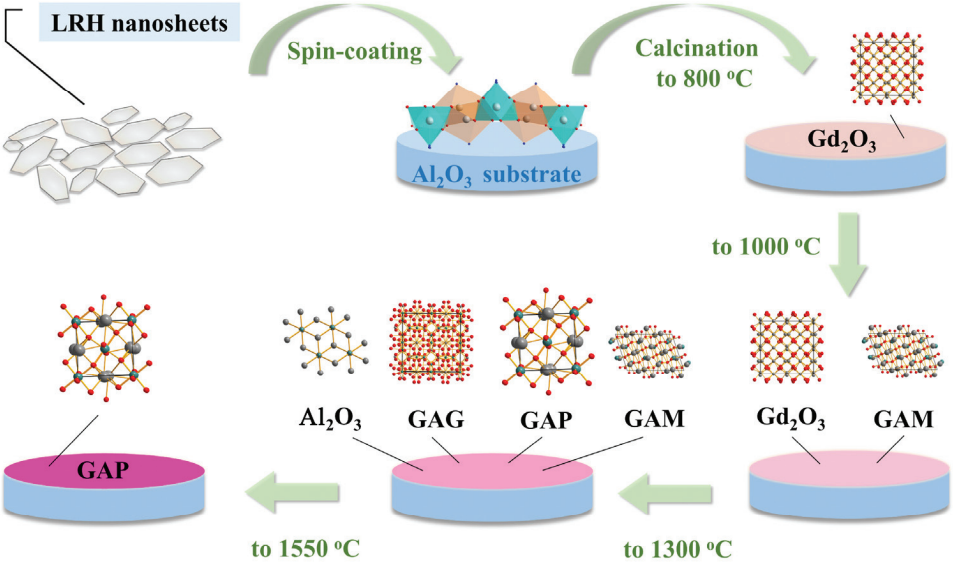

Figure 3. Schematic illustration for the fabrication of $GdAlO_3$ (GAP) ceramic films using exfoliated nanosheets as the rare-earth source. The intermediates GAM and GAG represent $Gd_4Al_2O_9$ and $Gd_3Al_5O_{12}$, respectively.

The SEM morphology of the films calcined at 1300 and 1550 °C is shown in Figure 5a,b. Traditionally, the obtained grain size of bulk ceramic is around 10–30 μm, because the ceramic is prepared by the traditional method at a high temperature range from 1700 °C to 1800 °C with the help of vacuum sintering [29–31]. Here, the sizes of most grains for the ceramic film at 1300 °C are 0.3–1 μm (Figure 5a). The grain size is up to 2–5 μm with the temperature elevated up to 1550 °C (Figure 5b). However, the grains are much smaller than those in bulk ceramic. First, the reaction temperature for ceramic film (1550 °C in air) is lower than that for bulk ceramic. Second, the reaction takes place on the interface, so the element diffusion is interface diffusion, which is rather slower than the volume diffusion for bulk ceramic. Therefore, the growth speed of the grains is much smaller than that for bulk ceramic.

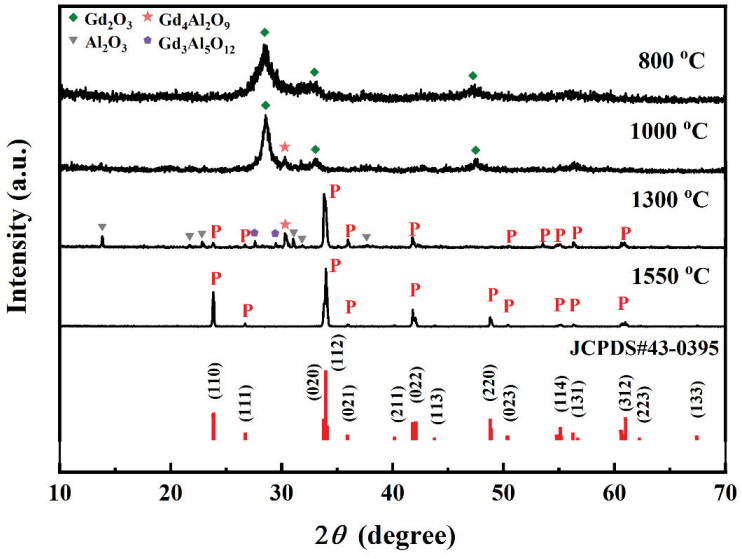

Figure 4. XRD patterns of the ceramic film calcined at different temperatures.

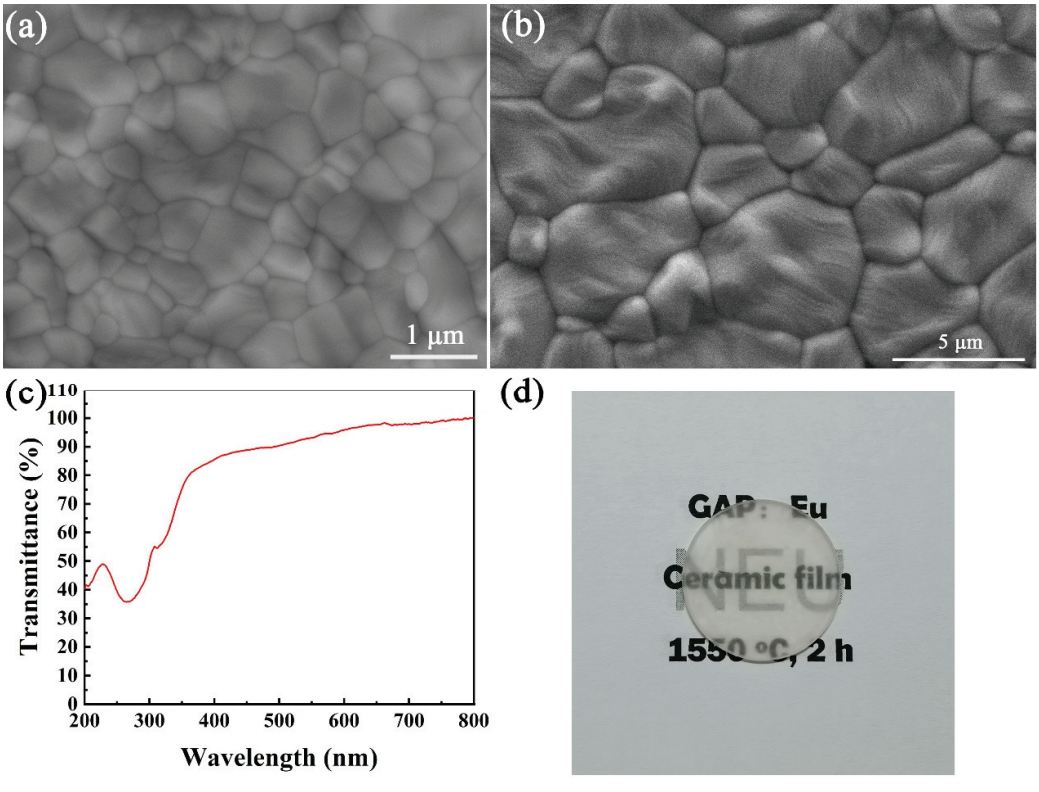

Figure 5. (**a**,**b**) FE-SEM images of the ceramic film calcined at 1300 °C and 1550 °C. (**c**) Transmittance curve and (**d**) appearance of the ceramic film calcined at 1550 °C.

3.3. Optical Properties of GAP:Eu^{3+} Transparent Ceramic Film

Transmittance of the prepared GAP:Eu^{3+} ceramic film was analyzed in Figure 5c. A broad and strong band is found in the transmittance curve at the range of 250–400 nm, which is arising from the charge-transfer absorption of O^{2-}-Eu^{3+} [32]. The shoulder near the intense band is assigned to the $^8S_{7/2}$-^6I_J transition of Gd^{3+} [33]. However, the transmittance curve is gentle and the value keeps above 90%, indicating that the transmittance of ceramic film is higher than 90%. Because the bare amorphous alumina substrate has a transmittance of ~99%, the ceramic film with the transmittance higher than 90% is highly transparent. Putting ceramic film (coated on the amorphous alumina) on the words shows that the words can also be observed clearly (Figure 5d), which confirms that GAP:Eu^{3+} ceramic film has high transmittance.

Figure 6 shows the photoluminescence excitation emission spectra of GAP:Eu^{3+} transparent ceramic film. Monitoring the wavelength at 618 nm, a broad and strong band is observed in PLE spectra at the range of 200–300 nm, whose maximum is located at 254 nm. The electron transition of O^{2-}-Eu^{3+} mainly contributes to the intense band (Figure 6a), which is usually called the charge-transfer band (CTB) [32]. However, the very weak peaks at the wavelength range of 300–500 nm are assigned to the intra-4f electronic transitions of the Eu^{3+} ion, but they are almost invisible because of the rather strong CTB. Under the UV light excitation at 254 nm, the GAP:Eu^{3+} transparent ceramic film outputs a red emission with multiple sharp peaks. The emission peaks at the range of 500–800 nm are assigned to the typical transition of Eu^{3+} from the excited energy level of $^5D_0$ to the ground energy level of ^7F_J (J = 0, 1, 2, 3, 4) [32]. Because the relative intensity of different J-level transitions is closely related to the symmetrical environment of Eu^{3+} ion, the coordination environment of Eu^{3+} in the host can be evaluated by the intensity of Eu^{3+} transitions. On the basis of the Judd–Ofelt theory, when the Eu^{3+} ion occupies a site with an inversion center, the magnetic dipole transition of $^5D_0$-$^7F_1$ is allowed, but the electric dipole transition of $^5D_0$-$^7F_2$ is forbidden [34,35]. In Figure 6b, the intensity of $^5D_0$-$^7F_1$ transition at 595 nm is obviously weaker than that of $^5D_0$-$^7F_2$ transition at 618 nm, so most Eu^{3+} ions occupy an asymmetry site. The symmetry of these sites is lower than that of the perfect crystal (D_{2d}), which leads to the appearance of $^5D_0$-$^7F_2$ transition at 618 nm and thus contributes to its emission intensity. Notably, the width of the peak around 617 nm indicates the overlap of bands corresponding to $^5D_0$-$^7F_2$ transitions (Figure 6b). Therefore, the outputted signal is red instead of orange. The CIE coordinate diagram of transparent ceramic film indicates that the color coordinate is (0.644, 0.355), located in the region of red color (Figure 6c). The CIE coordinate for the red emission of Eu^{3+} ions is close to the value in Ref. [13]. It not only depends upon the asymmetric ratio, but also on the higher energy emission levels. The appearance of the transparent ceramic film under UV light directly confirms the emission color is red. The transparent ceramic film also exhibits a stable thermality since its emission intensity only loses about 17% by increasing the environment temperature from 25 to 150 °C (Figure S2).

The lifetime of GAP:Eu^{3+} ceramic film is analyzed in Figure 6d through the fluorescence decay curve. The tested data are matched well with a single exponential, according to the following formula: $I = A\exp(-t/\tau)+B$, where τ is fluorescence lifetime (ms), t is decay time (ms), I is fluorescence intensity, and A and B are constants [19,36,37]. Through the calculation from the formula, the fluorescence lifetime of the film is determined to be ~1.570 ms. For most Eu^{3+}-doped oxides, the lifetimes in the literature are in the range of 1.4–2.0 ms, which are in the domain of the lifetimes for transparent ceramic film [38–40].

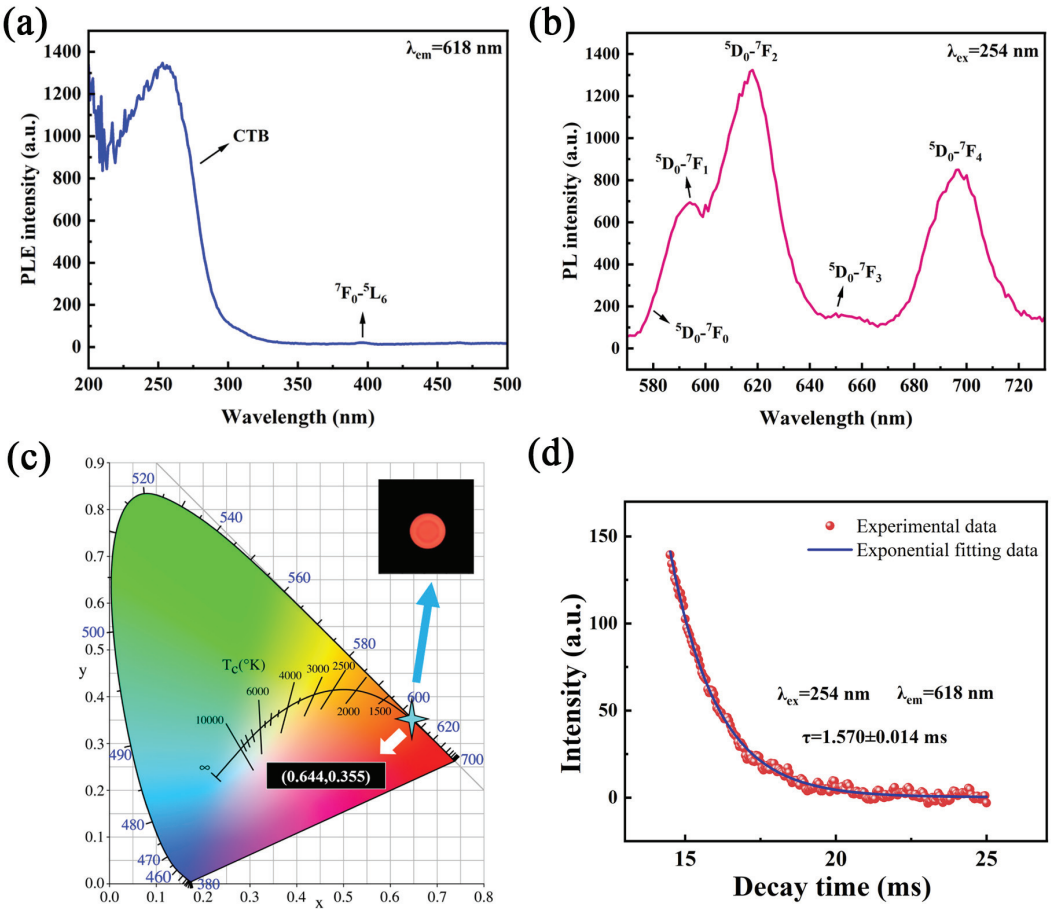

Figure 6. (**a**) PLE, (**b**) PL spectra, (**c**) CIE chromaticity diagram, and (**d**) fluorescence decay curve with fitting results of the ceramic film calcined at 1550 °C.

4. Conclusions

In this work, the two-dimensional guidance strategy has been successfully carried out for the perovskite-structured aluminate ceramic film. Through the interfacial reaction, $GdAlO_3:Eu^{3+}$ (GAP:Eu^{3+}) films of transparent ceramic were fabricated using the exfoliated layered gadolinium hydroxide nanosheets as the rare-earth source. The final films were tested by the characterization techniques, including XRD, SEM, TEM, FT-IR, PLE/PL spectroscopy, temperature-dependent PL spectroscopy, and luminescence decay analysis. The perovskite film of transparent ceramic can be obtained by calcining the LRH nanosheets on the substrate of amorphous alumina at 1550 °C in air for 120 min. Because the reaction takes place at the interface, the temperature-dependent element diffusion takes the dominant role and more reactants participate in the reaction with increasing calcination temperature. The grains for ceramic film increase up to 2–5 μm by elevating the temperature to 1550 °C, but the grains are much smaller than that for bulk ceramic. The lower temperature and interface diffusion contribute to the smaller grains. The ceramic film exhibits a high transmittance above 90% at the visible wavelength range. Upon UV excitation at 254 nm, the ceramic film emits intense red light with a lifetime of ~1.570 ms.

Supplementary Materials: The following supporting information can be downloaded at: https://www.mdpi.com/article/10.3390/coatings12121927/s1, Figure S1: EDS elemental mapping analysis of the film calcined at different temperatures; Figure S2: (a) Temperature-dependent PL spectra and (b) relative integral intensity of 618-nm emission bands.

Author Contributions: Conceptualization, methodology, T.Z. and Q.Z.; software, validation, formal analysis, investigation, resources, data curation, writing—original draft preparation, L.C. and J.Y.; writing—review and editing, visualization, T.Z.; supervision, project administration, funding acquisition, T.Z. and Q.Z. All authors have read and agreed to the published version of the manuscript.

Funding: This work was supported in part by the Natural Science Foundation of Liaoning Province (Grant 2020-MS-081), and National Natural Science Foundation of China (Grant 51302032 and U21A2045).

Institutional Review Board Statement: Not applicable.

Informed Consent Statement: Not applicable.

Data Availability Statement: This study did not report any public data.

Conflicts of Interest: The authors declare no conflict of interest.

References

1. Schubert, E.F.; Kim, J.K. Solid-state Light Sources Getting Smart. *Science* **2005**, *308*, 1274–1278. [CrossRef] [PubMed]
2. Zhou, Q.; Dolgov, L.; Srivastava, A.M.; Zhou, L.; Wang, Z.L.; Shi, J.X.; Dramicanin, M.D.; Brik, M.G.; Wu, M.M. Mn^{2+} and Mn^{4+} Red Phosphors: Synthesis, Luminescence and Applications in WLEDs. A Review. *J. Mater. Chem. C* **2018**, *6*, 2652–2671. [CrossRef]
3. Sun, B.H.; Zhang, L.; Zhou, T.Y.; Shao, C.; Zhang, L.; Ma, Y.L.; Yao, Q.; Jiang, Z.G.; Selim, F.A.; Chen, H. Protected-annealing Regulated Defects to Improve Optical Properties and Luminescence Performance of Ce:YAG Transparent Ceramics for White LEDs. *J. Mater. Chem. C* **2019**, *7*, 4057–4065. [CrossRef]
4. Yoon, S.W.; Park, H.K.; Ko, K.Y.; Ahn, J.; Do, Y.R. Various Nanofabrication Approaches towards Two-dimensional Photonic Crystals for Ceramic Plate Phosphor-capped WhiteF Light-emitting Diodes. *J. Mater. Chem. C* **2014**, *2*, 7513–7522. [CrossRef]
5. Park, H.K.; Yoon, S.W.; Choi, D.Y.; Do, Y.R. Fabrication of Wafer-scale TiO_2 Nanobowl Arrays via a Scooping Transfer of Polystyrene Nanospheres and Atomic Layer Deposition for Their Application in Photonic Crystals. *J. Mater. Chem. C* **2013**, *1*, 1732–1738. [CrossRef]
6. Zhu, Q.; Ding, S.N.; Xiahou, J.Q.; Li, S.Y.; Sun, X.D.; Li, J.G. A Groundbreaking Strategy for Fabricating YAG:Ce^{3+} Transparent Ceramic Films via Sintering of LRH Nanosheets on a Sapphire Substrate. *Chem. Commun.* **2020**, *56*, 12761–12764. [CrossRef]
7. Grabmaier, B.C. *Luminescent Materials*; Springer: Berlin, Germany, 1994; pp. 71–90.
8. Dorenbos, P.; Bougrine, E.; De Haas, J.T.M.; Van Eijk, C.W.E.; Korzhik, M.V. Scintillation Properties of $GdAlO_3$:Ce crystals. *Radiat. Eff. Defects Solids* **1995**, *135*, 321–323. [CrossRef]
9. Srivastava, A.M.; Brik, M.G. The Nature of Mn^{4+} Luminescence in the Orthorhombic Perovskite, $GdAlO_3$. *Opt. Mater.* **2017**, *63*, 207–212. [CrossRef]
10. Jovanić, B.R.; Andreeta, J.P. $GdAlO_3$:Cr^{3+} as a New Pressure Sensor. *Phys. Scr.* **1999**, *59*, 274–276. [CrossRef]
11. Wang, X.L.; Yang, Z.; Li, J.Y.; Fu, W.F.; Tang, P.; Chen, Y.F.; Guo, J.; Gao, Z.H.; Huang, Y.; Tao, Y. Hydrothermal Synthesis, Morphology and Luminescent Properties of $GdAlO_3$:Eu^{3+} Microcrystals. *J. Alloys Compd.* **2014**, *614*, 40–43. [CrossRef]
12. Shilpa, C.J.; Jayaram, A.K.; Dhananjaya, N.; Nagabhushana, H.; Prashantha, S.C.; Sunitha, D.V.; Sharma, S.C.; Shivakumara, C.; Nagabhushana, B.M. $GdAlO_3$:Eu^{3+}:Bi^{3+} Nanophosphor: Synthesis and Enhancement of Red Emission for WLEDs. *Spectrochim. Acta Part A Mol. Biomol. Spectrosc.* **2014**, *133*, 550–558. [CrossRef] [PubMed]
13. Jisha, P.K.; Naik, R.; Prashantha, S.C.; Nagabhushana, H.; Sharma, S.C.; Nagaswarupa, H.P.; Anantharaju, K.S.; Prasad, B.D.; Premkumar, H.B. Facile Combustion Synthesized Orthorhombic $GdAlO_3$:Eu^{3+} Nanophosphors: Structural and Photoluminescence Properties for WLEDs. *J. Lumin.* **2015**, *163*, 47–54. [CrossRef]
14. Michail, C.; Kalyvas, N.; Valais, I.; David, S.; Seferis, I.; Toutountzis, A.; Karabotsos, A.; Liaparinos, P.; Fountos, G.; Kandarakis, I. On the Response of $GdAlO_3$:Ce Powder Scintillators. *J. Lumin.* **2013**, *144*, 45–52. [CrossRef]
15. Kumar, P.; Singh, D.; Gupta, I.; Singh, S.; Kumar, V. Emerging green light emission of Er^{3+}-activated single phased $GdAlO_3$ phosphors for lighting applications. *Luminescence* **2022**, *ahead of print*.
16. Deng, T.L.; Jiang, X.B.; Zhang, Q.Y. Sustainably adjusting the up-conversion white-emitting luminescence properties of $GdAlO_3$:Er^{3+}/Yb^{3+}/Tm^{3+} phosphors. *Front. Chem.* **2020**, *8*, 788. [CrossRef]
17. Sheoran, S.; Singh, K.; Tanwar, V.; Singh, S.; Samantilleke, A.; Singh, D. Synthesis and Spectroscopic Investigations of Trivalent Europium-doped $Z_2Si_3O_8$ (Z = Mg, Ca and Sr) Nanophosphors for Display Applications. *Rare Metals* **2021**, *40*, 2610–2617. [CrossRef]
18. Xie, J.H.; Wang, J.; Qiu, G.H.; Li, X.B.; Huang, W.T.; Zhang, R.R.; Lin, T.; Wang, L.X.; Zhang, Q.T. A Strategy to Achieve Efficient Green-emission Dual-mode Luminescence of Yb^{3+}, Er^{3+} Doped $NaBiF_4$. *Rare Metals* **2021**, *40*, 2040–2048. [CrossRef]

19. Yao, J.; Zhu, Q.; Li, J.G. Garnet Transparent Ceramic Film of $Y_3Al_5O_{12}$:Eu^{3+} Fabricated through an Interface Reaction of Layered Rare-earth Hydroxide Nanosheets on Amorphous Alumina. *Appl. Surf. Sci.* **2022**, *579*, 152226. [CrossRef]
20. Zhu, Q.; Wang, X.J.; Li, J.G. Recent Progress in Layered Rare-earth Hydroxide (LRH) and its Application in Luminescence. *J. Adv. Ceram.* **2017**, *6*, 177–186. [CrossRef]
21. Zhu, Q.; Li, J.G.; Zhi, C.Y.; Li, X.D.; Sun, X.D.; Sakka, Y.; Golberg, D.; Bando, Y. Layered Rare-earth Hydroxides (LRHs) of $(Y_{1-x}Eu_x)_2(OH)_5NO_3{\cdot}nH_2O$ (x = 0–1): Structural Variations by Eu^{3+} Doping, Phase Conversion to Oxides, and the Correlation of Photoluminescence Behaviors. *Chem. Mater.* **2010**, *22*, 4204–4213. [CrossRef]
22. Li, J.G.; Sakka, Y. Recent Progress in Advanced Optical Materials Based on Gadolinium Aluminate Garnet ($Gd_3Al_5O_{12}$). *Sci. Technol. Adv. Mater.* **2015**, *16*, 014902. [CrossRef]
23. Hu, L.F.; Ma, R.Z.; Ozawa, T.C.; Sasaki, T. Exfoliation of layered europium hydroxide into unilamellar nanosheets. *Chem. Asian J.* **2010**, *5*, 248–251. [CrossRef] [PubMed]
24. Geng, F.X.; Xin, H.; Matsushita, Y.; Ma, R.Z.; Tanaka, M.; Izumi, F.; Iyi, N.; Sasaki, T. New layered rare-earth hydroxides with anion-exchange properties. *Chem. Eur. J.* **2008**, *14*, 9255–9260. [CrossRef] [PubMed]
25. Geng, F.X.; Matsushita, Y.; Ma, R.Z.; Xin, H.; Tanaka, M.; Iyi, N.; Sasaki, T. Synthesis and properties of well-crystallized layered rare-earth hydroxide nitrates from homogeneous precipitation. *Inorg. Chem.* **2009**, *48*, 6724–6730. [CrossRef] [PubMed]
26. Gadsden, J.A. *Infrared Spectra of Minerals and Related Inorganic Compounds*; Butterworth: Newton, MA, USA, 1975; pp. 101–120.
27. Nakamoto, K. *Infrared Spectra of Inorganic and Coordination Compounds*; John Wiley & Sons: New York, NY, USA, 1963; pp. 56–78.
28. Zhu, Q.; Li, S.Y.; Wang, Q.; Qi, Y.; Li, X.D.; Sun, X.D.; Li, J.G. Grafting of Terbium (III) Complexes onto Layered Rare-earth Hydroxide Nanosheets to Fabricate Novel Optical Fiber Temperature Sensors. *Nanoscale* **2019**, *11*, 2795–2804. [CrossRef] [PubMed]
29. Li, J.; Chen, F.; Liu, W.B.; Zhang, W.X.; Wang, L.; Ba, X.W.; Zhu, Y.J.; Pan, Y.B.; Guo, J.K. Co-precipitation Synthesis Route to Yttrium Aluminum Garnet (YAG) Transparent Ceramics. *J. Eur. Ceram. Soc.* **2012**, *32*, 2971–2979. [CrossRef]
30. Wen, L.; Sun, X.D.; Xiu, Z.M.; Chen, S.W.; Tsai, C.T. Synthesis of Nanocrystalline Yttria Powder and Fabrication of Transparent YAG Ceramics. *J. Eur. Ceram. Soc.* **2004**, *24*, 2681–2688. [CrossRef]
31. Zhu, Q.Q.; Li, S.X.; Yuan, Q.; Zhang, H.; Wang, L. Transparent YAG:Ce Ceramic with Designed Low Light Scattering for High-power Blue LED and LD Applications. *J. Eur. Ceram. Soc.* **2021**, *41*, 735–740. [CrossRef]
32. Zhu, Q.; Fan, Z.S.; Wang, S.; Xiahou, J.Q.; Li, J.G. Uniform Colloidal Spheres for RE_3BO_6 (RE = Eu-Yb, Y) and Excitation-dependent Luminescence of Y_3BO_6:Eu^{3+} Red Phosphor. *J. Am. Ceram. Soc.* **2019**, *102*, 7448–7461. [CrossRef]
33. Wang, Z.W.; Qu, Q.; Ji, H.P.; Hao, X.F.; Li, J.S. Available Manganese-containing Chemicals and Synthesis Methods for Mn^{4+}-activated Phosphors. *Chin. J. Lumin.* **2022**, *43*, 662–675. [CrossRef]
34. Zhu, Q.; Li, J.G.; Li, X.D.; Sun, X.D. Morphology-dependent Crystallization and Luminescence Behavior of (Y, Eu)$_2O_3$ Red Phosphors. *Acta Mater.* **2009**, *57*, 5975–5985. [CrossRef]
35. Syrbu, L.; Ursaki, V.V.; Tiginyanu, I.M.; Dolgaleva, K.; Boyd, R.W. Red and green nanocomposite phosphors prepared from porous GaAs templates. *J. Opt. A Pure Appl. Opt.* **2007**, *9*, 401–404. [CrossRef]
36. Sun, H.C.; Zhu, Q.; Li, J.G. Local Charge Regulation by Doping Li^+ in $BaGa_2O_4$:Bi^{3+} to Generate Multimode Luminescence for Advanced Optical Morse Code. *Ceram. Int.* **2022**, *48*, 9640–9650. [CrossRef]
37. Zhao, B.Q.; Zhu, Q.; Sun, X.D.; Li, J.G. Co-doping Zn^{2+}/Sn^{4+} in $ZnGa_2O_4$:Cr^{3+} for Dynamic Near-infrared Luminescence and Advanced Anti-counterfeiting. *Ceram. Int.* **2021**, *47*, 17000–17007. [CrossRef]
38. Mao, Q.; Shen, B.; Yang, T.; Zhong, J.S.; Wu, G.Q. A Double Perovskite-based Red-emitting Phosphor with Robust Thermal Stability for Warm WLEDs. *Ceram. Int.* **2020**, *46*, 19328–19334. [CrossRef]
39. Raju, G.S.R.; Jung, H.C.; Park, J.Y.; Moon, B.K.; Balakrishnaiah, R.; Jeong, J.H.; Kim, J.H. The Influence of Sintering Temperature on the Photoluminescence Properties of Oxyapatite Eu^{3+}:$Ca_2Gd_8Si_6O_{26}$ Nanophosphors. *Sens. Actuator B-Chem.* **2010**, *146*, 395–402. [CrossRef]
40. Bai, X.; Song, H.W.; Yu, L.X.; Yang, L.M.; Liu, Z.X.; Pan, G.H.; Lu, S.Z.; Ren, X.G.; Lei, Y.Q.; Fan, L.B. Luminescent Properties of Pure Cubic Phase Y_2O_3/Eu^{3+} Nanotubes/Nanowires Prepared by a Hydrothermal Method. *J. Phys. Chem. B* **2005**, *109*, 15236–15242. [CrossRef] [PubMed]

coatings

MDPI

Article

Effect of Mo and C Additions on Eta Phase Evolution of WC-13Co Cemented Carbides

Xun Li [1], Xianwei Zhang [2], Junfei Zhang [2], Qiang Zhang [2], Vincent Ji [3] and Jinlong Liu [1,*]

[1] Key Laboratory for Anisotropy and Texture of Materials (Ministry of Education), School of Materials Science and Engineer, Northeastern University, Shenyang 110819, China
[2] Liaoning Wuhuan Special Materials and Intelligent Equipment Industry Technology Research Institute Co., Ltd., Shenyang 113122, China
[3] Institut de Chimie Moléculaire et Des Matériaux d'Orsay, CNRS UMR 8182, Université Paris-Saclay, 91405 Orsay, France
* Correspondence: liujl@atm.neu.edu.cn; Tel.: +86-24-83681455; Fax: +86-24-83686455

Abstract: The WC-13Co (wt.%) cemented carbide was prepared by simple pressureless sintering, and the influence of Mo and C additions on the eta evolution and mechanical properties was analyzed by XRD, SEM, EDS, XPS, and Vickers hardness tester. The results show that the addition of Mo has an important influence on the composition, size, and distribution of the eta phase and Mo_2C phase. When the Mo content increases from 0 to 2.5%, the Mo-enriched eta phase grows abnormally and the area fraction of the eta phase significantly increases to 40%, leading to an obvious increase in hardness from 1232 HV_{30} to 1321 HV_{30}, and a decrease in fracture toughness from 12.5 $MPa{\cdot}m^{1/2}$ to 9.8 $MPa{\cdot}m^{1/2}$. The addition of carbon black effectively inhibits the formation of the eta phase in the samples with 2.5% Mo. Moreover, adding Mo can suppress WC coarsening in a high-carbon content, which is different from the obvious growth of WC grains in a high-carbon environment in traditional research. Finally, the mechanism of eta phase evolution during the sintering process of WC-Co cemented carbides containing Mo is discussed systematically.

Keywords: WC-Co; cemented carbide; eta phase; Mo

Citation: Li, X.; Zhang, X.; Zhang, J.; Zhang, Q.; Ji, V.; Liu, J. Effect of Mo and C Additions on Eta Phase Evolution of WC-13Co Cemented Carbides. *Coatings* **2022**, *12*, 1993. https://doi.org/10.3390/coatings12121993

Academic Editor: Michał Kulka

Received: 31 October 2022
Accepted: 16 December 2022
Published: 19 December 2022

1. Introduction

The WC-Co cemented carbides consisting of WC grains coated by Co binders have excellent mechanical properties, including high hardness, high wear resistance, and favorable fracture toughness [1]. It is widely used in metal-cutting, mining, construction, and rock drilling [2]. Alloying is an effective method to improve the mechanical properties of WC-Co cemented carbides. Li et al. [3] found that Cu-doped WC-Co cemented carbides have excellent comprehensive performances. The average WC grain size decreases as Cu is added, and the grain size distribution narrows. The addition of Al can greatly improve the hardness and density of the WC-Co cemented carbides, but its fracture toughness decreases [4]. The addition of the Cr element promotes the segregation of the M_7C_3 phase around the eta phase, which can inhibit the growth of the eta phase, and leads to the finer and more dispersed eta phase [5].

Recently, some reports showed that the addition of Mo [6] or Mo_2C [7], which obviously enhanced the wettability between WC grains and binder phases, is beneficial to improving the mechanical properties of WC-Co cemented carbides. Some studies further indicated that hardness [8], fracture toughness [9], and bending strength increase with the addition of Mo in cemented carbide. Moreover, Guo et al. [10] also reported that Mo is helpful to improve the corrosion resistance of WC-6Co cemented carbide in both acidic and alkaline solutions.

In addition, the phase is a key factor in the mechanical properties of cemented carbides. Especially for high-temperature sintering, the phases in W-C-Co ternary phase diagram system are very complex, and the possible phases include eta phases (Co_6W_6C and Co_3W_3C),

ditungsten carbide (W_2C), and the intermediate Co_7W_6 phase [11]. However, the effect of Mo addition on the formation and growth of the phase is still very limited. The current work mainly focused on investigating the effect of Mo addition on the phase of WC-13Co cemented carbides, and the difference in microstructure evolution of WC-13Co cemented carbide containing Mo is further explored in the sintering environments of both low-carbon and high-carbon.

2. Experimental Procedure

Commercial tungsten carbides (5.92% C, 0.094% O, W ≥ 93.98, S ≤ 0.001%, P ≤ 0.001%, others ≤ 0.001%, wt.%, average particle size of 1.5 μm, Xiamen golden egret special alloy Co., Ltd., Xiamen, China, Figure 1a), Co powders (Co ≥ 99.9%, Mn ≤ 0.0001%, Cu ≤ 0.0003%, others ≤ 0.005%, average particle size of 0.8 μm, 99.9 wt.% purity, Xiamen golden egret special alloy Co., Ltd., Xiamen, China, Figure 1b), Mo powders (Mo ≥ 99.0%, average particle size of 2 μm, Shanghai Macklin Biochemical Technology Co., Ltd., Shanghai, China, Figure 1c) were selected as raw materials. Table 1 shows the nominal chemical compositions of WC-13Co cemented carbides with different additives of Mo and carbon black. The carbon content of the sample is calculated using the following formula: $C_{total}\% = (C_{WC} + C_{carbon})/M_{total}$, where $C_{total}\%$ is the proportion of C in the sample, C_{WC} is the weight of C in the WC powder, C_{carbon} is the weight of carbon black added, and the M_{total} is the total weight of the sample. The C_{total} is important for evaluating the carbon content in the sample, although it ignores the carbon loss during the sintering process.

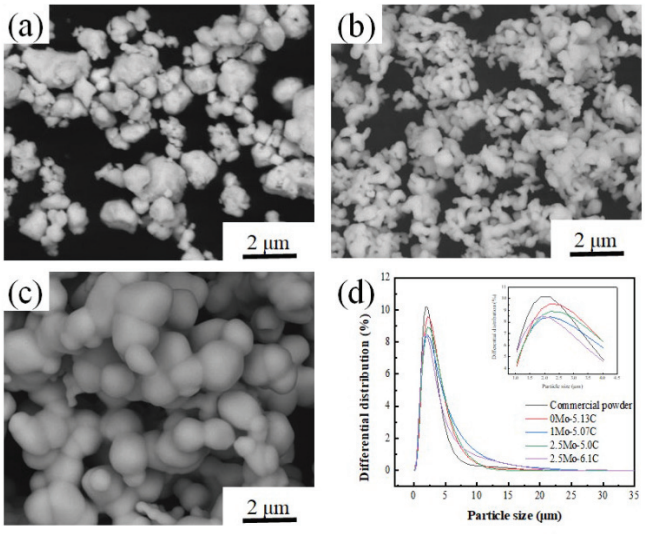

Figure 1. SEM of (**a**) WC powders, (**b**) Co powders, (**c**) Mo powders, (**d**) Size distribution of commercial WC and ball-milled powders.

Table 1. The nominal chemical compositions of WC-13Co cemented carbides (wt.%).

Samples	WC	Co	Mo	C	C_{total}
0Mo-5.13C	87	13	0	0	C5.13
1Mo-5.07C	86	13	1	0	C5.07
2Mo-5.01C	85	13	2	0	C5.01
2.5Mo-5.0C	84.5	13	2.5	0	C5.0
2.5Mo-5.3C	84.5	13	2.5	0.3	C5.3
2.5Mo-5.45C	84.5	13	2.5	0.45	C5.45
2.5Mo-5.75C	84.5	13	2.5	0.75	C5.75
2.5Mo-6.1C	84.5	13	2.5	1.1	C6.1

The raw materials were ball-milled for 24 h in air atmosphere by adding alcohol. The purpose of ball milling is mainly to mix the powder evenly. The mass ratio of ball-to-powder was 4:1 and rotational velocity was 240 rpm. After milling, the powders were dried at 70 °C for 5 h in a vacuum and then screened by 80 mesh griddles. Then the particle size of the powder was measured with a laser particle size analyzer (Zhu Hai OMEC Instruments Co., Ltd., Zhuhai, China) as shown in Figure 1d. After ball milling, the size of composite powder containing WC, Co, Mo, and carbon black is similar to the size of WC before ball milling.

Afterward, the powders were pressed into a mold with a diameter of 20 mm under 240 MPa. Finally, they were sintered by a pressureless method. The sintering parameters are as follows. The samples were heated from room temperature to 1000 °C at a rate of 10 °C/min, and then to 1430 °C at a heating rate of 5 °C/min and kept at 1430 °C for 1 h, and later were cooled in furnace. The sintering process is carried out under Ar atmosphere, and the operation process of Ar gas is as follows. A vacuum pump was used to pump down the air from the furnace and Ar gas was aerated to the furnace up to atmosphere pressure, and then draw out the Ar gas. After filling and pumping out Ar gas 5 times, the Ar gas was filled again for sintering under atmosphere pressure. The type of furnace used is the Tubular experimental furnace (GSL-1700X, Hefei Kejing Co., Ltd., Hefei, China).

The phase identification of WC-Co and Mo/C-doped WC-Co alloys was measured using XRD-7000 (Shimadzu Co., Ltd., Japan, Cu target). During XRD image analysis, the scanning speed is 5°/min and the scanning angle is 20°–80°. The microstructure was observed by Quanta 250FEG SEM (Czech FEI Co., Ltd., Czech Republic) and the grain size was determined by the software of Image-Pro Plus. Vickers hardness tester was selected to estimate the hardness of alloys. When testing the hardness, the loading force used is 30 kg, which is applied for 10 s. Based on the indentation of Vickers hardness, the total length of indentation crack was obtained to calculate the fracture toughness of alloys (K_{1C}: MPa·$m^{1/2}$). The etching agent for observing the optical microstructure is the mixed 10% potassium hydroxide solution with 10% potassium ferricyanide, and the etching method is to drop the etching agent onto the degreased cotton and then gently wipe the sample with the degreased cotton. X-ray photoelectron spectroscopy (XPS, Model Axis Supra, Shimadzu-Kratos Analytical Ltd., Manchester, UK) data were measured by monochromatized Al Kα X-ray radiation (1486.6 eV).

3. Results and Discussion

3.1. Microstructure and Composition

The XRD patterns of WC-13Co cemented carbide with different Mo and C contents were shown in Figure 2. When the Mo element is added, WC hard phase, Co binder phase, and eta phases were identified in each sample as shown in Figure 2a. The relative intensity of the eta phase diffraction peak enhances with the increase of the Mo content. The WC-Co binary phase diagram indicates that two eta phases are present in the WC-Co system in the low-carbon content, namely, M_6C and $M_{12}C$ [12], which are also named Co_3W_3C and Co_6W_6C [13]. The eta phases form in the sintering process [14]. Among them, the M_6C phase is the high-temperature phase and exists above 1150 °C. With the fall in temperature, it starts to transform into the $M_{12}C$ phase. The M_6C and $M_{12}C$ type carbides have similar FCC crystal structures [15]. In Figure 2b, an interesting phenomenon is that the Mo_2C phase becomes detectable in the samples added Mo and carbon black, accompanied by the decrease of the eta phase. Liu et al. [16] reported that the Mo_2C phase can form below 900 °C when Mo is added to cemented carbide with a high carbon content. The reaction of Mo with carbon black weakened the effect of Mo on the promotion of the eta phase.

Based on the XRD data, the lattice constants were further calculated, as shown in Table 2. It can be seen that the lattice constants of the WC and eta phases did not change significantly when 0%–2.5% Mo was added to the WC-13Co cemented carbide and 0%–1.1% C was added to the WC-13Co-2.5Mo cemented carbide, which indicates that the addition of Mo and C does not cause large lattice strain. Mo and W have very similar atomic radii

(W: 1.37 Å, Mo: 1.36 Å) [17], thus Mo in the place of W will not produce a large lattice strain.

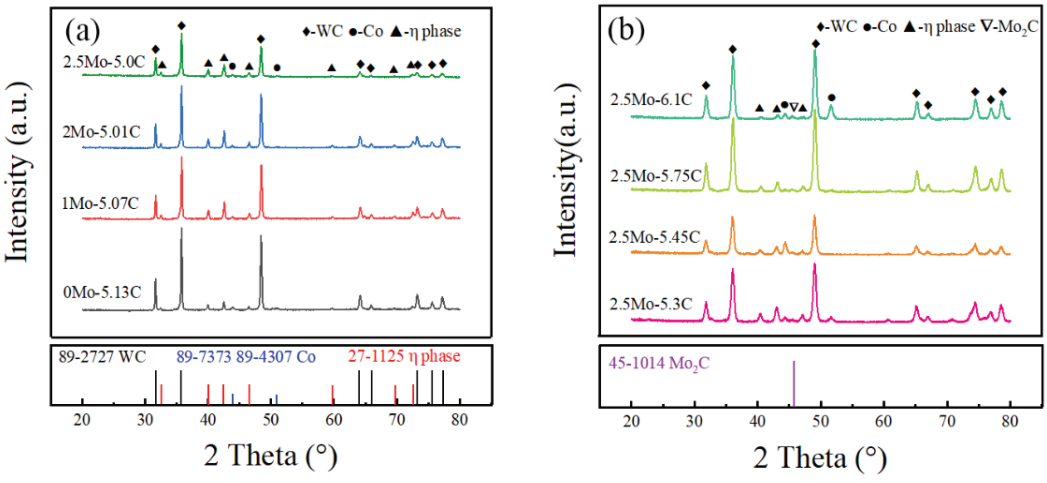

Figure 2. XRD results of WC-13Co alloys with different contents of Mo and C, (**a**) WC-13Co-x%Mo, (**b**) WC-13Co-2.5Mo-x%C.

Table 2. Lattice constants of WC and eta phase of various compositions.

Component	WC		Eta Phase
	a	b	a = b = c
0Mo-5.13C	2.90511	2.83594	11.06816
1Mo-5.07C	2.90568	2.83645	11.06775
2Mo-5.01C	2.90464	2.83501	11.05768
2.5Mo-5.0C	2.90543	2.83578	11.06578
2.5Mo-5.3C	2.90644	2.83722	11.05969
2.5Mo-5.45C	2.90599	2.83707	11.0609
2.5Mo-5.75C	2.90453	2.83563	11.03769
2.5Mo-6.1C	2.90495	2.83613	11.03866

Figure 3 illustrates the optical microstructure and Figure 4 further demonstrates the statistical area fraction of the eta phase. The black region in Figure 3 is the corroded eta phase. It is worth noting that the eta phase is very sensitive to the Mo addition. When 2.5% Mo was used to replace WC, the content of C in the alloy decreased by 0.13, and the proportion of the eta phase doubled, from 19.5% to 40%. However, the proportion of the eta phase only decreased from 40% to 34.2% when the addition of carbon black increased from 0 to 0.3%. According to the calculated phase diagram, the ratio of the eta phase should be close to zero for the WC-13Co with a composition of 0Mo-5.13C, and the formation of a large area fraction of the eta phase in Figure 3a is mainly caused by the loss of carbon during sintering [18]. When the content of carbon black reaches 1.1%, the proportion of the eta phase decreases to 4%. Carbon black effectively inhibits the formation of the eta phase in the sample of 2.5Mo-6.1C.

In the WC-Co phase diagram, low-carbon content is the main reason for the formation of the eta phase. The eta phase was also successfully eliminated by increasing the carbon content when producing the inhomogeneous cemented carbides with fine-grained structure via one-step transformation using coarse WC, WO_3, C, and Co as raw materials by Tang et al. [19].

The eta phase can be clearly observed in the BSE-SEM images as shown in Figure 5. With the addition of Mo from 0% to 2.0%, both the area fraction and the size of the eta phase increase sharply. In the 0Mo-5.13C sample, the eta phase size is relatively small, and most eta phases are slightly larger than WC grains, but in the samples with 2.0% Mo and 2.5% Mo, the size of some eta phases reaches about 10 μm, almost ten times higher than the size of WC grains. With the increase of carbon black in the sample with 2.5% Mo, the large size eta phase disappeared.

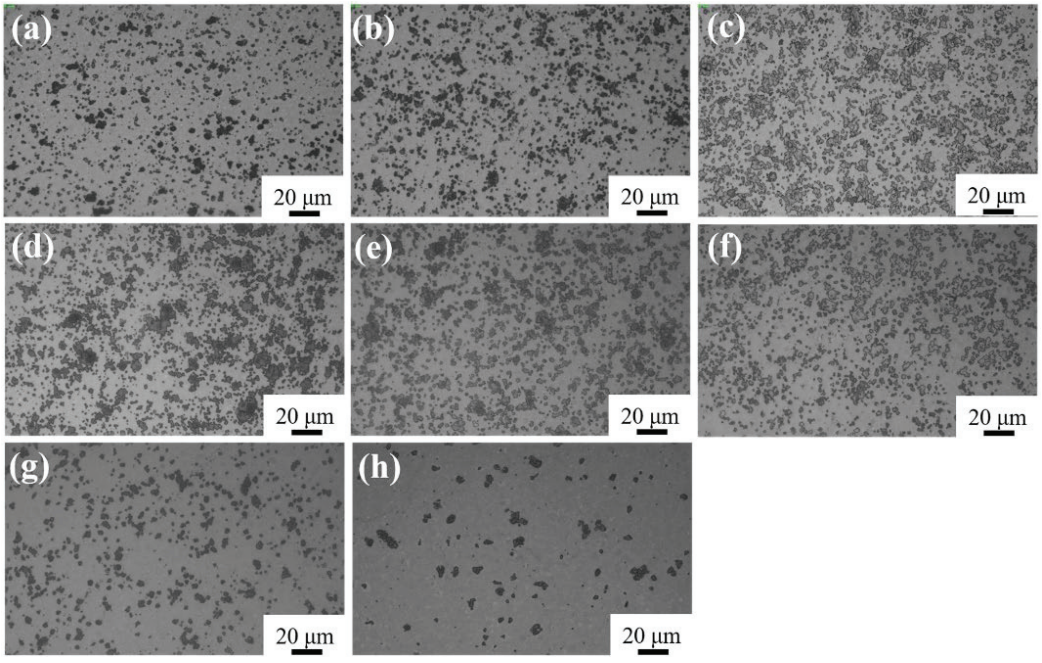

Figure 3. Optical microstructure of WC-13Co with different contents of Mo and C, (**a**) 0Mo-5.13C, (**b**) 1Mo-5.07C, (**c**) 2Mo-5.01C, (**d**) 2.5Mo-5.0C, (**e**) 2.5Mo-5.3C, (**f**) 2.5Mo-5.45C, (**g**) 2.5Mo-5.75C, (**h**) 2.5Mo-6.1C.

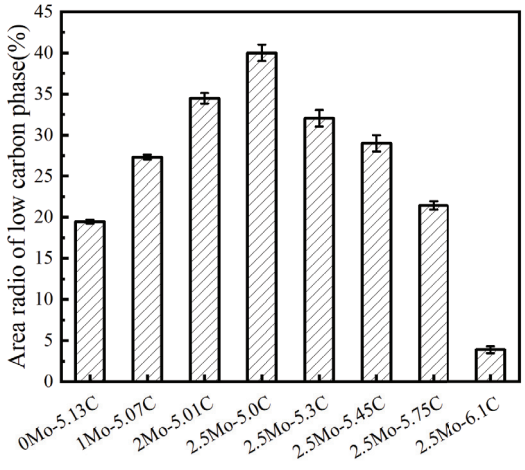

Figure 4. Area fraction of eta phase of WC-13Co with different additions of Mo and C.

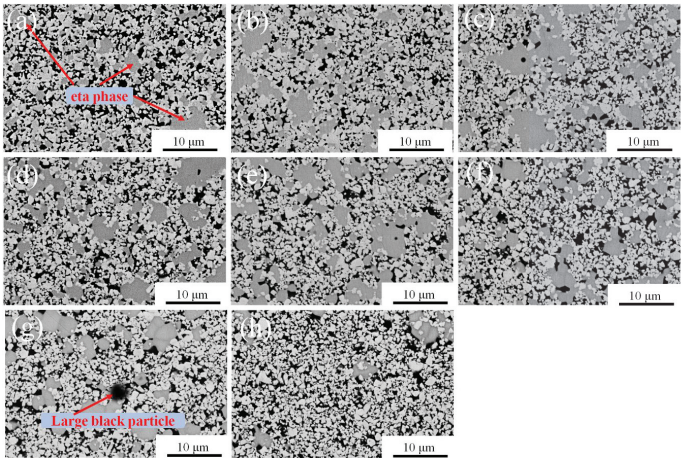

Figure 5. BSE-SEM microstructure of alloys, (**a**) 0Mo-5.13C, (**b**) 1Mo-5.07C, (**c**) 2Mo-5.01C, (**d**) 2.5Mo-5.0C, (**e**) 2.5Mo-5.3C, (**f**) 2.5Mo-5.45C, (**g**) 2.5Mo-5.75C, (**h**) 2.5Mo-6.1C.

The distribution of WC grains is shown in Figure 6. As Mo content increases from 0 to 2.5%, WC grain size decreases from ~0.85 to ~0.73 μm. It is well known that the growth and coarsening of WC grains are caused by the Ostwald ripping mechanism. The addition of molybdenum can reduce the solubility of WC in the liquid phase, thus preventing the growth of WC in the liquid phase [20]. Furthermore, Mo precipitates on WC particles, leading to the formation of (W, Mo) C solid solution [16], which slows down the dissolution of WC in the liquid phase, thus inhibiting the dissolution and growth of WC particles.

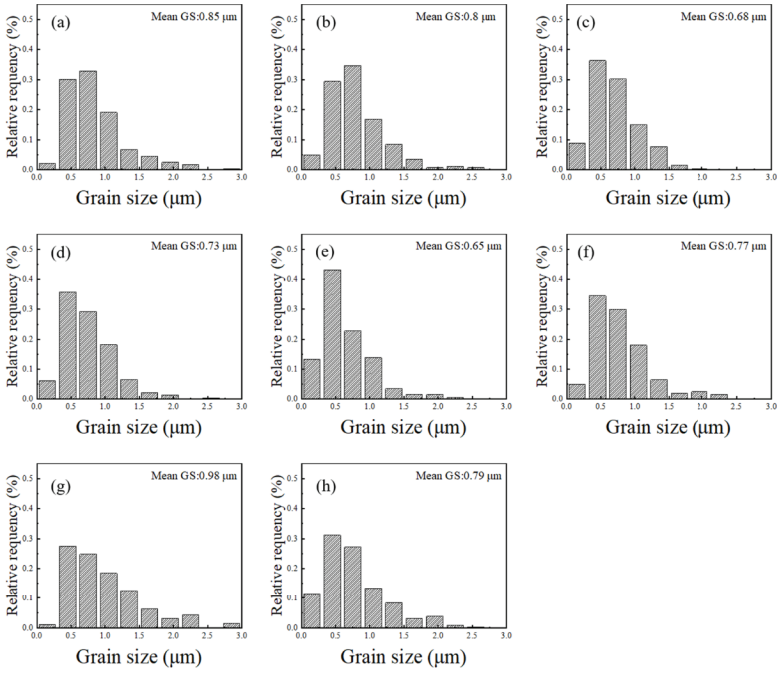

Figure 6. The grain size distribution in WC-13Co with different additions of Mo and C, (**a**) 0Mo-5.13C, (**b**) 1Mo-5.07C, (**c**) 2Mo-5.01C, (**d**) 2.5Mo-5.0C, (**e**) 2.5Mo-5.3C, (**f**) 2.5Mo-5.45C, (**g**) 2.5Mo-5.75C, (**h**) 2.5Mo-6.1C.

In contrast, with the increase of carbon black content from 0 to 0.75%, the WC grain size increases from ~0.73 μm to ~0.98 μm. High-carbon content can promote the WC coarsening [21], but with the further increase of carbon black to 1.1%, the WC grain size decreases to ~0.79 μm. Wei et al. [22] also observed a similar phenomenon, which can be explained by the existence of free carbon in the high-carbon content. The free carbon hinders the solid solution of W and C atoms in the Co phase during liquid phase sintering, which is beneficial to suppress the coarsening of grains during sintering.

The eta phase in the 2.5Mo-5.0C sample was further analyzed by EDS as exhibited in Figures 7 and 8. Surprisingly, it is in the eta phase that the Mo element is mainly enriched in the 2.5Mo-5.0C sample as shown in Figures 7b and 8b. The black binder phase is mainly composed of the Co and W elements. Therefore, in the process route of preparing WC-13Co cemented carbide by powder metallurgy with WC and Co powders as raw materials, when Mo powder is contained in the raw materials, Mo is mainly concentrated in the eta phase if sintering in low-carbon content.

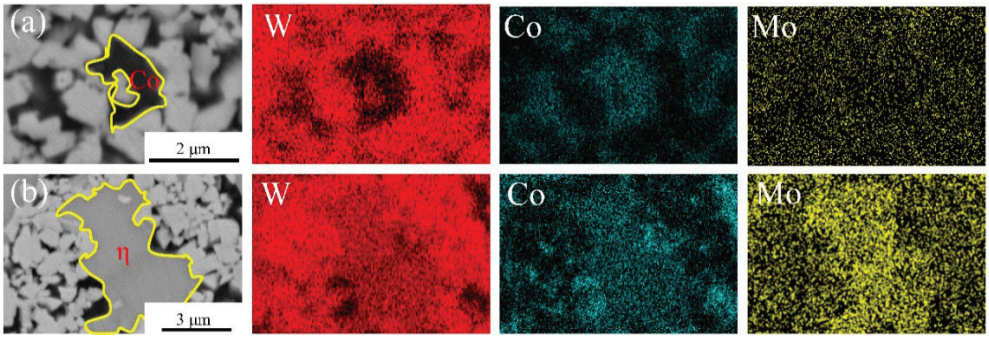

Figure 7. Mapping of elements distribution of the 2.5Mo-5.0C sample. (**a**) Co phase and (**b**) eta phase.

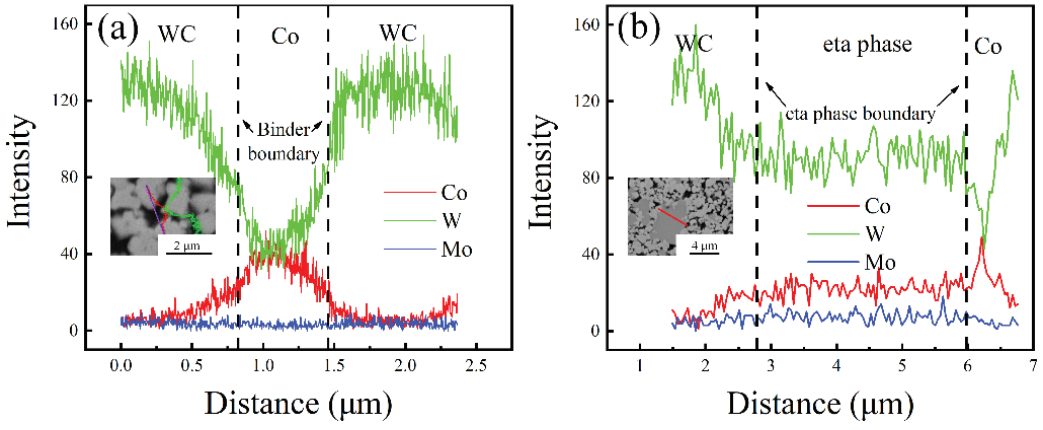

Figure 8. Elements distribution of (**a**) Co phase and (**b**) eta phase in the 2.5Mo-5.0C sample.

It is worth noting that some large black particles are observed in Figure 5g. Its composition was analyzed by EDS in Figure 9. The results show that this large particle is enriched with Mo and C. According to the X-ray analysis in Figure 2, this large black particle should be the Mo_2C. It can be seen from Figure 5 that such large spherical particles are a low-frequency occurrence. Guo [7] observed that a small-sized Mo_2C phase forms by the reaction of Mo and C at about 900 °C during the sintering process of WC-6Co alloys. Figure 9 also indicates that a large amount of Mo is enriched in the eta phase in the

2.5Mo-5.75C sample, which is consistent with the observation results of the eta phase of the 2.5Mo-5.0C sample as shown in Figures 7 and 8.

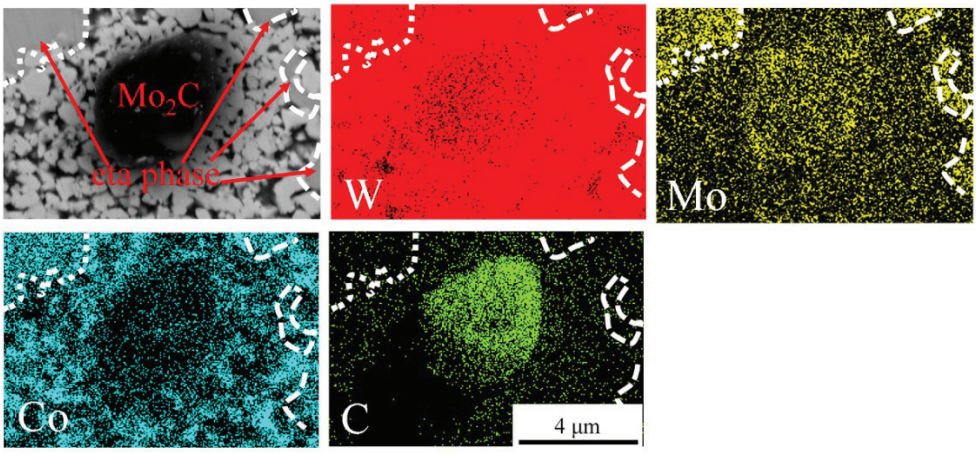

Figure 9. Mapping of element distribution of the 2.5Mo-5.75C sample.

Figure 10 compares the Mo $3d_{3/2}$ and Mo $3d_{5/2}$ XPS spectra of 2.5Mo-5.0C and 2.5Mo-6.1C samples. The main peak of the 2.5Mo-5.0C sample is characterized by Mo $3d_{3/2}$ and Mo $3d_{5/2}$ features at 228.43 and 232.56 eV, while the main peak of 2.5Mo-6.1C sample is characterized by Mo^{2+} $3d_{3/2}$ and Mo^{2+} $3d_{5/2}$ features at 228.05 [23] and 231.27Ev [24] and [25]. Based on the data of XPS, the percentage content of Mo with different valence states was estimated. The fraction of Mo^{2+} and Mo is about 69% and 31% in the 2.5Mo-6.1C sample. Considering the XRD analysis in Figure 2, Mo^{2+} mainly exists in Mo_2C. It should be pointed out that it is useful to estimate the approximate proportion of these atoms and ions according to the statistical theory, although this estimation cannot accurately describe the percentage content of Mo^{2+} and Mo.

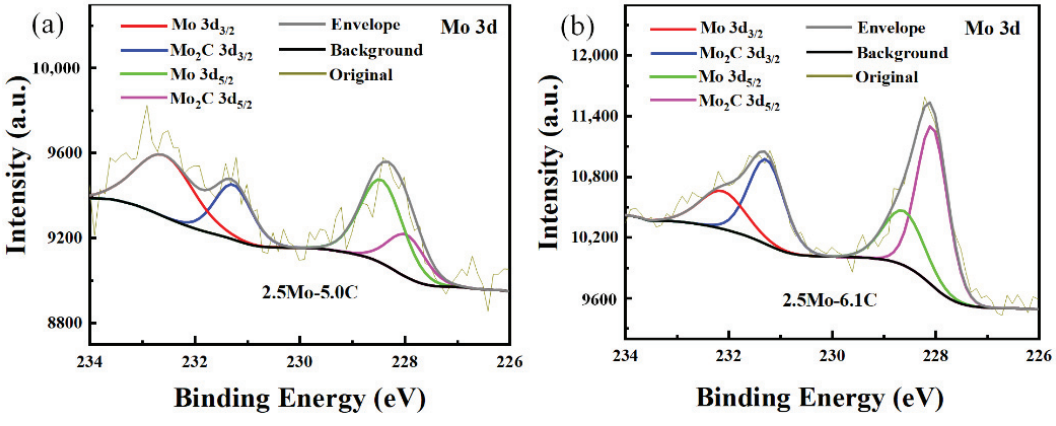

Figure 10. XPS survey spectra of 2.5Mo-5.0C (**a**) and 2.5Mo-6.1C (**b**) samples.

To sum up, when Mo is added to WC-Co cemented carbide, the content of C determines its existing state. In low-carbon contents, Mo is mainly distributed in the eta phase, partially replacing the positions of W and Co atoms. When the eta phase is formed, Mo can infinitely replace W, forming an infinite solid solution and Mo is not observed in the Co binder phase. According to the reports [17], the radius of W and Mo atomic is very close (W: 1.37 Å,

Mo: 1.36 Å). In a high-carbon environment, the Mo element preferentially exists in Mo_2C, and a small amount of Mo appears in the eta phase partially replacing the lattice position of W and Co.

3.2. Mechanical Properties

Figure 11 illustrates the hardness and fracture toughness of all samples. The alloy without adding Mo has the lowest hardness value. When the Mo content increases from 0 to 2.5%, the eta phase grows abnormally and the area fraction of the eta phase significantly increases to 40%, leading to an obvious increase in hardness from 1232 HV_{30} to 1321 HV_{30}, and the decrease in fracture toughness from 12.5 MPa·$m^{1/2}$ to 9.8 MPa·$m^{1/2}$. This is different from the experimental results of Wang [20]. They found that the increase of Mo improved the fracture toughness because Mo slows down the transformation from FCC-Co to HCP-Co. From Figures 5, 7 and 8, it is deduced that Mo is mainly concentrated in the eta phase in the samples of 0Mo-5.13C, 1Mo-5.07C, 2Mo-5.01C, and 2.5Mo-5.0C. The appearance of a large-sized eta phase is harmful to fracture toughness.

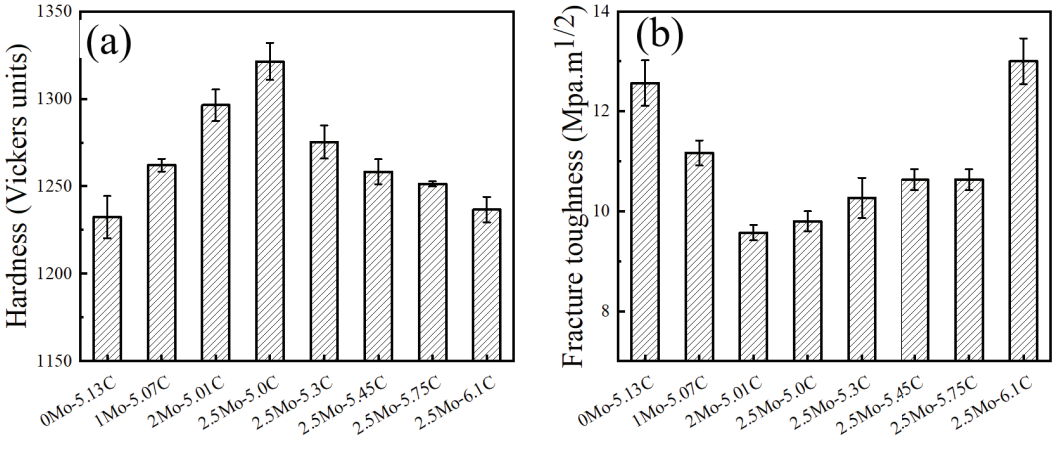

Figure 11. The hardness (**a**) and fracture toughness of different cemented carbides (**b**).

After adding carbon black to samples with 2.5% Mo added, the eta phase was restrained. Compared with the fracture toughness of 9.8 MPa·$m^{1/2}$ in the 2.5Mo-5.0C sample without adding carbon black, the fracture toughness of the 2.5Mo-6.1C sample increased by about 32%. The fracture toughness and hardness of the 2.5Mo-6.1C sample are slightly higher than those of the 0Mo-5.13C sample, which is very important to the preparation of WC-Co cemented carbide containing Mo for improving the corrosion resistance.

The hardness of WC–Co cemented carbides is strongly dependent on the content of the Co binder [26], the grain size of WC, and the eta phase [27]. The eta phase enhances the WC–Co but decreases the toughness. After the addition of 1%, 2%, or 2.5% Mo, a large amount of Co reacts and converts to the eta phase, which leads to the decrease of the Co binder phase, the decrease of grain size (Figure 6), and the increase of eta (Figures 4 and 5). All of these factors lead to the increase in the hardness of the cemented carbide. Therefore, the hardness increases with the increase of Mo content in Figure 11. However, after adding carbon black, the content of the eta phase decreases, the content of the Co binder increases, the grain size increases, and the hardness decreases. It should be noted that the sample of 2.5Mo-6.1C also has a small grain size, but its hardness is low, which is mainly due to the large reduction of the eta phase and the increase of the proportion of the Co binder phase. The fracture toughness of WC–Co cemented carbides is chiefly affected by the free path of the Co binder phase [28]. It can be seen from Figure 5 that the distribution of the Co phase is relatively uniform, thus the higher the content of the Co phase, the better the fracture

toughness. The specimen prepared with the carbon addition of 1.1 wt.% has the lowest content of eta and the highest fracture toughness of 13 MPa·m $^{1/2}$.

Figure 12 demonstrates crack propagation in 0Mo-5.13C and 2.5Mo-5.0C, which have higher and lower fracture toughness, respectively. The length of the crack affects the calculation of the value of fracture toughness. In Figure 12a, the type of crack propagation includes intergranular and transgranular fractures [29]. More cracks in the 0Mo-5.13C sample are extended between WC particles, while the large-sized eta phase in the 2.5Mo-5.0C sample leads to the formation of long flat transgranular cracks as shown in Figure 12b, which significantly reduces the fracture toughness [30].

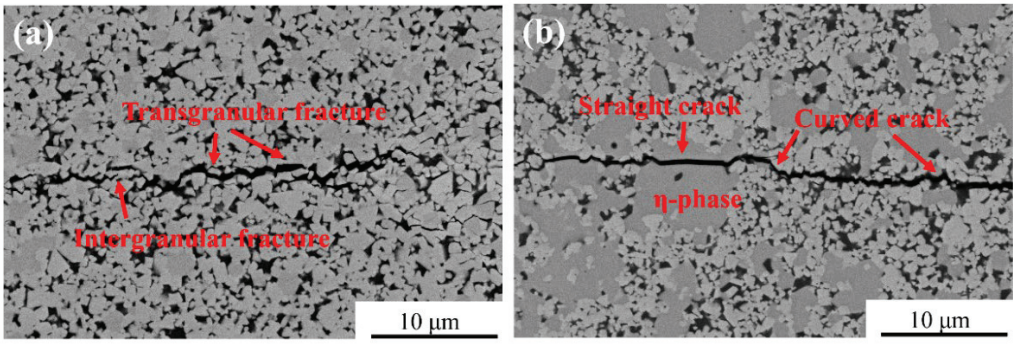

Figure 12. Crack microstructure of (**a**) 0Mo-5.13C, and (**b**) 2.5Mo-5.0C samples.

3.3. Influence Mechanism of the Addition of Mo

According to the Ostwald ripening mechanism, WC grains will grow gradually due to the dynamic balance of dissolution and precipitation of WC in the Co binder phase when WC-Co cemented carbide is prepared by liquid phase sintering. Wang et al. [20] pointed out that the addition of Mo precipitates on the surface of WC grains, thus hindering the growth of WC grains and resulting in the refinement of the WC grains of sintering WC-Co cemented carbides. In this study, it is found that Mo has more influence on the development of the phases in both low-carbon and high-carbon contents. In low-carbon content, Mo mainly concentrates in the eta phase, as shown in Figures 5 and 7, and Mo significantly promotes the development of the eta phase. In a high-carbon environment, Mo mainly exists in the Mo_2C phase, as shown in Figures 2 and 10. In contrast, the addition of Mo has relatively less effect on the size of WC grains.

Moreover, Guo et al. [7] reported on the small-sized Mo_2C formed by the reaction between Mo and C in WC-Co alloys, and that most of them are distributed in the Co binder phase. Different from the reports, it is observed in Figure 9 that some Mo_2C particles with larger sizes above 3 μm form by the reaction of Mo and C, although the number of large-sized Mo_2C particles is very small. It is inferred that the reduction of the size of Mo powder in raw materials is helpful to eliminate the large-sized Mo_2C particle.

Based on the above analysis, Figure 13 illustrates the reaction diagram in the heating process of sintering: (i) for the Composition Design I without adding Mo, the alloy is composed of the WC grain, the Co binder, and eta phase after sintering in the low-carbon contents; (ii) for the Composition Design II of adding Mo powder in the sample with low-carbon content, the eta phase of [W, Co, Mo] C forms by the reaction of Mo, Co, and WC when the temperature rises to 900–1100 °C, and Mo mainly concentrates in the eta phases; (iii) for the Composition Design III of adding Mo powder and sintering in a high-carbon environment, the Mo_2C preferentially forms by the reaction of Mo and C at 900–1100 °C and the remaining part of Mo mainly exists in the eta phase of [W, Co, Mo] C after sintering.

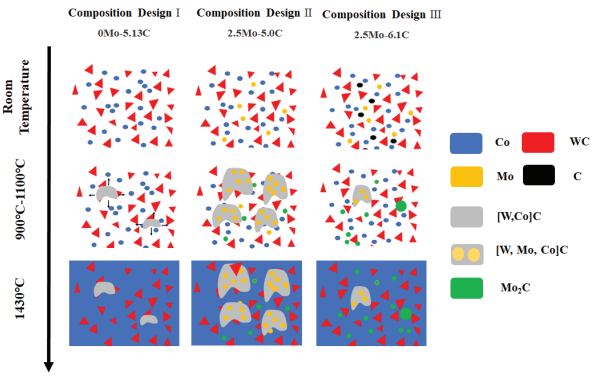

Figure 13. The reaction diagram in the heating process of sintering in WC-Co cemented carbides adding different contents of Mo and C.

4. Conclusions

The addition of Mo in WC-13Co cemented carbides has an obvious impact on the composition, size, and distribution of the eta phase and Mo_2C phase, and shows different results in low-carbon and high-carbon contents.

Without the addition of Mo, the eta phase of the WC-13Co cemented carbides is composed of the elements of Co, W, and C. After adding 2.5% Mo in low-carbon contents, the eta phase is composed of Co, W, Mo, and C. With the increase of Mo content from 0 to 2.5% in WC-13Co cemented carbides, the Mo-enriched eta phase grows abnormally and the area fraction of the eta phase significantly increases from 19.4% to 40%, leading to an obvious increase in hardness from 1232 HV_{30} to 1321 HV_{30}, and the decrease in fracture toughness from 12.5 $MPa{\cdot}m^{1/2}$ to 9.8 $MPa{\cdot}m^{1/2}$. With the increase of carbon black content from 0 to 1.1% in WC-13Co-2.5Mo cemented carbides, the formation of the eta phase is inhibited and a small number of large-sized Mo_2C occurs. The fracture toughness clearly increases from 9.8 $MPa{\cdot}m^{1/2}$ to 13 $MPa{\cdot}m^{1/2}$ while the hardness decreases from 1321 HV_{30} to 1237 HV_{30}.

In view of the beneficial effect of Mo addition on mechanical properties and corrosion resistance of WC-Co cemented carbides found in previous reports, it is believed that this work can contribute to the control of the eta phase of WC-Co cemented carbides containing Mo for industrial production.

Author Contributions: Conceptualization, J.L. and V.J.; methodology, J.L. and X.L.; formal analysis, X.L.; investigation, X.L. and X.Z.; resources, X.Z., J.Z. and Q.Z.; writing—original draft preparation, X.L.; writing—review and editing, J.L. All authors have read and agreed to the published version of the manuscript.

Funding: This work was funded by the Fundamental Research Funds for the Central Universities (No. N2002008), and the Science and Technology Plan Project of Shenfu Demonstration District (2021JH05).

Institutional Review Board Statement: Not applicable.

Informed Consent Statement: Not applicable.

Data Availability Statement: Not applicable.

Conflicts of Interest: The authors declare no conflict of interest.

References

1. Lu, Z.; Du, J.; Sun, Y.; Su, G.; Zhang, C.; Kong, X. Effect of ultrafine WC contents on the microstructures, mechanical properties and wear resistances of regenerated coarse grained WC-10Co cemented carbides. *Int. J. Refract. Met. Hard Mater.* **2021**, *97*, 105516. [CrossRef]
2. Rayón, E.; Bonache, V.; Salvador, M.D.; Roa, J.J.; Sánchez, E. Hardness and Young's modulus distributions in atmospheric plasma sprayed WC–Co coatings using nanoindentation. *Surf. Coat. Technol.* **2011**, *205*, 4192–4197. [CrossRef]

3. Li, J.; Cheng, J.; Chen, P.; Chen, W.; Wei, B.; Liu, J. Effects of partial substitution of copper for cobalt on the microstructure and properties of ultrafine-grained WC-Co cemented carbides. *J. Alloys Compd.* **2018**, *735*, 43–50. [CrossRef]
4. Fazili, A.; Derakhshandeh, M.R.; Nejadshamsi, S.; Nikzad, L.; Razavi, M.; Ghasali, E. Improved electrochemical and mechanical performance of WC-Co cemented carbide by replacing a part of Co with Al_2O_3. *J. Alloys Compd.* **2020**, *823*, 153857. [CrossRef]
5. Yu, B.; Li, Y.; Lei, Q.; Nie, Y. Microstructures and mechanical properties of WC-Co-xCr-Mo cement carbides. *J. Alloys Compd.* **2019**, *771*, 636–642. [CrossRef]
6. Lin, N.; Wu, C.H.; He, Y.H.; Zhang, D.F. Effect of Mo and Co additions on the microstructure and properties of WC-TiC-Ni cemented carbides. *Int. J. Refract. Met. Hard Mater.* **2012**, *30*, 107–113. [CrossRef]
7. Guo, Z.; Xiong, J.; Yang, M.; Song, X.; Jiang, C. Effect of Mo_2C on the microstructure and properties of WC–TiC–Ni alloy. *Int. J. Refract. Met. Hard Mater.* **2008**, *26*, 601–605. [CrossRef]
8. Genga, R.M.; Cornish, L.A.; Akdogan, G. Effect of Mo_2C additions on the properties of SPS manufactured WC–TiC–Ni alloys. *Int. J. Refract. Met. Hard Mater.* **2013**, *41*, 12–21. [CrossRef]
9. Lin, Z.; Xiong, J.; Guo, Z.; Zhou, W.; Wan, W.; Yang, L. Effect of Mo_2C addition on the microstructure and fracture behavior of (W, Ti) C-based alloys. *Ceram. Int.* **2014**, *40*, 16421–16428. [CrossRef]
10. Guo, S.; Bao, R.; Yang, J.; Chen, H.; Yi, J. Effect of Mo and Y_2O_3 additions on the microstructure and properties of fine WC-Co cemented carbides fabricated by spark plasma sintering. *Int. J. Refract. Met. Hard Mater.* **2017**, *69*, 1–10. [CrossRef]
11. Ban, Z.G.; Shaw, L.L. On the reaction sequence of WC–Co formation using an integrated mechanical and thermal activation process. *Acta Mater.* **2001**, *49*, 2933–2939. [CrossRef]
12. Guillermet, A.F. Thermodynamic properties of the Co-W-C system. *Metall. Trans. A* **1989**, *20*, 935–956. [CrossRef]
13. Markström, A.; Frisk, K.; Sundman, B. A revised thermodynamic description of the Co-W-C system. *J. Phase Equilib. Diffus.* **2005**, *26*, 152–160. [CrossRef]
14. Janusz, L. Positions of the carbon atoms in Fe_6W_6C. *J. Less Common Met.* **1964**, *7*, 318–320.
15. Janisch, D.S.; Garel, M.; Eder, A.; Lengauer, W.; Dreyer, K.; van den Berg, H. Sintering, characterization, and analysis of functional gradient hardmetals. *Int. J. Refract. Met. Hard Mater.* **2008**, *26*, 179–189. [CrossRef]
16. Liu, N.; Xu, Y.; Li, Z.; Chen, M.; Li, G.; Zhang, L. Influence of molybdenum addition on the microstructure and mechanical properties of TiC-based cermets with nano-TiN modification. *Ceram. Int.* **2003**, *29*, 915–925. [CrossRef]
17. Zhou, Y.; Lin, Y.; Zhang, F.; Jiang, Y.; Wei, S.; Xu, L.; Chong, X.; Li, Z.; Feng, J. Lattice stability, mechanical and thermal properties of a new class of multicomponent (Fe, Mo, W)$_6$C η carbides with different atomic site configurations. *Ceram. Int.* **2022**, *48*, 5107–5118. [CrossRef]
18. Rabouhi, H.; Khelfaoui, Y.; Khireddine, A. Comparative study by image analysis of WC-Co alloys elaborated by liquid phase sintering and hot isostatic pressing. *Int. Inform. Eng. Technol. Assoc.* **2020**, *44*, 263–269. [CrossRef]
19. Tang, Y.; Wang, S.; Xu, F.; Hong, Y.; Luo, X.; He, S.; Chen, L.; Zhong, Z.; Chen, H.; Xu, G.; et al. Effect of carbon content on the properties of inhomogeneous cemented carbides with fine-grained structures produced via one-step transformation. *J. Alloys Compd.* **2021**, *882*, 160638. [CrossRef]
20. Wang, Y.; Liu, W.; Zhong, C.; Wu, J.; Ye, Y. Effects of partial substitution of Cu for Co on the microstructure and properties of WC-Co-Mo cemented carbides. *Ceram. Int.* **2021**, *47*, 13519–13527. [CrossRef]
21. Konyashin, I.; Hlawatschek, S.; Ries, B.; Lachmann, F.; Dorn, F.; Sologubenko, A.; Weirich, T. On the mechanism of WC coarsening in WC–Co hard metals with various carbon contents. *Int. J. Refract. Met. Hard Mater.* **2009**, *27*, 234–243. [CrossRef]
22. Wei, C.; Song, X.; Fu, J.; Lv, X.; Wang, H.; Gao, Y.; Zhao, S.; Liu, X. Effect of Carbon Addition on Microstructure and Properties of WC–Co Cemented Carbides. *J. Mater. Sci. Technol.* **2012**, *28*, 837–843. [CrossRef]
23. Perret, N.; Wang, X.; Delannoy, L.; Potvin, C.; Louis, C.; Keane, M.A. Enhanced selective nitroarene hydrogenation over Au supported on β-Mo_2C and β-Mo_2C/Al_2O_3. *J. Catal.* **2012**, *286*, 172–183. [CrossRef]
24. Weigert, E.C.; Esposito, D.V.; Chen, J.G. Cyclic voltammetry and X-ray photoelectron spectroscopy studies of electrochemical stability of clean and Pt-modified tungsten and molybdenum carbide (WC and Mo_2C) electrocatalysts. *J. Power Sources* **2009**, *193*, 501–506. [CrossRef]
25. Hara, Y.; Minami, N.; Itagaki, H. Synthesis and characterization of high-surface area tungsten carbides and application to electrocatalytic hydrogen oxidation. *Appl. Catal. A-Gen.* **2007**, *323*, 86–93. [CrossRef]
26. Tabrizi, A.T.; Pouzesh, M.; Laleh, F.F.; Aghajani, H. Evaluation of the corrosion resistance of WC-Co coating on AZ91 applied by electro spark deposition. *Powder Metall. Prog.* **2020**, *20*, 30–40. [CrossRef]
27. Da Costa, F.A.; De Medeiros, F.F.P.; Da Silva, A.G.P.; Gomes, U.U.; Filgueira, M.; De Souza, C.P. Structure and hardness of a hard metal alloy prepared with a WC powder synthesized at low temperature. *Mater. Sci. Eng. A* **2008**, *485*, 638–642. [CrossRef]
28. Fang, Z.; Griffo, A.; White, B.; Lockwood, G.; Belnap, D.; Hilmas, G.; Bitler, J. Fracture resistant super hard materials and hardmetals composite with functionally designed microstructure. *Int. J. Refract. Met. Hard Mater.* **2001**, *19*, 453–459. [CrossRef]
29. Chang, S.H.; Chang, M.H.; Huang, K.T. Study on the sintered characteristics and properties of nanostructured WC–15 wt.% (Fe–Ni–Co) and WC–15 wt.% Co hard metal alloys. *J. Alloys Compd.* **2015**, *649*, 89–95. [CrossRef]
30. Pristinskiy, Y.; Peretyagin, N. Comparative studies on mechanical properties of WC-Co composites sintered by SPS and conventional techniques. *MATEC Web Conf.* **2017**, *129*, 02028. [CrossRef]

coatings

MDPI

Article

Influence of the Nitrogen Flux Ratio on the Structural, Morphological and Tribological Properties of TiN Coatings

Xiaojing Fu [1,2], Shuming Guo [1,2], Yong Wan [3,*], Qiang Li [1,2], Bingchang Liu [1,2] and Hui Zheng [1,2]

[1] Shandong Provincial University Laboratory for Protected Horticulture, Weifang University of Science and Technology, Weifang 262700, China
[2] University Featured Laboratory of Materials Engineering for Agricultural Machinery of Shandong Province, Weifang University of Science and Technology, Weifang 262700, China
[3] School of Mechanical Engineering, Qilu University of Technology (Shandong Academy of Sciences), Jinan 250353, China
* Correspondence: wanyong@qlu.edu.cn

Abstract: In this study, the structural characteristics of TiN coatings deposited by DC magnetron sputtering on the surface of AISI 304 stainless steel were modulated by performing deposition at four different nitrogen flux ratios. The XRD results indicated that the coatings mainly contained face-centered cubic TiN phase. The experimental results showed that the nitrogen flux ratio played a major role in determining the microstructure and the mechanical and tribological properties of the TiN coatings. SEM images revealed that the thickness of the TiN coatings decreased linearly as the nitrogen flux ratio increased from 0.25 to 0.55. However, the grain size had a nonlinear relationship with the nitrogen flux ratio. When the nitrogen flux ratio was 0.45, the grain size was only 5.3 nm. Theoretical and experimental analysis showed that the TiN coating deposited at a nitrogen flux ratio of 0.45 had the best mechanical properties, which due to its minimum grain size and (111) orientation, and the best tribological performance under unlubricated conditions, may have been due to its higher fracture toughness and plastic deformation resistance among the four TiN coatings.

Keywords: TiN coatings; nitrogen flux ratio; microstructure; tribological properties

Citation: Fu, X.; Guo, S.; Wan, Y.; Li, Q.; Liu, B.; Zheng, H. Influence of the Nitrogen Flux Ratio on the Structural, Morphological and Tribological Properties of TiN Coatings. *Coatings* **2023**, *13*, 78. https://doi.org/10.3390/coatings13010078

Academic Editor: Ben Beake

Received: 5 November 2022
Revised: 30 December 2022
Accepted: 30 December 2022
Published: 31 December 2022

1. Introduction

Titanium nitride (TiN) coatings have been widely used as wear-protective hard coatings in automobiles, impellers, and cutting cools because of their good mechanical and tribological properties [1–3]. In addition, the high thermal stability, chemical stability and low resistivity of TiN coatings make them widely used not only as protective coatings for mechanical tools, but also in the decoration [4] and micro-electronic industries [5]. Especially with the development of micro-electromechanical systems (MEMS) and precision machinery, the demand for thin TIN coatings with high wear resistance and high hardness of several hundred nanometers thickness has greatly increased. In recent years, TiN has also become commonly used as a protective surface coating for orthopedic implants and cardiac valves [6] due to its excellent biocompatibility and hemocompatibility [7]. These applications require highly dense coatings and have typical deposition temperatures lower than 450 °C [8]. Improving the wear resistance of a surface coating can extend the lifespan of an implant, thus reducing costs to patients. Physical vapor deposition (PVD) is widely utilized for the deposition of TiN coatings to improve the tribological properties of the mechanical components. Among the different PVD methods, DC magnetron sputtering can be used to obtain high-density TiN coatings that generate little gas pollution and strong adhesion between the deposited coating and the substrate [9]. However, most of the problems associated with TiN production are due to its requirements of high voltages and temperatures. Much of the literature has reported the preparation of TiN coatings at high temperatures [10,11]. Gerlach et al. [12] prepared a TiN coating by reactive evaporation

at 1023 K. However, the effects of deposition parameters on the microstructure, and the mechanical and tribological properties of TiN coatings have rarely been studied at low temperatures [13]. The microstructure and properties of a coating can be adjusted by changing the deposition parameters [14]. TiN coatings with a high density and excellent mechanical and tribological properties can be obtained by optimizing the deposition process.

To understand the relationship between the process parameters, microstructure, and properties of TiN coatings deposited at low temperatures, various studies have been carried out. The nitrogen flux ratio during the deposition of a TiN coating influences some major properties of the coatings. Therefore, in this report, TiN coatings were deposited by DC magnetron sputtering to investigate the effect of the nitrogen flux ratio on the structural, morphological and tribological behavior of the low-temperature deposited TiN coatings. The nitrogen flux ratio was varied from 0.25, 0.35, 0.45, to 0.55 under an Ar/N_2 atmosphere at a deposition temperature of 300 °C.

2. Experimental Section

2.1. Deposition of TiN Coatings

Before deposition, the AISI 304 stainless steel samples (Ra = 20 nm) were washed ultrasonically in anhydrous ethanol, petroleum ether, and deionized water for 15 min each and then dried with nitrogen for later use. DC magnetron sputtering of a Ti target (99.9%) was used to prepare TiN coatings on the cleaned samples. When the pressure inside the sputtering chamber stabilized at the set value of 4.0×10^{-3} Pa, the specimens were etched with Ar^+ for 20 min at a low-duty cycle (30%) and a high bias voltage (−800 V). During the deposition stage, the flow rate of argon gas (99.9%) was 60 mL/min, and the working pressure was approximately 5.0×10^{-1} Pa at −50 V and 7 A. First, a Ti transition layer was sputtered on the flats for 15 min, and then the nitrogen flow was turned on. At that moment, the sputtering chamber contained a mixture of Ar and N_2 (99.9%) with different nitrogen flux ratios $R(N_2) = f(N_2)/f(Ar + N_2)$, and the pressure was maintained at 5×10^{-1} Pa by adjusting the grating. Deposition was continued at a constant temperature of 300 °C for 4 h. The TiN coatings obtained at $R(N_2)$ = 0.25, 0.35, 0.45 and 0.55 were denoted as TiN-0.25, TiN-0.35, TiN-0.45 and TiN-0.55, respectively.

2.2. Characterization of TiN Coatings

The phase structure of the TiN coatings was characterized by X-ray diffraction (XRD, Bruker, Karlsruhe, Germany) using Cu Kα radiation. Small-angle glancing mode (1.5°) with scattering angles from 20 to 90° was used to avoid interference by the substrate peaks. Scanning electron microscopy (SEM, MERLIN Compact, Jena, Germany) was used to characterize the surface, abrasion, and cross-sectional morphology of the TiN coatings. The surface morphology and roughness of the samples were investigated with atomic force microscopy (AFM, Bruker, Karlsruhe, Germany). The chemical composition of wear scars was analyzed by energy-dispersive X-ray spectroscopy (EDS, MERLIN Compact, Jena, Germany). The adhesion between the TiN coatings and the substrate was measured using a UMT-3 (CETR, Bruker, Rheinstetten, Germany) with a load range of 0–30 N and scratch length of 3 mm. The device collected the acoustic signal of the peeling coatings to determine the critical load (L_c) of coating adhesion. It is generally believed that there are at least two stages during the deformation and failure of a coating. The former represents the loading force when a coating peels for the first time (L_{c1}), and the latter represents the loading force when the coating is completely peeled off (L_{c2}) [15].

Tribological properties of the TiN coating were assessed by UMT-3 under unlubricated conditions. The tests were carried out in ball-on-flat reciprocating mode using a GCr15 ball with a diameter of 9.525 mm at room temperature (20 ± 5 °C) and a relative humidity of 70 ± 5%. Before the test, samples and balls were cleaned ultrasonically in acetone for 15 min. During the tribological experiments, the stroke was 6 mm, the frequency was 2 Hz and the normal load was 20 N with a maximum Hertzian contact pressure of 1.45 GPa. To ensure the reliability of the test results, the same experimental conditions were tested

three times. The friction sensor with a 20 N load was 2.5 mN, which was accurate enough to measure the friction coefficient in the order of millesimals under that load.

3. Results and Discussion

3.1. Microstructure and Morphology of TiN Coatings

The XRD patterns of the substrate and TiN coatings deposited at different $R(N_2)$ are shown in Figure 1. The peaks at diffraction angles of 36.8, 42.6, 62.1 and 73.8° corresponded to TiN(111), TiN(200), TiN(220), and TiN(222), respectively. The XRD pattern of the TiN coatings showed that the four coatings mainly existed as face-centered cubic TiN phase (JCPDS-ICDD NO. 87-0629). The TiN-0.25, TiN-0.35 and TiN-0.45 coatings showed two strong peaks for TiN(111) and TiN(200), and another relatively weak peak for TiN(220). For the TiN-0.45 coating, the strongest peak was at 36.8°, illustrating that the TiN coating preferred the (111) orientation. The sharp peak indicated good crystallinity [16]. Some theories and hypotheses state that the preferred orientation of TiN depends on the lowest total energy, which is the result of competition between strain energy and surface energy [17]. When $R(N_2)$ was small, the TiN coating had no obvious preferred orientation, but when $R(N_2)$ gradually increased to 0.45, the sputtering power of the nitrogen was lower than that of Ar, and the average free path and adsorption energy of particles decreased upon increasing $R(N_2)$. The adsorbed atoms did not have enough mobility to move on the surface and migrate to the (111) plane at lower energy position, so they formed columnar structures perpendicular to the surface due to competitive grain growth. When $R(N_2)$ continued to increase to 0.55, the preferred TiN orientation changed from (111) to (200), because upon increasing the nitrogen flux ratio, the degree of nitriding of the coating increased. Its deposition rate decreased, leading to an increase in the surface diffusion capacity of the deposited particles [18]. This is consistent with previous studies [19,20].

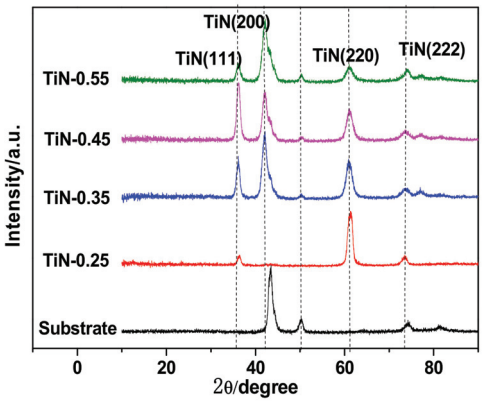

Figure 1. XRD pattern of the TiN coatings.

The texture coefficient, grain size and lattice parameters of the microstructure were calculated from the XRD patterns of the coatings. The texture coefficient (T_c) determining the degree of the preferred orientation was calculated by formula (1) [21]:

$$T_c = \frac{I_{m(hkl)} / I_{0(hkl)}}{1/n \sum_1^n I_{m(hkl)} / I_{0(hkl)}} \quad (1)$$

where $I_{m(hkl)}$ is the integrated intensity of the hkl plane, $I_{0(hkl)}$ is the relative intensity of the hkl plane obtained from the JCPDS card, and n is the number of reflections. As shown in Figure 2, the texture coefficient of the TiN coatings was calculated from their respective XRD patterns using Equation (1). For each $R(N_2)$, the value of n was 4. As the $R(N_2)$

increased, the value of T_c for the TiN(111) orientation increased first and then decreased, in which the largest value of T_c was observed at $R(N_2) = 0.45$.

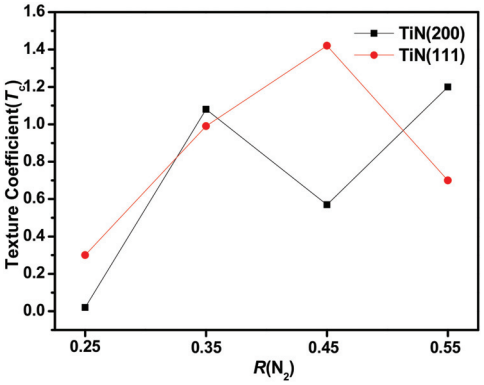

Figure 2. The texture coefficient of the TiN coating at different $R(N_2)$.

Figure 3a depicts the distribution of the lattice parameters of the TiN coatings at different $R(N_2)$. The lattice parameters increased from 4.240 Å to 4.266 Å as $R(N_2)$ increased from 0.25 to 0.55 (JCPDS No.87-0629), obtained using MDI Jade 6 software [22]. In this report, the resulting increase in the lattice parameters is consistent with previous reports [23,24]. The lattice parameter is generally 4.240 Å at ambient temperature. Soudgren et al. proposed that lower lattice parameters may be attributed to a reduction in the ratio of N and Ti in the TiN coatings [23].

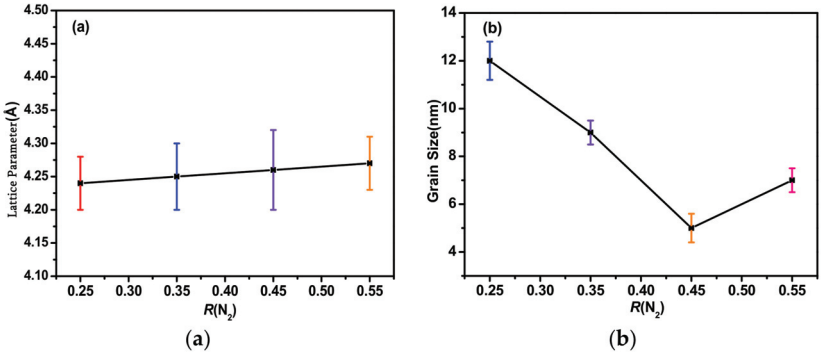

Figure 3. (**a**) Lattice parameter and (**b**) grain size of the TiN coating at different $R(N_2)$.

Scherer's formula was used to calculate the grain size of the TiN coatings [25].

$$D = \frac{0.9\lambda}{B\cos\theta} \quad (2)$$

where λ is the wavelength of the X-ray source (1.54056 Å), B is the FWHM of diffraction lines, and θ is the diffraction angle. The grain size approximately showed a decreasing trend as the nitrogen flux ratio increased, as shown in Figure 3b. This was because the mobility of the deposited atoms decreased, resulting in less diffusion. On the other hand, the sputtering energy of the atoms decreased as the sputtering rate decreased under a high nitrogen flux ratio. The formation of nanoparticles in the coating is affected by the ion energy, ion flux, trace impurities, texture and other factors [26]. Adatoms with low energy had less mobility to slip on the surface, and were dispersed across the grains and grain

boundaries to form coarse grains. Therefore, the grain size of the TiN coating decreased as the nitrogen flux ratio increased. However, when $R(N_2)$ was 0.55, the grain size of the TiN coating increased, and agglomerated particles appeared due to the random Brownian motion of the particles. This made it possible for the particles to collide and adhere directly at a high nitrogen flux ratio [27].

Figure 4 shows the surface morphology and cross-sectional FESEM micrographs (insert) of the TiN coatings. The deposit rates of the TiN coatings were calculated based on the thickness and deposit time. The largest and smallest values were 4.3 nm/min and 2.8 nm/min at $R(N_2)$ = 0.25 and 0.55, respectively. The thickness of the TiN coatings decreased linearly as the nitrogen flux ratio increased from 0.25 to 0.55 because the sputtering rate of Ti decreased as the nitrogen flux ratio increased [28].

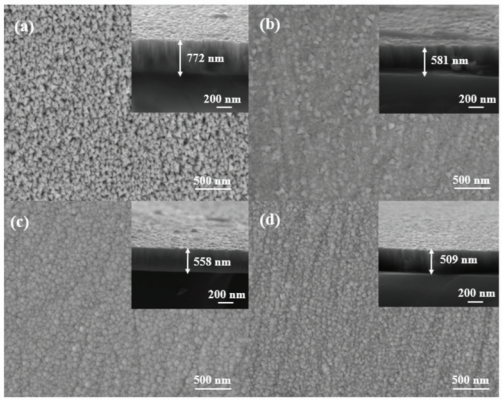

Figure 4. Surface morphology and cross-sectional images (insert) of (**a**) TiN-0.25 (**b**) TiN-0.35 (**c**) TiN-0.45 (**d**) TiN-0.55 coatings.

The surface morphology of the TiN coatings changed obviously at different nitrogen flux ratios. As shown in Figure 4a, the grains of the TiN-0.25 coating showed a tri-pyramid shape and uneven particle size with large gaps. When the nitrogen flux ratio increased, the particles size became smaller, and the structure became denser (Figures 4 and 5). However, when $R(N_2)$ increased to 0.55, large particles reappeared, which is consistent with changes in the grain size. Combining Figures 1 and 4 shows that the preferred orientation changed from (200) to (111), the surface of the coating became uniform, and dense particles with a clear interface formed. Hence, the TiN-0.45 coating exhibited a dense columnar microstructure with well-defined grain boundaries.

3.2. Mechanical Performance of TiN Coatings

The mechanical properties of the TiN coatings measured by nano-indentation tests are shown in Table 1. Nano-indentation is a common method for determining the Young's modulus of coatings. The accuracy of the test is strongly influenced by the surface quality of the material [29], so the roughness and grain size differences of the coating surface may be the main reason for the large deviations in its elastic modulus and hardness. The hardness and elastic modulus of the TiN coatings dramatically decreased as the nitrogen flux ratio increased. The mechanical properties of the coatings were affected by grain size, internal microstress, orientation, and other factors. According to the Hall–Petch relationship, the hardness of the material is inversely proportional to the grain size [30]. Combined with the results of the previous grain size calculations, our conclusions are consistent with this relationship. The TiN-0.45 coating had the greatest hardness and elastic modulus of 26.1 GPa and 329.5 GPa, respectively, which was similar to most of the previous studies on TiN [31]. One previous study [32] indicated that the (111) texture coefficient is a key factor of coating hardness, which is due to the hardest orientation of TiN being (111).

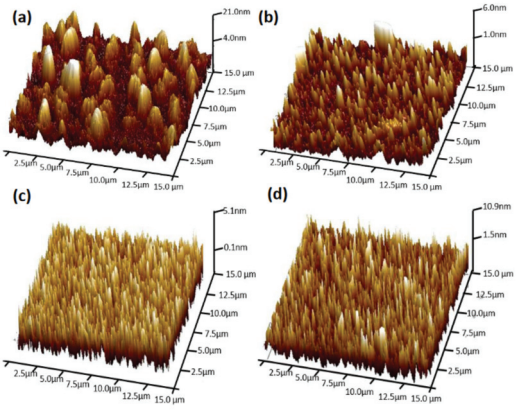

Figure 5. Three-dimensional representation (15 × 15 µm^2) of the surface morphology of the (**a**) TiN-0.25 (**b**) TiN-0.35 (**c**) TiN-0.45 (**d**) TiN-0.55 coating.

Table 1. Mechanical properties of the TiN coatings.

$R(N_2)$	Roughness (nm)	Hardness (GPa)	Elasticity modulus (GPa)	H/E	H^3/E^2 (GPa)
0.25	26.03 ± 0.15	18.50 ± 4.10	278.0 ± 28.7	0.067 ± 0.008	0.082 ± 0.012
0.35	6.81 ± 0.12	23.32 ± 2.21	315.2 ± 31.1	0.074 ± 0.012	0.128 ± 0.017
0.45	1.46 ± 0.08	26.14 ± 2.07	329.5 ± 28.7	0.080 ± 0.007	0.165 ± 0.025
0.55	3.90 ± 0.14	20.87 ± 3.52	296.8 ± 30.1	0.007 ± 0.006	0.103 ± 0.009

Figure 6 shows the adhesion results of the TiN coating. The magnitude of the acoustic signal depended on the peeling of the coating. The location of the first crack (L_{c1}) was determined by combining the acoustic signal and the scratch morphology of the TiN coating at $R(N_2)$ = 0.25, 0.35, 0.45 and 0.55, which occurred at 1.8, 3.1, 13.6 and 7.8 N, respectively. The loads at which the coating completely peeled off (L_{c2})) were 2.3, 5.0, 17.2 and 8.8 N, respectively. This suggests that the adhesion between the TiN coating and steel substrate increased and then decreased with the increase in nitrogen flux ratio. The adhesion was influenced by the thickness, microstrain and atomic arrangement [33]. When $R(N_2)$ was less than 0.45, the microstrain increased, and the film thickness decreased. Therefore, the thickness overcame the effect of microstrain and improved the adhesion. As the nitrogen flux ratio continued to increase, the energy of the adsorbed atoms decreased, so atoms were severely attenuated, the compactness of the coating decreased, and the microstrain increased. Combined, these effects reduced the adhesion of the TiN coatings. As shown in Figure 6c, the TiN-0.45 coating had a few chips in its surface but no significant coating shedding. The L_{c2} of this coating is comparable to the Ti-TiN-multilayer PVD coatings with a thickness of about 2.7 µm [34].

3.3. Tribological Performance

Figure 7 shows the friction coefficient (COF) and wear rates for the uncoated and TiN-coated steel under unlubricated conditions at a load of 20 N. The TiN-coated steel showed a lower COF than the uncoated steel. The most striking case was for the TiN-0.45 coating, which showed the smallest COF of 0.36. Correspondingly, the TiN-0.45 coating possessed the lowest wear rate of 12.4 × 10^{-5} $mm^3N^{-1}m^{-1}$, which was only one-eighth of the uncoated steel (96.8 × 10^{-5} $mm^3N^{-1}m^{-1}$).

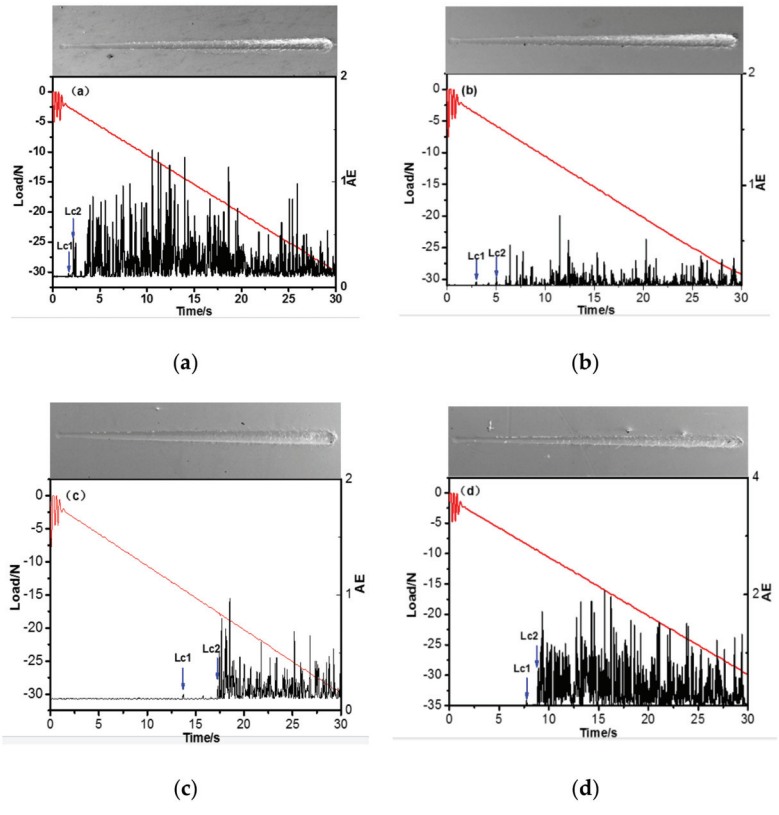

Figure 6. The scratch morphologies and results of scratch test of the (**a**) TiN-0.25 (**b**) TiN-0.35 (**c**) TiN-0.45 (**d**) TiN-0.55 coating. (Red line is load, black line is acoustic emission intensity (AE).)

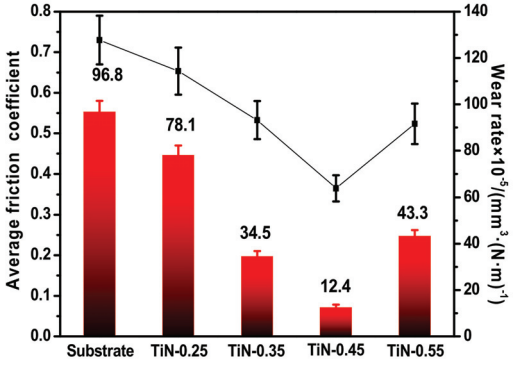

Figure 7. Wear rates and friction coefficient for the steel substrate and the TiN coating sliding against GCr15 steel ball under unlubricated conditions. (Line graph is friction coefficient, and bar graph is wear rates.)

Figures 8 and 9 show SEM images of the morphology of the wear track for flats and dual steel balls after tribological tests at a load of 20 N under unlubricated conditions. For the steel/steel system (Figure 8a), the surface of the wear track on the substrate steel was full of furrows and scratches. The width of the wear track was about 1096.3 μm and the diameter of the grinding steel ball reached 1074.5 μm. The TiN-0.25 coating showed a

wear track surface morphology similar to that of the uncoated steel, indicating that the TiN-0.25 coating was almost worn out. This observation was confirmed by EDS analysis (Table 2), as indicated by the lower number of Ti and N atoms and larger number of Fe atoms inside the wear track. The other TiN coatings showed wear tracks with different surface morphologies. Especially for the TiN-0.45 coating (Figure 8d), a smoother surface was observed for the wear track on both the flat and steel ball, suggesting it had excellent wear resistance. The EDS analysis in Table 2 also supports the SEM observation.

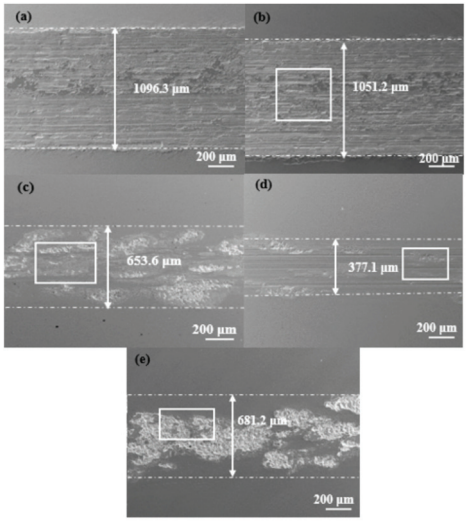

Figure 8. SEM images morphology for wear scars on the (**a**) substrate and TiN coating at $R(N_2)$ of (**b**) 0.25, (**c**) 0.35 (**d**) 0.45 (**e**) 0.55 at load of 20 N under unlubricated conditions. White square is the EDS test area.

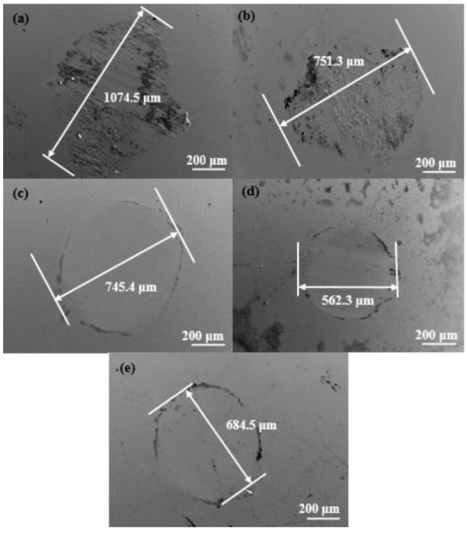

Figure 9. SEM images of morphology for wear scars on the dual ball sliding against (**a**) substrate and TiN coatings at $R(N_2)$ of (**b**) 0.25, (**c**) 0.35 (**d**) 0.45 (**e**) 0.55 at load of 20 N under unlubricated conditions.

Table 2. EDS analysis of the wear scars corresponding to the white frame in Figure 8 of the four TiN coatings under 20 N load under unlubricated conditions.

$R(N_2)$	Element (at.%)			
	Ti	N	Fe	Cr
0.25	22.57	4.40	30.77	42.26
0.35	52.98	24.26	17.94	4.82
0.45	60.45	28.76	10.01	0.78
0.55	56.33	16.81	23.08	3.78

The values of H/E and H^3/E^2 are more suitable for predicting the failure resistance of PVD coatings during unlubricated sliding [35]. A higher value of H/E means that stress can be distributed over a larger area, thereby delaying the failure of a coating. The higher value of H^3/E^2 means a coating possesses greater toughness, thus improving a sample's resistance to mechanical failure. This is consistent with the tribological properties of the TiN coating. Of the four TiN coatings, the TiN-0.45 coating had the largest H/E and H^3/E^2 value and, therefore, the best wear resistance.

4. Conclusions

TiN coatings deposited at different nitrogen flux ratios presented different microstructures and mechanical properties. The effects of nitrogen flux ratio on the microstructure were studied in terms of lattice orientation, grain size and lattice coefficient. The influence of nitrogen flux on the coating deposition rate, elastic modulus, adhesion and other mechanical properties of the TiN coatings was analyzed in detail. The following is a summary of our conclusions:

1. The phase structure of the TiN coatings deposited at $R(N_2)$ = 0.25, 0.35, 0.45, and 0.55 was mainly face-centered cubic TiN. All TiN coatings had obvious columnar crystals. The TiN-0.45 coating possessed the densest columnar microstructure of the four TiN coatings.
2. The nitrogen flux ratio strongly affected the mechanical properties of the coating, and the TiN-0.45 coating had the best mechanical properties (hardness, elasticity modulus, H/E, and H^3/E^2) due to its minimum grain size and (111) orientation. In addition, the thickness of the TiN coating was inversely correlated with $R(N_2)$ and decreased from 772 nm to 509 nm as $R(N_2)$ decreased.
3. The TiN-0.45 coating had the largest values of H/E and H^3/E^2 and, therefore, the best wear resistance among the four TiN coatings.

Author Contributions: Conceptualization, S.G.; Methodology, Y.W. and Q.L.; Investigation, X.F. and S.G.; Data curation, S.G., B.L. and H.Z.; Writing—original draft, X.F.; Supervision, Q.L.; Funding acquisition, X.F. and Y.W. All authors have read and agreed to the published version of the manuscript.

Funding: The authors acknowledge the financial support by National Natural Science Foundation of China (51975304), Scientific Research Funding of Weifang University of Science and Technology, China, under Grant No. KJRC2022011.

Institutional Review Board Statement: Not applicable.

Informed Consent Statement: Not applicable.

Data Availability Statement: Not applicable.

Conflicts of Interest: The authors declare no conflict of interest.

References

1. Xi, Y.; Bai, Y.; Gao, K.; Pang, X.; Yang, H.; Yan, L.; Volinsky, A.A. Residual stress and microstructure effects on mechanical, tribological and electrical properties of TiN coatings on 304 stainless steel. *Ceram. Int.* **2018**, *44*, 15851–15858. [CrossRef]
2. Bobzin, K. High-performance coatings for cutting tools. *CIRP J. Manuf. Sci. Technol.* **2017**, *18*, 1–9. [CrossRef]
3. Sawada, S.; Tamai, T.; Hattori, Y. Effect of contact force on the friction coefficient of electroplated TiN films for automotive applications. *J. Jpn. Inst. Met.* **2009**, *73*, 659–665. [CrossRef]
4. Lousa, A.; Esteve, J.; Mejia, J.P.; Devia, A. Influence of deposition pressure on the structural mechanical and decorative properties of TiN thin films deposited by cathodic arc evaporation. *Vacuum* **2007**, *81*, 1507–1510. [CrossRef]
5. Ma, Y.; Wang, X.; Gu, X.; Zhang, H.; Lu, J.; Liu, H. Fabrication of Metallic Micro-Parts Reinforced with Nano-and Micro-Sized TiN Particles via Laser Shock Processing. *J. Mater. Eng. Perform.* **2022**, *31*, 786–800. [CrossRef]
6. Franks, W.; Schenker, I.; Schmutz, P.; Hierlemann, A. Impedance characterization and modeling of electrodes for biomedical applications. *IEEE Trans. Biomed. Eng.* **2005**, *52*, 1295–1302. [CrossRef]
7. Jeyachandran, Y.; Narayandass, S.; Mangalaraj, D.; Areva, S.; Mielczarski, J. Properties of titanium nitride films prepared by direct current magnetron sputtering. *Mater. Sci. Eng. A* **2007**, *445*, 223–236. [CrossRef]
8. Toth, L.E. *Refractory Materials, Transition Metal Carbides and Nitrides*; Academic Press Inc.: New York, NY, USA, 1971; Volume 7, p. 88.
9. Shukla, K.; Rane, R.; Alphonsa, J.; Maity, P.; Mukherjee, S. Structural, mechanical and corrosion resistance properties of Ti/TiN bilayers deposited by magnetron sputtering on AISI 316L. *Surf. Coatings Technol.* **2017**, *324*, 167–174. [CrossRef]
10. Hua, M.; Ma, H.; Li, J.; Mok, C. Tribological behaviours of patterned PVD TiN spot coatings on M2 steel coated with different bias voltages. *Surf. Coat. Technol.* **2006**, *200*, 3612–3625. [CrossRef]
11. Pihosh, Y.; Goto, M.; Kasahara, A.; Oishi, T.; Tosa, M. Influence of reacting nitrogen gas consistence on the properties of TiN films prepared by rf. magnetron sputtering. *Appl. Surf. Sci.* **2005**, *244*, 244–247. [CrossRef]
12. Gerlach, J.; Höche, T.; Frost, F.; Rauschenbach, B. Ion beam assisted MBE of GaN on epitaxial TiN films. *Thin Solid Film.* **2004**, *459*, 13–16. [CrossRef]
13. Chen, G.S.; Guo, J.J.; Lin, C.K.; Hsu, C.-S.; Yang, L.C.; Fang, J.S. Evaluation of radio-frequency sputter-deposited textured TiN thin films as diffusion barriers between copper and silicon. *J. Vac. Sci. Technol. A Vac. Surf. Film.* **2002**, *20*, 479–485. [CrossRef]
14. Arshi, N.; Lu, J.; Joo, Y.K.; Lee, C.G.; Yoon, J.H.; Ahmed, F. Study on structural, morphological and electrical properties of sputtered titanium nitride films under different argon gas flow. *Mater. Chem. Phys.* **2012**, *134*, 839–844. [CrossRef]
15. Stanishevsky, A.; Lappalainen, R. Tribological properties of composite Ti (N, O, C) coatings containing hard amorphous carbon layers. *Surf. Coatings Technol.* **2000**, *123*, 101–105. [CrossRef]
16. Bin, D.; Tao, Y.; Hu, Z. The microstructure, mechanical and tribological properties of TiN coatings after Nb and C ion implantation. *Appl. Surf. Sci.* **2013**, *284*, 405–411. [CrossRef]
17. Pelleg, J.; Zevin, L.Z.; Lungo, S.; Croitoru, N. Reactive-sputter-deposited TiN films on glass substrates. *Thin Solid Film.* **1991**, *197*, 117–128. [CrossRef]
18. Lu, G.; Yu, L.; Ju, H.; Zuo, B.; Xu, J. Influence of nitrogen content on the thermal diffusivity of TiN films prepared by magnetron sputtering. *Surf. Eng.* **2020**, *36*, 192–198. [CrossRef]
19. Banerjee, R.; Singh, K.; Ayyub, P.; Totlani, M.K.; Suri, A.K. Influence of the Ar/N_2 ratio on the preferred orientation and optical reflectance of reactively sputter deposited titanium nitride thin films. *J. Vac. Sci. Technol. A Vac. Surf. Film.* **2003**, *21*, 310–317. [CrossRef]
20. Li, T.Q.; Noda, S.; Tsuji, Y.; Ohsawa, T.; Komiyama, H. Initial growth and texture formation during reactive magnetron sputtering of TiN on Si (111). *J. Vac. Sci. Technol. A Vac. Surf. Film.* **2002**, *20*, 583–588. [CrossRef]
21. Wang, Y.; Tang, W.; Zhang, L. Crystalline size effects on texture coefficient, electrical and optical properties of sputter-deposited Ga-doped ZnO thin films. *J. Mater. Sci. Technol.* **2015**, *31*, 175–181. [CrossRef]
22. Material Data Inc. *MDI Jade 6 User's Manual*; Material Data Inc.: Livermore, CA, USA, 2004.
23. Arshi, N.; Lu, J.; Koo, B.H.; Lee, C.G.; Ahmed, F. Effect of nitrogen flow rate on the properties of TiN film deposited by e beam evaporation technique. *Appl. Surf. Sci.* **2012**, *258*, 8498–8505. [CrossRef]
24. Sundgren, J.E. Structure and properties of TiN coatings. *Thin Solid Film.* **1985**, *128*, 21–44. [CrossRef]
25. Warren, B.E. *X-ray Diffraction*; Addison Wesley Publishing Co.: London, UK, 1969.
26. Chawla, V.; Jayaganthan, R.; Chandra, R. Structural characterizations of magnetron sputtered. *Mater. Charact.* **2008**, *59*, 1015–1020. [CrossRef]
27. Mohapatra, S.S.; Ranjan, S.; Dasgupta, N.; Mishra, R.K.; Thomas, S. *Nano-Carriers for Drug Delivery: Nanoscience and Nanotechnology in Drug Delivery*; Elsevier: Amsterdam, The Netherlands, 2019. [CrossRef]
28. Kiahosseini, S.R.; Larijani, M.M. Effects of nitrogen gas ratio on the structural and corrosion properties of ZrN thin films grown on biodegradable magnesium alloy by ion-beam sputtering. *Appl. Phys. A* **2017**, *123*, 759. [CrossRef]
29. Qasmi, M.; Delobelle, P. Influence of the average roughness R_{ms} on the precision of the Young's modulus and hardness determination using nanoindentation technique with a Berkovich indenter. *Surf. Coat. Technol.* **2006**, *201*, 1191–1199. [CrossRef]
30. Lee, J.H.; Nathanael, A.J.; Hong, S.I. Effect of nitrogen flow rate on the structure and properties of TiN thin films deposited onto β-type Ti-15Mo-3Nb-3Al-0.2Si alloy Substrates by Reactive Magnetron Sputtering. *Adv. Mater. Res.* **2012**, *557*, 1998–2001. [CrossRef]

31. Lia, J.; Zheng, H.; Sinkovits, T.; Hee, A.C.; Zhao, Y. Mono and multiple TiN(/Ti) coating adhesion mechanism on a Ti–13Nb–13Zr alloy. *Appl. Surf. Sci.* **2015**, *355*, 502–508. [CrossRef]
32. Huang, J.H.; Lau, K.W.; Yu, G.P. Effect of nitrogen flow rate on structure and properties of nanocrystalline TiN thin films produced by unbalanced magnetron sputtering. *Surf. Coat. Technol.* **2005**, *191*, 17–24. [CrossRef]
33. Huang, J.H.; Ho, C.H.; Yu, G.P. Effect of nitrogen flow rate on the structure and mechanical properties of ZrN thin films on Si(1 0 0) and stainless steel substrates. *Mater. Chem. Phys.* **2007**, *102*, 31–38. [CrossRef]
34. Ali, R.; Sebastiani, M.; Bemporad, E. Influence of Ti–TiN multilayer PVD-coatings design on residual stresses and adhesion. *Mater. Des.* **2015**, *75*, 47–56. [CrossRef]
35. He, C.; Zhang, J.; Xie, L.; Ma, G.; Du, Z.; Wang, J.; Zhang, D. Microstructure, mechanical and corrosion properties of TiN/Ni nano-multilayered films. *Rare Metals.* **2019**, *38*, 979–988. [CrossRef]

coatings

MDPI

Article

Microstructure Evolution and Hardness Improvement of WC-Co Composites Sintered with Fe Substituting Part of Co Binder

Xun Li [1], Junfei Zhang [2], Qiang Zhang [2], Xianwei Zhang [2], Vincent Ji [3] and Jinlong Liu [1,*]

[1] Key Laboratory for Anisotropy and Texture of Materials, Ministry of Education, Northeastern University, Shenyang 110819, China
[2] Liaoning Wuhuan Special Materials and Intelligent Equipment Industry Technology Research Institute Co., Ltd., Shenyang 113122, China
[3] Institut de Chimie Moléculaire et Des Matériaux d'Orsay, Université Paris-Saclay, 91405 Orsay, France
* Correspondence: liujl@atm.neu.edu.cn

Abstract: WC-13Co (wt.%) composite with Fe added was prepared by pressureless sintering, and its microstructure and mechanical properties were analyzed by X-ray Diffraction (XRD), Scanning Electronic Microscopy (SEM), Energy Dispersive Spectroscopy (EDS) and Vickers hardness tester. The effect of Fe and C content on the microstructure of the eta phase, binder phase, grain size and porosity, as well as mechanical properties in the W-Co-Fe-C system, was discussed quantitatively. The position of added Fe in the lattice of the composites is clarified. When 2%–4% Fe was added, Fe existes in both the binder phase and the low-carbon eta phase. In the lattice of the eta phase, Fe occupies the position of Co and Fe uniformly existes in the binder with the structure of simple cubic when the composites is in the eutectic phase region. Differently from the previous report that the growth of WC in liquid Fe was severely limited, the size of WC in the W-Co-Fe-C system increases from 1.14 μm to 1.21 μm when the content of Fe increases from 0 to 4%, which indicates that the growth behavior of WC in liquid CoFe was different from that in liquid Fe, but closer to that in liquid Co. The sample added both 2% Fe and 1% C has the optimum matching of hardness and toughness. Compared with the hardness of 979 HV_{30} in the sample without adding Fe and C, the hardness of the sample with both 2% Fe and 1% C added achieved 1071 HV_{30}, which is increased by 9.4% under the conditions of a slight increase in fracture toughness.

Keywords: WC-Co; Fe; eta phase; grain growth; hardness; toughness

Citation: Li, X.; Zhang, J.; Zhang, Q.; Zhang, X.; Ji, V.; Liu, J. Microstructure Evolution and Hardness Improvement of WC-Co Composites Sintered with Fe Substituting Part of Co Binder. *Coatings* **2023**, *13*, 116. https://doi.org/10.3390/coatings13010116

Academic Editor: Emerson Coy

Received: 7 December 2022
Revised: 21 December 2022
Accepted: 4 January 2023
Published: 8 January 2023

1. Introduction

Composites can obtain comprehensive properties that cannot be achieved by the single component material [1–4], and they are an important achievement of material technology during the development of human civilization. More than 100 years ago, in order to replace expensive diamonds, the WC-Co composite, which was composed of hard WC particles and tough Co binder, was invented by powder sintering in the cutting processing industry [5]. At present, this material has been widely used in wear-resistant parts and the cutting tools of mining, machinery, oil mining, aerospace and other industries [6]. For each country, Co is a limited resources and is widely used not only in WC-Co composites as binders [7], but also in other important alloys, such as ultra-high strength martensitic steel for aircraft landing gear [8], high-performance Co-based soft magnetic materials [9], and high efficiency lithium batteries for new energy vehicles, which have developed rapidly in recent years [10]. Therefore, researchers have been considering new alternative binders for many years. In particular, the new European chemicals regulation clearly proposes to consider partially replacing Co with Fe and Ni [11]. Both Fe and Ni are transition metals close to Co element in the periodic table and have similar affinity with carbon and tungsten.

The replacement of Co with Fe and Ni has been a research focus of WC-Co composites. Uhrenius' [12] work showed that the calculated phase diagram based on Thermo Calc databases can be used to predict the corresponding C content in the two-phase region WC + fcc (face-centered cubic) under different Fe, Ni and Co content combinations in the new Fe-Ni-Co-W-C composites. Shon et al. [13] fabricated the WC-10Co (wt.%), WC-10Ni and WC-10Fe composites by the high-frequency induction heating sintering (HFIHS) method and further discussed the effects of Fe and Ni on sintering behavior, density, grain size and mechanical properties of the composites. Soria-Bairrun et al. [14] added Cr to the binder of WC-Co-Fe-Ni composite, and found that, compared with the phase diagram of WC-FeNiCo based on Thermocalc, the position of the carbon window and the temperature of solidus and liquidus are significantly affected by the content of Cr.

After replacing Co with other metal elements, the microstructure evolution changed significantly in WC-based composites. Marek Tarraste et al. [15] fabricated the WC-FeCr composites using ferrite chromium steel as the binder metal and found that the addition of about 2% carbon in WC-30%FeCr composites can hinder the formation of the eta phase. Wittmann [16] investigated the effect of VC and other inhibitors on the growth of WC grains when Ni and Fe are used as binders and found that VC is the most effective grain growth inhibitor in WC-Ni hard metals, while the growth of WC grains is strongly restricted even if no growth inhibitor is added in Fe-binder composites.

Furthermore, it is possible to obtain higher mechanical properties and corrosion resistance through the replacement of reasonable content of Fe and Ni [17]. Kakeshita et al. [18] found that the toughness of WC-(Fe-Ni-C) composites is higher than that of common WC-Co composite by controlling martensitic transformation strengthening. Guo et al. [19] investigated the influence of heat treatment on the toughness of WC-(Fe-Ni-C) composites, and results showed that isothermal heat treatment can also effectively improve the toughness. Chang et al. [20] reported that, compared with WC-Co composites, the sintered nanostructured WC-(Co-Ni-Fe) composites have better corrosion resistance and mechanical properties.

The efforts above have shown that Fe has become an important alloying element to replace Co in WC-Co-based composites. On the other hand, completely replacing Co with Fe or Ni leads to a sharp decline in the performance of composites, and the composites showed an extremely narrow carbon window (about 40% of WC-Co composites) at binder contents of $\leq$10 wt.%, resulting in difficult control of the stability and reliability of products in the factory.

At present, the research on WC-Co composites with added Fe has paid more attention to the calculated phase diagram, WC grain growth, mechanical properties and corrosion resistance. The research on the composition and distribution of the eta phase as well as the occupation of Fe atoms in the lattice of WC-Co composites adding Fe is still limited. Moreover, although the current experimental work has illustrated a good agreement with the calculated phase diagram of WC-Co containing Fe based on CALPHAD, more experimental data are needed, especially on the eta phase formation side, to better compare the experimental and calculation [21].

In this work, WC-Co-based composites with different Fe contents were prepared by powder metallurgy. The key factors affecting the mechanical properties, such as the density, eta phase and WC grain size, as well as the composition and structure of the binders, were studied. The occupation of Fe atoms in the crystallographic lattice of the composites after the addition of Fe powder was also explored.

2. Experimental Procedure

Commercial tungsten carbide powder (6.1% C, W $\geq$ 93.72, $p \leq 0.001$%, S $\leq$ 0.001%, 0.094% O, others $\leq$ 0.001%, wt.%, average particle size of 2 μm, Xiamen golden egret special alloy Co., Ltd., Xiamen, China, Figure 1a), Co powder (Co $\geq$ 99.9%, Mn $\leq$ 0.0001%, Cu $\leq$ 0.0003%, others $\leq$ 0.005%, average particle size of 0.8 μm, 99.9 wt.% purity, Xiamen golden egret special alloy Co., Ltd., Xiamen, China, Figure 1b), Fe powder (Fe $\geq$ 99.0%,

average particle size of 10 μm, Qinghe county Kegong Metallurgical Materials Co., Ltd., Xingtai, China, Figure 1c), W powder (W ≥ 99.0%, average particle size of 1.2 μm, Xiamen golden egret special alloy Co., Ltd., Xiamen, China, Figure 1d) and carbon black (average particle size of 200 nm, Xiamen golden egret special alloy Co., Ltd., Xiamen, China) were selected as raw materials. Table 1 shows the nominal chemical compositions of different WC-Co composites. The carbon content is calculated as follows: Ct% = (C1 + C2)/Mt, where Ct% is the weight of total carbon in the sample, C1 is the weight of carbon in WC powder, C2 is the weight of adding carbon black, and Mt is the total weight of sample. The Ct is important for evaluating the carbon content in the sample, although it ignores the carbon loss during the sintering process.

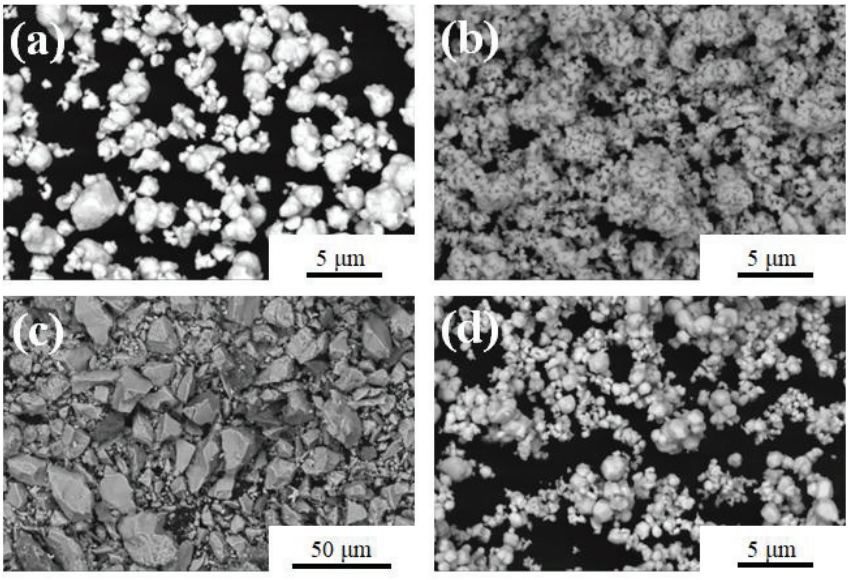

Figure 1. BSE-SEM of raw powders. (**a**) WC, (**b**) Co, (**c**) Fe, (**d**) W.

Table 1. The nominal chemical compositions of WC-13(Co-Fe) composites (wt.%).

Samples	WC	Co	Fe	W	C	Ctotal
0Fe-5.3C	87	13	0	0	0	C5.3
1Fe-5.3C	87	12	1	0	0	C5.3
2Fe-5.3C	87	11	2	0	0	C5.3
3Fe-5.3C	87	10	3	0	0	C5.3
4Fe-5.3C	87	9	4	0	0	C5.3
2Fe-5.1C	83.7	11	2	3.3	0	C5.1
2Fe-5.5C	87	11	2	0	0.25	C5.5
2Fe-6.3C	87	11	2	0	1	C6.3

Various weighed powders and ethanol were put into the ball mill. The weight ratio of the ball to powder was 4:1, and the ball milling lasted for 24 h. Then, the mixed materials were placed in a 70 °C vacuum drying furnace, and the drying time was 5 h. After drying, the powder was sieved with an 80 mesh sieve and pressed into a mold with a diameter of 20 mm under the pressure of 240 Mpa. Finally, the pressed blank was heated in a tubular experimental furnace (GSL-1700X, Hefei Kejing Co., Ltd., Hefei, China) from room temperature to 1000 °C at the rate of 10 °C/min, then heated to 1430 °C at the rate of 5 °C/min, kept at 1430 °C for 1 h, and then cooled in the furnace. The atmosphere for oxidation prevention was argon during sintering.

The prepared samples were ground and polished to analyze the phase by XRD-7000 (Shimadzu Co., Ltd., Kyoto, Japan, Cu target.). The selected angle was 20°–80° and the scanning speed was 5°/min. Quanta 250FEG SEM (FEI Co., Ltd., Hillsboro, OR, USA) equipped with energy dispersive spectroscopy (EDS) was used to analyze the microstructure and chemical element distribution. Image Pro Plus image analysis software was used to measure WC grain size. After sintering, the electronic analytical scale (JHY-600Q, Xiamen Jinheyuan Technology Co., Ltd., Xiamen, China) was used to measure the bulk density, which is calculated using the Archimedes principle. The pressure of the indenter for measuring Vickers hardness was 30 kg, lasting for 10 s. Moreover, in view of the high toughness of the samples 0Fe-5.3C and 2Fe-6.3C, the hardness tests at 50 kg pressure and 10 s were carried out on the two samples in order to observe the crack morphology.

3. Results and Discussion

3.1. The Microstructure of WC-Co-Fe Composites

The XRD patterns of different samples are illustrated in Figure 2, and the composites of 0Fe-5.3C, 1Fe-5.3C, 2Fe-5.3C, 3Fe-5.3C, 4Fe-5.3C, 2Fe-5.1C and 2Fe-5.5C are composed of three phases: WC, binder and eta phase. Only binder phase and WC exist in samples 2Fe-6.3C. Moreover, with the increase of Fe content, the peak value of the eta phase increases, indicating that the formation of eta phase is promoted by replacing Co with Fe. In the environment of low-carbon content, the reaction between WC and Co contributes to the formation of the eta phase, which is usually called M_6C and $M_{12}C$ [22] (or Co_3W_3C and Co_6W_6C [23]). The addition of C leads to the disappearance of the eta phase in the 2Fe-6.3C sample.

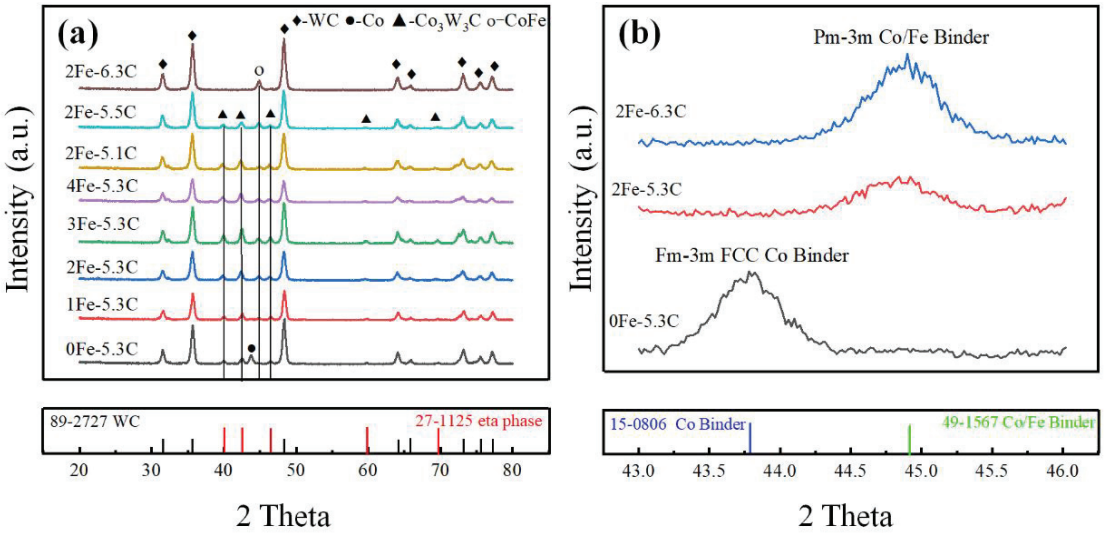

Figure 2. XRD patterns of WC-13 (Co-Fe) composites with different contents of Fe and C (**a**) and the enlarged XRD patterns between 43° and 46° (**b**).

Furthermore, the crystal structure of the binder phase changes with the addition of Fe and C. The binder phase in the 0Fe-5.3C sample is Co-binder, corresponding to the lattice constant of 3.57. After 2%–4% Fe is added, the CoFe-binder is formed, corresponding to the lattice constants of 2.82. Through adding 1% C in the 2Fe-6.3C sample, the eta phase is eliminated and the sample is a two-phase material, consisting of B2 ordered (simple cubic, sc) CoFe and WC, and the Co-binder phase of fcc cannot be observed. In addition, the content of added Fe has no obvious effect on the lattice constant of the eta phase. The

lattice constant of the eta phase is about 11.04 in all samples of 0Fe-5.3C, 1Fe-5.3C, 2Fe-5.3C, 3Fe-5.3C, 4Fe-5.3C, 2Fe-5.1C and 2Fe-5.5C. The occupation of Fe in the lattice of the eta phase of WC-Co composites has been reported [24], and the results of this study are in agreement with it, and it is difficult to observe the change of the corresponding 2θ angle in the XRD pattern due to the very similar atomic radii of Fe and Co (Fe: 1.27 Å, Co: 1.26 Å).

As mentioned above, there are more eta phases in the sample added with Fe, which indicates that Fe promotes the expansion of the upper limit of C in the fcc + WC + eta phase region. Figure 3 demonstrates the phase diagram of WC-13Co and WC-9Co-4Fe calculated by Thermo-Calc software. It can be seen that, with the increase of Fe, the carbon content range of the WC + fcc two-phase region increases from 5.19%–5.36% to 5.33%–5.42%; that is, the addition of Fe expands the range of carbon content in the phase diagram corresponding to the WC + fcc two-phase region in the WC-Co-Fe system. It should be pointed out that there is a large carbon loss in the sintering process, as reported by [25,26], so the nominal C content in Table 1 is significantly higher than the carbon content in the phase diagram in Figure 3.

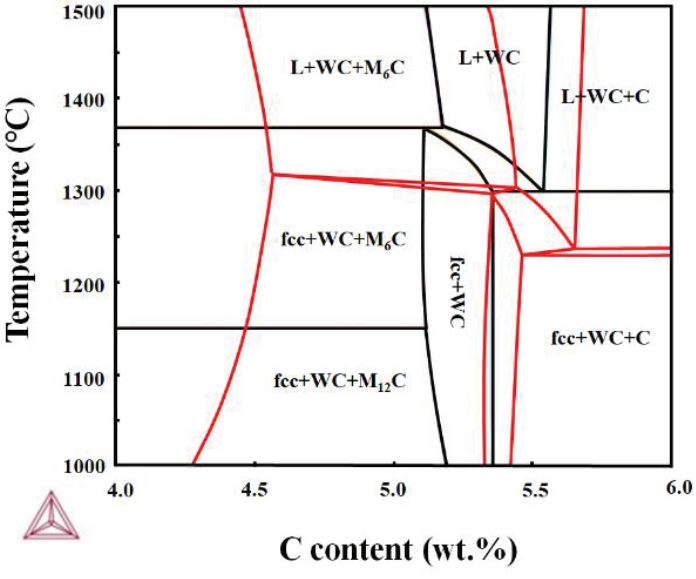

Figure 3. Isopleth calculated with ThermoCalc software using TCFE10 database corresponding to the WC-13Co (Black) and WC-9Co-4Fe (Red) composites.

The eta phase can be clearly observed in the BSE-SEM images in Figure 4. With the addition of Fe from 0 to 4.0%, the area fraction and the size of the eta phase increase sharply. In the 0Fe-5.3C sample, the eta phase size is relatively small, and most eta phases are slightly larger than WC grains and, moreover, in the samples adding 4% Fe, the size of some eta phases reache ~10 μm, which is more than five times the WC size. With the increase of carbon black in the sample adding of 2% Fe, the fraction of the eta phase gradually decreases and it finally disappears in the sample of 2Fe-6.3C.

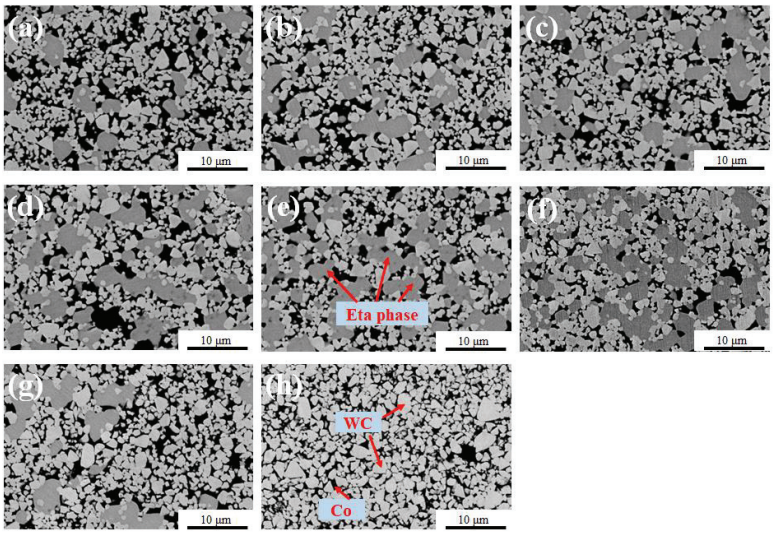

Figure 4. BSE-SEM microstructure of composites, (**a**) 0Fe-5.3C, (**b**) 1Fe-5.3C, (**c**) 2Fe-5.3C, (**d**) 3Fe-5.3C, (e) 4Fe-5.3C, (**f**) 2Fe-5.1C, (**g**) 2Fe-5.5C, (**h**) 2Fe-6.3C.

Figure 5 further illustrates the statistical area fraction of the eta phase. The eta phase is very sensitive to the addition of Fe. Under the same carbon content conditions, when 4% Fe was used to replace 4% Co, the proportion of the eta phase increased more than twice, from 20% to 45.3%. When the added content of C reached 1%, the proportion of the eta phase decreased to 0% in the sample of 2% Fe. Carbon black effectively inhibits the formation of the eta phase in the 2Fe-6.3C sample. Wei et al. [27] also eliminated the eta phase by adding carbon when using the WO_2, Co_3O_4 and C as raw materials to manufacture WC-Co composites.

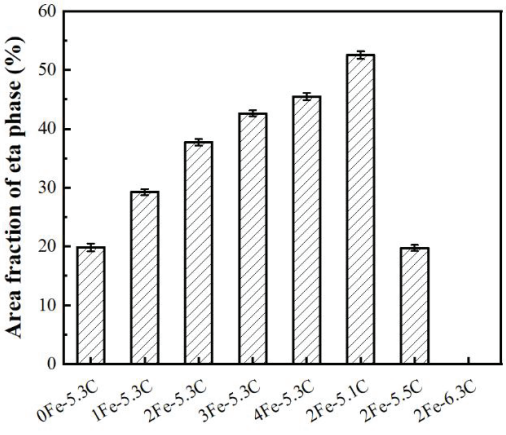

Figure 5. Area fraction of the eta phase of different WC-13 (Co-Fe) composites.

The eta phase and Co in the 2Fe-5.3C sample are further analyzed by EDS as exhibited in Figures 6 and 7. In addition to replacing Co in the binder (Figure 6a), the added Fe also exists in the eta phase (Figure 6b) in 2Fe-5.3C sample, while in the 2Fe-6.3C sample, Fe only exists in the binder (Figure 6c) due to the disappeared eta phase, as shown in Figures 2 and 5. Moreover, the Co content in the binder and eta phases of the 2Fe-5.3C sample is higher than the Fe content, as seen in Figure 7.

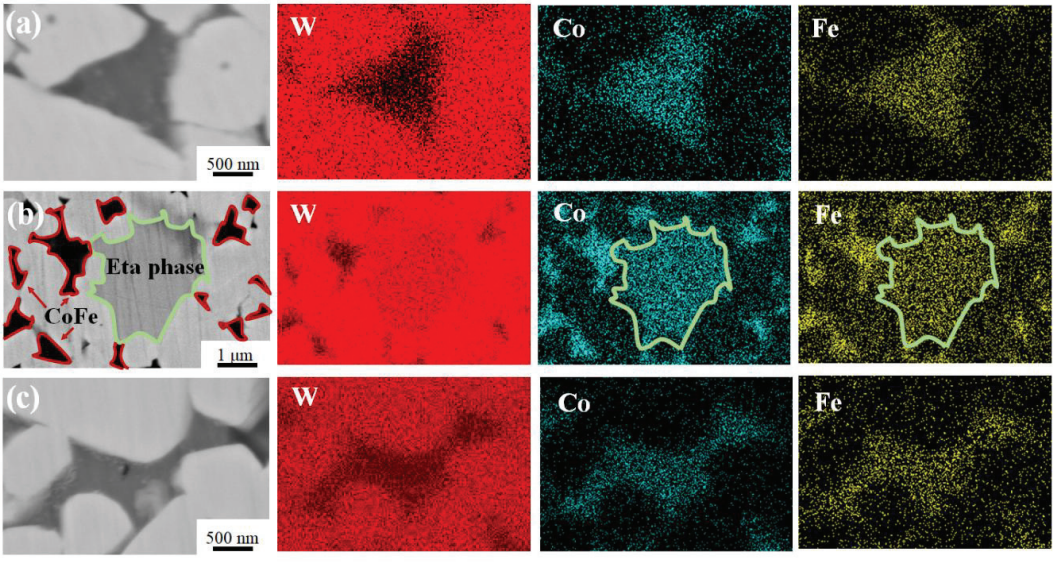

Figure 6. EDS mapping of element distribution of different samples, (**a**) the binder phase of 2Fe-5.3C sample, (**b**) the binder and eta phases of 2Fe-5.3C sample, (**c**) the binder phase of 2Fe-6.3C sample.

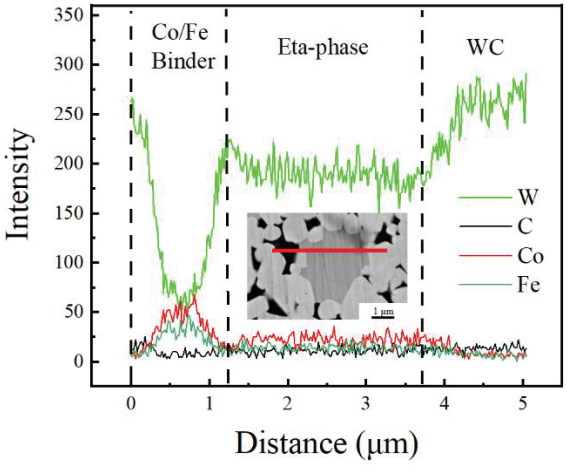

Figure 7. Elements' distribution of binder phase, eta phase and WC phase in the 2Fe-5.3C sample.

To sum up, for the sample without an eta phase such as 2Fe-6.3C, Fe mainly exists in the binder, forming a solid solution with B2 ordered structure (Figure 2). When the WC-13 (Co-Fe) composite is sintered at low-carbon content, such as 1Fe-5.3C, 2Fe-5.3C, 3Fe-5.3C, 4Fe-5.3C, 2Fe-5.1C and 2Fe-5.5C, Fe exists in both the eta phase and B2 ordered binder, which has been confirmed by EDS analysis in Figure 6. In the eta phase, Fe occupies the Co position instead of the W position, which can be identified by comparing the diffraction peaks of the eta phase of 0Fe-5.3C and 2Fe-5.3C samples in Figure 2. If Fe occupies the W position, the lattice constant will be greatly changed due to the large difference between the atomic radii of Fe and W. Figure 8 demonstrates the schematic diagram of atomic occupancy of Fe in the lattice of WC-13 (Co-Fe) composites.

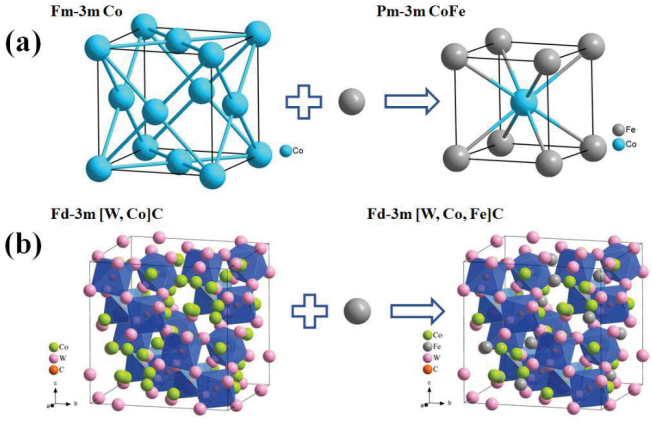

Figure 8. Crystal structure diagram of (**a**) binder phase of Co and CoFe and (**b**) eta phase of [W, Co]C and [W, Co, Fe]C.

Figure 9 illustrates the distribution of the grain size of the composites. With the Fe content increase from 0 to 4% (Figure 9a–e), the grain size of WC increases slightly from 1.14 μm to 1.21 μm, which is different from the previous report that the growth of WC was hindered by adding Fe [16]. The growth of the WC grains was primarily related to the dissolution and re-precipitation of WC grains in the binder phase during liquid phase sintering [28]. Roulon et al. [11] found that the solubility of WC in liquid Fe is lower than that in liquid Co. Wittmann et al. [16] reported that the substitution of Fe for Co as a binder would strongly limit the growth of WC grains during liquid sintering.

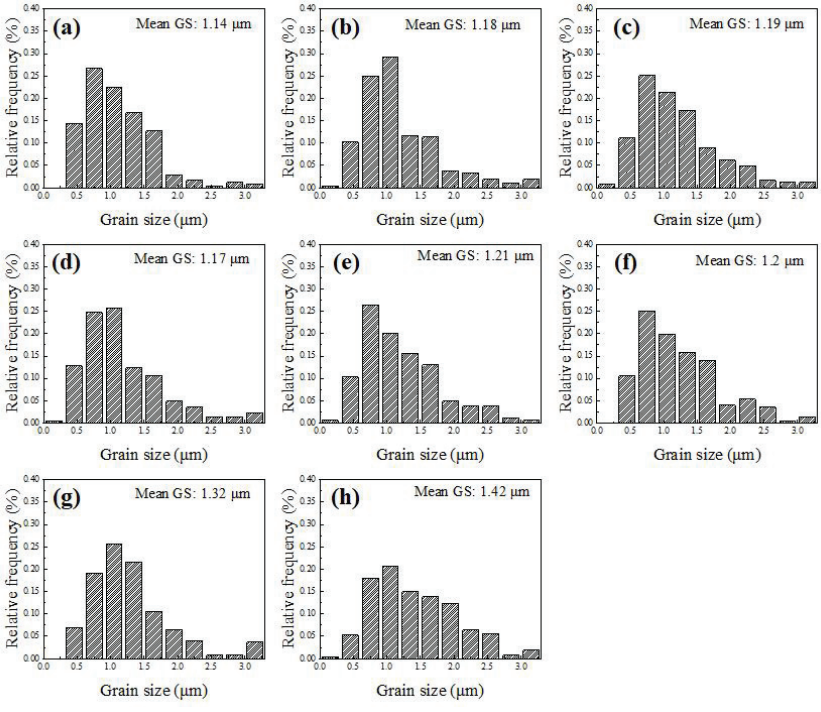

Figure 9. The grain size distribution in WC-13Co with different additions of Fe and C: (**a**) 0Fe-5.3C, (**b**) 1Fe-5.3C, (**c**) 2Fe-5.3C, (**d**) 3Fe-5.3C, (**e**) 4Fe-5.3C, (**f**) 2Fe-5.1C, (**g**) 2Fe-5.5C, (**h**) 2Fe-6.3C.

The results in Figure 9 demonstrate that the growth behavior of WC in liquid CoFe is close to that of liquid Co but completely different from that of liquid Fe. Moreover, with the increase of the content of carbon added, the grain size of the composites further increased from 1.21 μm to 1.42 μm. Konyashin et al. [29] pointed out that the high-carbon environment is more conducive to the WC coarsening in WC-Co hard metals, although the influence of carbon content on the grain growth behavior in the W-C-Co-Fe system is still unclear.

3.2. Analysis of the Density

Figure 10 illustrates that the density of the WC-13 (Co-Fe) composite decreases gradually with the increase of Fe content. The densification of WC-Co composites mainly depends on the volume shrinkage and the closure of micro-pores during liquid sintering. The high content of liquid metal and the good wettability between WC and the liquid metal are important factors for densification sintering. Both the XRD pattern in Figure 2 and the volume fraction of the eta phase in Figure 5 demonstrate that the proportion of the eta phase increases with the increase of Fe content. This means that, during the sintering process, the liquid Co decreases, which leads to the inhibition of shrinkage behavior and the decrease of density.

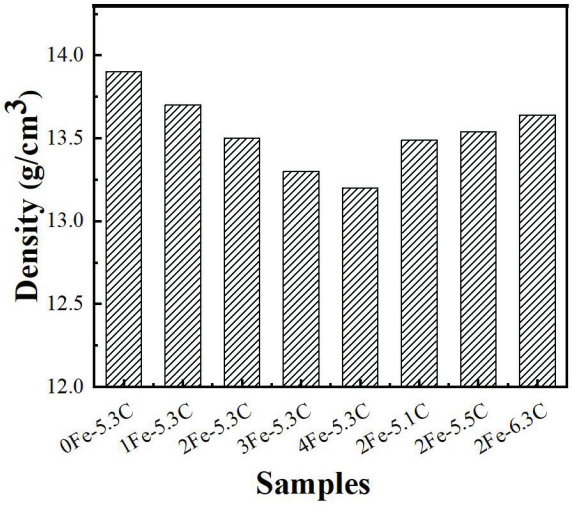

Figure 10. The effects of addition of Fe and C on the densities of WC-13 (Co-Fe) composites.

Figures 11 and 12a further demonstrate the distribution and area fraction of micro-pore with different additions of Fe and C. With the increase of Fe content from 1% to 4%, the area fraction of micro-pore increased from 0.21% to 1.03%, while with the increase of C content the area fraction of micro-pore significantly decreased, and the fraction in the 2Fe-6.3C sample decreased to 0.30%. This is consistent with the change trend of density in Figure 10. According to the EDS analysis in Figure 12b, the content of all elements of W, Fe and Co is extremely low in the micro-pore, which is useful to prove the existence of the micro-pore in the composites containing Fe.

With the addition of C, the fraction of eta phase decreases and the content of liquid Co increases. Interestingly, comparing the density of 2Fe-6.3C and 0Fe-5.3C samples, the density of the 2Fe-6.3C sample was lower than that of 0Fe-5.3C samples, although the eta phase in the 2Fe-6.3C sample was completely eliminated. The reasons for the decrease in density include: (i) the density of Fe is lower than that of Co; (ii) the increase of porosity. It can be seen from Figure 11 that there are some micro-pores in the 2Fe-6.3C sample, which can be explained by the lower wettability of WC in CoFe than in Co [30,31].

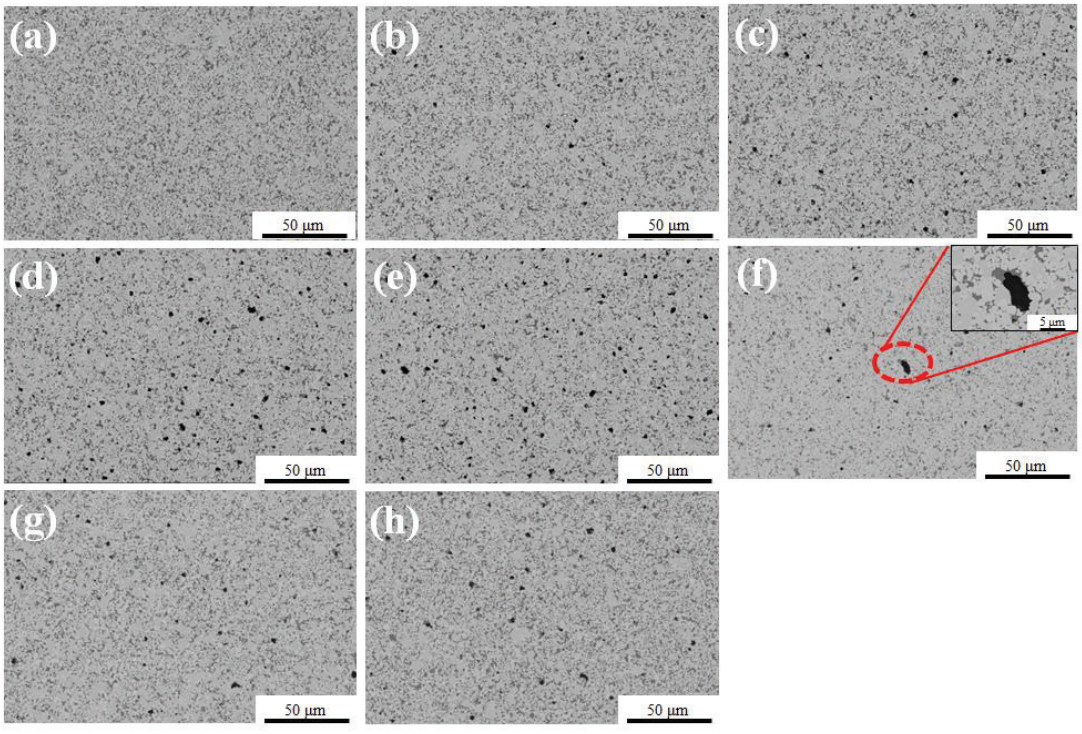

Figure 11. BSE-SEM microstructure of different composites, (**a**) 0Fe-5.3C, (**b**) 1Fe-5.3C, (**c**) 2Fe-5.3C, (**d**) 3Fe-5.3C, (**e**) 4Fe-5.3C, (**f**) 2Fe-5.1C, (**g**) 2Fe-5.5C, (**h**) 2Fe-6.3C.

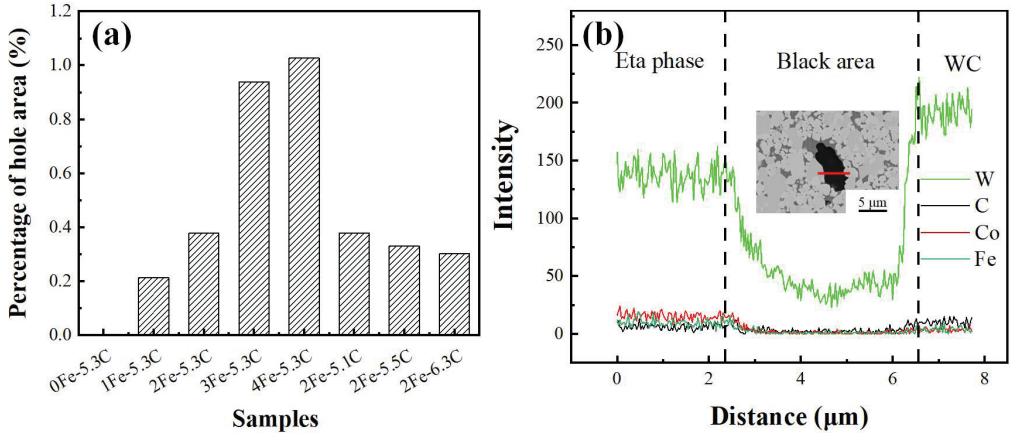

Figure 12. (**a**) Area fraction of the micro-pore in different WC-13 (Co-Fe) composites and (**b**) the EDS analysis around the micro-pore in the 2Fe-5.1C sample.

3.3. Mechanical Properties

When powder metallurgy is used to fabricate WC-Co composites, the key to the sintering process is to remove porosity and make the composite compact, and to bond different WC grains together with metal. Especially in the process of liquid phase sintering, WC particles rearrange, dissolve and precipitate in the liquid phase binder, thus further

removing the composite porosity. The hardness H affected by porosity can be described by the following formula [32]:

$$H = H_0 \exp(-b\rho) \quad (1)$$

where ρ is the porosity, and H_0 and b are constants. With the increase of porosity, the hardness decreases rapidly. The quantitative effect of grain size on hardness can be expressed by the Hall-Petch relationship [33]:

$$H = H_0 + kd^{-\frac{1}{2}} \quad (2)$$

where H_0 and k are constants, and d is the grain size of WC. The hardness decreases with the increase of grain size. However, when the addition of Fe increased from 0 to 4%, the porosity ρ and the grain size d increased (Figures 3 and 6), but hardness also increased (Figure 13). This is because the hardness of WC-Co-based composites is also affected by the eta phase. It is well known that the higher the content of the eta phase, the lower the proportion of the binder phase. The eta phase is an intermetallic compound, and its hardness is significantly higher than that of the metal binder phase. Therefore, the eta phase is the dominant factor affecting the hardness in samples of 0Fe-5.3C, 1Fe-5.3C, 2Fe-5.3C, 3Fe-5.3C, 4Fe-5.3C, 2Fe-5.1C. When the Fe content increases from 0 to 4%, the eta phase grows abnormally and the area fraction of the eta phase significantly increases to 45.3%, leading to an obvious increase in hardness from 979 HV_{30} to 1185 HV_{30}, and the increase in average crack length from 0 μm to 47 μm.

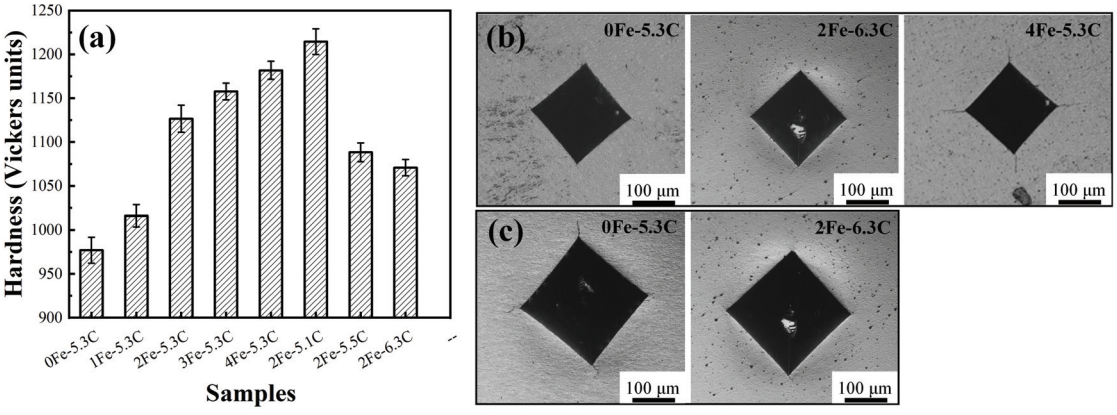

Figure 13. The hardness (**a**) and the micrographs of Vickers' indentations and induced surface cracking in different WC-Co-Fe samples under 30 kg (**b**) and 50 kg (**c**) pressure, respectively.

On the other hand, the addition of C increases the grain size, and especially, significantly, decreases the eta phase, leading to the clear decrease of hardness, although the decrease of porosity (Figure 3) is beneficial to the increase of hardness. Therefore, the 2Fe-6.3C sample without eta phase has lower hardness than other samples containing 2% Fe. Surprisingly, compared with the hardness 979 HV_{30} of the 0Fe-5.3C sample without Fe addition, the hardness of the 2Fe-6.3C sample clearly increases to 1071 HV_{30} by adding Fe and C and, moreover, it also has good fracture toughness and the average crack length decreases to 0 μm, as shown in Figure 13b. The disappearance of the eta phase can strengthen the skeleton structure of WC, which is very beneficial to synergistically increasing the hardness and toughness [34].

As the cracks cannot be observed in the 0Fe-5.3C and 2Fe-6.3C samples in the hardness test under 30 kg pressure (Figure 13b), the pressure of hardness was increased to 50 kg and two samples had obviously different crack morphology. Clear cracks appeared at the corners of the Vickers hardness indentation in the 0Fe-5.3C sample, while the 2Fe-6.3C

sample still had no cracks. However, unlike hardness, fracture toughness is more difficult to assess accurately, especially in brittle materials. The Godse and Gurland's model (GGM) given in the literature [35] can evaluate the fracture toughness in WC-Co composites with 10%–25% Co. The model formula is as follows.

$$K_{Ic} = \sqrt{R(\lambda + d)E'\sigma_B \frac{(1 - CV_{WC})}{C_1}} \tag{3}$$

where C, d and V_{WC} are the contiguity, grain size and volume fraction of the carbide phase, respectively; λ is the binder mean free path; R is a floating parameter calculated on the basis of best fitting with experimental results, C_1 is taken from McMeeking's work as 0.54, E' is the ratio of elastic modulus to Poisson's ratio, σ_B is the binder effective flow stress. E' can be calculated by using Equation (4) for plane stress:

$$E' = \frac{E}{1 - V^2} \tag{4}$$

where E and V are elastic modulus and Poisson's ratio. According to reports [36], 600 Gpa and 619 Gpa were used for E and 0.23 and 0.22 for V in 0Fe-5.3C and 2Fe-6.3C samples, respectively. Additionally, σ_B is the effective flow stress of binder, calculated by using Equation (5) as proposed by Sigl and Fischmeister:

$$\sigma_B = 480 + \frac{1550}{\lambda}[\text{MPa}] \tag{5}$$

The adjacency degree and the mean free path of the Co phase can be measured from the SEM image. In the 0Fe-5.3C sample they are 0.27 and 0.39 μm, while in the 2Fe-6.3C sample they are 0.31 and 0.42 μm. It is noted that the grain size of the 2Fe-6.3C sample is larger than that of 0Fe-5.3C, which is in agreement with the report [37] that the average free path of the Co phase increases with the increase of WC grain size. Then, the K_{IC} can be calculated by the Formula (3). The K_{IC} of the 0Fe-5.3C sample and the 2Fe-6.3C sample is 29.6 MPa·m$^{1/2}$ and 31 MPa·m$^{1/2}$, respectively. Eta phase exists in the 0Fe-5.3C sample, which is unfavorable to the fracture toughness [38]. The calculation results show that the fracture toughness of the 2Fe-6.3C sample is slightly higher than that of the 0Fe-5.3C sample, which are consistent with the experimental results in Figure 13c.

The toughness of WC-based composites is mainly contributed by the metal binder phase. The eta phase was completely eliminated in the 2Fe-6.3C sample, as seen in Figures 2 and 5, leading to the highest proportion of binder phase compared with other samples in Figure 13a. Furthermore, the density of Fe (7.86 g/cm^3) is significantly lower than that of Co (8.9 g/cm^3). Therefore, after replacing Co with Fe of the same weight, the volume fraction of the binder increases, resulting in a higher average free path of the 2Fe-6.3C sample. In addition, CoFe binder has higher hardness than Co binder. This is because Fe replaces the occupation of Co in the binder based on the crystal structure diagram as illustrated in Figure 8, which inevitably leads to lattice distortion and solution strengthening. Moreover, the formation of the B2 ordered structure further produces the ordered strengthening. Thus, the strengthening of the binder phase induced by the addition of Fe is the main reason that the hardness of the 2Fe-6.3C sample is significantly higher than that of the 0Fe-5.3C sample.

It should be pointed out that the hardness of WC based composites is significantly lower than that reported in low pressure sintering and SPS sintering [36] due to the simple pressureless sintering method adopted in this paper. However, the samples have excellent fracture toughness, especially the 2Fe-6.3C sample, which did not crack in the hardness test. This is significantly higher than the reported WC-13Co composite [39].

Consequently, adding 2% Fe to the WC-13Co composites increases the porosity, but by adjusting the carbon content, the hardness can be significantly improved without obviously damaging the toughness, although the porosity will damage the bending property [13].

When WC-based composites perform with low requirements for bending strength, the beneficial exploration of the current study can provide a useful reference on the control of the eta phase, binder phase and porosity for saving cobalt resources and reducing raw material costs in industrial production.

4. Conclusions

WC-13 (Co-Fe) composites were prepared by pressureless sintering at 1430 °C. The effects of Fe and C additions on the microstructure and mechanical properties of composites were investigated. The conclusions were drawn as follows.

- ✓ The addition of Fe significantly promoted the formation of eta phase in WC-13 (Co-Fe) composites, and slightly promoted the growth of WC. With the increase of Fe content from 0 to 4%, the content of the eta phase increases significantly from 20% to 45.3%, and the grain size of WC increases from 1.14 μm to 1.21 μm. The addition of C inhibited the eta phase and further promoted the growth of WC. With the increase of C content from 0 to 1%, the content of the eta phase decreases from 37.6% to 0, and the grain size of WC increases from 1.19 μm to 1.42 μm.
- ✓ The added Fe mainly exists in the eta phase and the binder phase. Compared with the WC-13Co composite, the added Fe occupies the Co position instead of the W position in the lattice of the eta phase. When the eta phase is eliminated by adjusting the content of C, Fe uniformly exists in the binder, and after adding a relatively small amount of 2% Fe, the binder phase of fcc-Co transforms into sc-CoFe.
- ✓ WC-13 (Co-Fe) composites with 2% Fe and 1% C added obtain good matching of hardness and toughness. The fracture toughness is slightly higher than that of WC-13% Co without the addition of Fe and C, and the hardness also increases by 9.4%. The hardness of composites is mainly controlled by the content of WC and eta phases, and is not very sensitive to porosity.

Author Contributions: Conceptualization, J.L. and V.J.; methodology, J.L. and X.L.; formal analysis, X.L.; investigation, X.L. and J.Z.; resources, X.Z., J.Z. and Q.Z.; writing—original draft preparation, X.L.; writing—review and editing, J.L.; All authors have read and agreed to the published version of the manuscript.

Funding: This work was funded by the Fundamental Research Funds for the Central Universities (No. N2002008), and Science and Technology Plan Project of Shenfu Demonstration District (2021JH05).

Institutional Review Board Statement: Not applicable.

Informed Consent Statement: Not applicable.

Data Availability Statement: Not applicable.

Conflicts of Interest: The authors declare no conflict of interest.

References

1. Yu, K.; Ma, H.T.; Guo, Y.H.; Sun, Z.; Dong, Y.; Alexandrov, I.V.; Prokofiev, E.A.; Chang, H. Microstructure evolution and mechanical properties of copper coated graphene nanoflakes/pure titanium matrix composites. *Mater. Charact.* **2022**, *194*, 112433. [CrossRef]
2. Ozer, M.; Aydogan, S.I.; Cinici, H.; Ozer, A. Effects of sintering techniques and parameters on microstructure and mechanical properties of Al-15Si-2,5Cu-0.5Mg compacts and Al-15Si-2,5Cu-0.5Mg/B_4C composites. *Mater. Today Commun.* **2022**, *30*, 103192. [CrossRef]
3. Ghabezi, P.; Harrison, N.M. Indentation characterization of glass/epoxy and carbon/epoxy composite samples aged in artificial salt water at elevated temperature. *Polym. Test.* **2022**, *110*, 107588. [CrossRef]
4. Wang, R.; Deng, J.X.; Zhang, Z.H.; Lu, Y.; Li, X.; Wu, J. Microstructure and tribological properties of Ni_3Al-Cr_3C_2/Ni_3Al micro-laminate composite films fabricated by electrohydrodynamic atomization technique. *Vacuum* **2022**, *200*, 110979. [CrossRef]
5. Lu, Z.Y.; Du, J.; Sun, Y.; Su, G.; Zhang, C.; Kong, X. Effect of ultrafine WC contents on the microstructures, mechanical properties and wear resistances of regenerated coarse grained WC-10Co cemented carbides. *Int. J. Refract. Met. Hard Mater.* **2021**, *97*, 105516. [CrossRef]

6. Rayón, E.; Bonache, V.; Salvador, M.D.; Roa, J.; Sánchez, E. Hardness and Young's modulus distributions in atmospheric plasma sprayed WC-Co coatings using nanoindentation. *Surf. Coat. Technol.* **2011**, *205*, 4192–4197. [CrossRef]
7. Garcia, J. Influence of Fe-Ni-Co binder composition on nitridation of cemented carbides. *Int. J. Refract. Met. Hard Mater.* **2012**, *30*, 114–120. [CrossRef]
8. Li, H.Y.; Dong, C.F.; Xiao, K.; Li, X.; Zhong, P. Relationship Between Microstructure and Corrosion Behavior of Cr12Ni3Co12Mo4W Ultra-High-Strength Martensitic Stainless Steel. *Acta Metall. Sin.* **2016**, *29*, 1064–1072. [CrossRef]
9. Thomas, S.V.; Willard, M.A.; Martone, A.; Heben, M.J.; Solomon, C.V.; Welton, A.; Boolchand, P.; Ewing, R.C.; Wang, C.; Bud'Ko, S.L.; et al. Processing of soft magnetic fine powders directly from as-spun partial crystalline $Fe_{77}Ni_{5.5}Co_{5.5}Zr_7B_4Cu$ ribbon via ball mill without devitrification. *IEEE Trans. Magn.* **2020**, *56*, 1–9. [CrossRef]
10. Pu, J.; Han, M.T.; Wang, T.; Zhu, X.; Lu, M.; Chen, J.; Liu, W.; Dai, Y.; Tan, Y. The enhanced confinement effect of double shell hollow mesoporous spheres assembled with nitrogen-doped copper cobaltate nanoparticles for enhancing lithium-sulfur batteries. *Electrochim. Acta.* **2022**, *404*, 139597. [CrossRef]
11. Roulon, Z.; Missiaen, J.M.; Lay, S. Carbide grain growth in cemented carbides sintered with alternative binders. *Int. J. Refract. Met. Hard Mater.* **2020**, *86*, 105088. [CrossRef]
12. Uhrenius, B.; Pastor, H.; Pauty, E. On the composition of Fe-Ni-Co-WC-based cemented carbides. *Int. J. Refract. Met. Hard Mater.* **1997**, *15*, 139–149. [CrossRef]
13. Shon, I.J.; Jeong, I.K.; Ko, I.K.; Doh, J.M.; Woo, K.D. Sintering behavior and mechanical properties of WC-10Co, WC-10Ni and WC-10Fe hard materials produced by high-frequency induction heated sintering. *Ceram. Int.* **2009**, *35*, 339–344. [CrossRef]
14. Biurrun, T.S.; Cabezas, L.L.; Cuadrado, J.N.; Lopez, F.I.; Martinez-Pampliega, R.; Sánchez-Moreno, J.M. Densification of WC-Fe-Ni-Co-Cr cemented carbides processed by HIP after sintering: Effect of WC powder particle size. *Int. J. Refract. Met. Hard Mater.* **2023**, *110*, 105994. [CrossRef]
15. Tarraste, M.; Kübarsepp, J.; Juhani, K.; Mere, A.; Kolnes, M.; Viljus, M.; Maaten, B. Ferritic chromium steel as binder metal for WC cemented carbides. *Int. J. Refract. Met. Hard Mater.* **2018**, *73*, 183–191. [CrossRef]
16. Wittmann, B.; Schubert, W.D.; Lux, B. WC grain growth and grain growth inhibition in nickel and iron binder hardmetals. *Int. J. Refract. Met. Hard Mater.* **2002**, *20*, 51–60. [CrossRef]
17. Gao, Y.; Luo, B.H.; He, K.J.; Zhang, W.W.; Bai, Z.H. Effect of Fe/Ni ratio on the microstructure and properties of WC-Fe-Ni-Co cemented carbides. *Ceram. Int.* **2018**, *44*, 2030–2041. [CrossRef]
18. Kakeshita, T.; Wayman, C.M. Martensitic transformations in cermets with a metastable austenitic binder I: WC-(Fe-Ni-C). *Mater. Sci. Eng. A* **1991**, *141*, 209–219. [CrossRef]
19. Guo, Z.X.; Xiong, J.; Yang, M.; Wang, J.; Sun, L.; Wu, Y.; Chen, J.; Xiong, S. Microstructure and properties of Ti(C,N)-Mo_2C-Fe cermets. *Int. J. Refract. Met. Hard Mater.* **2009**, *27*, 781–783. [CrossRef]
20. Chang, S.H.; Chang, P.Y. Investigation into the sintered behavior and properties of nanostructured WC-Co-Ni-Fe hard Metal alloys. *Mater. Sci. Eng. A* **2014**, *606*, 150–156. [CrossRef]
21. Schubert, W.D.; Fugger, M.; Wittmann, B.; Useldinger, R. Aspects of sintering of cemented carbides with Fe-based binders. *Int. J. Refract. Met. Hard Mater.* **2015**, *49*, 110–123. [CrossRef]
22. Guillermet, A.F. Thermodynamic properties of the Co-W-C system. *Metall. Trans. A* **1989**, *20*, 935–956. [CrossRef]
23. Markström, A.; Frisk, K.; Sundman, B. A revised thermodynamic description of the Co-W-C system. *J. Phase Equilib. Diffus.* **2005**, *26*, 152–160. [CrossRef]
24. Fernandes, C.M.; Vilhena, L.M.; Pinho, C.M.S.; Oliveira, F.; Soares, E.; Sacramento, J.; Senos, A. Mechanical characterization of WC-10wt% AISI 304 cemented carbides. *Mater. Sci. Eng. A* **2014**, *618*, 629–636. [CrossRef]
25. Zhou, P.; Peng, Y.B.; Buchegger, C.; Du, Y.; Lengauer, W. Experimental investigation and thermodynamic assessment of the C-Co-Fe-Ni-W system. *Int. J. Refract. Met. Hard Mater.* **2016**, *54*, 60–69. [CrossRef]
26. Rabouhi, H.; Khelfaoui, Y.; Khireddine, A. Comparative study by image analysis of WC-Co alloys elaborated by liquid phase sintering and hot isostatic pressing. *Ann. Chim.-Sci. Mater.* **2020**, *44*, 263–269. [CrossRef]
27. Wei, C.B.; Song, X.Y.; Fu, J.; Lv, X.; Wang, H.; Gao, Y.; Zhao, S.; Liu, X. Effect of Carbon Addition on Microstructure and Properties of WC-Co Cemented Carbides. *J. Mater. Sci. Technol.* **2012**, *28*, 837–843. [CrossRef]
28. Chang, S.H.; Chang, M.H.; Huang, K.T. Study on the sintered characteristics and properties of nanostructured WC-15 wt% (Fe-Ni-Co) and WC-15 wt% Co hard metal alloys. *J. Alloys Compd.* **2015**, *649*, 89–95. [CrossRef]
29. Konyashin, I.; Hlawatschek, S.; Ries, B.; Lachmann, F.; Dorn, F.; Sologubenko, A.; Weirich, T. On the mechanism of WC coarsening in WC-Co hardmetals with various carbon contents. *Int. J. Refract. Met. Hard Mater.* **2009**, *27*, 234–243. [CrossRef]
30. Upadhyaya, G.S.; Bhaumik, S.K. Sintering of submicron WC-10wt.%Co hard metals containing nickel and iron. *Mater. Sci. Eng. A* **1988**, *105–106*, 249–256. [CrossRef]
31. Pan, Y.F.; Liu, A.J.; Huang, L.; Du, Y.; Jin, Y.; Yang, X.; Zhang, J. Effects of metal binder content and carbide grain size on the microstructure and properties of SPS manufactured WC-Fe composites. *J. Alloys Compd.* **2019**, *784*, 519–526. [CrossRef]
32. Gao, Y.; Luo, B.H.; He, K.J.; Jing, H.B.; Bai, Z.H.; Chen, W.; Zhang, W.W. Mechanical properties and microstructure of WC-Fe-Ni-Co cemented carbides prepared by vacuum sintering. *Vacuum* **2017**, *143*, 271–282. [CrossRef]
33. Liu, G.H.; Li, R.D.; Yuan, T.C.; Zhang, M.; Zeng, F. Spark plasma sintering of pure TiCN: Densification mechanism, grain growth and mechanical properties. *Int. J. Refract. Met.* **2017**, *66*, 68–75. [CrossRef]

34. Yang, G.J.; Gao, P.H.; Li, C.X.; Li, C.J. Simultaneous strengthening and toughening effects in WC-(nanoWC-Co). *Scr. Mater.* **2012**, *66*, 777–780. [CrossRef]
35. Godse, R.; Gurland, J. Applicability of the critical strain fracture criterion to WC-Co hard metals. *Mater. Sci. Eng. A* **1988**, *105–106*, 331–336. [CrossRef]
36. Sheikh, S.; M'Saoubi, R.; Flasar, P.; Schwind, M.; Persson, T.; Yang, J.; Llanes, L. Fracture toughness of cemented carbides: Testing method and microstructural effects. *Int. J. Refract. Met.* **2015**, *49*, 153–160. [CrossRef]
37. Xu, Z.H.; Ågren, J. A modified hardness model for WC-Co cemented carbides. *Mater. Sci. Eng. A* **2004**, *386*, 262–268. [CrossRef]
38. Li, X.; Zhang, X.W.; Zhang, J.F.; Zhang, Q.; Ji, V.; Liu, J.L. Effect of Mo and C additions on eta phase evolution of WC-13Co cemented carbides. *Coatings* **2022**, *12*, 1993. [CrossRef]
39. Liu, K.; Wang, Z.H.; Yinet, Z.B.; Cao, L.; Yuan, J. Effect of Co content on microstructure and mechanical properties of ultrafine grained WC-Co cemented carbide sintered by spark plasma sintering. *Ceram. Int.* **2018**, *44*, 18711–18718. [CrossRef]

coatings

MDPI

Article

Ultrasonic-Induced Grain Refinement in Laser Cladding Nickel-Based Superalloy Reinforced by WC Particles

Jizhuang Wang [1], Jianzhong Zhou [1,*], Teng Zhang [1], Xiankai Meng [2], Pengfei Li [1], Shu Huang [1] and Hao Zhu [1]

[1] School of Mechanical Engineering, Jiangsu University, Zhenjiang 212013, China
[2] Institute of Advanced Manufacturing and Modern Equipment Technology, Jiangsu University, Zhenjiang 212013, China
* Correspondence: zhoujz@ujs.edu.cn

Abstract: Laser cladding was used to prepare three composite coatings, i.e., Inconel 718 nickel-based superalloy (IN718), IN718-50 wt.% WC created by adding tungsten carbide (WC) particles and IN718-50 wt.% WC assisted by ultrasonic vibration. The phase composition, microstructure evolution, microhardness, residual stress and tribological properties of the three coatings were studied. The addition of WC enhances hardness and improves tribological properties, but also causes aggregation and considerable formation of carbides associated with rough structure. Ultrasonic vibration greatly refines the solidification microstructure, as it can break the growing dendrites, reduce the aggregation of reinforced particles and refine solidified structure. The average microhardness of the latter two composite coatings was increased by 36.37% and 57.15%, respectively, compared with the first IN718 coating, and the last composite coating (ultrasonic assistance) had the lowest COF (0.494). The WC particles and refined carbides converted the wear mechanism from adhesive wear to abrasive wear. In addition, the resultant stress on the surface of the composite coating roughly doubled after adding 50 wt.% WC, and only increased by 49.53% with ultrasonic treatment. The simulation results indicate that acoustic cavitation mainly occurs in the middle and bottom of the molten pool and proper frequency ultrasonic is conducive to the generation of the cavitation effect.

Keywords: laser cladding; IN718 nickel-based superalloy; tungsten carbide; ultrasonic; acoustic cavitation

Citation: Wang, J.; Zhou, J.; Zhang, T.; Meng, X.; Li, P.; Huang, S.; Zhu, H. Ultrasonic-Induced Grain Refinement in Laser Cladding Nickel-Based Superalloy Reinforced by WC Particles. *Coatings* **2023**, *13*, 151. https://doi.org/10.3390/coatings13010151

Academic Editor: Alexander D. Modestov

Received: 7 December 2022
Revised: 8 January 2023
Accepted: 9 January 2023
Published: 11 January 2023

1. Introduction

IN718 is a precipitate-strengthened superalloy based on Ni-Fe-Cr elements, possessing high yield strength and good resistance to heat, creep and corrosion, and therefore has been widely used in the manufacturing of gas turbine blades, engine casings, pumps and molds [1,2]. Under high-temperature, overloading and alternating-loading severe serving conditions, the failure of nickel-based alloy components is mainly caused by surface abrasion, corrosion and fatigue spalling, resulting in the scrapping of a large number of expensive mechanical parts [3,4]. Therefore, numerous surface modification techniques are used to improve surface performances of these parts to prolong service life. In recent years, with the merits of good metallurgical bonding, convenience for automation and controllable thickness, laser cladding technology has been widely used in preparing functional coatings on surfaces [5,6].

However, it is difficult for pure nickel-based coating to meet practical application requirements. Therefore, ceramic particles (such as TiC, WC, Al_2O_3 and ZrO_2) possessing the properties of good thermal stability, high hardness and superior wear resistance are added into nickel-based alloy powder to fabricate metal-based ceramic composite coatings with excellent performance [7–10]. Therefore, WC particles having a fine affinity with nickel-based alloys are ideal materials for improving the wear properties of nickel-based coatings [11–13]. Xia et al. [14] studied the tribological properties of laser melting GH3536-WC composite coatings reinforced by coarse and fine WC particles, concluding that the

more uniform distribution of fine WC particles can significantly enhance the effect of dispersion strengthening under the same WC content. Shen et al. [15] fabricated NiCrSiBC-WC composite coatings with different WC content to investigate the mechanism of grain refinement and crack behavior, and found that high WC content can refine solidified structures obviously while also causing increases in the tensile stress and crack susceptibility of coatings. In fact, due to the differences in physical properties between ceramic particles and Ni-based alloy as well as the rapid melting/solidification characteristics of laser cladding, metallurgical defects such as uneven distribution of WC ceramic particles, cracks and pores are more likely to appear in the composite coating [16–18].

Ultrasonic vibration, as a type of auxiliary field, has been applied in the solidification process of molten metal to refine the growth of microstructures via the synergistic effect of ultrasonic cavitation and acoustic streaming [19,20]. Based on mathematical deduction and analysis, Zhu et al. [21] proposed that the degree of undercooling and nucleation rate of the molten pool increase with increasing amplitude and frequency of the ultrasonic vibration. Moreover, Fan and Chen et al. [22] conducted a series of experiments on ultrasonic-field-assisted gas tungsten arc cladding high-entropy alloys and found that the size of grains and crystal boundary decrease with an increase in ultrasonic power. In addition, the acoustic streaming and thermal effect of ultrasonic in the molten pool were studied using numerical simulation. At present, most research mainly focuses on the field of pure superalloy coating, while the mechanism of ultrasonic vibration on the distribution and decomposition of reinforced particles as well as the morphologies of precipitated carbides in the composite coatings is still insufficiently studied.

In this study, IN718 coating, IN718-50 wt.% WC and IN718-50 wt.% WC (ultrasonic assistance) composite coatings were prepared by laser cladding. The phase composition, microstructure evolution, microhardness, wear resistance and residual stress of the three coatings were investigated. In addition, both the sound pressure distribution and cavitation process in the molten pool were analyzed by numerical simulation.

2. Materials and Methods

2.1. Materials

The raw materials were spherical IN718 alloy powder (particle size: 40–100 μm) and spherical WC particles (particle size: 30–70 μm), as shown in Figure 1, which were then mechanically mixed by a planetary ball mill for 180 min. Finally, the mixed powder was dried in a vacuum drying oven at 373.15 K for 30 min. The chemical composition of bonding metal IN718 alloy powder is shown in Table 1. The forged In718 alloy with the dimensions of 58 mm × 38 mm × 6 mm was used as the substrate. Before the experiment, the surface of the substrate was grinded with sandpaper and washed with acetone solution to remove oil stains.

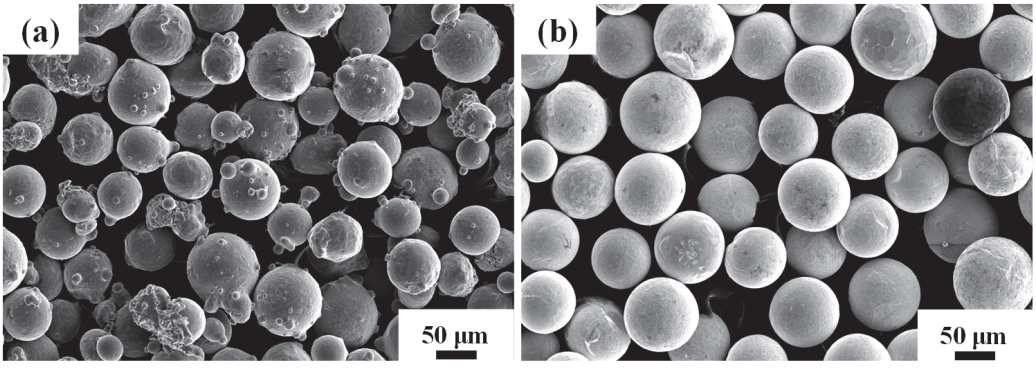

Figure 1. SEM images of powders. (**a**) Spherical IN718; (**b**) spherical WC.

Table 1. Chemical composition of bonding metal IN718 alloy powder (wt.%).

Elements	Ni	Cr	Nb	Mo	Al	Si	Ti	Fe
wt.%	52.3	19.01	5.07	3.06	0.57	0.35	1.00	Bal.

2.2. Experimental Procedure

The experiment was carried out on a composite device, and the details of the overall layout diagram are shown in Figure 2. The whole device is composed of two parts, including the laser cladding system and the ultrasonic vibration device. The laser cladding system consists of a continuous fiber laser (IPG-YLS-2000-TR, Ipg Photonics Corporation, Oxford, MA, USA), a powder feeder (Acunity, Acunity GmbH, North Rhine-Westphalia, Germany) and a six-axis industrial robot (KUKA, KUKA Schweissanlagen, Augsburg, Germany). The ultrasonic vibration device (CYCS-300TJ, Chiyu Ultrasonic Equipment, Jinhua, China) is composed of a piezoelectric transducer, an acoustic horn and an ultrasonic regulator. The resonant frequency of ultrasonic generator is adjustable from15 kHz to 60 kHz, and the maximum amplitude is 30 μm. The perpendicular relation and tight junction between the horn and the substrate were double-checked before the experiment to ensure the introduction of ultrasonic.

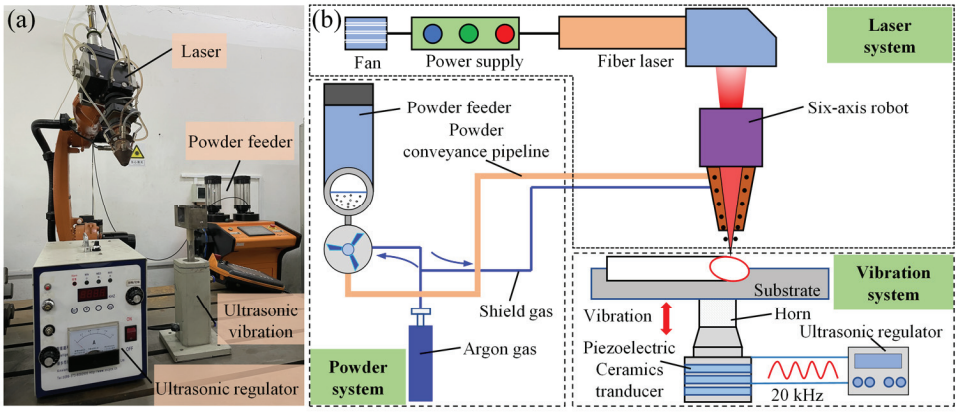

Figure 2. Setup for laser cladding with ultrasonic assistance. (**a**) Overall layout diagram; (**b**) schematic diagram of ultrasonic-assisted laser cladding processing system.

Based on the optimization results of previous experiments, the process parameters of laser cladding are listed in Table 2 [18,20,23]. The IN718 coating, IN718-50 wt.% WC and IN718-50 wt.% WC (ultrasonic assistance) composite coatings were fabricated, and were marked as Coating A, Coating B and Coating C, respectively. Figure 3a,b show their dimensions and the scanning strategy, respectively. Moreover, all coatings and the single track were fabricated using the same process parameters of laser cladding.

Table 2. The process parameters used in preparation of coatings.

Laser Cladding	Value	Ultrasonic Vibration	Value
Laser power (w)	1300	Ultrasonic power (w)	300
Scanning speed (mm/min)	450	Amplitude (μm)	20
Power feeding rate (g/min)	16	Angular frequency (kHz)	20
Overlapping ration (%)	50	Wavelength (mm)	1.7

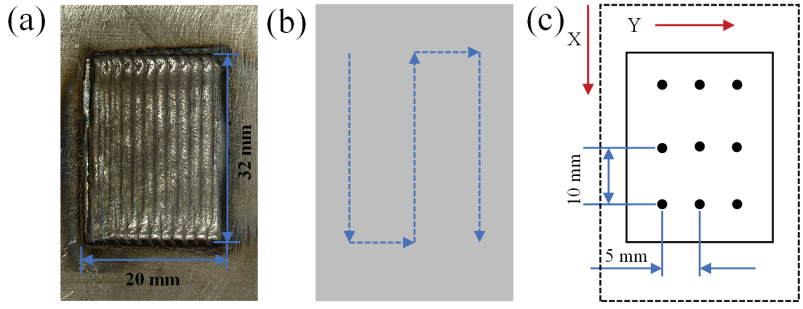

Figure 3. (**a**) Top view of the laser cladding coating; (**b**) laser scanning path; (**c**) residual stress testing points.

2.3. Microstructure and Properties Characterization

Samples were prepared using wire-cutting machine for metallographic observation and phase detection. The metallographic samples were etched by aqua regia solution (HCl: HNO_3 = 3: 1) for 220 s to observe the microstructure under scanning electron microscopy (SEM, S-3400N, Japan) and optical microscope (OM, Axio-Lab.A1, Carl Zeiss AG, Baden-Wurttemberg, Germany). X-ray diffractometer (XRD, Bruker D8 Advance, Bruker, Karlsruhe, Germany) was used to analyze the phase of coatings. The residual stress on the surface of coatings was obtained by the $\sin^2\psi$ method with a Proto-LXRD instrument (X-350A, Aurora Group Company, Vancouver, Canada). The high voltage of the X-ray was 22 kV and the current was 6 mA. Cr-Kα characteristic X-ray filtered by nickel and the diffraction plane 220 were utilized for the measurement. The stress constant was −601 MPa/deg.

The mechanical properties of different coatings were measured by Vickers microhardness tester (MHVS-1000BZ, Yizhong Precision Instrument, Shanghai, China) and friction and wear tester (HT-1000, Kaihua Technology Company, Lanzhou, China). The load and hold time of the microhardness test were set as 0.2 kg and 15 s, respectively. Before friction and wear test, the surface of coatings was grounded with sandpapers from 400# to 2000# and then polished with diamond polishing agents to obtain high-quality smooth surface. In addition, the material of grinding balls (φ = 5 mm) was Si_3N_4. The wear tests were carried out with a load of 1500 g and a constant duration of 20 min.

3. Results and analysis

3.1. Cross-Sectional Morphologies of Different Coatings

Figure 4 shows the cross-sectional morphologies of three coatings fabricated by laser cladding. It can be found that Coating A contains many pores, while the main defects of Coating B are longitudinal and transverse cracks, as shown in Figure 4a,b. Due to the rapid solidification in the laser cladding process, pores are caused by shielding gas and air which cannot escape out of the molten pool in time, as shown in Figure 4(a1,a2). Under natural conditions, melt flow in the molten pool is not strong enough to overcome agglomeration and sedimentation of WC particles because of considerable density differences (Table 3), as shown in Figure 4(b2). Carefully observing Figure 4(b1,b2), it can be seen that transverse cracks occur at the interface between the coating and the substrate, while longitudinal cracks are observed in the overlapping area. The longitudinal cracks propagate in the direction of the highest temperature gradient, i.e., the preferentially growing direction of dendrites, and then penetrate the whole composite coating. The transverse cracks are induced by the difference of the coefficient of thermal expansion in different regions, especially the reinforced WC particles which tend to cluster toward the bottom of the coating. The micro-jetting and acoustic streaming generated by ultrasonic can effectively promote the internal flow of the melt pool, and thus the WC particles are relatively evenly

distributed across the cladding layer. In addition, there are no obvious pores and cracks in the cross-section of the coating, as shown in Figure 4c.

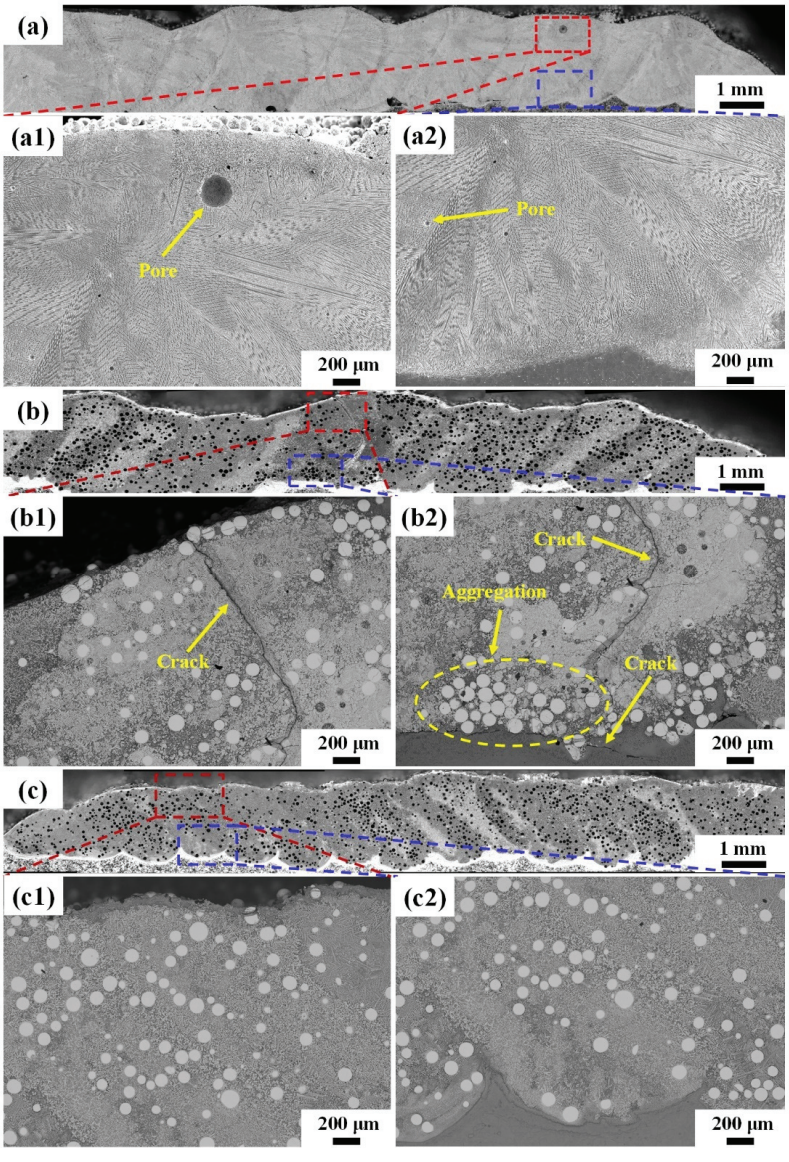

Figure 4. Cross-sectional morphologies of different coatings: (**a**) Coating A; (**b**) Coating B; (**c**) Coating C; 1 and 2 represent partial enlarged images of the top and bottom regions respectively.

Table 3. Physical properties of bonding metal IN718 alloy and WC particles.

Materials	Density	Expansion Coefficient	Elastic Modulus	Melting Point
	g cm^{-3}	10^{-6} K^{-1}	Gpa	K
IN718	8.24	11.8–18.7	199.9–240	1523
WC	16.5	6.5–7.4	650–710	2798

3.2. Microstructure of Coatings

3.2.1. Phase Composition Analysis

Figure 5a shows the XRD patterns of the three coatings. Tungsten carbide particles possessing high thermal stability and chemical inertness experience almost no conversion or chemical reactions under individual heating. The possible decomposition reactions of WC particles in the molten pool were calculated using HSC thermodynamic software. The Gibbs free enthalpy (**Δ**G) of WC decomposing into W_2C and WC turns out to be negative only when temperature surpasses 2614 K (as shown in Figure 5b), which means this reaction can proceed spontaneously with the rise in temperature. However, with strong thermal convection and high-density energy in the molten pool, tungsten carbide particles can decompose into W_2C even at low temperatures (873 K~1143 K), as reported by Nerz et al. [24]. The free enthalpy of decarburization reaction (2) is positive, which means that it cannot proceed spontaneously without external force. In fact, the non-equilibrium solidifying characteristics of the laser cladding process, including high cooling rate (up to 7800 K/s) and strong thermal convection (up to 0.5 m/s) induced by the Marangoni effect, promote the forward process of the reaction [25,26].

$$2WC \rightarrow W_2C + C \quad (1)$$

$$W_2C \rightarrow 2W + C \quad (2)$$

$$WC + W + L \rightarrow M_3W_3C \quad (3)$$

$$M + C \rightarrow MC \quad (4)$$

where L means Fe-C liquid phase and M means Cr elements in the IN718 alloy.

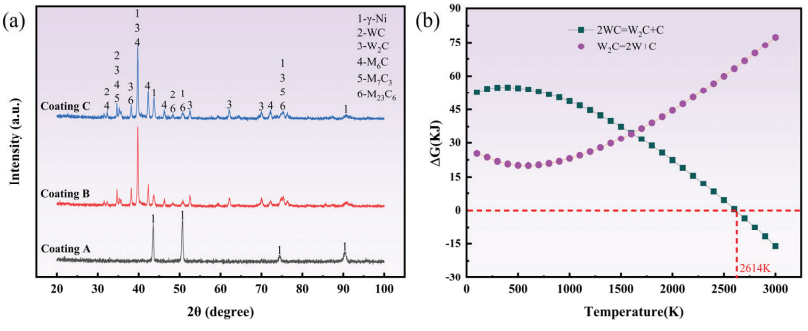

Figure 5. (**a**) XRD patterns of the three coatings; (**b**) relationship between temperature and free enthalpy.

Therefore, under high-intensity laser irradiation, WC decomposes into W_2C and C at the beginning, and then the intermediate product (W_2C) proceeds to undergo the decarburization reaction. During the dynamic decomposition process, the W and C elements can react with the active elements (such as Fe, Mo and Cr elements) in the molten pool to precipitate carbides with different shapes and crystalline structures. The XRD pattern shows that the dominant phase in Coating A is $Fe_{0.64}Ni_{0.36}$ supersaturated solid solution (namely γ-Ni). With the addition of numerous WC particles, the phases of Coating B and Coating C are mainly γ-Ni, WC, W_2C, M_6C (Fe_3W_3C and Fe_3Mo_3C), M_7C_3 (Cr_7C_3) and $M_{23}C_6$ ($Cr_{23}C_6$) [15,27].

Attentive examination of Figure 5a reveals some detailed information: the main peak position of Coating A is 50.7038° and those of Coating B and Coating C are 39.7464° and 39.7656°, respectively. The left shift of the diffraction peak is closely related to the increase in residual stress caused by a considerable number of precipitated carbides, which is consistent with prior studies [14,25]. The mean grain size of the coating can be deduced

from the Scherrer equation [28]. The full width at half maximum (FWHM) of the XRD diffraction peak is calculated by

$$L = \frac{0.9\lambda}{\beta\cos\theta} \tag{5}$$

where L is the mean grain size, λ is the X-ray wavelength, β is the FWHM and θ is half the scattering angle. According to this equation, the FWHM is inversely proportional to the mean grain size. Fitting the main peaks of XRD curves using Gaussian functions, the FWHM values of Coatings A, B and C are measured to be 0.31849, 0.25541 and 0.26437, respectively. Therefore, the mean grain size of the three coatings first increases and then decreases. It is noted that the grain size of precipitated carbides is generally larger than the γ-Ni phases of IN718 alloy, and this kind of microstructure is more refined with the application of ultrasonic (as is shown in Figure 6), corresponding with the above inference.

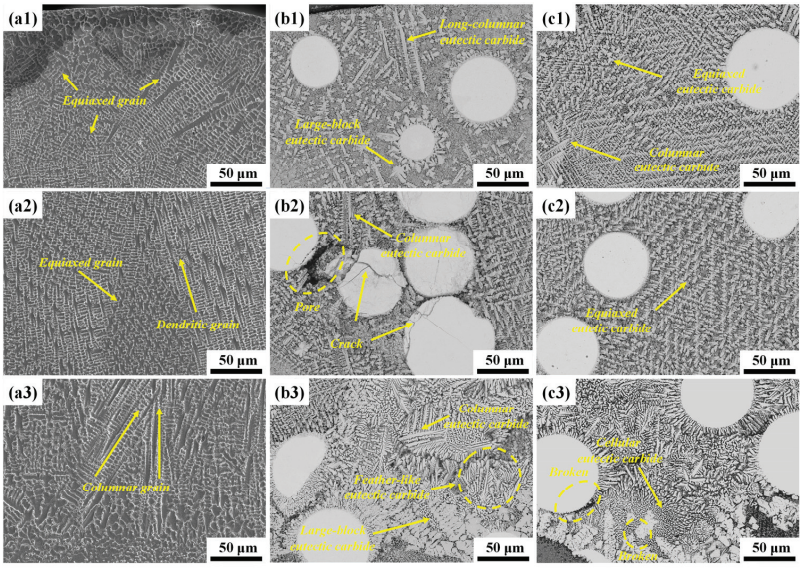

Figure 6. Typical microstructure on cross-section. (**a1**–**a3**), (**b1**–**b3**) and (**c1**–**c3**) are the cross-sectional morphologies of Coating A, Coating B and Coating C, respectively. 1, 2 and 3 represent the top region, middle region and bottom region, respectively.

3.2.2. Microstructure Analysis

The typical microstructure of Coating A is shown in Figure 6. According to the constitutional supercooling criterion, the morphology of a solidified structure depends on the combined parameters of temperature gradient G and solidification rate R [29]. The solidification rate R is defined as the rate of normal advance at the solidification interface, which can be expressed as [26]:

$$R = V_s \cdot i \cdot n^* \tag{6}$$

where V_s, i and n^* correspond to the laser scanning velocity, the unit vector of scanning direction and the interface normal vector of the solidification front, respectively. Therefore, the value of solidification rate R gradually decreases in the depth direction. The surface of the molten pool is at the gas–liquid interface where it is affected by a strong dual action of thermal radiation and thermal convection, while the interior is mainly affected by thermal convection caused by the Marangoni effect. As a result, the temperature gradient G gradually decreases in the depth direction. The morphology of the solidified structure is determined by the morphological parameters G/R; the larger the value, the rougher the microstructure. Meanwhile, the size of the solidified structure decreases with the increase

in the cooling rate $G \times R$ [30]. Therefore, the microstructure of Coating A sequentially presents as fine equiaxed grains, dendritic crystal and coarse columnar grains from the top to bottom of the coating, as shown in Figure 6(a1–a3).

When adding 50 wt.% WC particles, the microstructure undergoes a dramatic shift from single γ-Ni solid solution phase to a large number of precipitated carbides. At the top region of Coating B, the direct laser radiation and endothermic decomposition of tungsten carbide both promote the higher temperature gradient G and cooling rate $G \times R$ around WC particles [14]. Thus, WC particles act as heterogeneous nucleation sites for precipitated carbides which appear as long columnar and large block carbides with sharp edges, as shown in Figure 6(b1). Due to the addition of a high content of WC particles, obvious cracks and pores occur in the cluster regions of multiple particles at the middle region of Coating B, as shown in Figure 6(b2). It is noted that cracks initiate at the edges of WC particles and gradually extend to the interior, presenting as brittle fracture of multiple clustered particles. These phenomena are mainly related to local stress concentration and poor flowability of IN718 melt caused by the agglomeration of WC particles [15,27]. At the bottom region of Coating B, the WC particles with high density tend to sink, and the precipitated carbides become granular and columnar in shape rather than block-shaped, and clustered in flocculent and chrysanthemum shapes. In addition, mixed microstructures such as feather-like, long columnar and large block carbides with obvious dendrite orientation form, as shown in Figure 6(b3).

After introducing ultrasonic vibration into the molten pool, the solidified microstructure is refined, apparently because of the synergetic effects between acoustic streaming and cavitation. The acoustic streaming and micro-jet emitted by the collapse of cavitation bubbles both accelerate the thermal convection of the molten pool, which is conducive to reducing the temperature gradient G. Thus, plenty of fine equiaxed carbides are generated at the top of Coating C, as shown in Figure 6(c1). Moreover, the solidification rate R decreases with increasing depth, which leads to the formation of columnar carbides. The refinement of the microstructure is more remarkable at the bottom region associated with less ultrasonic attenuation, as shown in Figure 6(c2,c3). The epitaxial growth of dendrites as well as the large block eutectic carbides are broken on the side near the bottom. In addition, fine dispersed carbides in the shape of cells and arborization are generated.

A map scanning analysis of a whole WC particle and the surrounding area in the metal-base ceramic coatings was carried out, as shown in Figure 7. A dissolution–diffusion layer can be obviously observed around the WC particle, with strips and blocks of tungsten-rich dendrites growing perpendicular to the edges. The W elements are mainly enriched in the surrounding bright white carbides, while the Cr, Fe and C elements are relatively evenly distributed within the coatings. Based on previous studies [18,31], five main phases are observed in Figure 7, namely the bright white tungsten carbide phase (1), the white W_2C phase in the dissolved diffusion layer (2), the block as well as striped eutectic carbide phases (3) and (4), and the dark grey IN718 matrix phase (5). The eutectic carbide phase is produced by the metallurgical combination of W elements released by the thermal decomposition of WC with elements from IN718 alloy at locations relatively far from the WC particles, and contains more Fe, Cr and Ni elements. The chemical compositions of typical phases are shown in Table 4. The results show that the weight ratio of W and C elements in the block carbide is higher than that of the strip carbide, which contains more Nb and Cr elements.

Several typical decomposition characteristics of WC particles are generalized according to the microstructure SEM images in different coatings, as shown in Figure 8. Figure 8a,c are extracted from Coating B, while the others are from Coating C. Firstly, WC particles with a small size are prone to experiencing disintegration and diffusion at high thermal energy densities, while the decomposition type of large WC particles is dissolution–diffusion. Secondly, the main differences between Coating B and Coating C are the morphologies and sizes of precipitated carbides. In Figure 8a, the splitting decomposition of small-scale WC particles occurs at a high temperature, then reacts with the active elements in

the IN718 matrix, which finally precipitate large block carbides with sharp edges and microcracks. However, when ultrasonic is introduced into the molten pool, the edges of carbides become more rounded and their size reduces, as shown in Figure 8b. The same phenomenon can be found in the morphology of the large WC particles. During the cladding process, the energy in the molten pool is not sufficient to cause complete dissolution of large WC particles. The borders of the WC particle are slightly eroded by molten IN718 alloy and form a shallow alloyed reaction layer which is mainly composed of the intermediate product (W_2C) from the decarburization reaction of tungsten carbide. At the same time, the surrounding carbides present as block and strip shapes, as shown in Figure 8c. In Figure 8d, the decomposition of WC particles increases obviously because of the completely disappearance of the shell-core structure, and rounded carbides nucleated at the WC particle grow radially after ultrasonic treatment. Meanwhile, the microstructure and size of precipitated carbides are generally refined.

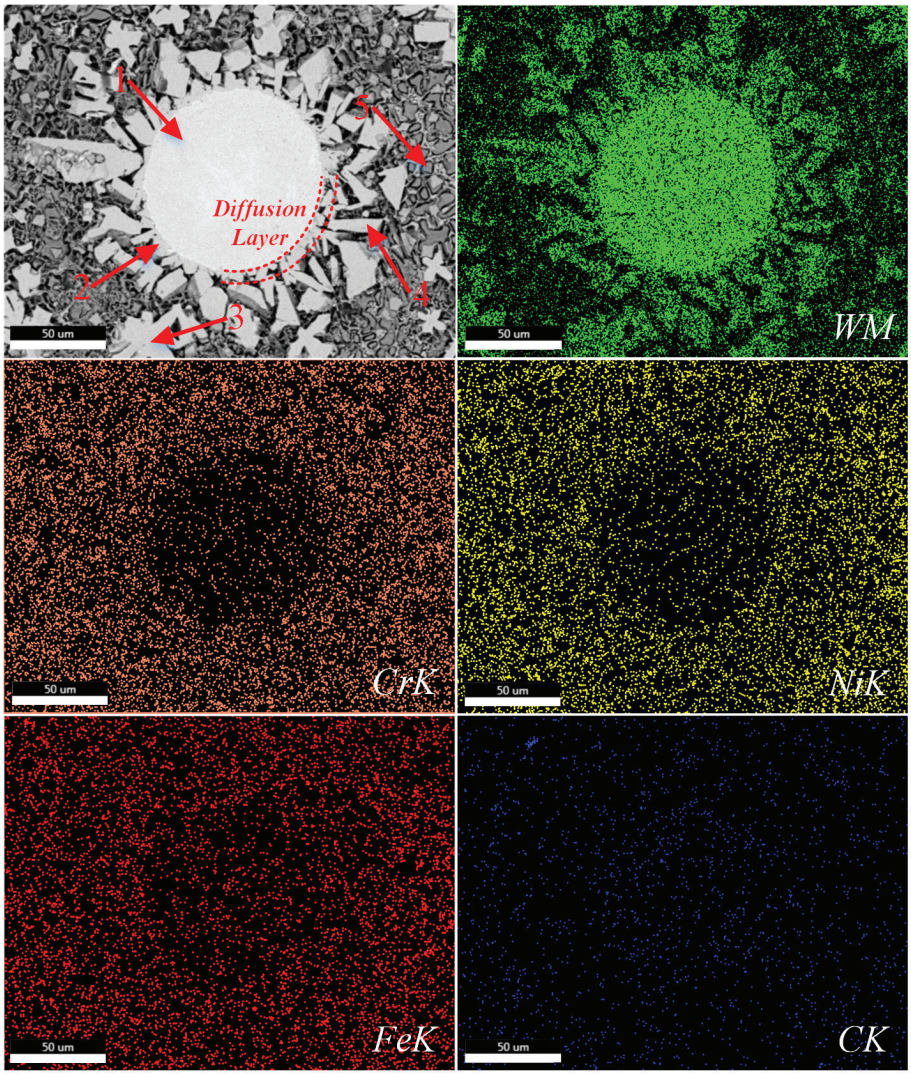

Figure 7. EDS map scanning results of typical microstructure in composite coatings.

Table 4. Chemical compositions of different phases in the composite coating.

Point	Phase	Composition (wt.%)						
		W	C	Ni	Fe	Cr	Mo	Nb
1	WC	78.63	10.13	1.62	2.35	0.96	0.09	6.22
2	W_2C	75.65	6.56	1.05	1.64	0.70	0.18	14.21
3	Block carbide	49.10	9.65	15.25	6.94	9.23	1.03	8.79
4	Strip carbide	42.21	6.54	11.41	4.49	11.64	1.32	22.39
5	Ni matrix	12.35	2.1	45.85	17.58	15.25	0.76	6.11

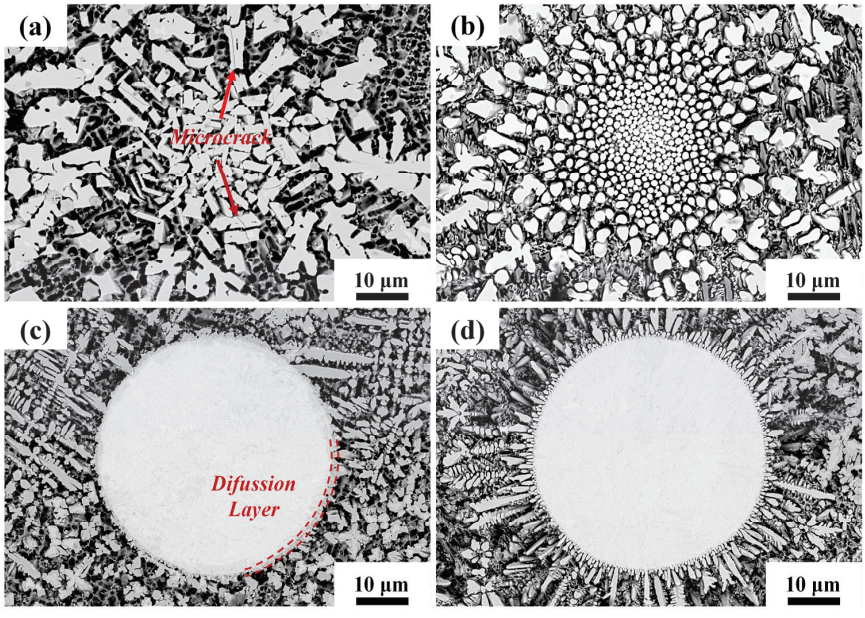

Figure 8. Thermal decomposition characteristics of WC particles during laser cladding process with and without ultrasonic: (**a**,**b**) disintegration–diffusion type for WC particles with small size; (**c**,**d**) dissolution–diffusion type for WC particles with large size.

3.3. Performance of Composite Coating

3.3.1. Microhardness

Figure 9 shows the microhardness distribution along the depth direction of the three coatings. The average microhardness of Coatings A, B and C is 304.27 $HV_{0.2}$, 414.93 $HV_{0.2}$ and 478.15 $HV_{0.2}$, respectively. The microhardness of Coating C increases by 63.22 $HV_{0.2}$ (15.25%) compared with Coating B and is 1.36 times that of Coating A. The enhancement of microhardness in Coating B and Coating C can be ascribed to a large number of precipitated carbides after the addition of WC particles. According to the Hall–Petch formula [32], there is a nonlinear inverse relationship between microhardness and grain size. Thus, the microstructure refinement caused by ultrasonic, as shown in Figure 6, can effectively enhance the microhardness of Coating C. Meanwhile, the fluctuation of microhardness along the depth direction is gentle, which indicates that the homogenization of particle distribution and microstructure has improved significantly.

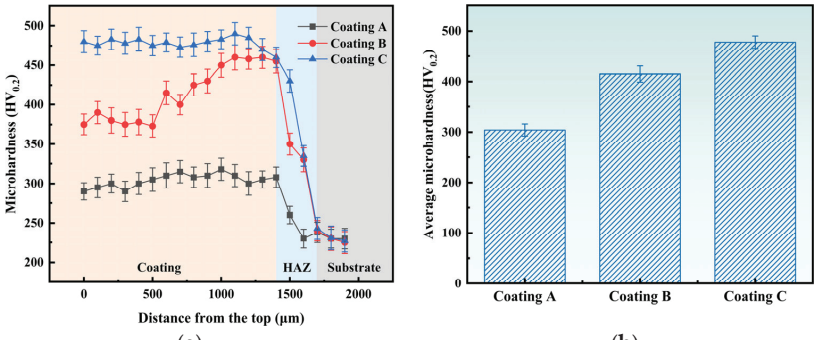

Figure 9. (**a**) Microhardness of different coatings along the depth direction; (**b**) average hardness of cladding layers of different coatings.

3.3.2. Residual Stress

The residual stress of WC-reinforced composite coatings prepared by laser cladding was made up of two parts: thermal stress and shrinkage stress [31]. Thermal stress was generated due to high-temperature ingredients, especially at the interface between the coating and the substrate, while shrinkage stress was induced by the incompatible coefficient of thermal expansion between carbides and nickel-based alloy [15,33]. The generation mechanism of residual stress is shown in Figure 10. Basing on the laser scanning path shown in Figure 3b, the direction along the laser scanning path was set as x, while that perpendicular to it was set as y. Nine points selected evenly on the surface of coatings were measured to obtain the average residual stress. Then, the residual stress component of x direction was set as σ_x, and the residual stress component of y direction was set as σy. Eventually, the resultant stress—which was the vector sum of σ_x and σ_y—was set as σ_t, as shown in Figure 11.

The results indicate that residual tensile stresses are widespread on the surface of coatings, and the residual stress component σ_x is the principal stress, similar to the results of previous studies [34]. With the addition of numerous WC particles, σ_x and σ_y of Coating B increased significantly. It is noteworthy that the gap between σ_x and σ_y on Coating C decreased due to the homogenized effect of ultrasonic. Based on the synthesis results, the resultant stress σ_t for Coating A was 237.19 MPa, while these values increased to 460.43 MPa and 354.68 MPa for Coating B and Coating C, respectively. According to previous studies, the bulk precipitated carbides with sharp edges and uneven distribution of WC particles all increase residual stress levels [14,33]. In short, the distribution of WC particles was improved, and the formation of bulk precipitated carbides with sharp edges was inhibited by ultrasonic, as shown in Figures 6 and 8. Therefore, the resultant stress σ_t of Coating C showed a 22.95% decrease compared with Coating B.

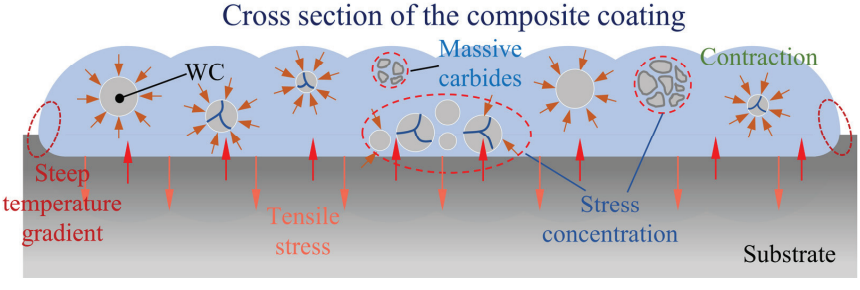

Figure 10. Mechanism of residual stress generation during laser cladding.

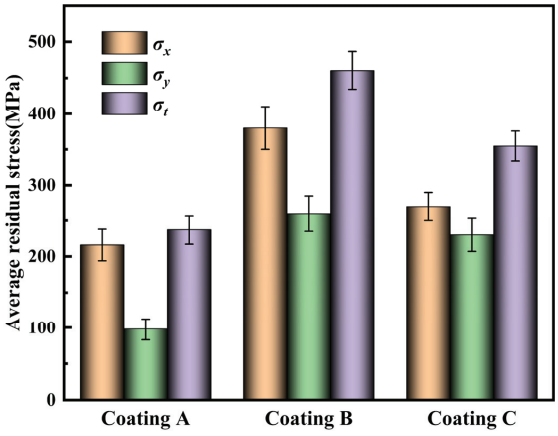

Figure 11. Average residual stress of different coatings.

3.3.3. Tribological Properties

The friction and wear curves of the three coatings are shown in Figure 12a. The friction and wear curves of the three coatings can be divided into two stages: the rapid growth stage and the steady wear stage. In the initial stage, due to the flatness of the sample and the cold-welding effect of wear debris between friction pairs, the grind ball needed greater friction force to overcome the above negative factors. Therefore, the friction and wear coefficient increased significantly. After a period of running-in, as the cold-welding areas were cut off, the friction and wear coefficient decreased sharply, and all curves entered a relatively stable stage after 6 min. The mean coefficients of friction (COFs) for Coatings A, B and C are 0.605, 0.546 and 0.494, respectively. Therefore, the abrasion curve of Coating C is the most stable, and also has the smallest COF. In addition, the abrasion curve of Coating C is more stable than those of the other coatings and it was the first to enter the steady wear stage. This can be attributed to the more uniform distribution of WC particles and grain refinement induced by ultrasonic, as shown in Figures 4 and 6.

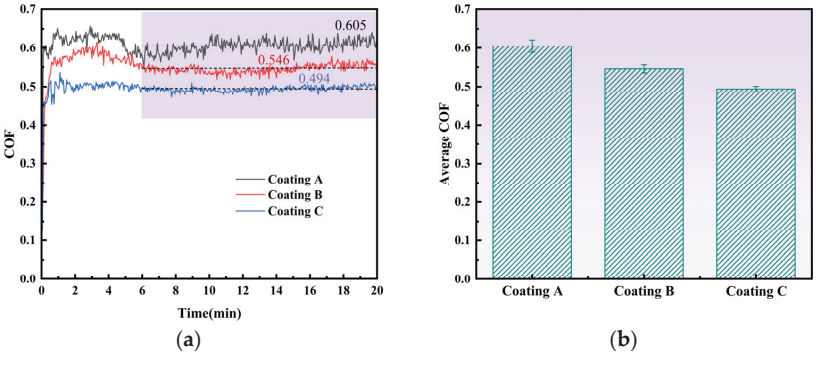

Figure 12. (**a**) Friction and wear curves of different coatings; (**b**) average COF.

In order to further study the wear mechanism of various coatings, the morphologies of worn surfaces were observed by SEM, as shown in Figure 13. The wear scar width decreases successively from 1.058 mm on Coating A to 0.397 mm on Coating C, which means the wear resistance of the coating was improved. For Coating A, which was prepared by IN718 alloy powder, large wear debris, obvious plowing grooves and spalling pits in the sliding direction were found (Figure 13a). The WC particles and precipitated carbides

enhance the wear resistance of the coating. As shown in Figure 13(a2,a3), the WC particles and granular-lump carbides with high hardness can improve surface resistance to local plastic deformation and destruction capabilities. Compared with Coating A and Coating B, Coating C has the smallest wear debris, which can be attributed to the uniform distribution of WC particles and formation of fine dispersed carbides. Acoustic streaming and cavitation induced by ultrasonic promote the even particle distribution in the upper region of the coating and grain refinement. Coating C has excellent friction performance caused by precipitation and grain refinement strengthening.

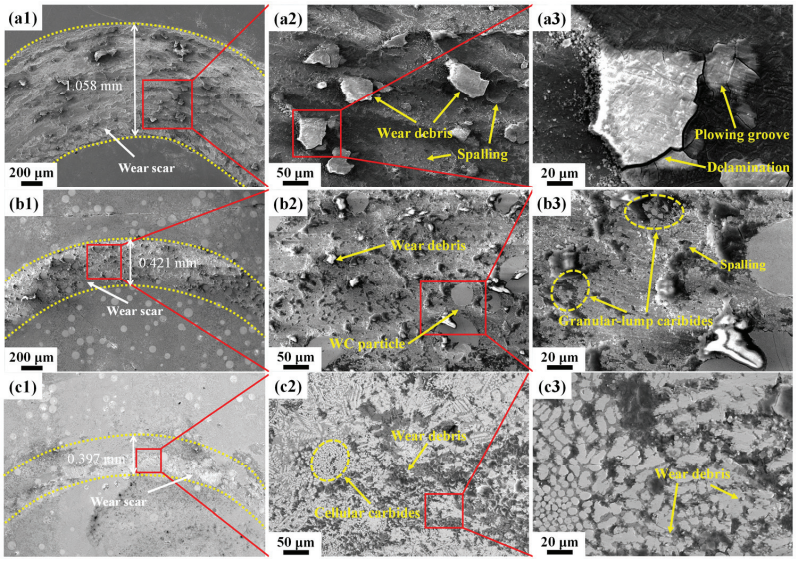

Figure 13. Worn surface morphology of different coatings. (**a1**–**a3**) Coating A; (**b1**–**b3**) Coating B; (**c1**–**c3**) Coating C.

4. Discussion

Numerous recent research works indicate that dendrite fragmentation and microstructure refinement in metal solidification processes with ultrasonic treatment are mainly ascribed to the cavitation effect of ultrasonic [21,35,36]. The cavitation effect is the result of the dynamic interaction between sound pressure and bubbles. Figure 14 shows the two-dimensional model for finite element simulation. The model is predigested to an integration of two semi-ellipses by gauging the cross-section of the single-track cladding layer.

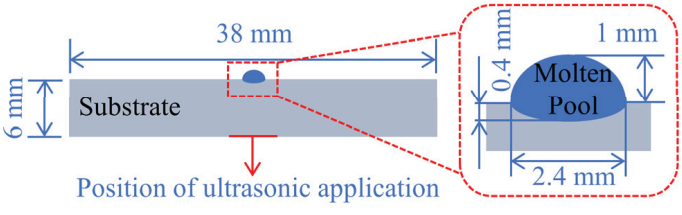

Figure 14. Numerical simulation model for ultrasonic effect.

When high-intensity ultrasonic is introduced into the molten pool, the tiny bubbles in liquid metal are subjected to periodic action of sound pressure. When there is a cavitation

nucleus with initial radius R_0 in the molten pool, the cavitation threshold of the molten pool in the form of sound pressure is expressed as [37]:

$$P_B = P_0 - P_v + \frac{2}{3\sqrt{3}}\left[\frac{\left(\frac{2\sigma}{R_0}\right)}{P_0 - P_v + \frac{2\sigma}{R_0}}\right]^{\frac{1}{2}} \tag{7}$$

where P_0 = 101 kPa is the liquid static pressure, P_v = 0 kPa is the saturated steam pressure, σ = 1.5 N/m is the liquid surface tension coefficient of the IN718 alloy molten pool and R_0 = 5 μm is the initial radius of the cavitation bubble. The corresponding cavitation threshold P_B in liquid IN718 metal is 0.3 MPa, calculated by Equation (5). The ultrasonic input position is located at the bottom of the substrate, the same as in the experimental setup. The molten pool and the substrate are modelled separately with the pressure-acoustic, frequency-domain and solid mechanics modules in COMSOL Multiphysics software. In order to simplify the model, the influences of the WC particle's distribution and dissolution on physical parameters such as liquid metal density and dynamic viscosity are ignored. The entire molten pool is assumed to be filled with the melting IN718 alloy to characterize the function of ultrasonic. The Y-axis sinusoidal displacement $A(t)$ on the middle of the substrate's bottom is set as

$$A(t) = Am\sin(2\pi ft) \tag{8}$$

where A_m = 20 μm is the vibration amplitude and ω = 20 kHz is the ultrasonic frequency. A sound-soft boundary is applied to simulate the vapor–liquid interface at the top of the molten pool, and the acoustic impedance of the top boundary is nil. At the same time, an acoustic-structure boundary coupling model was used to calculate the actual distribution of sound pressure of the molten pool in this work and the results are shown in Figure 15.

Figure 15a shows the transient sound pressure distribution in the molten pool and the displacement of the substrate which was extracted from 1 μs to 6 μs in the first period of ultrasonic (50 μs). It is remarked that regions with the actual value of sound pressure surpassing the cavitation threshold (0.3 MPa) are mainly distributed in the middle and lower parts of the molten pool. Figure 15b shows the average, maximum and minimum sound pressures of the whole molten pool within ten ultrasonic cycles. The results show that the sound pressure in the molten pool gradually tends to be stable despite large amplitude oscillation with time, which is mainly caused by the attenuation effect associated with the propagation of sound waves in the fluid. In order to further investigate the expansion, contraction and collapse process of cavitation bubbles in the molten pool, the evolution law of individual cavitation bubbles under different sound pressure fields is analyzed based on the Rayleigh–Plesset model [38]:

$$\begin{aligned} &R\frac{d^2R}{dt^2} + \frac{3}{2}\left(\frac{dR}{dt}\right)^2 \\ &= \frac{1}{\rho}\left[\left(P_0 + \frac{2\sigma}{R_0} - P_v\right)\left(\frac{R_0}{R}\right)^{3k} - 2\frac{\sigma}{R} - 4\mu\frac{1}{R}\frac{dR}{dt} - P_0 + P_v + P_m\sin(\omega t)\right] \end{aligned} \tag{9}$$

where R is the real-time radius of the cavitation bubble; t is time; k is the ratio of the specific heat at a constant pressure to specific heat at a constant volume of gas in the bubble, taking 4/3; and μ is the dynamic viscosity of molten IN718 alloy, taking 0.005 Pa·s. Additionally, $P_m sin(\omega t)$ is the acoustic pressure in the cladding pool substituted with the simulated values, as shown in Figure 15, to solve this differential equation.

The Rayleigh–Plesset equation is solved using the differential equation interface in COMSOL Multiphysics software, and the evolution law of the cavitation bubble under specific sound pressure amplitude, initial radius and ultrasonic frequency is calculated as shown in Figure 16. The horizontal coordinate is the ratio of time to ultrasound period and the vertical coordinate is the ratio of the real-time radius of the cavitation bubble to the initial radius, showing the variation of the cavitation bubble radius over ten ultrasound periods.

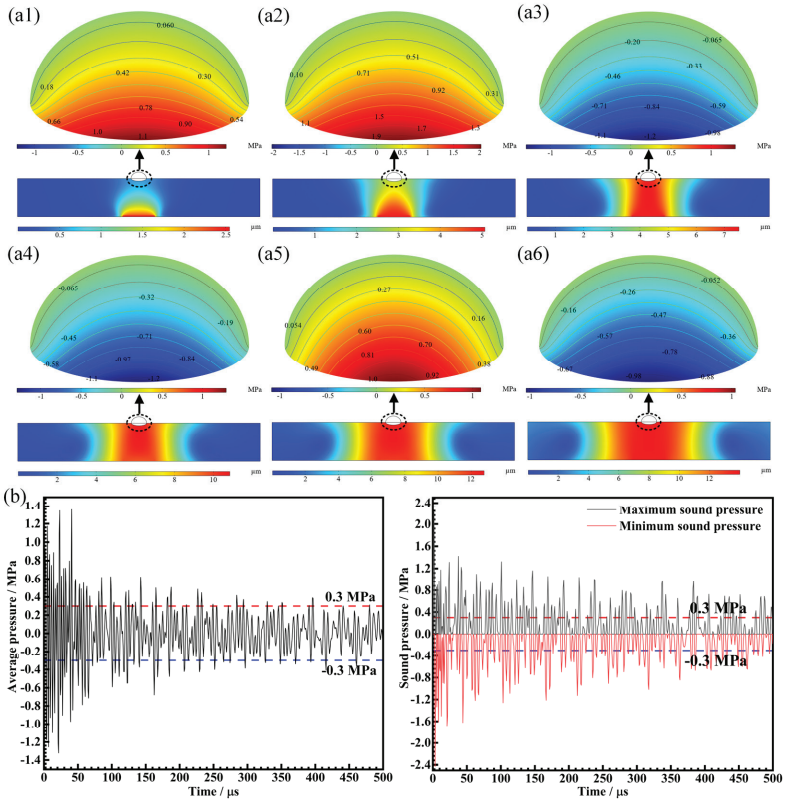

Figure 15. Simulation results of sound pressure in the molten pool: (**a**) sound pressure and vibration amplitude at 1 us to 6 us with 1 us time interval; (**b**) average, maximum and minimum sound pressures in the molten pool; 1–6 represents each microsecond from 1 us to 6 us.

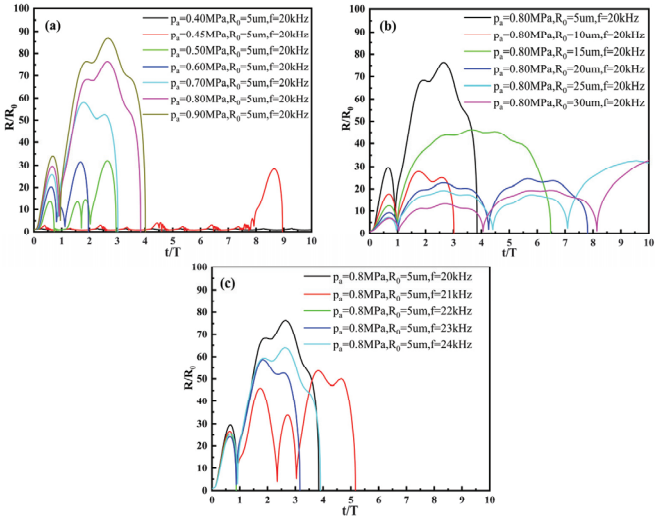

Figure 16. Influence of characteristic parameters on cavitation process. (**a**) Ultrasonic amplitude; (**b**) initial radius; (**c**) ultrasonic frequency.

When the radius of cavitation bubbles and ultrasonic frequency are certain, the evolution law of the bubble's radius with different sound pressures from 0.40 MPa to 0.90 MPa is shown in Figure 16a. The results indicate that only when the sound pressure in the molten pool is much higher than the cavitation threshold can the radius of cavitation bubbles vary significantly. The cavitation bubbles with various radii are invariably in the condition of moderate amplitude and nonlinear oscillation at an acoustic pressure of 0.8 MPa; some do not even collapse within ten sound pressure cycles, as shown in Figure 16b.

Based on the R–P equation to predict the effect of ultrasonic frequency on cavitation bubble radius, Figure 16c shows that under the sound pressure field with the sound pressure of 0.8 MPa and the initial radius of 5 μm, the collapse times of the cavitation bubbles at frequencies of 20 kHz, 21 kHz, 22 kHz, 23 kHz and 24 kHz are 3.85 T, 5.16 T, 0.87 T, 3.16 T and 3.90 T, respectively. Moreover, the maximum radii of the cavitation bubbles during dynamic evolution are 76.36, 53.57, 25.50, 58.62 and 63.88 times the initial radius, respectively. At an ultrasonic frequency of 20 kHz, the intensity of cavitation is guaranteed to include higher radius variation and moderate collapse time. Some experimental observations indicated that when the ultrasonic frequency increased to a certain value, no ultrasonic cavitation occurred or cavitation could not be detected, resulting in a more stable pressure value in the flow field [39]. The main reason for this anomaly is that at higher ultrasonic frequencies, the cavitation bubbles do not have enough time to expand and contract under the effect of alternating strong positive and negative pressures, and the difficulty of generating the cavitation effect increases. Therefore, low-frequency ultrasonic was used in this study.

In this study, the size of the molten pool formed by laser irradiation was approximately equivalent to the width of a single-track cladding layer, which is about 2.4 mm. According to the laser scanning speed (450 mm/min), the existence time of the molten pool was estimated to be about 0.32 s, which was long enough to cover the annihilation time of the cavitation bubbles (about 0.00005 s). Therefore, the solidification process of the molten pool can experience up to ~10^3 cavitation.

Based on the above cavitation simulation, the ultrasonic used in this experiment can generate the cavitation effect, and the cavitation intensity can be guaranteed. On the one hand, a large number of cavitation bubbles are generated and then swell up at the initial stage of ultrasonic cavitation; these bubbles absorb considerable heat from the liquid metal. Therefore, the overall undercooling degree of the molten pool increases, which is conducive to decreasing the grain size. On the other hand, acoustic streaming and microjets generated by the collapse of cavitation bubbles both promote the internal flow of melt as well as the uniform distribution of solute elements in the coating. The combined action of the above two factors refines the microstructure of the coating. Some laboratory observations using synchrotron radiation indicated that acoustic cavitation and acoustic streaming can break the growing dendrites into tiny fragments, and these fragments then act as the nucleus of heterogeneous nucleation [40,41].

The schematic illustration of grain refinement in the molten pool is shown in Figure 17. Under the action of a high-energy density laser, WC particles decompose and react with elements in the IN718 matrix to precipitate massive carbides with sharp edges and coarse structure, as shown Figure 17a,b. After introducing ultrasonic into the molten pool, acoustic cavitation and the acoustic streaming effect greatly improve thermal convection and mass transfer, which promote the decomposition of WC particles, and the size of carbides is refined, as shown in Figure 17c,d. Moreover, the tiny fragments from growing dendrites act as the nucleus of heterogeneous nucleation, which can result in the growth of equiaxed grains.

In short, the enhancements in mechanical properties (microhardness, residual stress and wear resistance) of IN718-WC composite coatings can be attributed to precipitation strengthening and microstructure refining induced by fine dispersed carbides.

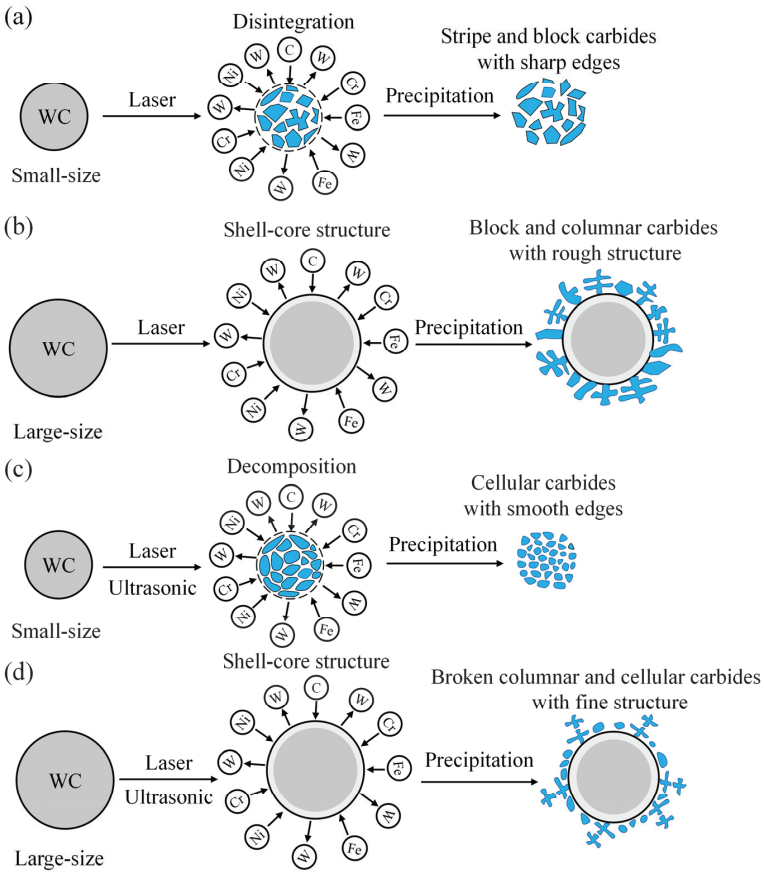

Figure 17. A schematic of grain refinement including small and large size WC particles in laser cladding: (**a**,**b**) without ultrasonic vibration; (**c**,**d**) with ultrasonic vibration.

5. Conclusions

IN718 coating, IN718-50 wt.% WC and IN718-50 wt.% WC (ultrasonic assistance) composite coatings were prepared by laser cladding. The influences of decomposition of WC particles and ultrasonic vibration on composition, microstructure evolution, microhardness, residual stress and tribological prosperities have been systematically analyzed. The following main conclusions can be drawn:

(1) The main phase in laser cladding IN718 coating is the γ-Ni phase. With the addition of numerous WC particles, the phase compositions are converted into γ-Ni, WC, W_2C, M_6C (Fe_3W_3C and Fe_3Mo_3C), M_7C_3 (Cr_7C_3) and $M_{23}C_6$ ($Cr_{23}C_6$) due to considerable generation of precipitated carbides with various shapes and sizes.

(2) The decomposition of WC particles can greatly enhance microhardness and wear resistance of composite coatings. Meanwhile, acoustic streaming and cavitation can homogenize the distribution of WC particles and refine the microstructure. Therefore, the composite coating assisted by ultrasonic has the highest microhardness (478.15 $HV_{0.2}$) and the lowest COF (0.494).

(3) Massive particles and carbides can increase residual stress on the surfaces of coatings, while ultrasonic vibration can inhibit the formation of massive carbides with sharp edges. Thus, the resultant residual stress and the gap between σ_x and σ_y can be effectively decreased.

(4) The cavitation effect is mainly concentrated at the bottom of the molten pool. The ultrasonic used in this work can guarantee the intensity of cavitation, including through higher radius variation and moderate collapse time.

Author Contributions: Conceptualization, J.Z.; methodology, J.Z.; validation, J.W. and T.Z.; formal analysis, T.Z. and P.L.; investigation, J.W.; resources, J.Z., X.M., H.Z. and S.H.; data curation, J.W.; writing—original draft preparation, J.W.; writing—review and editing, J.Z.; visualization, J.W. and P.L.; supervision, J.Z.; project administration, J.Z.; funding acquisition, J.Z., X.M., S.H. and H.Z. All authors have read and agreed to the published version of the manuscript.

Funding: This research was funded by the National Natural Science Foundation of China (grant number 51875265).

Institutional Review Board Statement: Not applicable.

Informed Consent Statement: Not applicable.

Data Availability Statement: Not applicable.

Conflicts of Interest: The authors declare no conflict of interest.

References

1. Mandal, V.; Tripathi, P.; Kumar, A.; Singh, S.S.; Ramkumar, J. A study on selective laser melting (SLM) of TiC and B4C reinforced IN718 metal matrix composites (MMCs). *J. Alloys Compd.* **2022**, *901*, 163527. [CrossRef]
2. Wang, T.; Zhu, L.; Song, H.; Wang, H. Effect of WC-17Co content on microstructure and properties of IN718 composites prepared by laser cladding. *Opt. Laser Technol.* **2022**, *148*, 107780. [CrossRef]
3. Chen, T.; Deng, Z.; Liu, D.; Zhu, X.; Xiong, Y. Bioinert TiC ceramic coating prepared by laser cladding: Microstructures, wear resistance, and cytocompatibility of the coating. *Surf. Coat. Technol.* **2021**, *423*, 127635. [CrossRef]
4. Lei, J.; Shi, C.; Zhou, S.; Gu, Z.; Zhang, L.-C. Enhanced corrosion and wear resistance properties of carbon fiber reinforced Ni-based composite coating by laser cladding. *Surf. Coat. Technol.* **2018**, *334*, 274–285. [CrossRef]
5. Hu, Y.; Wang, L.; Yao, J.; Xia, H.; Li, J.; Liu, R. Effects of electromagnetic compound field on the escape behavior of pores in molten pool during laser cladding. *Surf. Coat. Technol.* **2020**, *383*, 125198. [CrossRef]
6. Li, M.; Zhang, Q.; Han, B.; Song, L.; Cui, G.; Yang, J.; Li, J. Microstructure and property of Ni/WC/La_2O_3 coatings by ultrasonic vibration-assisted laser cladding treatment. *Opt. Lasers Eng.* **2020**, *125*, 105848. [CrossRef]
7. Xu, S.; Cai, Q.; Li, G.; Lu, X.; Zhu, X. Effect of scanning speed on microstructure and properties of TiC/Ni60 composite coatings on Ti6Al4V alloy by laser cladding. *Opt. Laser Technol.* **2022**, *154*, 108309. [CrossRef]
8. Jiang, C.; Zhang, J.; Chen, Y.; Hou, Z.; Zhao, Q.; Li, Y.; Zhu, L.; Zhang, F.; Zhao, Y. On enhancing wear resistance of titanium alloys by laser cladded WC-Co composite coatings. *Int. J. Refract. Met. Hard Mater.* **2022**, *107*, 105902. [CrossRef]
9. Chen, Y.; Zhou, J.; Li, P.; Huo, K.; Meng, X. Effect of Electromagnetic Field on Wear Resistance of Fe901/Al_2O_3 Metal Matrix Composite Coating Prepared by Laser Cladding. *Materials* **2022**, *15*, 1531. [CrossRef]
10. Obadele, B.A.; Andrews, A.; Olubambi, P.A.; Mathew, M.T.; Pityana, S. Effect of ZrO 2 addition on the dry sliding wear behavior of laser clad Ti6Al4V alloy. *Wear* **2015**, *328–329*, 295–300. [CrossRef]
11. Jing, P.; Wang, H.; Chen, W.; Chen, L.; Yin, H.; Wu, H.; Li, D. Effect of Ti addition on microstructure and tribological properties of laser cladding Ni35/WC coating in an oxygen-free environment. *Surf. Coat. Technol.* **2022**, *440*, 128480. [CrossRef]
12. Wang, X.; Zhou, S.; Dai, X.; Lei, J.; Guo, J.; Gu, Z.; Wang, T. Evaluation and mechanisms on heat damage of WC particles in Ni60/WC composite coatings by laser induction hybrid cladding. *Int. J. Refract. Met. Hard Mater.* **2017**, *64*, 234–241. [CrossRef]
13. Li, G.J.; Li, J.; Luo, X. Effects of high temperature treatment on microstructure and mechanical properties of laser-clad NiCrBSi/WC coatings on titanium alloy substrate. *Mater. Charact.* **2014**, *98*, 83–92. [CrossRef]
14. Xia, Y.; Chen, H.; Liang, X.; Lei, J. Circular oscillating laser melting deposition of nickel-based superalloy reinforced by WC: Microstructure, wear resistance and electrochemical properties. *J. Manuf. Process.* **2021**, *68*, 1694–1704. [CrossRef]
15. Shen, X.; He, X.; Gao, L.; Su, G.; Xu, C.; Xu, N. Study on crack behavior of laser cladding ceramic-metal composite coating with high content of WC. *Ceram. Int.* **2022**, *48*, 17460–17470. [CrossRef]
16. Wang, L.; Yao, J.; Hu, Y.; Zhang, Q.; Sun, Z.; Liu, R. Influence of electric-magnetic compound field on the WC particles distribution in laser melt injection. *Surf. Coat. Technol.* **2017**, *315*, 32–43. [CrossRef]
17. Zhang, N.; Liu, W.; Deng, D.; Tang, Z.; Liu, X.; Yan, Z.; Zhang, H. Effect of electric-magnetic compound field on the pore distribution in laser cladding process. *Opt. Laser Technol.* **2018**, *108*, 247–254. [CrossRef]
18. Huo, K.; Zhou, J.; Dai, F.; Xu, J. Particle distribution and microstructure of IN718/WC composite coating fabricated by electromagnetic compound field-assisted laser cladding. *Appl. Surf. Sci.* **2021**, *545*, 149078. [CrossRef]
19. Han, X.; Li, C.; Yang, Y.; Gao, X.; Gao, H. Experimental research on the influence of ultrasonic vibrations on the laser cladding process of a disc laser. *Surf. Coat. Technol.* **2021**, *406*, 126750. [CrossRef]

20. Zhang, T.; Zhou, J.; Lv, J.; Meng, X.; Li, P.; Huang, S. A novel hybrid ultrasonic and electromagnetic field assisted laser cladding: Experimental study and synergistic effects. *J. Mater. Process. Technol.* **2022**, *307*, 117658. [CrossRef]
21. Zhu, L.; Yang, Z.; Xin, B.; Wang, S.; Meng, G.; Ning, J.; Xue, P. Microstructure and mechanical properties of parts formed by ultrasonic vibration-assisted laser cladding of Inconel *Surf. Coat. Technol.* **2021**, *410*, 126964. [CrossRef]
22. Fan, Q.; Chen, C.; Fan, C.; Liu, Z.; Cai, X.; Lin, S.; Yang, C. Ultrasonic induces grain refinement in gas tungsten arc cladding AlCoCrFeNi high-entropy alloy coatings. *Mater. Sci. Eng. A* **2021**, *821*, 141607. [CrossRef]
23. Xu, J.; Zhou, J.; Tan, W.; Huang, S.; Wang, S.; He, W. Ultrasonic vibration on wear property of laser cladding Fe-based coating. *Surf. Eng.* **2020**, *36*, 1261–1269. [CrossRef]
24. Nerz, J.; Kushner, B.; Rotolico, A. Microstructural evaluation of tungsten carbide-cobalt coatings. *J. Therm. Spray Technol.* **1992**, *1*, 147–152. [CrossRef]
25. Sadhu, A.; Choudhary, A.; Sarkar, S.; Nair, A.M.; Nayak, P.; Pawar, S.D.; Muvvala, G.; Pal, S.K.; Nath, A.K. A study on the influence of substrate pre-heating on mitigation of cracks in direct metal laser deposition of NiCrSiBC-60%WC ceramic coating on Inconel *Surf. Coat. Technol.* **2020**, *389*, 125646. [CrossRef]
26. Gan, Z.; Yu, G.; He, X.; Li, S. Numerical simulation of thermal behavior and multicomponent mass transfer in direct laser deposition of Co-base alloy on steel. *Int. J. Heat Mass Transf.* **2017**, *104*, 28–38. [CrossRef]
27. Wang, Q.; Li, Q.; Zhang, L.; Chen, D.X.; Jin, H.; Li, J.D.; Zhang, J.W.; Ban, C.Y. Microstructure and properties of Ni-WC gradient composite coating prepared by laser cladding. *Ceram. Int.* **2022**, *48*, 7905–7917. [CrossRef]
28. Li, W.; Di, R.; Yuan, R.; Song, H.; Lei, J. Microstructure, wear resistance and electrochemical properties of spherical/non-spherical WC reinforced Inconel 625 superalloy by laser melting deposition. *J. Manuf. Process.* **2022**, *74*, 413–422. [CrossRef]
29. Gan, Z.; Yu, G.; He, X.; Li, S. Surface-active element transport and its effect on liquid metal flow in laser-assisted additive manufacturing. *Int. Commun. Heat Mass Transf.* **2017**, *86*, 206–214. [CrossRef]
30. Lippold, J.C. *Welding Metallurgy and Weldability*; John Wiley & Sons: Hoboken, NJ, USA, 2014.
31. Abioye, T.E.; Folkes, J.; Clare, A.T.; McCartney, D.G. Concurrent Inconel 625 wire and WC powder laser cladding: Process stability and microstructural characterisation. *Surf. Eng.* **2013**, *29*, 647–653. [CrossRef]
32. Tan, H.; Luo, Z.; Li, Y.; Yan, F.; Duan, R. Microstructure and wear resistance of Al2O3–M7C3/Fe composite coatings produced by laser controlled reactive synthesis. *Opt. Laser Technol.* **2015**, *68*, 11–17. [CrossRef]
33. Zhou, S.; Zeng, X.; Hu, Q.; Huang, Y. Analysis of crack behavior for Ni-based WC composite coatings by laser cladding and crack-free realization. *Appl. Surf. Sci.* **2008**, *255*, 1646–1653. [CrossRef]
34. Tian, J.; Xu, P.; Liu, Q. Effects of stress-induced solid phase transformations on residual stress in laser cladding a Fe-Mn-Si-Cr-Ni alloy coating. *Mater. Des.* **2020**, *193*, 108824. [CrossRef]
35. Ji, F.; Qin, X.; Hu, Z.; Xiong, X.; Ni, M.; Wu, M. Influence of ultrasonic vibration on molten pool behavior and deposition layer forming morphology for wire and arc additive manufacturing. *Int. Commun. Heat Mass Transf.* **2022**, *130*, 105789. [CrossRef]
36. Yuan, D.; Shao, S.; Guo, C.; Jiang, F.; Wang, J. Grain refining of Ti-6Al-4V alloy fabricated by laser and wire additive manufacturing assisted with ultrasonic vibration. *Ultrason. Sonochem.* **2021**, *73*, 105472. [CrossRef]
37. Jamshidi, R.; Brenner, G. Dissipation of ultrasonic wave propagation in bubbly liquids considering the effect of compressibility to the first order of acoustical Mach number. *Ultrasonics* **2013**, *53*, 842–848. [CrossRef]
38. Geng, L.; Chen, J.; Escaler, X. Improvement of cavitation mass transfer modeling by including Rayleigh–Plesset equation second order term. *Eur. J. Mech.—B/Fluids* **2020**, *84*, 313–324. [CrossRef]
39. Lv, T.; Li, Y. Simulation of Ultrasonic Flow Polishing inside the Mold Cavity. *Front. Manuf. Eng.* **2015**, *3*, 20–24. [CrossRef]
40. Wang, F.; Eskin, D.; Mi, J.; Wang, C.; Koe, B.; King, A.; Reinhard, C.; Connolley, T. A synchrotron X-radiography study of the fragmentation and refinement of primary intermetallic particles in an Al-35 Cu alloy induced by ultrasonic melt processing. *Acta Mater.* **2017**, *141*, 142–153. [CrossRef]
41. Wang, B.; Tan, D.; Lee, T.L.; Khong, J.C.; Wang, F.; Eskin, D.; Connolley, T.; Fezzaa, K.; Mi, J. Ultrafast synchrotron X-ray imaging studies of microstructure fragmentation in solidification under ultrasound. *Acta Mater.* **2018**, *144*, 505–515. [CrossRef]

coatings

MDPI

Article

Glass-Ceramic Protective Coatings Based on Metallurgical Slag

Alexander V. Gorokhovsky [1,2], Gleb Yu. Yurkov [3], Igor N. Burmistrov [1,*], Angel F. Villalpando-Reyna [4], Denis V. Kuznetsov [1], Alexander A. Gusev [1], Bekzod B. Khaidarov [1], Yuri V. Konyukhov [1], Olga V. Zakharova [1] and Nikolay V. Kiselev [1,5]

[1] Department of Functional Nanosystems and High Temperature Materials, National University of Science and Technology (MISIS), 119049 Moscow, Russia
[2] Department of Chemistry and Chemical Technology, Yuri Gagarin State Technical University of Saratov, 410054 Saratov, Russia
[3] N.N. Semenov Federal Research Center of Chemical Physics, Russian Academy of Sciences, 119334 Moscow, Russia
[4] Department of Engineering Ceramics, The Center for Research and Advanced Studies of the National Polytechnic Institute (CINVESTAV) Unidad Saltillo, Ramos Arizpe CP25900, Coahuila, Mexico
[5] Engineering Center, Plekhanov Russian University of Economics, 36 Stremyanny Lane, 117997 Moscow, Russia
* Correspondence: glas100@yandex.ru

Abstract: Pyroxene glass-ceramic enamels based on combinations of blast furnace slag and some additives were produced and investigated. The batch compositions and technological regimes of enameling were developed to produce high temperature protective coatings for carbon steel (ASTM 1010/1008). The composition of raw materials was selected to match the values of the thermal expansion coefficients of the glass-ceramic coating (~$11 \cdot 10^{-6}$ K^{-1}) and metal substrate (~$12 \cdot 10^{-6}$ K^{-1}) taking into account the temperatures of fluidization (T_f ~ 800°) and crystallization (T_c = 850−1020 °C) of the corresponding glasses. The covered and thermally treated samples of carbon steel were produced using single-layer enameling technology and investigated to specify structure, phase composition and properties of the coating and coating-steel interface. The obtained coatings were characterized with excellent adhesion to the steel (impact energy ~3 J) and protective properties. The closed porous structure of the coatings promoted low thermal conductivity (~1 W/(m·K)) and high (up to 1000 °C) thermal resistance, whereas the pyroxene-like crystalline phases supported high wear and chemical resistance as well as micro-hardness (~480 MPa) and thermal shock resistance (>30 cycles of 23–700 °C). The obtained cheap coatings and effective protective coatings could be used at the temperatures up to 1100 °C in the corrosive atmosphere and under the action of abrasive particles.

Keywords: glass-ceramics; carbon steel; protective coating; structure; properties

Citation: Gorokhovsky, A.V.; Yurkov, G.Y.; Burmistrov, I.N.; Villalpando-Reyna, A.F.; Kuznetsov, D.V.; Gusev, A.A.; Khaidarov, B.B.; Konyukhov, Y.V.; Zakharova, O.V.; Kiselev, N.V. Glass-Ceramic Protective Coatings Based on Metallurgical Slag. *Coatings* **2023**, *13*, 269. https://doi.org/10.3390/coatings13020269

Academic Editor: Devis Bellucci

Received: 28 November 2022
Revised: 19 January 2023
Accepted: 19 January 2023
Published: 24 January 2023

1. Introduction

Modern engineering techniques demand the creation of new coatings, which must have high efficiency under the action of temperature and an aggressive environment. Among protective ceramic coating systems for industrial and engineering applications, glass–ceramic coatings have advantages of chemical resistance, high temperature stability and superior mechanical properties such as abrasion, impact etc., as compared to other coating materials applied by different forms of thermal spraying (physical and chemical vapor deposition (PVD and CVD), plasma, etc.) [1]. In addition, the ceramic coatings produced by sputtering technologies [2–5] usually are brittle, expensive, and difficult to deposit with low-cost processes.

The sol-gel process enables the synthesis of ceramic coating on the steel surfaces with a protective layer based on SiO_2, ZrO_2, Al_2O_3, TiO_2. These materials, easily deposited on surfaces with inexpensive processes, showed excellent chemical stability, and improve the

corrosion resistance of metal substrates at low temperatures [6], however, their thermal refractory properties are not high enough. Besides imparting required functional properties such as heat, abrasion and corrosion resistance to suit particular end use requirements, the glass-ceramic coatings in general also provide good adherence, defect free surface and refractoriness [1,7]. However, most of the glass-ceramic coatings described in the literature were developed for stainless steel [8]. The data on protective glass-ceramic coatings recommended for carbon steels are not so extensive.

Some glass-ceramic compositions based on the system of SiO_2-Al_2O_3-CaO-MgO-Fe_2O_3-MnO_2-K_2O-Na_2O were developed by Zubekhin and coauthors to coat carbon steels [9,10]. A wear resistant glass-ceramic coating system based on SiO2-B2O3-Al2O3 glass was reported by [11]. A glass-ceramic coating with quartz additions has been developed in [12], as a single coat without prior chemical treatment of the surface, by using the dipping technique on low carbon alloyed steel. A number of TiO_2 and P_2O_5 nucleated glass-ceramic coating compositions in the system of RO-R′$_2$O-Al_2O_3-SiO_2 (R = Ca, Mg; R′ = Na, K, Li) have been studied for application on various grades of steel and alloy, including mild steel, with an aim of protecting them against mechanical wear and chemical corrosion [13]. A novel environmental barrier double-layer coating system for mild steel consisting of a perhydropolysilazane bond coat and a polysilazane-based glass/ceramic composite topcoat has been developed in [14]. An anti-fouling ceramic coating was developed and applied to carbon steel in the work [15]. Anti-fouling testing and thermal conductivity measurements were performed to evaluate the performance of this coating. However, the modern industry requires that the coatings must have greater efficiency under aggressive environments and can be used in the thermal shock conditions.

Here, it is necessary to note that glass-ceramic materials based on various combinations of industrial waste have been intensively investigated in the last decades and indicated excellent wear, chemical and thermal resistance [16–21]. Among them, the pyroxene-type glass-ceramic materials are very attractive, due to their excellent exploitation properties such as chemical, thermal and wear resistance [21,22].

We proposed that the glass compositions based on industrial waste such as blast furnace slag, fly ash and neutralized sludge of nickel electroplating could represent the glass-forming systems with the chemical composition very similar to that required for the formation of pyroxene-like glass compositions. It is also important that possible varying of the above-mentioned industrial wastes practically does not influence the crystallization behavior of the pyroxene-type glasses due to varied chemical composition of the pyroxen-like solid solutions [22].

In this regard, the aim of this study is to develop a pyroxene-type glass-ceramic coating based on the combination of different industrial wastes using the traditional enamel fritting technique applied to common carbon steel (ASTM 1010/1008) substrates. It is proposed that such coatings could be formed using the single-layer enameling technology (1 coat–1 firing), which minimizes the consumption of raw materials and energy resources due to decreased number of the technological operations. The protective properties of the obtained coatings were investigated taking into account their hardness, wear, chemical and thermal-shock resistance as well as their thermal conductivity.

2. Materials and Methods

2.1. Design of Glass Composition

The pyroxene-like glass-ceramic materials could be obtained using the raw material mixtures with the chemical composition varied in the range (wt.%): SiO_2 (35–60), Al_2O_3 (2–15) 3, Fe_2O_3 (1–26), % CaO (9–25), MgO (1–20), R_2O (0–12) [22]. Taking into account the gradual global transition from non-renewable raw materials to renewable (plant-based) ones has intensified, the industrial wastes combined with some additives were applied to prepare fritted vitreous materials. The chemical compositions of the applied raw materials are reported in Table 1.

Table 1. Chemical composition (wt.%) of different industrial wastes and other raw materials used to formulate glass coating composition.

Oxide	Raw Materials							
	Fly Ash	Lime Stone Dust	Dolomite Dust	Silica Sand	Soda Ash	Dried Gavanic Slurry	Blast Furnace Slag	Bento-nite
Na_2O	0.6	0.5	-	-	58.5	-	-	2.1
MgO	0.7	1.2	20.6	-	-	-	11	2.1
Al_2O_3	24.1	2.6	-	-	-	-	14.5	24.2
SiO_2	59.7	6.7	0.2	98.5	-	-	33.0	64.1
K_2O	1.5	0.7	-	-	-	-	-	0.7
CaO	4.6	86.1	32.5	-	-	25.6	40.0	2.2
TiO_2	1.5	-	-	-	-	-	-	0.2
Fe_2O_3	6.5	1.5	-	-	-	12.3	0.5	2.4
P_2O_5	0.1	0.5	-	-	-	-	-	-
Cr_2O_3	-	-	-	-	-	1.1	-	-
NiO	-	-	-	-	-	37.7	-	-
SO_3	-	-	-	-	-	21.5	-	-

These raw materials allow preparing the pyroxene-type glasses with their various combinations. In any case, the blast furnace slag can be considered as the main component of the batch due to its high content of the oxides which participate in the vitrification processes and crystallization of pyroxenes (CaO, MgO, Al_2O_3, Fe_2O_3, SiO_2). The admixtures of fly ash, silica sand, dolomite and limestone dusts (wastes of the crushed stone production) were selected to optimize the glass composition for the following crystallization, whereas soda ash admixtures were used to regulate the glass transition and fluidization processes (T_g, T_f).

It is known that the pyroxene-like glasses have a trend of the surface crystallization in the temperature range of enameling (700–900 °C), however, controlling the nucleation and crystal growth rates allows obtaining the glass-ceramic materials, which have high contents of crystalline phases in the glass matrix, using NiO and Cr_2O_3 as nucleating agents [23]. That is why, the dried slurry obtained by neutralization of liquid wastes of the nickel electroplating and characterized with high content of nickel and chromium oxides, was introduced in the raw material mixtures too. In addition, it is necessary to note that a presence of NiO promotes wetting of the steel surface by silicate melts [24].

The batch compositions reported in Table 2 were considered to meet the pyroxene-like chemical composition requirements for the glass destined for the protective coating. Table 3 presents the theoretical chemical compositions of the glasses based on these raw material mixtures. The industrial wastes produced in the plants of Severstal Inc. (Cherepovets, Russia) were used here as raw materials.

Table 2. Raw material mixtures used to formulate glass composition.

Raw Material	Batch Number				
	1	2	3	4	5
Fly Ash	30	-	30	-	-
Limestone	38	-	-	-	-
Silica Sand	15	23	17	24	24
Galvani Slurry	7	12	7	13	14
Soda Ash	10	8	8	13	13
Dolomite dust	-	17	38	20	19
Slag	-	40	-	30	30

Table 3. Theoretical chemical composition of the glasses based on the formulated raw material mixtures (Table 2) and their calculated (theor.) and measured (exp.) CTE values.

Oxide	Number of Glass Composition (Corresponding Batch)				
	1	**2**	**3**	**4**	**5**
Na_2O	7.5	5.1	6.3	9.2	9.9
MgO	0.8	8.6	10.6	8.9	8.6
Al_2O_3	16.3	11.7	10.6	5.2	5.5
SiO_2	46	39	44.1	40.4	41.3
CaO	26	27	19.8	26.4	26.0
TiO_2	0.5	-	0.5	-	-
Fe_2O_3	4	1.8	2.6	2.1	2.3
NiO	3.2	6.2	2.5	7.5	6.4
K_2O	0.7	-	0.5	-	-
Cr_2O_3	0.1	0.1	0.1	0.2	0.2
CTE (theor.) $\times 10^6$ K^{-1}	10	8.6	8.3	10.6	11.5
CTE (exp.)	9.7 ± 0.2	8.6 ± 0.2	8.4 ± 0.1	10.3 ± 0.3	11.6 ± 0.2

It was assumed that cracking and peeling defects would not occur in the coatings during their formation as when they were exposed to thermal shock and aggressive environment, these coatings will be characterized with optimal values of the coefficient of the thermal expansion (CET). That is why the theoretical CET values were calculated in accordance with [25] for each formulated glass composition to guarantee the compatibility of the coating and the substrate over the temperature range of the expected applications.

The steel ASTM 1010/1008 was selected as a substrate taking into account that this type of carbon steel is used for a wide variety of applications that need high strength and toughness in the form of plates, sheets, bars, and tubes.

The thermo-mechanical behavior of all the investigated materials was determined by dilatometry (Netzsch DIL 402 PC equipment, Selb, Germany) in the temperature range from 20 to 800 °C with a rate of 3 K·min^{-1} using the samples of glass (glass-ceramics) and steel (substrate) of square parallel bases with 6 mm per side and 40 mm length. It was determined that the CTE value of the metal substrate varied from $12.2 \cdot 10^{-6}$ K^{-1}(in the range of 20–100 °C) to $15 \cdot 10^{-6}$ K^{-1}(in the range of 20–800 °C). That is why, the batch, which allows producing the glass composition No 5 characterized with $CTE_{theor.} < CTE_{steel}$ but closer to CTE_{steel} (Table 3), was chosen for the following experiments, taking into account traditional requirements of the enameling [25,26]. Some preliminary experiments were conducted on the fusion and crystallization of the glass compositions based on the batches No 1–5 and confirmed the correctness of the choice of the batch No 5 as the optimal composition in terms of the thermal expansion properties (experimental CTE values).

2.2. Glass Frits and Raw Material Mixtures

The selected batch No 5 was dry homogenized in the rotating drum and melted in alumina crucibles at 1450 °C for 2 h using a Lindberg-Blue high-temperature electric furnace BF51433. To produce a glass frit, the glass-forming melt was poured onto a stainless-steel plate, in order to temper the melt and prevent surface crystallization, and further was ground in a two-station Retsch PM400 planetary mill for 30 min. The glass frit was screened until passing the #325 mesh, considering that this particle size favors green coating of the metal substrates [25,27,28].

The temperatures of vitrification (T_g) and crystallization (T_c) of the parent glass was determined using the DTA technique (calorimeter Perkin Elmer DTA7), whereas the temperature of fluidization (T_f) was estimated taking into account the data of dilatometry too. These results were applied to select the temperature of firing which allowed the formation of the protective glass-ceramic coating by the single-layer enameling technique. This technique is especially promising due to the decreased number of coating operations and

firings. A single-layer enameling prevents warping of thin and large-size metal substrates; the coating becomes more elastic and impact resistant and has reduced thickness.

To form the glass-ceramic coatings, the glass frit (95 wt.%) was dry mixed with powdered bentonite clay (5 wt.%). The obtained mixture was used to produce a slurry (dispersion) prepared in accordance with [24,25,27] an aqueous solution (weight ratio of 1:2) contained 5 wt.% of $Na_2B_4O_7$ (purity of 99%, MosReactiv) and phenol sulfonic acid dispersant (Tamol, BASF) (0.5%). Subsequently, this dispersion was magnetically stirred for 30 min and maturated for 24 h (stabilization).

Three slurries with different water contents (40, 50 and 60 wt.%) were used to form green coatings of different thicknesses.

2.3. Pretreatment and Coating of the Substrate

Rectangular specimens of 25 × 50 × 5 mm^3 were used as a substrate and prepared by cutting the commercial steel plate (ASTM 1008/1010), containing 1.87 wt.% of carbon. To obtain the surface characteristics of a substrate required for the enameling, a chemical treatment of the steel specimens was applied to remove the adhering oxides and surface grease.

The chemical treatment process consisted of immersing the steel specimens in the acidic solution composed of 80 mL of 1 M H_2SO_4 and 7.2 g of NaCl [25]. The specimens were introduced in this solution heated up to 80 °C for 15 min. Subsequently, the treated samples were washed in hot water at 95 °C for 1 min to remove residues from the acid solution. After that, the treated specimens were immersed in a solution formed by Na_2CO_3 (5 g/L) and Na_3PO_4 (3 g/L) at 60 °C for 6 min to inhibit the previous acidic action. Finally, each specimen was dried at 90 °C for 20 min in an oven.

Each specimen of the obtained metal substrate was coated by immersion in the dispersion based on fritted glass. The obtained green coating was dried in an oven at 90 °C for 30 min and further thermally treated at the temperature selected for firing (820, 850 °C).

The muffle furnace was preheated up to 40 °C above the required temperature; subsequently, the green coated specimens were introduced into the hot furnace. Additionally, an evaluation of the time required for the formation of homogeneous coating was performed. It was determined that the burning time of 5 min ensured the total fusion of the green coating and made it possible to avoid generating any cracks or detachment of the coating during the cooling.

2.4. Microstructure Analysis and Materials Characterization

The microstructure and chemical composition of the protective layer, obtained after coating and firing, was investigated by scanning electron microscopy (Philips XL30ESEM, SEMTech Solutions, Inc., North Billerica, MA USA) equipped with an energy dispersive spectrometer (EDS, EDAX Pegasus, EDAX, LLC, Pleasanton, CA USA) conducted at 20 kV.

The phase composition of the bulk glass-ceramics and coatings obtained onto the steel surface was carried out using a Philips PW3040 difractometer (CuKα radiation with a nickel filter operating 40 kV and 100 mA). The reflection positions and relative intensities of the XRD patterns were compared to the catalog of the International Center for Diffraction Data (ICDD-2008).

The chemical resistance of the glass-ceramic material used to produce the coatings was estimated by the following standards based on measurement of weight losses:

- water resistance (IRS-3502, Japan): 2 g of the powdered glass-ceramics (fraction of 0.5–0.8 mm) was treated in 50 mL of distilled water for 5 h, filtered and dried for 12 h and weighed;
- chemical resistance to the action of basic and acidic aqueous solutions (GOST 10134-62, Russia): 10 g of powdered glass-ceramics (fraction of 0.5–0.8 mm) were treated in 100 mL of 1 M NaOH or 1 M HCl solutions, respectively, for 3 h at 96 °C; filtered and dried for 12 h and weighed.

Microhardeness of the coatings was measured in accordance with the standard ASTM E384-99 (Tukon microhardness tester, Vickers indenter) using an indentation load of 50 g for 20 s.

To measure the thermal shock resistance of the coating, six coated specimens were heated in an electrical furnace up to 700 °C and then immersed in water at 23 °C (heating–cooling cycle). The number of cycles required to cause any failure was recorded for each specimen.

To estimate wear resistance (wear loss in mg·cm^2) we used a modification of the ASTM abrasion standard (G65, by sand between a specimen and a rubber wheel tested for 50,000 revolutions with a rate of 200 ± 10 rpm at a load of 45 N) for coating evaluation to rank the relative abrasion resistance and compare the abrasion resistance with that of the uncoated steel surface.

The thermal endurance was estimated by standing the coated steel specimens at 1000 °C with heating and cooling rates of 10 K/min and holding times of 30 min. The thermal conductivity was measured at room temperature and 700 °C in air by the Hot Disk Transient Plan Source (TPS) method according to ISO 22007-2.

The coating-substrate adhesion was estimated in accordance with the Russian standard GOST 24788-2018 which determines minimal acceptable impact energy of the enamel protective coating as 0.6 J. The impact strength (impact energy) test of the coating was carried out on flat areas of the coated metal substrate by the action of a steel ball freely falling from a certain height. After the impact, the surface was tested to recognize any cracking or chipping of the coating. A value of the impact strength was determined as the impact energy which favored delamination of any part of the protective coating from the metal substrate.

3. Results

3.1. Chemical and Phase Composition (Frits and Coatings)

3.1.1. Chemical Composition

The chemical composition of glass No 5 used as a frit to produce the coatings, in accordance with the data of energy-dispersive X-ray spectroscopy (EDS) and inductively coupled plasma (ICP) analysis, included (wt.%): Na_2O (8.9), MgO (7.8), Al_2O_3 (7.9), SiO_2 (41.9), CaO (24.9), Fe_2O_3 (2.5), NiO (5.9), K_2O (0.2), Cr_2O_3 (0.2).

3.1.2. Thermal Behavior

The DSC data obtained for the coarse (0.6–0.8 mm) and thin (0.1–0.16 mm) powders of the parent glass (No 5) are reported in Figure 1a. It is possible to note that the temperature of glass transition of the investigated composition Tg~720 °C and temperature of fluidization is about 800 °C. At the same time, the exothermal peaks of the surface and bulk crystallization appear in the range of 850 and 1020 °C, respectively. The main crystallization process for the coarse powder takes place at T > 1000 °C, while the surface crystallization dominates for the thin powder used to produce glass frit. Taking into account these data, the temperatures 820 and 850 °C have been selected for firing the protective coatings based on the fritted glass No 5. The temperatures of 820–850 °C could allow fluidization as crystallization processes in the glass-forming composition. The temperatures above 850 °C are not recommended for carbon steel enameling [24,25].

The XRD analysis data obtained for the coatings produced at 820 and 850 °C are reported in Figure 1b. A firing at 820 °C did not allow obtaining the glass-ceramic coating, whereas at 850 °C crystallization processes take place in the system investigated; that is why the following experiments were conducted using a firing of green coatings at 850 °C.

3.2. Structure

The microphotographs of the obtained coatings are reported in Figure 2. The structure of the external surface for the coating fired at 850 °C is well crystallized (Figure 2b),

continuous and homogeneous, and has some inclusions of open pores. The structure of the coating formed at 820 °C is more rough and inhomogeneous (Figure 2c).

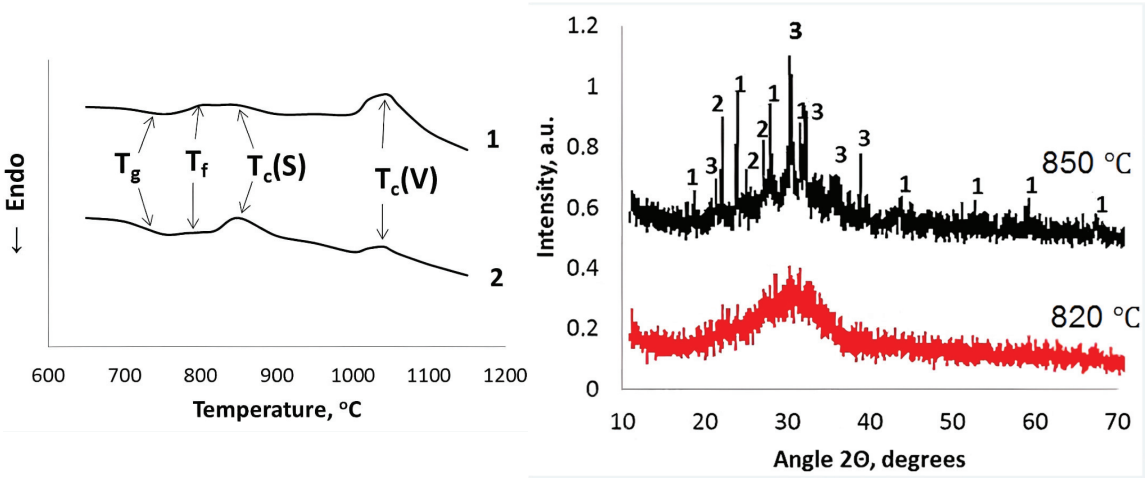

(**a**) (**b**)

Figure 1. DSC data obtained for the coarse (1) and thin (2) powders of glass frit (**a**) and XRD patterns of the coarse glass powder fired at 820 and 850 °C (**b**). 1—nepheline, 2—gehlenite, 3—pyroxene. T_g, T_f, T_c(S) and T_c(V)–the temperatures of glass transition, fluidization, surface and bulk crystallization, respectively.

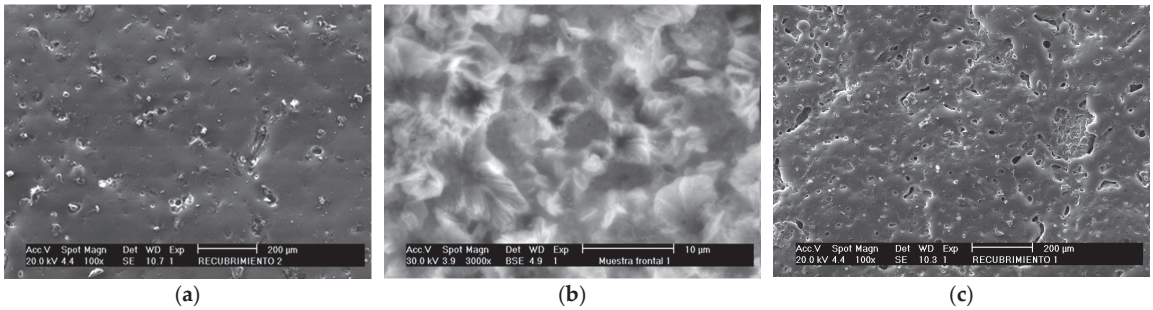

(**a**) (**b**) (**c**)

Figure 2. Microphotographs (SEM) of the protective coating fired at 850 °C (**a**,**b**) and at 820 °C (**c**).

The cross-section microphotographs (Figure 3) indicate that the obtained coating has a glassy matrix and contains closed pores of a different diameter. The size of pores increases in the direction of the external surface, while, near the coating-metal interface these pores almost disappear. Nepheline ($NaAlSiO_4$), gehlenite ($Ca_2Al_2SiO_7$) and pyroxenes (Ca, Mg, Fe, Al) Si_2O_6 represent the crystalline phases of the coating. The pyroxen-like crystals form the main crystalline phase in accordance with the XRD data (Figure 1b). It is important that the crystals are mainly formed either on the coating-steel interface or on the surface of closed pores (Figure 3) and on the external surface of the coating (Figure 2b).

The coating fired at 820 °C is characterized with a very low content of the crystalline phases (Figure 3b) and contains pores near the coating-steel interface (Figure 3b).

It is necessary to note that for the coarse glass powder treated at 820 °C the XRD patterns do not present any reflections of crystalline phases (Figure 1b), whereas, in the structure of the protective coating based on thin glass powder with some additives (clay,

borax), several pores demonstrate initial stages of the surface crystallization (Figure 3b), although in the most part of these pores a surface is free of crystals (Figure 3c).

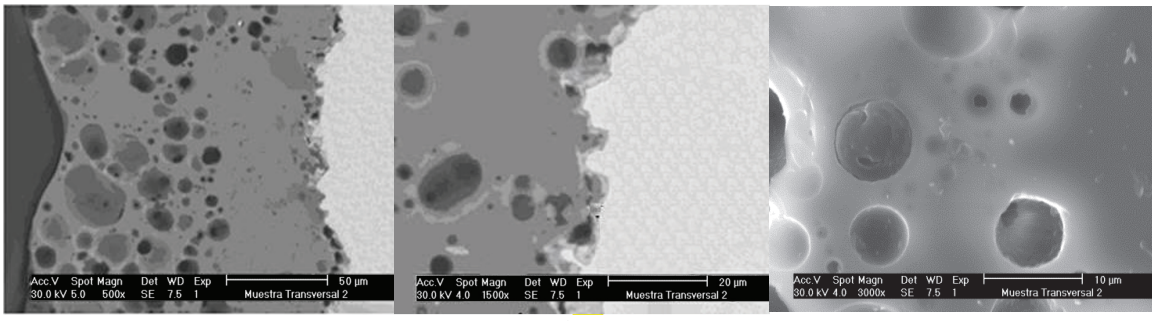

(**a**) (**b**) (**c**)

Figure 3. Cross-section micrographs of the coatings produced at 850 °C (**a**) and 820 °C (**b**,**c**).

The data of the EDS point analysis (Figure 4, Table 4) indicate a presence of the chemical elements of the substrate and fritted glass.

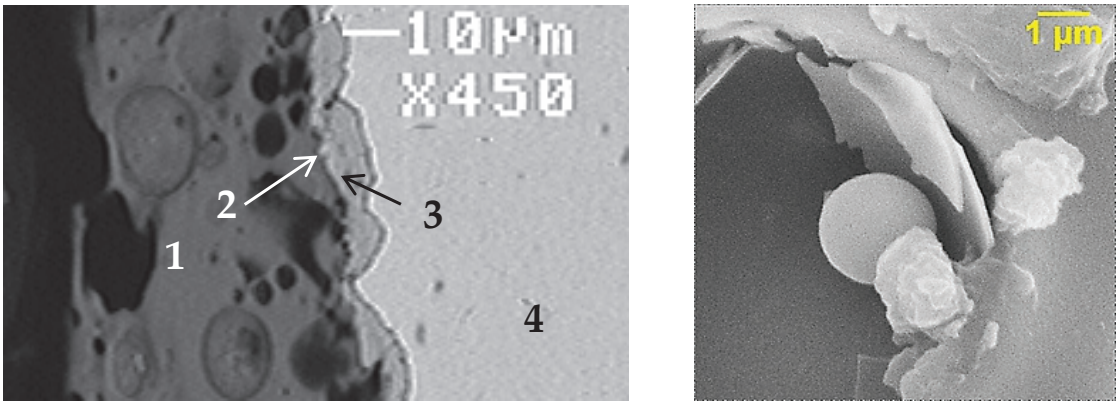

(**a**) (**b**)

Figure 4. SEM images of the coating-steel interface formed at 820 °C (**a**) and the trace from a ball impact (6 J) on the surface of the coating obtained at 850 °C (**b**), the elemental composition corresponding to points 1-4 is shown in Table 4.

Table 4. Chemical composition of the metal substrate, different zones of the interface and coating (marked in Figure 4). Data of the EDS point analysis.

Numer of the EDS Point Analysis	Content of the Chemical Elements, at.%								
	Si	**Ca**	**Fe**	**Ni**	**Na**	**Mg**	**Al**	**O**	**C**
1	23.5	14.9	0.6	3.0	4.7	6.5	1.9	44.9	-
2	2.2	1.5	54.8	3.1	0.2	-	0.5	37.7	-
3	0.9	1.0	64.6	3.3	-	-	-	30.7	-
4	-	-	99.1	-	-	-	-	-	0.9

3.3. Properties

The steel ball impacts (adhesion tests) indicated high adhesion of the coating to the steel surface. The impacts with the energy value of 1 J only promoted a cracking of walls of

some pores located near the external surface of the coating (Figure 4b) and did not cause delamination of the coating.

The properties characterizing other protective functions of the resulting coatings are given in Table 5 and considered in the Discussion.

Table 5. Some properties of the protective coatings fired at 850 °C.

Content of H_2O in the Slurry, %	Properties									
	Thickness, μm		Weight Losses in Aqueous Solutions, %			Microhardness, MPa	** Relative Wear Resistance, %	*** Thermal Shock Resistance	Impact Energy, J	Thermal Conductivity at 700 °C, W/(m·K)
	Coating	* Interface Layer	H_2O	Acidic	Alkali					
40	150–180	4–10	0	0.5	6.3	440 ± 32	122	22	3.1	1.0
50	110–135	3–8	0	0.2	4.8	459 ± 20	132	25	3.3	0.8
60	80–110	2–5	0	0.1	5.0	481 ± 21	154	>30	3.6	1.1

* glass-ceramic coating–metal substrate, ** comparison with the uncoated steel, *** quantity of the thermal cycles 23–700 °C.

4. Discussion

Thus, the glass-ceramic coatings, produced using the combination of blast furnace slag, dried galvanic slurry of the nickel electroplating and some additives have excellent protective properties. They meet the standard requirements (GOST 24788-2018) related to the impact strength (impact energy) and are characterized with a good adhesion to the carbon steel surfaces. Impact energy values were higher than 0.6 J and reached 3.1–3.6 J, whereas such characteristics reported in the literature ranged between 1.1 and2.4 J [1,13,29].

In comparison with similar protective glass-ceramic coatings proposed earlier for the carbon steels [9–15,27–30], the obtained coating is characterized with some very attractive exploitation properties.

The experimental data indicate that the developed protective coating has excellent chemical resistance in water and alkali aqueous solutions and acceptable resistance under the action of strong acids.

Abrasion resistance of the coating (1.6 ± 0.1 mg/cm^2) increased in 54%, in comparison with the uncoated parent steel surface, and was higher than one reported in previous works (2–3 mg/cm^2 after 50,000 cycles of RWAT [1,12]). The hardness of the obtained coating is slightly less of the best characteristics for the analogs (480 MPa and 500–600 MPa [9–11], respectively), however, it is acceptable taking into account high wear resistance and corresponds to the data obtained for the bulk pyroxene-type glass-ceramics [20–22,30].

The thermal conductivity of the coating is also much better for this one mentioned for the analogs (1.1 and 2.6 W/(m·K) [15], respectively).

Spherical pores of various diameters located in the external part of the coating can be considered as a filler of the glassy matrix. In fact, the obtained coating is filled with ceramic porous particles characterized with high mechanical strength and low thermal conductivity. Such structural features of the coating also promote high mechanical properties, thermal and thermal-shock resistance.

Good adhesion of the coating to a surface of the carbon steel substrate and low thermal conductivity promote an excellent thermal shock resistance (more than 30 cycles of 23–700 °C, in comparison with 15–20 cycles of 23–400 °C [1,13]).

The boiling water resistance (100%) as well as acid (>99%) and alkali (~95%) resistance of the obtained coatings are better for the analogs described in the literature (98%–99%, 95%–98%, 92%–94%, respectively, [1,9,10,12,13,31]). The cause of this phenomenon can be explained by dominant surface crystallization of the pyroxene-like glass compositions. As a result, a presence of the chemically resistant ceramic layers as onto the external surface of the coating as on the surfaces of pores, provide improved chemical durability.

It is necessary to note that a thickness of the glass-ceramic coating based on metallurgical slag can be regulated with the H_2O contents in the slurry used to form green coating by dipping (Table 4). The obtained results allow one to suggest that an increase

in the viscosity of the slurry based on fritted enamel increases a thickness of the film due to the substrate-coating interaction. However, more thick coatings are characterized with worse thermal shock and wear resistances, whereas very thin coatings have worse abrasion resistance and relatively high thermal conductivity. That is why the slurries containing 50–55 wt.% of H_2O could be recommended to produce the glass-ceramic coatings of the proposed composition characterized with improved protective properties.

The following factors influencing protective properties of the proposed coating have to be taken into account.

A presence of about 6 wt.% of NiO in the chemical composition of fritted glass, used to produce the coating, promotes two useful processes.

The first, in accordance with [22,23,28,30], is related to the nucleation of crystalline phases in the molten silicate glasses. However, in spite of a presence of NiO and Cr_2O_3 supporting the crystallization of pyroxenes [21], a surface crystallization dominates in the system investigated; a bulk crystallization only takes place at T > 1000 °C (Figure 1a). Nonetheless, the nucleants favor an intensive growth of the pyroxene-like crystals from the steel-coating interface into a volume of the protective coating (Figure 3a), improving the mechanical strength and thermal-shock resistance of the coating.

In addition, a presence of NiO in the glass composition promotes a perfect adhesion between the coating and metal substrate, achieved due to an appearance of the intermediate layer. This layer has a thickness of 2–8 μm (Figures 3 and 4, Table 4) and, in accordance with the EDS point analysis data, contains the components of fritted glass and metal substrate (SiO_2, CaO, NiO, Fe_2O_3). Thus, it is possible to assume that the phases supporting adhesion, in particular α-Fe_2O_3 and ferrites ($NiFe_2O_4$), formed during a firing as a result of the redox processes [31].

$$Fe + NiO = Fe_2O_3 + Ni$$

$$NiO + Fe_2O_3 = NiFe_2O_4.$$

The data of the EDS point analysis (Figure 4, Table 4) indicate that interdiffusion occurs at the interface during the firing of green coatings [26]. The interlayer is formed as a result of the metal substrate oxidation and diffusion of the glass components into the Fe_2O_3 structure. It is important that Ni has a trend of incorporation into the structure of the interface layer in the metal form; this is indicated by a gradual decrease in the amount of oxygen in the intermediate layer, when moving from the steel surface to the glass-ceramic coating. Such gradient structure of the interlayer prevents micro-cracking of the ductile metal substrate, which recently has been discovered to be dangerous during the destruction of brittle coatings [32]. In our case the interlayer provides perfect adherence of the coating due to its good impact strength and wear resistance.

Thus, the developed glass–ceramic coating material based on industrial wastes, such as metallurgical slag and waste of nickel electroplating, is useful for specialized engineering and industrial applications. A presence of the pyroxene-like crystalline phases, characterized with high toughness, hardness, thermal, wear and chemical resistance promotes improved exploitation properties in comparison with the analogs containing inclusions of quartz, alumina, magnesium aluminium titanate, lithium titanium silicate or sodium silicates [9–15,31]. Due to high mechanical strength and abrasion resistance, the pyroxene-type glass-ceramic coating has a good potential for its applications for the carbon steel constructions which are used in the conditions where an abrasive action accelerates a failure.

It is important to note that the developed coatings can be produced by the simple one-stage technique of enameling. Such a technique allows one to obtain protective coatings onto the surface of large-sized samples of carbon steel. In our case, the ASTM 1008/1010 carbon steel plates with a size of 4 × 150 × 200 mm were coated using the investigated glass-ceramic composition. However, some special equipment has to be developed to coat the samples of a higher scale. This research as well as more detailed investigation of the mechanical and other exploitation properties will be conducted in the near feature taking into account the requirements of the potential consumers.

5. Conclusions

The raw material mixtures based on the combination of powdered blast furnace slag and wastes of nickel electroplating as well as some technological additives (silica sand and soda ash) allow producing the ASTM 1008/1010 carbon steel glass-ceramic coating by the simple one-stage enameling technique, using the 50% aqueous dispersions of the fritted pyroxene-type glass powder with admixtures of bentonite clay, borax and surfactant, and with the following thermal treatment at 850 °C.

The obtained coatings have some structural features: (1) well developed gradient coating-steel interface layer formed, most likely by α-Fe_2O_3, $NiFe_2O_4$, Fe and Ni; (2) closed spherical pores with the ceramic walls, located near the external surface; (3) totally crystallized external surface formed by nepheline ($NaAlSiO_4$), gehlenite ($Ca_2Al_2SiO_7$) and pyroxene-like crystals.

These structural features promote improved adherence, mechanical properties, thermal shock and chemical resistance of the coating, which allow one to recommend them for the carbon steel constructions used in the aggressive conditions of high temperatures, abrasive action and chemically aggressive media.

Author Contributions: Conceptualization, A.V.G.; methodology, G.Y.Y. and Y.V.K.; validation, I.N.B. and N.V.K.; investigation, A.F.V.-R., A.A.G., B.B.K. and O.V.Z.; data curation, D.V.K.; writing—original draft preparation, G.Y.Y.; writing—review and editing, A.V.G. All authors have read and agreed to the published version of the manuscript.

Funding: This research was partially financially supported by the Ministry of Science and Higher Education of the Russian Federation in the framework of Strategic Academic Leadership Program "Priority 2030", NUST "MISIS" grant No K2-2020-009.

Institutional Review Board Statement: Not applicable.

Informed Consent Statement: Not applicable.

Data Availability Statement: Not applicable.

Conflicts of Interest: The authors declare no conflict of interest.

References

1. Majumdar, A.; Jana, S. Glass and glass-ceramic coatings, versatile materials for industrial and engineering applications. *Bull. Mater. Sci.* **2001**, *24*, 69–77. [CrossRef]
2. Fukahori, R.; Nomura, T.; Zhu, C.; Sheng, N.; Okinaka, N.; Akiyama, T. Thermal analysis of Al–Si alloys as high-temperature phase-change material and their corrosion properties with ceramic materials. *Appl. Energy* **2016**, *163*, 1–8. [CrossRef]
3. Quenard, S.; Roumanie, M. A Simple Method for a Protective Coating on Stainless Steel against Molten Aluminum Alloy Comprising Polymer-Derived Ceramics, Oxides and Refractory Ceramics. *Materials* **2021**, *14*, 1519. [CrossRef] [PubMed]
4. Gladczuk, L.; Patel, A.; Paur, S.C.; Sosnowski, M. Tantalum films for protective coatings of steel. *Thin Solid Film.* **2004**, *467*, 150–157. [CrossRef]
5. Parchovianský, M.; Parchovianská, I.; Švancárek, P.; Motz, G.; Galusek, D. PDC Glass/Ceramic Coatings Applied to Differently Pretreated AISI441 Stainless Steel Substrates. *Materials* **2020**, *13*, 629. [CrossRef]
6. Wang, D.; Bierwagen, G.P. Sol–gel coatings on metals for corrosion protection. *Prog. Org. Coat.* **2009**, *64*, 327–338. [CrossRef]
7. Donald, I.W.; Mallinson, P.M.; Metcalfe, B.L.; Gerrard, L.A.; Fernie, J. A Recent developments in the preparation, characterization and applications of glass- and glass–ceramic-to-metal seals and coatings. *J. Mat. Sci.* **2011**, *46*, 1975–2000. [CrossRef]
8. Ceylan, I.; Gökdemir, H.; Cengiz, T.; Cicek, B. Development of CaO-rich blast furnace slag containing fluorine mica-based glass ceramic coatings. *Ceram. Int.* **2021**, *47*, 29988–29994. [CrossRef]
9. Gurnovich, N.V.; Zubekhin, A.P. Synthesis of one-layer glass-enamel coatings for domestic products. *Glass Ceram.* **1994**, *51*, 325–327. [CrossRef]
10. Zubekhin, A.P.; Zhabrev, V.A.; Kondyurin, A.M. Glass formation and crystallization in the SiO_2-Al_2O3-CaO-MgO-Fe_2O_3-MnO_2-K_2O-Na_2O for synthesizing heat resistant coatings. *Glass Ceram.* **1993**, *50*, 227–230. [CrossRef]
11. Han, Y.; Yao, S.; Zhang, W.; Gu, M.; Yao, Y. A Novel Wear Resistant Glass-Ceramic Coating Material. *Mater. Sci. Forum* **2011**, *686*, 521–527. [CrossRef]
12. Ataiwi, A.H.; Mahmood, I.A.; Mohmmed, J.H. Studying and Modeling The Effects of Quartz Addition and Heat Treatment on Corrosion Properties of Ceramic Coating. *Eng. Tech. J.* **2011**, *29*, 2564–2579.
13. Biswas, K.K.; Datta, S.; Das, S.K.; Ghose, M.C.; Mazumdar, A.; Roy, N. Glass-ceramic Coatings for Steel and Nimonic Alloy. *Trans. Ind. Ceram. Soc.* **1986**, *45*, 43–45. [CrossRef]

14. Günthner, M.; Schütz, A.; Glatzel, U.; Wang, K.; Bordia, R.K.; Greißl, O.; Krenkel, W.; Motz, G. High performance environmental barrier coatings, Part I: Passive filler loaded SiCN system for steel. *J. Eur. Ceram. Soc.* **2011**, *31*, 3003–3010. [CrossRef]
15. Nguyen, M.D.; Bang, J.W.; Kim, Y.H.; Bin, A.S.; Hwang, K.H.; Pham, V.H.; Kwon, W.T. Anti-fouling ceramic coating for improving the energy efficiency of steel boiler systems. *Coatings* **2018**, *8*, 353. [CrossRef]
16. Bernardo, E.; Bonomo, E.; Dattoli, A. Optimisation of sintered glass–ceramics from an industrial waste glass. *Ceram. Int.* **2010**, *36*, 1675–1680. [CrossRef]
17. Rawlings, R.D.; Wu, J.P.; Boccaccini, A.R. Glass-ceramics: Their production from wastes—A Review. *J. Mater. Sci.* **2006**, *41*, 733–761. [CrossRef]
18. Dávalosa, J.; Bonilla, A.; Villaquirán-Caicedo, M.A.; de Gutiérrez, R.M.; Rincón, J.M. Preparation of glass–ceramic materials from coal ash and rice husk ash: Microstructural, physical and mechanical properties. *Bol. Soc. Esp. Ceram. V.* **2021**, *60*, 183–193. [CrossRef]
19. Zhao, S.; Liu, B.; Ding, Y.; Zhang, J.; Wen, Q. Study on Glass-Ceramics Made from MSWI Fly Ash, Pickling Sludge and Waste Glass by One-Step Process. *J. Clean. Prod.* **2020**, *271*, 122674. [CrossRef]
20. Gorokhovsky, A.; Escalante-Garcia, J.I. Inorganic Wastes in Manufacture of Glass and Glass-Ceramics: Quartz-Feldspar Waste of Ore Refining, Metallurgical Slag, Limestone Dust, and Phosphorus Slurry. *J. Am. Ceram. Soc.* **2002**, *85*, 285–287. [CrossRef]
21. Gorokhovsky, A.; Gorokhovsky, V.; Mescheryakov, D.; Mendez-Nonel, J.; Escalante Garcia, J.I.; PechCanul, M.I.; Vargas-Gutierrez, G. Inorganic wastes in manufacturing of glass-ceramics: Slurry of phosphorous fertilizer production and oil shale ash. *Mat. Lett.* **2001**, *51*, 281–284. [CrossRef]
22. Lonelli, C.; Manfredini, T.; Paganelli, M.; Pozzi, P.; Pellacani, G.C. Crystallization of some anorthite-diopside glass precursors. *J. Mater. Sci.* **1991**, *26*, 5041–5046. [CrossRef]
23. Dahotre, N.B.; Kadolkar, P.; Shah, S. Refractory ceramic coatings: Processes, systems and wettability/adhesion. *Surf. Interface Anal.* **2001**, *31*, 659–672. [CrossRef]
24. Eppler, R.A.; Eppler, D.R. *Glazes and Glass Coatings*; The American Ceramic Society Inc.: Columbus, OH, USA, 2000.
25. Colomban, P. Glazes and enamels. In *Encyclopedia of Glass Science, Technology, History, and Culture*; The American Ceramic Society: Columbus, OH, USA, 2021; pp. 1309–1325. [CrossRef]
26. Guo, T.; Pang, X.; He, J.; Qiao, L. Discontinuous cracking of TiN films on a steel substrate induced by an adhesive interlayer. *Philos. Mag. Lett.* **2019**, *99*, 199–207. [CrossRef]
27. Bragina, L.L.; Zubekhin, A.P. *Technology of Enamels and Protective Coatings*; YuRGTU (NPI): Novocherkassk, Russia, 2003; pp. 54–96. (In Russian)
28. Diaz, C.; Salgado, S.; Jordan, R.; Cruz, E.; Zayas, M.E. Glass ceramic made from anodizing plant industrial waste. *Am. Ceram. Soc. Bull.* **2003**, *82*, 9601–9604.
29. Wang, D. Effect of crystallization on the property of hard enamel coating on steel substrate. *Appl. Surf. Sci.* **2009**, *255*, 4640–4645. [CrossRef]
30. Mejia-Ramirez, E.; Gorokhovsky, A.; Escalante-Garcia, J.I. Crystallization behavior of glasses in the system of Na_2O-CaO-MgO-Fe_2O_3-Al_2O_3-SiO_2 with high contents of nickel oxide. *J. Non-Cryst. Solids* **2007**, *353*, 366–373. [CrossRef]
31. Berdzenishvili, I.G. Functional Corrosion-Resistant Enamel Coatings and Their Adherence Strength. *Acta Phys. Pol. A* **2012**, *121*, 178–180. [CrossRef]
32. Guo, T.; Chen, Y.; Cao, R.; Pang, X.; He, J.; Qiao, L. Cleavage cracking of ductile-metal substrates induced by brittle coating fracture. *Acta Mater.* **2018**, *152*, 77–85. [CrossRef]

coatings

MDPI

Article

Novel Method for Deposition of Gas-Tight SiC Coatings

Sergey Shikunov, Alexei Kaledin, Irina Shikunova, Boris Straumal * and Vladimir Kurlov

Osipyan Institute of Solid State Physics, the Russian Academy of Sciences, Ac. Osipyan Street 2, Chernogolovka 142432, Russia
* Correspondence: straumal@issp.ac.ru

Abstract: A new high-temperature method for the deposition of gas-tight silicon carbide protective coatings with low gas permeability has been developed. The free carbon atoms form during the high-temperature pyrolysis of hydrocarbon molecules. In turn, carbon reacts with molten silicon contained in the subsurface substrate layers and/or with silicon vapor. The source of silicon vapor serves the molten silicon in the heated zone of a reactor furnace. Such coatings effectively protect SiC-C-Si and SiC-C-$MoSi_2$ ceramics, carbon–carbon composite materials, structural graphite, and refractory metals and alloys from oxidation. The conducted tests show the high thermal oxidation and thermal shock stability of deposited protective coatings, as well as their good adhesion to the substrates.

Keywords: silicon carbide; coatings; deposition; high-entropy alloys; gas permeability; thermal oxidation; thermal shock stability

Citation: Shikunov, S.; Kaledin, A.; Shikunova, I.; Straumal, B.; Kurlov, V. Novel Method for Deposition of Gas-Tight SiC Coatings. *Coatings* **2023**, *13*, 354. https://doi.org/10.3390/coatings13020354

Academic Editor: Qi Zhu

Received: 27 December 2022
Revised: 28 January 2023
Accepted: 1 February 2023
Published: 3 February 2023

1. Introduction

Graphite, carbon–carbon composite materials (CCCMs), and silicon carbide-based composites containing carbon are widely used in the design of various devices, machines, and mechanisms. In particular, they are used in the development of aviation and rocket technologies. The application of these materials is limited to temperatures below 450–500 °C. At higher temperatures, carbon is oxidized by the oxygen contained in the air. High-density silicon carbide (SiC) ceramics (such as reaction-bonded silicon carbide) usually contain some residual silicon. This fact limits their applicability due to thermal oxidation or degradation when operating in an alkaline environment.

Therefore, the development of high-temperature protective coatings on carbon- and silicon-containing materials is an urgent task [1]. These so-called "functional coatings" can be used for the following purposes:

- Isolation of the substrate material from contact with an oxidizing atmosphere in order to prevent corrosion;
- Increasing the wear resistance of the surface of the product;
- Increase in the strength of the product;
- Surface engineering, etc.

Silicon carbide is one of the most commonly used materials for protective coatings due to its resistance to temperature variations, high corrosion resistance, and good wear resistance at high temperatures in an oxidizing environment [2–4]. SiC thin films and coatings on high-temperature materials can be deposited by chemical vapor deposition (CVD) [5–8], metal organic chemical vapor deposition (MOCVD) [9], and reactive chemical vapor deposition (RCVD) [10]. SiC coatings are also deposited by high-speed plasma deposition [11–13], thermal evaporation [14], and magnetron sputtering [15,16]. Chemical surface modification [17], sol–gel technology [18], electrolytic and electrophoretic deposition from liquid solutions [19,20], plasma chemical vapor deposition [21–23], and reactive diffusion coating [24] are also used to deposit SiC.

CVD is the most common method for the deposition of protective SiC coatings on carbon-containing materials. This is because of its versatility and technological ripeness. CVD allows for gas-tight, homogeneous coatings to be obtained (on large-dimension parts) with precise thickness control and improved surface morphology. These properties ensure the good protective ability of SiC coatings. The disadvantages of CVD include the high cost of reagents, low deposition rates, and difficulties with adhesion when applied to some materials due to the impossibility of forming buffer layers.

There are also other methods for the deposition of SiC coatings. Thus, to protect carbon fibers and nanotubes from oxidation, as well as to form a buffer layer, the coating can be deposited in such a way that the surface of the carbon material does not deteriorate. This can be achieved if carbon is excluded from the reaction. For example, fibers can be impregnated with mixtures of reagents containing carbon and silicon subjected to hydrolysis, followed by heat treatment such as a gradual temperature increase up to 1400 °C [25]. Additionally, to obtain a composite material, the carbon powders can be coated with a SiC layer before subsequent sintering [26].

On the contrary, the participation of silicon in the formation of a coating on SiC ceramics with a high content of residual silicon permits the production of continuous SiC coatings when only a carbon-containing component is supplied. This approach ensures not only the protection of silicon-containing material, but also the manufacturing of hermetic (gas-tight) joints for ceramic parts [27]. Pastes or slurries consisting of a finer carbon filler fraction than the siliconized graphite being coated can also be used for deposition of SiC coatings. In this way, after siliconization, the dense SiC layer is formed on the surface of the product [28]. Due to the high content of SiC and reactive bonding with the protected material, such SiC coating exhibit good adhesion and wear resistance.

In this paper, we consider a new method for the deposition of tight SiC coatings with low gas permeability. Such SiC coatings permit improvements to the thermal oxidative resistance of ceramic materials containing residual carbon and silicon, as well as carbon–carbon composite materials, especially graphites and refractory metals and alloys. We also characterized the properties of materials, coatings, and products obtained using the developed deposition technology.

2. Materials and Methods

The technique for applying a gas-tight silicon carbide coating to a substrate material is based on the direct interaction of carbon formed during the high-temperature pyrolytic decomposition of hydrocarbon molecules (for example, methane) with a silicon melt contained in the surface layer of the material to be coated and/or silicon vapor. The source of silicon vapor is the silicon melt placed in the thermal zone of the furnace [29].

The layout of the reactor for deposition of a gas-tight SiC coating is shown in Figure 1. The process was carried out in a vacuum high-temperature furnace with a graphite heater and carbon thermal insulation. In the lower part of the thermal zone of the furnace, a crucible with silicon was located on a support, above which the coated part was placed upon special tooling. The furnace was evacuated using a fore-vacuum pump and was smoothly heated to a temperature of 1500–1800 °C until silicon melted in the crucible. After that, with the help of a gas flow regulator, methane was supplied to the thermal zone of the furnace. After reaching the required thickness of coating, the supply of methane to the thermal zone of the furnace was stopped and the heater was turned off. The coating growth rate can vary from 10 to 100 μm/h depending on the application mode and the type of surface to be protected. The vacuum supply system was left on until the furnace was completely cooled down.

Grain size of the SiC coating (from microcrystalline to nanoscale), the fraction of void, the atomic structure of grain boundaries, the composition of polytypes, and the morphology of SiC depend on the temperature in the interaction zone and the pressure of hydrocarbon gas. In this case, depending on the deposition conditions, one can controllably obtain either

coating from SiC nanoparticles with a controlled content of nanopores or poreless coatings consisting of nano- or microcrystals with uniform granulometric composition.

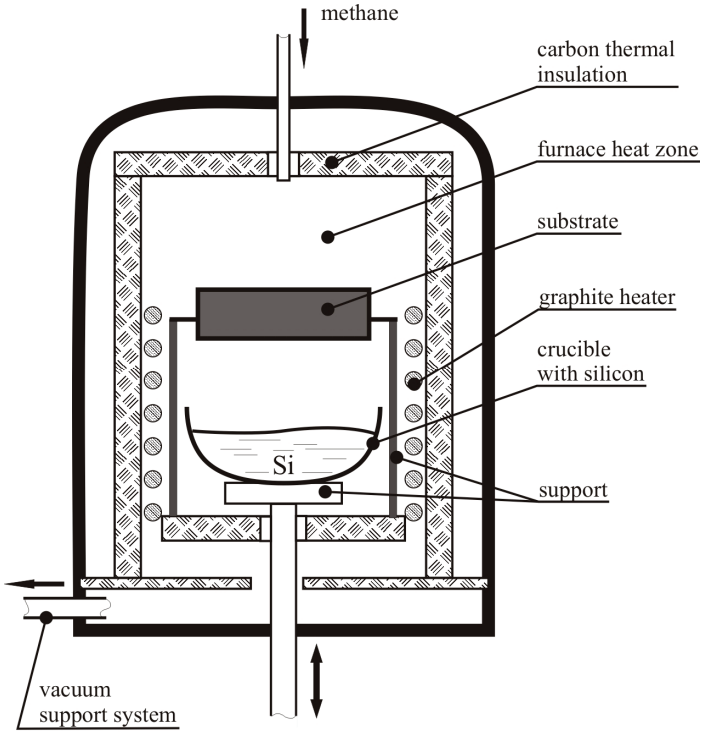

Figure 1. The layout of the reactor for deposition of gas-tight SiC coatings.

At low temperature (1500–1600 °C) in the reaction zone, the coating structure was formed of SiC nanoparticles ranging in size from 10 to 80 nm, which were agglomerated into clusters up to several tens of microns in size (Figure 2a). These clusters compose an ordered structure on the surface of the material, forming a porous coating in one or more layers (Figure 2b,c). Such coatings have significant advantages for a number of specific applications. For example, for materials operating under conditions of intense radiation, a large positive role is played by the presence of nanocavities, which ensure the rapid emergence and annihilation of radiation defects.

At higher temperatures (1700–1800 °C), gas-tight protective coatings are formed from micro- and nanocrystals (Figure 3).

Depending on the composition of the protected material, carbon and silicon can be used to form a coating both from external or internal sources. External sources are either a crucible with a silicon melt placed in the thermal zone of the furnace or carbon from the thermal decomposition of a gaseous hydrocarbon. Internal sources are residual silicon and carbon contained in the near-surface substrate layer. Information on the components involved in the formation of coatings on various materials is given in Table 1.

Application of the developed technique makes it possible to obtain air-tight polycrystalline silicon carbide coatings with thicknesses from 300 nm to hundreds of micrometers and even several millimeters. Depending on the feed rate, pressure, and temperature of the components in the interaction zone, it is possible to change the grain size of the SiC coating from dozens of nanometers to hundreds of micrometers.

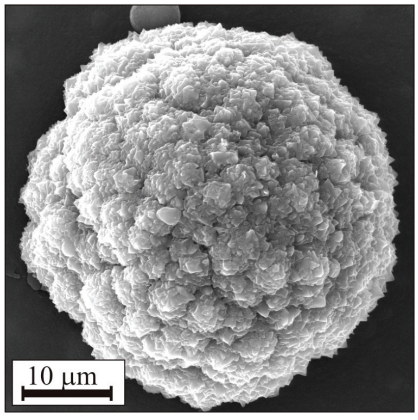

(**a**)

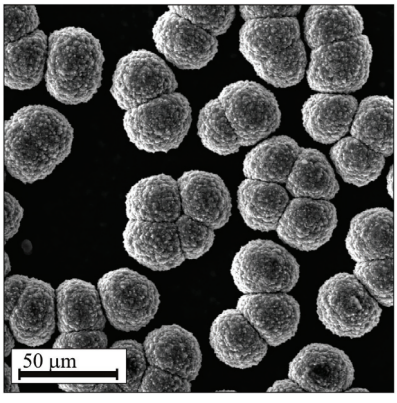

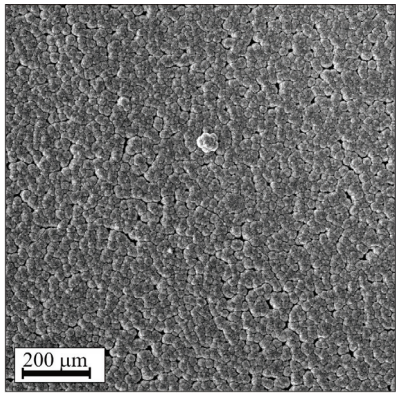

(**b**) (**c**)

Figure 2. Porous coating formed of SiC nanoparticles from 10 to 80 nm in size, agglomerated into clusters. (**a**) SiC nanoparticles ranging in size from 10 to 80 nm agglomerated into clusters up to several tens of microns in size; (**b**) clusters in an ordered structure on the surface of the material; (**c**) resulted porous coating in one or more layers.

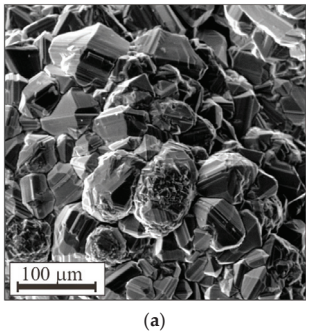

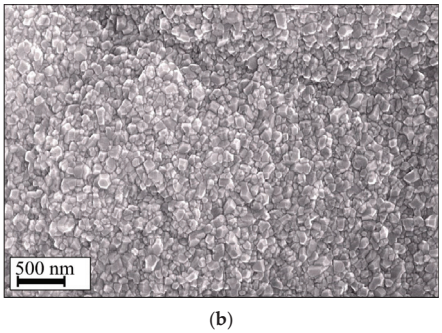

(**a**) (**b**)

Figure 3. Gas-tight protective coatings formed by micro-F (**a**) and nanocrystals (**b**).

Table 1. Features of SiC coating deposition on various refractory materials.

Substrate Material	Carbon from the Substrate	Silicon from the Substrate	Carbon from the External Source	Silicon from the External Source
CCCMs and graphite	yes	no	yes	yes
SiC-C-Si, siliconized graphites	yes	yes	yes	yes
SiC-C-$MoSi_2$	yes	no	yes	yes
Modified RSiC	no	yes	yes	yes
Metals and alloys	no	no	yes	yes

3. Results and Discussion

In this section we describe the deposition of protective SiC coatings on various high-temperature materials. The features of the formation of coatings on various materials and their influence on the characteristics of products are considered. Oxidation resistance at high temperatures, thermal shock resistance, and the influence on mechanical properties are described.

3.1. Deposition of Protective SiC Coatings on the Carbon–Carbon Composite Materials and Graphites

Carbon–carbon composite materials (CCCMs) and graphites have high strength and thermal stability in vacuum or inert environments. However, they can be oxidized by the oxygen in air at above 450–500 °C. The oxidation leads to corrosion and loss of strength and therefore limits the applicability of CCCMs and graphites. To protect CCCMs from oxidation, deposition modes were used, in which a dense SiC coating about 10 μm thick with a small grain size (80 nm) was formed. Such coating protects the substrate material from reactions with environmental components. The SiC coating also leads to a noticeable change in the size and mechanical characteristics of the coated composite material.

A CCCM with a SiC gas-tight coating is shown in Figure 4. The carbon from the surface layer of the CCCM partially participated in the formation of the SiC coating. This ensures the high adhesion of the SiC coating to the substrate and high protective properties with a thin coating.

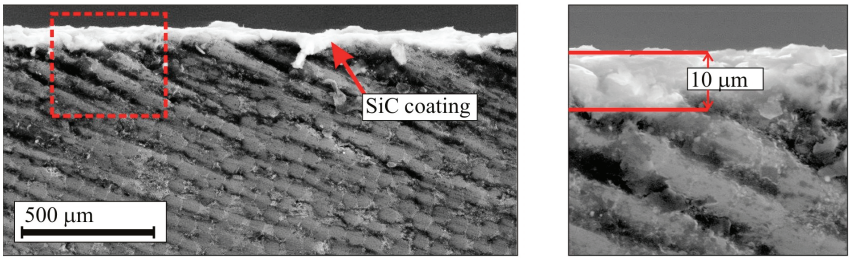

Figure 4. Cross-section of a CCCM with a protective gas-tight SiC coating (**a**) and its enlarged fragment (**b**).

To determine the thermal oxidative resistance of the coatings, tests were carried out on a specially prepared CCCM sample with a SiC coating. The experimental conditions were as follows: air velocity head 4–6 GPa, temperature T = 1700 °C, test time of 10 min. Figure 5 shows the test thermograms for a CCCM sample with a protective SiC coating and its appearance before and after testing. Figure 6 shows the temperature distribution over the area of the sample. Despite the local overheating of the sample surface (Figure 4), the continuity of the coating was not disturbed. The weight loss of the sample after testing was 14.6 mg, which was less than 0.1% of the total weight of the sample. Tests for thermo-oxidative resistance demonstrated the promising features of the developed technique for deposition of silicon carbide coatings on CCCMs. The coating has good protective properties up to temperatures of 1700–1750 °C.

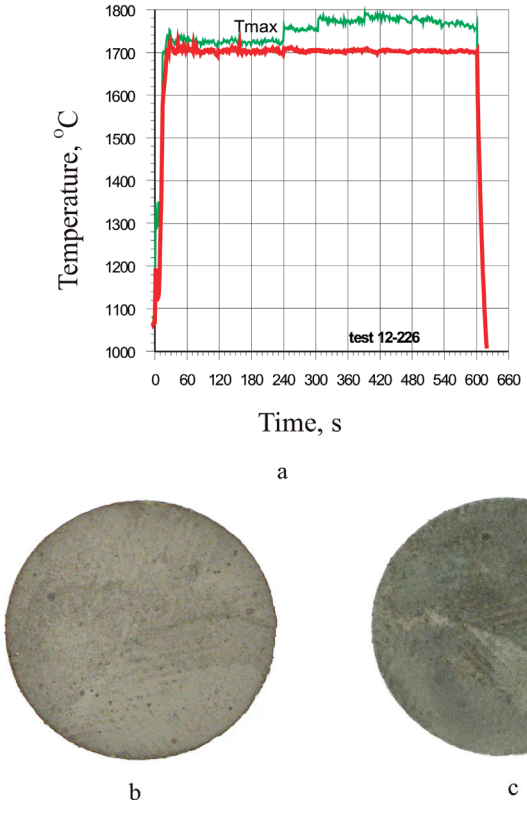

Figure 5. Test thermograms for a CCCM sample 50 mm in diameter with a protective SiC coating (**a**) and its appearance before (**b**) and after (**c**) testing.

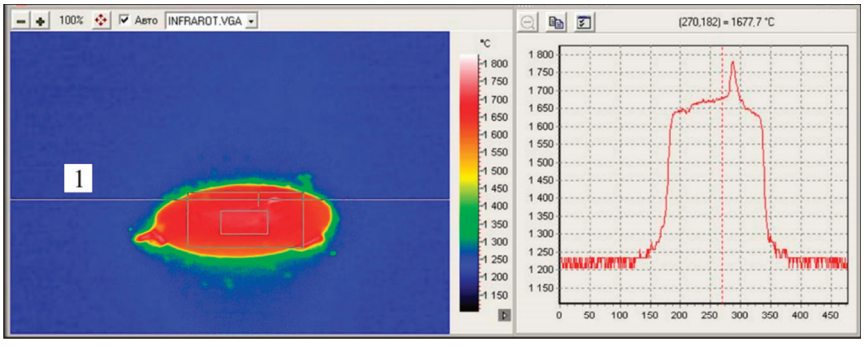

Figure 6. Temperature distribution over the area of the CCCM sample with a protective SiC coating.

Tight SiC coatings with low gas permeability were also deposited on graphite parts with various geometries to protect them from oxidation. The maximum dimensions of products to be coated are limited only by the dimensions of the thermal zone of the installation. Figure 7 shows examples of SiC coatings of uniform thickness that were deposited on graphite parts with various geometries.

Figure 7. Examples of gas-tight SiC coatings of uniform thickness on the large graphite parts with complicated geometries.

Graphite can be used as a removable substrate to obtain polycrystalline silicon carbide in complex shapes. Figure 8 shows SiC tubes and a magnetron sputtering target made by depositing a thick layer of silicon carbide on rectangular graphite rods and a plate. After coating, the graphite was removed by annealing in air at a temperature of 1100 °C. This technique allows you to obtain macroscopic articles of various configurations from nanostructured SiC.

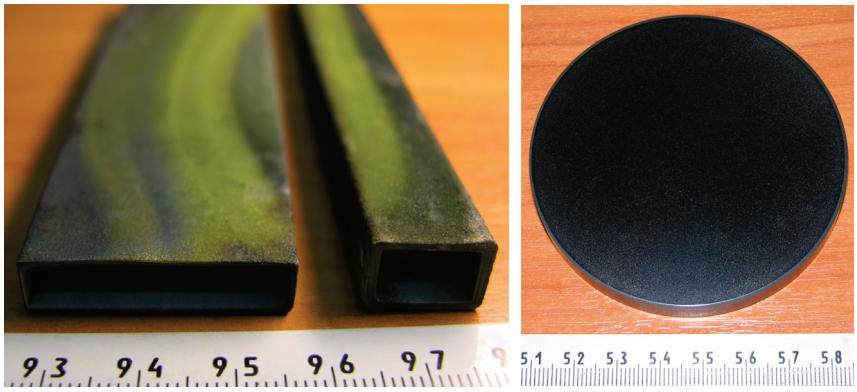

(**a**) (**b**)

Figure 8. SiC rectangular tubes with a wall thickness of 1–1.5 mm (**a**) and a SiC magnetron sputtering target of 70 mm in diameter and 6 mm in thickness (**b**), which were obtained by deposition onto removable graphite substrates.

3.2. Deposition of Protective SiC Coatings on SiC-C-Si and Siliconized Graphites

Relatively light and wear-resistant SiC-C-Si ceramics are well suited for manufacturing complex-shaped parts. As for carbon materials, their operating conditions are limited to temperatures of 450–500 °C due to the oxidation of residual carbon. In the absence of residual carbon, their operating conditions are limited to temperatures of 1100 °C due to the oxidation of residual silicon. The atmosphere of water vapor and alkali metal salts accelerates the destruction of SiC-C-Si ceramics. Thus, a protective SiC coating should significantly limit the corrosion of such ceramics.

Polycrystalline SiC coatings with a thickness of 20–100 μm were deposited on the parts made of SiC-C-Si ceramics. These parts were produced by the impregnation of porous carbon matrices with liquid silicon. The porous carbon matrices had different residual silicon and carbon content in the volume [30,31]. It can be seen in the cross section of the coated substrate (Figure 9) that the part of the residual silicon in the near-surface open pores was involved in the formation of the coating. Single pores in the near-surface layer of the material do not have any noticeable effect on the mechanical properties of ceramics, especially in front of their significant increase from the presence of the SiC coating. The coating itself has multiple continuous bonds to the carbon and silicon carbide of the material, providing strong bonding to the substrate.

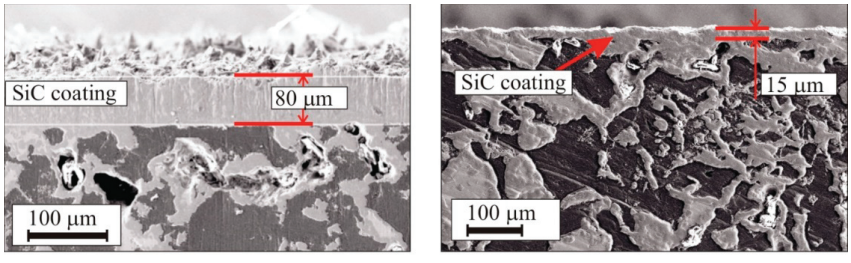

a b

Figure 9. Cross section of a SiC-C-Si ceramic substrate with a deposited protective gas-tight SiC thick (**a**) and thin (**b**) coating.

To determine the temperature stability of protective SiC coatings on SiC-C-Si ceramics, the decrease in the mass of samples due to carbon burnout when exposed to high temper-

ature in an oxidizing atmosphere was evaluated. Figure 10 shows cross sections of the SiC-C-Si/50-40-10 ceramics without a protective coating (Figure 10a) and with a gas-tight SiC coating after annealing in air at 1000 °C for 60 h (Figure 10b). It can be seen that the structure of the material without a protective coating is severely damaged due to carbon burnout from the bulk of the material. Information about the changes in the weight of the samples is given in Table 2. The weight of parts with SiC coatings changed by less than 1%, which indicates that the coating has high functional quality.

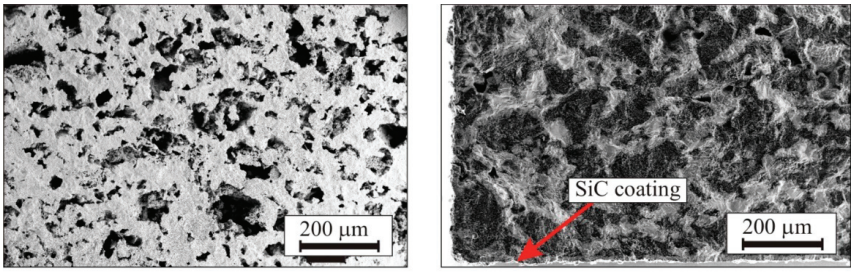

Figure 10. Microstructure of composite material SiC-C-Si/50-40-10 without a coating (**a**) and with a gas-tight SiC coating (**b**) after annealing at 1000 °C in air for 60 h.

Table 2. Weight of samples from SiC-C-Si/50-40-10 ceramics without a coating and with a protective SiC coating before and after annealing.

Sample Description	Weight of Sample before Annealing, g	Weight of Sample after Annealing, g	Weight Loss, %
Sample 1, without coating	29.35	18.76	36.08
Sample 2, without coating	25.19	16.33	35.17
Sample 3, with protective SiC coating	28.82	28.68	0.48
Sample 4, with protective SiC coating	24.21	24.05	0.66

The deposition of a SiC coating on SiC-C-Si ceramics can also improve the mechanical properties of the material by reducing the contribution of surface defects during bending and compression testing. Table 3 shows the measurement results of mechanical testing of the uncoated and coated SiC-C-Si specimens.

Table 3. Comparison of the strength characteristics of SiC ceramics with SiC-C-Si/50-40-10 composition without coating and with a gas-tight SiC coating.

Property	Without Coating	With Coating, 20 °C	With Coating, 1000 °C
Compression strength, MPa	398 ± 19	472 ± 11	483 ± 8
Bending strength, MPa	126 ± 6	204 ± 11	203 ± 7

The SiC film deposited according to the developed method is sufficiently conformal. In other words, its thickness on the walls of complex structures is comparable to the thickness of the film on the horizontal sections of these structures. This means that the method can be used to apply protective coatings on parts that are very complex in shape.

Using the developed method for manufacturing ceramic parts with complex shapes and the technique of applying protective SiC coatings, high-temperature equipment was manufactured. Namely, inserts for thermocouples were produced and used in the test bench for a gas turbine engine (Saturn, Rybinsk). Figure 11 shows the water-cooled metal case of a gas flow thermometer with five SiC inserts for the placement of thermocouples [32,33].

In the test bench for the gas turbine engine, a test cycle was carried out where the total operating time of the equipment was about 8 h; the thermogram (Figure 12) shows that the maximum measured temperature was 1465 °C.

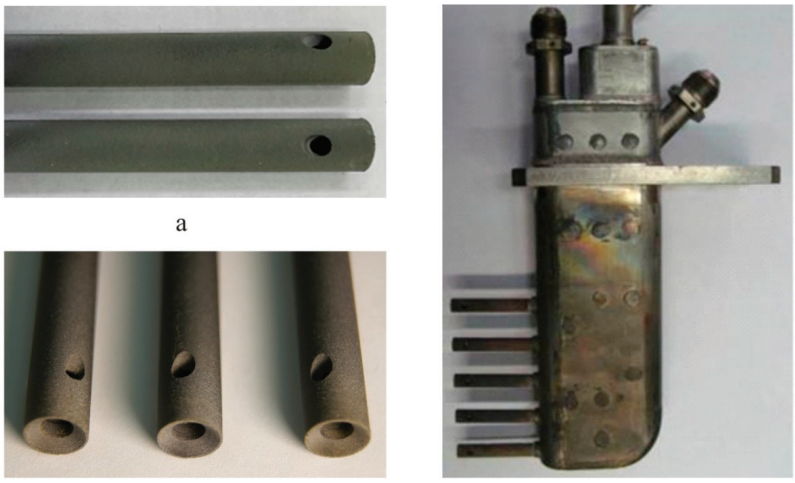

Figure 11. Thermal probes for temperature measurement in a high-temperature gas flow with brake chambers (**a**,**b**) and a comb with thermal probes as an assembly (**c**).

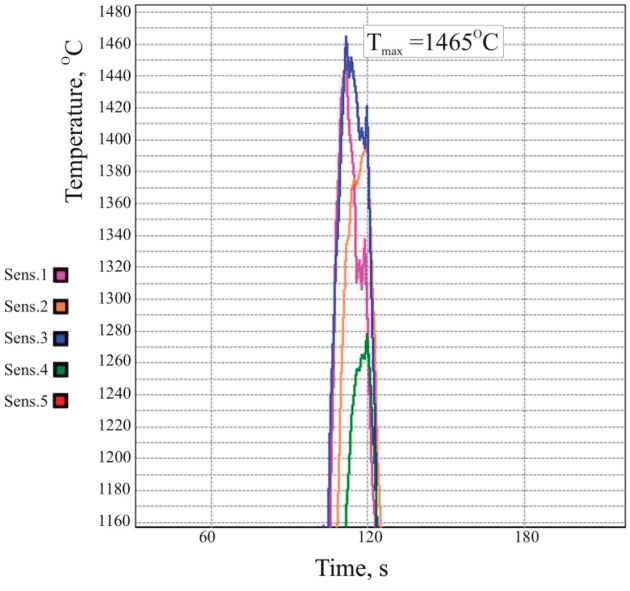

Figure 12. Thermogram recorded by thermocouples placed in silicon carbide inserts with a protective SiC coating.

3.3. Deposition of SiC Coatings on SiC-C-$MoSi_2$ Ceramic Products

SiC has good chemical compatibility and thermal stability with $MoSi_2$, so the strength and toughness of SiC-based composites enriched in the $MoSi_2$ phase can be greatly improved. Figure 13 shows the microstructure of a SiC-C-$MoSi_2$ composite material with

a silicon carbide protective coating. The coating makes it possible to prevent both the high-temperature oxidation of carbon particles (which are present in the material's structure) and the low-temperature oxidation of molybdenum disilicide. Such stability is necessary during the long-term operation of such a material in the temperature range of 600–900 °C [34,35]. The coating was deposited by the gas-phase method through the exposure of the composite sample in the thermal zone of the furnace, where silicon vapors and products of high-temperature pyrolytic decomposition of methane molecules were present.

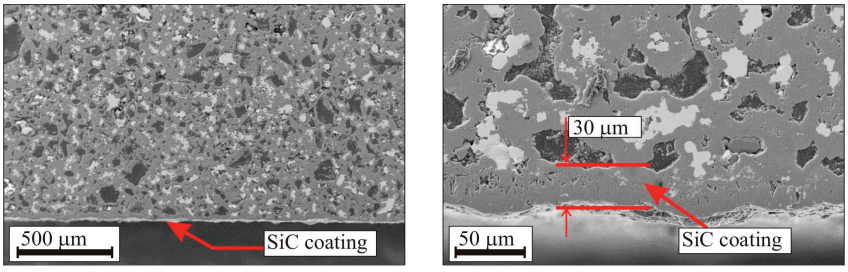

Figure 13. Micrograph of the structure of a SiC-C-$MoSi_2$ ceramic composite material with a protective SiC coating: black areas represent carbon, dark gray represents SiC, and light gray represents $MoSi_2$. (**a**) low magnification; (**b**) high magnification.

Additionally, this method can be used to obtain protective coatings for SiC-based composites reinforced with refractory metal wire, such as molybdenum, tungsten, niobium, etc. [36,37].

3.4. Deposition of SiC Coatings on Products from SiC-Si Material

A silicon carbide gas-tight coating can be deposited on materials containing residual silicon, such as modified recrystallized silicon carbide (mRSiC) or reaction-bonded silicon carbide (RBSiC). Such protective SiC coatings significantly increase the thermal and oxidative resistance of mRSiC or RBSiC (Figure 14) due to the protection against oxidation of residual silicon contained in the material.

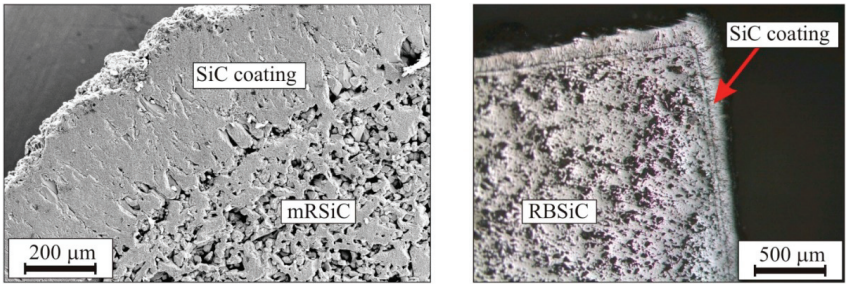

Figure 14. Protective SiC coating on recrystallized (**a**) and reaction-bonded (**b**) SiC.

Heaters made of recrystallized SiC ceramics "age" during operation. Due to oxidation, the cross section of the working part of the heater decreases and its electrical resistance increases. As a result, zones of local overheating are formed. In places of overheating, more intense oxidation occurs, which in turn causes a further decrease in the cross section of the heater and an increase in temperature. The process proceeds at an increasing rate and leads to the burnout of the heater. We have developed a technique for modifying RSiC [38]. This technology increases the mechanical strength and thermal shock resistance of the material.

The dependence of electrical resistivity on temperature becomes more stable. Therefore, the manufacture of an mRSiC heater with a protective SiC coating is of great interest as this would increase the resistance of the heater to oxidation.

To confirm the effectiveness of the above method for manufacturing heating elements from mRSiC, a prototype heater was prepared and tested. A heating element of made of mRSiC with an outer diameter of 12 mm and a length of 180 mm was made from the working parts of a standard heating element. The protective silicon carbide coating was deposited on its surface (Figure 14a).

The tests were carried out on a stand (see the scheme in Figure 15). A computer-controlled power supply heated the heater up to ~1600 °C for two minutes, which was followed by cooling for one minute. The cycle was repeated afterwards. At the end of each heating cycle, the values of the current flowing through the heater and the voltages on the current leads were recorded.

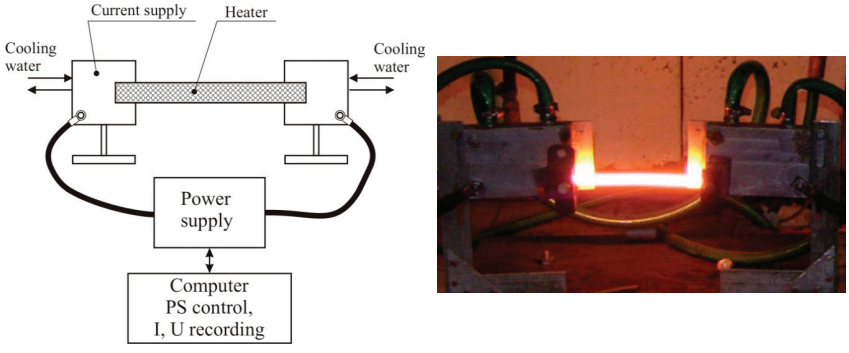

Figure 15. Scheme of the stand and a photograph of the testing process for the mRSiC heater with a protective SiC coating.

In Figure 16, the dependence of heater resistance vs. the number of warm-up/cool-down cycles is plotted. After 2000 cycles, the change in the electrical resistance of the heater was less than 5%. The stability of electrical resistance confirms the good protective properties of the SiC coating and its high adhesion to the heater surface.

3.5. Deposition of SiC Coatings on SiC-C-$MoSi_2$ Ceramic Products

The protective SiC gas-tight coating can also be deposited on refractory metals and metal alloys. Figure 17a shows a SiC-coated molybdenum plate that was used as a heater in an oxidizing atmosphere at a temperature of 1500 °C for about 10 h. Heater contact zones at the edges were not protected by the coating.

To achieve good adhesion with the SiC coating and prevent its delamination and destruction during temperature cycling, an intermediate layer of silicide was formed on the surface of metal (Figure 17b). In order for this to be achieved before methane was supplied to the chamber, the metal was preliminarily held in silicon vapor to form a silicide layer on its surface. Further, after the start of methane supply to the interaction zone, a silicon carbide coating was formed on a silicide layer.

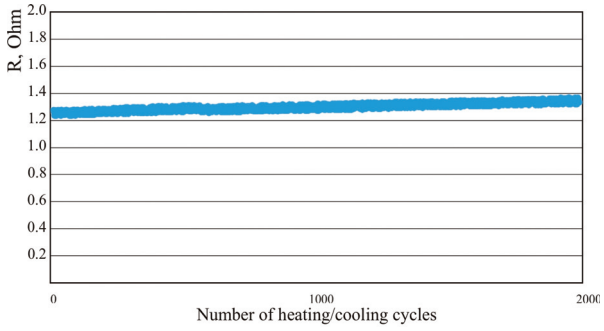

Figure 16. Dependence of heater resistance on the number of heating/cooling cycles.

(**a**)

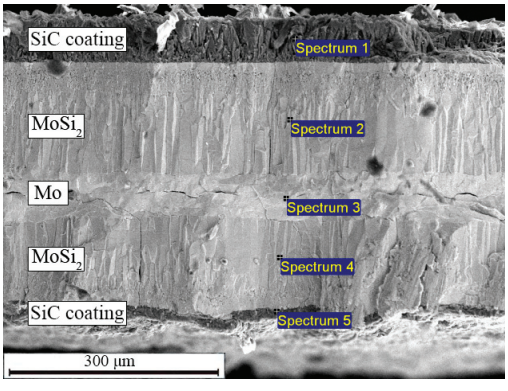

Spectrum	C	Si	Mo
Spectrum 1	78.48	21.52	
Spectrum 2		64.83	35.17
Spectrum 3		2.03	97.97
Spectrum 4		64.64	35.36
Spectrum 5	57.52	41.73	0.75
Max.	78.48	64.83	97.97
Min.	57.52	2.03	0.75

All results in atomic%

(**b**)

Figure 17. Protective gas-tight SiC coating on a molybdenum heating element (**a**). Phase analysis of the heating element's cross section (**b**).

4. Conclusions

The conventional CVD method for SiC deposition includes various precursors (monomethylsilane, methyltrichlorosilane, tetramethylsilane, etc.). In contrast to CVD, the proposed high-temperature method of the gas-phase deposition of protective SiC coatings has a number of significant advantages. These are the following:

- The deposition rate is approximately two orders of magnitude higher;
- The adhesion of the protective coating to the surface of a carbon- and/or silicon-containing material is significantly higher. This is because the process is carried out at a high temperature with the participation of carbon and silicon located directly in the substrate material;
- Simpler technological equipment;
- Low cost due to the speed of coating deposition and the use of more accessible and cheaper components compared to silicon-containing precursors.

Thus, a high-temperature method for the deposition of protective SiC coatings onto SiC-C-Si and SiC-C-$MoSi_2$ ceramics, CCCMs, graphite, refractory metals, and metal alloys has been developed. The tests carried out showed high thermal-oxidative and thermal

shock resistance and good adhesion, with protective coatings also capable of withstanding harsh environments.

Author Contributions: Conceptualization, S.S. and V.K.; methodology, A.K. and I.S.; formal analysis, A.K. and I.S.; writing—original draft preparation, V.K.; writing—review and editing, B.S.; supervision, B.S. and V.K.; project administration, V.K.; funding acquisition, V.K. All authors have read and agreed to the published version of the manuscript.

Funding: This research received no external funding.

Institutional Review Board Statement: Not applicable.

Informed Consent Statement: Not applicable.

Data Availability Statement: All the data required to reproduce these experiments are present in the article.

Conflicts of Interest: The authors declare no conflict of interest.

References

1. Raj, R. Fundamental research in structural ceramics for service near 2000 °C. *J. Amer. Ceram. Soc.* **1993**, *9*, 2147. [CrossRef]
2. Elizarova, Y.A.; Zakharov, A.I. High-temperature protective coatings of the functional purpose. *New Refract.* **2020**, *10*, 52. [CrossRef]
3. Filonov, K.N.; Kurlov, V.N.; Klassen, N.V.; Kudrenko, E.A.; Steinman, E.A. Peculiarities of nanostructured silicon carbide films and coatings obtained by novel technique. *Bull. Russ. Ac. Sci. Phys.* **2009**, *73*, 1374. [CrossRef]
4. Locke, C.W. *SiC Films and Coatings: Amorphous, Polycrystalline, and Single Crystal Forms: In Silicon Carbide Biotechnology*, 2nd ed.; Elsevier: Amsterdam, The Netherlands, 2012; Volume 379; Available online: http://books.google.com/books?hl=en&lr=&id=tdRnnGs0UsgC&oi=fnd&pg=PA17&dq=info%3 (accessed on 20 December 2022).
5. Dhanaraj, G.; Dudley, M.; Chen, Y.; Ragothamachar, B.; Wu, B.; Zhang, H. Epitaxial ghrowth and characterization of silicon carbide films. *J. Cryst. Growth* **2006**, *287*, 344. [CrossRef]
6. Zhang, W.G.; Hüttinger, K.J. CVD of SiC from methyltrichlorosilane. Part I: Deposition rates. *Chem. Vapor Depos.* **2001**, *7*, 167. [CrossRef]
7. Park, K.-I.; Kim, J.-H.; Lee, H.-K.; Kim, D.K. High temperature mechanical properties of CVD-SiC thin films. *Mod. Phys. Lett. B* **2009**, *23*, 3877. [CrossRef]
8. Powell, J.A.; Larkin, D.J.; Matus, L.G.; Choyke, W.J.; Bradshaw, J.L.; Henderson, L.; Yoganathan, M.; Yang, J.; Pirouz, P. Growth of high quality 6H-SiC epitaxial films on vicinal (0001) 6H-SiC wafers. *Appl. Phys. Lett.* **1990**, *15*, 1442. [CrossRef]
9. Landry, C.C.; Barron, A.R. MOCVD of alumina-silica oxidation resistant coatings on carbon fibers. *Carbon* **1995**, *33*, 381. [CrossRef]
10. Baklanova, N.I.; Zima, T.M.; Boronin, A.I.; Kosheev, S.V.; Titov, A.T.; Isaeva, N.V.; Graschenkov, D.V.; Solntsev, S.S. Protective ceramic multilayer coatings for carbon fibers. *Surf. Coat. Technol.* **2006**, *201*, 2313. [CrossRef]
11. Han, M.X.; Zhou, W.; Zheng, D.H.; Tu, R.; Zhang, S.; Goto, T. High-speed deposition of SiC thick film by halide precursor. *Key Eng. Mater.* **2014**, *616*, 37. [CrossRef]
12. Károlya, Z.; Bartha, C.; Mohai, I.; Balázsi, C.; Sajó, I.E.; Szépvölgyi, J. Deposition of silicon carbide and nitride based coatings by atmospheric plasma spraying. *Int. J. Appl. Ceram. Technol.* **2013**, *10*, 72. [CrossRef]
13. Tului, M.; Giambi, B.; Lionetti, S.; Pulci, G.; Sarasini, F.; Valente, T. Silicon carbide based plasma sprayed coatings. *Surf. Coat. Technol.* **2012**, *207*, 182. [CrossRef]
14. Wielage, B.; Wilden, J.; Schnick, T.; Wank, A. Development of SiC-composite feedstock for HVOF applications. *Proc. Int. Therm. Spray Conf.* **2002**, *2002*, 749. [CrossRef]
15. Tang, H.D.; Tan, S.H.; Huang, Z.R. SiC coatings deposited by RF magnetron sputtering. *Key Eng. Mater.* **2007**, *280–283*, 1309. [CrossRef]
16. Ordine, A.; Achete, C.; Mattos, O.; Margarit, I.C.P.; Camargo, S.S., Jr.; Hirsch, T. Magnetron sputtered SiC coatings as corrosion protection barriers for Steels. *Surf. Coat. Technol.* **2000**, *133–134*, 583. [CrossRef]
17. Gadiou, R.; Serverin, S.; Gibot, P.; Vix-Guterl, C. The synthesis of SiC and TiC protective coatings for carbon fibers by the reactive replica process. *J. Europ. Ceram. Soc.* **2008**, *28*, 2265. [CrossRef]
18. Kerans, R.J.; Hay, R.S.; Parthasarathy, T.A.; Cinibulk, M.K. Interface design for oxidation-resistant ceramic composites. *J. Amer. Ceram. Soc.* **2002**, *85*, 2599. [CrossRef]
19. Zhitomirsky, I.; Petric, A. Cathodic electrodeposition of ceramic coatings for oxidation protection of materials at elevated temperatures. *Can. J. Metal. Mater. Sci.* **2002**, *41*, 497. [CrossRef]
20. Sheveleva, I.V.; Zemskova, L.A.; Voit, A.A.; Zheleznov, S.V.; Kuryavyi, V.G. Relationship between electrochemical and structural properties of modified carbon fibers. *Russ. J. Appl. Chem.* **2007**, *80*, 240. [CrossRef]

21. Daves, W.; Krauss, A.; Behnel, N.; Häublein, V.; Bauer, A.; Frey, L. Amorphous silicon carbide thin films (a-SiC:H) deposited by plasma-enhanced chemical vapor deposition as protective coatings for harsh environment applications. *Thin Solid Films* **2011**, *519*, 5892. [CrossRef]
22. Loboda, J.; Seifferly, J.A.; Dall, F.C. Plasma-enhanced chemical vapor deposition of a-SiC:H films from organosilicon precursors. *J. Vacuum Sci. Technol. A* **1994**, *12*, 90. [CrossRef]
23. Dai, P.Y.; Wang, Y.Z.; Liu, G.L.; Wang, B.; Shi, Y.G.; Yang, J.F.; Qiao, G.J.; Wang, H.J. Fabrication of highly dense pure SiC ceramics via the HTPVT method. *Acta Mater.* **2011**, *59*, 6257. [CrossRef]
24. Paccaud, O.; Derré, A. Silicon carbide coating by reactive pack cementation—Part II: Silicon monoxide/carbon reaction. *Chem. Vapor Dep.* **2000**, *6*, 41. [CrossRef]
25. Kablov, E.N.; Kuznetcov, N.T.; Sarkisov, P.D.; Graschenkov, D.V.; Sevast'yanov, V.G.; Orlova, L.A.; Simonenko, E.P. Method for Protecting Carbon-Containing Materials with Silicon Carbide. Patent RU 2350580, 27 March 2009.
26. Nakamura, M.; Tojo, T.; Miyamoto, Y. Synthesis of ceramic bonded carbon using SiC-coated carbon particles and spark plasma sintering. *Int. J. Appl. Ceram. Technol.* **2012**, *9*, 1076. [CrossRef]
27. Lessing, P.A.; Erickson, A.W.; Kunerth, D.C. Thermal cycling of siliconized-SiC at high temperatures. *J. Mater. Sci.* **2001**, *36*, 1389. [CrossRef]
28. Krödel, M.R.; Ozaki, T. HB-Cesic composite for space optics and structures. *Proc. SPIE* **2007**, *6666*, 1. [CrossRef]
29. Kurlov, V.N.; Shikunova, I.A.; Shikunov, S.L.; Ershov, A.E. Method of Applying Gastight Coating of Silicon Carbide. Patent RU 2601049, 27 October 2016.
30. Shikunov, S.L.; Kurlov, V.N. SiC-based composite materials obtained by siliconizing carbon matrices. *Tech. Phys.* **2017**, *62*, 1869. [CrossRef]
31. Kurlov, V.N.; Shikunov, S.L.; Shikunova, I.A. Composition of Carbon Blank for Obtaining SiC/C/Si Ceramics and Method for Obtaining SiC/C/Si Products. Patent RU 2573146, 24 December 2014.
32. Kurlov, V.N.; Shikunova, I.A.; Shikunov, S.L. High Temperature Probe for Measurements in Gas Flow. Patent RU 165789, 10 November 2016.
33. Kurlov, V.N.; Shikunov, S.L.; Shikunova, I.A.; Surmin, N.V.; Tihomirova, E.V.; Grishihin, S.A. Thermocouple Comb for Measuring the Temperature Field of a Gas Flow. Patent RU 160313, 10 March 2016.
34. McKamey, C.G.; Tortorelli, P.F.; DeVan, J.H.; Carmichael, C.A. A Study of pest oxidation in polycrystalline $MoSi_2$. *J. Mater. Res.* **1992**, *7*, 2747. [CrossRef]
35. Meschter, P.J. Low temperature oxidation of molybdenum disilicide. *Metall. Trans. A* **1992**, *23*, 1763. [CrossRef]
36. Mainzer, B.; Lin, C.; Frieß, M.; Riedel, R.; Riesch, J.; Feichtmayer, A.; Fuhr, M.; Almanstötter, J.; Koch, D. Novel ceramic matrix composites with tungsten and molybdenum fiber reinforcement. *J. Eur. Ceram. Soc.* **2021**, *41*, 3030. [CrossRef]
37. Kaledin, A.V.; Shikunov, S.L.; Straumal, B.B.; Kurlov, V.N. SiC-based composite material reinforced by molybdenum wire. *Metals* **2023**, *13*, 313. [CrossRef]
38. Kurlov, V.N.; Shikunov, S.L.; Shikunova, I.A. Method for Obtaining Products from Silicon Carbide Ceramics. Patent RU 2740984, 22 January 2021.

coatings

MDPI

Article

Enhanced Performance in Si_3N_4 Ceramics Cutting Tool Materials by Tailoring of Phase Composition and Hot-Pressing Temperature

Shuai Guo [1,2], Fusheng Zhu [1], Zhimeng Xiu [1], Mu Zhang [1,2,*] and Xudong Sun [1,2,*]

[1] Key Laboratory for Anisotropy and Texture of Materials (Ministry of Education), School of Materials Science and Engineering, Northeastern University, Shenyang 110819, China
[2] Foshan Graduate School of Innovation, Northeastern University, Foshan 528311, China
* Correspondence: zhangm@mail.neu.edu.cn (M.Z.); xdsun@mail.neu.edu.cn (X.S.)

Abstract: In this study, a type of micro-nano Si_3N_4 matrix ceramic cutting tool material was successfully prepared by controlling the addition amount of $TiC_{0.7}N_{0.3}$ and the hot-pressing sintering temperature. The effects of different volume fractions of $TiC_{0.7}N_{0.3}$ on the microstructure, mechanical properties, particle size distribution, and relative density of Si_3N_4 ceramic tools at the same temperature were investigated. The results show that the addition of $TiC_{0.7}N_{0.3}$ makes the β-Si_3N_4 grains with different diameters and aspect ratios interlaced and tightly bonded, thus achieving the strengthening and toughening effects. In addition, the effects of different hot-press sintering temperatures on the properties of Si_3N_4 ceramic tool materials were studied. It was concluded that the density of the material increased with the increase of the hot-pressing temperature. The relative density, flexural strength, and fracture toughness of the samples with 1 vol% $TiC_{0.7}N_{0.3}$ added at 1750 °C and 30 MPa pressure reached 99.22%, 993 MPa, and 9.81 MPa·$m^{1/2}$, respectively.

Keywords: Si_3N_4; ceramic cutting tool; hot-pressing sintering; $TiC_{0.7}N_{0.3}$; self-toughening

Citation: Guo, S.; Zhu, F.; Xiu, Z.; Zhang, M.; Sun, X. Enhanced Performance in Si_3N_4 Ceramics Cutting Tool Materials by Tailoring of Phase Composition and Hot-Pressing Temperature. *Coatings* **2023**, *13*, 475. https://doi.org/10.3390/coatings13020475

Academic Editor: Ben Beake

Received: 16 January 2023
Revised: 11 February 2023
Accepted: 14 February 2023
Published: 20 February 2023

1. Introduction

With the development of modern manufacturing technology, the use of various new difficult-to-machine materials is increasing, such as iron-based, nickel-based, cobalt-based, titanium-based superalloys, ultra-high strength steel, and high wear-resistant cast iron. Therefore, the cutting and machining of such materials are becoming increasingly important. However, with the current use of traditional hard alloy or high-speed steel and other tool materials to process, tool life is very low or even impossible to process. This prompted people to study and manufacture suitable-for-processing engineering materials for use as tool materials. Because of the outstanding performance of high-toughness ceramic tools, ceramic tools are considered to be the most prominent and widely useful option. In modern machining, ceramic materials have become the most promising utility tool materials due to their excellent heat resistance, high-temperature oxidation resistance, high hardness, and wear resistance [1–5].

Although ceramics cutting tools play an increasingly important role in cutting difficult-to-machine materials, ceramics cutting tools suffer from relatively low fracture toughness and ductility due to the inherent brittleness of ceramic materials [6]. Therefore, some scholars have focused their research on improving the fracture toughness of conventional ceramic tool materials to meet the requirements of high-speed precision cutting processing. Some researchers choose to prepare a coating (cBN coating, [7] TiAlN coating, [8,9] WS_2/Zr soft-coating [10]) on the surface of the ceramic tool to achieve the purpose of improving the tool life, study the wear mechanism of the tool during cutting, and prepare a composite ceramic tool with good performance. These coatings can effectively prevent the internal

ceramic material from being corroded, thereby increasing the service life of the tool. Mikołajczyk et al. [11] studied a new selective exchange worn cutting edge (SEWCE) scheme, which achieved the effect of reducing tool cost. Wang et al. [12] fabricated Si_3N_4 ceramic cutting tools with high fracture toughness by introducing tungsten particles and changing nitrogen pressure. Lucchini et al. [13] found that although the Al_2O_3/Mo composite increases the toughness of the ceramic cutting tool, there is a performance defect in some material cutting due to the too-low adhesion between the Al_2O_3 matrix and the Mo dispersion. TiCN-based materials have the characteristics of high hardness and high melting point, so they are also widely used in various metal-based ceramic materials [14–17]. It has been reported that adding 10–30 wt.% coarse TiCN to ultrafine TiCN metal-based ceramics can significantly improve the fracture toughness and strength of the material [18]. In the past, there were very few studies on TiCN-toughened silicon nitride ceramic materials. The $TiC_{0.7}N_{0.3}$ used in this experiment is a continuous solid solution formed by TiC and TiN, both of which have high hardness and high melting points. Most academic research focuses on the performance improvement of Si_3N_4 by TiC or TiN [4,10,19–21], while $TiC_{0.7}N_{0.3}$ is mostly used to improve the performance of other ceramic materials.

In this study, Si_3N_4-based ceramic materials with good overall performance were prepared from two commercial ultrafine Si_3N_4 powders by controlling the addition of $TiC_{0.7}N_{0.3}$ and different sintering temperatures. In addition, the chemical composition, microstructure, and micro-interface of the Si_3N_4-based ceramics were characterized, and the mechanical properties of the ceramics were measured. In addition, the bimodal particle size distribution phenomenon and the self-toughening principle of β-Si_3N_4 are discussed.

2. Experimental Procedures

Two sizes of commercial α-Si_3N_4 powders (α > 92.5 wt.%, D_{50} = 0.8 μm and D_{50} = 0.35 μm, oxygen content = 1.20 wt.%, Shanghai Ansame Fine Ceramics Co., Ltd., Shanghai, China) were used. Al_2O_3 (purity ≥ 99.9 wt.%, Shanghai Aladdin Biochemical Technology Co., Ltd., Shanghai, China), Y_2O_3 (purity ≥ 99.5 wt.%, Shanghai Aladdin Biochemical Technology Co., Ltd., Shanghai, China), and $TiC_{0.7}N_{0.3}$ ultrafine powder (purity ≥ 98%, D_{50} = 200 nm, Shijiazhuang Huatai Ceramic Materials Factory, Shijiazhuang, China) were used as raw materials. The 0.8 μm Si_3N_4 powder was marked as Si_3N_4-80, and the 0.35 μm Si_3N_4 powder was marked as Si_3N_4-35. In this experiment, a combined Y_2O_3-Al_2O_3 sintering aid was selected, and the Si-Al-O-N and Y-Si-O-N liquid phases formed during the sintering process allowed for more than adequate sintering of the Si_3N_4 [22,23]. The starting composition was determined to be Si_3N_4-80:Si_3N_4-35:Y_2O_3:Al_2O_3 = 87:5:6:2 by mass ratio, and the powder was weighed and planetarily ground in ethanol at a speed of 300 rpm using Si_3N_4 balls for 10 h. After the planetary milling, the mixed slurry was poured out and placed in an oven for drying at a drying temperature of 60 °C. The ground and dried powder was passed through an 80-mesh sieve and recorded as the initial powder SN. According to different $TiC_{0.7}N_{0.3}$ contents and different hot-pressing temperatures, it is divided into five experimental schemes, SN1, SN2, SN3, SN4, and SN5, for hot-pressing sintering at 30 MPa pressure, as shown in Table 1.

Table 1. Starting powder composition (vol%) and sintering parameter.

Sample	SN	$TiC_{0.7}N_{0.3}$	Temperature (°C)
SN1	100	/	1650
SN2	99	1	1650
SN3	97	3	1650
SN4	99	1	1700
SN5	99	1	1750

The samples obtained by sintering were cut into several standard samples of 40 mm × 5 mm × 6 mm with a diamond cutter, and the standard samples were polished and ground until the surface was mirror-like for various performance tests. Relative densities of Si_3N_4 tool material were evaluated by the Archimedes method. Phase characteriza-

tion was performed by X-ray diffraction (XRD; PW3040/60, Panalytical Ltd, Netherlands, The Netherlands). Backscatter observation and energy spectrum analysis were performed on the polished surface of the specimen using a scanning electron microscope of SSX-550 (Shimadzu, Kyoto, Japan). The Vickers hardness of the material was measured with a 450SVD^{TM} Vickers hardness tester (Walbert Measuring Instruments (Shanghai) Co., Ltd., Shanghai, China), the indentation load was 10 Kg, and the diamond indenter was loaded on the surface of the sample for 15 s. The single-edge notched beam (SENB) method was used to test the fracture toughness of the material. The strength of the material was measured using the three-point flexural strength method. The surface of the ground and polished sample strip was tested on a SANS computer-controlled electronic universal testing machine (Shenzhen Xinsansi Material Testing Co., Ltd., Shenzhen, China).

3. Results and Discussion

Figure 1 shows the morphology of the SN2 mixed powder. In the SN2 composite powder of various raw materials mixed and dispersed by ball milling, the particles are separated from each other, the small particles are dispersed between the large particles, and there is no agglomeration between the large and small particles. This shows that the composite powder after dispersion treatment is evenly mixed and has good dispersibility, which is beneficial for the subsequent experiments.

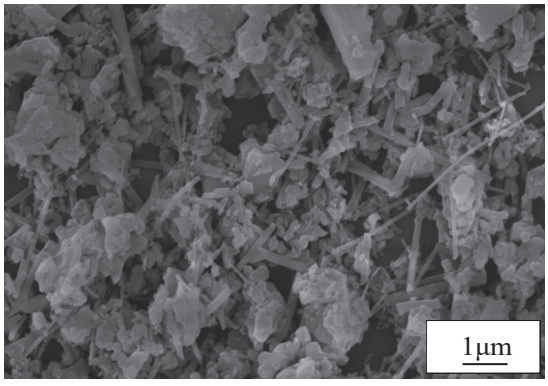

Figure 1. SEM image of SN2 sample powder before hot-pressing sintering.

X-ray diffraction (XRD) phase analysis was performed on the pre-compact body and sintered body before and after hot-pressing sintering, respectively, to determine the phase change before and after sintering, as shown in Figure 2. Based on the analysis of the XRD pattern, it can be seen that the Si_3N_4 before sintering is mainly α-Si_3N_4, and there is only β-Si_3N_4 remaining in the sample after sintering, indicating that during the sintering process, the α-Si_3N_4 in the initial powder is all converted into columnar β-Si_3N_4 [24,25]. In addition, oxygen-containing sintering aids react with surface SiO_2 and Si_3N_4 to form a liquid phase of oxynitride at a high temperature. That is, during the high-temperature sintering process of Si_3N_4, Al_2O_3 enters the Si_3N_4 crystal, and Al^{3+} and O^{2-} ions replace part of the Si^{4+} and N^{3-} ions in the Si_3N_4 lattice, respectively. This forms the Si-Al-O-N (which is β-sialon) phase, Y_2O_3 becomes Y-N apatite, and the Y-Si-O-N phase appears. The resulting liquid phase can provide a solvent for bond breaking, reconstruction, and phase transition; phase transition usually occurs only at the solid-liquid phase contact because the sintering and densification of Si_3N_4 are affected by the solubility and viscosity of the liquid phase [26–28]. During the phase transition, the unstable and easily soluble α-Si_3N_4 dissolves into the liquid phase, while the stable and insoluble β phase is precipitated, and this liquid phase becomes the grain boundary phase when cooled. It can be seen from XRD (Figure 2) that the $TiC_{0.7}N_{0.3}$ phase exists before and after sintering. Therefore, it can be

inferred that $TiC_{0.7}N_{0.3}$ does not undergo phase transformation during the experiment but is uniformly dispersed in the Si_3N_4 matrix.

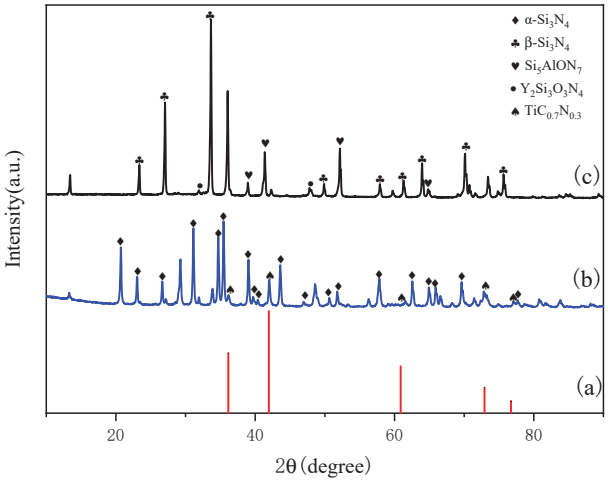

Figure 2. X-ray diffraction (XRD) patterns of SN2 samples before and after sintering at 1650 °C for 1 h: (**a**) Standard data for $TiC_{0.7}N_{0.3}$ (PDF#42-1489); (**b**) Sample before sintering; (**c**) Sample after sintering.

Table 2 presents the mechanical properties of materials with different $TiC_{0.7}N_{0.3}$ additions. Figure 3 shows the relationship between the relative density, hardness, flexural strength, fracture toughness of the material, and the amount of $TiC_{0.7}N_{0.3}$ added. It can be seen from Figure 3a that with the increase of the addition amount of the second phase $TiC_{0.7}N_{0.3}$, the relative density of the material has a downward trend. However, the relative density is more than 98%, which can be regarded as densification at the same time, and the overall hardness has an increasing trend. This is because $TiC_{0.7}N_{0.3}$ has the characteristics of high hardness [29,30]. In the meantime, the addition of $TiC_{0.7}N_{0.3}$ is equivalent to adding a hard second phase, so it can be expected that when the addition amount continues to increase, the hardness of the material will further increase.

Furthermore, adding 1 vol% of $TiC_{0.7}N_{0.3}$ can significantly improve the flexural strength of the material, but when the addition is 3 vol%, it decreases significantly. It can be seen from Figure 3b that the fracture toughness increases gradually with the increase in the addition amount. The toughening effect of $TiC_{0.7}N_{0.3}$ on the matrix material is mainly due to the difference in thermal expansion coefficient and elastic modulus between the Si_3N_4 matrix and the dispersed phase particles of $TiC_{0.7}N_{0.3}$. In the process of material preparation, when sintering and cooling, local residual stress will inevitably be generated. When the residual stress is greater than a certain value, microcracks will be generated. During the propagation of the main crack, the energy required for the propagation of the main crack is consumed by microcracks, thereby improving the fracture toughness of the material. Among the four performance indicators of the material, under the premise that the relative density, Vickers hardness, and fracture toughness do not change much, the flexural strength of the material added with 1 vol% $TiC_{0.7}N_{0.3}$ is the best. Therefore, among the three samples with different compositions, the best comprehensive performance is the sample with the $TiC_{0.7}N_{0.3}$ addition of 1 vol%.

Table 2. Effect of $TiC_{0.7}N_{0.3}$ content on the mechanical properties of materials.

Sample	Relative Density (%)	Bending Strength (MPa)	Fracture Toughness ($MPa \cdot m^{1/2}$)	Vickers Hardness (GPa)
SN1	99.42	809	9.10	15.9
SN2	98.78	916	9.47	15.8
SN3	98.90	856	9.89	16.1

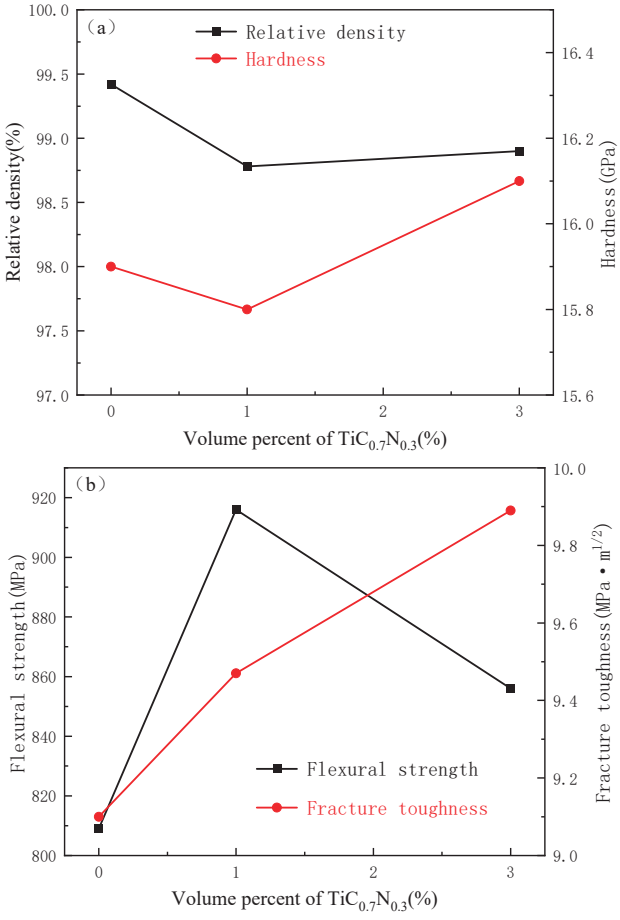

Figure 3. The effect of different volume fractions of $TiC_{0.7}N_{0.3}$ in SN1, SN2, and SN3 on the properties: (**a**) Relative density and Vickers hardness; (**b**) Flexural strength and fracture toughness.

Figure 4 is the backscattered photos of the polished surface of the sample without and with 1 vol% and 3 vol% $TiC_{0.7}N_{0.3}$ added. It can be seen in Figure 4a–c that the black parts are distributed in stripes of different sizes, and the white areas are evenly distributed. With the increase of $TiC_{0.7}N_{0.3}$ addition, the size of the black strips gradually decreased. The uniform distribution of the black and white areas indicates that the powders are well-mixed and have no serious agglomeration. Figure 5a,b is the energy spectrum (EDS) analysis of points A and B in Figure 4c, respectively. Combined with the XRD phase analysis of the sintered body (Figure 2c), it can be seen that point A, that is, the white area in the figure, is mainly the Y-Si-O-N phase, and there is also a small amount of the Si-Al-O-N phase. Point B, which is the black area in the figure, is mainly the β-Si_3N_4 phase and also has a small amount of Al, indicating that it also contains a small amount of the Si-Al-O-N phase. Since the addition of $TiC_{0.7}N_{0.3}$ is very small, the Ti is not obvious in the energy spectrum. As a result, it is difficult to determine whether it is distributed at the grain boundaries of β-Si_3N_4 or involved in the nucleation of β-Si_3N_4 and located at its crystal lattice.

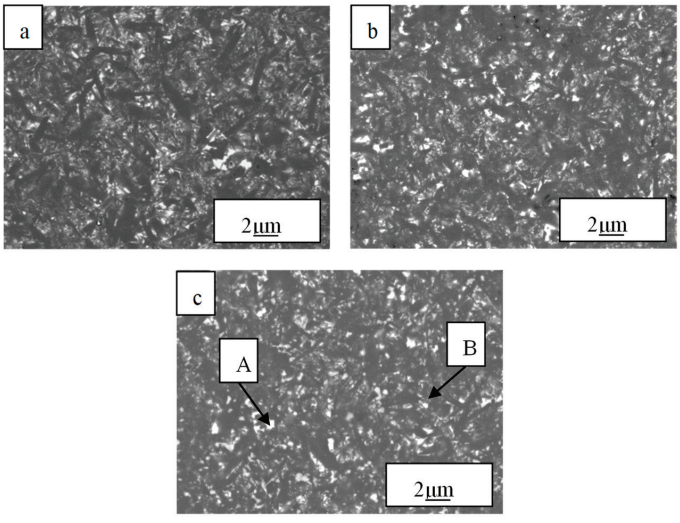

Figure 4. Backscattering photos of the polished surface of samples with different $TiC_{0.7}N_{0.3}$ contents: (**a**) without $TiC_{0.7}N_{0.3}$; (**b**) 1 vol% $TiC_{0.7}N_{0.3}$; (**c**) 3 vol% $TiC_{0.7}N_{0.3}$.

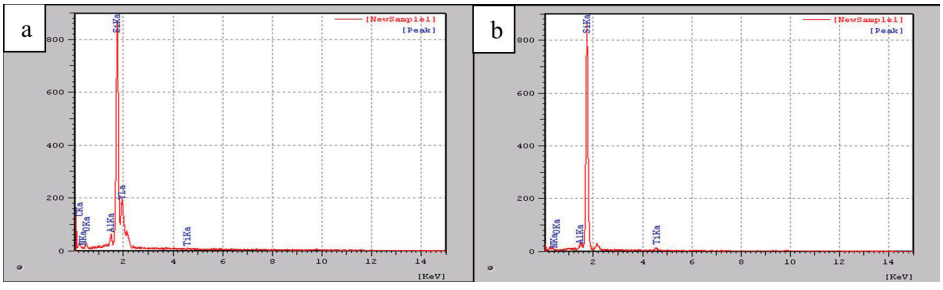

Figure 5. Energy spectrum analysis (**a**) Point A in Figure 4c; (**b**) Point B in Figure 4c.

It can be seen from Figure 6 that with the change in the addition amount of $TiC_{0.7}N_{0.3}$, the microstructure of the material has undergone a relatively obvious change. The Si_3N_4 matrix in the sintered body is all long columnar β-Si_3N_4 grains with different diameters and aspect ratios interlaced with each other, and the fractures are rough. From the fracture morphology of the material (Figure 6a–c), it can be clearly seen that the holes and part of the grain section are left by the grain pulling out. This indicates that the fracture mode is a combination of intergranular fracture and transgranular fracture. The long columnar β-Si_3N_4 has the effect of strengthening and toughening similar to fibers and whiskers. This is the self-toughening of Si_3N_4, and it is also an important reason why the flexural strength and fracture toughness of Si_3N_4-based ceramic tool materials are higher than other tool materials. At the same time, a small amount of β-Si_3N_4 in the raw material exists in the form of seed crystals, and self-toughening Si_3N_4 ceramics can also be synthesized [31,32]. In addition, a small number of irregularly shaped and deep holes can be seen from the fracture of the material. These are the pores inside the material, indicating that the density of the material is not enough, especially the pores in Figure 6b are more obvious, and the number of pores is slightly more than the other two. This also corresponds to the lowest relative density of the sample added with 1 vol% $TiC_{0.7}N_{0.3}$ measured earlier. It can also be seen from Figure 6 that with the increase of $TiC_{0.7}N_{0.3}$ addition amount, the average grain size gradually decreases.

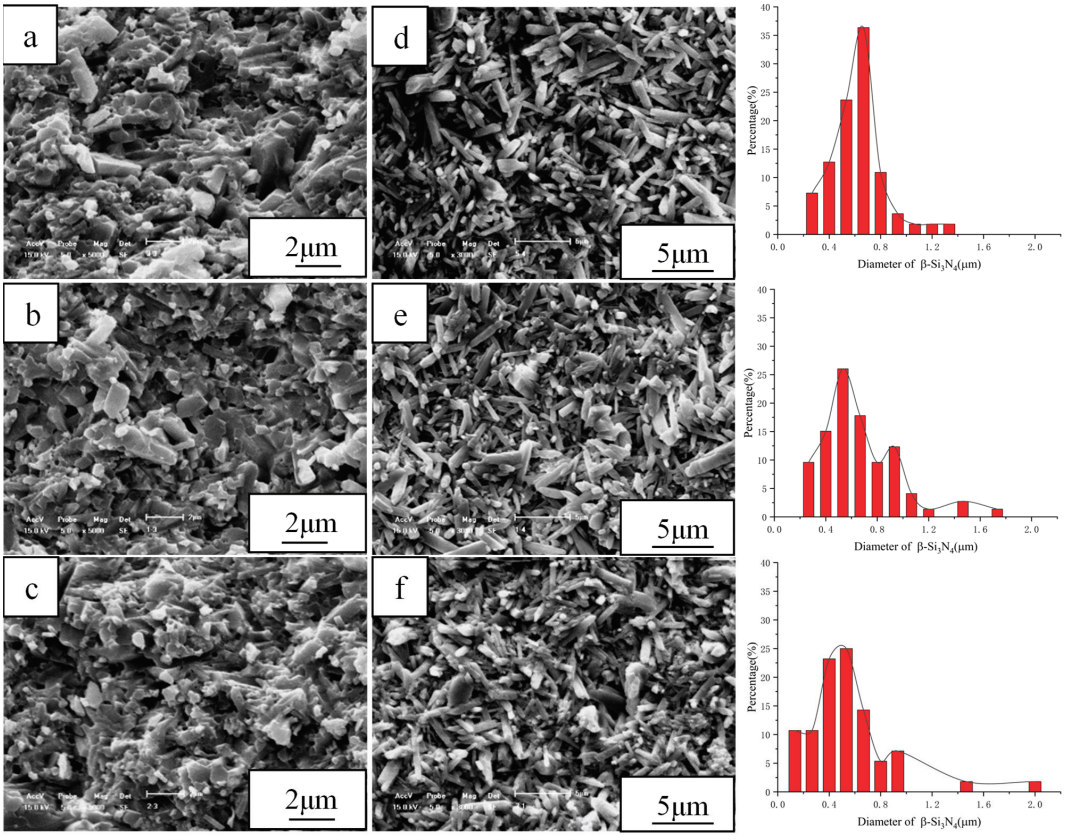

Figure 6. (**a**–**c**) are the fracture scan photos of no addition, the addition of 1 vol%, and the addition of 3 vol% $TiC_{0.7}N_{0.3}$, respectively; (**d**–**f**) are the scanning photos of the corroded surface without adding, adding 1 vol%, and adding 3 vol% $TiC_{0.7}N_{0.3}$, respectively. On the right are the diameter distributions of the three corresponding β-Si_3N_4 grains.

It can be seen from Figure 6d–f of the corroded surface topography that the grains without $TiC_{0.7}N_{0.3}$ are more uniform and have little difference in size. After adding a small amount of $TiC_{0.7}N_{0.3}$, due to the pinning effect of the second phase particles, the growth of part of the grains is prevented so that the diameter and aspect ratio range of the overall grains increases. Small grains are embedded between large grains, and the structure is more tightly packed. This is also the reason why the flexural strength increases after adding 1 vol% $TiC_{0.7}N_{0.3}$. When the addition amount is 3 vol%, the number of small grains is too large, which weakens the self-toughening effect of Si_3N_4. Therefore, the flexural strength starts to decrease again while the fracture toughness continues to increase, which is still due to the difference in thermal expansion coefficient and elastic modulus between the Si_3N_4 matrix and the dispersed phase particles of $TiC_{0.7}N_{0.3}$.

It can be clearly seen from the particle size distribution diagram on the right that the diameter of β-Si_3N_4 grains in the sample without $TiC_{0.7}N_{0.3}$ is concentrated between 0.4 and 0.8 μm. After adding 1 vol% $TiC_{0.7}N_{0.3}$, the diameters of β-Si_3N_4 grains are concentrated between 0.3 and 1 μm. After adding 3 vol% $TiC_{0.7}N_{0.3}$, the diameters of β-Si_3N_4 grains are concentrated between 0.1 and 0.65 μm. It shows that the addition of $TiC_{0.7}N_{0.3}$ reduces the diameter of some β-Si_3N_4 grains in the sample and increases the diameter distribution range. It can also be seen that the diameter of β-Si_3N_4 grains has a bimodal distribution, especially the bimodal distribution of the 1 vol% $TiC_{0.7}N_{0.3}$ sample

is more obvious. At the same time, when the grain size of β-Si_3N_4 in the Si_3N_4 matrix presents a bimodal distribution, its mechanical properties are greatly improved [33–35]. This is also an important reason for the improvement of the mechanical properties of the material after adding a small amount of $TiC_{0.7}N_{0.3}$.

The above discussion can be concluded that the addition of $TiC_{0.7}N_{0.3}$ has a certain effect on the relative density and hardness of ceramic tool materials. However, $TiC_{0.7}N_{0.3}$ exists as a hard second phase in the Si_3N_4 grain boundary, and the second phase particles act as pegging. When the addition amount is 1 vol%, the β-Si_3N_4 grains have an overall bimodal structure. Different diameters of β-Si_3N_4 are interlaced with each other, which makes the flexural strength of ceramic tools much higher.

In the process of hot-pressing sintering, the influence of hot-pressing temperature on the properties of materials is also very obvious. The addition of sintering aids can reduce the sintering temperature, and the optimal sintering temperature of different sintering aid combinations is also different. It can be seen from Figure 2c that the mixed powder with 1 vol% $TiC_{0.7}N_{0.3}$ that was hot-pressed and sintered at a sintering temperature of 1650 °C for one hour, the α → β phase transition was complete. Therefore, when the sintering temperature increased to 1700 and 1750 °C, the phase composition of SN2, SN4, and SN5 samples did not change after sintering. It was still the four phases of β-Si_3N_4, Si-Al-O-N (which is β-sialon), Y-Si-O-N, and $TiC_{0.7}N_{0.3}$. In XRD images (Figure 7), the difference between the three images is only the difference in peak strength.

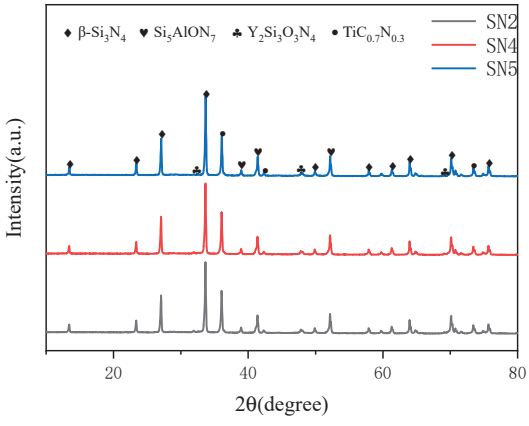

Figure 7. XRD patterns of samples at different hot-pressing temperatures: The sintering temperatures of SN2, SN4, and SN5 samples were 1650, 1700, and 1750 °C, respectively.

Table 3 presents the mechanical properties of the materials prepared at different hot-pressing sintering temperatures. Figure 8 shows the relationship between the relative density, hardness, flexural strength, fracture toughness of the material, and hot-pressing sintering temperature. It can be seen from Figure 8 that with the increase of hot-pressing temperature, the relative density of the material increases gradually, indicating that increasing the hot-pressing sintering temperature can promote the densification of the material. The Vickers hardness of the material had almost no change, indicating that the hardness of the material is mainly affected by its composition and phase, and is little affected by the hot-pressing temperature. In addition, the flexural strength and fracture toughness of the material increased significantly with the increase in hot-pressing temperature, which may be related to the increase in the material density or the change in grain size, which can be verified by the microstructure and morphology. Some researchers claim that the α-Si_3N_4 powder can be completely densified under the temperature of about 1850 °C and the pressure hot-pressing of 23 MPa [36]. However, our temperature has not reached 1850 °C at present, so by increasing the hot-pressing sintering temperature, the comprehensive performance of the Si_3N_4-based ceramic tool material can be further improved.

Table 3. Effect of hot-pressing temperature on the mechanical properties of materials.

Sample	Relative Density (%)	Bending Strength (MPa)	Fracture Toughness (MPa·m$^{1/2}$)	Vickers Hardness (GPa)
SN2	98.78	916	9.47	15.8
SN4	99.04	961	9.95	15.9
SN5	99.22	993	9.81	15.9

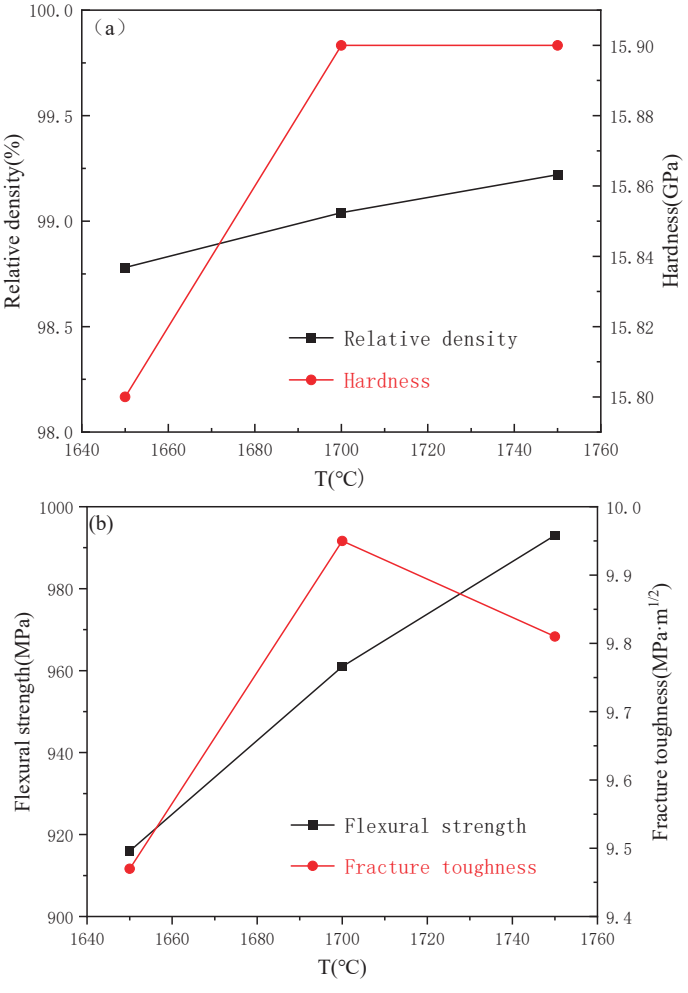

Figure 8. Comparison of performance parameters of SN2, SN4, and SN5 samples at different sintering temperatures: (**a**) Relative density and Vickers hardness; (**b**) Flexural strength and fracture toughness.

Figure 9 shows the scanned photographs of the fracture cross-sections at three hot pressing temperatures. When sintered at 1650 °C, the β-Si_3N_4 seeds in the raw material grow through the Ostwald maturation mechanism. Due to the relatively low sintering temperature, the overall grain radius is relatively small, and there are many pores at the grain boundary. The $TiC_{0.7}N_{0.3}$ in the raw material is uniformly dispersed in the Si_3N_4 matrix. Because its thermal expansion coefficient and elastic modulus are different from those of Si_3N_4, β-Si_3N_4 grains with different diameters and different aspect ratios are interlaced and tightly combined with each other during the sintering process to achieve the effect of reinforcement and toughening.

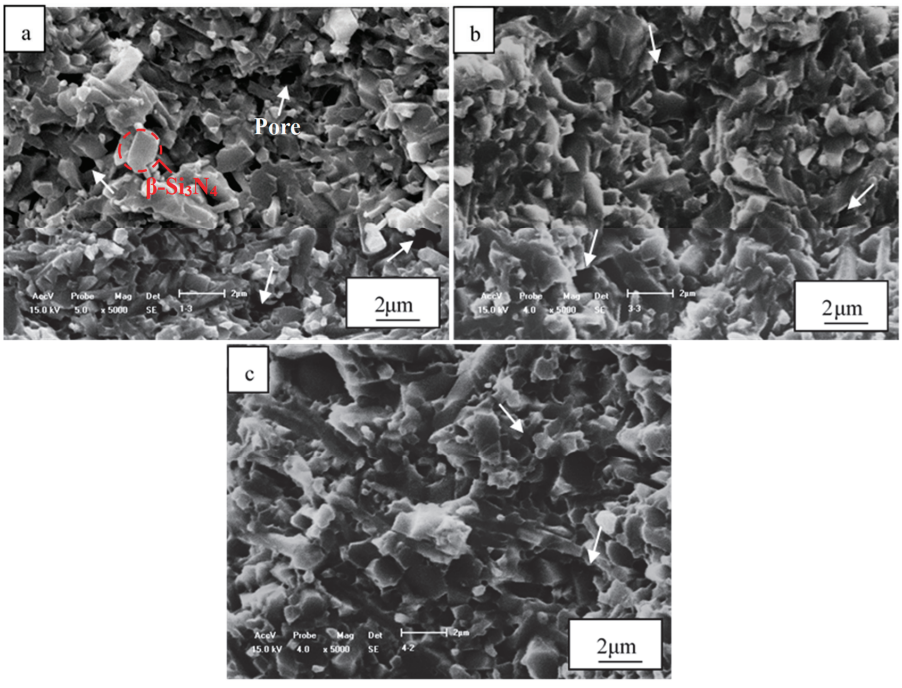

Figure 9. The fracture surfaces SEM of SN2, SN4, and SN5 samples sintered at different temperatures: (**a**) 1650 °C; (**b**) 1700 °C; (**c**) 1750 °C.

In the sintering process, there are two main factors affecting the crystal growth, one is the diffusion rate of solute atoms, and the other is the deposition rate of solute atoms at the particle-matrix interface [37]. In this experiment, with the increase of temperature under the same conditions, the diffusion rate of solute atoms increases greatly, making the grain size of β-Si_3N_4 larger. At the same time, the density of the material increases, and the porosity defect decreases so that the mechanical properties such as flexural strength, fracture toughness, and hardness are improved.

At the same time, we can also draw from Figure 9, with the change of hot-pressing sintering temperature, the intrinsic reasons for the change of mechanical properties of materials. With the increase of hot-pressing sintering temperature, the phenomenon of grain pull-out during fracture becomes more and more obvious, and the fracture is rougher; that is, the holes left after grain pulling out are larger and deeper. This indicates that the diameter and length of the grains increased. Due to the existence of rod-like β-Si_3N_4, crack deflection and bridging occur during crack propagation, which increases the crack deflection angle, consumes more energy, and inhibits crack propagation [26,35]. Furthermore, the larger the rod size, the better the effect. The β-Si_3N_4 particles at 1750 °C are larger than other samples, so the performance is better. It may be that the increase in temperature makes a large amount of liquid phase to be formed at the grain boundary during the sintering process, which increases the crystal phase transformation rate and makes the particle diameter of β-Si_3N_4 larger. Compared with those shown in Figure 9a,b, the fracture surface (Figure 9c) seems to be denser, and the number of irregularly-shaped deeper pores at the fracture is significantly reduced. This basically conforms to the relative density variation trend of samples at different temperatures shown in Table 3. Therefore, increasing the sintering temperature is helpful to improve the flexural strength and fracture toughness of the samples.

Figure 10 is the distribution curve of the aspect ratio of β-Si_3N_4 grains in samples with hot-pressing sintering temperatures of 1650, 1700, and 1750 °C. It can be seen that with the increase in hot-pressing temperature, the aspect ratio of β-Si_3N_4 grains increases significantly. This makes the inter-grain interleaving of Si_3N_4 more complex so that the overall mechanical properties are relatively high. This is the same as the previous experimental results. At the same time, the mechanical properties still show an increasing trend as the temperature continues to increase. The increase in grain diameter and aspect ratio enhances the self-toughening effect of the material and improves the overall performance [38].

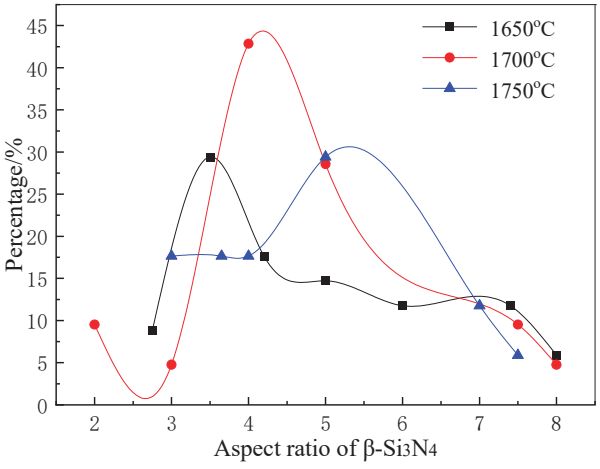

Figure 10. The distribution curves of the aspect ratio of β-Si_3N_4 grains in SN2, SN4, and SN5 at different hot-pressing temperatures.

4. Conclusions

In this study, the mechanical properties of Si_3N_4 ceramic tool materials were improved by adding a new $TiC_{0.7}N_{0.3}$ sintering aid to the traditional sintering additive combination of Al_2O_3 and Y_2O_3. Using different sintering temperatures, Si_3N_4 ceramic tool materials with excellent bending strength and fracture toughness were prepared. The relationship between the microstructure and mechanical properties of the prepared Si_3N_4 ceramics was systematically characterized and discussed. Based on the experimental results and discussion, the following conclusions are drawn:

(1) The added $TiC_{0.7}N_{0.3}$ and the matrix Si_3N_4 have different thermal expansion coefficients and elastic moduli; they prevent the growth of part of the grains so that the β-Si_3N_4 grains with different diameters and different aspect ratios are staggered and tightly combined with each other. At the same time, because $TiC_{0.7}N_{0.3}$ has the characteristics of high hardness and high strength, it is uniformly dispersed in the matrix of Si_3N_4 as a hard second phase, and the effect of strengthening and toughening is achieved. In addition, the effect of adding 1 vol% $TiC_{0.7}N_{0.3}$ is relatively the best; the flexural strength and fracture toughness are 916 MPa and 9.47 MPa·$m^{1/2}$, respectively.

(2) Use of the Ostwald maturation mechanism to explain the grain growth process at different temperatures. By increasing the temperature of hot-pressing sintering, the degree of grain growth is greater, the degree of the interlacing of β-Si_3N_4 grains with different diameters and different aspect ratios is also gradually increased, and the mechanical properties of the material are also improved. The relative density, flexural strength, and fracture toughness reached 99.22%, 993 MPa, and 9.81 MPa·$m^{1/2}$, respectively, when the hot-pressing sintering temperature was 1750 °C. However, there is still a great potential for improvement in numerical value.

Author Contributions: Conceptualization, S.G. and M.Z.; methodology, S.G. and F.Z.; validation, S.G., F.Z. and M.Z.; formal analysis, S.G., F.Z. and Z.X.; investigation, S.G.; resources, F.Z.; data curation, F.Z.; writing—original draft preparation, S.G.; writing—review and editing, X.S.; visualization, Z.X.; supervision, X.S. and M.Z.; project administration, X.S.; funding acquisition, M.Z. and X S. All authors have read and agreed to the published version of the manuscript.

Funding: This research was funded by the National Natural Science Foundation of China (52072063, 51872033, 51732007) and a research start-up fund from the Foshan Graduate School of Innovation of Northeastern University.

Institutional Review Board Statement: Not applicable.

Informed Consent Statement: Not applicable.

Data Availability Statement: Not applicable.

Conflicts of Interest: The authors declare no conflict of interest.

References

1. Tan, D.-W.; Zhu, L.-L.; Wei, W.-X.; Yu, J.-J.; Zhou, Y.-Z.; Guo, W.-M.; Lin, H.-T. Performance improvement of Si_3N_4 ceramic cutting tools by tailoring of phase composition and microstructure. *Ceram. Int.* **2020**, *46*, 26182–26189. [CrossRef]
2. Souza, J.V.C.; Nono, M.C.A.; Ribeiro, M.V.; Machado, J.P.B.; Silva, O.M.M. Cutting forces in turning of gray cast iron using silicon nitride based cutting tool. *Mater. Des.* **2009**, *30*, 2715–2720. [CrossRef]
3. Lü, Z.; Deng, L.; Tian, Q.; Zhao, X. Cutting performance of Si_3N_4/TiC micro-nanocomposite ceramic tool in dry machining of hardened steel. *Int. J. Adv. Manuf. Technol.* **2017**, *95*, 3301–3307. [CrossRef]
4. Kwon, W.T.; Kim, Y.W. Cutting performance of Si_3N_4 based SiC ceramic cutting tools. *KSME Int. J.* **2004**, *18*, 388–394. [CrossRef]
5. Zhao, J.; Yuan, X.; Zhou, Y. Cutting performance and failure mechanisms of an Al_2O_3/WC/TiC micro- nano-composite ceramic tool. *Int. J. Refract. Met. Hard Mater.* **2010**, *28*, 330–337. [CrossRef]
6. van Luttervelt, C.A.; Childs, T.H.C.; Jawahir, I.S.; Klocke, F.; Venuvinod, P.K.; Altintas, Y.; Armarego, E.; Dornfeld, D.; Grabec, I.; Leopold, J.; et al. Present Situation and Future Trends in Modelling of Machining Operations Progress Report of the CIRP Working Group 'Modelling of Machining Operations'. *CIRP Ann.* **1998**, *47*, 587–626. [CrossRef]
7. Tu, L.; Tian, S.; Xu, F.; Wang, X.; Xu, C.; He, B.; Zuo, D.; Zhang, W. Cutting performance of cubic boron nitride-coated tools in dry turning of hardened ductile iron. *J. Manuf. Process.* **2020**, *56*, 158–168. [CrossRef]
8. Liu, W.; Chu, Q.; He, R.; Huang, M.; Wu, H.; Jiang, Q.; Chen, J.; Deng, X.; Wu, S. Preparation and properties of TiAlN coatings on silicon nitride ceramic cutting tools. *Ceram. Int.* **2018**, *44*, 2209–2215. [CrossRef]
9. Şap, S.; Usca, Ü.; Uzun, M.; Kuntoğlu, M.; Salur, E. Performance evaluation of AlTiN coated carbide tools during machining of ceramic reinforced Cu-based hybrid composites under cryogenic. *Pure-Minim. Quant. Lubr. Dry Regimes* **2022**, *56*, 3401–3421.
10. Xing, Y.; Deng, J.; Zhang, K.; Wang, X.; Lian, Y.; Zhou, Y. Fabrication and dry cutting performance of Si_3N_4/TiC ceramic tools reinforced with the PVD WS2/Zr soft-coatings. *Ceram. Int.* **2015**, *41*, 10261–10271. [CrossRef]
11. Mikolajczyk, T.; Paczkowski, T.; Kuntoglu, M.; Patange, A.; Binali, R. Research on Using an Unconventional Tool for Increasing Tool Life by Selective Exchange of Worn Cutting Edge. *Appl. Sci.* **2023**, *13*, 460. [CrossRef]
12. Wang, L.; Qi, Q.; Zhang, H.; Yang, X.; Liu, Z.; Ge, S.; Peng, X.; Liu, X.; Huang, Z. High tough W-added silicon nitride ceramics. *Ceram. Int.* **2019**, *45*, 19055–19059. [CrossRef]
13. Lucchini, E.; Lo Casto, S.; Sbaizero, O. The performance of molybdenum toughened alumina cutting tools in turning a particulate metal matrix composite. *Mater. Sci. Eng. A* **2003**, *357*, 369–375. [CrossRef]
14. Hu, Z.; Zhao, Z.; Deng, X.; Lu, Z.; Liu, J.; Qu, Z. Microstructure and mechanical behavior of TiCN reinforced $AlSi_{10}Mg$ composite fabricated by selective laser melting. *Mater. Chem. Phys.* **2022**, *283*, 125996. [CrossRef]
15. Yang, Y.; Dang, W.; Liu, J.; Zhang, H.; Gu, S.; Lei, C.; Chen, Y. Effect of the Addition of Ultrafine Powders on the Microstructure and Mechanical Properties of TiCN-Based Cermets. *J. Ceram. Sci. Technol.* **2022**, *13*, 15–22.
16. Meng, J.; Lu, J.; Wang, J.; Yang, S. Tribological behavior of TiCN-based cermets at elevated temperatures. *Mater. Sci. Eng. A* **2006**, *418*, 68–76. [CrossRef]
17. Wang, B.; Liu, Z. Cutting performance of solid ceramic end milling tools in machining hardened AISI H13 steel. *Int. J. Refract. Met. Hard Mater.* **2016**, *55*, 24–32. [CrossRef]
18. Xiong, H.; Wen, Y.; Gan, X.; Li, Z.; Chai, L. Influence of coarse TiCN content on the morphology and mechanical properties of ultrafine TiCN-based cermets. *Mater. Sci. Eng. A* **2017**, *682*, 648–655. [CrossRef]
19. Lee, B.T.; Yoon, Y.J.; Lee, K.H. Microstructural characterization of electroconductive Si_3N_4-TiN composites. *Mater. Lett.* **2001**, *47*, 71–76. [CrossRef]
20. Kgoete, F.M.; Popoola, A.P.I.; Fayomi, O.S.I.; Adebiyi, I.D. Spark plasma sintered Ti-6Al-4V-Si_3N_4-TiN ternary composites: Effect of combined microsized Si_3N_4 and TiN addition on microstructure and mechanical properties for aerospace application. *J. Alloys Compd.* **2018**, *769*, 817–823. [CrossRef]

21. Huang, J.L.; Chang, Y.L.; Lu, H.H. Fabrication of multilaminated Si_3N_4-Si_3N_4/TiN composites and its anisotropic fracture behavior. *J. Mater. Res.* **1997**, *12*, 2337–2344. [CrossRef]
22. Miyazaki, H.; Hyuga, H.; Yoshizawa, Y.-I.; Hirao, K.; Ohji, T. Correlation of wear behavior and indentation fracture resistance in silicon nitride ceramics hot-pressed with alumina and yttria. *J. Eur. Ceram. Soc.* **2009**, *29*, 1535–1542. [CrossRef]
23. Tsuge, A.; Nishida, K.; Komatsu, M. Effect of Crystallizing the Grain-Boundary Glass Phase on the High-Temperature Strength of Hot-Pressed Si_3N_4 Containing Y_2O_3. *J. Am. Ceram. Soc.* **1975**, *58*, 323–326. [CrossRef]
24. Zhu, X.; Sakka, Y. Textured silicon nitride: Processing and anisotropic properties. *Sci. Technol. Adv. Mater.* **2008**, *9*, 033001. [CrossRef]
25. Hampshire, S. Silicon nitride ceramics—Review of structure, processing and properties. *J. Achiev. Mater. Manuf. Eng.* **2007**, *24*, 43–50.
26. Liao, S.; Zhou, L.; Jiang, C.; Wang, J.; Zhuang, Y.; Li, S. Thermal conductivity and mechanical properties of Si_3N_4 ceramics with binary fluoride sintering additives. *J. Eur. Ceram. Soc.* **2021**, *41*, 6971–6982. [CrossRef]
27. Cinibulk, M.K.; Thomas, G.; Johnson, S.M. Fabrication and Secondary-Phase Crystallization of Rare-Earth Disilicate-Silicon Nitride Ceramics. *J. Am. Ceram. Soc.* **1992**, *75*, 2037–2043. [CrossRef]
28. Shen, Z.; Zhao, Z.; Peng, H.; Nygren, M. Formation of tough interlocking microstructures in silicon nitride ceramics by dynamic ripening. *Nature* **2002**, *417*, 266–269. [CrossRef]
29. Xiong, J.; Guo, Z.; Wen, B.; Li, C.; Shen, B. Microstructure and properties of ultra-fine $TiC_{0.7}N_{0.3}$ cermet. *Mater. Sci. Eng. A* **2006**, *416*, 51–58. [CrossRef]
30. Gao, J.; Song, J.; Lv, M.; Cao, L.; Xie, J. Microstructure and mechanical properties of $TiC_{0\cdot7}N_{0.3}$-HfC cermet tool materials. *Ceram. Int.* **2018**, *44*, 17895–17904. [CrossRef]
31. Wang, B.; Yang, J.; Guo, R.; Gao, J.-Q.; Yang, J.-F. Microstructure characterization of hot-pressed β-silicon nitride containing β-Si_3N_4 seeds. *Mater. Charact.* **2009**, *60*, 894–899. [CrossRef]
32. Dai, J.; Li, J.; Chen, Y.; Yang, L. Effect of the residual phases in β-Si_3N_4 seed on the mechanical properties of self-reinforced Si_3N_4 ceramics. *J. Eur. Ceram. Soc.* **2003**, *23*, 1543–1547. [CrossRef]
33. Perera, D.S.; Mitchell, D.R.G.; Leung, S. High aspect ratio β-Si_3N_4 grain growth. *J. Eur. Ceram. Soc.* **2000**, *20*, 789–794. [CrossRef]
34. Hirosaki, N.; Okamoto, Y.; Munakata, F.; Akimune, Y. Effect of seeding on the thermal conductivity of self-reinforced silicon nitride. *J. Eur. Ceram. Soc.* **1999**, *19*, 2183–2187. [CrossRef]
35. Hu, J.; Zhang, B.; Li, C.; Wang, L.; Wang, S.; Shi, Z.; Yang, J. Fabrication of Si_3N_4 ceramics with high thermal conductivity and flexural strength via novel two-step gas-pressure sintering. *J. Eur. Ceram. Soc.* **2022**, *42*, 4846–4854. [CrossRef]
36. Deeley, G.G.; Herbert, J.M.; Moore, N.C. Dense Silicon Nitride. *Powder Metall.* **1961**, *4*, 145–151. [CrossRef]
37. German, R.M. Coarsening in Sintering: Grain Shape Distribution, Grain Size Distribution, and Grain Growth Kinetics in Solid-Pore Systems. *Crit. Rev. Solid State Mater. Sci.* **2010**, *35*, 263–305. [CrossRef]
38. Hirao, K.; Watari, K.; Hayashi, H.; Kitayama, M. High Thermal Conductivity Silicon Nitride Ceramic. *MRS Bull.* **2001**, *26*, 451–455. [CrossRef]

coatings

MDPI

Article

Characteristics and Cutting Performance of CVD Al_2O_3 Multilayer Coatings Deposited on Tungsten Carbide Cutting Inserts in Turning of 24CrMoV5-1 Steel

Maoxiang Zhu [1,2,3,*], Soufyane Achache [1,2], Mariane Prado Motta [4], Alexandre Delblouwe [1], Cyril Pelaingre [4], Alexis Carlos García-Wong [3], Jean-François Pierson [3] and Frédéric Sanchette [1,2]

1 LASMIS, Université de Technologie de Troyes, Antenne de Nogent, Póle Technologique de Sud Champagne, 52800 Nogent, France
2 Nogent International Centre for Coating Innovation, LRC CEA-LASMIS, UTT, Antenne de Nogent, Póle Technologique de Sud Champagne, 52800 Nogent, France
3 Institut Jean Lamour, UMR CNRS 7198, Université de Lorraine, 54000 Nancy, France
4 CIRTES SA, 88100 Saint-Dié-des-Vosges, France
* Correspondence: maoxiang.zhu@univ-lorraine.fr

Abstract: In this work, TiN/Ti(C,N)/Al_2O_3 multilayer coatings were deposited using an industrial-scale thermal CVD system. Two polymorphs of Al_2O_3, the stable α- and the metastable κ-Al_2O_3, were obtained by the deposition of specific bonding layers at the Al_2O_3/Ti(C,N) interface. The comparable hardness and elastic moduli of α- and κ-Al_2O_3 multilayer coatings were measured. The tribological behavior of Al_2O_3 multilayer coatings was studied at room temperature using 24CrMoV5-1 balls; friction coefficients were comparable for both α- and κ-Al_2O_3 multilayer coatings. As a result of the relatively high hardness of coatings and the generation of abrasive wear particles, larger wear tracks were observed on balls. In Rockwell C tests, good adhesion at Al_2O_3/Ti(C,N)-based layer's interface was reported in κ-Al_2O_3 multilayer coatings, which could be attributed to the deposition of κ-bonding layers consisting of needle-shaped grains. The cutting performances in the turning-roughing of 24CrMoV5-1 steel under different parameters—cutting speed, feed, and depth of cut—were investigated. Herein, κ-Al_2O_3 multilayer coatings showed the longest tool life, double of that of a commercial CVD Al_2O_3 multilayer coating. The results obtained could enrich the existing database for the development of prediction models of tool wear and machined surface quality and help improve tool performance for the machining of 24CrMoV5-1 steel.

Keywords: chemical vapor deposition; Al_2O_3; wear-resistant coatings; tungsten carbide cutting inserts; cutting performance

Citation: Zhu, M.; Achache, S.; Motta, M.P.; Delblouwe, A.; Pelaingre, C.; García-Wong, A.C.; Pierson, J.-F.; Sanchette, F. Characteristics and Cutting Performance of CVD Al_2O_3 Multilayer Coatings Deposited on Tungsten Carbide Cutting Inserts in Turning of 24CrMoV5-1 Steel. *Coatings* **2023**, *13*, 883. https://doi.org/10.3390/coatings13050883

Academic Editor: Petr M. Pivkin

Received: 16 April 2023
Revised: 3 May 2023
Accepted: 5 May 2023
Published: 8 May 2023

1. Introduction

Metal cutting is a manufacturing process achieved through different operations, mainly categorized as turning, milling, and drilling [1]. During metal cutting, high forces act at contact zones between the tool and workpiece. The chip formation involves the plastic deformation at shear zones, generating contact stress and heat in cutting tools, which are subjected to abrasive and adhesive wear. When using workpiece materials with relatively high thermal conductivities, the generated heat is transported away with chip flow over the tool rake face [2–5]. In the case of continuous cylindrical turning, the workpiece rotates around its center axis, while a sharp-edged tool is set to a certain depth of cut for performing a facing operation towards the workpiece rotational center [6]. In contact zones, high temperatures are reached, where thick coatings (≈5–20 μm) with low thermal conductivities are accepted as favorable since they provide a thermal barrier to the substrate, and the generated heat is deflected into the chip, preventing the plastic deformation of the underlying substrate [1,7].

CVD α- and κ-Al_2O_3 coatings were found to be efficient to protect cutting tools from crater wear on the rake face, due to their low adhesion tendency in contact with metals and excellent chemical stability at high temperatures [8]. α- and κ-Al_2O_3 differ in their crystal structure, grain size and thermal conductivity; the low thermal conductivity of κ-Al_2O_3, approx. three times lower than α-Al_2O_3, suggests that this metastable phase of alumina could be an excellent thermal barrier for cutting tools [9]. However, κ-Al_2O_3 can transform irreversibly to α-Al_2O_3 at high temperatures, resulting in a volume contraction of approx. 8% due to the heat generated during thermal CVD process and metal cutting [10]. It was also reported that the mechanical properties of CVD α-Al_2O_3 coatings could be enhanced by choosing an optimized texture for the α-Al_2O_3 phase [11]. Consequently, CVD Al_2O_3 coatings have continuously been optimized with respect to the phase and film texture control.

In previous studies, CVD TiN/Ti(C,N)/Al_2O_3 multilayer coatings were extensively studied [12,13]. It was shown that the growth of α- and κ-Al_2O_3 on Ti(C,N) could be controlled with the deposition of bonding layers at the Al_2O_3/Ti(C,N)-based layer's interface [12]. The epitaxial growth of α-Al_2O_3 on rutile as well as that of κ-Al_2O_3 on needle-like Ti(C,N) were reported [12,13]. It is essential to achieve the phase control to compare the performance of CVD α- and κ-Al_2O_3 multilayer coatings in the present work.

In this work, 24CrMoV5-1 was selected as the workpiece material, which is widely used to produce molds for light metals and plastics. Based on a previous study, tungsten carbide tools with coatings of hard refractory materials such as Ti(C,N) and Al_2O_3 were used for turning operations of 24CrMoV5-1 steel herein [14]. The aim of the present work is to study mechanical and tribologicial properties of CVD α- and κ-Al_2O_3 multilayer coatings and to investigate the effects of operational conditions on tool wear. The cutting performances of coated tungsten carbide inserts were characterized and compared to that of a commercial CVD Al_2O_3 multilayer coating.

2. Materials and Methods

2.1. Sample Preparation

Four CVD Al_2O_3 multilayer coatings were deposited, corresponding to the following samples: A, B, A1 and B1. All coatings were deposited using an industrial-scale thermal CVD system (Ionbond BernexTM BPXpro 325S, IHI group, Olten, Switzerland). The process was described in a previous study, principally composed of four systems: reactor, $AlCl_3$ generator, by-products treatment system, gaseous and liquid precursors ($TiCl_4$ and CH_3CN) supply systems [15]. As shown in Figure 1, the multilayers in samples A and B were deposited on 30 mm diameter cemented carbide substrates (WC-Co 6 wt.%) to study the mechanical and tribological properties of CVD Al_2O_3 coatings. All substrates were mirror-polished (1μm diamond slurry) and cleaned using ethanol.

This coating architecture is described as: TiN buffer layer/TiN gradient layer (Grad 1)/MT-Ti(C,N); gradient layer (Grad 2)/MT-Ti(C,N)/MT-Ti(C,N); gradient layer (Grad 3)/HT-Ti(C,N); gradient layer (Grad 4)/HT-Ti(C,N); and α- or κ-bonding layer/Al_2O_3. For clarity, the TiN buffer layer acts as a diffusion barrier of Co from the substrate, Ti(C,N) layers provide high hardness and good wear resistance; bonding layers help to control the growth of α- and κ-Al_2O_3 on Ti(C,N); and the Al_2O_3 top layer can improve the oxidation resistance of coatings. Herein, α-Al_2O_3 was obtained in samples A and A1, whereas κ-Al_2O_3 was obtained in samples B and B1. Importantly, multilayers with a 0.8 μm thick TiN top layer were deposited in samples A1 and B1 on tungsten carbide inserts for the turning of 24CrMoV5-1 steel. TiN top layers can facilitate the wear detection. TiN top layers in samples A1 and B1 were deposited at 1005 °C and 70 mbar from a $TiCl_4$-H_2-N_2 gas mixture (H_2: balance, N_2: 39.4 vol.%, $TiCl_4$: 1.70 vol.%, the total flow rate: 34.0 L.min^{-1}). Due to an increasing deposition temperature in the CVD process, MT (medium-temperature) and HT (high-temperature) Ti(C,N) layers, as well as different gradient layers, were deposited in order to enhance the process continuity and the coating adhesion. The detailed deposition parameters are given in Tables 1 and 2.

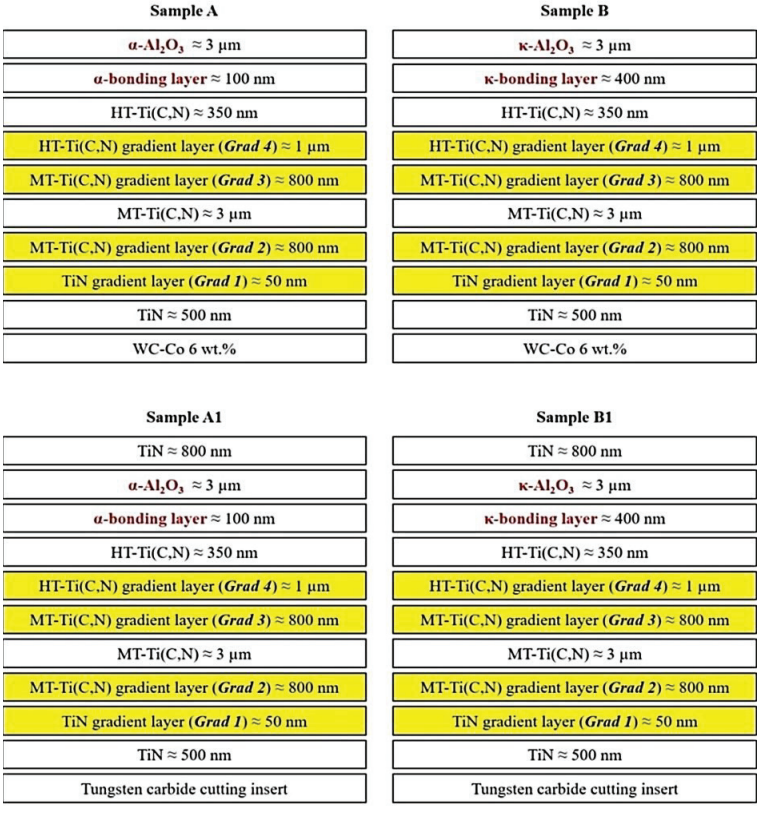

Figure 1. Schematic representation of the coating architecture of samples A, B, A1 and B1.

Table 1. The deposition parameters of different layers in samples A, B, A1 and B1.

Parameters	TiN	MT-Ti(C,N)	HT-Ti(C,N)	α-Bonding Layer	κ-Bonding Layer	Al_2O_3
Temperature (°C)	900	880	1005	1005	1005	1005
Pressure (mbar)	70	70	70	70	70	70
Deposition time (min)	40	60	15	15	15	120
Total flow rate (L.min^{-1})	33.8	26.1	32.5	26.0	32.5	25.0
H_2 (vol.%)	balance					
N_2 (vol.%)	39.6	20.3	18.4	-	9.2	-
$TiCl_4$ (vol.%)	1.3	2.4	1.4	-	1.2	-
CH_3CN (vol.%)	-	0.8	-	-	-	-
CH_4 (vol.%)	-	-	3.4	-	2.2	-
CO_2 (vol.%)	-	-	-	3.8	-	4.0
CO (vol.%)	-	-	-	-	0.9	-
$AlCl_3$ (vol.%)	-	-	-	-	0.4	1.6
HCl (vol.%)	-	-	-	-	-	2.0
H_2S (vol.%)	-	-	-	-	-	0.3

Table 2. The deposition parameters of different gradient layers.

Parameters	*Grad 1*	*Grad 2*	*Grad 3*	*Grad 4*
Temperature (°C)	900 → 890	890 → 880	880 → 890	890 → 1005
Pressure (mbar)	70	70	70	70
Deposition time (min)	10	15	15	60
Total flow rate (L.min^{-1})	33.9	26.1	26.1	26.2
H_2 (vol.%)	balance			
N_2 (vol.%)	39.5	20.3	20.3	16.8
$TiCl_4$ (vol.%)	1.6	2.2	2.3	1.6
CH_3CN (vol.%)	-	0.8	0.8	-
CH_4 (vol.%)	-	-	-	5.3

2.2. Characterization

X-ray diffraction (XRD) studies were carried out using a Bruker D8 Advance diffractometer (Bruker, Billerica, MA, USA) operating at 40 kV/40 mA with Kα radiation of Cu (λ $K\alpha_1$ = 1.54059 Å and λ $K\alpha_2$ = 1.54443 Å). Phase identifications were conducted in Bragg–Brentano geometry with a step size of 0.02° for a 2θ-range from 20° to 60°. Peak positions were determined by fitting the diffraction peaks with the Pseudo–Voigt function, and the software MAUD (version 2.92) was used. The instrumental contribution was determined using the standard material® 640d.

Surface morphology was observed using a Zeiss Gemini 500 scanning electron microscope (SEM, Jena, Germany), and cross-sectional fractures were prepared by a FIB/SEM FEI Helios NanoLab 600i (FEI, Hillsboro, OR, USA) equipped with platinum gas injection system. The FIB column used a gallium liquid metal ion source operating at an accelerating voltage up to 30 kV. A Pt-layer was primarily deposited to protect the coating surface from ion beam damage. However, the film thickness is more than 11 µm, which exceeds the limit of the FIB/SEM used, and only the Al_2O_3 and Ti(C,N)-based layer's interface was highlighted.

The average surface roughness *Ra* was evaluated by an AltiSurf© 500 optical profilometer (Altimet, Thonon-Les-Bains, Switzerland) with a scanning rate of 50 µm/s, using a measurement length of 5 mm on ten different positions at the coating surface. Surface profiles were characterized after ball-on-disc tests with a scanning rate of 50 µm/s (analyzed area: 2.5 × 2.5 mm^2).

The hardness and modulus of samples A and B were evaluated by a Nano-indenter HYSITRON TI980 using a Berkovitch diamond tip with a maximum load of 11 mN. Loading and unloading rates were 2 mN/s with a residence time of 2 s at the maximum load. Prior to measurements, the coating surface was mirror-polished to eliminate asperities and to obtain an average roughness *Ra* less than 15 nm. Twenty-five indentations were performed for each sample and an average value was considered. The Oliver and Pharr method and the Poisson's ratio of 0.24 for both α- and κ-Al_2O_3 were used for calculations [16,17]. Vickers hardness $HV_{0.05}$ values were measured using a Wilson® TUKONTM 1202 (Buehler, Leinfelden-Echtergingen, Germany): ten indentations were performed for each sample, and an average value was considered [18].

A CSM tribometer was used for ball-on-disc tests. Samples A and B were tested using 6 mm diameter grade 24CrMoV5-1 balls (workpiece material for cutting tests) without lubricant. A normal force of 10 N (maximum of the tribometer used) was applied; the sliding distance was 1000 m with a speed of 10 cm/s and a rotational radius of 2.5 mm. Wear tracks on coating surfaces were observed by an optical microscope KEYENCE VH-Z250R (KEYENCE, Bois-Colombes, France). Rockwell C tests were carried out for samples A and B to investigate the film adhesion and its brittleness; a conical diamond indenter with a load of 150 kg was used [19].

Furthermore, Ø 200 × 300 mm annealed bars of 24CrMoV5-1 (Dijon, France: ANFOR NFA) with a hardness of 220 HB were selected as the workpiece material; its composition

(C: 0.39 wt.%, Si: 1.03 wt.%, Mn: 0.33 wt.%, Cr: 5.07 wt.%, Ni: 0.16 wt.%, Mo: 1.23 wt.%, V: 0.39 wt.%, P: 0.02 wt.% and S: <0.001 wt.%) is given in a previous study [14]. The tool holder DCLNL 3232 P16 was used with uncoated (CNMX 16 06 12 E8 CH01) and coated (CNMX 16 06 E8 CFX 1025) inserts provided by Evatec Tools. According to the ISO standard 3002:1982, the tool cutting edge angle (k_r) is 95°, the tool cutting edge inclination (λ_s) is −6°, the orientation of the cutting face (γ_o) is −6° and the orientation of the flank (α_o) is 6°.

A spinner TC600 CNC lathe machine was used for the cylindrical turning of 24CrMoV5-1 steel; the experimental set-up is shown in Figure 2 [14]. A water–oil mixture (8.5% S-Aero Fluch soluble oil) was used as lubricant during turning. Cutting edge temperatures were measured by an Actarus® System (CIRTES, Saint-Dié-des-Vosges, France); a temperature probe was 1 mm under the cutting edge. A triaxial piezoelectric dynamometer-Kistler 9257B and accelerometer-Kistle 8763B were placed to measure cutting forces and accelerations in feed, in tangential and radial directions with reference to tools [14,20]. Herein, cutting parameters, cutting forces, accelerations, and temperature are inputs of the "Machine Learning Model", which can provide an estimation of tool wear and machined surface roughness as outputs [14].

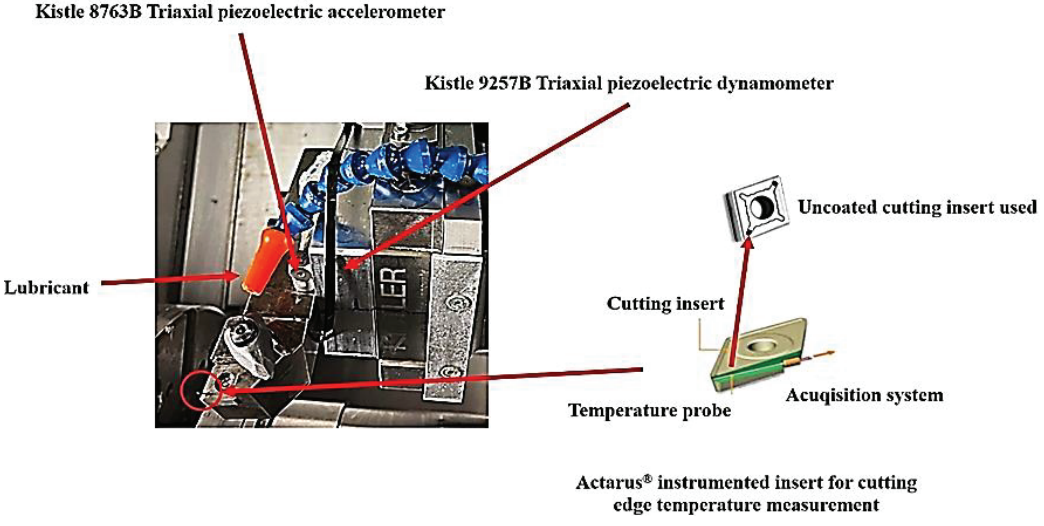

Figure 2. Cutting forces, accelerations and cutting-edge temperatures measurement systems.

The COM (Couple Tool-Material) protocol defined on the standard NF E 66-520 was devoted to the determination of cutting parameters, for a precise association of tool, workpiece material and machining operation. This protocol provides the guidelines for choosing minimum values for cutting speed-Vc, as well as maximum and minimum values of depth of cut-a_p and feed-f. The determination of these values is based on cutting parameters and other process information (cutting forces, accelerations, cutting edge temperatures, roughness of the machined surface, tool wear, chip shape, etc.).

Herein, 39 experiments were carried out following the COM protocol using commercial coated inserts from Evatec Tools to choose the optimum cutting parameters. As can be seen in Table 3, cutting speed-Vc was increased from 150 to 500 m/min in the series (A), feed-f was increased from 0.2 to 0.6 mm/rev in the series (B), and depth of cut-a_p was increased from 1 to 5.5 mm in the series (C). These parameters (Vc: 150–500 m/min, f: 0.2–0.6 mm/rev and a_p: 1–5.5 mm) were suggested by Evatec Tools for turning-roughing operations.

Table 3. Experiments carried out for the determination of cutting parameters: cutting speed-*Vc* (m/min), feed-*f* (mm/rev) and depth of cut-a_p (mm).

Series	Experience Number	*Vc* (m/min)	*f* (mm/rev)	a_p (mm)
(A)	1 to 3	150	0.3	2.5
	4 to 6	240	0.3	2.5
	7 to 9	340	0.3	2.5
	10 to 12	500	0.3	2.5
(B)	13 to 15	240	0.2	2.5
	16 to 18	240	0.3	2.5
	19 to 21	240	0.45	2.5
	22 to 24	240	0.6	2.5
(C)	25 to 27	240	0.35	1
	28 to 30	240	0.35	2.5
	30 to 32	240	0.35	3.5
	33 to 36	240	0.35	4.5
	37 to 39	240	0.35	5.5

Each experiment repeated three times consists of performing a cylindrical turning operation for about 30 s with given cutting parameters, to obtain stable signals of temperature and a visible evolution of tool wear. Accelerations and cutting-edge temperatures were measured, and specific cutting force-*kc* (cutting force per unit area of cut) was calculated according to the standard NF ISO 3002-4. Tool flank wear-*Vb* was measured as the average width of the flank land by an optical microscope according to the ISO standard 3685:1993. At the end of each experiment, an average roughness *Ra* of the machined surface was measured by a portable roughness tester: Mitutoyo SJ 210 (Mitutoyo, Roissy, France). A new cutting edge was used for each experiment.

Based on the results obtained from 39 experiments and the "Machine Learning Model", cutting parameters were determined: cutting speed—240 (m/min), feed—0.35 (mm/rev) and depth of cut—3.5 (mm). In these conditions, a low flank wear with a low machined surface roughness was obtained for turning of 24CrMoV5-1 steel using commercial coated cutting inserts (CNMX 16 06 E8 CFX 1025) from Evatec Tools (Evatec tools, Thionville, France). However, it was not possible to characterize this $TiN/TiB_2/Al_2O_3$ commercial coating in terms of coating thickness, composition or microstructure. Afterwards, tool-life tests were carried out according to the ISO standard 3685:1993 using these determined parameters. When tool flank wear-*Vb* reached 300 μm or edge breakage occurred, the cutting edge was considered as reaching the end of life. The results obtained are discussed in Section 3.5.

3. Results and Discussion

3.1. Structure, Morphology and Microstructure Analyses

The X-ray diffractograms of samples A, A1, B and B1 are presented in Figures 3 and 4. It is shown that α-Al_2O_3 was obtained in samples A and A1, due to the deposition of the α-bonding layer that was obtained by oxidizing the uppermost part of the HT-Ti(C,N) layers. This oxidizing step resulted in the formation of rutile; the epitaxial growth of α-Al_2O_3 on rutile was evidenced [12]. On the contrary, κ-Al_2O_3 was obtained in samples B and B1, due to the deposition of κ-bonding layer composed of Ti(C,N) needle-shaped grains [12]. Compared with Figure 3, diffraction peaks belonging to TiN were pronounced in Figure 4, since 800 nm thick TiN top layers were deposited in both samples A1 and B1 to facilitate the wear detection after the manufacturing process.

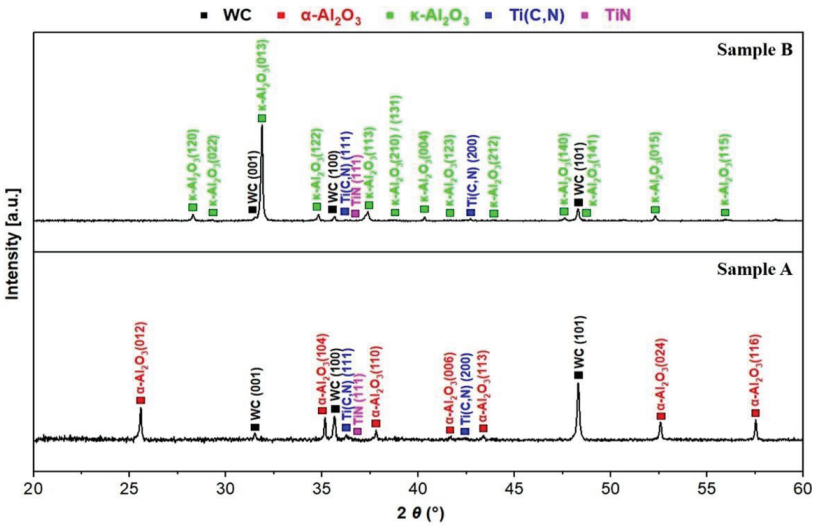

Figure 3. X-ray diffractograms of samples A and B.

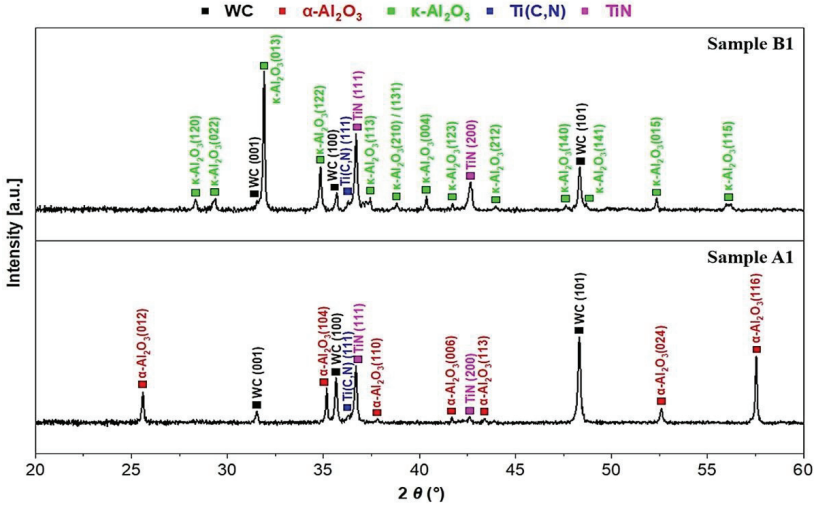

Figure 4. X-ray diffractograms of samples A1 and B1.

Figure 5 shows surface morphologies and cross-sectional microstructures of samples A and B. Sample A consists of facetted grains, in agreement with earlier observations reported [12,21,22]. Previous studies found that κ- to α-Al_2O_3 phase transformation can occur during the CVD deposition process, and α-Al_2O_3 obtained through this phase transformation shows large equiaxed grains [21,23]. Herein, neither diffraction peaks originating from κ-Al_2O_3, nor large equiaxed grains was observed, and the phase transformation is ruled out. In contrast, sample B is composed of small, rounded grains, thus a similar morphology was reported [12]. Some cracks were observed due to thermal stresses generally found in CVD coatings. Cross-sectional fractures were prepared by FIB, the Al_2O_3 and Ti(C,N)-based layer's interface was highlighted, and Ti(C,N) needle-shaped grains were grown to promote the nucleation of κ-Al_2O_3 in sample B.

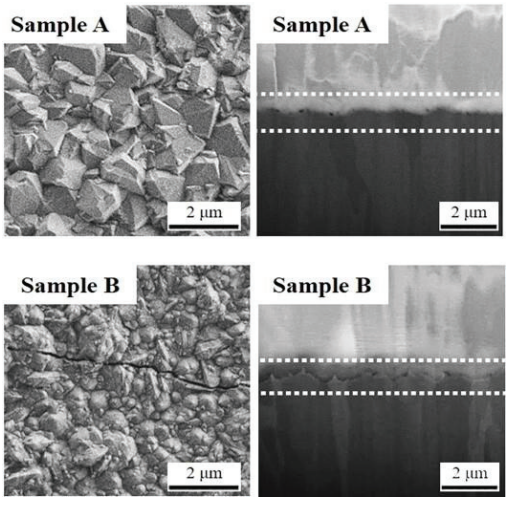

Figure 5. SEM images showing surface morphologies (top view) and cross-sectional fractures of samples A and B. Note that top layers in these two samples are α- and κ-Al_2O_3, respectively.

3.2. Nano- and Micro-Indentation

The hardness of 28.0 ± 0.8 GPa and 25.6 ± 0.4 GPa was measured for samples A and B, in good agreement with earlier studies: polycrystalline α-Al_2O_3 exhibits slightly higher hardness than κ-Al_2O_3 [24–27]. Young's moduli of 333 ± 6 GPa and 292 ± 6 GPa were measured for samples A and B. Accordingly, Ruppi et al. reported elastic moduli of 390 ± 44 GPa and 340 ± 15 GPa for CVD α- and κ-Al_2O_3 multilayer coatings [25]. However, Rebelo de Figueiredo et al. obtained lower moduli of 280 ± 8 GPa and 250 ± 6 GPa [24]. It is believed that the mechanical properties of CVD Al_2O_3 are strongly dependent on deposition conditions. Additionally, elastic properties of CVD Al_2O_3 coatings depend also on residual stress state [27,28]. High tensile residual stresses could provoke low moduli. Regarding CVD coatings, thermal stresses induced by dissimilar coefficients of thermal expansion play a crucial role, and the stress behavior of anisotropic α-Al_2O_3 is not independent from the in-plane orientation [27,29,30]. Such a conclusion requires further investigations.

The Vickers hardness of 27.3 ± 1.1 and 25.9 ± 1.0 GPa was measured for samples A and B, respectively. Comparable values of approx. 29.4 GPa were reported for both CVD α- and κ-Al_2O_3 multilayer coatings from the company Bernex. Since the applied indentation load was relatively small in both the present study and company measurement standard, no visible radial or lateral cracks were observed at the surroundings of the imprints by an optical microscope.

3.3. Ball-on-Disc Test

As shown in Figure 6, friction coefficients (μ) of 0.76 and 0.72 were determined for samples A and B, respectively. This could be attributed to relatively high surface roughness *Ra*, which is 125 nm and 108 nm for samples A and B. Accordingly, a slightly lower μ of sample B could be related to its smaller grain size [31,32]. As shown in Figure 7, wear tracks were observed on the surfaces of samples A and B, while larger tracks were found on 24CrMoV5-1 balls. It is speculated that the counterpart crushed coating surface asperities and abrasive wear particles were generated. Furthermore, the counterpart shows an adhesion tendency to the coating surface, leading to the stick-slip phenomenon and scattering friction forces [33]. Meanwhile, coatings exhibit much higher hardness levels than 24CrMoV5-1 steel, which could also be responsible for larger tracks on balls [34,35].

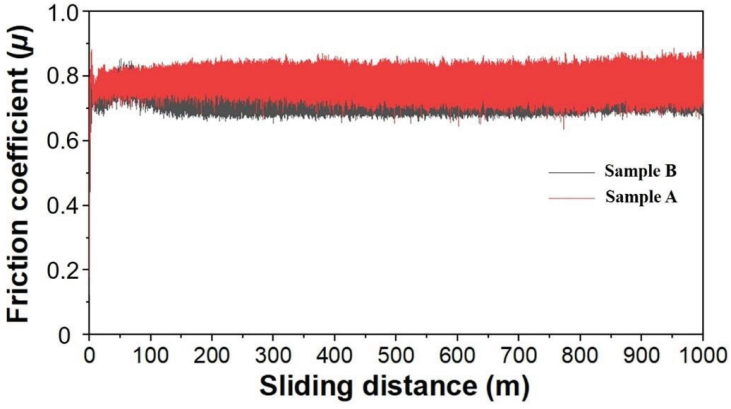

Figure 6. Friction coefficients measured using 6 mm diameter 24CrMoV5-1 balls at room temperature in air atmosphere without lubricant.

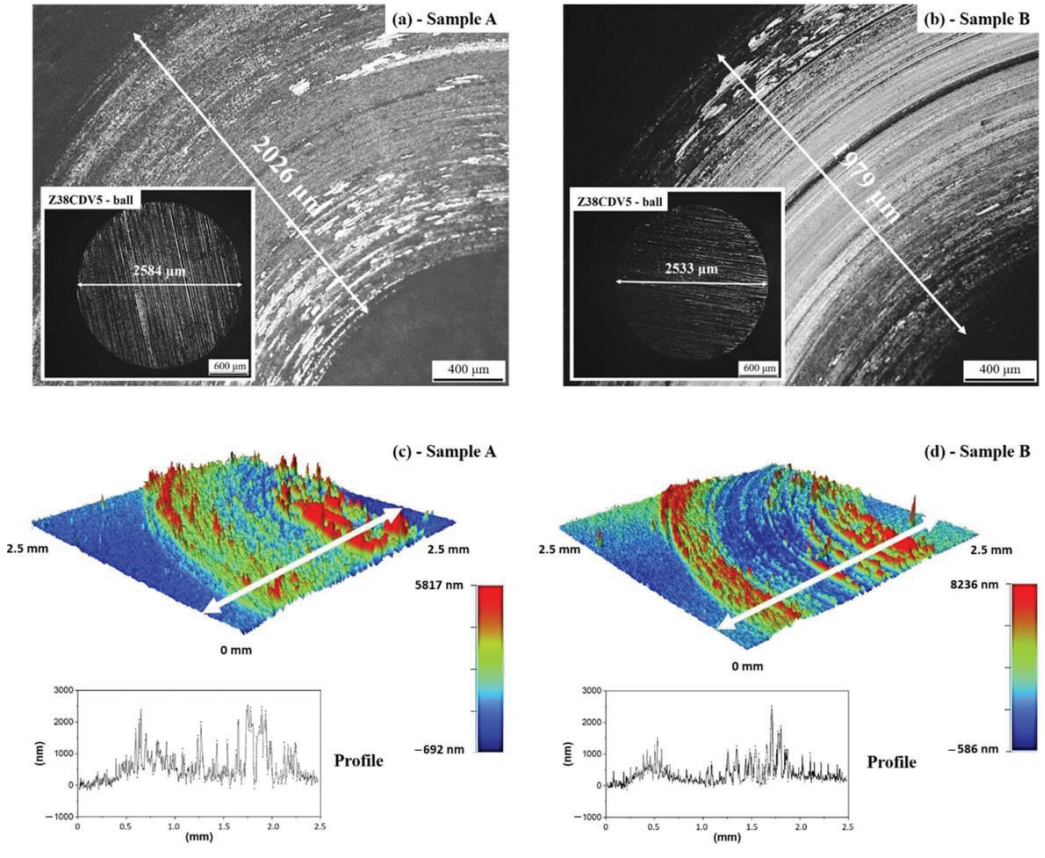

Figure 7. (**a**,**b**) Optical microscope images of wear tracks on the surface of samples A and B. (**c**,**d**) 3D profilometer images of wear tracks.

3.4. Rockwell C Test

As shown in Figures 8 and 9, samples A and B were characterized by SEM after Rockwell C tests. In general, coatings under extreme stress conditions show two different

aspects. On the one hand, the normal components of the stress tensor could be responsible for the brittle failures of coatings [36]. Normal stresses greater than the coating strength can provoke coherence release or chipping. In this case, the mechanical properties of coatings, such as the internal cohesion, play an important role. On the other hand, interfacial bonds between the coatings and the substrates—the so-called adhesion—are key. The release of interfacial bonds could be correlated to the shear stress components of stress tensors, which could result in micro- or macro-delamination.

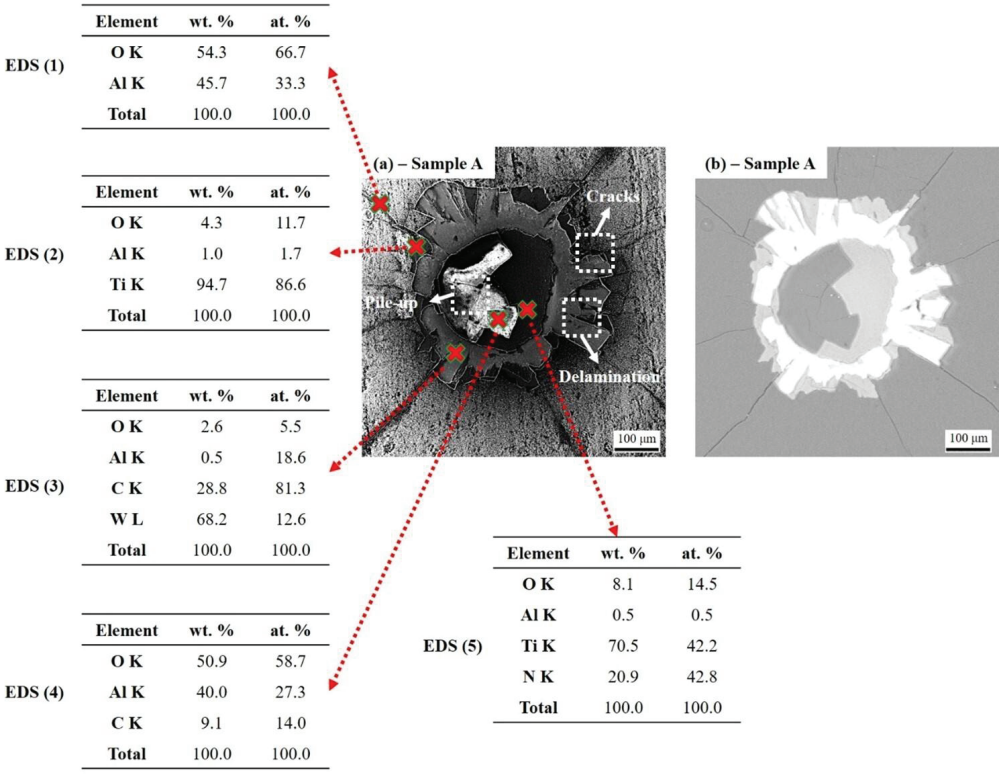

Figure 8. SEM images and EDS analyses of sample A after Rockwell C test. (**a**) Secondary electron (SE) image and (**b**) Backscattered electron (BSE) image.

As shown in Figure 8, extended delamination and radial cracks surrounding the imprint are observed. As can be seen in Figure 8a,b, film delamination with buckling at the center of the imprint is evidenced. In EDS analysis (1), an Al_2O_3 layer was detected. In EDS analyses (2) and (3), Ti(C,N)-based layers and a substrate were characterized. It was observed in EDS analyses (4) and (5) that Al_2O_3 layers pile up at the center of imprint, and Ti(C,N)-based layers were exposed. As shown in Figure 9, film delamination and cracks at the vicinity of imprint were observed, similar to sample A. On the contrary, no significant buckling at the center of the imprint could be observed in sample B, consistent with EDS analysis (4). EDS analysis (1) demonstrates that only an Al_2O_3 layer was detected, whereas Ti(C,N)-based layers and a cemented carbide substrate were characterized in EDS analyses (2) and (3).

In such case, it is difficult to conclude whether the fracture results from cohesive or adhesive failures, so the so-called mixed failure mode is considered. This kind of failure could be caused by a combination of normal and shear stresses. At least, the poor delamination at the center and small radial cracks at the surrounding of imprint indicate

that sample B shows a better adhesion between the Al_2O_3 and based layers, compared with sample A. However, these results must be put into perspective with respect to the nature of the substrate. However, indentations were performed on these coatings deposited on cemented carbide substrates, whereas in conventional Rockwell C tests, a quenched and tempered high-speed steel (62 HRC) substrate is used.

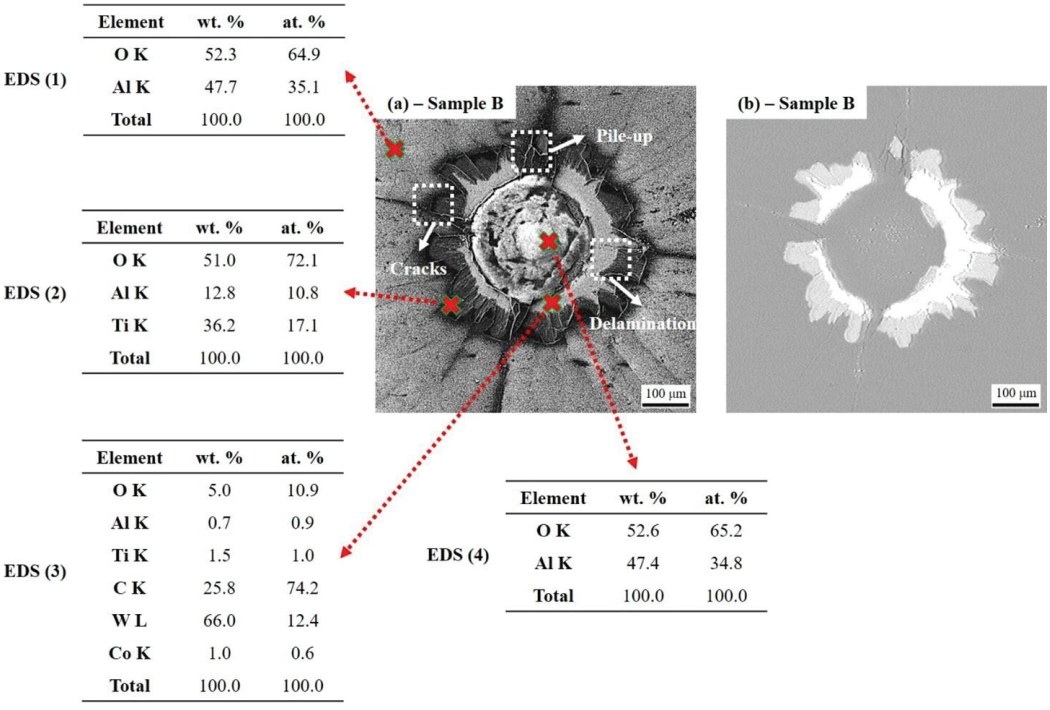

Figure 9. SEM images and EDS analyses of sample B after Rockwell C test. (**a**) Secondary electron (SE) image and (**b**) Backscattered electron (BSE) image.

3.5. Metal Cutting Test

Tool-life tests consist of executing cutting experiments with the same cutting edge until the end of life. Using the determined cutting parameters in Section 2.2, tool-life tests of 24CrMoV5-1 steel using sample A1 and B1 coated cutting inserts, commercial uncoated and coated cutting inserts were carried out according to the ISO standard 3685:1993. It is noticeable that cutting-edge radiuses are comparable before and after the deposition of CVD Al_2O_3 multilayer coatings (samples A1 and B1). Regarding commercial uncoated inserts, edge breakage occurred after the very first seconds. It is shown clearly that these uncoated inserts are not adaptable to the severe cutting conditions applied.

Tool-life plots are shown in Figure 10. Flank wear, cutting edge temperature, roughness of the machined surface, accelerations and cutting forces were measured every 30 s during the cutting tests, as displayed in Figure 11. In these conditions, sample B1 (the coated tungsten carbide cutting insert) exhibits the longest tool life of approx. 650 s, double that of commercial coated inserts. In this study, tool life was evaluated by flank wear-*Vb*; when flank wear reaches 300 µm or edge breakage occurs, the tool reaches the end of its life.

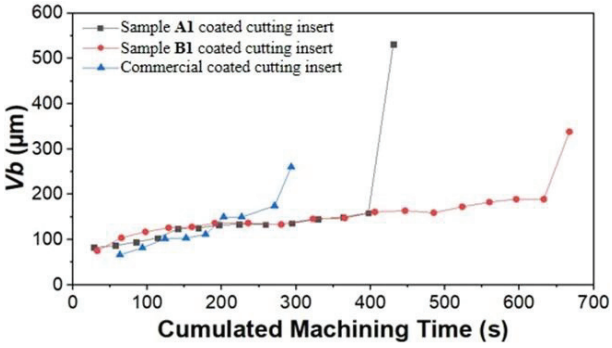

Figure 10. Tool-life plots for cutting tests of 24CrMoV5-1 steel.

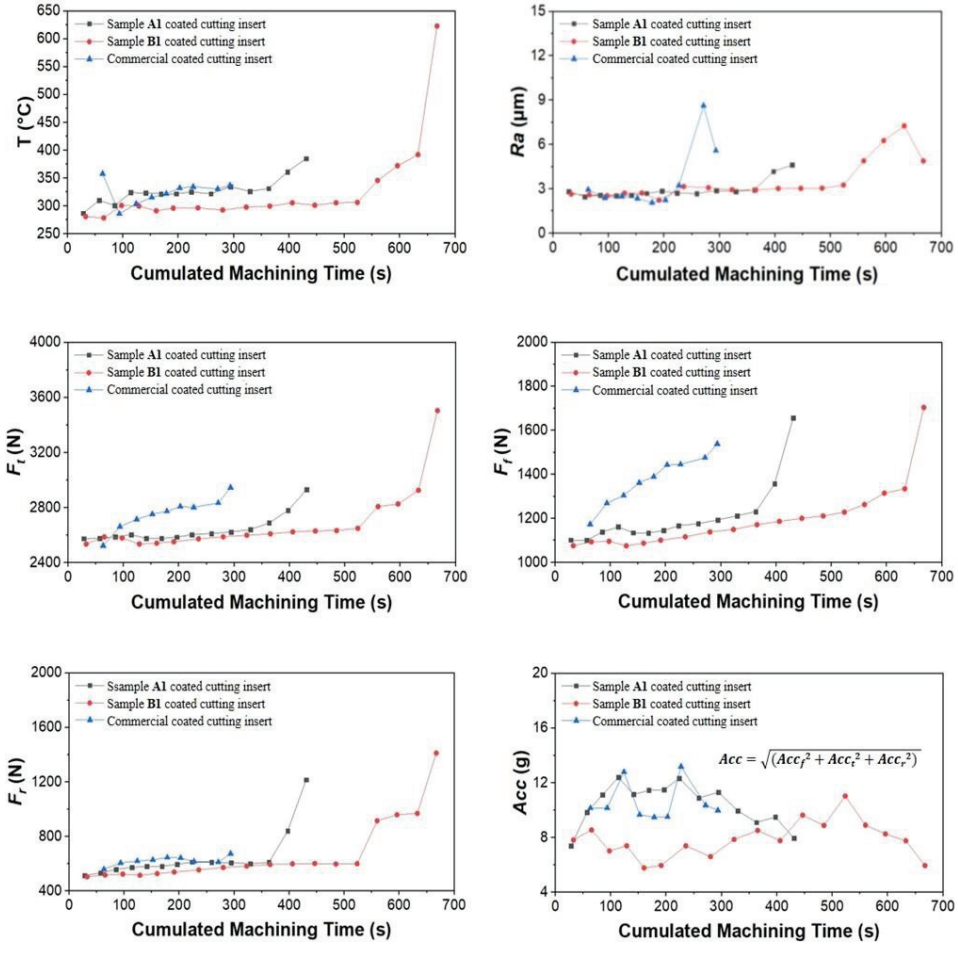

Figure 11. Evolution of cutting-edge temperature-T, average roughness of machined surface-*Ra*, cutting forces in tangential-F_t, feed-F_f and radial-F_r directions, as well as accelerations-*Acc* (vibrations in tangential-Acc_t, feed-Acc_f and radial-Acc_r directions) with increasing machining time during tool-life tests.

As can be seen in Figure 11, while cumulated machining time increased, cutting temperatures did not increase until the end of life. As aforementioned, the generated heat in the shear zone could be transported away with chip flow. In this respect, CVD Al_2O_3 is considered a good thermal barrier for preventing the plastic deformation of substrates [1,7,8]. Compared with α-Al_2O_3, κ-Al_2O_3 shows a much smaller thermal conductivity. This could be a plausible explanation for the lower cutting-edge temperatures measured during cutting tests using sample B1 coated cutting inserts [9]. Concerning the roughness of the machined surface, comparable results of approx. 3 µm were obtained at the end of tool life in all three tests.

Cutting forces in different directions were measured. Cutting forces in all directions for tool-life tests using commercial coated cutting inserts were always higher than those using sample A1 and B1 coated inserts, particularly F_t and F_f, indicating that more important powers were required on the spindle for turning using commercial coated inserts. Accelerations in all directions were measured and root mean square values were considered. Indeed, accelerations correlated to cutting vibrations could significantly influence tool service life and tool deflection, and the vibration of tool tip could seriously deteriorate the quality of the machined surface. In this study, smaller accelerations were measured during the test using sample B1 coated cutting inserts. In contrast, it is speculated that large grain size and the higher hardness and roughness of sample A1 generated important vibrations. This could be responsible for the significant chipping reported in Figure 12a.

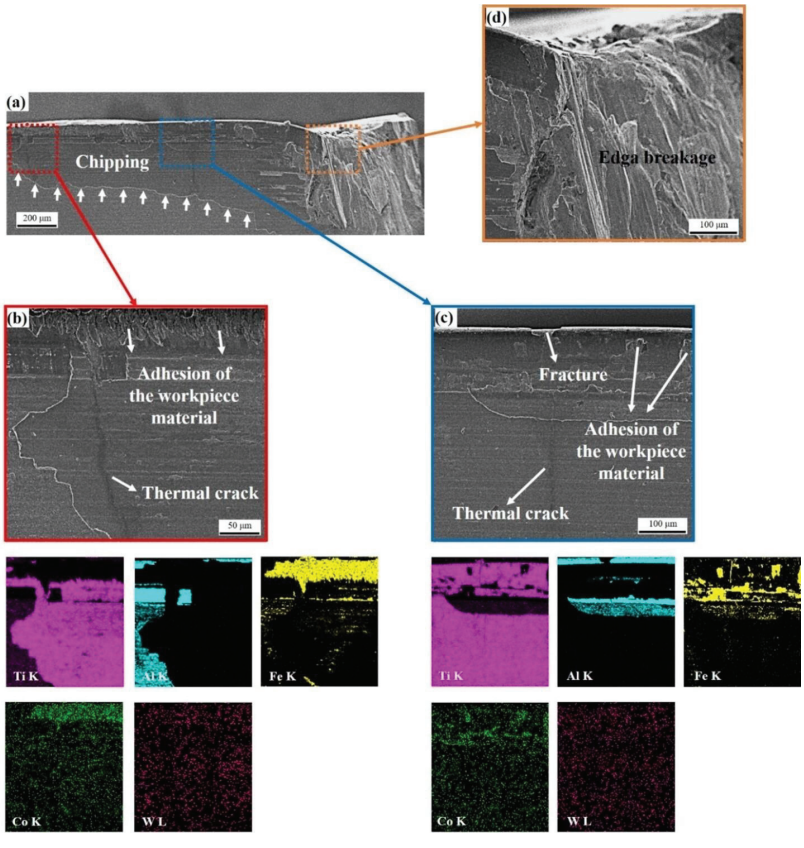

Figure 12. SEM images and EDS analyses of the sample A1 (CVD α-Al_2O_3 coating) coated insert after cutting test of 24CrMoV5-1 steel. (**a**) Flank face of the cutting insert. (**b**,**c**) SEM images corresponding to the red and blue areas indicated in (**a**). (**d**) The cutting edge.

As shown in Figures 12 and 13, sample A1 and B1 coated inserts were characterized, but we could not characterize this commercial coating due to an industrial confidential issue. Important chipping on the flank face of sample A1 can be observed, showing that wear penetrated the α-Al_2O_3 layer, revealing Ti(C,N)-based layers, which is not the case for sample B1 except for a small area near the cutting edge. As sample B1 exhibits a good adhesion at the Al_2O_3/Ti(C,N)-based layer's interface, this could be a plausible explanation for its good performance in these cutting tests.

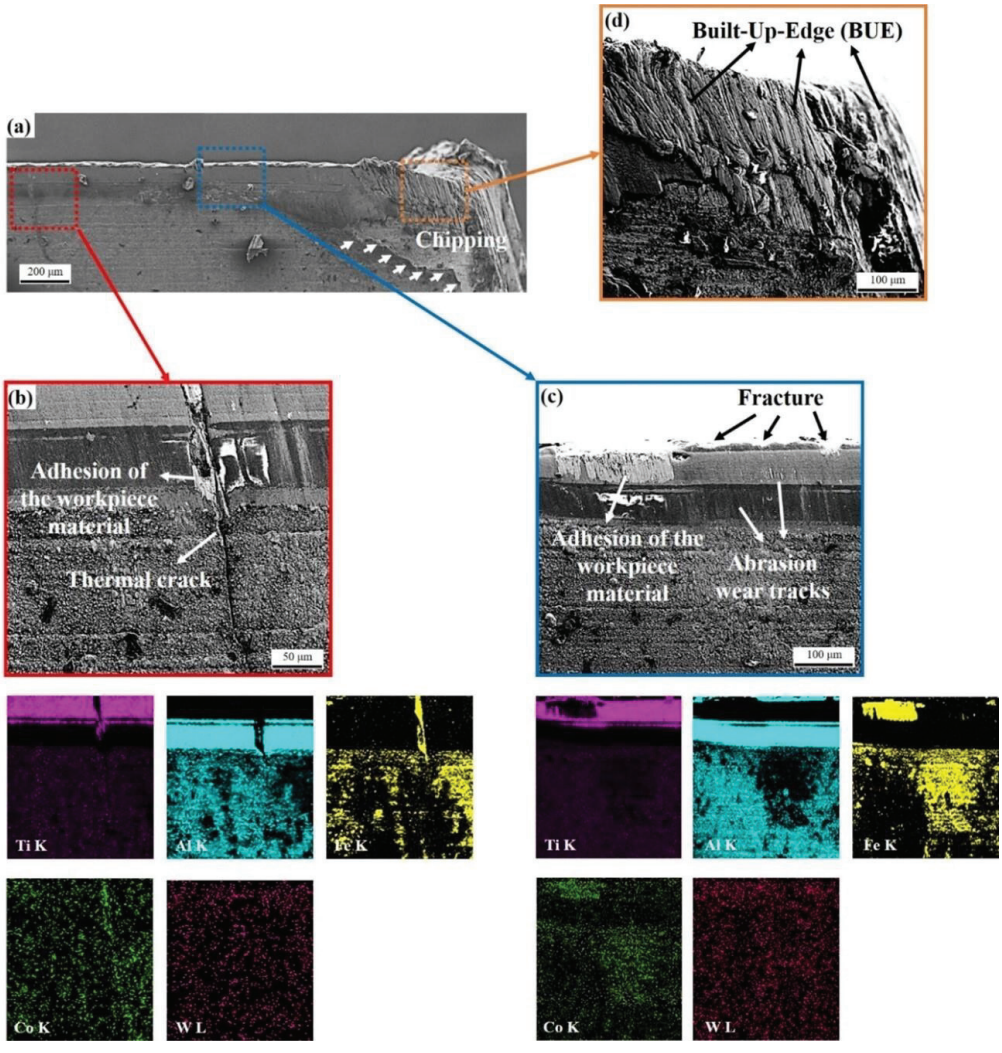

Figure 13. SEM images and EDS analyses of the sample B1 (CVD κ-Al_2O_3 coating) coated insert after cutting test of 24CrMoV5-1 steel. (**a**) Flank face of the cutting insert. (**b**,**c**) SEM images corresponding to the red and blue areas indicated in (**a**). (**d**) The cutting edge.

Figure 12b,c shows SEM images of sample A1 corresponding to the red and blue squares indicated in Figure 12a. EDS analyses were conducted. The adhesion of the workpiece material to the tool surface and visible cracks were observed. However, the diffusion of cobalt from the substrate is not evident, but it could be possible in the zone

where the adhesion of the workpiece material occurs. A similar phenomenon is found in sample B1, as shown in Figure 13b,c, but the diffusion of Co from tungsten carbide substrates into coatings needs further cross-sectional EDS analyses. Accordingly, the adhesion of the workpiece material on tools could generate progressive tool wear. It was suggested that diffusion of Fe and Cr from the workpiece material through grain boundaries into coatings accelerated the degradation of coatings [37]. Furthermore, Ti and Al appear in very limited zones, similar to sample B1. It is assumed that the delamination only occurred at the Al_2O_3/Ti(C,N)-based layer's interface, but Ti(C,N)-based layers are adherent to cutting inserts.

Regarding sample B1, as shown in Figure 13a,d, the Built-Up-Edge (BUE) is observed, due to the adhesion of the workpiece material. Moreover, since the cutting-edge temperature was low (approx. 300 °C), only thermal cracks were observed, but there was no evidence for secondary cracks resulting from κ- to α-Al_2O_3 phase transformation.

4. Conclusions

In this work, four CVD Al_2O_3 multilayer coatings were deposited without (samples A and B) and with thin TiN top layers (samples A1 and B1). The morphology, microstructure, and mechanical and tribological properties of samples A and B were studied, while turning operations of 24CrMoV5-1 with uncoated and coated tools (commercial coating, samples A1 and B1) were carried out. The main results can be summarized as follows:

(1) By means of nano-indentation, hardness levels of 28.0 ± 0.8 and 25.6 ± 0.4 Gpa and Young's moduli of 333 ± 6 and 292 ± 6 GPa were measured for CVD α- and κ-Al_2O_3 coatings, respectively. Due to the anisotropic properties of α-Al_2O_3, the influence of film texture on its mechanical properties needs further investigations. Vickers hardness levels of 27.3 ± 1.1 and 25.9 ± 1.0 GPa were measured for CVD α- and κ-Al_2O_3 coatings, comparable with CVD α- and κ-Al_2O_3 coatings from the company Bernex.

(2) In tribotests using 24CrMoV5-1 balls, friction coefficients of approx. 0.7 were measured for samples A and B, respectively. The effects of grain size, hardness and surface roughness were discussed. In Rockwell C tests, poor delamination but no evident bulking at the center of imprint indicate that sample B could be a good adherent coating.

(3) Cutting parameters for tool-life tests of 24CrMoV5-1 were determined according to the COM protocol: cutting speed—240 (m/min), feed—0.35 (mm/rev) and depth of cut—3.5 (mm). In this study, commercial uncoated inserts were not adaptable. Sample B1 coated inserts exhibited the longest tool life of approx. 11 min, double of that of commercial coated inserts from Evatec Tools. Compared to sample A1, good adhesion between κ-Al_2O_3 and Ti(C,N)-based layers was evidenced in sample B1. The large grain size and high hardness and surface roughness of sample A1 could be responsible for important vibrations that could seriously deteriorate the tool service life.

The results obtained can enrich the existing database for the development of prediction models of tool wear and machined surface quality. They can also help in improving the tool performance for the turning-roughing of 24CrMoV5-1 steel, as the tool life has been dramatically improved compared with the existing commercial CVD Al_2O_3 multilayer coating. Further works will focus on the optimization of multilayer coating architecture and film texture to improve the adhesion and mechanical properties. The crater wear on the tool rake face also needs more investigations, to study the tool-chip interface.

Author Contributions: Conceptualization, M.Z. and S.A.; methodology, M.Z., S.A., M.P.M., A.D. and A.C.G.-W.; software, M.Z., M.P.M. and C.P.; validation, J.-F.P. and F.S.; formal analysis, M.Z.; investigation, M.Z. and M.P.M.; resources, J.-F.P. and F.S.; writing—original draft preparation, M.Z.; writing—review and editing, M.Z., J.-F.P. and F.S.; supervision, J.-F.P. and F.S. All authors have read and agreed to the published version of the manuscript.

Funding: This research was funded by Groupement d'Intérêt Public Haute-Marne (GIP 52).

Institutional Review Board Statement: Not applicable.

Informed Consent Statement: Not applicable.

Data Availability Statement: No new data were created or analyzed in this study. Data sharing is not applicable to this article.

Acknowledgments: The authors would like to acknowledge the fruitful collaboration with CIRTES SA. The authors thanks Sylvie Migot for the FIB preparation. The "Centre de Compétences" 3M and X-gamma of the Institut Jean Lamour are acknowledged for the access to their equipment. Special thanks to the Groupement d'Intérêt Public Haute-Marne (GIP 52) for its financial support to this work.

Conflicts of Interest: The authors declare no conflict of interest.

References

1. Schalk, N.; Tkadletz, M.; Mitterer, C. Hard coatings for cutting applications: Physical vs. chemical vapor deposition and future challenges for the coatings community. *Surf. Coat. Technol.* **2021**, *429*, 127949. [CrossRef]
2. M'Saoubi, R.; Ruppi, S. Wear and thermal behaviour of CVD α-Al_2O_3 and MTCVD Ti(C,N) coatings during machining. *CIRP Ann.* **2009**, *58*, 57–60. [CrossRef]
3. Nemetz, A.W.; Daves, W.; Klünsner, T.; Ecker, W.; Teppernegg, T.; Czettl, C.; Krajinović, I. FE temperature- and residual stress prediction in milling inserts and correlation with experimentally observed damage mechanisms. *J. Mater. Process. Technol.* **2018**, *256*, 98–108. [CrossRef]
4. Nemetz, A.W.; Daves, W.; Klünsner, T.; Ecker, W.; Schäfer, J.; Czettl, C.; Antretter, T. Cyclic heat-up and damage-relevant substrate plastification of single- and bilayer coated milling inserts evaluated numerically. *Surf. Coat. Technol.* **2019**, *360*, 39–49. [CrossRef]
5. Krajinović, I.; Daves, W.; Tkadletz, M.; Teppernegg, T.; Klünsner, T.; Schalk, N.; Mitterer, C.; Tritremmel, C.; Ecker, W.; Czettl, C. Finite element study of the influence of hard coatings on hard metal tool loading during milling. *Surf. Coat. Technol.* **2016**, *304*, 134–141. [CrossRef]
6. Tzeng, C.J.; Lin, Y.H.; Yang, Y.K.; Jeng, M.C. Optimization of turning operations with multiple performance characteristics using the Taguchi method and Grey relational analysis. *J. Mater. Process. Technol.* **2009**, *209*, 2753–2759. [CrossRef]
7. Nemetz, A.W.; Daves, W.; Klünsner, T.; Praetzas, C.; Liu, W.; Teppernegg, T.; Czettl, C.; Haas, F.; Bölling, C.; Schäfer, J. Experimentally validated calculation of the cutting edge temperature during dry milling of Ti6Al4V. *J. Mater. Process. Technol.* **2020**, *278*, 116544. [CrossRef]
8. Bobzin, K. High-performance coatings for cutting tools. *CIRP J. Manuf. Sci. Technol.* **2017**, *18*, 1–9. [CrossRef]
9. Cahill, D.G.; Lee, S.M.; Selinder, T.I. Thermal conductivity of κ-Al_2O_3 and α-Al_2O_3 wear-resistant coatings. *J. Appl. Phys.* **1998**, *83*, 5783–5786. [CrossRef]
10. Halvarsson, M.; Vuorinen, S. The influence of the nucleation surface on the growth of CVD α-Al_2O_3 and κ-Al_2O_3. *Surf. Coat. Technol.* **1995**, *76–77*, 287–296. [CrossRef]
11. Ruppi, S. Influence of Process Conditions on the Growth and Texture of CVD Alpha-Alumina. *Coatings* **2020**, *10*, 158. [CrossRef]
12. Zhu, M.; Achache, S.; Emo, M.; Ramírez, A.B.; Pierson, J.F.; Sanchette, F. Influence of the nucleation surface on the growth of epitaxial Al_2O_3 thermal CVD films deposited on cemented carbides. *Mater. Des.* **2022**, *216*, 110601. [CrossRef]
13. Zhu, M.; Achache, S.; Boulet, P.; Virfeu, A.; Pierson, J.F.; Sanchette, F. Effects of deposition parameters on the microstructure and mechanical properties of Ti(C,N) produced by moderate temperature chemical vapor deposition (MT-CVD) on cemented carbides. *Vacuum* **2022**, *195*, 110650. [CrossRef]
14. Motta, M.P.; Pelaingre, C.; Delamézière, A.; Ayed, L.B.; Barlier, C. Machine learning models for surface roughness monitoring in machining operations. *Procedia CIRP* **2022**, *108*, 710–715. [CrossRef]
15. Uny, F.; Achache, S.; Larmi, S.; Ghanbaja, J.; Fischer, E.; Pons, M.; Blanquet, E.; Schuster, F.; Sanchette, F. Deposition and characterization of (Ti, Al)N coatings deposited by thermal LPCVD in an industrial reactor. *Surf. Coat. Technol.* **2019**, *358*, 923–933. [CrossRef]
16. Oliver, W.C.; Pharr, G.M. An improved technique for determining hardness and elastic modulus using load and displacement sensing indentation experiments. *J. Mater. Res.* **1992**, *7*, 1564–1583. [CrossRef]
17. Konstantiniuk, F.; Tkadletz, M.; Czettl, C.; Schalk, N. Fracture Properties of α– and κ–Al_2O_3 Hard Coatings Deposited by Chemical Vapor Deposition. *Coatings* **2021**, *11*, 1359. [CrossRef]
18. Qin, Y.F.; Zhu, L.Y.; He, J.N.; Yin, F.X.; Nan, Z.S.; Zhao, L.J. Microstructure and tribological properties of TiCN-Al_2O_3 composite coatings fabricated by reactive plasma spraying. *Vacuum* **2018**, *147*, 149–157. [CrossRef]
19. Vidakis, N.; Antoniadis, A.; Bilalis, N. The VDI 3198 indentation test evaluation of a reliable qualitative control for layered compounds. *J. Mater. Process. Technol.* **2003**, *143–144*, 481–485. [CrossRef]
20. Le Coz, G.; Marinescu, M.; Devillez, A.; Dudzinski, D.; Velnom, L. Measuring temperature of rotating cutting tools: Application to MQL drilling and dry milling of aerospace alloys. *Appl. Therm. Eng.* **2012**, *36*, 434–441. [CrossRef]
21. Ruppi, S. Deposition, microstructure and properties of texture-controlled CVD α-Al_2O_3 coatings. *Int. J. Refract. Met. Hard Mater.* **2005**, *23*, 306–316. [CrossRef]

22. Ruppi, S. Enhanced performance of α-Al_2O_3 coatings by control of crystal orientation. *Surf. Coat. Technol.* **2008**, *202*, 4257–4269. [CrossRef]
23. Trinh, D.H.; Back, K.; Pozina, G.; Blomqvist, H.; Selinder, T.; Collin, M.; Reineck, I.; Hultman, L.; Högberg, H. Phase transformation in κ- and γ-Al_2O_3 coatings on cutting tool inserts. *Surf. Coat. Technol.* **2009**, *203*, 1682–1688. [CrossRef]
24. De Figueiredo, M.R.; Abad, M.D.; Harris, A.J.; Czettl, C.; Mitterer, C.; Hosemann, P. Nanoindentation of chemical-vapor deposited Al_2O_3 hard coatings at elevated temperatures. *Thin Solid Films* **2015**, *578*, 20–24. [CrossRef]
25. Ruppi, S.; Larsson, A.; Flink, A. Nanoindentation hardness, texture and microstructure of α-Al_2O_3 and κ-Al_2O_3 coatings. *Thin Solid Films* **2008**, *516*, 5959–5966. [CrossRef]
26. Riedl, A.; Schalk, N.; Czettl, C.; Sartory, B.; Mitterer, C. Tribological properties of Al_2O_3 hard coatings modified by mechanical blasting and polishing post-treatment. *Wear* **2012**, *289*, 9–16. [CrossRef]
27. Konstantiniuk, F.; Tkadletz, M.; Kainz, C.; Czettl, C.; Schalk, N. Mechanical properties of single and polycrystalline α-Al_2O_3 coatings grown by chemical vapor deposition. *Surf. Coat. Technol.* **2021**, *410*, 126959. [CrossRef]
28. Graça, S.; Trabadelo, V.; Neels, A.; Kuebler, J.; Le Nader, V.; Gamez, G.; Döbeli, M.; Wasmer, K. Influence of mosaicity on the fracture behavior of sapphire. *Acta Mater.* **2014**, *67*, 67–80. [CrossRef]
29. Norton, A.D.; Falco, S.; Young, N.; Severs, J.; Todd, R.I. Microcantilever investigation of fracture toughness and subcritical crack growth on the scale of the microstructure in Al_2O_3. *J. Eur. Ceram. Soc.* **2015**, *35*, 4521–4533. [CrossRef]
30. Stylianou, R.; Velic, D.; Daves, W.; Ecker, W.; Tkadletz, M.; Schalk, N.; Czettl, C.; Mitterer, C. Thermal crack formation in TiCN/α-Al_2O_3 bilayer coatings grown by thermal CVD on WC-Co substrates with varied Co content. *Surf. Coat. Technol.* **2020**, *392*, 125687. [CrossRef]
31. Davidge, R.W.; Riley, F.L. Grain-size dependence of the wear of alumina. *Wear* **1995**, *186–187*, 45–49. [CrossRef]
32. Mukhopadhyay, A.K.; Yiu-Wing, M. Grain size effect on abrasive wear mechanisms in alumina ceramics. *Wear* **1993**, *162–164*, 258–268. [CrossRef]
33. Holmberg, K.; Matthews, A.; Ronkainen, H. Coatings tribology-contact mechanisms and surface design. *Tribol. Int.* **1998**, *31*, 107–120. [CrossRef]
34. Bull, S.J.; Bhat, D.G.; Staia, M.H. Properties and performance of commercial TiCN coatings. Part 2: Tribological performance. *Surf. Coat. Technol.* **2003**, *163–164*, 507–514. [CrossRef]
35. Leyland, A.; Matthews, A. On the significance of the H/E ratio in wear control: A nanocomposite coating approach to optimised tribological behaviour. *Wear* **2000**, *246*, 1–11. [CrossRef]
36. Ma, L.; Howard, I.; Pang, M.; Wang, Z.; Su, J. Experimental Investigation of Cutting Vibration during Micro-End-Milling of the Straight Groove. *Micromachines* **2020**, *11*, 494. [CrossRef] [PubMed]
37. List, G.; Nouari, M.; Géhin, D.; Gomez, S.; Manaud, J.P.; Le Petitcorps, Y.; Girot, F. Wear behaviour of cemented carbide tools in dry machining of aluminium alloy. *Wear* **2005**, *259*, 1177–1189. [CrossRef]

coatings

MDPI

Article

Mechanical Properties and Wear Resistance of CrSiN Coating Fabricated by Magnetron Sputtering on W18Cr4V Steel

Changqing Cui [1,*] and Chunyan Yang [2]

[1] College of Mechanical Engineering, Baicheng Normal University, Baicheng 137000, China
[2] College of Computer Science, Baicheng Normal University, Baicheng 137000, China; liht13@mails.jlu.edu.cn
* Correspondence: bsccq@bcnu.edu.cn; Tel.: +86-15593190528

Abstract: To increase the service life of tool materials and further meet the demands of modern high-speed machining, a Si-doping CrN coating consisting of Si_3N_4 amorphous and CrN nanocrystalline was fabricated on top of W18Cr4V high-speed steel. The effect of coating thickness on its structure and properties was investigated by means of X-ray diffraction (XRD), scanning electron microscope (SEM), transmission electron microscope (TEM), scratch test, nano-indenter, and friction–abrasion tester. The thickness of the coating was modulated by the deposition time. The results show that the coating consists of a CrN phase distributed into an amorphous Si_3N_4 matrix. As the thickness increased, the surface defects decreased, and the residual compressive stress, hardness, and elastic modulus as well as the H/E and H^3/E^2 factors increased, improving the wear resistance significantly. The adhesion between coating and substrate increased first and then decreased, and it reached the maximum when the coating thickness was 1.9 μm (deposition 60 min). Moreover, the effect of toughness on wear resistance and the wear mechanisms is discussed.

Keywords: CrSiN coating; structure; thickness; mechanical property; residual stress; wear resistance

Citation: Cui, C.; Yang, C. Mechanical Properties and Wear Resistance of CrSiN Coating Fabricated by Magnetron Sputtering on W18Cr4V Steel. *Coatings* **2023**, *13*, 889. https://doi.org/10.3390/coatings13050889

Academic Editor: Manuel António Peralta Evaristo

Received: 17 April 2023
Revised: 30 April 2023
Accepted: 6 May 2023
Published: 9 May 2023

1. Introduction

At present, the development of high-speed cutting and dry cutting technology puts forward higher requirements for tool materials and cutting performance, and the cutting tools which are covered by coatings exhibit an important way to improve their surface properties by endowing them with higher hardness and wear resistance [1–4]. In addition to fabrication techniques and methods, the type and structure of the coating is a significant factor in the lifetime of the cutting tools. In the past decades, the tools coated with a transition metal nitride coating, such as TiN [2,5,6], CrN [5], NbN [6], and ZrN [4], demonstrated that they were well resistant to wear. They combine the advantages of high strength and toughness of the steel matrix and high hardness and wear resistance of the coating not only to enable high-speed cutting of tools but also to enhance machining accuracy and quality of the workpiece. Particularly, CrN coatings are expected to be technologically important in many tribocorrosion-resistant applications due to their good wear resistance, corrosion resistance, and oxidation resistance [7].

However, the binary CrN film applied to machining tools, cutting tools, and molds exposed problems with low oxidation temperatures, poor wear resistance, and low thermal hardness [8,9]. Previous reports [1,3,7,10–13] have shown that the Si-doped CrN coatings had better performance than CrN. The addition of Si can refine the grain and improve the hardness, and Si is likely to form the Si_3N_4 amorphous phase with N atoms, which can reduce the columnar crystals of film, obtain more grain boundaries, and prolong the diffusion path of oxygen, thus improving the hardness and high-temperature stability of the coating and inhibiting the formation of cracks in the layers. In addition, Cr and Si in the CrSiN coating can form oxide films of SiO_2 and Cr_2O_3 that are resistant to high-temperature corrosion [10,13]. As a result, CrSiN coatings, with their high hardness and strength, low

friction coefficient, better oxidation resistance, and high thermal shock resistance, have attracted increasing attention in the area of cutting tools and have become one of the important research directions in hard coatings. Scholars at home and abroad have studied the effect of deposition temperature [14,15], matrix bias [15], periodic layers [1], nitrogen flow rate [14], and other process parameters on the performance of CrSiN coating, but the effects of coating thickness on structure and properties have been less reported. In this work, a CrSiN coating with a composite structure is fabricated at various deposition times to obtain different thicknesses, and the influence of the coating thickness on the structure and properties is systematically investigated.

2. Experimental Details

W18Cr4V (commercial high-speed steel) with a dimension of 15 mm × 15 mm × 2 mm was used as the substrate. After grinding, polishing, and ultrasonic cleaning in acetone, anhydrous ethanol, and deionized water rinsing, the steel was loaded into a vacuum chamber. Under a united action of a DC and a bias voltage supply, a pure Cr target and a Si target were first pre-sputtered to ensure the purity of the coating and to produce a micro-convex structure on the W18Cr4V surface to enhance the adhesion between the coating and the steel substrate. A thin bottom Cr layer was then prepared by DC magnetron sputtering in an argon atmosphere. Next, a mixture of Ar and N_2 was introduced into the chamber, and a CrN layer was prepared by DC-sputtering the Cr target. Finally, a CrSiN top layer was deposited in a mixture of Ar and N_2 by co-sputtering Cr and Si targets with DC and Rf power supplies. Table 1 summarizes the deposition parameters used in this study.

Table 1. Processing parameters for coating deposition.

Layer	Bias Voltage (V)	Ar Flow (sccm)	N_2 Flow (sccm)	Power DC(A)/RF(W)	Time (min)
Cr	−50	30	0	0.5/0	5
CrN	−50	30	10	0.5/0	10
CrSiN	−50	30	10	0.5/180	15, 30, 60, 120

The background vacuum was lower than 1×10^{-3} Pa.

The working pressure was 0.5 Pa.

The deposition temperature was 300 °C.

The distance between the target and the substrate was 60 mm.

The deposition times were set to 15 min, 30 min, 60 min, and 120 min. For the sake of illustration, we refer to them T1, T2, T3, and T4, respectively.

A D8 Advance X-ray diffractometer (XRD; Bruker, Billerica, MA, USA) was used to analyze phase structure with a 3-degree grazing incidence, the scanning speed was 8°/min, and the step was 0.05 degree. The Debye–Scherrer equation, shown in Equation (1), is employed to calculate the grain size. The surface morphology was observed by means of JSM-6700 scanning electron microscopy (SEM, FEI, Hillsboro, OR, USA) and Tecnai F20 transmission electron microscopy (TEM, FEI, Hillsboro, OR, USA). A WS-2005 scratch tester (Zhongke Kaihua Co., Ltd., Lanzhou, China) was used to evaluate the adhesion, with a load of 20 N, a scratch length of 3 mm, and a loading rate of 20 N/min, and the scratch morphology was observed by an optical microscope (OM, CR 30-T1000, Suzhou, China) [16,17].

$$D = \frac{k\lambda}{\beta \cos\theta} \quad (1)$$

where k is a constant equal to 0.89, β is half-width of the diffraction peak (in radian), λ is the wavelength of 0.154 nm (Cu k_α), θ is the Bragg Angle (°), and D is the grain size (nm).

The surface mechanical properties were carried out with 3 mN load (kept for 10 s) via a nano-indenter (KLA-Tencor, Milpitas, CA, USA). The loading and unloading speed were

5 mN/min, the indentation depth to eliminate the influence of the W18Cr4V steel [18–20], and it was necessary to measure at least 5 points to avoid error [18]. The error bar was calculated as a standard deviation of the average tested data, which was a result of the variation in the local mechanical properties of the coating [21]. An SFT-2M model pin-on-disk tester (Zhongke Kaihua Co., Ltd., Lanzhou, China) was employed to measure the coefficient of friction (COF) and wear loss rate in a dry environment against a ϕ 6 mm Al_2O_3 ball rotating at 300 rpm (30 °C, relative humidity of 60%). A 200 g normal load was applied for 15 min, and the wear track was observed by using an optical microscope (OM, CR 30-T1000, LTD, Suzhou, China). Residual stress was evaluated by using FST1000 film stress tester (Supro Instruments Co., Ltd., Shenzen, China), measuring the curvature radius (W18Cr4V steel). The value was calculated by Stoney's equation (Equation (2)) [22].

$$\sigma = \frac{E_s}{1-\nu_s}\frac{t_s^2}{6t_f}\left(\frac{1}{R_1}-\frac{1}{R_2}\right) \quad (2)$$

where E_s and ν_s are the elasticity modulus and the Poisson's ratio of the substrate, R_1 and R_2 are the curvature radii of the substrate before and after deposition, and t_s and t_f represent the thicknesses of substrate and coating, respectively. The E_s and ν_s in this investigation are 0.22 and 180 GPa, respectively.

3. Results and Discussion

Figure 1a–d show the cross sections of the coatings. It is clearly observed that the thickness of the CrSiN coating increases significantly from 0.8 to 4.0 μm. The thicknesses are 0.8 μm (T1), 1.2 μm (T2), 1.9 μm (T3), and 4.0 μm (T4), respectively. Each interface is well bonded and uniform in thickness, without obvious defects. Moreover, Figure 1a–d show that the CrSiN coating is well-compact, with a relatively flat cross section, no columnar crystal structure, and that each deposited layer is well-bonded to the other without significant pores, leading to its strong resistance to crack expansion. The addition of Si can refine the columnar crystal structure of the coating and improve the compactness of the coating. Figure 1a–d demonstrate that the coating structure becomes compact as the thickness increases. The compact structure is able to avoid the abrupt sinking of the tip during indentation testing, resulting in high hardness. In addition, elemental analysis of point A on the surface of the T1 coating reveals the presence of Fe, Mo, and V, originating from the W18Cr4V substrate, due to the thin thickness of the T1 sample. In addition, C and O are detected on the surface of the T4 coating due to surface contamination. Excluding the effects of surface contamination and matrix elements, we can say that the thickness has little influence on the element content in the coating, and the main components of the coating are Cr, Si, and N.

Figure 2 presents the surface morphology of the four group samples. Figure 2a exhibits some pits and white particles on the film surface, where pits and particles of various sizes and shapes are clearly visible. The broad pits are clearly visible, and the coating is not completely covered or continuous, which leads to a poor surface density. Figure 2b shows the distribution of a large number of small-sized irregular white particles and some pits and pinholes on the surface of the T2 sample. The number of white particles increases but is significantly reduced in size compared with the T1 sample, resulting in a reduction in surface roughness. In addition, the white particles are concentrated mostly in the lower left, while the upper right is smooth and flat, with no visible particles and a reduced number of pits, indicating an improved surface quality for the T2 coating. Figure 2c illustrates that the T3 coating has only a few white particles on its surface, no pits or pores are observed, and it is smooth and flat. Figure 2d shows that the surface of the T4 coating has few shallow pits and white particles, the number of white particles further decreases, and the coating has a smoother surface. The surface morphology in Figure 2 illustrates that the coating roughness decreases and the surface density improves with the increase in coating thickness.

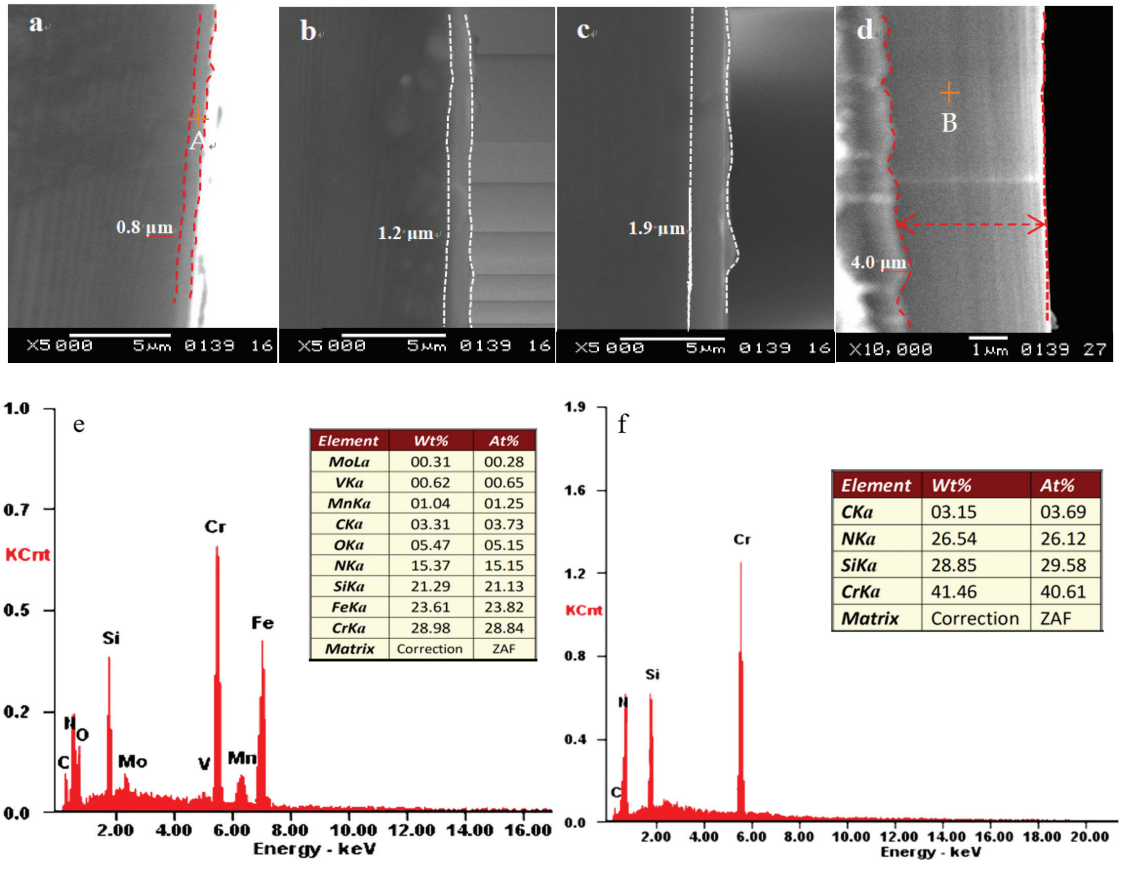

Element	Wt%	At%
MoLa	00.31	00.28
VKa	00.62	00.65
MnKa	01.04	01.25
CKa	03.31	03.73
OKa	05.47	05.15
NKa	15.37	15.15
SiKa	21.29	21.13
FeKa	23.61	23.82
CrKa	28.98	28.84
Matrix	Correction	ZAF

Element	Wt%	At%
CKa	03.15	03.69
NKa	26.54	26.12
SiKa	28.85	29.58
CrKa	41.46	40.61
Matrix	Correction	ZAF

Figure 1. Cross section of the samples, (**a**) T1; (**b**) T2; (**c**) T3; (**d**) T4; (**e**) EDS analysis of the point A; and (**f**) EDS analysis of the point B.

3.1. Microstructure

Figure 3 presents the coating XRD pattern. It is clear that coatings of different thickness have the same shape and crystal plane index of the diffraction peak. There are two types of phase consisting of FCC-CrN phase and Cr phase; the CrN phase corresponds to the (111), (200), (220), and (311) planes (PDF#06-0694), and the Cr phase located at 44.2° corresponds to the (210) index (PDF#19-0323). The CrN phase is formed from the top CrSiN layer, and the Cr phase is formed from the bottom Cr layer. Figure 3 shows that the peak intensity decreases with increasing coating thickness, and the half-width of the diffraction peak increases with an increase of coating thickness, indicating that the grain size of the coating was reduced and more amorphous phases formed. According to Debye–Scherrer, as shown in Equation (1), the grain size reduces a little with an increase in coating thickness—the values are 13.5 nm, 11.8 nm, 10.2 nm, and 8.9 nm, respectively. The reason for the decrease in the grain size with thickness is attributed mainly to thermodynamics. When the coating is deposited for 15 min, the coating thickness is only 0.8 μm, and it tends to grow in a linear fashion, which leads to a relatively high crystallinity in some crystal orientations. On the contrary, the T4 coating with a thickness of 4.0 μm possesses a long time to diffusion and growth. It tends to grow in several orientations; thus, the film is uniform and dense. In addition, no diffraction peaks are detected in Figure 3 for the Si or Si_3N_4 phases, which is most likely due to the amorphous structure generated by Si with N_2

atoms. Therefore, the Si-contained phases are not observed in Figure 3. This is consistent with other studies [10,23].

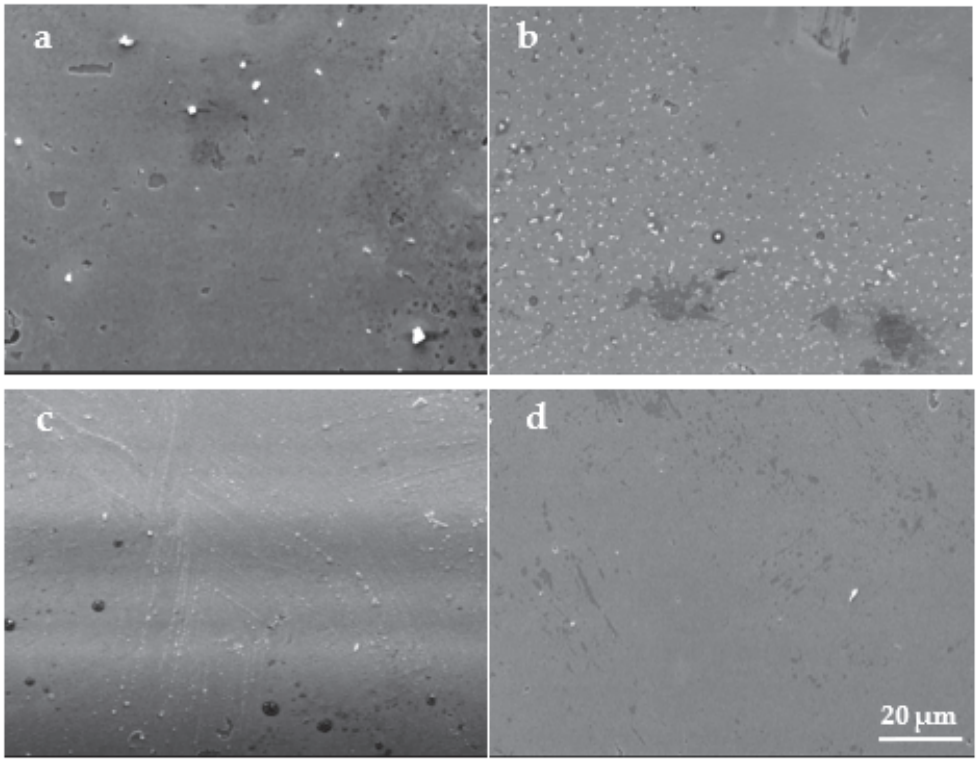

Figure 2. Surface morphology of the coatings: (**a**) T1; (**b**) T2; (**c**) T3; and (**d**) T4.

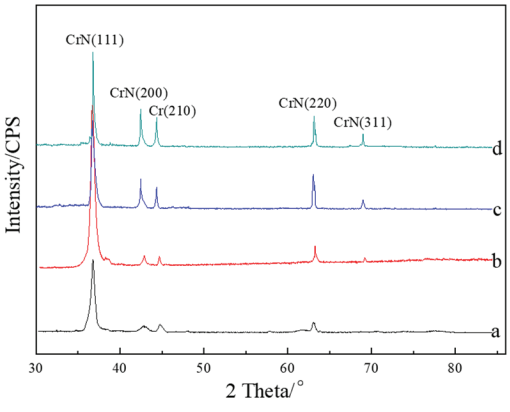

Figure 3. XRD patterns of the coating: a—T4; b—T3; c—T2; and d—T1.

Figure 4 shows the TEM images of the T4 and T1 coatings. It is clearly observed that the structure of the T4 coating is a mixed structure consisting of tiny CrN nanocrystalline and amorphous phases, combining with the XRD pattern, and we know that the CrN nanocrystal is mainly in the (111) index. The selected area electronic diffraction (SAED) in Figure 4c1 (yellow box area in Figure 4a) demonstrates that the T4 sample formed a

large mount of amorphous phases. In contrast, the T1 coating shows a distinct interface consisting of a Cr base layer, a CrN interlayer, and a CrSiN top layer. The Cr layer has the (210) crystal plane with a d-spacing of 2.05 Å, the CrN interlayer shows two indexes of (111) and (200) with d-spacing of 2.4 Å and 2.07 Å, and the CrSiN top layer exhibits d-spaces of 1.25 Å and 2.4 Å, corresponding to the (311) and (111) plane indexes. The SAED image in Figure 4c2 demonstrates the formation of a CrN polycrystalline phase. Following the EDS analysis in the red box region in Figure 4b, we know that this region is dominated by Si and N elements, 40.13 at% and 53.48 at%, respectively, close to 3:4. From this, we deduce that the amorphous phase is Si_3N_4 and that the structure of the T1 coating is a mixture of CrN polycrystalline and Si_3N_4 amorphous phases. Figure 4 demonstrates that as the coating thickness increases, the crystallinity of the coating and the size of the grains decrease significantly, which is in strong agreement with the XRD results.

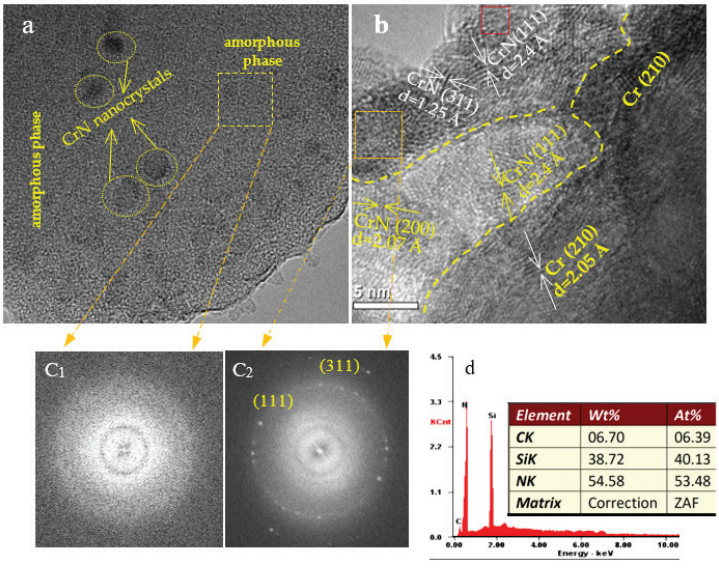

Figure 4. TEM images of the samples: (**a**) T4; (**b**) T1; (**c$_1$**) SAED image of the T4, (**c$_2$**) SAED image of the T1 and (**d**) EDS analysis of the red box area in (**b**).

3.2. Mechanical Properties

Table 2 shows the specific parameters of the nano-indentation, and the corresponding plots can be seen in Figure 5. It is visible that the hardness (H) is approximately 11.75 GPa, 16.15 GPa, 22.77 GPa, and 25.45 GPa, respectively, and the elastic modulus (E) is approximately 130.9 GPa, 148.5 GPa, 180.2 GPa, and 192.6 GPa, respectively. Figure 5 illustrates that the values of *H* and *E* increase with the deposition thickness, suggesting that the mechanical properties of the coating improve. The results demonstrate the good mechanical properties of the composite structure consisting of the nanocrystalline CrN and the amorphous phase, and the tiny CrN grains help to further enhance the mechanical properties of the coating. This is because the strong interfaces between amorphous phase and CrN nanocrystalline effectively prevented dislocation proliferation and grain boundary sliding, which increased the coating hardness [24].

Table 2. The specific parameters of the nano-indentation test.

Parameters	T1	T2	T3	T4
H/GPa	11.75 ± 0.80	16.15 ± 1.10	22.77 ± 1.07	25.45 ± 1.25
E/GPa	130.9 ± 3.0	148.5 ± 4.5	180.2 ± 6.0	192.6 ± 7.2
H/E	0.090 ± 0.005	0.109 ± 0.0065	0.126 ± 0.006	0.132 ± 0.0071
H^3/E^2(GPa)	0.095 ± 0.012	0.191 ± 0.015	0.364 ± 0.030	0.444 ± 0.035

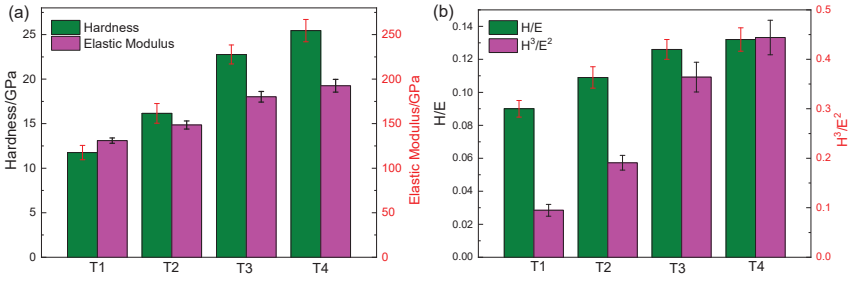

Figure 5. Mechanical property index of the nano-indentation test: (**a**) H and E; (**b**) Elasticity factor (H/E) and shaping factor (H^3/E^2).

In addition, the ratios H/E and H^3/E^2 are two important factors to assess the mechanical properties of the sample, as shown in Table 2 and Figure 5b. The T4 coating exhibits the highest H/E and H^3/E^2 ratio of all the coatings, and the corresponding values are 0.132 and 0.444, respectively. However, the T1 coating exhibits the lowest H/E and H^3/E^2 ratios among all the coatings, namely 0.09 and 0.095. Table 2 and Figure 5 suggest that the H/E and H^3/E^2 values increase with increasing coating thickness. Therefore, it also indicates that an increased coating thickness results in better mechanical properties.

Figure 6 exhibits the relationship between the residual stress and the thickness, according to Equation (2). It is clearly observed that the residual compressive stress of the coating increases with an increasing thickness. When the thickness ranges from 0.8 to 1.9 μm, the increase in residual stress is relatively flat with the thickness. When the coating thickness is in the range of 1.9 to 4.0 μm, the residual stress increases rapidly, and the maximum is −1287 ± 39 MPa when the thickness is approximately 4.0 μm. This demonstrates that the residual stress increases as the thickness increases, especially when the thickness excesses 2.0 μm, which increases the risk of the film peeling off from the matrix due to the high residual stress.

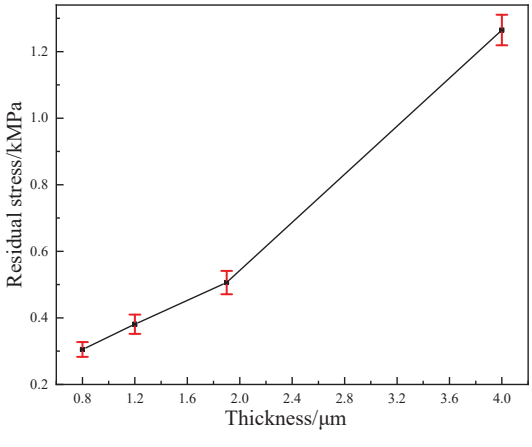

Figure 6. Relationship between residual stress and coating thickness.

The total stress of the film consists of two parts, an internal stress due to imperfections, defects, and lattice deformations in the crystal, and an external stress due to the lattice mismatch between the film and the substrate and different expansion coefficients. During the film growth process, a fraction of the sputtered particles from the target are inserted into the film. At the same time, as the film grows, surface atoms are moved deeper into the growing film by the bombardment of sputtered particles. The interstitial particles and surface atoms of the sputtered particles result in a reduction of the lattice constant and, hence, of the compressive stress. As a result, the compressive stress increases as the film thickness increases. In addition, as the film grows, the diffraction peak widens, the grain size decreases, the grain strengthening effect increases, and the compressive stress gradually increases due to the impact pinning effect of high-velocity particles. As the film thickness increases, the film hardness gradually increases. When the film thickness is sufficiently large, the composite hardness of the film substrate is essentially the same as that of the film, and the effect of the matrix vanishes.

Figure 7 shows the OM morphology during the scratch test. The adhesion properties of the coatings illustrated in Figure 7 are quite different due to the different mechanical properties and surface densities, as well as the coating thickness. As the coating thickness increases, the adhesion first increases and then decreases. The T1 coating presents an adhesion of 4.8 N, the T2 sample shows an adhesion of 7.2 N, and the T3 coating shows that it does not detach continuously from the substrate throughout the scraping process, indicating its highly bonded nature. In the case of the T4 sample, Figure 7d shows that the decrease in adhesion is due mainly to the larger residual stress, and that the T4 coating undergoes continuous peeling when the dynamic load exceeds 9.9 N, so that the adhesion is defined as 9.9 N, which is lower than that of the T3 coating.

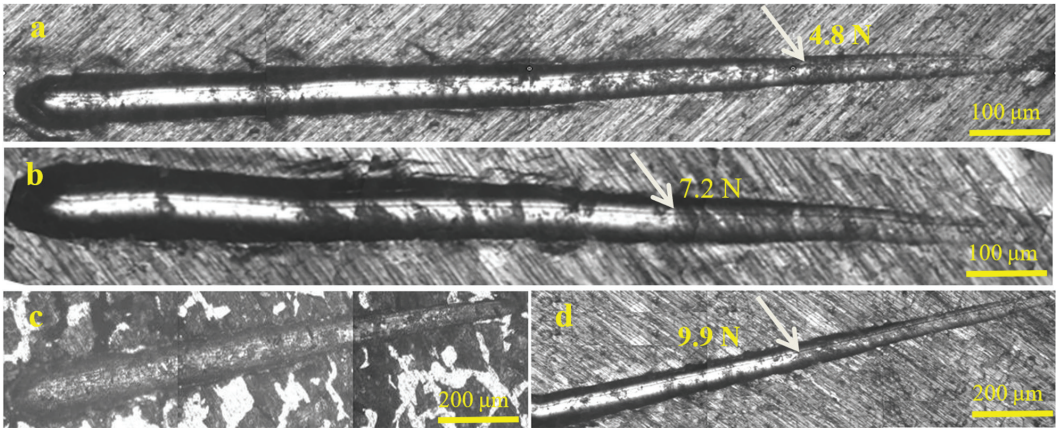

Figure 7. Scratch morphology of the coatings taken by OM: (**a**) T1; (**b**) T2; (**c**) T3; and (**d**) T4.

The lowest adhesion that the T1 sample shows is dominated by the surface defects (pits, pinholes, and white particles), and the defects breaks the continuity of the coated surface and leads to an increase in the roughness of the coated surface, which is the main factor responsible for the decrease in the binding force, which leads to the critical load of the T1 coating of approximately 4.8 N. As shown in Figure 7a, a very long white linear scratch is clearly visible, and it is clear that the matrix was exposed continuously at a load of 4.8 N. In summary, Figure 7 illustrates that the adhesion of the coating increases first with an increase in the thickness, then begins to decrease. The complete and smooth surface with few defects, as well as its highest mechanical properties resulted in its highest adhesion among the four groups.

3.3. Wear Resistance

Figure 8 shows the coefficient of friction (COF) and wear loss rate (WLR) of all coatings. Figure 8a illustrates that the COFs of all test samples exhibit an abrupt fluctuation at the very beginning stage. All the CrSiN films exhibit COFs of 0.2~0.5 and WLRs of (5.83~9.05) $\times$ 10^{-7} $mm^3/N{\cdot}m$. It can be observed that the COF of the T1 coating includes three distinct stages: a run-in period, a continuous decreasing period, and a stable period. During the run-in period, the COF is very high, with a value of approximately 0.88, due to the large actual contact of its defective surface. However, it soon reaches a decreasing stage that exhibits effective protection from the substrate, and this decreasing phase persists for approximately 780 s of the test. The COF then enters a stable period, with a stable value of approximately 0.43. In contrast, the T2 coating is composed of only two phases, including a run-in period and a continuous fluctuation period. During the run-in phase, the COF is approximately 0.5, it soon decreases and increases against at 140 s duration, after which it reaches a stable fluctuation stage with an average value of approximately 0.42. This may be attributed to a mount of white particles which acts as isolation and load-bearing sites, leading to large and persistent fluctuations, in which the wear process is not stable. In the case of T3 and T4 coatings, they exhibit a very smooth friction process with very little fluctuation during the entire friction process, the COFs of them are approximately 0.27 and 0.34, respectively, which is related to grain orientation [25].

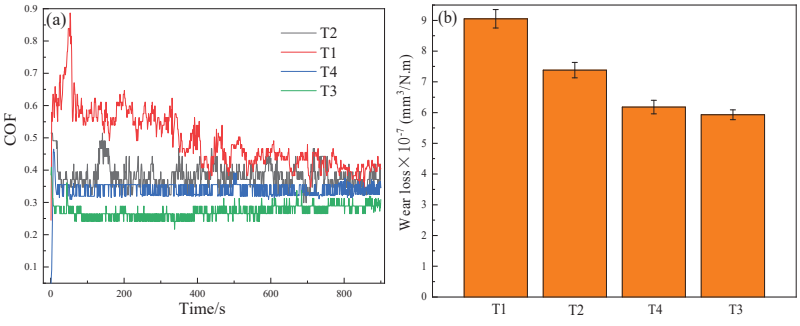

Figure 8. Results of friction–wear test: (**a**) Friction coefficient and (**b**) Wear loss rate.

Figure 8b displays the WLRs of the samples. It is clear that the T1 coating shows the maximum of 9.05 $\times$ 10^{-7} $mm^3/N{\cdot}m$, and the T3 coating has the minimum of 5.83 $\times$ 10^{-7} $mm^3/N{\cdot}m$. The WLRs are consistent with COFs, namely, the T1 sample has the worst wear resistance, whereas the T3 sample has the best wear resistance.

Figure 9 shows the wear tracks for the tested samples. Severe scratches and furrows as well as detachments along the wear scar were observed in Figure 9a,b, and several ploughs and some white wear particles appeared, as well as a little black debris distributed around the edges of the wear track, which indicates that the T1 and T2 coatings belong to abrasive wear and adhesive wear [26]. In addition, the track widths of the T1 and T2 coatings are relatively broad, suggesting their relatively poor wear resistance among the four groups. In contrast, Figure 9c,d only show a number of furrows; the appearance of the furrows indicates the coating belongs to abrasive wear [26]. In addition, the track widths of the T3 and T4 coatings are greatly decreased in comparison with the T1 and T2 coatings, especially for the T3 sample, which has the smallest abrasion mark width. From this, we know that the wear mechanisms of coatings are severe abrasive wear and mild adhesive wear. Moreover, as the coating thickness increases from 0.8 to 4.0 μm, the width and depth of the wear track decrease, implying that the wear resistance improves with an increase of coating thickness. The wear resistance of the T4 sample degrades, which is not a result of its surface density and inter-structure, but rather due to the large residual stress resulting from the large thickness.

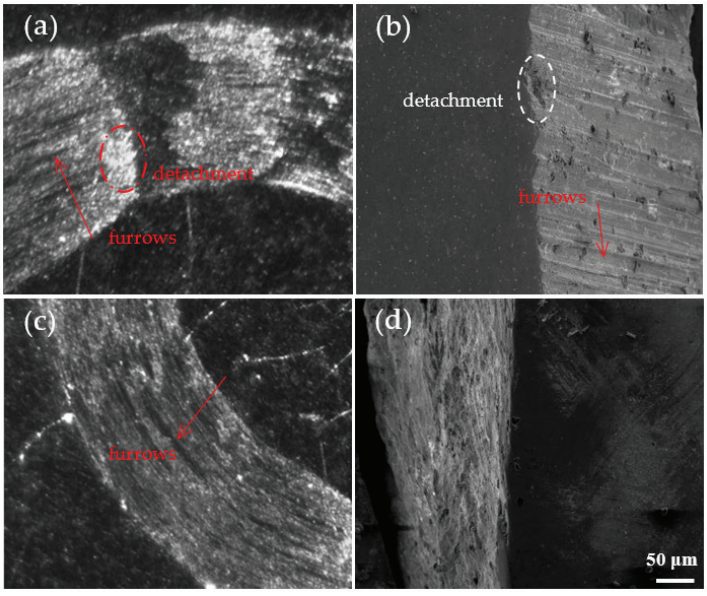

Figure 9. Wear tracks of the coatings: (**a**) T1; (**b**) T2; (**c**) T4; and (**d**) T3.

To further investigate the wear resistance of the coating, the coating toughness was used to illustrate the wear resistance. The H, E, H/E, and H^3/E^2 values of the hard coatings suggested alternating fracture toughness for evaluating wear resistance, and the coatings with H/E>0.1 possessed high elasticity and wear resistance [15,27,28]. In addition, the high H/E ratio is helpful in decreasing the ploughing effect and obtaining a low COF [26]. In the case of the T4 coating, the values of H, E, H/E, and H^3/E^2 exhibit maximum values of 25.45, 192.6 0.132, and 0.444 GPa (Table 2), respectively. That is to say, the T4 coating has the best toughness to resist deformation and wear failure. Thus, the COF and WLR of the coating are the lowest, but this does not take into account the effect of the variation of the coating thickness on the residual stress. In fact, Figure 7 demonstrates that the compress residual stress of the T4 sample is much larger than that of the T3 coating, resulting in wear resistance of the T4 coating being lower than that of the T3.

Moreover, for a hard coating, the factors of H/E and H^3/E^2 are closely related to cracking resistance and plastic deformation, which is often used to assess wear resistance [26–28]. From Table 2, it is seen that the T1 coating shows the lowest toughness (H/E = 0.09), and the T3 coating exhibits the highest toughness (H/E = 0.126) and excellent resistance to plastic deformation (H^3/E^2 = 0.364 GPa). This is also evidence that the T3 coating has good wear resistance. In addition, according to a report [26], higher hardness of the hard coating means higher load-carrying capacity, which is very helpful in reducing plastic yielding and actual contact area with the counterpart, resulting in the amount of wear reduced. However, reports [26,29] tell us that satisfying H/E (>0.1) and H^3/E^2 (0.15~0.3 GPa) are important conditions for good lubrication and good wear resistance, but the T4 coating in this work has the highest H^3/E^2 ratio beyond the range of 0.15~0.3 GPa. Therefore, according to all the results in this paper and reports [26,29], the optimal deposition time is 60 min (thickness of 1.9 μm).

4. Conclusions

The effect of thickness on the structure, mechanical properties, and wear resistance of CrSiN films deposited on the surface of W18Cr4V by DC and RF magnetron sputtering is investigated in this work. The details are summarized as follows:

(1) The crystal phase of coating is a mixture of nano-sized CrN and amorphous Si_3N_4 phase, and the size of CrN phase reduces as the coating thickness increases.

(2) With the increase in coating thickness, the surface roughness, grain size, and the number of defects decrease, whereas the toughness, wear resistance, and mechanical properties significantly improved. The coating is well bonded with the substrate. When the coating thickness increases, the adhesion first increases and then decreases, and the residual stress increases. The T3 sample with a thickness of 1.9 μm has the largest adhesion, and the T4 sample with a thickness of 4.0 μm has the largest compress residual stress.

(3) The T4 coating with a thickness of 4.0 μm possesses the highest hardness, elasticity modulus, H/E, and H^3/E^2 ratios. The T3 coating with a thickness of 1.9 μm possesses the lowest COF and WLR, whereas the T1 coating with a thickness of 0.8 μm possesses the lowest hardness, elasticity modulus, and the highest COF and WLR.

(4) The toughness and residual stress, which have a close relationship with thickness, are the important factors affecting the wear resistance of the CrSiN coating, but the excessive ratio of H/E and H^3/E^2 and high residual stress are not helpful in enhancing wear resistance, Thus, in this work, the T3 coating with a thickness of 1.9 μm is preferred for wear resistance application.

Author Contributions: C.C., conceptualization, supervision, writing—original draft, and data curation; C.Y., methodology, investigation, formal analysis, and writing—review and editing. All authors have read and agreed to the published version of the manuscript.

Funding: This research received no external funding.

Institutional Review Board Statement: Not applicable.

Informed Consent Statement: Not applicable.

Data Availability Statement: Not applicable.

Conflicts of Interest: There are no conflict of interest in this work, including financial interests, personal relationships, or other aspects that influence the work published.

References

1. Cai, F.; Zhang, J.; Wang, J.; Zheng, J.; Wang, Q.; Zhang, S. Improved adhesion and erosion wear performance of CrSiN/Cr multi-layer coatings on Ti alloy by inserting ductile Cr layers. *Tribol. Int.* **2021**, *153*, 106657. [CrossRef]
2. Li, H.T.; Sun, P.F.; Cheng, D.H.; Liu, Z.M. Effects of deposition temperature on structure, residual stress and corrosion behavior of Cr/TiN/Ti/TiN films. *Ceram. Int.* **2021**, *47*, 34909–34917. [CrossRef]
3. Li, W.; Liu, P.; Meng, J.; Zhang, K.; Ma, F.; Liu, X.; Chen, X.; He, D. Microstructure and mechanical property of TiSiN nanocomposite film with inserted CrAlN nanomultilayers. *Surf. Coat. Technol.* **2016**, *286*, 313–318. [CrossRef]
4. Deng, J.X.; Liu, J.H.; Ding, Z.L.; Niu, M. Unlubricated friction and wear behaviors of ZrN coatings against hardened steel. *Mater. Des.* **2008**, *29*, 1828–1834. [CrossRef]
5. Leonov, A.A.; Denisova, Y.A.; Denisov, V.V.; Syrtanov, M.S.; Shmakov, A.N.; Savostikov, V.M.; Teresov, A.D. Structure and properties of CrN/TiN multi-layer coatings obtained by vacuum-arc plasma-assisted deposition method. *Coatings* **2023**, *13*, 351. [CrossRef]
6. Sugumaran, A.A.; Purandare, Y.; Shukla, K.; Khan, I.; Ehiasarian, A.; Hovsepian, P. TiN/NbN nanoscale multilayer coatings deposited by high power impulse magnetron sputtering to protect medical-grade CoCrMo alloys. *Coatings* **2021**, *11*, 867. [CrossRef]
7. Shao, T.; Ge, F.F.; Dong, Y.; Li, K.; Li, P.; Sun, D.E.; Huang, F. Microstructural effect on the tribo-corrosion behaviors of magnetron sputtered CrSiN coatings. *Wear* **2018**, *416–417*, 44–53. [CrossRef]
8. Aissani, L.; Alhussein, A.; Zia, A.W.; Mamba, G.; Rtimi, S. Magnetron sputtering of transition metal nitride thin films for environmental remediation. *Coatings* **2022**, *12*, 1746. [CrossRef]

9. Tranca, D.E.; Sobetkii, A.; Hristu, R.; Anton, S.R.; Vasile, E.; Stanciu, S.G.; Banica, C.K.; Fiorentis, E.; Constantinescu, D.; Stanciu, G.A. Structural and mechanical properties of CrN thin films deposited on Si substrate by using magnetron techniques. *Coatings* **2023**, *13*, 219. [CrossRef]
10. Zhou, Z.C.; Zhang, H.; Zhang, X.; Chang, W.J.; Song, L.L.; Huang, C.; Duo, S.W. Friction and wear behavior of CrSiN coatings deposited by plasma enhanced magnetron sputtering. *Surf. Technol.* **2020**, *8*, 185–191. (In Chinese)
11. Wang, Q.M.; Kim, K.H. Microstructure control of Cr-Si-N films by a hybrid arc ion plating and magnetron sputtering process. *Acta Mater.* **2009**, *57*, 4974–4987. [CrossRef]
12. Chang, W.J.; Zhang, H.; Chen, Y.Y.; Li, J.; Zhang, X.; Jiang, P.Z.; Fan, X.W.; Duo, S.W. Tribological performances of CrSiN coatings deposited by high power pulse magnetron sputtering. *Solid State Phenom.* **2018**, *281*, 540–545. [CrossRef]
13. Chen, H.; Ye, Y.; Wang, C.; Ma, X.; Wang, H.; Liu, W. Understanding the corrosion and tribological behaviors of CrSiN coatings with various Si contents in HCl solution. *Tribol. Int.* **2019**, *131*, 530–540. [CrossRef]
14. Shah, H.N.; Jayaganthana, R.; Kaur, D. Influence of reactive gas and temperature on structural properties of magnetron sputtered CrSiN coatings. *Appl. Surf. Sci.* **2011**, *257*, 5535–5543. [CrossRef]
15. Chang, L.C.; Sung, M.C.; Chen, Y.I. Effects of bias voltage and substrate temperature on the mechanical properties and oxidation behavior of CrSiN films. *Vacuum* **2021**, *194*, 110580. [CrossRef]
16. Sveen, S.; Andersson, J.; M'saoubi, R.; Olsson, M. Scratch adhesion characteristics of PVD TiAlN deposited on high speed steel, cemented carbide and PCBN substrates. *Wear* **2013**, *308*, 133–141. [CrossRef]
17. Capote, G.; Silva, G.F.; Trava-Airoldi, V.J. Effect of hexane precursor diluted with argon on the adherent diamond-like properties of carbon films on steel surfaces. *Thin Solid Film.* **2015**, *589*, 286–291. [CrossRef]
18. Wang, W.L.; Yu, L.H.; Xu, J.H. Preparation of CrSiN-Ag films and evaluation of their properties. *Mater. Prot.* **2018**, *51*, 12–17. (In Chinese)
19. Li, H.T.; Sun, P.F.; Cheng, D.H. Structure and properties of a-C:H:Si:O films deposited by cage-like hollow cathode discharge on AZ31 alloy. *Tribol. Int.* **2022**, *175*, 107848. [CrossRef]
20. Li, H.T.; Sun, P.F.; Cheng, D.H. Structure and properties of DLC films deposited on Mg alloy at different C_2H_2 flows of magnetron sputtering process. *Coatings* **2021**, *11*, 815. [CrossRef]
21. Daghbouj, N.; Sen, H.; Čížek, J.; Lorinčík, J.; Karlík, M.; Callisti, M.; Čech, J.; Havránek, V.; Li, B.; Krsjak, V.; et al. Characterizing heavy ions-irradiated Zr/Nb: Structure and mechanical properties. *Mater. Des.* **2022**, *219*, 110732. [CrossRef]
22. Bouabibsa, I.; Lamri, S.; Sanchette, F. Structure, mechanical and tribological properties of Me-doped diamond-like carbon (DLC) (Me=Al, Ti or Nb) hydrogenated amorphous carbon coatings. *Coatings* **2018**, *8*, 370. [CrossRef]
23. Zhu, L.-H.; Song, C.; NI, W.-Y.; Liu, Y.-X. Effect of 10% Si addition on cathodic arc evaporated TiAlSiN coatings. *Trans. Nonferrous Met. Soc. China* **2016**, *26*, 1638–1646. [CrossRef]
24. Su, K.; Liu, D.M.; Shao, T.M. Microstructure and mechanical properties of TiAlSiN nano-composite coatings deposited by ion beam assisted deposition. *Sci. China (Technol. Sci.)* **2015**, *58*, 1682–1688. [CrossRef]
25. AlMotasem, A.T.; Daghbouj, N.; Sen, H.S.; Mirzaei, S.; Callisti, M.; Polcar, T. Influence of HCP/BCC interface orientation on the tribological behavior of Zr/Nb multilayer during nanoscratch: A combined experimental and atomistic study. *Acta Mater.* **2020**, *249*, 118832. [CrossRef]
26. Cao, H.S.; Liu, F.J.; Li, H.; Luo, W.Z.; Qi, F.G.; Lu, L.W.; Zhao, N.; Ouyang, X.P. Effect of bias voltage on microstructure, mechanical and tribological properties of TiAlN coatings. *Trans. Nonferrous Met. Soc. China* **2022**, *32*, 3596–3609. [CrossRef]
27. Chen, X.; Du, Y.; Chung, Y.W. Commentary on using H/E and H^3/E^2 as proxies for fracture toughness of hard coatings. *Thin Solid Film.* **2019**, *688*, 137265. [CrossRef]
28. Li, H.; Liu, Z.; Li, J.; Huang, J.; Kong, J.; Wu, Q.; Xiong, D. Effects of Hf addition on the structure, mechanical and tribological properties of CrN film. *Surf. Coat. Technol.* **2020**, *397*, 126067. [CrossRef]
29. Musil, J.; Novák, P.; Čerstvý, R.; Soukup, Z. Tribological and mechanical properties of nanocrystallineTiC/a-C nanocomposite thin films. *J. Vac. Sci. Technol. A* **2010**, *28*, 244–249. [CrossRef]

coatings

MDPI

Article

Sunlight-Activated Long Persistent Luminescent Coating for Smart Highways

Mao Zheng [1], Xin Li [1], Yu Bai [1], Shijun Tang [1], Peiyang Li [2] and Qi Zhu [2,*]

[1] Sichuan Shugong Expressway Mechanisation Engineering Co., Ltd., Chengdu 610000, China; scjjzhengmao@163.com (M.Z.); xin15884884328@163.com (X.L.); baixiaobai02131218@163.com (Y.B.); tangshijun715@126.com (S.T.)

[2] Key Laboratory for Anisotropy and Texture of Materials (Ministry of Education), School of Materials Science and Engineering, Northeastern University, Shenyang 110819, China; lipeiyangneu@126.com

* Correspondence: zhuq@smm.neu.edu.cn

Abstract: With the whole society's demand for intelligence, the smart highway has become the inevitable trend of road development. Luminescent road marking made of long persistent luminescent coating is a new type of functional marking that is designed with long afterglow luminescent material as the raw material and has many features such as safety, beauty and energy saving. Here, $SrA1_2O_4:Eu^{2+},Dy^{3+}$ green long afterglow phosphors were prepared using a high-temperature solid state method. The green phosphors obtained at 1350 °C have two traps with a shallow trap depth of 0.66 eV and a deep trap depth of 0.8 eV. The green afterglow can be seen in the dark for more than 8 h after sunlight excitation for 2 h. The green long persistent luminescent coatings were synthesized using the blending method. The uniformity of each component can be improved by adding 1.25% SiO_2 into the luminescent coatings. The addition of 3.5% $CaCO_3$ will improve the compactness of the coatings and reduce water absorption. After soaking in water for 120 h, the afterglow intensity of the coating decreases to 76% of the original, showing good water resistance. After daylight excitation in different weather conditions (cloudy, sunny, rainy), the afterglow can reach more than 5 h; therefore, it can be applied to a smart highway.

Keywords: $SrA1_2O_4:Eu^{2+},Dy^{3+}$; luminescent coating; afterglow; smart highway

Citation: Zheng, M.; Li, X.; Bai, Y.; Tang, S.; Li, P.; Zhu, Q. Sunlight-Activated Long Persistent Luminescent Coating for Smart Highways. *Coatings* **2023**, *13*, 1050. https://doi.org/10.3390/coatings13061050

Academic Editor: Mathieu G. Silly

Received: 12 May 2023
Revised: 31 May 2023
Accepted: 4 June 2023
Published: 6 June 2023

1. Introduction

Due to the promotion of energy conservation and emission reduction all over the world, long afterglow materials have attracted great attention with their excellent characteristics. Long afterglow materials can store energy and emit light of different colors at the same time under the irradiation of different light sources (ultraviolet light, visible light or near infrared light), electron beams or high energy rays. When the external energy stops irradiating, the stored energy can be slowly released in the form of light to achieve non-electric luminescence; therefore, it is also known as luminous material [1,2]. At present, several green long afterglow phosphors with excellent persistence properties have been reported such as $SrAl_2O_4:Eu^{2+},Dy^{3+}$ [3], $Li_2MgGeO_4:Mn^{2+}$ [4], $Ca_2MgSi_2O_7:Eu^{2+},Dy^{3+}$ [5], $Ba_2SiO_4:Eu^{2+},Ho^{3+}$ [6], $Ga_4GeO_8:Tb^{3+}$ [7], $Sr_3Ga_4O_9:Tb^{3+}$ [8], and $Zn_2SiO_4:Mn^{2+},Pr^{3+}$ [9]. Among them, $SrA1_2O_4:Eu^{2+},Dy^{3+}$ is one of the most studied green long afterglow phosphors. It has several advantages, including stable luminescence, high efficiency, less toxicity than sulfide, and good afterglow luminescence properties [10–12]. In addition, it can be excited effectively by sunlight or visible light to emit green light. The main synthesis methods reported by researchers include sol-gel, combustion and high-temperature solid state methods [13–16], all of which can produce a sample with a long green afterglow.

As an environment-friendly material, long afterglow phosphor has been widely used in safety signs, emergency signals and persistent pigments [17–19]. Since the 21st century, due to the rapid development of science and technology, especially the rapid development

of artificial intelligence and big data, intelligent transportation has become an inevitable trend of road development. In order to meet the needs of a smart highway, new pavement materials with self-capture [20], self-illumination [21], self-regulation of temperature [22] and self-healing functions [23] have been proposed. In recent years, long afterglow phosphor has received much attention among luminescent coatings [24–27]. With the deepening of technology research and application, the use of long afterglow energy storage luminescent coatings made of road markings can improve the recognition and safety in dust, haze or other harsh environments; at the same time, it will also save a lot of power resources. However, the research of luminescent coating based on road marking is still in its infancy, and there are still many theoretical and application problems to be solved. For example, the luminescent coating prepared by adding phosphor into the coating cannot achieve the ideal luminescent effect and cannot guarantee the stability of luminescent coating in the external environment. Therefore, the research on the best components and processes of the long afterglow energy storage luminescent coating has become a hot topic. The composition of luminescent coating is mainly composed of film-forming material, long afterglow phosphors, fillers and additives [28]. The film-forming material has the ability to adhere to substances and form a film. It is the base of paint, sometimes also known as the base material. The addition of the fillers SiO_2 and $CaCO_3$ can improve the compactness and uniformity of each component in luminous coatings, along with reducing the cost.

In this study, we successfully synthesized the $SrA1_2O_4:Eu^{2+},Dy^{3+}$ phosphor using a high-temperature solid state method. The phosphor was selected as the raw material for luminescent coating and acrylic emulsion was used as the film-forming material. Using the blending method, $SrA1_2O_4:Eu^{2+},Dy^{3+}$ phosphors, acrylic emulsion, SiO_2 and $CaCO_3$ were mixed evenly under the action of additives to obtain green long persistent luminescent coatings. X-ray diffraction (XRD), field-emission scanning electron microscopy (FE-SEM), excitation (PLE) spectrum, emission (PL) spectrum, afterglow spectrum and afterglow decay curves were used to characterize the phosphor and coatings. Through composition regulation, green long persistent luminescent coating was successfully prepared, which exhibited a potential application in a smart highway.

2. Experimental Section

2.1. Preparation of Phosphor

The $SrAl_2O_4:0.01Eu^{2+},0.02Dy^{3+}$ phosphor was prepared using a high-temperature solid state method. The raw materials were analytical-grade reagents $SrCO_3$, Al_2O_3, Eu_2O_3, Dy_2O_3 and H_3BO_3, all purchased from Sinopharm Chemical Reagent Co. LTD (Shanghai, China) with a purity of 99.9%. The ingredients were accurately weighed according to the stoichiometric ratio, and then 5% of the mass of the matrix material H_3BO_3 was weighed as the flux. After grinding the powders in agate mortar for 30 min, the phosphor was obtained by calcination for 2 h in a reducing atmosphere of 10% H_2/90% N_2 at 1350 °C.

2.2. Preparation of Long Persistent Luminescent Coating

The film-forming substance was acrylic emulsion purchased from Hebei Taiji Chemical Industry Co. LTD (chemically pure, Hebei, China). The additives were a thickening agent, film-forming agent, anti-sedimentation agent and silane coupling agent purchased from Shenzhen Jitian Chemical Co. LTD (chemically pure, Shenzhen, China), and the fillers were SiO_2 and $CaCO_3$ purchased from Sinopharm Chemical Reagent Co. LTD (99.99% pure, Shanghai, China). First, the required reagents were weighed according to the raw material ratio. Using the blending method, water, thickening agent, SiO_2 and $CaCO_3$ were mixed and then mixed with acrylic emulsion and film-forming agent directly. After stirring for 10 min, $SrAl_2O_4:Eu^{2+},Dy^{3+}$ phosphors, anti-sedimentation agent and silane coupling agent were added, following by stirring for 15 min, to obtain a green long persistent luminescent coating.

2.3. Characterization Techniques

The purity of the phase was measured by X-ray diffraction (XRD, Model SmartLab, Rigaku, Tokyo, Japan). The diffraction data were detected at 40 kV/40 mA, and the Cu Kα radiation was filtered by nickel. The scanning speed and scanning range were 10.0° 2θ/min and 10°–70°, respectively. The microscopic morphology of the samples was observed with field-emission scanning electron microscopy (FE-SEM, Model S-4800, Hitachi, Tokyo, Japan) at an acceleration voltage of 15 kV. The photoluminescence spectra, afterglow spectra and afterglow decay curves of phosphor and luminescent coating were measured by a Model JY FL3-21 spectrophotometer (Horiba, Kyoto). After exposure to a 365 nm UV light for 5 min at room temperature, the thermoluminescence glow curve of the phosphor was measured on a spectrometer (Model FJ-427A TL, Beijing Nuclear Instrument Factory, Beijing, China) at a heating rate of 1 $K \cdot s^{-1}$.

3. Results and Discussion

Figure 1a shows the XRD pattern of the $SrAl_2O_4:Eu^{2+},Dy^{3+}$ phosphor. It can be seen that all diffraction peaks of the sample match well with the peaks of the standard diffraction of $SrAl_2O_4$ (JCPDS No. 34-0379), indicating that a pure phase sample has been obtained. The diffraction peaks are very sharp, which indicates the high crystallinity of the sample. Figure 1b shows the FE-SEM morphology of the $SrAl_2O_4:Eu^{2+},Dy^{3+}$ phosphor, in which it can be seen that the selected particle size is approximately 15 μm. The elemental mapping results in Figure 1c confirm that all elements are evenly distributed in the particle. It is further proved that the sample obtained is a solid solution.

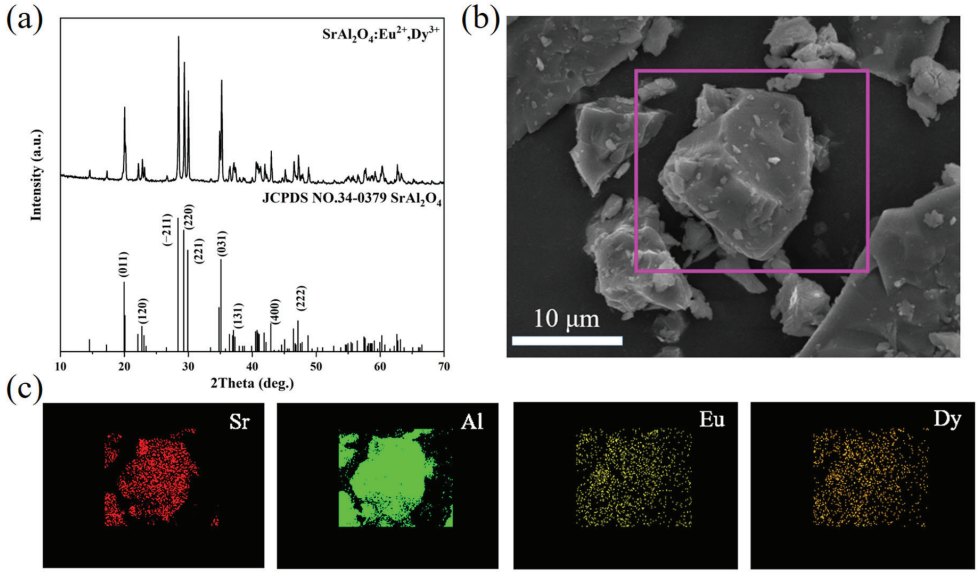

Figure 1. (**a**) XRD pattern and (**b**) FE-SEM image of the $SrAl_2O_4:Eu^{2+},Dy^{3+}$ phosphor. (**c**) Elemental mapping images of Sr, Al, Eu and Dy for the selected particle.

Figure 2a shows the photoluminescence excitation (PLE) and photoluminescence (PL) spectra of the $SrAl_2O_4:Eu^{2+},Dy^{3+}$ phosphor. The PLE spectrum monitored at 522 nm contains a broad band from 300 nm to 500 nm, with the maximum at ~397 nm. Thus, the sample can be effectively excited by daylight or visible light. When excited by UV light at 397 nm, the sample exhibits a green emission with a peak at 522 nm, which is attributed to the $5d^1$–$4f^7$ transition of Eu^{2+} [29]. Figure 2b shows the afterglow spectrum of the $SrAl_2O_4:Eu^{2+},Dy^{3+}$ sample. The afterglow emission wavelength is 522 nm, which is

assigned to the $5d^1$–$4f^7$ transition of Eu^{2+} [30]. The CIE chromaticity diagram is utilized to analyze the afterglow emission color and indicates that the color is located in the green region with coordinate of (0.284, 0.543), as shown in Figure 2c. The afterglow decay curve in Figure 2d describes how the green afterglow of the sample can last more than 1000 s, which is detected at 522 nm after 5 min excitation by a 365 nm UV lamp. The afterglow phenomenon is determined by the existence of traps in the materials. The thermoluminescence (TL) curve is an important method to characterize the trap in phosphors [31]. In Figure 2e, the traps of the sample are tested and analyzed. The TL curve of phosphor covers a wide range from 320 K to 420 K, with two peaks centered at 342 K and 395 K. The following function is used to calculate the depth of the trap (E) [32]:

$$E = \frac{T_m}{500} \tag{1}$$

where T_m is the temperature of the peak maximum in the TL curves (Kelvin temperature). The trap depths of the sample are 0.68 eV for 342 K and 0.79 eV for 395 K, respectively. Among them, the shallow trap at 0.68 eV leads to a high initial afterglow intensity and the deep trap at 0.79 eV leads to long lasting afterglow phenomena. After sunlight excitation for 2 h, a green afterglow lasting more than 8 h in the dark can be seen by the naked eye (Figure 2f). Therefore, $SrAl_2O_4$:Eu^{2+},Dy^{3+} can serve as a potential long afterglow luminescence material for application in a smart highway.

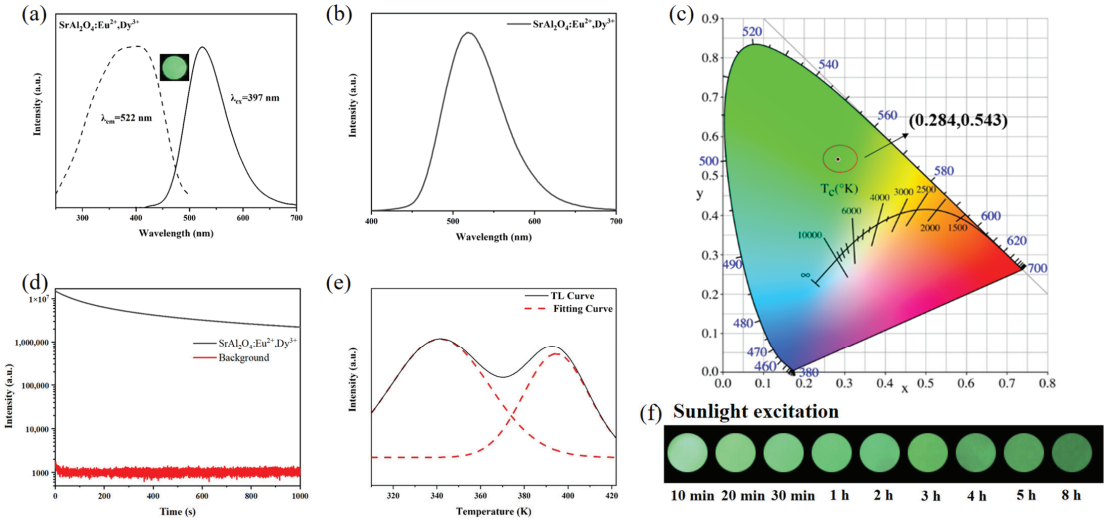

Figure 2. (**a**) PLE and PL spectra of $SrAl_2O_4$:Eu^{2+},Dy^{3+} phosphor, with inset showing the digital photo under 365 nm UV light irradiation of phosphor. (**b**) Afterglow spectrum, (**c**) CIE chromaticity coordinates, (**d**) afterglow decay curve and (**e**) TL glow curve of the $SrAl_2O_4$:Eu^{2+},Dy^{3+} phosphor obtained after 5 min illumination with 365 nm UV light. (**f**) Afterglow images of $SrAl_2O_4$:Eu^{2+},Dy^{3+} phosphor taken after sunlight excitation for 2 h.

The green long persistent luminescent coating is prepared by using the blending method. Then, it is coated on the substrate and dried at room temperature to obtain the green luminescent coating (Figure 3), which can be tested and analyzed later.

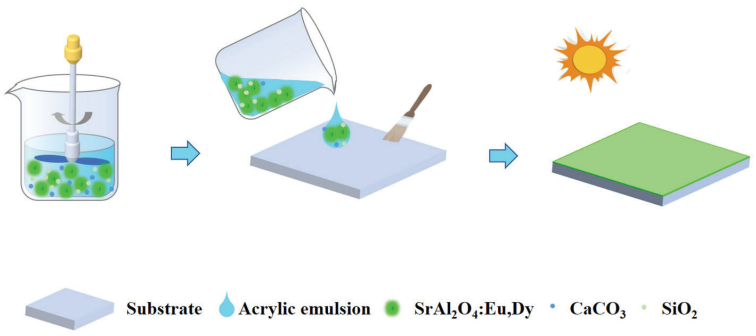

Figure 3. Schematic illustration of the preparation process of luminescent coating.

As can be seen from the XRD pattern in Figure 4a, the diffraction peaks of green luminescent coating correspond exactly to the positions of the diffraction peaks of $SrAl_2O_4:Eu^{2+},Dy^{3+}$ phosphor, but the peak intensity drops a lot [33,34]. The crystal structure of phosphor is not changed when $SrAl_2O_4:Eu^{2+},Dy^{3+}$ phosphor is used to prepare luminescent coating. Therefore, the characterization and analysis of green luminescent coating can be carried out. Figure 4b shows an FE-SEM image of the cross section of green luminescent coating. The irregularly shaped particles of approximately 10–30 μm in the luminescent coating are $SrAl_2O_4:Eu^{2+},Dy^{3+}$ phosphor, indicating that there is no agglomeration of phosphor during the preparation of luminescent coating [35,36]. The element mapping analysis (Figure 4c) is performed on the selected region of the luminescent coating cross section. It is shown that Sr, Al, C, Si and Ca elements are detected. Furthermore, the $SrAl_2O_4:Eu^{2+},Dy^{3+}$ phosphor, SiO_2 powder and filler $CaCO_3$ are dispersed in the acrylic emulsion, and the green luminescent coating with uniform dispersion of each component is obtained.

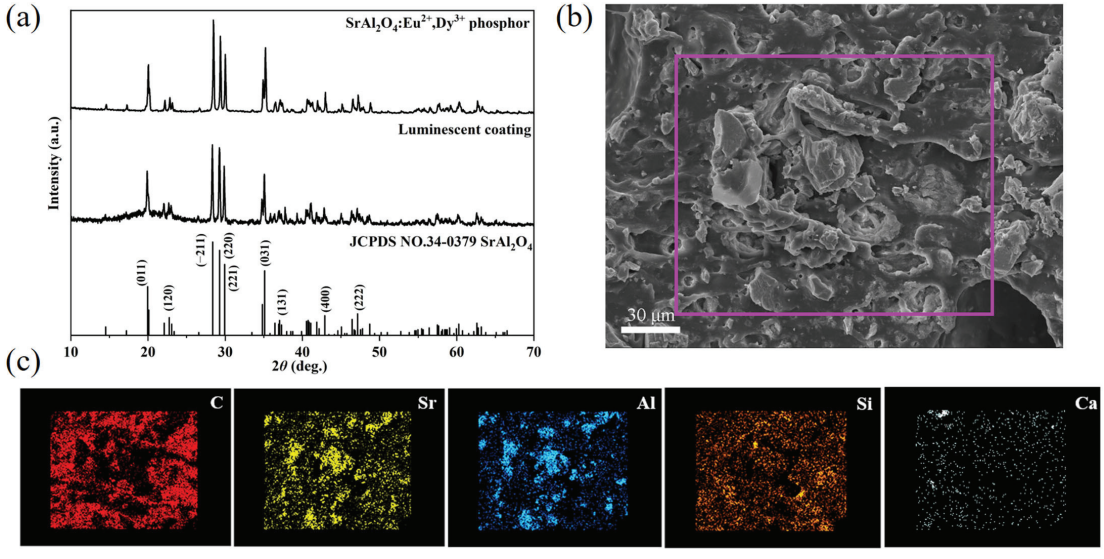

Figure 4. (**a**) XRD patterns of $SrAl_2O_4:Eu^{2+},Dy^{3+}$ phosphor and luminescent coating. (**b**) FE-SEM image for cross section of luminescent coating. (**c**) Elemental mapping images of C, Sr, Al, Si and Ca for the selected region.

Figure 5 shows cross sections of the morphology of the luminescent coating with different SiO_2 contents. It can be seen that when the incorporation content is small, pores

will be generated in the coating (Figure 5a), which will affect the compactness of the luminescence coating. If the content is too high, the components in the coating will gather (Figure 5e), which may affect the luminescence performance. Therefore, the proper addition of 1.25% SiO_2 to the luminescence coating will make the coating more evenly dispersed (Figure 5d), and thus, make it achieve the best luminous effect [37,38].

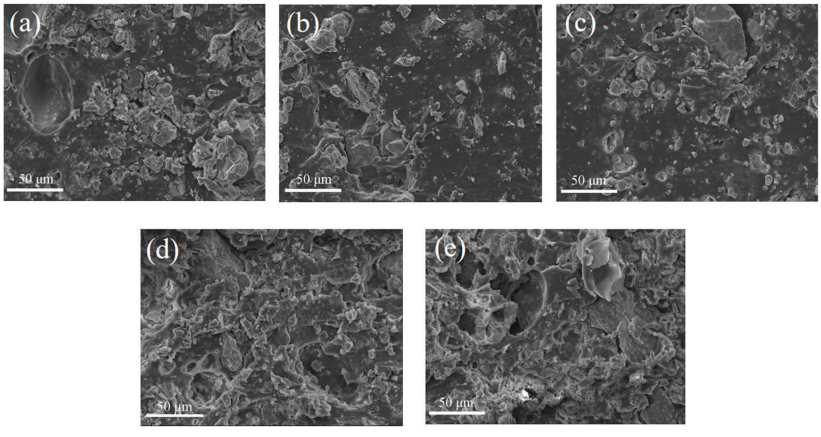

Figure 5. FE-SEM images of luminescent coating cross sections with different SiO_2 contents: (**a**) 0.5%, (**b**) 0.75%, (**c**) 1%, (**d**) 1.25% and (**e**) 1.5%.

The water absorption of a material is closely related to its porosity and pore structure characteristics. The water absorption of luminescent coatings with different $CaCO_3$ contents are tested and calculated according to the following formula [39]:

$$m_t = \frac{(m_2 - m_1)}{m_1} 100\% \tag{2}$$

where m_t is water absorption of the sample, m_1 is mass of the sample before soaking and m_2 is mass of the sample after soaking. It can be seen from Figure 6 that all curve trends are divided into two stages. At the initial stage, the water absorption of the luminescent coating increases rapidly with the increase in soaking time. After about five days, the water absorption of coatings basically no longer has a large change, reaching saturation. At the saturation stage, the water absorption of the luminescent coating mixed with 3.5% $CaCO_3$ is the lowest, which is close to 26%. As depicted in Figure 6, the initial water absorption is nonlinearly fitted using Equation (3) [40]:

$$m_t = K \cdot t^n \tag{3}$$

where m_t is the water absorption of the coating at time t and K and n are constants. When the process exhibits ideal Fickian behaviour, n is equal to 0.5. The n values of the luminescent coatings with different $CaCO_3$ contents are all close to 0.5. Therefore, the diffusion behavior of water in the coatings basically conforms to the ideal Fickian behavior. On this basis, the diffusion coefficient can be calculated using Equation (4) [41]:

$$\frac{m_t}{m_s} = \frac{4\sqrt{D}}{L\sqrt{\pi}} \sqrt{t} \tag{4}$$

where m_t is the water absorption of the coating at time t, m_s is the water absorption of the coating when it is saturated, L is the coating thickness (cm) and D is the diffusion coefficient ($cm^2 \cdot s^{-1}$). Equation (4) shows that m_t/m_s is proportional to $t^{1/2}$ and such that the diffusion coefficient can be obtained by linear fitting [42]. It can be seen from Figure 7 that with the

increase in $CaCO_3$ content, the diffusion coefficient increases first and then decreases, and the diffusion coefficient of the coating mixed with 3.5% $CaCO_3$ is the lowest. Therefore, appropriate addition of $CaCO_3$ will improve the density of the luminescent coating and reduce the water absorption. The hardness of the luminescent coating with 3.5% $CaCO_3$ is 0.5 GPa, as tested by an automatic microhardness tester.

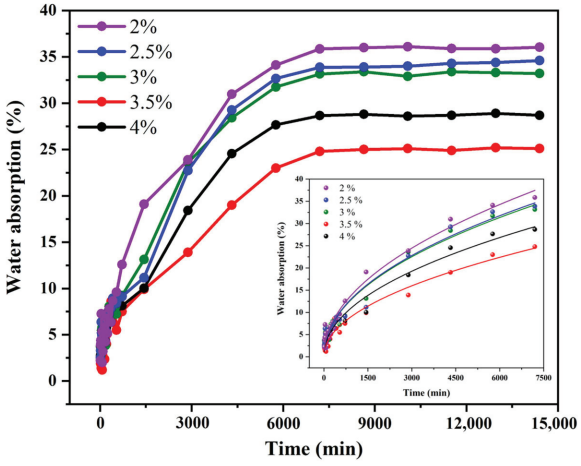

Figure 6. Water absorption of luminescent coatings with different $CaCO_3$ contents. The inset is the fitting diagram of water absorption.

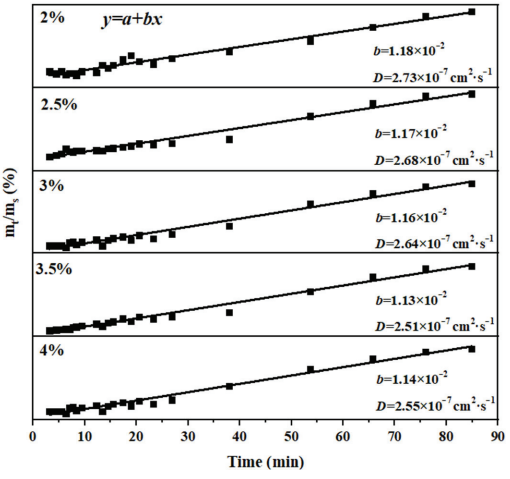

Figure 7. The relationship between water absorption and immersion time of luminescent coatings with different $CaCO_3$ contents.

Figure 8 shows the PLE spectra, PL spectra, afterglow spectra and afterglow decay curves of luminescent coatings with different ratios of phosphor to emulsion. As shown in Figure 8a, the excitation spectra include a broad band centered around 397 nm. Therefore, the green luminescent coatings can be effectively excited by sunlight or visible light. In addition, under the excitation of 397 nm, the emission of the luminescent coating is a broad peak ascribed to the $5d^1$–$4f^7$ transition of Eu^{2+}. The optimal emission peak is located at 522 nm (Figure 8b). Theoretically, if the phosphor content of the luminescent coating is too small, its total emission intensity will be weak. With the increase in the amount of

phosphor, the emission intensity of the coating will increase. The results obtained in this experiment correspond to that, with the decrease in the phosphor content, the intensity of the excitation and emission peaks of luminescent coatings decrease. After 5 min of irradiation by a 365 nm UV lamp, the afterglow spectra and afterglow decay curves of the green coatings with different ratios of phosphor to emulsion were analyzed. As shown in Figure 8c, the afterglow emission wavelength of all luminescent coatings is located at 522 nm. With the reduction of long afterglow phosphor contents, the intensity of the afterglow decreases. Figure 8d shows the afterglow decay curves of green luminescent coatings. All of the curves show a similar trend: the intensity of the afterglow decays very fast in the first few minutes and gradually slows down over time. Considering the practical application of luminescent coatings, the coating is exposed to sunlight for 2 h (Figure 8e). It can be clearly seen that the afterglow brightness of each coating darkens with the increase in time, and the afterglow time can last for more than 5 h. Due to the high price of long afterglow phosphor, if its use content is too large, the cost of luminescent paint will increase. Considering the luminescent effect and cost, this work shows that the best ratio of phosphor to emulsion is 1:2.

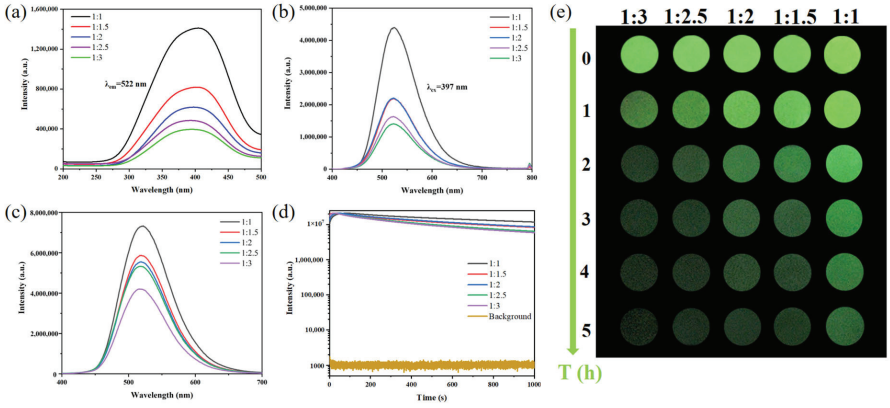

Figure 8. (**a**) PLE spectra and (**b**) PL spectra of luminescent coatings with different ratios of phosphor to emulsion. (**c**) Afterglow spectra and (**d**) afterglow decay curves of luminescent coatings with different ratios of phosphor to emulsion obtained after 5 min illumination with 365 nm UV light. (**e**) Afterglow images of luminescent coatings taken after sunlight excitation for 2 h with different ratios of phosphor to emulsion.

Figure S1 shows the PLE spectra, PL spectra, afterglow spectra and afterglow decay curves of luminescent coatings with different SiO_2 contents. It can be seen that the addition of SiO_2 does not affect the luminous color of the luminescent coating. Figure S1c shows the afterglow spectra and afterglow decay curves of the luminescent coatings. Incorporation of SiO_2 with increasing concentrations from 0.5% to 1.25% causes an increase in the afterglow intensity. When the SiO_2 content is 1.5%, the afterglow intensity decreases. This is because the components in the luminescent coatings are evenly dispersed when the 1.25% SiO_2 powder is added, as shown in the above FE-SEM image in Figure 5d. Thus, $SrAl_2O_4:Eu^{2+},Dy^{3+}$ phosphor can achieve the best luminous effect in the luminescent coating. Figure S1e shows the afterglow photos of the luminescent coating after sunlight excitation for 2 h which can prove that the afterglow brightness is the highest when 1.25% SiO_2 is added, which corresponds to the above spectra. Therefore, the optimal incorporation of SiO_2 is determined to be 1.25%.

Figure S2 shows the PLE spectra, PL spectra, afterglow spectra and afterglow decay curves of luminescent coatings with different $CaCO_3$ contents. It can be seen that the peak shape and peak position of PLE/PL spectra do not change after the addition of $CaCO_3$.

With the increase in $CaCO_3$ content, the intensity of the excitation and emission peaks of the coatings increase first and then decrease, and the luminescence reaches the highest intensity when the coating is mixed with 3.5% $CaCO_3$. After 5 min of irradiation by a 365 nm UV lamp, the afterglow spectra and afterglow decay curves of luminescent coatings were obtained, as shown in Figure S2c,d. It can be seen that the afterglow emission wavelength is 522 nm. With the increase in $CaCO_3$ content, the afterglow intensity of luminescent coatings first increases and then decreases. Figure S2e shows the afterglow images of the luminescent coating. With the increase in time, the brightness of the afterglow of the coating darkens, and the change of intensity corresponds to the afterglow decay curves. When 3.5% $CaCO_3$ is added, luminescent coating has the best afterglow performance. The results show that when the coating has the best compactness, it has the highest afterglow intensity. Therefore, the optimum content of $CaCO_3$ is determined to be 3.5%.

The water resistance of luminescent coating with different $CaCO_3$ contents is systematically tested, as shown in Figure 9a. After soaking in water for 120 h, the surface of the coating is smooth without blistering. It can be seen from the afterglow emission spectra in Figure 9b that the afterglow emission of the coatings is located at 522 nm and the peak position does not change. Corresponding to the variation trend of the afterglow emission intensity of the coatings without soaking water, the afterglow intensity is the highest when 3.5% $CaCO_3$ is added. Figure 9c shows the afterglow decay curves measured by the luminescent coatings doped with 3.5% $CaCO_3$ soaked in water for different lengths of time. The afterglow intensity of the coating gradually decreases with the increase in soaking time. The inset in Figure 9c is the afterglow photo of the coating excited by the ultraviolet lamp at 365 nm after soaking for 120 h, which can still output a bright green afterglow. Figure 9d shows the change rate of the afterglow intensity obtained at different times. After soaking for 120 h, the afterglow intensity reaches 76% of the original at 1000 s, indicating that the luminescent coating has good water resistance and practical applicability.

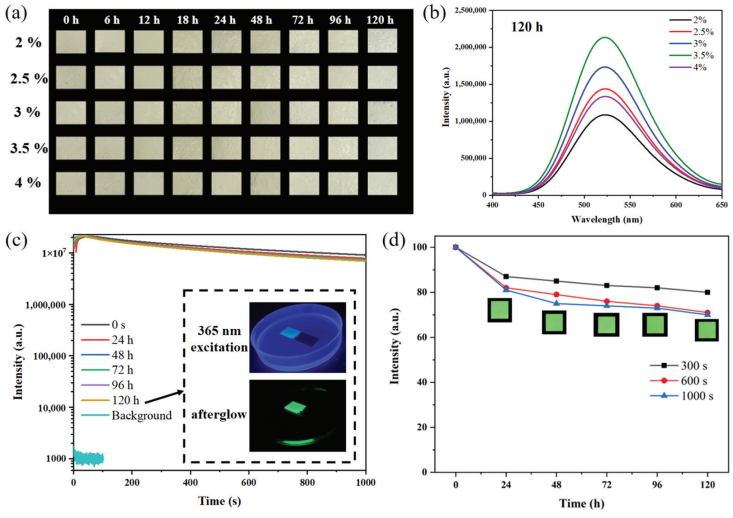

Figure 9. (**a**) Photographs of luminescent coatings with different $CaCO_3$ contents after immersion in water. (**b**) Afterglow spectra of luminescent coatings with different $CaCO_3$ contents after immersion in water for 120 h obtained with 5 min illumination of 365 nm UV light. (**c**) Afterglow decay curves of 3.5% $CaCO_3$ doped luminescent coating after immersion in water for different lengths of time obtained after 5 min illumination with 365 nm UV light. The inset is the afterglow image of 3.5% $CaCO_3$ doped luminescent coating after immersion in water for 120 h taken after 10 s illumination with 365 nm UV light. (**d**) The change rate of afterglow intensity of 3.5% $CaCO_3$ doped luminescent coating after immersion in water for different lengths of time. The inset is the afterglow images at 1000 s after excitation.

Figure 10 shows the afterglow photos of the luminescent coating during daylight excitations on cloudy, sunny and rainy days in different weather. With the increase in time, there is little difference in the brightness of the afterglow obtained under different weather conditions, and the afterglow can last for more than 5 h. This shows that weather conditions have no effect on the intensity of the coating afterglow. Therefore, this kind of luminescent coating can meet the application requirements of a smart highway.

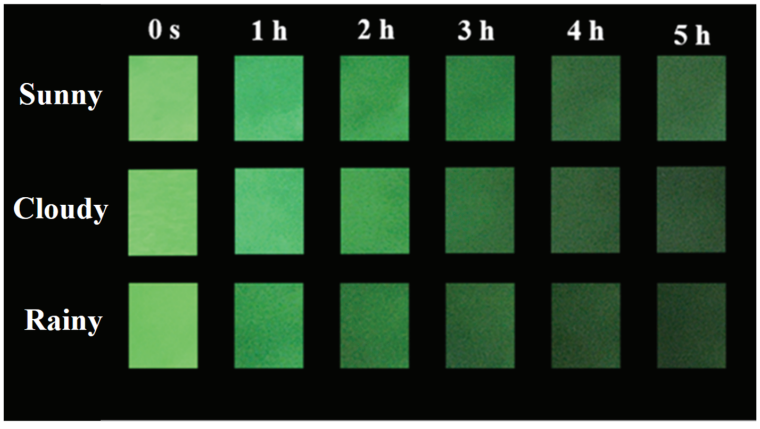

Figure 10. Afterglow images of luminescent coatings taken after sunlight excitation for 2 h in different weather conditions.

4. Conclusions

In this work, we successfully synthesized $SrAl_2O_4:Eu^{2+},Dy^{3+}$ green long afterglow phosphor via high-temperature solid state reactions in a reducing atmosphere. The phosphor was used as a raw material to prepare a green long persistent luminescent coating using the blending method. The main methods of characterization were XRD, FE-SEM, PL/PLE, TL, afterglow spectra, afterglow decay curves and water absorption. The green phosphor calcined at 1350 °C has two traps of appropriate depths, a shallow trap (0.66 eV) and a deep trap (0.8 eV), showing good afterglow properties. After 2 h of sunlight excitation, the afterglow can reach more than 8 h. The optimum ratios of different substances in the long persistent luminescent coating were determined. The ratio of phosphor to emulsion is 1:2, and the incorporation amounts of SiO_2 and $CaCO_3$ are 1.25% and 3.5%, respectively. The addition of SiO_2 improves the uniformity of each component in the coating and makes the coating achieve the best luminous effect. By adding $CaCO_3$ to adjust its content, the compactness of the coating is improved, and the water absorption is reduced. After soaking for 120 h, the afterglow intensity decreased to 76% of the original. When it is applied in practice, the afterglow intensity of luminescent coatings is not significantly affected after daylight excitation in different weather conditions (cloudy, sunny, rainy), and can reach more than 5 h; therefore, it can be applied to a smart highway.

Supplementary Materials: The following supporting information can be downloaded at: https://www.mdpi.com/article/10.3390/coatings13061050/s1, Figure S1: (**a**) PLE spectra, and (**b**) PL spectra of luminescent coatings with different SiO_2 contents. (**c**) Afterglow spectra, and (**d**) Afterglow decay curves of luminescent coatings with different SiO_2 contents obtained after 5 min illumination with 365 nm UV light. (**e**)Afterglow images of luminescent coatings taken after sunlight excitation for 2 h with different SiO_2 contents. Figure S2: (**a**) PLE spectra, and (**b**) PL spectra of luminescent coatings with different $CaCO_3$ contents. (**c**) Afterglow spectra, and (**d**) Afterglow decay curves of luminescent coatings with different $CaCO_3$ contents obtained after 5 min illumination with 365 nm UV light. (**e**) Afterglow images of luminescent coatings taken after sunlight excitation for 2 h with different $CaCO_3$ contents.

Author Contributions: M.Z.: data curation, formal analysis. X.L.: data curation, formal analysis. Y.B.: data curation, formal analysis. S.T.: data curation. P.L.: data curation, formal analysis, writing—original draft. Q.Z.: resources, supervision, conceptualization, writing—review and editing, conceptualization. All authors have read and agreed to the published version of the manuscript.

Funding: Natural Science Foundation of Liaoning Province (Grant No. 2020-MS-081).

Institutional Review Board Statement: Not applicable.

Informed Consent Statement: Not applicable.

Data Availability Statement: Data available on request from the authors.

Acknowledgments: This work was supported in part by the Natural Science Foundation of Liaoning Province (Grant 2020-MS-081).

Conflicts of Interest: The authors declare no conflict of interest.

References

1. Xu, J.; Tanabe, S. Persistent luminescence instead of phosphorescence: History, mechanism, and perspective. *J. Lumin.* **2018**, *205*, 581–620. [CrossRef]
2. Hölsä, J. Persistent Luminescence Beats the Afterglow: 400 Years of Persistent Luminescence. *Electrochem. Soc. Interface* **2009**, *18*, 42–45. [CrossRef]
3. Matsuzawa, T.; Aoki, Y.; Takeuchi, N.; Murayama, Y. A New Long Phosphorescent Phosphor with High Brightness, $SrAl_2O_4$: Eu2 +, Dy3 +. *J. Electrochem. Soc.* **1996**, *143*, 2670. [CrossRef]
4. Jin, Y.; Hu, Y.; Chen, L.; Ju, G.; Wu, H.; Mu, Z.; He, M.; Xue, F. Luminescent properties of a green long persistent phosphor Li_2MgGeO_4:Mn^{2+}. *Opt. Mater. Express* **2016**, *6*, 929–937. [CrossRef]
5. Zhang, C.; Gong, X.; Cui, R.; Deng, C. Improvable luminescent properties by adjusting silicon-calcium stoichiometric ratio in long afterglow phosphors $Ca_{1.94}MgSi_2O_7$:$Eu^{2+}{}_{0.01}$,$Dy^{3+}{}_{0.05}$. *J. Alloys Compd.* **2016**, *658*, 898–903. [CrossRef]
6. Wang, C.; Jin, Y.; Lv, Y.; Ju, G.; Liu, D.; Chen, L.; Li, Z.Z.; Hu, Y. Trap distribution tailoring guided design of super-long-persistent phosphor Ba_2SiO_4:Eu^{2+},Ho^{3+} and photostimulable luminescence for optical information storage. *J. Mater. Chem. C* **2018**, *6*, 6058–6067. [CrossRef]
7. Fu, X.; Liu, Y.; Meng, Y.; Zhang, H. Long afterglow green luminescence of Tb^{3+} ion in Ga_4GeO_8 through persistent energy transfer from host to Tb^{3+}. *J. Lumin.* **2021**, *237*, 118149. [CrossRef]
8. Wang, J.; Chen, W.; Peng, L.; Han, T.; Liu, C.; Zhou, Z.; Qiang, Q.P.; Shen, F.J.; Wang, J.; Liu, B. Long persistent luminescence property of green emitting $Sr_3Ga_4O_9$:Tb^{3+} phosphor for anti-counterfeiting application. *J. Lumin.* **2022**, *250*, 119066. [CrossRef]
9. He, X.; Zhang, H.; Xie, F.; Tao, C.; Xu, H.; Zhong, S. Enhanced afterglow performance of Zn_2SiO_4:Mn^{2+} by Pr^{3+} doping and mechanism. *Ceram. Int.* **2022**, *13*, 19358–19366. [CrossRef]
10. Rojas-Hernandez, R.E.; Rubio-Marcos, F.; Rodriguez, M.Á.; Fernandez, J.F. Long Lasting Phosphors: $SrAl_2O_4$: Eu, Dy as the Most Studied Material. *Renew. Sust. Energ. Rev.* **2018**, *81*, 2759–2770. [CrossRef]
11. Liepina, V.; Millers, D.; Smits, K. Tunneling Luminescence in Long Lasting Afterglow of $SrAl_2O_4$: Eu, Dy. *J. Lumin.* **2017**, *185*, 151–154. [CrossRef]
12. Qiu, Z.F.; Zhou, Y.Y.; Lv, M.K.; Zhang, A.Y.; Ma, Q. Combustion Synthesis of Long-Persistent Luminescent MAl_2O_4: Eu^{2+}, R^{3+} (M= Sr, Ba, Ca, R= Dy, Nd and La) Nanoparticles and Luminescence Mechanism Research. *Acta Mater.* **2007**, *55*, 2615–2620. [CrossRef]
13. Luo, X.H.; Cao, W.H.; Xiao, Z.H. Investigation on the Distribution of Rare Earth Ions in Strontium Aluminate Phosphors. *J. Alloys Compd.* **2006**, *416*, 250–255. [CrossRef]
14. Cordoncillo, E.; Julian-Lopez, B.; Martínez, M.; Sanjuán, M.L.; Escribano, P. New Insights in the Structure-Luminescence Relationship of Eu: $SrAl_2O_4$. *J. Alloys Compd.* **2009**, *484*, 693–697. [CrossRef]
15. Peng, T.Y.; Yang, H.P.; Pu, X.L.; Hu, B.; Jiang, Z.C.; Yan, C.H. Combustion Synthesis and Photoluminescence of $SrAl_2O_4$: Eu, Dy Phosphor Nanoparticles. *Mater. Lett.* **2004**, *58*, 352–356. [CrossRef]
16. Peng, T.Y.; Li, H.J.; Yang, H.P.; Yan, C.H. Synthesis of $SrAl_2O_4$: Eu, Dy Phosphor Nanometer Powders by Sol-Gel Processes and Its Optical Properties. *Mater. Chem. Phys.* **2004**, *85*, 68–72. [CrossRef]
17. Zang, L.X.; Shao, W.H.; Kwon, M.S.; Zhang, Z.G.; Kim, J. Photoresponsive Luminescence Switching of Metal-Free Organic Phosphors Doped Polymer Matrices. *Adv. Opt. Mater.* **2020**, *8*, 2000654. [CrossRef]
18. Poelman, D.; Van der Heggen, D.; Du, J.R.; Cosaert, E.; Smet, P. Persistent Phosphors for the Future: Fit for the Right Application. *J. Appl. Phys.* **2020**, *128*, 240903. [CrossRef]
19. Chiatti, C.; Fabiani, C.; Pisello, A.L. Long Persistent Luminescence: A Road Map Toward Promising Future Developments in Energy and Environmental Science. *Annu. Rev. Mater. Sci.* **2021**, *51*, 409–433. [CrossRef]
20. Wang, H.; Jasim, A.; Chen, X.D. Energy harvesting technologies in roadway and bridge for different applications-A comprehensive review. *Appl. Energy* **2018**, *212*, 1083–1094. [CrossRef]

21. Wiese, A.; Washington, T.; Tao, B.; Weiss, W.J. Assessing performance of glow-in-the-dark concrete. *Transp. Res. Record.* **2015**, *2508*, 31–38. [CrossRef]
22. Tian, Y.X.; Ma, B.; Liu, F.W.; Li, N.; Zhou, X.Y. Thermoregulation effect analysis of microencapsulated phase change thermoregulation agent for asphalt pavement. *Constr. Build. Mater.* **2019**, *221*, 139–150. [CrossRef]
23. Gallego, J.; del Val, M.A.; Contreras, V.; Páez, A. Heating asphalt mixtures with microwaves to promote self-healing. *Constr. Build. Mater.* **2013**, *42*, 1–4. [CrossRef]
24. Zhang, M.; Li, F.; Jiang, S.; Lin, Y.C.; Chen, F.; Zhao, X.; Shen, Y. $CaAl_2O_4$: Eu^{2+}, Nd^{3+} Anti-Corrosive Coating and Its Afterglow-Catalytic Process. *Opt. Mater.* **2021**, *116*, 111049. [CrossRef]
25. Bispo-Jr, A.G.; Lima, S.A.; Carlos, L.D.; Ferreira, R.A.; Pires, A.M. Phosphor-Based Green-Emitting Coatings for Circadian Lighting. *J. Lumin.* **2020**, *224*, 117298. [CrossRef]
26. Xiong, G.; Zhang, Z.; Qi, Y. Effect of the Properties of Long Afterglow Phosphors on the Antifouling Performance of Silicone Fouling-Release Coating. *Prog. Org. Coat.* **2022**, *170*, 106965. [CrossRef]
27. Al-Qahtani, S.D.; Al-nami, S.Y.; Alkhamis, K.; Al-Ahmed, Z.A.; Binyaseen, A.M.; Khalifa, M.E.; El-Metwaly, N.M. Simple Preparation of Long-Persistent Luminescent Paint with Superhydrophobic Anticorrosion Efficiency from Cellulose Nanocrystals and an Acrylic Emulsion. *Ceram. Int.* **2022**, *48*, 6363–6371. [CrossRef]
28. Thejo Kalyani, N.; Jain, A.; Dhoble, S.J. Persistent Phosphors for Luminous Paints: A Review. *Luminescence* **2022**, *37*, 524–542. [CrossRef]
29. Dutczak, D.; Jüstel, T.; Ronda, C.; Meijerink, A. Eu^{2+} Luminescence in Strontium Aluminates. *Phys. Chem. Chem. Phys.* **2015**, *17*, 15236–15249. [CrossRef]
30. Korthout, K.; Van den Eeckhout, K.; Botterman, J.; Nikitenko, S.; Poelman, D.; Smet, P.F. Luminescence and X-ray Absorption Measurements of Persistent $SrAl_2O_4$: Eu, Dy Powders: Evidence for Valence State Changes. *Phys. Rev. B* **2011**, *84*, 085140. [CrossRef]
31. Guo, C.F.; Tang, Q.; Zhang, C.X.; Huang, D.X.; Su, Q. Thermoluminescent Properties of Eu^{2+} and RE^{3+} Co-doped Phosphors $CaGa_2S_4$:Eu^{2+},RE^{3+} (RE=Ln, Excluding Pm, Eu and Lu). *J. Lumin.* **2007**, *126*, 333–338. [CrossRef]
32. Van den Eeckhout, K.; Bos, A.J.; Poelman, D.; Smet, P.F. Revealing Trap Depth Distributions in Persistent Phosphors. *Phys. Rev. B* **2013**, *87*, 045126. [CrossRef]
33. Poulose, A.M.; Shaikh, H.; Anis, A.; Alhamidi, A.; Kumar, N.S.; Elnour, A.Y.; Al-Zahrani, S.M. Long persistent luminescent hdpe composites with strontium aluminate and their phosphorescence, thermal, mechanical, and rheological characteristics. *Materials* **2022**, *15*, 1142. [CrossRef]
34. Poulose, A.M.; Anis, A.; Shaikh, H.; Alhamidi, A.; Siva Kumar, N.; Elnour, A.Y.; Al-Zahrani, S.M. Strontium aluminate-based long afterglow pp composites: Phosphorescence, thermal, and mechanical characteristics. *Polymers* **2021**, *13*, 1373. [CrossRef]
35. Wang, L.; Shang, Z.; Shi, M.; Cao, P.; Yang, B.; Zou, J. Preparing and testing the reliability of long-afterglow $SrAl_2O_4$:Eu^{2+},Dy^{3+} phosphor flexible films for temperature sensing. *RSC Adv.* **2020**, *10*, 11418–11425. [CrossRef] [PubMed]
36. Lin, J.D.; Chen, C.C.; Lin, C.F. Influence of sol–gel-derived ZnO:Al coating on luminescent properties of Y_2O_3:Eu^{3+} phosphor. *J. Sol-Gel Sci. Technol.* **2019**, *92*, 562–574. [CrossRef]
37. Shi, X.; Dou, R.; Ma, T.; Liu, W.; Lu, X.; Shea, K.J.; Song, J.L.; Jiang, L. Bioinspired lotus-like self-illuminous coating. *ACS Appl. Mater. Interfaces* **2015**, *7*, 18424–18428. [CrossRef]
38. Wan, M.; Jiang, X.; Nie, J.; Cao, Q.; Zheng, W.; Dong, X.; Fan, Z.H.; Zhou, W. Phosphor powders-incorporated polylactic acid polymeric composite used as 3D printing filaments with green luminescence properties. *J. Appl. Polym. Sci.* **2019**, *137*, 48644. [CrossRef]
39. Perez, C.; Collazo, A.; Izquierdo, M.; Merino, P.; Novoa, X.R. Characterisation of the Barrier Properties of Different Paint Systems: Part II. Non-Ideal Diffusion and Water Uptake Kinetics. *Prog. Org. Coat.* **1999**, *37*, 169–177. [CrossRef]
40. Perez, C.; Collazo, A.; Izquierdo, M.; Merino, P.; Novoa, X.R. Characterisation of the Barrier Properties of Different Paint Systems: Part I. Experimental Set-Up and Ideal Fickian Diffusion. *Prog. Org. Coat.* **1999**, *36*, 102–108. [CrossRef]
41. Zhang, J.T.; Hu, J.M.; Zhang, J.Q.; Cao, C.N. Studies of Impedance Models and Water Transport Behaviors of Polypropylene Coated Metals in NaCl Solution. *Prog. Org. Coat.* **2004**, *49*, 293–301. [CrossRef]
42. Zhang, J.T.; Hu, J.M.; Zhang, J.Q.; Cao, C.N. Studies of Water Transport Behavior and Impedance Models of Epoxy-Coated Metals in NaCl Solution by EIS. *Prog. Org. Coat.* **2004**, *51*, 145–151. [CrossRef]

coatings

MDPI

Article

Investigation of Structural and Tribological Characteristics of TiN Composite Ceramic Coatings with Pb Additives

Aleksandr Lozovan, Svetlana Savushkina *, Maksim Lyakhovetsky, Ilya Nikolaev, Sergey Betsofen and Ekaterina Kubatina

Moscow Aviation Institute, National Research University, 121552 Moscow, Russia; loz-plasma@yandex.ru (A.L.); lyakhovetsky@yandex.ru (M.L.); racer4500@yandex.ru (I.N.); s.betsofen@gmail.com (S.B.); tisaprmp@gmail.com (E.K.)

* Correspondence: sveta_049@mail.ru; Tel.: +7-(499)-158-4312

Abstract: Solid lubricating composite TiN coatings with Pb additives were obtained on steel and titanium substrates in the process of reactive magnetron sputtering of separate cathodes. Columnar, columnar nanostructured and composite nanostructured TiN coatings with different contents (3–13%) of a lubricating component (Pb) were obtained by deposition onto rotating and stationary substrates. It was found that deposition at a rotating substrate and 3% Pb content in the TiN matrix led to a columnar crystallite coating structure. With an increase in its content to 8%, columnar crystallites in the structure become less pronounced, and the coating becomes columnar nanostructured. In nanostructured composite coating with 12% Pb, the soft component is distributed both in the matrix and in the form of inclusions. XRD analysis of the composite nanostructured TiN–Pb coating indicates a textureless state. In this case, the diffraction lines of all present phases (Pb, PbO, TiN) are characterized by a significant broadening, indicating that the size of the subgrains are in range of 10–20 nm. Tribological tests of the coatings were carried out at room temperature and under conditions of stepwise heating. The nanostructured composite coating showed the best tribological characteristics due to a high Pb content, a relatively high microhardness (817 HV) and a textureless state with a low grain size. This coating had a low friction coefficient (~0.1) over 50,000 test cycles, both at room temperature and under conditions of stepwise heating up to 100 °C and 200 °C.

Keywords: solid lubricant coating; titanium nitride; lead; nanostructured coating; composite coating; tribological testing; friction coefficient; stepwise heating

Citation: Lozovan, A.; Savushkina, S.; Lyakhovetsky, M.; Nikolaev, I.; Betsofen, S.; Kubatina, E. Investigation of Structural and Tribological Characteristics of TiN Composite Ceramic Coatings with Pb Additives. *Coatings* **2023**, *13*, 1463. https://doi.org/10.3390/coatings13081463

Academic Editor: Qi Zhu

Received: 25 July 2023
Revised: 12 August 2023
Accepted: 17 August 2023
Published: 20 August 2023

1. Introduction

An increase in the loads of thermal machines and the desire to reduce the weight of products lead to a gradual replacement of the liquid lubricants system in favor of alternative solutions. Solid lubricant coatings (SLC) can resist wear for a long time at elevated temperatures and high contact pressures [1–3]. Such coatings should have high wear resistance to ensure a long service life and a low friction coefficient. Various combinations of oxide, nitride, and carbide ceramics, wear-resistant metals, and intermetallic compounds are promising materials as a matrix for SLC [4–7].

Solid lubricants currently used at high temperatures can be divided into three categories [8,9]: (1) soft metals (Ag, Cu, Au, Pb, In and etc.); (2) fluorides (e.g., CaF_2, BaF_2 and CeF_3); and (3) metal oxides (e.g., V_2O_5, $Ag_2Mo_2O_7$). All three types of materials plastically deform and/or form low shear strength surfaces at elevated temperatures. They do not lubricate at relatively low temperatures, so they have been combined with low temperature lubricants to create "chameleon" coatings that adapt their surface during a temperature cycle from 25 °C to 1000 °C to reduce friction in this temperature range [1,2,10].

At present, various magnetron sputtering types are increasingly used for tribological coatings deposition in industry. The method makes it possible to vary the microstructure

of coatings, to change the grain size, phase composition and crystallographic orientation that creates a control mechanism in a wide range of coating properties. The most effective modern approaches of SLC properties increase are: (1) deposition of multicomponent coatings, when, along with the main metal component (for example, Ti, Zr), such elements as Al, Cr, Nb, Y, Si are introduced into the coating; (2) multilayer coatings containing alternating layers with the thickness from several nanometers to micrometers; (3) combined deposition methods accompanied with ion nitriding or ion implantation. In recent years, multicomponent coatings have attracted increased interest [11–18]. For example, in [11] it was shown that titanium nitride-based coatings doped with Al and Zr had higher heat resistance due to the formation of stable, dense oxides on the surface, which increased the performance of coated products at elevated temperatures. For a number of systems, it was found that three-component coatings had higher hardness and wear resistance compared to binary coatings based on these elements [12]. The addition of metalloids atoms with the formation, in particular carbonitride and oxynitride coatings, affect their properties in a more complex way. Generally, carbonitride coatings have a higher hardness and oxynitride coatings have a lower hardness compared to nitrides. Some elements (e.g., Y and Si) added in amounts up to 10% lead to amorphization of the coating structure [7,13–16]. For example, in works [7,12], the addition of Al and Si in TiN coatings was accompanied by a change in the crystallographic texture. The pronounced (111) texture of TiN coatings passed into a state close to textureless. In textureless TiN and ZrN coatings, the hardness was two times higher than in coatings with a pronounced (111) texture [19].

The authors of work [2] suppose that oxides are potentially the best choice for SLC under extreme conditions at high temperature since oxides are often structurally and chemically thermodynamically stable although there are exceptions. Solid solutions such as $(Al,Cr)_2O_3$ form a corundum phase in relatively low temperature PVD processes and may be promising for low friction and wear coatings, but they are metastable at moderate temperatures [20]. Recently, researchers have focused on understanding the tribological properties of various Magneli phases, as WO_x, VO_x, MoO_x and TiO_x [21].

In work [2], the authors added a silver to a binary oxide to create ternary oxides. Silver is a soft metal and self-lubricating at relatively high temperatures (T > 300 °C). Ag–O bonds are relatively weak. They enhance the shearing of crystal planes and lower the melting point of initial metal double oxides when incorporated into the ternary oxide crystal structure. Besides, elemental Ag does not easily oxidize and will improve the tribological properties of the surrounding oxide phases by increasing the toughness of the film. Ag adds effects to a solid nitride matrix. Its influence to tribological properties at different operating temperatures and the transport activity of silver depending on the deposition temperature conditions were studied by authors of works [22–26].

The concept of tribological oxidation with the formation of ternary oxides was first described in [27]. In this research, composite PbO–MoS_2 coatings, which formed a $PbMoO_4$ lubricating layer at elevated temperatures, were obtained. In a subsequent study focusing on the lead molybdate phase [28], the authors found that, although this material was abrasive at low temperatures, it showed reduced friction coefficients at high temperatures (~0.3–0.4 at 700 °C) [18]. It has been found that the presence of a soft metal with low oxygen bond strength in ternary oxides was effective decision for high temperature solid lubricants. The low bond strength results show that low melting point materials are soft and easy to shear and can degrade into a binary oxide and a soft metal to improve lubricity. Recently, such soft metals as Pb, Cu and In have attracted interest.

Thus, studies of the Ti-N-Cu system with the aim of developing both multilayer and composite wear-resistant coatings were carried out using various options of vacuum-arc [29] and magnetron [30,31] deposition and their hybrid application [32,33].

Copper is a soft metal with excellent thermal conductivity contributed to efficient dissipation of friction heat and therefore lower temperatures in the contact area. The main lubrication mechanism is their increased ductility and low shear strength at high temperatures. Thus, soft metals can plastically deform during sliding and conform to both

interacting surfaces, reducing friction and wear. Increased softening at high temperatures can lead to the pulling of soft metals from the interface, which limits their lubricating effect [34].

Lead has excellent tribological properties. In works [35,36], the magnetron sputtered with ion assistance TiN based solid lubricant coatings with the Pb addition showed the advantage of composite structure over a multilayer structure with alternating layers of a solid matrix and lubricant component. The development of these works has shown that an increase in the lubricant component in the matrix leads, on the one hand, to a decrease in the friction coefficient and, on the other hand, reduces the wear resistance of the coating.

In [37], the tribological behavior of PVD TiN coatings with the addition of indium was studied. Tribological studies showed an improvement of wear resistance over unmodified TiN thin films up to 450 °C. Observed deterioration in coating behavior at higher temperatures was attributed to indium oxidation.

In this work, composite TiN based SLC with different structure and Pb content have been formed by Ti and Pb cathodes co-sputtering of two separate magnetrons, and their tribological properties have been studied at room and elevated temperatures.

2. Materials and Methods

Solid lubricant nanostructured TiN coatings with Pb additives were formed on steel AISI 304 and titanium VT1 (99.0% Ti) samples in the process of reactive magnetron sputtering of separate cathodes (99.2% titanium, 99.5% pure lead).

Planar magnetrons with the size of both targets, 0.273 m × 0.112 m × 0.01 m, were placed vertically in the chamber at different distances d from the target to the substrate during the deposition of TiN–Pb coatings (Figure 1). The ion source was placed vertically opposite the substrate at a distance d_1 from it (Table 1). The screens made of steel were located next to them to reduce the possible transfer of sputtered atoms from one magnetron to another. Ar and N gases were fed into the vacuum chamber through an ion source.

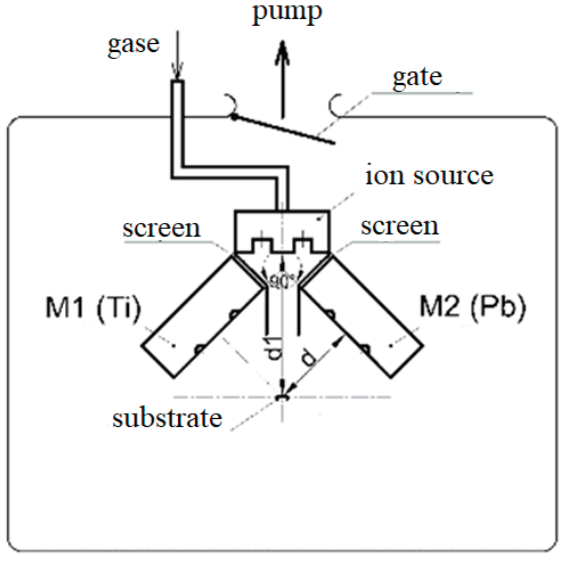

Figure 1. Scheme of TiN–Pb coatings deposition.

Table 1. Parameters of the coating deposition process. Q_{Ar}, Q_{N2}—gas flow rates; I_{Ti}, I_{Pb}—discharge currents; t—spraying duration; F—power supply frequency; d—target-substrate distance; d_1—substrate–ion source distance; n—substrate rotation speed.

No.	Substrate	P_{Ar+N2}, Pa	Q_{Ar}, cm^3/min	Q_{N2}, cm^3/min	I_{Ti}, A	I_{Pb}, A	t, min	F, kHz	d, mm	d_1, mm	n, rpm
1	steel	0.31	8.65	2.45	3.5	0.1	720	-	100	160	2
2	steel	0.25	8.54	4.1	3.5	0.1	350	-	100	160	2
3	steel	0.24	6.52	5.14	3.5	0.1	350	25	220	250	-
4	steel, Ti	0.24	6.49	5.18	3.5	0.1	350	40	220	250	-

The samples were cleaned in an ultrasonic bath in gasoline for 10–15 min before spraying. Then, they were placed into the chamber, and it was pumped out to a pressure of 5.3×10^{-4} Pa. The samples were cleaned using an ion source for 20 min at P_{Ar} = 0.13 Pa at a flow rate of Q_{Ar} = 6.49 cm^3/min. Then, the ion source was turned off. Ti and TiN transition layers were deposited for 10 min. Then, the main TiN + Pb coating layer was deposited. The main parameters of the coating deposition process are given in Table 1. Ti and Pb sputtering was carried out in the constant current mode with current stabilization when coatings 1 and 2 were deposited. For coatings 3 and 4, Ti sputtering was carried out in the constant current mode with current stabilization, and Pb sputtering was carried out in the medium frequency mode at 25 and 40 kHz and a duty cycle T = 80%. The total deposition time was 350 min for coatings 2–4 and 720 min for coating 1. During the deposition of samples 1 and 2, the substrate was rotated clockwise at a speed of 2 rpm.

The morphology and composition of the coatings were studied using a Quanta 600 scanning electron microscope (SEM, FEI Company, Eindhoven, The Netherlands) equipped with a TRIDENT XM4 energy dispersive X-ray microanalysis system. The thickness of the coatings was measured in a cross-section of the samples using SEM. The roughness was examined using an Olympus LEXT OLS 5000 confocal microscope (Olympus, Tokyo, Japan). 2D profiles were used to obtain the roughness parameters. X-ray phase analysis was performed by DRON-7 X-ray diffractometer (NPP "Burevestnik", Saint-Petersburg, Russia) in filtered CuKα radiation with a wavelength λ = 1.54178 Å. The microhardness of the coatings was evaluated on a Buehler Micromet 5101 instrument (Buehler, Lake Bluff, IL, USA) by indenting a Vickers pyramid with a load of 50 g.

Ball-on-disk tribological tests were carried out in the reciprocating wear mode with a displacement of 15 μm, a normal contact load of 1 N, a displacement frequency of 20 Hz, a cycles number of 50,000 (total sliding distance—1.5 m), an ambient temperature of 23 °C and a humidity of 37 ± 5%. A sphere with a diameter of 12.6 mm made of 100Cr6 steel (62–65 HRC) was used as a counter body. The influence of heating on the tribological properties of the coatings was studied in the stepwise heating mode up to 100 °C and 200 °C with holding at each temperature for 2 h. The coated samples were tested to determine the friction coefficient after each stage of heating.

Volumetric wear was analyzed using a confocal laser microscope LEXT OLS5000. The microscope software evaluates volumetric wear by integrating wear worn space points relative to the original surface. The transferred material of the counter body was estimated as the build-up volume in the wear patches. The build-up height exceeded the original level of the coating surface. In the case of its formation, the build-up volume corresponded to the volumetric wear of the counter body.

Also, tribological tests of the samples were carried out with a change in the loading parameters: displacement D = 5–60 μm; normal contact load F = 1–13 N; displacement frequency f = 20 Hz; the number of cycles n = 10,000. The friction coefficient and the mechanism of bodies interaction were analyzed in the testing process.

3. Results

3.1. Surface Structure and Elemental Composition

The coatings surface morphology on a steel substrate is characterized by globules with the size of ~1–5 μm (Figure 2). Coating 1 has the largest surface globules (Figure 2a), which may be due to the longer deposition time. The smallest size of surface globules was obtained for coating 3 (Figure 2c), while their highest packing density was obtained for coating 4 (Figure 2d). An enlarged image of the coating 4 globule structure is shown in Figure 2e. Differently oriented crystallites less than 0.1 μm in size are seen in the structure of the globule. Globules and cavities on the coatings surface could be formed in the presence of high compressive stresses. Thermal stresses arising as a result of temperature changes at the deposition completion can promote diffusion processes. In such a way, mass transfer of the deposited material can occur [38].

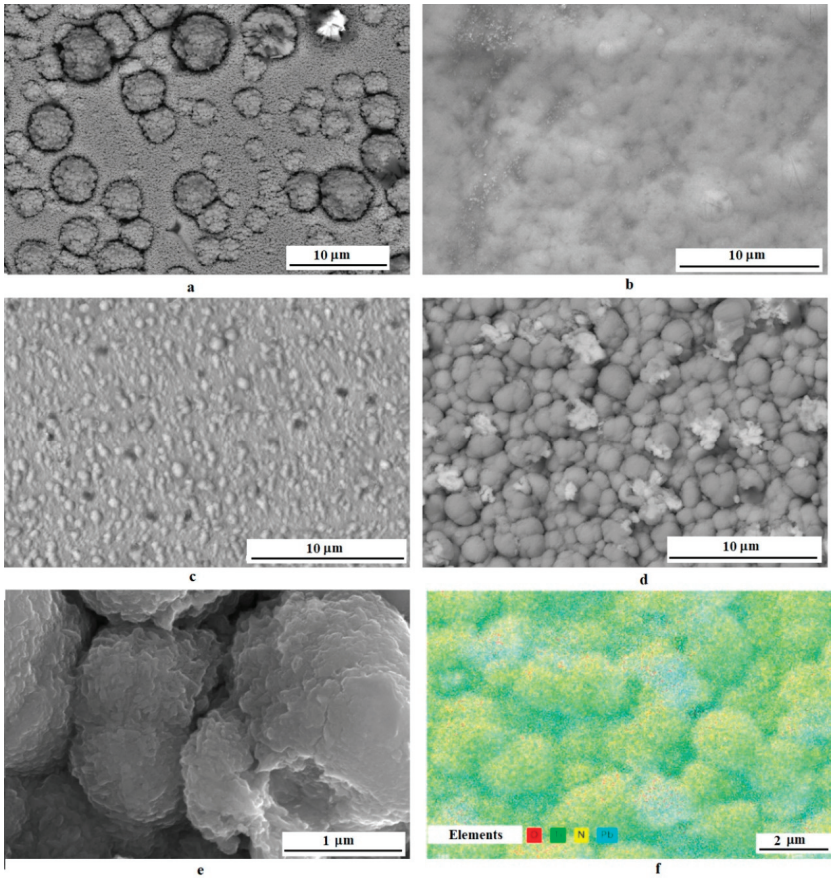

Figure 2. SEM images in backscattered electrons of the surface for coatings 1 (**a**), 2 (**b**), 3 (**c**), 4 (**d**), an enlarged image in secondary electrons of coating 4 globules (**e**) and a summary map of the elements distribution over the coating 4 surface (**f**).

X-ray microanalysis showed a uniform distribution of Pb over the surface for coatings 1–3 and the presence of areas with an increased content of Pb and O for coating 4 (Figure 2f). The thicknesses of coatings 1–4 are ~5.8, 3.8, 2.3 and 2.0 μm, according to the results of SEM studies on cross-sections. The average lead content is ~3, 8, 13 and 12 at.% for coatings 1–4, respectively. With an increase in the Q_{Ar}/Q_{N2} ratio, the TiN content in the coating

increases, and the Pb content decreases. The oxygen content in the surface layer of the coatings increases with an increase in the Pb content from 12 at.% (coating 1) to 40 at.% (coatings 3 and 4), which is associated with its oxidation.

3.2. Surface Roughness

In Figure 3, the coatings surface height maps obtained using a confocal microscope are shown. For coatings 1–3, the surface topography changes from the predominance of protrusions to a greater content of depressions with an increase in the lead content from 3 to 13%. A decrease in the roughness parameters R_a and R_q to 0.126 and 0.464 μm for coating 3 (Table 2) shows that the surface is getting smoother. R_a parameter and, more significantly, Rq parameter decreased with an increase in the lead content in the coatings, which may be due to the smoothing of the surface as a result of the lower thermal stresses action after the deposition process completion. The parameters R_a and R_q are higher for coating 4 with an uneven distribution of lead in the surface layer than for coatings 1–3. The roughness parameters R_{sk} and R_{ku} analysis allows the prediction of the tribological behavior of the coatings. R_{sk} parameter shows the asymmetry of the height distribution, and R_{ku} estimates the flatness or sharpness of the surface topography. Since the values of $R_{sk} > 0$ for all coatings, the protrusions dominate in the structure of all coatings. The smallest R_{sk} was obtained for coating 4, which indicates a significant proportion of depressions on the surface. The parameter R_{ku} is high for 1 coating due to individual sharp protrusions. R_{ku} shows a significant smoothing of the surface due to the reduction of the "sharpness" of the protrusions for coatings 2–4. Coating 1 is characterized by the highest values of R_{sk} and R_{ku}, which shows the predominance of higher and "sharper" protrusions on the surface. It was found in [39] that the following values of roughness parameters are satisfied to maintain an oxide coating low friction coefficient for a long time: R_a = 0.4 μm, $R_{sk} = -1.8$ and relatively high R_{ku} = 10. Thus, from the point of view of the obtained roughness parameters, coating 4 can have the lowest friction coefficient due to both a relatively low value of R_a and the lowest R_{sk}.

3.3. Cross-Section Coatings Structure

The coatings have a two-layer structure consisting of a Ti + TiN transition layer (1) up to 0.1 μm thick and the main coating TiN + Pb layer (2) (Figure 4). The inhomogeneity of the coating thickness is due to the globular structure of the surface. The globules height reaches 0.3 μm. Coating 1 has a columnar structure consisting of intergrown crystallites located perpendicular to the surface (Figure 4a). Such structure is typical for deposited TiN. It is characterized by the (111) texture component predominance [19]. In growth process, the deposited atoms diffuse over the surface until they enter the low-energy lattice sites and are included in the growing coating. The deposited atoms can change their positions in the crystal lattice due to diffusion and recrystallization processes [38]. The thickness of columnar crystallites (0.05–0.25 μm) increases with approaching to the surface of the coating. Their magnified image is shown in Figure 4a. The elements distribution map of coating 1 cross-section showed a uniform distribution of Pb in depth mainly along columnar crystallites, which may be due to the filling of intercrystallite spaces by it (Figure 4b). Coating 2 is columnar nanostructured. Columnar crystallites become less pronounced. Their thickness and length decrease, but a noticeable texture is retained, as in coating 1 (Figure 4a). The structure of coating 3 corresponds to the textureless state (Figure 4d). Columnar crystallites disappear, the structure becomes denser, nanocrystallites appear, which suggests the coating amorphous-crystalline state. Thus, for coatings 1–3, the structure with an increase in lead content from 3 to 13% changes from columnar to dense textureless. Coating 4 is composite nanostructured. On the one hand, its state is also close to textureless, but unlike coating 3, it consists of differently oriented nanocrystallites (Figure 4f). Lead is present both in the coating matrix and in the form of islands predominantly distributed in the surface layer of coating with a thickness of ~0.6 μm (Figure 4f). At the same time, its average content is less than that of coating 3. This suggests a smaller amount of Pb in the

matrix compared to coating 3, which may contribute to the nanostructured state. A special metastable state for the process of coating formation can lead to phase migration of the soft and fusible component and its higher concentration in the surface coating layer [40].

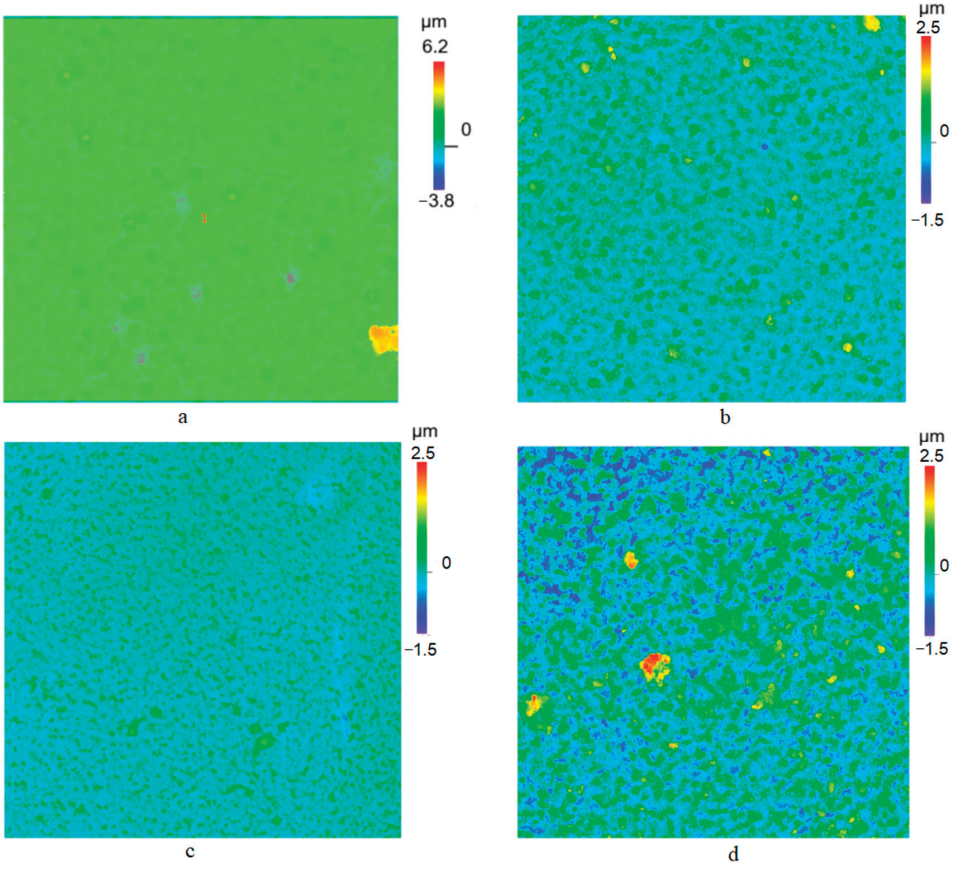

Figure 3. Surface height maps of coatings 1 (**a**), 2 (**b**), 3 (**c**), 4 (**d**) on a steel substrate.

Table 2. Roughness parameters of coatings 1–4.

No.	Pb, at.%	R_a, μm	R_q, μm	R_{sk}	R_{ku}
1	3	0.277	0.486	4.265	44.251
2	8	0.187	0.258	1.657	8.246
3	13	0.126	0.170	1.382	6.427
4	12	0.366	0.464	0.739	4.014

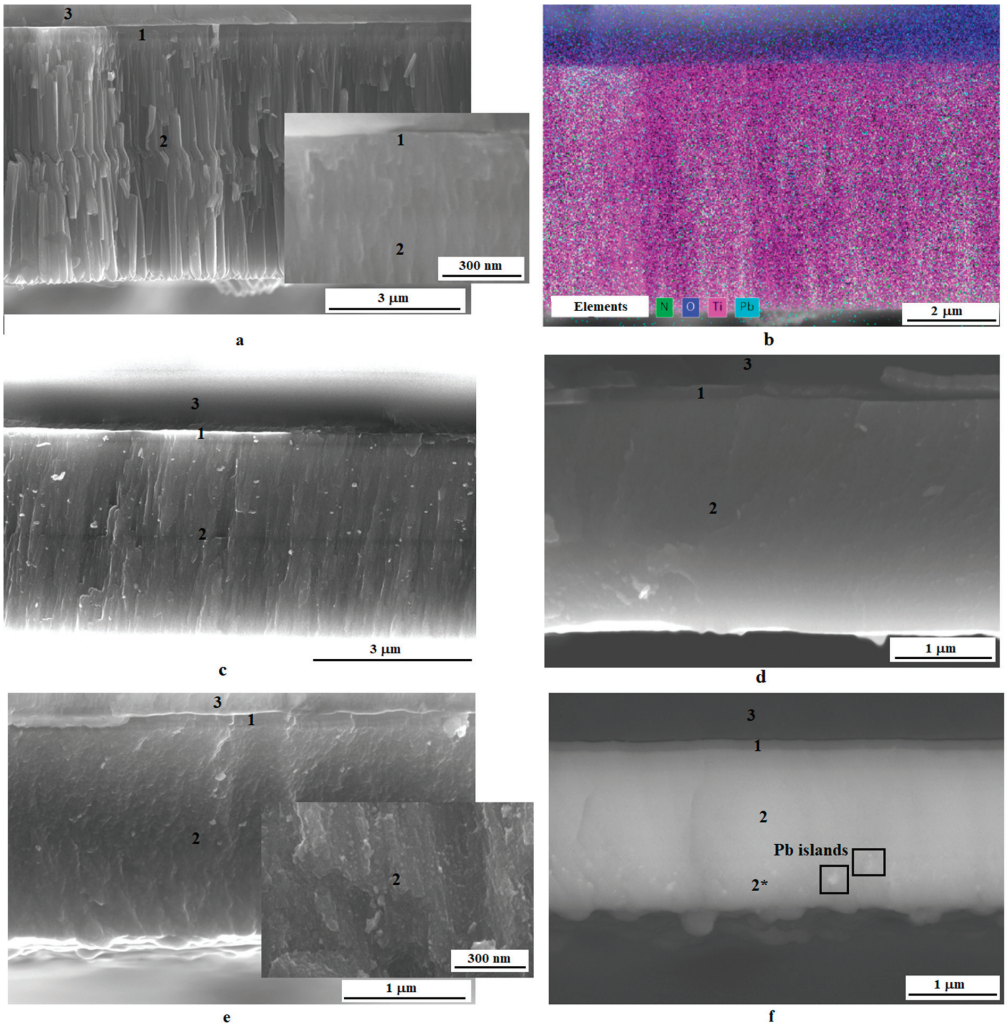

Figure 4. Cross-section structure SEM images in secondary electrons of the coatings 1 (**a**), 2 (**c**), 3 (**d**), 4 (**e**), a summary map of the elements distribution for coating 1 (**b**), SEM image of coating 4 in backscattered electrons (**f**). 1—Ti + TiN transition layer, 2—main TiN + Pb layer, 2*—surface layer with island-like Pb-containing inclusions, 3—substrate.

3.4. Phase Composition

Coatings 1 and 2 have a pronounced columnar structure. Usually such structure has pronounced (111) crystallographic texture. The XRD pattern of TiN–Pb coating 4 (Figure 5) indicates a textureless state. The diffraction lines of all present phases (Pb, PbO, TiN) are characterized by a significant broadening, indicating that the size of the subgrains are in range ~10–20 nm. It can be assumed that the absence of a columnar structure is associated with its discontinuous growth provided by Pb because it does not dissolve in the TiN matrix and has a weak tendency to nitridation. Formation of Pb and PbO phases nuclei on the surface of TiN crystallites promotes their growth interruption and their nanometer size retention. In addition, particles of Pb and PbO phases stimulate the formation of TiN nuclei of random orientations, which prevents the formation of a pronounced texture.

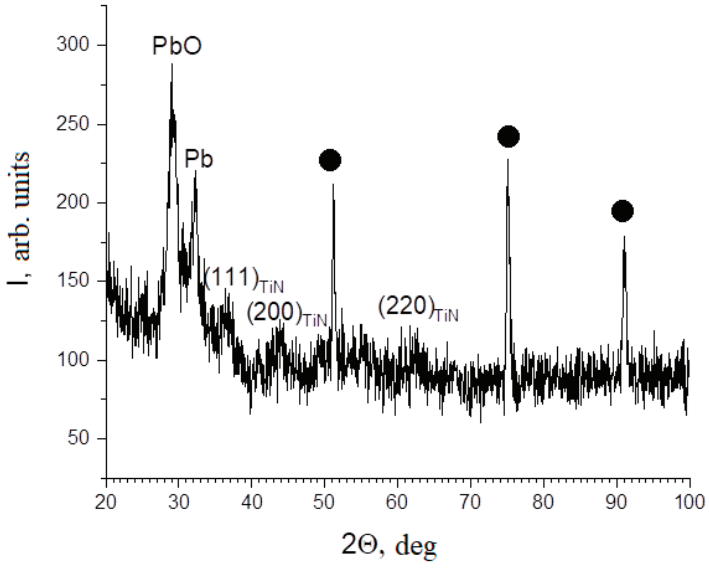

Figure 5. XRD pattern of TiN–Pb coating 4 on a steel substrate (●).

It was shown in [41] that an increase in the (111) texture component of TiN coating is accompanied to decrease in wear resistance. The textureless structure of the TiN coating may contribute to an increase in microhardness and wear resistance. Discontinuous structure and grain reduction provide strengthening in accordance with the Hall-Petch law.

3.5. Microhardness

The highest Vickers microhardness (919 HV_{50}) was obtained for columnar coating 1 with the greatest thickness (Table 3). The transition of the coating structure to a columnar nanostructured and textureless state, as well as a decrease in thickness, led to a decrease in microhardness. This is also associated with an increase in the content of the soft Pb component in the structure. For coating 3, the microhardness values become similar with those for the substrate—steel. An increase in Pb content can lead to the formation in the coating structure of such compounds as lead oxides, lead oxynitride, Ti_3PbO_7, $TiPbO_3$, etc. [42]. The hardness of these compounds is significantly inferior to TiN, which contributes to a general decrease in hardness, despite the compaction of the coating structure and a decrease in the size of crystallites. Despite its more than 2 times smaller thickness, the microhardness of the composite nanostructured coating 4 is 817 HV, which is not much inferior to the columnar coating. This must be due to the composite structure of the coating. In coating 4, surface layer lead is mainly present in the form of island inclusions, which makes it possible to maintain a solid matrix. The content of large Pb inclusions increases when approaching the surface. In addition, grains' size reduction provides strengthening in accordance with the Hall-Petch law.

3.6. Tribological Tests at Room Temperature

In tribological tests, the lowest friction coefficient (~0.1) was shown by nanostructured composite coating 4 (Figure 6). Its friction coefficient practically does not change during 50,000 test cycles. Textureless coating 3 also had low friction coefficient at the initial stage of testing. Already after 2000 cycles, it increases sharply, which is associated with the onset of the coating destruction. During subsequent cycles, the friction coefficient increases from 0.3 to 0.35. For columnar coating 1 and columnar nanostructured 2, the friction coefficient is ~0.27 during all 50,000 test cycles. Intensive destruction was accompanied by large oscillations in the friction coefficient. Small rises and decreases in the friction coefficient

during the experiment are associated with the accumulation of wear products in the contact zone and their removal outside the contact patch.

Table 3. Structure, Pb content and microhardness of the coatings.

No.	Thickness, μm	Pb, at.%	Structure	Microhardness, HV_{50}
1	5.8	3	Columned	919
2	3.8	8	Columned nanostructured	570
3	2.3	13	Textureless	283
4	2.0	12	Nanostructured composite	817

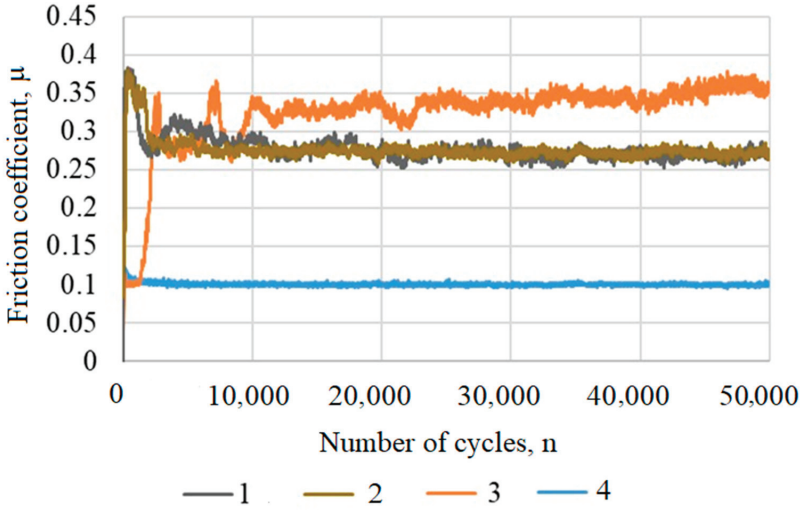

Figure 6. Comparison of friction coefficients of coatings 1–4 on a steel substrate when moving at 15 μm.

Figure 7 shows a comparison of the volumetric wear of the coatings and the material transfer from the counter body. An increase in the height of wear spots relative to the main coating and an increase in the friction coefficient indicated significant transfer of material from the counter body (steel) for coatings 1 and 2. Such a significant mass transfer should be associated with the rapid destruction of the coatings and the interaction of the substrate with the counter body, as can be seen in the graphs of the friction coefficient. "Sticking" was not observed for coatings 3 and 4. However, the volumetric wear of coating 3 is much higher.

3.7. Tribological Tests under Stepwise Heating Conditions

The effect of temperature on the tribological properties of the coatings was carried out with stepwise heating to 100 °C and 200 °C and a holding time of 2 h in a muffle furnace at each temperature. After heating tribological tests were carried out (Figure 8). Composite nanostructured coating 4 demonstrated the stability of tribological characteristics. The friction coefficient remained an approximate value of 0.1 during 50,000 test cycles, as after heating to 100 °C. After heating to 200 °C, it slightly increased up to 0.12. After heating to 100 °C, the friction coefficient of coating 3 increased already to 0.4 at the beginning of the tests (Figure 8a). After subsequent heating, it decreased to 0.3. Increased softening at high

temperatures can cause the soft component to be pulled away from the interface, which limits its lubricating effect.

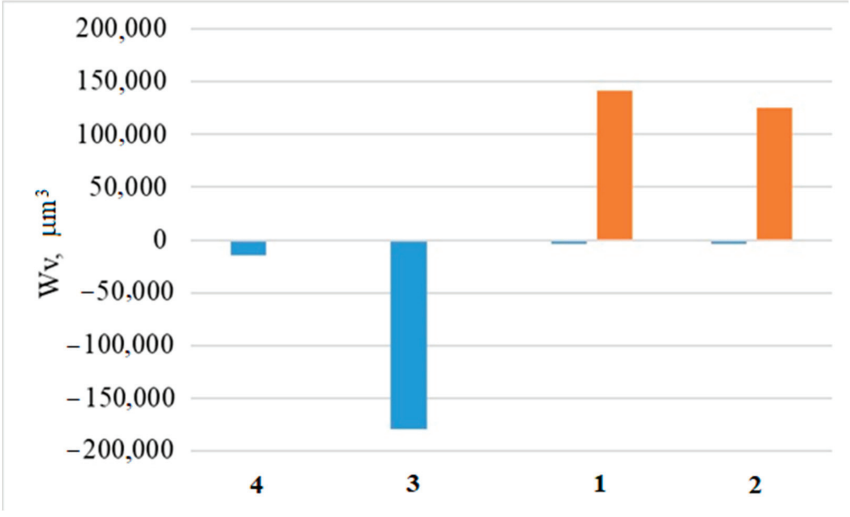

Figure 7. Volumetric wear of the coatings (blue columns) and material transfer from the counter body (orange columns).

Figure 9 shows images of wear patches. After heating to 200 °C, the coatings were subjected by rather strong oxidation that affected their tribological properties. Minor improvement in coating 3 tribological characteristics at the beginning of the tests could be due to the formation of oxides and oxynitrides of the system components.

3.8. XRD Analysis after Stepwise Heating

Some change in the properties of the coatings may be associated with the oxidation of the TiN–Pb system components, as well as the substrate. After heating reflections of Pb with FCC lattice and reflections of TiN are retained in addition to reflections from the substrate in XRD pattern of coating 4 (Figure 10). Reflection angles 2Θ~36° correspond to reflections (200) Pb and (111) TiN, and reflection angles 2Θ~62° correspond to reflections (311) Pb and (220) TiN, which cannot be uniquely identified as belonging to Pb or TiN.

The ratio of Pb reflection intensity (2Θ~36°) to PbO (2Θ~28°) increases compared to the diffraction pattern before heating (Figure 5). The diffraction lines of Pb, PbO and TiN are strongly broadened, which indicates the nanostructured state retention. A decrease in the signal-to-background ratio for Pb reflections compared to the XRD pattern before heating may indicate the formation of other oxide compounds with lead. In addition, oxygen atoms can also enter the TiN matrix, forming titanium oxynitride, which retains the original crystal structure (NaCl type). In this case, oxygen atoms replace some of the nitrogen atoms without forming TiO_2, and the signal-to-background ratio in the region of these reflections may decrease [43].

After heating, the intensity ratio of I_{Pb}/I_{PbO} reflections is much higher for coating 3 than for coating 4, which indicates less oxidation. Most likely, this is due to a more uniform distribution of Pb in the matrix and the absence of islands with its increased content in the surface layer of the coating.

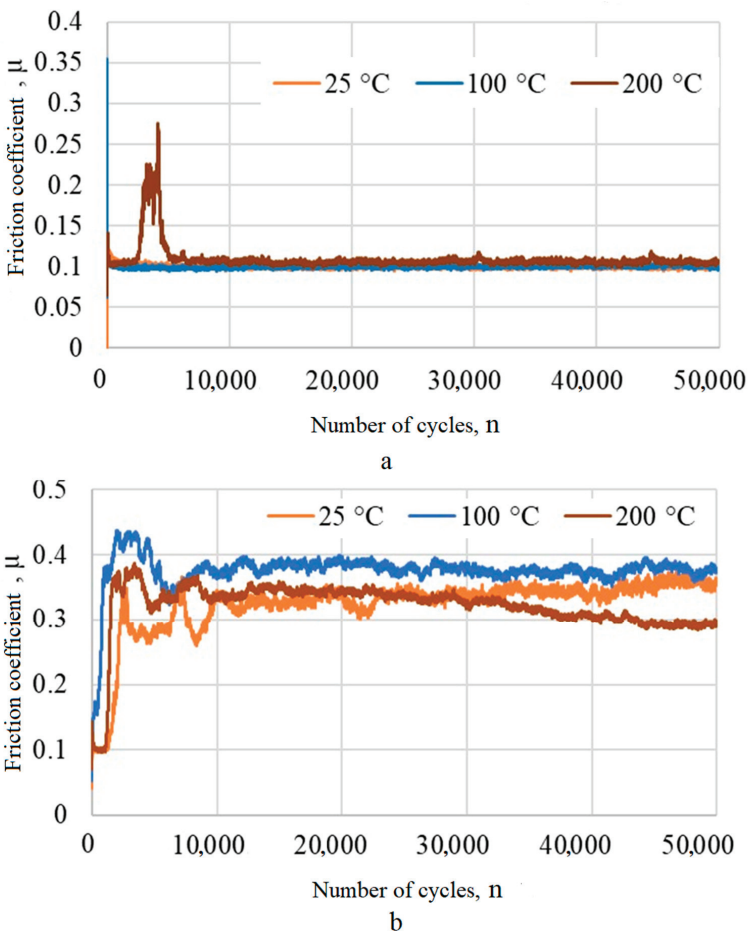

Figure 8. Friction coefficients of coatings 4 (**a**) and 3 (**b**) on a steel substrate during stepwise heating.

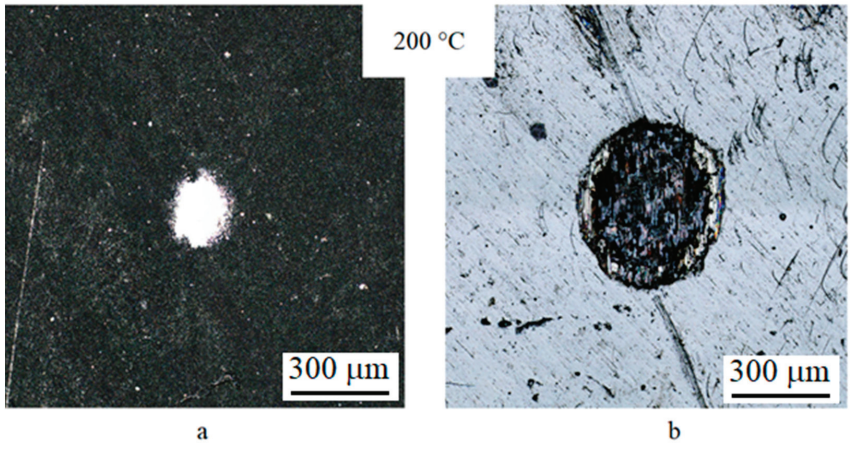

Figure 9. Images of wear patches after heating to 200 °C for coatings 4 (**a**) and 3 (**b**).

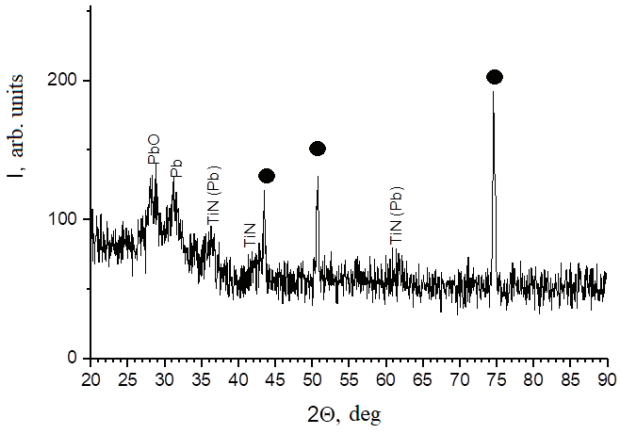

Figure 10. XRD pattern of coating 4 after stepwise heating up 200 °C. •—steel substrate.

3.9. Tribological Study of a Nanostructured Composite Coating at Various Loading Parameters

Coating 4 was studied in friction modes that differ in mechanisms of surface destruction, when fatigue processes, abrasive damage by wear products or adhesive wear can predominate [44,45]. The mechanism of friction during fretting was analyzed using an energy approach [46]. It consists in dissipation energy determining in the contact by measuring the instantaneous values of the friction force and displacement with a frequency at least 20 times higher than the frequency of bodies movement. The fretting hysteresis loops analysis makes it possible to estimate the modes of friction bodies interaction directly in the course of the experiment by calculating the slip index. Tribological tests were carried out in a wide range of loading parameters to obtain a fretting map. The resulting fretting map based on the hysteresis loops analysis is shown in Figure 11.

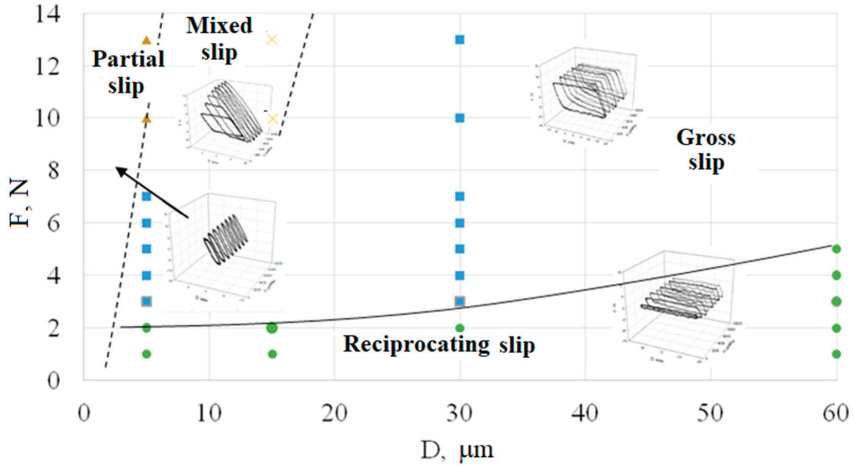

Figure 11. Fretting map of nanostructured composite coating 4 on titanium.

The process of abrasive and adhesive interaction of the bodies prevails in gross slip mode during fretting. The gross slip mode is indicated by blue squares in Figure 11. Fast fatigue failure dominates in mixed slip mode (yellow crosses). Fatigue failure with low cracking rate is observed in partial slip mode (brown triangles). The friction processes without the specific features of the friction bodies interaction in fretting corresponds to the

reciprocating slip mode (green circles). The wear patch obtained at D = 5 μm and F = 13 N is an uneven damage with dimensions of ~100 μm along the displacement axis and ~250 μm across (Figure 12a). The areas with a high lead content are visible on the coating surface in the form of light spots. Cracks up to 15 μm long are observed on the surface of the coating. They are located perpendicular to the direction of the bodies' friction (Figure 12b). The coating mechanism destruction corresponds to the process prevailing for the partial slip mode–fatigue failure. It occurs as a result of the sign-alternating friction force action in a contact in combination with the transition between slip zones and elastic bodies interaction. At loading parameters (D = 15 μm, F = 10 N), the process of fatigue failure is significantly getting worse. A network of cracks is formed over the entire area of the contact patch on the coating surface, which corresponds to a mixed slip mode (Figure 12c). The process of further destruction can lead to flaking of large agglomerates of the coating during friction and interaction of the counter body with the substrate. Also, under certain conditions the cracks could transit from the coating to the surface layer of the metal. In the gross slip mode (D = 30 μm and F = 3 N), the processes of abrasive interaction begin to prevail (Figure 12d). The shear relief of the coating along the bodies' direction motion is associated with the presence of a Pb soft component (Figure 12e). In this case, the lead plastically deformed during the slip, which reduced friction and wear. Figure 10f shows regions of the coating structure of differently oriented crystallites and "shear" regions, apparently corresponding to zones with a Pb high content.

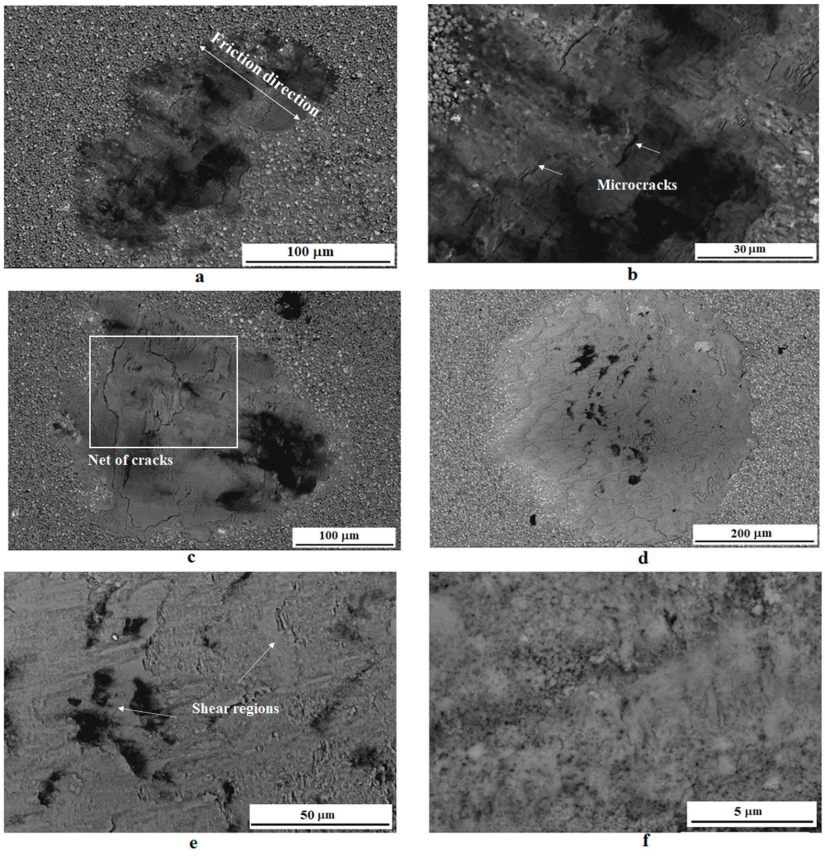

Figure 12. SEM images in backscattered electrons of TiN–Pb coating damage zone obtained at D = 5 μm and F = 13 N (**a**,**b**), at D = 15 μm and F = 10 N (**c**), at D = 30 μm and F = 3 N (**d**–**f**).

Elemental microanalysis of the wear patch obtained at loading parameters D = 15 μm, F = 10 N showed the transfer of the soft coating component to the edge region. It led to the coating preservation in this area and its destruction in the central regions accompanied by the formation of microcracks and the appearance of areas with increased titanium content (Figure 13a). The dissipation energy in the gross slip mode is the highest, which indirectly indicates a rather high wear rate. Elemental microanalysis of the wear patch shows the appearance of titanium zones up to 20 μm in size in the center (Figure 13) associated with the beginning of the process of complete coating wear to the metal. Mass transfer of the soft component is not observed in this mode.

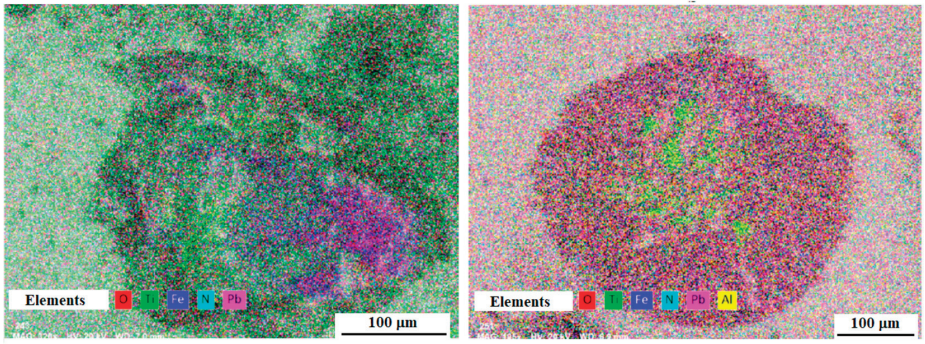

Figure 13. Summary maps of the elements' distribution of wear patches corresponding to loading parameters: D = 15 μm, F = 10 N (**a**) and D = 30 μm, F = 3 N (**b**).

The dissipation energy drops by more than 3 times, accompanied with a sharp decrease in the friction coefficient from 0.25 to 0.05 during the transition from the gross slip mode to the reciprocating slip mode. Thus, the reciprocating slip mode, as well as the partial slip mode, occur in narrow ranges of loads and displacements for TiN–Pb coating. The main mode of friction during the fretting is the gross slip mode. Mixed slip mode also occurs in a narrow range of the loads accompanied with the formation of a cracks network that can lead to its delamination. In the gross slip mode, the friction coefficient is set equal to ~0.25, which is significantly lower than the friction coefficient of TiN without Pb additives (~0.75–0.9) [25,26].

4. Discussion

The reactive deposition of TiN–Pb coatings is a multifactorial process complicated by a significant difference in the masses of Ti and Pb. The result is the different efficiency of the sputtered particles scattering process along the way to the substrate. Energy transfer during collisions of particles is maximum when their masses are equal. The masses of argon and titanium atoms are almost equal. As a result of successive collisions, Ti is effectively scattered by Ar slowing down and deviating at different angles. This effect ensures the deposition of titanium on the substrate by falling at an angle. On the other hand, nearly ballistic sputtering is realized for heavy lead atoms. They reach the substrates slightly deviating and losing a small amount of energy. By changing the angle of the ion beam, one can control such important properties of the coatings as structure, size of structural components, hardness, texture and morphology [47–49]. The structure of the formed coatings is usually also influenced by the substrate temperature, the chamber pressure, the initial surface roughness, and (especially at low temperature) the deposition rate and the angle of incidence of the deposited particles.

The deposition of sputtered Ti and Pb atoms on rotating substrates (coatings 1 and 2) provides their incidence angles in the range from 0 to 90° and leads to an increase in the coating thickness. This is due to such atoms involved in the process with direction of

arrival provided the self-shadowing effect. During the rotation and repeated passing of the substrate in front of the magnetrons, the atoms sputtered from the cathodes are deposited in a wide range of incidence angles from the normal (0–90°). This process is similar to the so-called "oscillation" deposition when the substrate oscillates in front of the sputtered target [50]. In this case, the substrate rotation rate is very important since the possibility of nucleation and growth direction of columnar crystallites also depends on it. Since the direction of vapor flow changes during the rotation, the direction of growth of individual columnar crystallites can change.

Sputtering of Pb in the medium frequency mode at 25 and 40 kHz for coatings 3 and 4 could contribute to their higher content in the coatings. The conditions of a stationary substrate and the medium-frequency Pb sputtering regime may promote to Pb-containing phases nuclei on the surface of TiN crystallites, their growth interruption and nanosized grains preservation. In addition, particles of Pb-containing phases could stimulate the formation of TiN nuclei of random orientations prevented the formation of a texture. A possible mechanism for this atomic densification is bombardment of the coating by high-energy argon atoms reflected from the cathode and sputtered heavy Pb atoms. This is due to the fact that both the average energy and the sputtered particles flux increase with the atomic mass of the target material.

Usually, TiN deposited coating has a pronounced columnar structure mostly combined with a pronounced crystallographic texture (111). TiN–Pb is a multicomponent coating. It has a structure formation mechanism different from two-component coatings. This is confirmed by changes in the crystallographic texture while in two-component coatings the texture is stably reproduced over a wide range of deposition coatings parameters. For example, it was found in [7,12] that the addition of Al and Si to TiN coating composition is accompanied by a transition of a pronounced texture (111) to a textureless state, microstructure refinement and the formation of a pseudo amorphous structure. As was found in [38], compressive stresses in the surface layer contribute to the formation of the deposited coating globular surface. As the lead content increases, the coating can become more fusible due to the presence of Pb and PbO phase inclusions. This can reduce the activation energy of diffusion processes. Under these conditions, volume diffusion becomes more significant, which can reduce internal stresses and prevent their accumulation. Increasing the fusibility of the coating can lead to an increase in the effects of recrystallization on the coating structure decreasing in the texture component as was obtained for coatings 2–4. An increase in the lead content with its uniform distribution in the coating can reduce the difference in thermal expansion of the substrate—steel and the coating with a TiN matrix. This can help to reduce the thermal stresses and the height of irregularities—the "globularity" of the surface. In this work it was found a decrease in the roughness of the coatings from 1 to 3. The composite structure of coating 4 did not lead to a decrease in roughness. It may indicate that a higher content of lead and Pb-containing phases in the TiN matrix can also lead to an increase in thermal stresses, phase migration of a soft and low-melting component into the surface layer [38].

Among the obtained coating (columnar, columnar nanostructured, textureless, nanostructured composite), nanostructured composite coating 4 showed the best tribological characteristics. In coating 4, the soft component is distributed both in the matrix and in the form of island-like inclusions predominantly in the surface layer. In columnar coatings (1 and 2), the crystallites are bound by a rather small area to the surface. In this case, the application of a load in the tangential direction can lead to their destruction. In addition, in the regions between the crystallites, there are often vertical pores in the form of channels through which the penetration of external environment products is possible. Therefore, the formation of a nanostructured textureless coating contributes to longer durability. Certainly, the friction coefficient, microhardness and roughness were essential in the testing process. In this case, the higher tribological characteristics stability of the composite nanostructured coating can be explained by the presence of soft island-like inclusions in the surface layer. This structure provides easier formation of shear regions under the loads, and the lower

content of lead in the matrix can maintain a relatively high microhardness. In the same time, a high content of Pb in the matrix (coating 3) can negatively influence wear resistance due to a decrease in microhardness, despite the low friction coefficient.

5. Conclusions

Solid lubricating ceramic composite TiN coatings with Pb additives were obtained on stationary and rotating substrates made of AISI 304 steel and titanium in the process of reactive magnetron sputtering of separate cathodes.

Columnar, columnar nanostructured, textureless and composite nanostructured TiN–Pb coatings with different Pb content (3–13%) were obtained by varying the deposition regimes. The columnar structure changes to a columnar nanostructured with an increase in the Pb content in the coating to 8%.

Deposition on a stationary substrate and the use of medium frequency sputtering of Pb lead to an increase in its content in the coatings and textureless state. The coatings include Pb, PbO and TiN phases. The diffraction lines are characterized by significant broadening, indicating nanometer size of the subgrains.

Tribological tests of the coatings were carried out at room temperature and under conditions of stepwise heating, as well as at various loading parameters. Among the obtained coating structures, the nanostructured composite coating showed the best tribological characteristics. In this coating the lead-containing components are distributed both in the matrix and in the form of inclusions contributed to relatively high microhardness (817 HV), a high Pb content and a textureless state with a low grain size. This provided a low friction coefficient (~0.1) over 50,000 test cycles, both at room temperature and under conditions of stepwise heating up to 100 °C and 200 °C.

Author Contributions: Conceptualization, A.L. and S.S.; methodology, I.N. and S.B.; software, E.K.; validation, M.L.; formal analysis, A.L.; investigation, S.S. and S.B.; resources, M.L.; data curation, A.L.; writing—original draft preparation, S.S. and A.L.; writing—review and editing, M.L.; visualization, E.K. and I.N.; supervision, A.L.; project administration, S.S.; funding acquisition, S.S. All authors have read and agreed to the published version of the manuscript.

Funding: This research was funded by Russian Science Foundation, project number 22-19-00754.

Institutional Review Board Statement: Not applicable.

Informed Consent Statement: Not applicable.

Data Availability Statement: Not applicable.

Conflicts of Interest: The authors declare no conflict of interest.

References

1. Aouadi, S.M.; Luster, B.; Kohli, P.; Muratore, C.; Voevodin, A.A. Progress in the development of adaptive nitride-based coatings for high temperature tribological applications. *Surf. Coat. Technol.* **2009**, *204*, 962–968. [CrossRef]
2. Aouadi, S.M.; Gao, H.; Martini, A.; Scharf, T.W.; Muratore, C. Lubricious oxide coatings for extreme temperature applications: A review. *Surf. Coat. Technol.* **2014**, *257*, 266–277. [CrossRef]
3. Lesnevskii, L.N.; Lezhnev, L.Y.; Lyakhovetskii, M.A.; Troshin, A.E.; Ushakov, A.M. Wear resistance of composite plasma coatings with graphite. *J. Mach. Manufact. Reliabil.* **2017**, *46*, 25–32. [CrossRef]
4. Ouyang, J.-H.; Li, Y.-F.; Zhang, Y.-Z.; Wang, Y.-M.; Wang, Y.-J. High-Temperature Solid Lubricants and Self-Lubricating Composites: A Critical Review. *Lubricants* **2022**, *10*, 177. [CrossRef]
5. Lenz, B.; Hoja, S.; Sommer, M.; Hasselbruch, H.; Mehner, A.; Steinbacher, M. Potential of Nitrided and PVD-MoS_2:Ti-Coated Duplex System for Dry-Running Friction Contacts. *Lubricants* **2022**, *10*, 229. [CrossRef]
6. Von Fieandt, K.; Paschalidou, E.-M.; Srinath, A.; Soucek, P.; Riekehr, L.; Nyholm, L.; Lewin, E. Multi-component (Al, Cr, Nb, Y, Zr) N thin films by reactive magnetron sputter deposition for increased hardness and corrosion resistance. *Thin Solid Films* **2020**, *693*, 137685. [CrossRef]
7. Betsofen, S.Y.; Plikunov, V.V.; Petrov, L.M.; Bannykh, I.O. Study of the phase composition and structure of multicomponent vacuum ion-plasma coatings (Ti, Nb, Me) N and (Zr, Nb) N (C), depending on their chemical composition and technology parameters. *Aviat. Ind.* **2007**, *4*, 9–15.

8. Bogdanski, M.S.; Sliney, H.E.; Della Corte, C. The effect of processing and compositional changes on the tribology of PM212 in air. *Lubric. Eng.* **1992**, *48*, 675–683.
9. Zabinski, J.S.; Sanders, J.H.; Nainaparampil, J.; Prasad, S.V. Lubrication using a microstructurally engineered oxide: Performance and mechanisms. *Tribol. Lett.* **2000**, *8*, 103–116. [CrossRef]
10. Muratore, C.; Voevodin, A.A. Chameleon coatings: Adaptive surfaces to reduce friction and wear in extreme environments. *Annu. Rev. Mater. Res.* **2009**, *39*, 297–324. [CrossRef]
11. Hasegava, H.; Kimura, A.; Suzuki, T. $Ti_{1-x}Al_xN$, $Ti_{1-x}Zr_xN$ and $Ti_{1-x}Cr_xN$ films synthesized by the AIP method. *Surf. Coat. Technol.* **2000**, *132*, 76–79. [CrossRef]
12. Yoo, Y.H.; Le, D.P.; Kim, J.G.; Kim, S.K.; Vinh, P.V. Corrosion behavior of TiN, TiAlN, TiAlSiN thin films deposited on tool steel in the 3.5 wt.% NaCl solution. *Thin Solid Films* **2008**, *516*, 3544–3548. [CrossRef]
13. Lewis, D.B.; Donohue, L.A. The influence of the yttrium content on structure and properties of $Ti_{1-x-y-z}Al_xCr_yY_zN$ PVD hard coatings. *Surf. Coat. Technol.* **1999**, *114*, 187–199. [CrossRef]
14. Kong, Q.; Li, J.; Li, H.; Liu, X.; Wang, Y.; Chen, J.; Zhou, H. Composition, microstructure, and properties of CrNx films deposited using medium frequency magnetron sputtering. *Appl. Surf. Sci.* **2011**, *257*, 2269–2274. [CrossRef]
15. Shuyong, T.; Zhang, X.; Wu, X.; Fang, F.; Jiang, J. Effect of substrate bias and temperature on magnetron sputtered CrSiN films. *Appl. Surf. Sci.* **2011**, *257*, 1850–1853.
16. Chang, C.-L.; Lin, C.-T.; Tsai, P.-C.; Ho, W.-Y.; Wang, D.-Y. Influence of bias voltages on the structure and wear properties of TiSiN coating synthesized by cathodic arc plasma evaporation. *Thin Solid Films* **2008**, *516*, 5324–5329. [CrossRef]
17. Discerens, M.; Patscheider, J.; Levy, F. Improving the properties of titanium nitride by incorporation of silicon. *Surf. Coat. Technol.* **1998**, *108–109*, 241–246. [CrossRef]
18. Mei, H.; Wang, R.; Zhong, X.; Wei, D.; Wang, Q. Influence of Nitrogen Partial Pressure on Microstructure and Tribological Properties of Mo-Cu-V-N Composite Coatings with High Cu Content. *Coatings* **2018**, *8*, 24. [CrossRef]
19. Ashmarin, A.A.; Betsofen, S.Y.; Petrov, L.M.; Lebedev, M.A. Effect of bias voltage on the texture of the TiN and ZrN coatings deposited by vacuum ion-plasma method. *Mat. Sci. Eng.* **2020**, *889*, 012019. [CrossRef]
20. Najafia, H.; Karimia, A.; Dessarzinb, P.; Morsteinb, M. Correlation between anionic substitution and structural properties in $AlCr(O_xN_{1-x})$ coatings deposited by lateral rotating cathode arc PVD. *Thin Solid Films* **2011**, *520*, 1597–1602. [CrossRef]
21. Gardos, M.N. Magnéli phases of anion-deficient rutile as lubricious oxides. Part I. Tribological behavior of single-crystal and polycrystalline rutile (Ti_nO_{2n-1}). *Tribol. Lett.* **2000**, *8*, 65–78. [CrossRef]
22. Mulligan, C.P.; Gall, D. CrN-Ag self-lubricating hard coatings. *Surf. Coat. Technol.* **2005**, *200*, 1495–1500. [CrossRef]
23. Kutschej, K.; Mitterer, C.; Mulligan, C.P.; Gall, D. High-temperature tribological behavior of CrN-Ag self-lubricating coatings. *Ad. Eng. Mat.* **2006**, *8*, 1125–1129. [CrossRef]
24. Stone, D.S.; Migas, J.; Martini, A.; Smith, T.; Muratore, C.; Voevodin, A.A.; Aouadi, S.M. Adaptive NbN/Ag coatings for high temperature tribological applications. *Surf. Coat. Technol.* **2012**, *206*, 4316–4321. [CrossRef]
25. Bondarev, A.V.; Kvashnin, D.G.; Shchetinin, I.V.; Shtansky, D.V. Temperature-dependent structural transformation and friction behavior of nanocomposite VCN-(Ag) coatings. *Mater. Des.* **2018**, *160*, 964–973. [CrossRef]
26. Bondarev, A.V.; Kiryukhantsev-Korneev, P.V.; Levashov, E.A.; Shtansky, D.V. Tribological behavior and self-healing functionality of TiNbCN-Ag coatings in wide temperature range. *Appl. Surf. Sci.* **2017**, *396*, 110–120. [CrossRef]
27. Zabinski, J.S.; Donley, M.S.; Dyhouse, V.J.; McDevitt, N.T. Chemical and tribological characterization of PbO-MoS_2 films grown by pulsed laser deposition. *Thin Solid Films* **1992**, *214*, 156–163. [CrossRef]
28. Zabinski, J.S.; Day, A.E.; Donley, M.S.; Dellacorte, C.; McDevitt, N.T. Synthesis and characterization of a high-temperature oxide lubricant. *J. Mat. Sci.* **1994**, *29*, 5875–5879. [CrossRef]
29. Peng, C.; Zhao, Y.; Jin, S.; Wang, J.; Liu, R.; Liu, H.; Shi, W.; Kolawole, S.K.; Ren, L.; Yu, B.; et al. Antibacterial TiCu/TiCuN Multilayer Films with Good Corrosion Resistance Deposited by Axial Magnetic Field-Enhanced Arc Ion Plating. *ACS Appl. Mater. Interfaces* **2019**, *11*, 125–136. [CrossRef]
30. Wei, C.B.; Tian, X.B.; Yang, Y.; Yang, S.Q.; Fu, K.Y.; Chu, P.K. Microstructure and tribological properties of Cu–Zn/TiN multilayers fabricated by dual magnetron sputtering. *Surf. Coat. Technol.* **2007**, *202*, 189–193. [CrossRef]
31. Mukhopadhyay, A.K.; Roy, A.; Bhattacharjee, G.; Das, S.C.; Majumdar, A.; Wulff, H.; Hippler, R. Surface Stoichiometry and Depth Profile of Ti_x-Cu_yN_z Thin Films Deposited by Magnetron Sputtering. *Materials* **2021**, *14*, 3191. [CrossRef]
32. Myunga, H.S.; Lee, H.M.; Shaginyan, L.R.; Han, J.G. Microstructure and mechanical properties of Cu doped TiN superhard nanocomposite coatings. *Surf. Coat. Technol.* **2003**, *163–164*, 591–596. [CrossRef]
33. Zhu, Y.D.; Yan, M.F.; Zhang, Y.X.; Chen, H.T.; Yang, Y. Microstructure formation and evolution mechanism of Cu-Ti coating during dual-magnetron sputtering and thermo plasma nitriding. *Vacuum* **2016**, *134*, 25–28. [CrossRef]
34. Voevodin, A.A.; Muratore, C.; Aouadi, S.M. Hard coatings with high temperature adaptive lubrication and contact thermal management: Review. *Surf. Coat. Technol.* **2014**, *257*, 247–265. [CrossRef]
35. Lozovan, A.A.; Betsofen, S.Y.; Savushkina, S.V.; Lychovetsky, M.A.; Lesnevsky, L.N.; Nikolaev, I.A.; Kubatina, E.P. Influence of Sputtering Geometry and Conditions on the Structure and Properties of the TiN–Pb Solid Lubricating Coatings Fabricated by Magnetron Co-Sputtering of Two Separate Targets. *Russ. Metall.* **2022**, *11*, 1441–1448. [CrossRef]
36. Lozovan, A.A.; Lesnevsky, L.N.; Betsofen, S.Y.; Liakhovetsky, M.A.; Ushakov, A.M. Structure and properties of solid lubricating coatings based on the TiN-Pb system. *IOP Conf. Ser. Mat. Sci. Eng.* **2018**, *387*, 01204. [CrossRef]

37. Guleryuz, C.G.; Krzanowski, J.E.; Veldhuis, S.C.; Fox-Rabinovich, G.S. Machining performance of TiN coatings incorporating indium as a solid lubricant as placeholders for microreservoir formation. *Surf. Coat. Technol.* **2009**, *203*, 3370–3376. [CrossRef]
38. Thorton, J.A.; Hoffman, D.W. Stress—Related effects in thin films. *Thin Solid Films* **1989**, *171*, 5–31. [CrossRef]
39. Su, J.F.; Nie, X.; Hu, H. Friction and counterface wear influenced by surface profiles of plasma electrolytic oxidation coatings on an aluminum A356 alloy. *J. Vac. Sci. Technol. A* **2012**, *30*, 061402.
40. Yea, F.; Sun, X. Nanoindentation response analysis of TiN-Cu coating deposited by magnetron sputtering. *Prog. Nat. Sci. Mat. Int.* **2018**, *28*, 40–44. [CrossRef]
41. Lozovan, A.A.; Betsofen, S.Y.; Lyakhovetskiy, M.A.; Pavlov, Y.S.; Grushin, I.A.; Kubatina, E.P.; Nikolaev, I.A. Structure and properties of TiN–Pb composite coatings deposited on VT6 alloy by DC magnetron sputtering. *Russ. J. Non-Ferr. Met.* **2021**, *4*, 70–77. (In Russian) [CrossRef]
42. Saal, J.E.; Kirklin, S.; Aykol, M.; Meredig, B.; Wolverton, C. Materials Design and Discovery with High-Throughput Density Functional Theory: The Open Quantum Materials Database (OQMD). *JOM* **2013**, *65*, 1501–1509. [CrossRef]
43. Suciu, C.V.; Uchida, T. Modeling and Simulation of the Fretting Hysteresis Loop. Parallel, Grid, Cloud and Internet Computing. In Proceedings of the 3PGCIC 2010, International Conference on P2P, Fukuoka Institute of Technology, Fukuoka, Japan, 4–6 November 2010; p. 560.
44. Lesnevskiy, L.N.; Lyakhovetskiy, M.A.; Savushkina, S.V. Fretting wear of composite ceramic coating produced on D16 aluminum-based alloy using microarc oxidation. *J. Frict. Wear.* **2016**, *37*, 268–273. [CrossRef]
45. Subramanian, B.; Muraleedharan, C.V.; Ananthakumar, R.; Jayachandran, M. A comparative study of titanium nitride (TiN), titanium oxy nitride (TiON) and titanium aluminum nitride (TiAlN), as surface coatings for bio implants. *Surf. Coat. Technol.* **2011**, *205*, 5014–5020. [CrossRef]
46. Fouvry, S.; Kapsa, P.; Vincent, L. Quantification of fretting damage. *Wear* **1996**, *200*, 186–205. [CrossRef]
47. Dervaux, J.; Cormier, P.-A.; Moskovkin, P.; Douheret, O.; Konstantinidis, S.; Lazzaroni, R.; Lucas, S.; Snyders, R. Synthesis of nanostructured Ti thin films by combining glancing angle deposition and magnetron sputtering: A joint experimental and modeling study. *Thin Solid Films* **2017**, *636*, 644–657. [CrossRef]
48. Robbie, K.; Brett, M.J. Sculptured thin films and glancing angle deposition: Growth mechanics and applications. *J. Vac. Sci. Technol.* **1997**, *15*, 1460–1465. [CrossRef]
49. Stempfle, P.; Besnard, A.; Martin, N.; Domatti, A.; Takadoum, J. Accurate control of friction with nanosculptured thin coatings: Application to gripping in microscale assembly. *Tribol. Int.* **2013**, *59*, 67–78. [CrossRef]
50. Jimenez, M.J.M.; Antunes, V.G.; Zagonel, L.F.; Figueroa, C.A.; Wisnivesky, D.; Alvarez, F. Effect of the period of the substrate oscillation in the dynamic glancing angle deposition technique: A columnar periodic nanostructure formation. *Surf. Coat. Technol.* **2020**, *383*, 125237. [CrossRef]

coatings

MDPI

Article

Research on the Corrosion Resistance of an Epoxy Resin-Based Self-Healing Propylene Glycol-Loaded Ethyl Cellulose Microcapsule Coating

Shudi Zhang [1,*], Linkun Liu [1], Yuheng Xu [1], Quanda Lei [1], Jiahui Bing [1] and Tao Zhang [2,*]

[1] School of Environmental and Chemical Engineering, Shenyang Ligong University, Shenyang 110159, China; 15670291571@163.com (L.L.); lovexyh2023@163.com (Y.X.); lqd317213741@163.com (Q.L.); 18342029676@163.com (J.B.)
[2] Chinese Academy of Sciences (Shenyang) Metals Research, Shenyang 110016, China
* Correspondence: zhangshudi@163.com (S.Z.); zhangtao@mail.neu.edu.cn (T.Z.)

Abstract: In this work, ethyl cellulose was used as a wall material, propanetriol as a core material, polyvinyl alcohol as a stabilizer and gelatin as an emulsifier. Self-healing microcapsules with a slow-release effect were prepared using the solvent evaporation method. Various analytical techniques, such as 3D confocal microscopy (LCSM), optical microscopy (OM), scanning electron microscopy (SEM), infrared spectroscopy (FT-IR), energy dispersive spectroscopy (EDS), thermal weight loss analysis (TGA), laser particle size tester and electrochemical impedance polarization, are utilized. The morphology, distribution, particle size, corrosion resistance and self-healing ability of the prepared microcapsules and resin-based coatings were characterized and analyzed. The results show that the cross-sectional core–shell structure is clearly seen in the LCSM, showing a smooth, hollow, spherical shape. OM and laser particle size testers have shown that the size of the microcapsules decreases over time. Also, in OM, the microcapsules are uniformly distributed in the emulsion with a smooth and non-adherent surface. In SEM, the microcapsule particle size is about 150 μm, the shell wall thickness is about 18 μm, and the hollow structure of ruptured microcapsules is obvious. FT-IR and TGA confirmed the successful encapsulation of the formulated microcapsules. The results show that when the core-wall mass ratio is 1.2:1 and the amount of microcapsule is 10% of the coating amount, the prepared microcapsule has high thermal stability and certain wear resistance. By electrochemical and immersion experiments, it was found that a 3.5 wt % NaCl solution has the best impedance, the lowest corrosion current density, and good adhesion and tensile toughness. The results showed that glycerol was successfully released from the broken microcapsules and self-healed, forming an anticorrosive coating with excellent corrosion resistance and self-healing ability.

Keywords: microencapsulation; E-51 epoxy resin; self-healing; corrosion resistance; AZ91D magnesium alloy

Citation: Zhang, S.; Liu, L.; Xu, Y.; Lei, Q.; Bing, J.; Zhang, T. Research on the Corrosion Resistance of an Epoxy Resin-Based Self-Healing Propylene Glycol-Loaded Ethyl Cellulose Microcapsule Coating. *Coatings* **2023**, *13*, 1514. https://doi.org/10.3390/coatings13091514

Academic Editors: Levente Csoka and JongHyeon Lee

Received: 29 June 2023
Revised: 27 July 2023
Accepted: 10 August 2023
Published: 27 August 2023

1. Introduction

Magnesium alloy has shown high application value in various applications in today's society. In the field of lightweight alloys, it is of great significance as a benefit mankind and to the promotion of further developments in science and technology. Magnesium alloys are also the lightest structural metal materials in the world [1–3]. They have the advantages of having a high specific strength sufficient toughness, and being lightweight and easy to transform, hence their pivotal in the development of society from ancient times to the present [4–7]. Therefore, magnesium alloys play an indispensable role in the fields of construction, aerospace, smart wearable, portable home, and so on, as well as in the energy and chemical industries. [5–8]. However, China is a large consumer of magnesium resources, it is not difficult to predict that under the development trend of today's world, further research and application of magnesium alloys will increase in significance [6–10].

Therefore, in this context, the poor corrosion resistance of magnesium alloy itself restricts the development of magnesium alloys. This situation urgently needs to be addressed [11–14]. The surface of magnesium alloys is similar to that of aluminum alloys; it also has a layer of magnesium oxide coating. However, the coating itself is loose, porous, soft and thin, and it is difficult to provide good corrosion protection [15–19]. This requires a layer of organic coating on the surface to prevent corrosion and improve its utilization. However, considering that it is not easy to dispose of the coating after the application or recycling of magnesium alloys, it is necessary to consider more environmentally friendly, highly efficient and long-lasting corrosion-resistant coatings [20–24]. In this context, coatings with self-repairing abilities and added microcapsules have emerged.

In recent years, self-healing microcapsules have achieved remarkable advantages in terms of biocompatibility and environmental friendliness, which has attracted much attention in various fields, such as materials chemistry, biopharmaceuticals and environmental sciences [25–29]. In particular, microencapsulation technology, with a core–shell structure and the synergistic effect of self-healing and slow release, has started to be explored for the corrosion and protection of alloy surfaces [30–34]. This is because microcapsules act as fillers in the preparation process to provide a good slow-release refinement and significantly improve the coating microstructure [34,35]. The self-healing ability of microcapsules is a very promising method for repairing microgaps in epoxy-resin-based magnesium alloy materials. There are two general types of self-healing microcapsules: One is the general type of microcapsule, and the other is the slow-release type of microcapsule. White SR [36] et al. attempted to design a general-type self-healing microcapsule by means of in situ polymerization. The microcapsules were composed of polyurea-formaldehyde resin-coated dicyclopentane, which is a general microcapsule of the resin-coated dicyclopentadiene type. The slow-release self-healing microcapsules are released from the wall material by controlling the core material within the core–shell structure. They can be used in alloy corrosion protection, chemical production as well as in the agricultural and food industries. Chen [37] designed a structurally robust microcapsule with a slow-release synergistic effect using a face complex of mesoglycan and chitosan from pectin as well as latex proteins. Cunha [38] studied bifunctional polyurea-formaldehyde microcapsules and successfully prepared microcapsules by mixing linseed oil and benzotriazole. Wang [39] prepared slow-release microcapsules that can act as a vitamin supplement using spray technology, while the natural antioxidant capacity and release rate of the microcapsules were tested for modulation. Amand [40] prepared a capsule structure with a synergistic effect of self-healing and slow release by varying the acetone content. The generated content of the core wall was also investigated, and when the microcapsules produced an effect, the core material flowed out, which in turn diffused to fill and bind the cracks.

Compared to existing literature reports, the uniqueness of this research lies in the fact that PVA itself has bonding, emulsification and dispersion properties, while gelatin itself is a macromolecular hydrophilic colloid, which can also be used for bonding. Therefore, the simultaneous addition of poly (vinyl alcohol) and gelatin provides stabilization as well as enhances aqueous phase viscosity to form a thin film, thereby increasing the encapsulation rate of the microcapsules. The wall material, ethyl cellulose, has the functions of bonding, filling and coating forming. However, there is limited research on the emulsifiers used in compounding. We analyzed the morphology of the microcapsules using a single emulsifier, as well as the lack of a certain heart–wall ratio and optimal mass fraction between the entire composition and the coating. This is the focus of this work. Finally, LCSM was used to observe the macroscopic morphology of the microcapsules, and the existence of core–shell structure was preliminarily determined. The particle size distribution and dispersion uniformity of the microcapsules in emulsion were evaluated using OM and a laser particle size analyzer. The micromorphologies of the microcapsules and the self-healing coatings were observed by scanning electron microscopy. In addition, FT-IR and TGA were used to verify that the microcapsules were successfully encapsulated. The basic properties of microcapsule coatings are tested via electrochemical Nyquist diagrams and Tafel

analyses, immersion experiments, adhesion tests and coating tensile tests. The purpose of this experiment was to show that the self-repairing coating with added microcapsules has excellent self-healing properties, corrosion resistance characteristics, adhesion, and self-healing tensile ductility under the action of a compounded emulsifier. Meanwhile, the impedance value in 3.5 wt.% NaCl solution was 8.242×10^4, which reached the optimum value. And it had the lowest corrosion current density and good adhesion and tensile toughness. Through the above corresponding series of experiments, it was able to be thoroughly analyzed that the glycerol was successfully released from the broken microcapsules for self-heal. The AZ91D magnesium alloy anticorrosive coating with excellent corrosion resistance and self-healing ability was formed. Compared to other experiments, the wall material, ethyl cellulose, itself is easy to degrade, green and has good biocompatibility as well as the function of bonding and filling. Finally, new theoretical support and empirical methods are provided for the corrosion and protection of magnesium alloy surfaces in this field.

2. Materials and Methods

2.1. Materials and Instruments

Main raw materials: AZ91D magnesium alloy (density 1.82 g/cm^3); ethyl cellulose (density 1.07 g/cm^3); propanetriol (relative molecular mass 92.09, colorless, odorless, sweet, clear and viscous liquid appearance; Sinopharm Chemical Reagent Co., Shanghai, China); polyvinyl alcohol (relative molecular mass 44.05, white flake, flocculent or powdery solid); Shanghai Sinopharm Chemical Reagent Co., Ltd., Shanghai, China); gelatin (also known as animal gelatin, gelatin belongs to a large molecule hydrocolloid; Tianjin Damao Chemical Reagent Factory, Tianjin, China); OP-10 (white and milky white paste; Shanghai Aladdin Biochemical Technology Co., Ltd., Shanghai, China); dichloromethane (relative molecular weight 84.93, colorless and transparent liquid; Tianjin Damao Chemical Reagent Factory, Tianjin, China); n-butanol (relative molecular weight 74.12, colorless and transparent liquid; Tianjin Damao Chemical Reagent Factory, Tianjin, China); xylene (relative molecular weight: 106.165; Tianjin Damao Chemical Reagent Factory, Tianjin, China); anhydrous ethanol (colorless liquid, with special fragrance; Tianjin Damao Chemical Reagent Factory, Tianjin, China); and E-51 Epoxy resin and supporting curing agent (Zhongtian Fine Chemical Co., Ltd., Zhoushan, Zhejiang Province).

Main experimental instruments: HH-S2 digital thermostatic water bath (Changzhou Yineng Experimental Instrument Factory, ChangZhou, China); DZF vacuum drying oven (Nanjing Suenrui Production Plant, Nanjing, China); 85-2 digital thermostatic magnetic stirrer (Changzhou Jintan Jingda Instrument Manufacturing Co., Ltd., Changzhou, China); CHINALAB 20 electronic balance (Anhui Tianping Machinery Co., Ltd., Chizhou, China); CHI660E-type electrochemical workstation (Gongyi Kerui Instrument Co., Ltd., Gongyi, China); VEGA3 XMU scanning electron microscope (Guangzhou Dongrui Technology Co., Ltd., Guangzhou, China); 3D confocal microscope (Xiamen Maina Optical Technology Co., Ltd., Xiamen, China); NMM-800TRF optical microscope (Dongguan Ruixian Optical Instrument Co., Ltd., Dongguan, China); FBS-50KNW tensile tester (Jinan Tianhua Testing Equipment Co., Ltd., Jinan, China); GD26-FTIR-650 Fourier transform infrared spectrometer (Zhongke Ruijie (Tianjin) Technology Co., Ltd., Tianjin, China); and TGA55 thermal weight loss analyzer (Nanjing Nanda Wanhe Technology Co., Ltd., Nanjing, China). The main experimental instruments are shown in Figure 1 below.

2.2. Sample Preparation

An AZ91D magnesium alloy with the size of 15 mm × 15 mm × 25 mm was selected And sanded with 600#, 800#, 1500# and 2000# sandpaper, in this order, until a metallic luster appeared. After, it was rinsed with deionized water for 3 minutes and put into a beaker filled with absolute ethanol. Ultrasonic shaking treatment was carried out for 5 min for the purpose of de-oiling. It was then removed, rinsed again with deionized water for 2 min, and put in alkaline washing solution. After rinsing with deionized water for 2 min,

it was degreased with acetone. Then, it was removed and rinsed with deionized water for 3 min and put in an acid washing solution. After rinsing with deionized water for 3 min, it was put into the vacuum drying oven and dried at 50 °C for use.

(**a**) (**b**)

Figure 1. Macroscopic view of the main experimental instruments: (**a**) scanning electron microscope; (**b**) 3D confocal microscopy (LSCM).

2.3. Experimental Content

2.3.1. Preparation of Microcapsules

Stirring was continued at 200 rpm for 5 min to obtain 250 mL of 0.8 wt.% PVA with 1 wt.% gelatin as a microencapsulated stabilizer. Next, 20 g of ethyl cellulose was fully dissolved in 100 mL of dichloromethane. 8 mL of propanetriol was added to the mixture of ethyl cellulose and dichloromethane. It was mechanically emulsified at 600 rpm in a constant temperature water bath at 45 °C and fully reacted for 4 h until the dichloromethane was completely evaporated. After the reaction, the microcapsules were isolated by filtering and rinsing with deionized water and were dried in a vacuum drying oven at 60 °C for use.

2.3.2. Preparation of Self-Healing Coatings

In the process of adding microcapsules into the coating, the influence of the amount and dispersion of microcapsules on the properties of the coating was researched. The designs are no add, 5% addition, 10% addition, and 20% addition. Twelve 25 mL beakers were taken and divided into three groups, a, b and c, resulting in three groups of 3 beakers each. 3.75 g of epoxy E-51 was put in each beaker. 1.25 g of hardener b was put in a beaker. The organic solvent in beaker c was put into a and b in an appropriate amount and stirred with a magnetic stirrer to mix thoroughly. Among them, 0 g, 0.5 g, 1 g, 2 g were added to each component and stirred for 30 min using a magnetic stirrer. Finally, the epoxy resin self-healing coating containing microcapsules with different mass fractions was uniformly coated on the surface of the magnesium alloy and then cured at 25 °C for 12 h and then at 60 °C for 24 h in a vacuum drying box.

2.4. Testing and Analysis

2.4.1. Electrochemical Test

The electrochemical impedance spectrum and polarization curves of the self-healing coatings were obtained using a CHI660E electrochemical workstation. The experimental tests were performed using a conventional three-electrode system. The specimen was the working electrode (exposed area of 1 cm^2), the saturated glycerol electrode (SCE) was the reference electrode, and the platinum electrode was the auxiliary electrode. The test solution was 3.5% N saturated aCl solution, and the test temperature was (25 ± 5) °C. The electrochemical impedance spectrum was scanned from 0.01 Hz to 100,000 Hz, the polarization curve was scanned at a voltage range of ±0.5 V relative to the open circuit potential, and the scan rate was 5 mV/S. To ensure accuracy and reproducibility, three sets of parallel tests were performed for each test.

2.4.2. Scanning Electron Microscopy and X-ray Diffraction Spectroscopy

A VEGA3 XMU scanning electron microscope (SEM) (Guangzhou Dongrui Technology Co., Ltd., Guangzhou, China) from TESCAN, with an accompanying energy spectrometer (EDS), was used to observe the prepared microcapsules as well as the microscopic morphology and microscopic characterization of the coatings, with a scanning voltage of 20 kV.

2.4.3. Microcapsules Particle Size and Macroscopic Morphology Analysis

3D confocal microscope (LCSM) (Xiamen Maina Optical Technology Co., Ltd., Xiamen, China), optical microscope (OM) (Dongguan Ruixian Optical Instrument Co., Ltd., Dongguan, China), and laser particle size tester (Kunshan Lugong Precision Instrument Co., Ltd., Kunshan, China) were used to characterize the macroscopic morphology, distribution in the compounded emulsion, particle size, and the aggregation of the prepared microcapsules. Among them, LCSM uses a 405 nm laser as the light source to initially determine the microcapsule roughness and core–shell structure.

2.4.4. Fourier Infrared Spectroscopy and Thermal Weight Loss Testing

The GD26-FTIR-650 Fourier infrared spectrometer (Zhongke Ruijie (Tianjin) Technology Co., Ltd., Tianjin, China) was used to view the organic functional group profile of the microcapsules. Among them, about 0.3 mg KBr was weighed and fully ground with microcapsules in an agate mortar, pressurized to 15–20 MPa and kept for 1 min for testing. The TGA55 heat loss tester (Nanjing Nanda Wanhe Technology Co., Ltd., Nanjing, China) was used for testing, and the sample was tested by opening the pure nitrogen valve and adjusting the outlet pressure to 0.1 MPa.

3. Results and Discussion

3.1. Characterization of Microcapsules

3.1.1. Microstructure and Particle Size Distribution

Figure 2 shows the SEM morphology and particle size distribution of the microcapsules and microstructure. Figure 2a shows the SEM image of microcapsules loaded with glycerol at 500 μm. It can be seen from the figure that the microcapsules are relatively uniform in both distribution and size. Local rupture appears, and the core–shell structure can be seen initially from the rupture. Figure 2b shows the SEM image of the microcapsules at 200 μm, and further magnification shows that the surface of the microcapsule is smooth and round and that the size distribution is relatively uniform. Figure 2c shows the SEM image of a single microcapsule, which is the moment when the magnification could be maximized and a clear image could be taken under the right conditions. At 100 μm, the synthesized capsule appears spherical, then becomes very round and smooth again. The core and wall states of the core–shell structure can be seen under reflection, in addition to the compact distribution of the capsule-forming structure. Figure 2d shows the SEM cross-section of the microcapsules rupture. The total thickness of the outer and inner walls of the capsule is about 15 μm, and Figure 2e shows the SEM image at a magnification of 100 μm. At this time, not only can the core–shell structure be clearly seen, but also the change distribution of microcapsule particle size can be seen. The observed results correspond to the particle size distribution detected by the laser particle size tester. Figure 2f shows the particle size distribution of the microcapsules, ranging from (150.424 $\pm$ 3.756) μm, which is consistent with the Gaussian nonlinear fitting results.

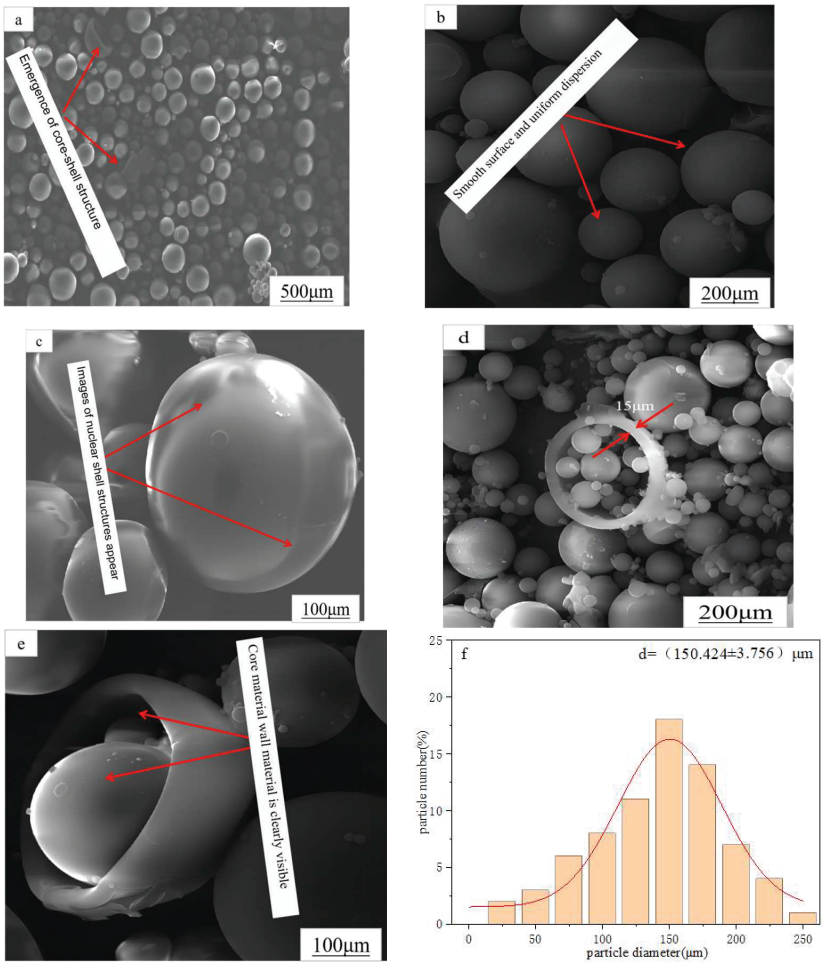

Figure 2. SEM images and size distribution of glycerol-loaded microcapsules: (**a**) microcapsule magnification at 500 μm; (**b**) microcapsule magnification at 200 μm; (**c**) microcapsule magnification at 100 μm; (**d**) ruptured microcapsule magnification at 200 μm; (**e**) ruptured microcapsule magnification at 100 μm; (**f**) size distribution of particle size.

3.1.2. Macroscopic Structure and Particle Dispersion

Figure 3 shows the macroscopic structure and particle size morphology of the microcapsules prepared under the 3D confocal microscopy (LCSM), optical microscopy (OM), and camera 2a. Figure 3a,b show the morphology of the capsule emulsion prepared under optimal conditions and the capsule emulsion dried in a vacuum drying oven, respectively. It can clearly be seen that the emulsions are green and transparent, the viscosity is moderate, and the dry powder is milky and delicate, which preliminarily indicates that the preparation method and process were successful. Figure 3c shows the dispersion of the emulsion under an optical microscopy (OM). It can be seen that the surface of the microcapsule obtained after mixing the water phase with oil is smooth and has no adhesion. The uniform distribution in the emulsion is attributed to the use of a gelatin and PVA compound emulsifier. The deposition rate of the polymer on the wall slowed down, forming a smooth-surfaced microcapsule. The microcapsule particle size is about 152 μm, as shown in Figure 3d. The inner capsule wall, outer capsule wall, and hollow of the

microcapsule are clearly seen in Figure 3e. Figure 3f shows the three-dimensional structure of the microcapsule measured under 3D confocal microscope. It can be seen that the outer capsule wall is locally depressed, indicating that the interior is hollow. The reason for the depression is that the outer capsule wall is resistant to friction and has toughness, which can undergo some deformation. As can be seen in Figure 3d–f, this is consistent with the results from scanning electron microscopy (SEM) and the laser particle size tester tests.

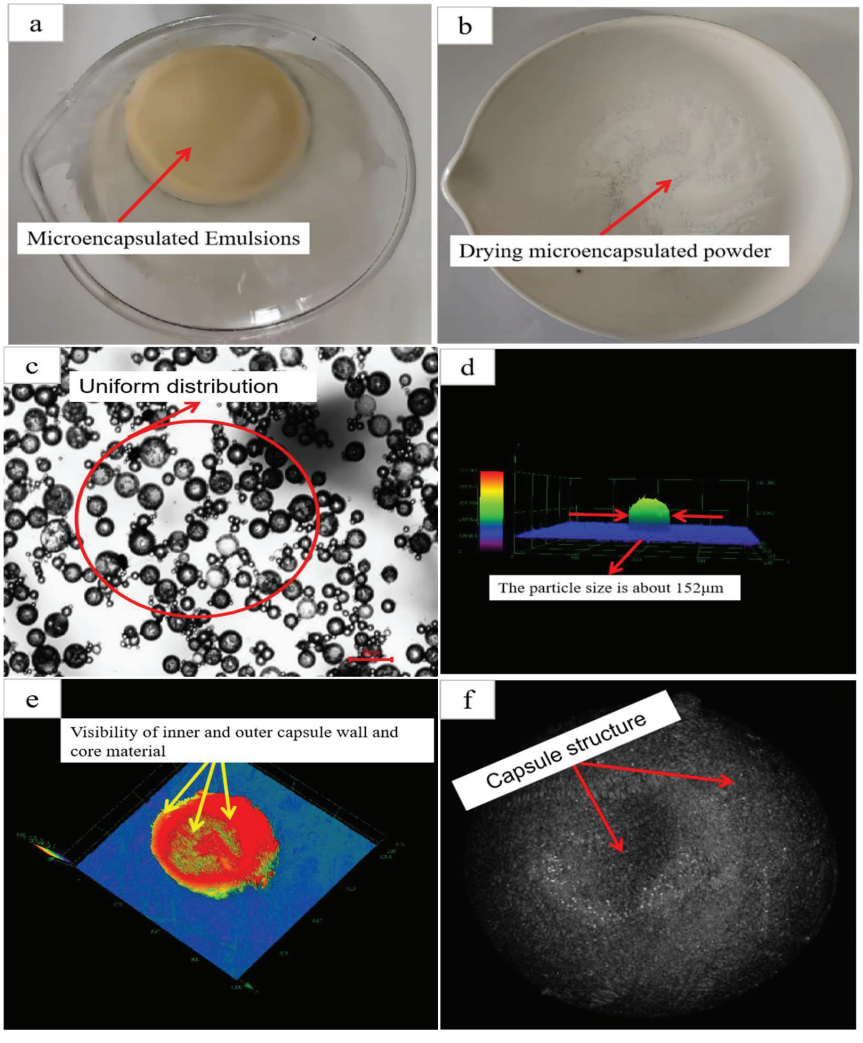

Figure 3. Macrostructure of prepared microcapsule and particle size under core–shell structure: (**a**) optimal emulsion; (**b**) microcapsule powder; (**c**) emulsion dispersion under optical microscope (OM); (**d**) particle size under 3D confocal microscope (LCSM); (**e**) inner capsule wall under 3D confocal microscope (LCSM); (**f**) capsule structure under 3D confocal microscope (LCSM).

3.1.3. Chemical Structure of Microcapsules

Figure 4a shows the FTIR spectrum of ethyl cellulose in the wall material. In the above peaks of organic functional groups, the tensile vibration of C-C aromatic ring ranges from 1586 to 1467 cm^{-1}. The characteristic peak corresponding to the microcapsules in Figure 4c is 1439 cm^{-1}. Meanwhile, the O-H-O asymmetric tensile vibration ranges from 1316 to

1289 cm^{-1}. The peak value of C-O-C stretching vibration is 1227 cm^{-1}. This corresponds to microcapsules at the characteristic peak of 1240 cm^{-1}. Figure 4b shows the FTIR spectrum of glycerol. There is a stretching vibration at the 3248 cm^{-1} peak for the -OH bond and an asymmetric stretching vibration at the 2913 cm^{-1} peak for the -CH_2 bond. There is a symmetric stretching vibration for the -CH_2 at the 2867 cm^{-1} peak and a bending vibration for the -CH_2 bond at the 1407 cm^{-1} peak. The symmetric stretching vibration peak of C-O ranges from 1132 to 1030 cm^{-1}, and that of the secondary alcohol is at 839 cm^{-1}. These peaks coincide with those of the microcapsule at 2964 cm^{-1}. The results showed that the characteristic peaks of ethyl cellulose and glycerol reacted in microcapsules. This also confirmed that glycerol was successfully encapsulated in the microcapsules.

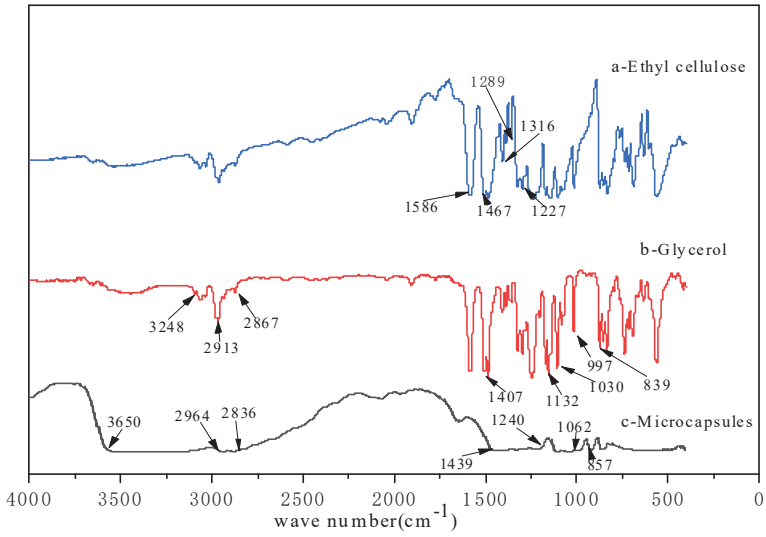

Figure 4. FTIR spectra of microcapsules, glycerol and ethyl cellulose: (**a**) ethyl cellulose; (**b**) glycerol; (**c**) microcapsules.

3.1.4. Conversion Efficiency of TGA and Microcapsules

Figure 5a,b show the heat weight loss curve and the conversion rate curve of microcapsules, respectively, and the initial decomposition temperature of ethyl cellulose is shown in Figure 5a at 465 °C. It has a higher initial decomposition temperature than the wood carbon structure, and the residue content is 29 wt.% at 800 °C, which easily forms a heat-stable carbon material. This is inherently because of the presence of the aromatic hydrocarbon skeleton structure in ethyl cellulose. Therefore, the initial decomposition temperature of glycerol is 150 °C, and the final decomposition temperature is 284 °C. The initial thermal degradation temperature of the microcapsules is 360 °C. It can be seen from the figure that the slope of the microcapsule curve is smaller than that of the ethyl cellulose curve. Combined with the Fourier infrared spectroscopy in Figure 4, it can be seen that glycerol is well encapsulated into the microcapsules. In Figure 5b, the thermogravimetric analysis of the figure shows that the microcapsule structure is synthesized by glycerol and the wall material. It can be seen from the TGA diagram of the microcapsules that the encapsulation rate of the microcapsules is 12 wt.%. This further indicates that the preparation of microcapsules was successful.

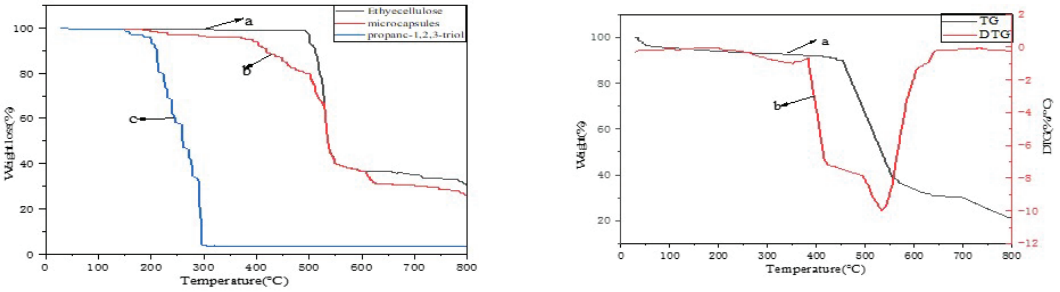

(**a**) (**b**)

Figure 5. Fourier infrared spectra (TGA) plots of self-healing microcapsules: (**a**) a, ethyl cellulose; b, microcapsules; c, propanetriol; (**b**) a, TG; b, DTG.

3.2. Characterization of Optimal Core-to-Wall Ratio of Microcapsules and Corrosion Resistance of Self-Healing Coatings

Figure 6 shows the optimal core–wall ratio and corrosion resistance test of self-healing coatings after the microcapsules with different mass fractions are soaked. In Figure 6a, when the core–wall ratio of microcapsules is 1:1, the proportion of spherical microcapsules with regular morphology is low in the total number of microcapsules. The surface is not polished, and there are more impurities attached. Due to the low core material ratio, the microcapsules adhere to each other, causing excess wall polymers to accumulate on the already formed microcapsules. In Figure 6b, when the core-to-wall ratio of 1.2:1, it is easily seen that the microcapsules are uniformly dispersed. The spherical structure of the microcapsule formed is smooth and more regular, and the surface is not adhered to anything. Figure 6c When the core–wall ratio is 1.5:1, the wall content is too low. During the mixing process, the microcapsule capsule is easy to break due to its thin wall shell. Therefore, when the mass ratio of core material to wall material is 1.2:1, the microcapsules synthesized with high sphericity have a regular shape and clear structure. There is no adhesion between microcapsules. The best results were prepared at this ratio. In Figure 6d–f, the scratch corrosion morphologies of magnesium alloys soaked in non NaCl solution, 3.5% NaCl solution for 24 h and 3.5% NaCl solution for 48 h, respectively, can be seed. The analysis showed that the corrosion of the epoxy coating without microcapsules was more significant than that of epoxy coating with microcapsules. And relative to the epoxy coatings with 5% and 20%, the epoxy coating with 10% microcapsules has good corrosion resistance. This indicates that there is an optimal concentration range for self-healing microcapsules to achieve maximum corrosion resistance. Excessive microcapsule content may compromise the water repellency of the coating, resulting in reduced corrosion resistance.

3.3. Characterization of Self-Healing Ability of Coating by Microcapsules with Different Mass Fraction Addition

Figure 7 shows the corrosion effect of the coated samples with different amounts of microcapsules in artificial seawater. For pure epoxy resins without microcapsules. With the increase in soaking time, corrosion appeared in the scratch area, and the corrosion outside the scratch was more obvious. As can be seen from figure b, when the microcapsule content is 5%, compared to the pure epoxy coating, the scratches become shallower and lighter under the same soaking time. This indicates an initial ability to self-healing, and when the microcapsule content is 10%, only a small amount of corrosion occurs around the coating. This indicates that the microcapsules will release the core material, propanetriol, over time when the coating is scratched or broken. However, glycerol is a polar molecule, and the unshared electron pair of the oxygen element on the polar group combines with the hydrogen ion. This causes cations to adsorb on the substrate surface, which changes the structure of the double electric layer on the surface of the substrate, producing a covering

effect, forming a hydrophobic coating and weakening the movement of hydrogen ions, chloride ions and water molecules. In turn, this weakens the access to the solution substrate and hinders charge transfer. Moreover, anode polarization occurs, thereby reducing the corrosion rate and self-healing, and hindering further corrosion. When the microcapsules content in d is 20%, the ratio between microcapsules and epoxy resin becomes larger. As a result, the epoxy resin inside the microcapsule cannot be evenly dispersed and cannot be scratched at the scratch site, and the corrosion resistance is weakened as the soaking time increases. It can be seen that when the microcapsule content is 10%, the self-healing ability is the best, which is consistent with Figure 6.

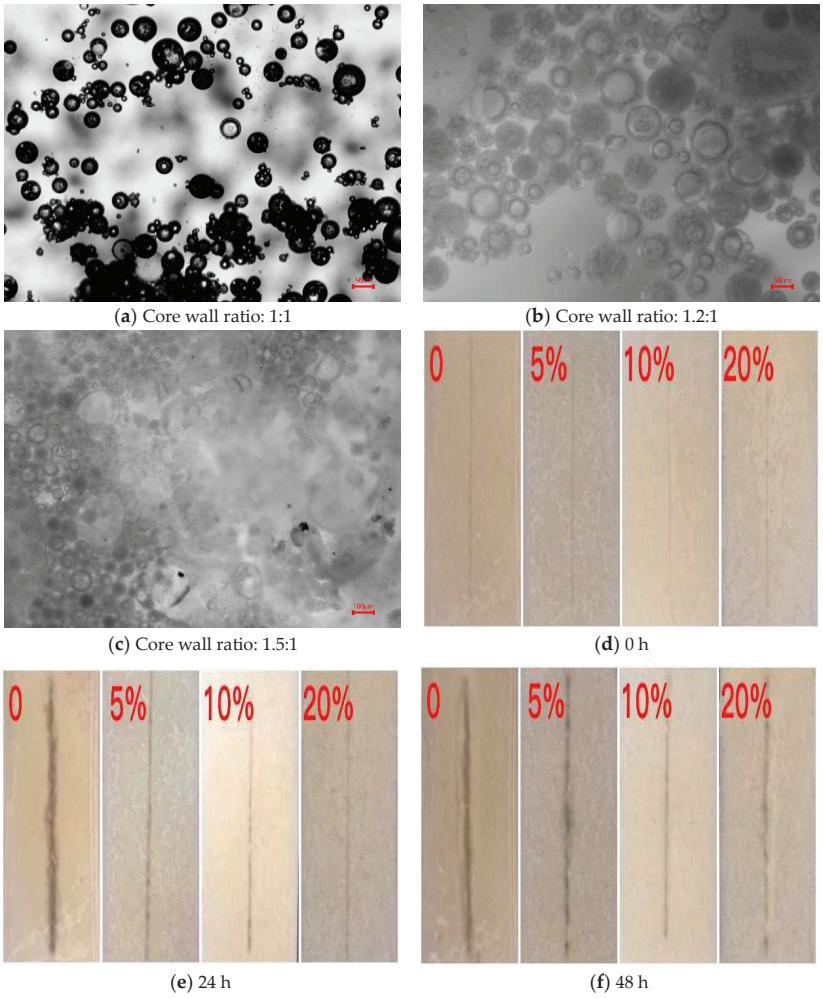

(**a**) Core wall ratio: 1:1 (**b**) Core wall ratio: 1.2:1

(**c**) Core wall ratio: 1.5:1 (**d**) 0 h

(**e**) 24 h (**f**) 48 h

Figure 6. In the impregnation corrosion resistance test, the best core–wall ratio of microcapsules and self-healing coatings with different mass fractions are the following: (**a**) core-to-wall ratio of 1.5:1; (**b**) core-to-wall ratio of 1.2:1; (**c**) core-to-wall ratio of 1.5:1; (**d**) no sodium chloride solution immersion; (**e**) 3.5% sodium chloride solution immersion for 24 h; (**f**) 3.5% sodium chloride solution immersion for 48 h.

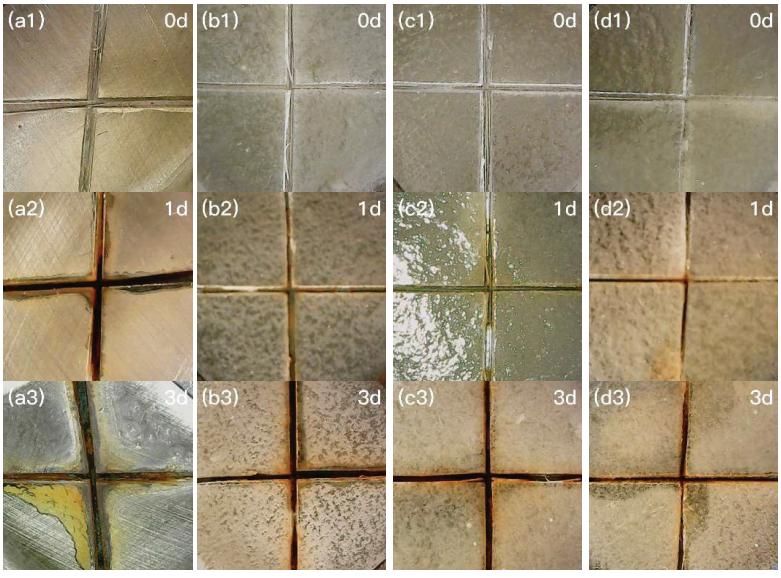

Figure 7. Corrosion effect of coatings with different self-healing microcapsule additions in artificial seawater: (**a**) no microcapsule addition (**a1** 0d, **a2** 1d, **a3** 3d); (**b**) microcapsule content 5% (**b1** 0d, **b2** 1d, **b3** 3d); (**c**) microcapsule content 10% (**c1** 0d, **c2** 1d, **c3** 3d); (**d**) microcapsule content 20% (**d1** 0d, **d2** 1d, **d3** 3d).

3.4. Electrochemical Test Characterization of Self-Healing Coatings

3.4.1. Electrochemical Impedance Spectroscopy

Figure 8 above shows the electrochemical impedance spectra of different self-healing microcapsules added to the 3.5% NaCl solution. Figure 8a shows the Nyquist diagram. The impedance modulus values in the low frequency region are 2.8×10^4, 3.6×10^4, 7.8×10^4, and 5.3×10^4, respectively. As the radius of the capacitive resistance of the capacitive arc in solution gradually increases, the corresponding resistance of the solvation layer also increases. The charge transfer resistance becomes more pronounced, which in turn hinders further erosion of the coating by the solute in solution. Moreover, when the microcapsule addition amount is 10 wt.%. The coating has the best self-healing ability, indicating that it has the best corrosion resistance at this moment. Compared to the pure epoxy coating without the addition of microcapsules, its corrosion resistance is poor. Also in the Byrd plot in Figure 8b, it can be seen that the $|Z|$ value increases continuously in the absence of the microcapsules up until they are added up at 10 wt.%, but the value decreases at a microcapsule content of 20 wt.%. This indicates that the self-healing coating exhibits optimal impedance coating volume with a stable passive response at 10 wt.% microcapsule content [40]. The self-healing epoxy coating successfully prevented the electrolyte solution from penetrating into the substrate and coating surface. The corrosion inhibitor released by the microcapsule is adsorbed at the corrosion site. It successfully inhibits the corrosion process. The appearance of double peaks can clearly be observed in Figure 8c, indicating that the self-healing coating was successfully coated at this time and has a double-layer structure. This indicates that the corrosion resistance of the coating is optimal when the microcapsule content is 10 wt.%. In Figure 9, the error between the data fitted in the figure and the experimental data is minimal, so the equivalent circuit can be used to fit the coating data of the optimal microcapsule addition amount, where CR and CP are, respectively, the annual corrosion rate and anti-corrosion efficiency on the Tafel curve. Ecorr mainly describes the corrosion thermodynamic trend of the coating, and Icorr is the corrosion current density. In general, the main criterion of corrosion resistance is determined by

the corrosion current density. The lower the current density, the lower the corrosion rate accordingly. Epoxy resin varnish coatings and self-healing coatings have orders of magnitude lower current densities compared to magnesium alloy substrates. In addition, the self-healing coating worked better in the sodium chloride solution. The reason is that the coating successfully resists the penetration of the electrolyte solution to the substrate and the coating surface. The corrosion inhibitor released by the microcapsule is adsorbed at the corrosion site. The corrosion process was successfully suppressed, which is also consistent with the polarization curve analysis in Figure 10 below.

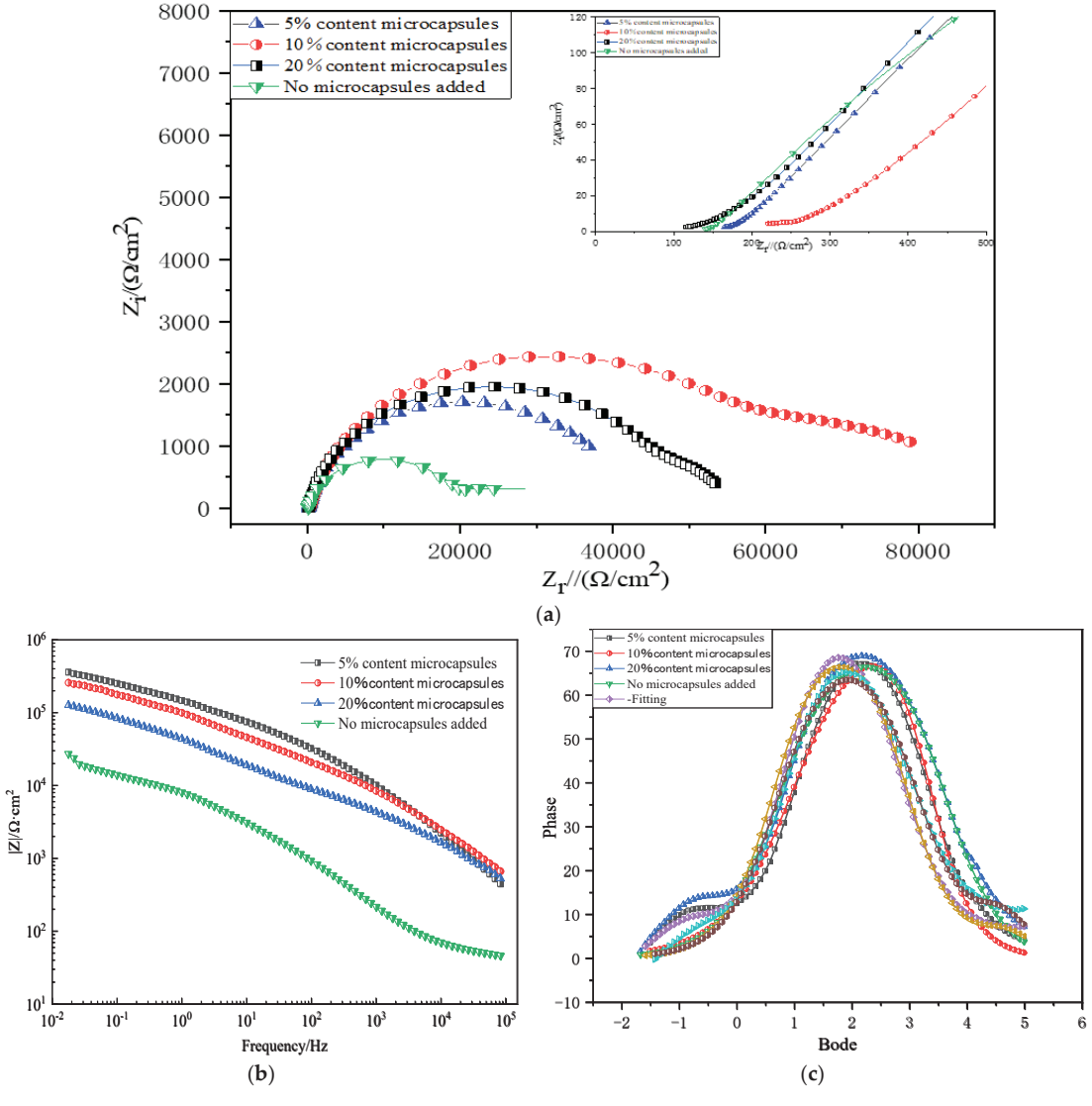

Figure 8. Electrochemical impedance spectra of coatings with different self-healing microcapsule additions in 3.5% NaCl solution: (**a**) Nyquist plot; (**b**) impedance vs. frequency Byrd plot; (**c**) Bode diagram of phase angle and frequency.

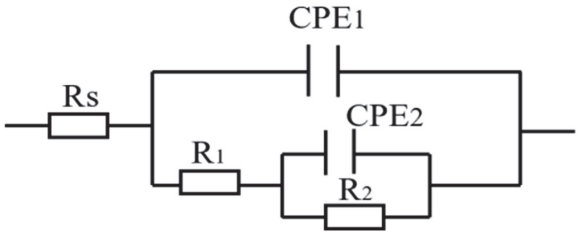

Figure 9. Equivalent circuit diagram of epoxy resin coating in 3.5% NaCl solution at optimal microcapsule addition.

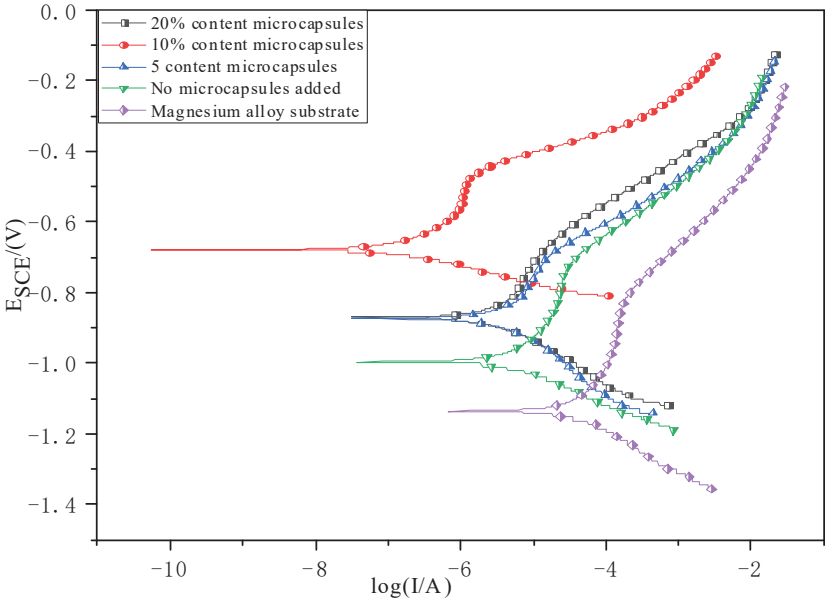

Figure 10. Polarization curve of epoxy resin coating in 3.5% NaCl solution at optimal microcapsule addition.

3.4.2. Electrochemical Polarization Curve Graph Analysis

Figure 10 shows the polarization curves of epoxy resin coatings in 3.5% NaCl solution at the optimal microcapsule dosage. Table 1 shows the Ecorr and icorr of the epoxy coating with different microcapsules added in 3.5% NaCl solution. Each set of experiments was conducted three times in parallel to exclude accidental errors. It can be concluded from the figure that when the addition of microcapsules reaches 20%, the anode arc can be observed. The corrosion potential and corrosion current density of magnesium alloy in a bare matrix are the worst, at -1.125 V and 1.562×10^{-5} A, respectively. With the addition of epoxy resin varnish, the corrosion potential and corrosion current density showed an obvious optimization trend. At this time, the corrosion potential and the corrosion current density are -1.014 V and 1.854×10^{-5} A, respectively. After that, according to the percentage content of microcapsule additives, the added amounts were 5 wt.%, 10 wt.% and 20 wt.%. The corresponding electrochemical measurement data showed a trend of first increasing and then decreasing, and reached the peak value when the microcapsule addition amount was 10 wt.%; that is, the optimal value was reached. The optimal corrosion potential and corrosion current density are -0.721 V and 1.86×10^{-7} A, respectively. In general, the corrosion resistance of self-healing coatings is mainly determined by the corrosion current density. The lower the corrosion current density, the lower the corresponding corrosion

rate of the self-healing coating. The self-healing coating without added microcapsules has a lower order of magnitude current density compared to the added microcapsules. This indicates that both coatings can provide corrosion protection to magnesium alloy substrates and slow down the corrosion rate. However, the self-healing coating is effective because it can release microcapsules, causing the slow-release healing of coating ruptures and adsorption on the broken parts, which can inhibit the corrosion process well. Table 2 shows the equivalent fitting of impedance using electrochemical fitting software, and the fitted equivalent circuit diagram of the coating is shown in Figure 9, which shows that the fitted data and the experimental data are similar. The result error is small, so the equivalent circuit diagram can be used to fit the experimental data. Rs represents the resistance of the solution, CPE1 and CPE2 represent the capacitance and resistance of the self-healing coating, and R1 and R2 represent the charge transfer resistance between the coating and the reaction resistance of the coating, respectively. Due to the rough surface and inhomogeneous electrochemical properties of the magnesium alloy substrate, a phase angle element is commonly used instead of the capacitance for interpreting the behavior of the high-frequency capacitive arcs. CPE1 and CPE2 represent the phase angle elements of the reaction interface and the two-layer corrosion products, respectively. The results show that the higher the fitting resistance of microcapsules, the better the corrosion resistance. When the mass fraction of the microcapsule is 10 wt.%, its corrosion resistance reaches its maximum. The results are consistent with those of the polarization curve.

Table 1. Ecorr and icorr of epoxy resin coatings with different microcapsule additions in 3.5% NaCl solution.

Microcapsules	E_{corr}/V	i_{corr}/(A/cm^2)
Uncoated	−1.125	1.562×10^{-5}
Pure epoxy resin coating	−1.014	1.854×10^{-5}
5 wt.% epoxy-based coating of microcapsules	−0.931	1.538×10^{-6}
Epoxy-based coating of 10 wt.% microcapsules	−0.721	1.86×10^{-7}
Epoxy-based coating of 20 wt.% microcapsules	−0.903	1.507×10^{-6}

Table 2. Tafel curve extrapolation results of epoxy resin coatings with different microcapsule additions in 3.5% NaCl solution.

Microcapsules	R_s Ω·cm^2	CPE_1 Ω^{-1}·S^{-n}·cm^2	n_1	R_1 Ω·cm^2	CPE_2 Ω^{-1}·S^{-n}·cm^2	n_2	R_2 Ω·cm^2	$R_1 + R_2$ Ω·cm^2
Uncoated	19.92	8.32×10^{-6}	0.87	8110	4.8×10^{-4}	0.61	15,890	24,000
Pure epoxy resin coating	12.13	8.94×10^{-6}	0.89	26,450	2.3×10^{-4}	0.85	13,150	39,600
5 wt.% epoxy-based coating of microcapsules	11.2	8.44×10^{-6}	0.89	14,080	1.7×10^{-4}	0.73	39,820	53,900
Epoxy-based coating of 10 wt.% microcapsules	9.8	1.33×10^{-5}	0.82	13,520	2.3×10^{-4}	0.85	68,900	82,420
Epoxy-based coating of 20 wt.% microcapsules	13.08	2.49×10^{-5}	0.84	28,900	4.4×10^{-4}	0.62	24,180	53,080

3.4.3. SEM Image and EDS Image of Self-Healing Coating

Figure 11 shows the planar SEM image, sectional SEM image and the corresponding sectional EDS spectra of the epoxy resin coating with optimal microcapsule dosage. At the magnification of Figure 11a, 200 μm, it can be seen that the encapsulated small particles are uniformly dispersed on the surface of the self-healing coating. This indicates that the microcapsules at the optimal content are well formed by stirring and curing after being added to the epoxy resin coating. When the coating is damaged by external forces, the microcapsules encapsulated in the coating can flow out in time to release the retarding agent, glycerin. In turn, the coating provides good protection against corrosion. Figure 11b shows the enlarged view in a. At this time, under the amplification size of 100 μm, the structure of the microcapsule can be seen increasingly clearly, and the dispersion is very

good. Figure 11c shows the cross-sectional SEM image of the epoxy resin coating at the optimal microcapsule dosage. Figure 11d shows the EDS energy spectrum of the corresponding cross section in Figure 11c, which corresponds to the overall face-swept element distribution. The thickness of the self-healing coating is 95–100 μm. It is clearly seen that the incorporation of microcapsules results in a tighter adhesion of the coating to the magnesium alloy substrate and thus excellent corrosion resistance.

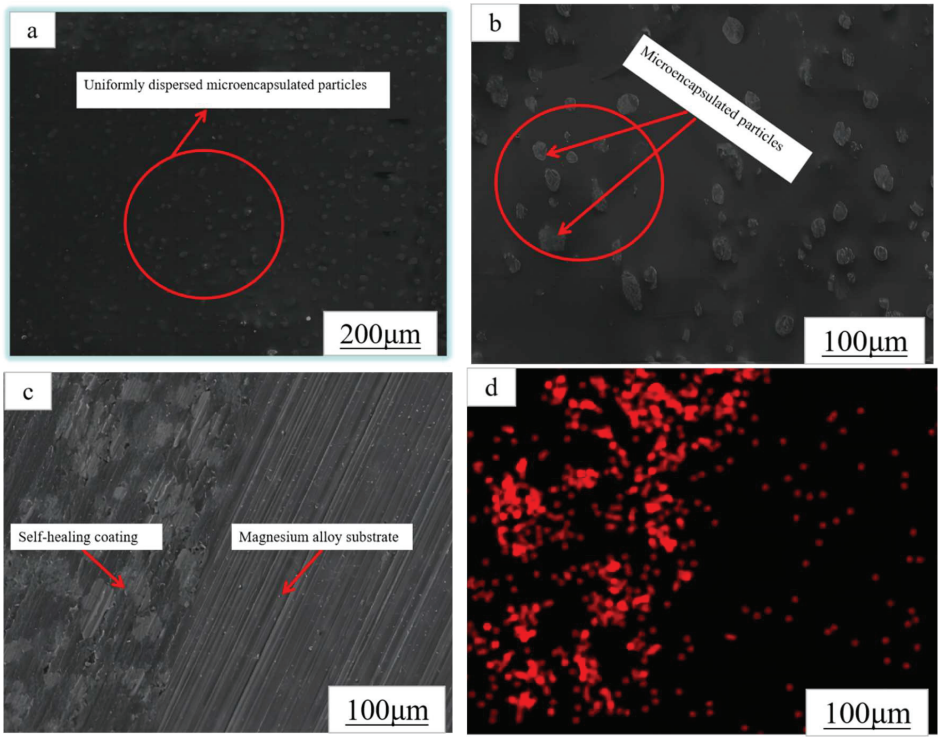

Figure 11. Plane SEM and cross-sectional SEM and EDS spectra of epoxy resin coatings at optimal microcapsule addition levels: (**a**) 200 micron SEM; (**b**) 100 micron SEM; (**c**) cross section of the self-healing coating was examined by SEM at 100 microns; (**d**) EDS spectra of self-healing coating cross section at 100 microns.

4. Conclusions

The present work is based on the preparation of loaded propanetriol microcapsules in micrometer vessels. Because ethyl cellulose is easily decomposed by heat, it is biodegradable and chemically stable. Glycerol itself, due to its lubricating and oiliness, can form a good hydrophobic coating with hydrogen ions on the surface of magnesium alloys. In turn, it can slow down hydrogen ions, chloride ions and water molecules from penetrating the epoxy resin coating, which can effectively reduce the corrosion resistance of the coating and enhance the self-healing performance of the coating, specifically as follows:

1. Microcapsules containing the corrosion inhibitor propanetriol are added into the epoxy resin to form a round and smooth spherical structure, which is uniformly dispersed into the coating.
2. The particle size of the propanetriol-loaded microcapsules was (150.424 ± 3.756) μm as observed by SEM, laser particle size tester, and 3D confocal microscopy.
3. The results of TGA and FTIR show that propanetriol, as a corrosion inhibitor, was effectively encapsulated inside the capsule wall as a core material for release retardation

when rupturing of the microcapsules occurred. The DTG curves of the microcapsules show that the capsule wall shell are loaded with about 12% of the printing agent.

4. SEM images of the plane and cross-section of the self-healing coating show that the microcapsules are evenly distributed in the epoxy resin layer, and the incorporation of microcapsules makes the coating adhere more closely to the magnesium alloy substrate.
5. The electrochemical experimental analysis shows that the microcapsules are successfully added into the epoxy resin coating. Glycerol, as a corrosion inhibitor, is able to be successfully released. It is adsorbed to the rupture site to form a hydrophobic coating layer for self-healing, which in turn attenuates the corrosion rate of the magnesium alloy.

Author Contributions: Conceptualization, L.L. and S.Z.; methodology, L.L.; software, L.L.; validation, S.Z., Q.L. and L.L.; formal analysis, S.Z.; investigation, L.L.; resources, S.Z.; data curation, L.L.; writing—original draft preparation, L.L.; writing—review and editing, L.L.; visualization, J.B. and S.Z.; supervision, Y.X.; project administration, T.Z. and S.Z.; funding acquisition, S.Z and T.Z. All authors have read and agreed to the published version of the manuscript.

Funding: This work was supported by the key project of National Natural Science Foundation of China: Research basis of "corrosion-functional" integrated protective coating on magnesium alloys (U21A2045), the National Natural Science Foundation of China (NSFC), "Study of conductive-corrosion resistant chemical conversion coating of magnesium alloy" (51771050), and the Basic Research Project of Liaoning Provincial Education Department (LJKMZ20220600).

Institutional Review Board Statement: Not applicable.

Informed Consent Statement: Not applicable.

Data Availability Statement: Not applicable.

Conflicts of Interest: The authors declare no conflict of interest.

References

1. Khisamov, R.; Shayakhmetov, R.; Yumaguzin, Y.M.; Kistanov, A.A. Work Function, Sputtering Yield and Microhardness of an Al-Mg Metal-Matrix Nanostructured Composite Obtained with High-Pressure Torsion. *Coatings* **2023**, *13*, 5007. [CrossRef]
2. Tun, K.S.; Brendan, T.Y.S.; Tekumalla, S.Y.; Gupta, M.J. Development from Alloys to Nanocomposite for an Enhanced Mechanical and Ignition Response in Magnesium. *Coatings* **2021**, *11*, 1792. [CrossRef]
3. Lei, C.; Di, M.; Zhao, Q.Z.; Yuan, D.H. Advances in bioorganic molecules inspired degradation and surface modifications on Mg and its alloys. *Mater. Eng.* **2022**, *3*, 723–745.
4. Yang, Q.X.; Tabish MH, M.; Wang, J.B.; Zhao, J.M. Enhanced Corrosion Resistance of Layered Double Hydroxide coatings on Mg Alloy: The Key Role of Cationic Surfactant. *Materials* **2022**, *15*, 2028. [CrossRef]
5. Wang, B.J.; Hou, J.Y.; Luan, J.Y.; Xu, D.K.; Sun, H.J.; Sun, J. The Corrosion Behaviors of an As-Rolled Mg-8Li (in wt.%) Alloy in Two Differently Concentrated NaCl Solutions. *Coatings* **2023**, *12*, 406. [CrossRef]
6. Salsabila, A.L.; Pratama, A.Y.; Nurrochman, A.A.; Hermawan, H.D. Preparation of Tannic Acid/Hyaluronic Acid Coating to Improve the Corrosion Resistance of Implant Material Based on AZ31B Magnesium Alloy. *Coatings* **2023**, *13*, 494. [CrossRef]
7. Li, T.L.; Zhao, Y.; Chen, M.F. Study on Enhancing the Corrosion Resistance and Photo-Thermal Antibacterial Properties of the Micro-Arc Oxidation Coating Fabricated on Medical Magnesium Alloy. *Int. J. Mol. Sci.* **2022**, *23*, 10708. [CrossRef] [PubMed]
8. Song, J.; She, J.; Chen, D.; Pan, F. Latest research advances on magnesium and magnesium alloys worldwide. *Magnes. Alloys.* **2021**, *9*, 705–747. [CrossRef]
9. Pargavi, B.S.L.; Dhanaji, T.U.; Dassani, S.J.; Somasundaram, M. Microstructural, Mechanical, and Corrosion Properties of AZXX Magnesium Alloy: A Review of Processing Methods. *Coatings* **2023**, *13*, 344.
10. Xu, D.K.; Li, C.Q.; Wang, B.J.; Han, E.H. Effect of icosahedral phase on the crystallographic texture and mechanical anisotropy of duplex structured Mg-Li alloys. *Mater. Des.* **2015**, *88*, 88–97. [CrossRef]
11. Chen, J.X.; Xu, Y.; Kolawole, S.F.D.; Wang, J.H.; Su, X.P.; Tian, L.I.; Yang, K. Systems, Properties, Surface Modification and Applications of Biodegradable Magnesium-Based Alloys: A Review. *Materials* **2022**, *15*, 5031. [CrossRef]
12. Sun, W.T.; Bian, G.X.; Jia, L.I.; Pai, J.J.; Ye, Z.H.; Wang, N.; Qi, J.T.; Li, T.J. Study of Trivalent Chromium Conversion Coating Formation at Solution—Metal Interface. *Metals* **2023**, *13*, 93. [CrossRef]
13. Rehman, Z.H.; Kim, J.S.; Churchill, D.G.; Koo, B.H. Tuning Corrosion Properties of the Bio-Inspired AZ-Series Mg Alloys Using Electrochemical Surface Treatment under Varying Experimental Regimes. *Coatings* **2022**, *12*, 1617. [CrossRef]

14. Li, M.; Hao, H.; Zhang, A.; Song, Y.; Zhang, X. Effects of Nd on microstructure and mechanical properties of as-cast Mg-8Li-3Al alloy. *J. Rare Earths* **2012**, *30*, 492–496. [CrossRef]
15. Rangaswamy, A.; Sudarsanam, P.; Benjaram, M. Rare earth doped CeO_2-based catalytic materials for diesel soot oxidation at lower temperatures. *Reddy J. High. Sch. Chem.* **2015**, *33*, 1162–1169. [CrossRef]
16. Liu, G.; Wang, J.; Bian, K.; Zhu, P. Preparation and characterization of nanostructured dibasic calcium phosphate coating on magnesium alloy wire. *Mater. Lett.* **2017**, *209*, 323–326. [CrossRef]
17. Yang, L.H.; Jiang, Q.T.; Zheng, M.; Hou, B.; Li, Y. Corrosion behavior of Mg-8Li-3Zn-Al alloy in neutral 3.5% NaCl solution. *J. Magnes. Alloy.* **2016**, *4*, 22–26. [CrossRef]
18. Dobkowska, A.; Adamczyk-Cieslak, B.; Mizera, J.; Kubásek, J.; Vojtěch, D. Corrosion Behaviour of Magnesium Lithium Alloys in NaCl Solution. *Solid. State. Phenom.* **2015**, *3763*, 87–90. [CrossRef]
19. Yang, J.; Zhang, P.; Zhou, Y.; Yan, F. The study of a phosphate conversion coating on magnesium alloy AZ91D: IV. Comparison of electrochemical behaviors in borate buffer and sodium chloride solutions. *Int. J. Electrochem. Sci.* **2019**, *14*, 11349–11357.
20. Thirumalaikumarasamy, D.; Shanmugam, K.; Balasubramanian, V. Comparison of the corrosion behaviour of AZ31B magnesium alloy under immersion test and potentiodynamic polarization test in NaCl solution. *J. Magnes. Alloy.* **2014**, *2*, 36–49. [CrossRef]
21. Xie, J.; Zhang, J.; Liu, S.; You, Z.; Zhang, Z.; Zhao, T.; Zhang, X.; Wu, R. Developing Mg-Gd-Dy-Ag-Zn-Zr Alloy with High Strength via Nano-Precipitation. *Nanomaterials* **2023**, *13*, 1219. [CrossRef]
22. Liu, F.; Song, Y.W.; Shan, D.Y.; Han, E.H. Corrosion behavior of AZ31 magnesium alloy in simulated acid rain solution. *Trans. Nonferrous Met. Soc. China* **2010**, *20*, 638–642. [CrossRef]
23. Ma, X.C.; Jin, S.Y.; Wu, R.Z.; Wang, J.X.; Wang, G.X.; Krit, B.; Betsofen, S. Corrosion behavior of Mg-Li alloys: A review. *Trans. Nonferrous Met. Soc. China* **2021**, *31*, 3228–3254. [CrossRef]
24. Zhang, Z.Y.; Zhang, J.; Zhao, X.Y.; Cheng, X.Q.; Jiang, S.M.; Zhang, Q.F. Effects of Al-Mg on the Microstructure and Phase Distribution of Zn-Al-Mg Coatings. *Coatings* **2023**, *13*, 46. [CrossRef]
25. Stojadinovic, S.; Radic, N.N.; Vasilic, R.K. ZnO Particles Modified MgAl Coatings with Improved Photocatalytic Activity Formed by Plasma Electrolytic Oxidation of AZ31 Magnesium Alloy in Aluminate Electrolyte. *Coatings* **2023**, *12*, 1503. [CrossRef]
26. Ashassi-Sorkhabi, H.; Moradi-Alavian, S.; Esrafifili, M.D.; Kazempour, A. Hybrid sol-gel coatings based on silanesamino acids for corrosion protection of AZ91 magnesium alloy: Electrochemical and DFT insights. *Prog. Org. Coating* **2019**, *131*, 191–202. [CrossRef]
27. Pommiers, S.; Frayret, J.; Castetbon, A.; Potin-Gautier, M.; Pommiers, S.; Frayret, J.; Castetbon, A.; Potin-Gautier, M. Alternative conversion coatings to chromate for the protection of magnesium alloys. *Corros. Sci.* **2014**, *84*, 135–146. [CrossRef]
28. Liang, F.; Shen, Y.; Pei, C.; Qiu, B.; Lei, J.; Sun, D. Microstructure evolution and corrosion resistance of multi interfaces AlTiAlN nanocomposite ficoatings on AZ91D magnesium alloy. *Surf. Coat. Technol.* **2019**, *357*, 83–92. [CrossRef]
29. Ernens, D.; Rooij, M.B.; Pasaribu, H.R.; Riet, E.J.; Haaften, W.M.; Schipper, D.J. Mechanical characterization and single asperity scratch behaviour of dry zinc and manganese phosphate coatings. *Tribol. Int.* **2018**, *118*, 474–483. [CrossRef]
30. Hu, L.; Gao, B.; Xu, N.; Sun, Y.; Zhang, Y.; Xing, P.F. Effect of Cerium and Magnesium on Surface Microcracks of Al–20Si Alloys Induced by High-Current Pulsed Electron Beam. *Coatings* **2022**, *12*, 61. [CrossRef]
31. Li, C.Q.; He, Y.B.; Huang, H.P. Effect of lithium content on the mechanical and corrosion behaviors of HCP binary Mg-Li alloys. *J. Magnes. Alloy.* **2021**, *9*, 569–580. [CrossRef]
32. Xu, W.; Birbilis, N.; Sha, G.; Wang, Y.; Daniels, J.; Xiao, Y.; Ferry, M. A high-specifific-strength and corrosion-resistant magnesium alloy. *Nat. Mater.* **2015**, *14*, 1229–1235. [CrossRef]
33. Zhiheng, G. Corrosion characteristics and protection technology of magnesium alloy. *Surf. Technol.* **2016**, *45*, 169–177.
34. Van, P.N.; Gupta, M.; Moon, S. Enhanced corrosion performance of magnesium pHospHate conversion coating on AZ31 magnesium alloy. *Trans. Nonferrous Met. Soc. China* **2017**, *27*, 1087–1095.
35. Gnedenkov, A.S.; Filonina, V.S.; Sinebryukhov, S.L.; Gnedenkov, S.V. A Superior Corrosion Protection of Mg Alloy via Smart Nontoxic Hybrid Inhibitor-Containing Coatings. *Molecules* **2023**, *28*, 2538. [CrossRef] [PubMed]
36. White, S.R.; Sottors, N.R.; Geubelle, P.H. Autonomic healing of polymer composites. *J. Nat.* **2011**, *21*, 6822–6829. [CrossRef] [PubMed]
37. Chen, Z.Y.; Zhao, S.J.; Yang, M. Structurally stable slow-release microcapsules stabilized by self-assembly pectin-chitosan-collagen in aqueous two-phase system. *J. Food Hydrocoll.* **2022**, *260*, 55–64.
38. Cunha, D.; Leal, D.A.; Santos, L.R.L. pH-sensitive micro-capsules based on biopolymers for active corrosion protection of carbon steel at different pH. *Surf. Coat.* **2020**, *67*, 1143–1153.
39. Chan, K.L.; Xu, C.Y.; Zhou, J.L. Multifunctional fabric coatings with slow-release fragrance and UV resistant properties from EC/silica hybrid microcapsules. *Carbohydr. Polym.* **2020**, *38*, 317–325.
40. Ahmad, M.; Qureshi, S.; Maqsood, S. Micro-encapsulation of folic acid using horse chestnut starch and β-cyclodextrin: Microcapsule characterization, release behavior & antioxidant potential during GI tract conditions. *Food Hydrocoll.* **2017**, *66*, 154–160.

coatings

MDPI

Article

Preparation of Conductive and Corrosion Resistant Phosphate Conversion Coating on AZ91D Magnesium Alloy

Shudi Zhang [1,*], Yuheng Xu [1], Linkun Liu [1], Quanda Lei [1], Jialin Dong [1] and Tao Zhang [2,*]

[1] School of Environmental and Chemical Engineering, Shenyang Ligong University, Shenyang 110159, China; lovexyh2023@163.com (Y.X.); 15670291571@163.com (L.L.); lqd317213741@163.com (Q.L.); 18845713710@163.com (J.D.)
[2] Chinese Academy of Sciences (Shenyang) Metals Research, Shenyang 110016, China
* Correspondence: zhangshuidi@163.com (S.Z.); zhangtao@mail.neu.edu.cn (T.Z.)

Abstract: The application of magnesium alloys in the 3C industry requires the coexistence of excellent corrosion resistance and good electrical conductivity. In this work, a conductive and corrosion-resistant phosphate conversion coating (PCC) on AZ91D magnesium alloy was investigated. The effects of strong oxidant ($KMnO_4$), additive (Na_2MoO_4), surface-active agent (OP-10) and their content in phosphating bath on PCCs were studied, and the mechanism of action of strong oxidant was analyzed. The results showed that the optimum content for $KmnO_4$, Na_2MoO_4 and OP-10 in phosphating bath was 3.0 g/L, 1.5 g/L and 1.0 g/L. The PCC formed at the phosphating bath at the optimum condition was completely covered, the coating on α phases had a bilayer structure and the β phases were protruded. The electrical contact resistance (ECR) of the PCC was as low as 4.91 Ω, the E_{corr} positively shifted about 27 mV, and the i_{corr} reduced significantly. The presence of $KMnO_4$ inhibited the formation of phosphate crystals and made the β phases protrude from the surface to form conductive spots, which improved the conductivity of PCCs.

Keywords: phosphate conversion coating; magnesium alloy; strong oxidant; corrosion resistance; electrical conductivity

Citation: Zhang, S.; Xu, Y.; Liu, L.; Lei, Q.; Dong, J.; Zhang, T. Preparation of Conductive and Corrosion Resistant Phosphate Conversion Coating on AZ91D Magnesium Alloy. *Coatings* **2023**, *13*, 1706. https://doi.org/10.3390/coatings13101706

Academic Editors: Alina Vladescu and Hideyuki Murakami

Received: 29 June 2023
Revised: 18 September 2023
Accepted: 20 September 2023
Published: 28 September 2023

1. Introduction

Magnesium alloys are the lightest engineering materials [1], which have promising applications in aerospace, military defense, biomedicine, transportation and the 3C industry [2–10] due to their excellent properties such as low density, high mechanical strength, high thermal conductivity and good electromagnetic compatibility [11]. Unfortunately, the poor corrosion resistance of magnesium alloys is still the biggest challenge of expanding their application range [12]. Surface treatment technology is an effective means to improve the corrosion resistance of magnesium alloys. Thus, the surface treatment technologies for magnesium alloys including anodic oxidation, micro-arc oxidation, organic coating, electroplating, chemical plating and chemical conversion treatment have experienced rapid development in the past decades [13–17]. As the applications of magnesium alloys in the 3C industry gradually expanded, in order to meet the requirements such as electromagnetic compatibility and electrostatic release, it is necessary to develop a surface treatment technology which can provide a coating with both excellent corrosion resistance and good electrical conductivity.

Chemical conversion treatment has gained widespread interest due to its low cost and simplicity of operation [18]. However, the chemical conversion coatings of magnesium alloys are usually composed of oxides and insoluble salts, which leads to the lack of conductivity of the coating itself [19]. Considering that the electrical contact resistance (ECR) is determined by the electrical conductivity of the material [20], and the charge transfer resistance (R_t) related to corrosion resistance is the resistance of metal atoms to lose electrons and become cations during the electrochemical reaction [21], the two are

irrelevant. Therefore, it is feasible to prepare conversion coatings with high corrosion resistance and low electrical contact resistance.

A few studies on the chemical conversion coatings with high corrosion resistance and low electrical contact resistance have been reported. Jian et al. [22] developed a permanganate conversion coating with a thickness of only 230 nm on AZ31 magnesium alloy; this coating has sufficient conductivity to ensure the magnetic shielding performance of AZ31 due to its low thickness. Duan et al. [23] proposed a design idea of a chemical conversion coating with high corrosion resistance and low ECR on AZ91D magnesium alloy, which was to make β-$Mg_{17}Al_{12}$ phase protrude from the surface as a conductive spot by using the micro-galvanic effect between different phases and adding VO_3^- as a strong oxidant to conversion solution to inhibit the deposition of coating on it. Zhou et al. [24] studied the phosphate conversion coatings (PCCs) with low electrical contact resistance on sand-cast and die-cast AZ91D magnesium alloy, and found that the PCCs of die-cast exhibit lower ECR and better corrosion resistance, which is attributed to the intensified micro-galvanic effect between different phases through the grain refinement of the die-cast alloy.

The main function of the phosphate conversion coatings is to improve the corrosion resistance of magnesium alloy. However, the current studies on conductive and corrosion-resistant PCCs mainly focus on how to improve their conductivity, and ignore the corrosion resistance. Therefore, the aim of this study is to prepare PCCs with low ECR and high corrosion resistance on AZ91D magnesium alloy. The pretreatment before phosphating was screened. The effects of strong oxidant ($KMnO_4$), additive (Na_2MoO_4), surface-active agent (OP-10) and their content in phosphating bath on PCCs were studied, and the mechanism of action of strong oxidant was analyzed by electrochemical measurement and scanning electron microscopy (SEM).

2. Materials and Methods

2.1. Sample Preparation

An AZ91D magnesium alloy was used as the substrate material; the content is shown in Table 1. After cutting into a dimension of 30 × 30 × 5 mm and mechanical polishing with up to 2000 grit SiC paper, plate samples were treated in different pretreatments as shown in Table 2 [25–27]. A phosphating bath containing 35 g/L $Ca(NO_3)_2{\cdot}4H_2O$, 20 g/L $NaH_2PO_4{\cdot}2H_2O$, 1~5 g/L $KMnO_4$, 0.5~2.5 g/L $Na_2MoO_4{\cdot}2H_2O$, 0.5~2.5 g/L OP-10 was used to treat the samples after pretreatments, and the process conditions were as follows: phosphating temperature 55 °C, reaction time 10 min, pH 3.0 (regulated with phosphoric acid). After being taken out of the bath, the samples were thoroughly washed using running deionized water, and then dried with cold air for subsequent tests.

Table 1. Elemental composition and content of AZ91D magnesium alloy (wt.%).

Element	Al	Zn	Mn	Si	Cu	Ni	Fe	Mg
Content	9.1	0.84	0.23	0.01	0.02	0.0021	0.005	Margin

Table 2. Formula and operating condition of pretreatment [25–27].

Sample Number	Formula and Operating Condition	
No. 1	$Na_3PO_4{\cdot}12H_2O$ 10 g/L NaOH 50 g/L 70 °C, 10 min	3 wt.% H_2SO_4 25 °C, 10 s
No. 2		3 wt.% HNO_3 25 °C, 10 s
No. 3		5 wt.% HCl 25 °C, 10 s
No. 4		30 wt.% H_3PO_4 25 °C, 30 s
No. 5		H_3PO_4 20 g/L $Na_3PO_4{\cdot}12H_2O$ 12 g/L 25 °C, 30 s
No. 6	Sonication cleanout in acetone for 5 min	

2.2. Surface Characterization

The appearances and surface morphologies of the phosphate coatings were observed using a digital camera (Sony ZV-1F, Shenzhen, China) and a scanning electron microscope (SEM, TESCAN MIRA3, Brno, Czech Republic), and the chemical compositions were identified using an energy dispersive spectroscopy (EDS, Oxford Instruments X-Max, Oxford, UK).

2.3. Electrical Contact Resistance (ECR) Measurement

The ECR measurement was analyzed with an ohmmeter, two probes were placed vertically on the sample with a distance of 1 cm, and a load of 120 g was applied. The arithmetic average of the measured results in three different areas of the sample was taken as the final test result.

2.4. Corrosion Tests

The time of $CuSO_4$ pitting corrosion test of the coating was carried out dropping a drop of 3 wt.% $CuSO_4$ solution on a 1 cm^2 area of the sample and recording the time when the droplet changed from blue to black. The arithmetic average of the test results in three different areas of the sample was taken as the final test result.

The potentiodynamic polarization (PDP) and electrochemical impedance spectroscopy (EIS) curves were measured using an electrochemical workstation (CH Instruments Ins CHI660E) in 3.5 wt.% NaCl solution at room temperature. A three-electrode cell was used, with the sample as the working electrode (with 1.0 cm^2 exposed area), a platinum electrode as the counter electrode, and a saturated calomel electrode (SCE, +0.242 V vs. SHE) as the reference electrode. Before the test, the sample was immersed in the test solution for about 30 min to stabilize the open circuit potential (OCP). The scanning rate of PDP tests was 5 mV/s, and the scanning range was OCP $\pm$ 0.5 V. The EIS tests were conducted at OCP values, and the scanning frequency range was from 10 mHz to 100 kHz. The data for the PDP and EIS curves were analyzed using tafel extrapolation and ZSimpWin software (ZSimpWin 3.60, http://www.echemsw.com/), respectively.

The immersion test was performed in 3.5 wt.% NaCl solution at room temperature. The appearances of samples were imaged every 12 h.

Each test was repeated at least three times to ensure reproducibility.

3. Results and Discussion

3.1. Effect of Pretreatment

Due to the strong chemical activity of magnesium alloys [28], the pretreatment before phosphating has a great influence on the phosphate coatings prepared later. Figure 1 shows the appearance of the samples after pretreatment and phosphating, the results of $CuSO_4$ pitting corrosion test and ECR measurement are shown in Figure 2. It is seen that the PCC with good corrosion resistance tend to have poor electrical conductivity. The coatings on sample No. 1, 2 and 3 are incomplete and heterogenous, with low ECR and poor corrosion resistance. The coatings on sample No. 4, 5 and 6 are compact and integral and have good corrosion resistance, but the electrical conductivity of No. 4 and 5 is poor. Therefore, process No. 6, which has both excellent corrosion resistance and good electrical conductivity, is selected as the pretreatment for the phosphate conversion coatings preparation.

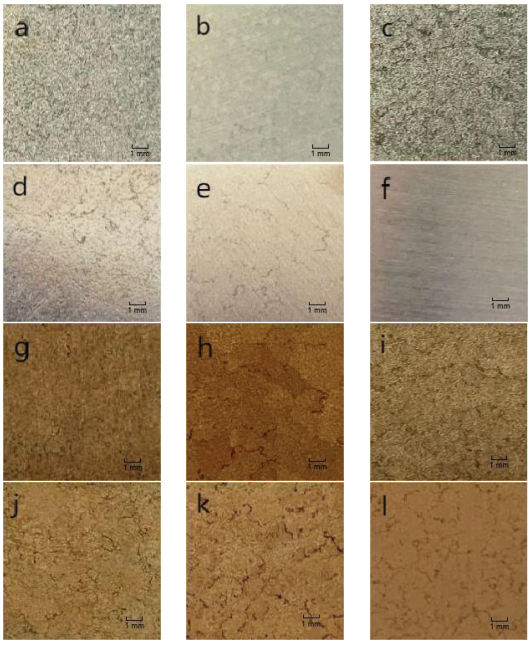

Figure 1. Appearance of samples treated with pretreatment and phosphating (**a**–**e**: samples after No. 1–No. 5 pretreatment; **f**: sample No. 6 only ultrasonic cleaned by acetone; **g**–**l**: sample No. 1–No. 6 after phosphating).

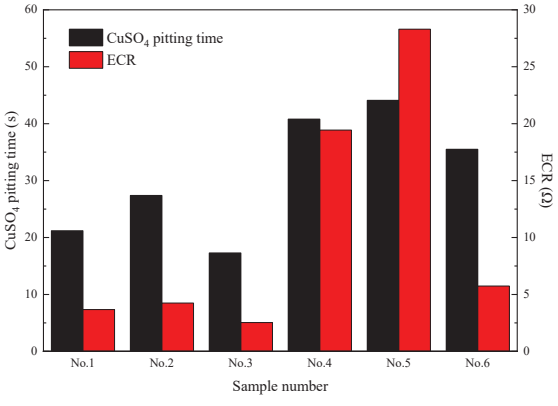

Figure 2. Curves of $CuSO_4$ pitting time and ECR of PCCs prepared by different pretreatments.

3.2. Effect of Strong Oxidant

In the present study, $KMnO_4$ is applied as the component of strong oxidant in the studied phosphating bath. Figure 3 presents the surface morphologies of samples treated in phosphating bath with $KMnO_4$, and the chemical compositions are shown in Table 3. It is seen from Figure 3b that the coating has a "riverbed" appearance, and numerous irregular bright spots can be seen on the surface. These bright spots are obviously raised, and clear grinding scratches can be seen on the surface, indicating that the coatings on them are very thin, or even that no coatings exist, as shown in Figure 3b. Combined with Table 3, the percentage of Al atoms in bright spots is much higher than that in the surrounding areas, and no Ca and P are detected, indicating that these areas are β-$Mg_{17}Al_{12}$ phase, it

is speculated that there is an extremely thin coating composed of Mg, Al and O on the surface, and the surrounding region is α-Mg phase, the main components of the upper coating are phosphates of Ca and Mg and oxides of Mg, Al and Mn. According to previous investigations [29], the action mechanism of $KMnO_4$ is speculated as follows:

$$MnO_4^- + 4H^+ + 3e^- \rightarrow MnO_2 + 2H_2O \quad (1)$$

$$Mg + H_2O - 2e^- \rightarrow MgO + 2H^+ \quad (2)$$

$$2Al + 3H_2O - 6e^- \rightarrow Al_2O_3 + 6H^+ \quad (3)$$

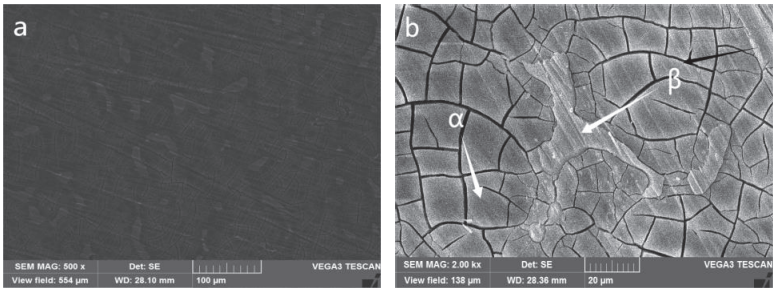

Figure 3. Surface morphologies of PCC with $KMnO_4$ (**a**: ×500; **b**: ×2000).

Table 3. Chemical composition of PCC with $KMnO_4$ by EDS equipped in SEM.

Atom (%)	Mg	Al	Ca	Mn	Mo	P	O
α phase	11.6	4.0	6.1	2.6	0.5	14.5	60.6
β phase	51.38	39.24	—	0.35	—	—	9.03

Figure 4 presents the surface morphologies of the coating formed at the phosphating bath free of $KMnO_4$, and the chemical compositions are shown in Table 4. It can be seen from Figure 4a,b that mass flake crystallization generated, and a few protruding β-$Mg_{17}Al_{12}$ phases are also visible, but these β phases are blocked by crystals. Combined with the chemical compositions shown in Table 4 and previous investigations [29], these crystals are presumed to be $CaHPO_4 \cdot 2H_2O$ formed by the deposition of Ca^{2+} due to the rapid rise in pH of solution surrounding the micro cathode β phase caused by the micro-galvanic effect. The following reactions of deposition of Ca^{2+} may occur in the studied phosphating bath:

$$H_2PO_4^{2-} \rightarrow HPO_4^{2-} + H^+ \quad (4)$$

$$Ca^{2+} + HPO_4^{2-} \rightarrow CaHPO_4\downarrow \quad (5)$$

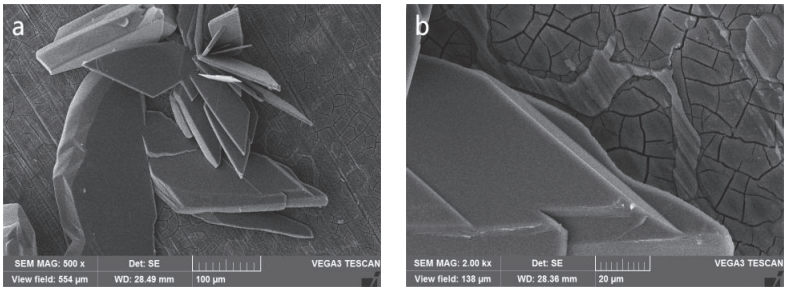

Figure 4. Surface morphologies of PCC without $KMnO_4$ (**a**: ×500; **b**: ×2000).

Table 4. Chemical composition of coating and crystallization of PCC without $KMnO_4$ by EDS equipped in SEM.

Atom (%)	Mg	Al	Ca	Mo	P	O
PCC	2.41	0.38	12.66	0.1	16.72	67.81
Crystal	0.42	—	21.77	—	12.86	64.95

Table 5 shows the ECR of two coatings measured by the two-point method. The ECR decreases from unmeasurable to 5.74 Ω with the addition of $KMnO_4$. Observe the phenomenon of parkerising, the number of bubbles generated by the reaction in the phosphating bath containing $KMnO_4$ is significantly reduced compared with that without $KMnO_4$. Combined with the surface morphologies above, it is seen that the introduction of $KMnO_4$ can effectively slow down the hydrogen evolution reaction in the reaction, inhibit the formation of $CaHPO_4{\cdot}2H_2O$ crystals and form an extremely thin oxide coating on the β phase, which finally protrude from the surface to become "conductive spots", and the conductivity of the phosphate conversion coating is improved.

Table 5. The ECR of phosphate conversion coating with and without $KMnO_4$.

Composition of Phosphating Bath	ECR (Ω)
Without $KMnO_4$	—
With $KMnO_4$	5.74

The results of the electrochemical tests for the PCCs formed at phosphating bath with different content of $KMnO_4$ are shown in Figure 5. The main fitting results of the PDP and EIS curves are summarized in Tables 6 and 7, respectively, and the equivalent electrical circuit (EEC) model used to fit the EIS curves is shown in Figure 6. R_s is the resistance of solution, R_1, CPE_1 and R_2, CPE_2 represent the resistance and capacitance of coating and double electric layer, respectively.

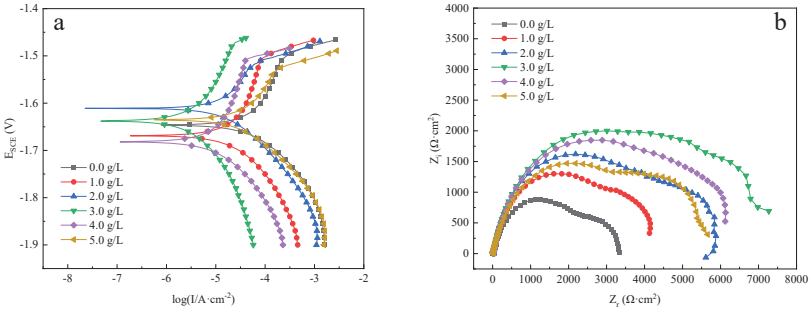

Figure 5. PDP and EIS curves of the PCCs obtained at different contents of $KMnO_4$ (**a**: PDP curves; **b**: EIS curves).

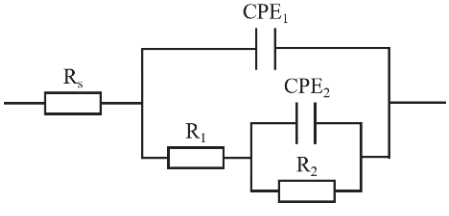

Figure 6. Equivalent circuit for EIS curve.

Table 6. Electrochemical parameters derived from the PDP curves of the PCCs obtained at different contents of $KMnO_4$.

Content of $KMnO_4$ (g/L)	E_{corr} (V)	i_{corr} (A/cm^2)
0.0	−1.646	5.27×10^{-5}
1.0	−1.669	3.61×10^{-5}
2.0	−1.611	2.04×10^{-5}
3.0	−1.638	9.62×10^{-6}
4.0	−1.682	1.39×10^{-5}
5.0	−1.635	2.86×10^{-5}

Table 7. Fitting results of EIS curves of the PCCs obtained at different contents of $KMnO_4$.

Content of $KMnO_4$ (g/L)	0.0	1.0	2.0	3.0	4.0	5.0
R_s ($\Omega \cdot cm^2$)	30.95	8.779	15.96	8.011	8.965	10.64
CPE_1/($\mu S \cdot s^{-n} \cdot cm^{-2}$)	2.697×10^{-5}	1.484×10^{-5}	1.215×10^{-5}	1.362×10^{-5}	1.375×10^{-5}	1.458×10^{-5}
n_1	0.8091	0.7914	0.8403	0.7817	0.7867	0.7759
R_1 ($\Omega \cdot cm^2$)	2486	3744	4478	5956	5798	4335
CPE_2 ($\mu S \cdot s^{-n} \cdot cm^{-2}$)	9.589×10^{-4}	5.534×10^{-4}	3.411×10^{-4}	2.598×10^{-4}	6.991×10^{-4}	3.071×10^{-4}
n_2	0.9244	0.8021	0.8947	0.8736	0.7641	0.8768
R_2 ($\Omega \cdot cm^2$)	780	675	1404	1357	568	1378
$R_1 + R_2$ ($\Omega \cdot cm^2$)	3266	4419	5882	7313	6357	5713

The results show that adding $KMnO_4$ into the phosphating bath can improve the corrosion resistance of the PCCs. It can be seen from Figure 5a and Table 6 that with the content of $KMnO_4$ increasing, the corrosion current (i_{corr}) of the coating decreases first and then increases, and the PCC exhibit the minimum i_{corr} of 9.62×10^{-6} A/cm^2 when the content of $KMnO_4$ is 3.0 g/L. As for the EIS curves in Figure 5b, the Nyquist curves all have similar characteristics and consist of two capacitive loops. The high-frequency capacitive loop is related to the process of charge transfer from magnesium alloy matrix to solution double layer during corrosion, while the low-frequency capacitive loop represents the process of Mg^{2+} diffusion to the sample surface. The order of dimension of the high-frequency capacitive loop is as follows: 3.0 g/L > 4.0 g/L > 2.0 g/L > 5.0 g/L > 1.0 g/L > 0.0 g/L. Combined with the data in Table 7, the coating resistance R_1 reaches the maximum of 5956 $\Omega \cdot cm^2$ at the content of $KMnO_4$ is 3.0 g/L. Therefore, the optimal content of $KMnO_4$ in the studied phosphating bath to form PCCs with the best corrosion resistance is 3.0 g/L.

In addition to corrosion resistance, low ECR is also the focus of conductive and corrosion-resistant phosphate conversion coatings. Therefore, $CuSO_4$ pitting corrosion test and contact resistance are used as the evaluation basis for corrosion resistance and electrical conductivity, respectively, to comprehensively screen the appropriate content of $KMnO_4$.

Figure 7 presents the results of the $CuSO_4$ pitting corrosion test and ECR measurement of PCCs with different $KMnO_4$ contents. It is seen that the concentration of $KMnO_4$ has a significant influence on the $CuSO_4$ pitting time and ECR. With the increase in $KMnO_4$ concentration, the pitting time of the coatings first increases and then decreases, which is consistent with the electrochemical test results above, and the ECR shows a trend of decrease, with the magnitude of the decreasing has lessened. In the formation of PCC, MnO_4^- will react with H^+, so that the pH between the solution and the alloy increases, thus promoting the deposition of phosphate and accelerating the formation of coating. However, when the content of $KMnO_4$ is too high, the surface of Mg alloy will be passivated, which will inhibit the subsequent deposition reaction, and the thickness of the coating will become thinner, the corrosion resistance will decrease, thus improving the electrical

conductivity [30–32]. When the concentration of $KMnO_4$ is 3.0 g/L, the coating has the longest pitting time and a low ECR. With the further increase in the concentration, the pitting time is significantly shortened, but the decrease in the ECR is not obvious. Therefore, the optimum content of $KMnO_4$ in the studied phosphating bath is 3.0 g/L.

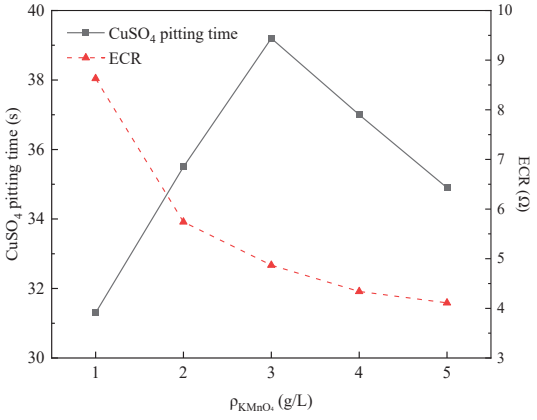

Figure 7. Curves of $CuSO_4$ pitting time and ECR of PCCs formed at different $KMnO_4$ content.

3.3. Effect of Additive

In the present study, Na_2MoO_4 is applied as the component of additive in the studied phosphating bath. Figure 8 presents the appearances of samples treated in phosphating bath with and without Na_2MoO_4 at various times during the 48 h immersion test, and the time interval of each photograph is 12 h. It is seen that both samples exhibited obvious pitting corrosion. The sample without Na_2MoO_4 showed obvious corrosion points at 24 h, while the sample containing Na_2MoO_4 showed corrosion points after 36 h. After the 48 h immersion test, the corroded area of both samples was intensified. However, the corroded area on the surface of sample with Na_2MoO_4 was less than that of sample without Na_2MoO_4. The result shows that adding Na_2MoO_4 into the phosphating bath can effectively improve the corrosion resistance of the coatings.

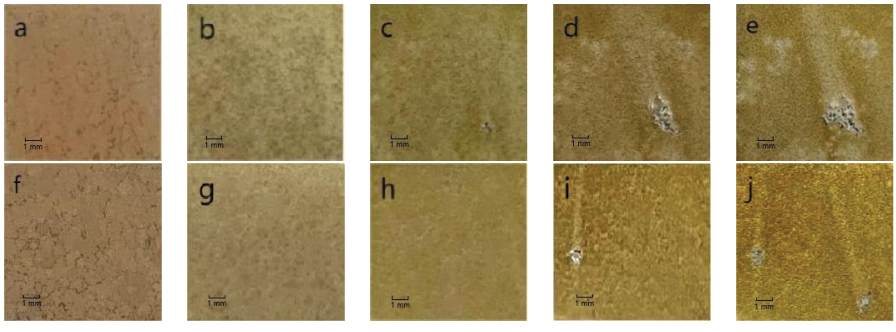

Figure 8. Appearances of samples treated in phosphating bath with and without Na_2MoO_4 at various times during the 48 h immersion test (**a**–**e**: without Na_2MoO_4, 0–48 h; **f**–**j**: with Na_2MoO_4, 0–48 h).

Figure 9 shows the results of electrochemical tests for the PCCs formed in the phosphating bath with different contents of Na_2MoO_4. The main fitting results of the PDP and EIS curves are summarized in Tables 8 and 9, respectively. MoO_4^{2-} can form insoluble $CaMoO_4$ with Ca^{2+}. A small amount of Na_2MoO_4 can increase the nucleation site in the phosphating process to promote the deposition of Ca^{2+} and accelerate the coating formation. However, when the concentration of Na_2MoO_4 is too high, cracks in the coating will be

thickened and many uneven coarse crystals will be generated on the surface, leading to the decline in corrosion resistance [33]. It can be seen from Figure 9 that with the increasing concentration of Na_2MoO_4, the i_{corr} of the coating decreases first and then increases, while the dimension of the high-frequency capacitive loop increases first and then decreases. According to the data in Tables 8 and 9, when the content of Na_2MoO_4 is 1.5 g/L, the i_{corr} of the PCC is the lowest (3.74×10^{-6} A/cm^2), and R1 reaches the maximum (7841 Ω·cm^2). Therefore, the optimal content of Na_2MoO_4 in the studied phosphating bath to form PCCs with the best corrosion resistance is 1.5 g/L.

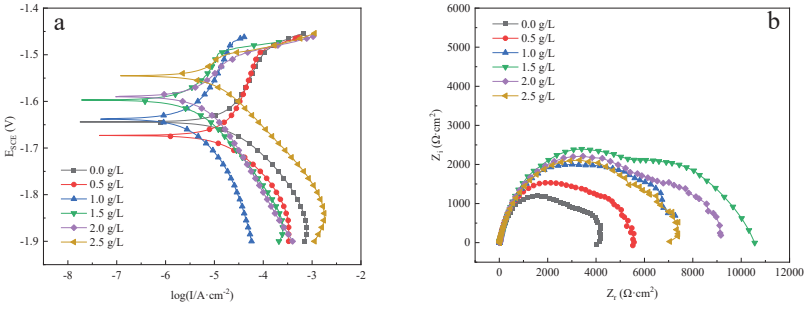

Figure 9. PDP and EIS curves of the PCCs obtained at different contents of Na_2MoO_4 (**a**: PDP curves; **b**: EIS curves).

Table 8. Electrochemical parameters derived from the PDP curves of the PCCs obtained at different contents of Na_2MoO_4.

Content of Na_2MoO_4 (g/L)	E_{corr} (V)	i_{corr} (A/cm^2)
0.0	−1.644	2.02×10^{-5}
0.5	−1.673	1.87×10^{-5}
1.0	−1.638	9.62×10^{-6}
1.5	−1.597	3.74×10^{-6}
2.0	−1.590	7.53×10^{-6}
2.5	−1.545	1.02×10^{-5}

Table 9. Fitting results of EIS curves of the PCCs obtained at different contents of Na_2MoO_4.

Content of Na_2MoO_4 (g/L)	0.0	0.5	1.0	1.5	2.0	2.5
R_s (Ω·cm^2)	11.34	10.72	8.011	9.342	12.73	12.1
CPE_1 (μS·s^{-n}·cm^{-2})	1.665×10^{-5}	1.481×10^{-5}	1.362×10^{-5}	1.575×10^{-5}	1.79×10^{-5}	1.859×10^{-5}
n_1	0.8395	0.827	0.7817	0.7392	0.8423	0.8357
R_1 (Ω·cm^2)	3226	4289	5956	7841	6638	6165
CPE_2 (μS·s^{-n}·cm^{-2})	4.725×10^{-4}	3.455×10^{-4}	2.598×10^{-4}	3.636×10^{-4}	6.126×10^{-4}	8.546×10^{-4}
n_2	0.9179	0.8701	0.8736	0.8127	0.8335	0.8314
R_2 (Ω·cm^2)	979	1187	1357	2278	2166	962
$R_1 + R_2$ (Ω·cm^2)	4205	5476	7313	10,119	8804	7127

Figure 10 shows the results of the $CuSO_4$ pitting corrosion test and ECR measurement of PCCs with different Na_2MoO_4 contents. It is seen that the concentration of Na_2MoO_4 has a great influence on the $CuSO_4$ pitting time, which increases first and then decreases with the increase in the content, reaching the maximum at 1.5 g/L, which is consistent with the results of electrochemical tests. However, the concentration of Na_2MoO_4 has

little effect on the ECR, which shows an upward trend, and the difference between the minimum 0.0 g/L and the maximum 2.5 g/L is about 1.5 Ω. Thus, 1.5 g/L is the optimum content of Na_2MoO_4 in the studied phosphating bath considering corrosion resistance and electrical conductivity.

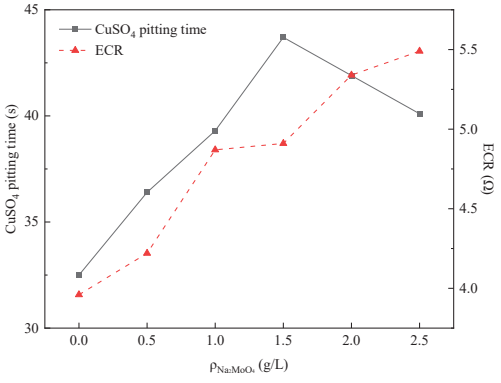

Figure 10. Curves of $CuSO_4$ pitting time and ECR of PCCs formed at different Na_2MoO_4 content.

3.4. Effect of Surface-Active Agent

In the present study, OP-10 is applied as the component of surface-active agent in the studied phosphating bath. Figure 11 presents the surface morphologies of PCCs formed in the phosphating bath with and without OP-10. It is seen that no matter whether OP-10 is contained in the phosphating bath or not, both coatings have a "dry riverbed" appearance. However, the cracks on the PCC containing OP-10 are significantly fewer than that without OP-10, and the crack width is also decreased. According to previous investigations [34], the composition of OP-10 is alkylphenol ethoxylates (APEO), which can reduce the tension between the metal and the solution interface, allowing the phosphating bath to moisten the surface rapidly, and can also reduce the adhesion ability of bubbles generated by the reaction, making them more easily separable from the sample surface, so that the compactness of the coating is improved.

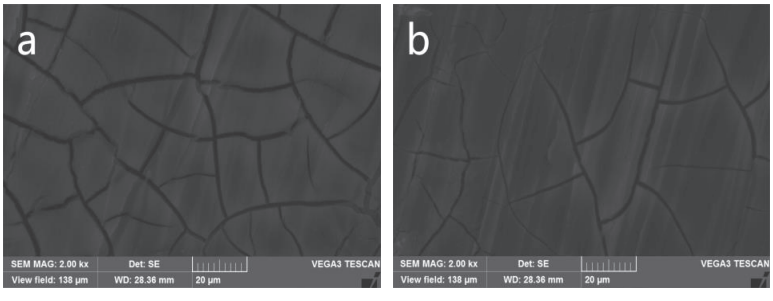

Figure 11. Surface morphologies of PCCs with and without OP-10 (**a**: without OP-10 ×2000; **b**: with OP-10 ×2000).

Figure 12 shows the results of electrochemical tests for the PCCs formed at phosphating bath with different contents of OP-10. The main fitting results of the PDP and EIS curves are summarized in Tables 10 and 11, respectively. It is seen that the i_{corr} of the coating decreases in the following order: 0.0 g/L > 2.5 g/L > 2.0 g/L >1.5 g/L > 0.5 g/L > 1.0 g/L. The i_{corr} reaches the minimum (3.74×10^{-6} A/cm^2) when OP-10 concentration is 1.0 g/L, and the coating resistance R_1 of the PCC reaches the maximum (7841 Ω·cm^2). Therefore,

the optimal content of OP-10 in the studied phosphating bath to form PCCs with the best corrosion resistance is 1.0 g/L.

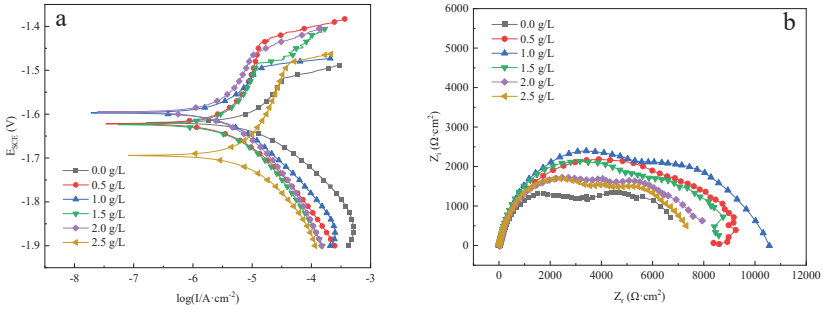

Figure 12. PDP and EIS curves of the PCCs obtained at different contents of OP-10 (**a**: PDP curves; **b**: EIS curves).

Table 10. Electrochemical parameters derived from the PDP curves of the PCCs obtained at different contents of OP-10.

Content of OP-10 (g/L)	E_{corr} (V)	i_{corr} (A/cm^2)
0.0	−1.619	1.35×10^{-5}
0.5	−1.622	7.52×10^{-6}
1.0	−1.597	3.74×10^{-6}
1.5	−1.624	8.19×10^{-6}
2.0	−1.595	9.45×10^{-6}
2.5	−1.694	1.01×10^{-5}

Table 11. Fitting results of EIS curves of the PCCs obtained at different contents of OP-10.

Content of OP-10 (g/L)	0.0	0.5	1.0	1.5	2.0	2.5
R_s (Ω·cm^2)	10.72	14.48	9.342	11.26	10.99	12.07
CPE_1 (μS·s^{-n}·cm^{-2})	1.484×10^{-5}	1.748×10^{-5}	1.575×10^{-5}	1.867×10^{-5}	1.611×10^{-5}	1.305×10^{-5}
n_1	0.7677	0.8481	0.7392	0.838	0.7655	0.7925
R_1 (Ω·cm^2)	3944	7468	7841	6126	5268	4957
CPE_2 (μS·s^{-n}·cm^{-2})	3.181×10^{-4}	6.223×10^{-4}	3.636×10^{-4}	4.685×10^{-4}	3.538×10^{-4}	2.905×10^{-4}
n_2	0.8529	0.7445	0.8127	0.8662	0.8763	0.8331
R_2 (Ω·cm^2)	2804	1347	2278	2292	2522	2261
$R_1 + R_2$ (Ω·cm^2)	6748	8815	10,119	8418	7790	7218

Figure 13 shows the results of the $CuSO_4$ pitting corrosion test and ECR measurement of PCCs with different OP-10 contents. It is seen that the ECR of coatings fluctuated between 4.4 Ω and 5.2 Ω, indicating that the concentration of OP-10 had no significant effect on electrical conductivity, while the pitting time increases first and then decreases with the increase in concentration, reaching the maximum at 1.0 g /L, which is consistent with the electrochemical test results. Therefore, the optimum content of OP-10 in the studied phosphating bath is 1.0 g/L.

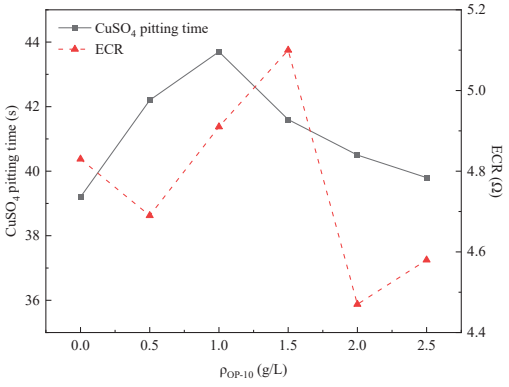

Figure 13. Curves of $CuSO_4$ pitting time and ECR of PCCs formed at different OP-10 content.

3.5. Performance Tests Results of PCC

From the results above, the optimum content for $KMnO_4$, Na_2MoO_4 and OP-10 in phosphating bath is 3.0 g/L, 1.5 g/L and 1.0 g/L, respectively.

Figure 14 shows the results of the electrochemical tests for the uncoated AZ91D magnesium alloy and the PCC formed at the optimum phosphating bath formulation. The main fitting results of the PDP are summarized in Table 12. The results show that PCC can provide good protection for the magnesium alloy. It can be seen from Figure 14a and Table 12 that the coated alloy has more positive E_{corr} and lower i_{corr} than the uncoated one. The E_{corr} positively shifts about 27 mV, and the i_{corr} decreases by more than 1 order of magnitude.

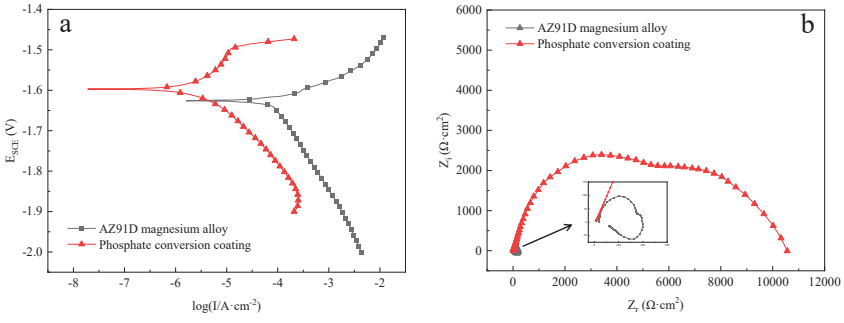

Figure 14. PDP and EIS curves of uncoated AZ91D magnesium alloy and PCC formed at the phosphating bath at the optimum condition (**a**: PDP curves; **b**: EIS curves).

Table 12. Electrochemical parameters derived from the PDP curves of uncoated AZ91D magnesium alloy and PCC formed at the phosphating bath at the optimum condition.

Sample	E_{corr} (V)	i_{corr} (A/cm^2)
Phosphate conversion coating	−1.597	3.74×10^{-6}
AZ91D magnesium alloy	−1.626	7.84×10^{-5}

As for the EIS curves in Figure 14b, the Nyquist curve of the PCC consisted of two capacitive loops, while that of the uncoated alloy has an obvious inductive loop in the low-frequency region. The shape of the impedance spectrum describes the type of electrochemical reactions that occur at the electrode surface. The low-frequency inductive loop corresponds to the adsorption process of Mg^{2+} on the alloy surface. A fully covered PCC

can block the contact between alloy and the test solution, thus hindering the generation and adsorption of Mg^{2+} on the surface. Therefore, no inductive loop appears in the Nyquist curve of the PCC.

Figure 15 presents the surface morphologies and the chemical compositions of PCC formed at the phosphating bath at the optimum condition. It is seen that the coating has a "dry riverbed" appearance and is covered completely. Clear irregular bright spots can be seen, which are raised β phases according to the previous results. The β phases combined with the ECR of the PCC is 4.91 Ω, demonstrating that β phases act as a conductive spot to achieve electrical conductivity.

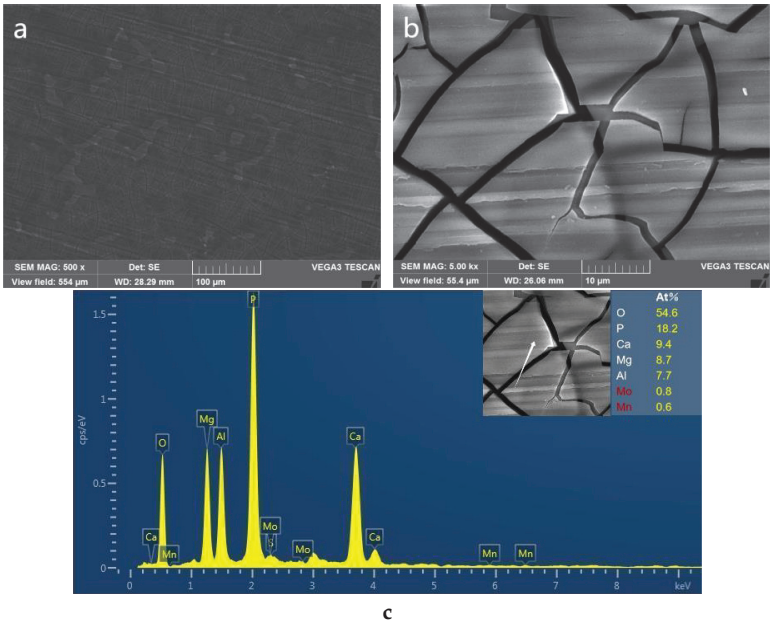

c

Figure 15. Surface morphologies and the chemical compositions of PCC formed at the phosphating bath at the optimum condition (**a**: ×500; **b**: ×2000; **c**: EDS).

Obvious scratches are visible on the surface, showing that the coating is thin, so that it cannot effectively cover the polishing marks. However, the bilayer structure can be clearly seen from the coating upon α phases in Figure 15b, which is consistent with the structure of Ca phosphate conversion coatings in previous investigations [35], indicating that the PCC has good corrosion resistance.

According to the chemical compositions shown in Figure 15c, the PCC consists of Ca, Mg, Al, O, P and a small amount of Mn and Mo, and it is speculated that the main coating-forming substances are phosphate of Ca and Mg and oxides of Mg and Al.

4. Conclusions

The conductive and corrosion-resistant phosphate conversion coating was prepared upon the surface of AZ91D magnesium alloy. The PCC was completely covered, and the main coating-forming substances were phosphate of Ca and Mg and oxides of Mg and Al. The coating on α phases had bilayer structure and the β phases protruded as conductive spots, which provided high corrosion resistance and low ECR.

The presence of strong oxidant $KMnO_4$ formed an extremely thin passive film on the protruded β phases and inhibited the formation of phosphate crystals to prevent the conductive spots from being obscured.

The optimum content for $KMnO_4$, Na_2MoO_4 and OP-10 in phosphating bath was 3.0 g/L, 1.5 g/L and 1.0 g/L, and the pretreatment before phosphating was sonication cleanout in acetone for 5 min after mechanical polishing.

Author Contributions: Conceptualization, Y.X. and S.Z.; methodology, Y.X.; software, Y.X.; validation, S.Z., J.D. and Y.X.; formal analysis, S.Z. and T.Z.; investigation, Y.X.; resources, S.Z.; data curation, Y.X.; writing—original draft preparation, Y.X.; writing—review and editing, Y.X.; visualization, L.L. and S.Z.; supervision, Q.L.; project administration, Y.X. and S.Z.; funding acquisition, S.Z. All authors have read and agreed to the published version of the manuscript.

Funding: This work was supported by the Key project of National Natural Science Foundation of China: Research basis of "corrosion-functional" integrated protective coating on magnesium alloys (U21A2045). the National Natural Science Foundation of China (NSFC), "Study of conductive-corrosion resistant chemical conversion coating of magnesium alloy" (51771050).

Data Availability Statement: Not applicable.

Conflicts of Interest: The authors declare no conflict of interest.

References

1. Song, J.F.; She, J.; Chen, D.L. Latest research advances on magnesium and magnesium alloys worldwide. *J. Magnes. Alloys* **2020**, *8*, 1–41. [CrossRef]
2. Luthringer, B.J.; Feyerabend, F.R.R.; Willumeit, M. Magnesium-based implants: A mini-review. *Magnes. Res.* **2014**, *24*, 142–154. [CrossRef] [PubMed]
3. Li, N.; Zheng, Y. Novel magnesium alloys developed for biomedical application: A review. *J. Mater. Sci. Technol.* **2013**, *29*, 489–502. [CrossRef]
4. Risky, U.P.; Hasan, B.; Akbar, T.P. Level of Activity Changes Increases the Fatigue Life of the Porous Magnesium Scaffold, as Observed in Dynamic Immersion Tests, over Time. *Sustainability* **2023**, *15*, 823.
5. Huang, G.; Zhang, L.; Song, B. Cold stamping for AZ31B magnesiumalloy sheet of cell phone house. *Trans. Nonferrous Met. Soc. China* **2010**, *20*, s608. [CrossRef]
6. Xu, T.C.; Yang, Y.; Peng, X.D. Overview of advancement and development trend on magnesium alloy. *J. Magnes. Alloys* **2019**, *7*, 536–544. [CrossRef]
7. Zheng, Y.; Ma, Y.L.; Zang, L.B. Microstructure, corrosion behavior, and surface mechanical properties of Fe oxide coatings on biomedical ZK60 Mg alloy. *Mater. Corros.* **2019**, *70*, 2292–2302. [CrossRef]
8. Li, N.; Yan, H.; Wu, Q. Fabrication of carbon nanotubes and rare earth Pr reinforced AZ91 composites by powder metallurgy. *Chin. J. Mech. Eng.* **2021**, *34*, 26. [CrossRef]
9. Zheng, Y.; Zhang, L.B.; Bi, Y.Z. Corrosion behavior of Fe/Zr composite coating on ZK60 Mg alloy by ion implantation and deposition. *Coatings* **2018**, *8*, 261. [CrossRef]
10. Yang, Y.; Xiong, X.M.; Chen, J. Research advances in magnesium and magnesium alloys worldwide in 2020. *J. Magnes. Alloys* **2021**, *9*, 705–747. [CrossRef]
11. Gray, J.E.; Luan, B. Protective coatings on magnesium and its alloys—A critical review. *J. Alloys Compd.* **2002**, *336*, 88–113. [CrossRef]
12. Pardo, A.; Merino, M.C.; Casajus, P. Corrosion behavior of Mg-Al alloys with Al-11Si thermal spray coatings. *Mater. Corros.* **2009**, *60*, 939–948. [CrossRef]
13. Yang, Q.H.; Chen, Z.; Xiong, Z.P. Research on the corrosion resistance of magnesium alloy anodizing films enhanced by SDBS. *Plat. Finish.* **2017**, *39*, 5.
14. Zhao, X.X.; Ma, Y.G.; Sun, N.A. Research Progress of Micro-arc Oxidation Process for Magnesium Alloy. *Foundry Technol.* **2013**, *34*, 45.
15. Chen, X.B.; Yang, H.Y.; Abbott, T.B. Corrosion-resistant electrochemical plating on magnesium alloys: A state-of-the-art review. *Corrosion* **2012**, *68*, 518–535. [CrossRef]
16. Hu, R.Y.; Chen, M. Effect of pretreatment on electroless nickel plating on AZ91D magnesium alloy. *Plat. Finish.* **2017**, *39*, 35.
17. Chen, X.B.; Birbilis, N.; Abbott, T.B. Effect of $[Ca^{2+}]$ and $[PO_3{}^{4-}]$ levels on the formation of calcium phosphateconversion coatings on die-cast magnesium alloy AZ91D. *Corros. Sci.* **2012**, *55*, 226. [CrossRef]
18. Cheng, I.C.; Fu, E.G.; Liu, L.D. Effect of fluorine anions on anodizing behavior of AZ91 magnesium alloy in alkaline solutions. *J. Electrochem. Soc.* **2008**, *155*, C219–C225. [CrossRef]
19. Liu, B.; Zhang, X.; Xiao, G.Y. Phosphate chemical conversion coatings on metallic substrates for biomedical application: A review. *Mat. Sci. Eng. C* **2015**, *47*, 97–104. [CrossRef]
20. Hung, S.M.; Lin, H.H.; Chen, W. Corrosion resistance and electrical contact resistance of a thin permanganate conversion coating on dual-phase LZ91 Mg-Li alloy. *J. Mater. Res. Technol.* **2021**, *11*, 1953–1968. [CrossRef]
21. Chen, X.B.; Birbilis, N.T.; Abbott, B. Review of corrosion-resistant conversion coatings for magnesium and its alloys. *Corrosion* **2011**, *67*, 35001. [CrossRef]

22. Jian, S.Y.; Chu, Y.R.; Lin, C.S. Permanganate conversion coating on AZ31 magnesium alloys with enhanced corrosion resistance. *Corros. Sci.* **2015**, *93*, 301–309. [CrossRef]
23. Duan, G.Q.; Yang, L.X.; Liao, S.J. Designing for the chemical conversion coating with high corrosion resistance and low electrical contact resistance on AZ91D magnesium alloy. *Corros. Sci.* **2018**, *135*, 197–206. [CrossRef]
24. Zhou, P.; Yang, L.X.; Hou, Y.J. Grain refinement promotes the formation of phosphate conversion coating on Mg alloy AZ91D with high corrosion resistance and low electrical contact resistance. *Corros. Commun.* **2021**, *1*, 47–57. [CrossRef]
25. Zeng, R.C.; Zhang, F.; Lan, Z.D. Corrosion resistance of calcium-modified zinc phosphate conversion coatings on magnesium-aluminium alloys. *Corros. Sci.* **2014**, *88*, 452. [CrossRef]
26. Chen, B.X. *The Research of Chemical Conversioncoating with High Corrosion Resistance and Lowelectrical Contact Resistance on AZ91D Magnesium Alloy Resisting Hot and Humid Environment*; Harbin Engineering University: Harbin, China, 2018.
27. Li, A.H. *Research on Surface Modification of Mg Alloy for Electro-Conductivity and Corrosion Protection*; South China University of Technology: Guangzhou, China, 2014.
28. Ismail, N.N.; Zuhailawati, H.; Abdalla, K. Effect of strontium pretreatment on zinc phosphate coating deposition on magnesium alloy. *Mater. Today* **2019**, *17*, 694–699. [CrossRef]
29. Duan, G.Q. *Investigation of the Conversion Coating with High Corrosion Resistance and Low Electrical Contact Resistance on Magnesium Alloy*; University of Science and Technology of China: Hefei, China, 2019.
30. Zhou, W.; Shan, D.; Han, E.H. Structure and formation mechanism of phosphate conversion coating on die-cast AZ91D magnesium alloy. *Corros. Sci.* **2008**, *50*, 329. [CrossRef]
31. Chen, X.B.; Zhou, X.; Abbott, T.B. Double-layered manganese phosphate conversion coating on magnesium alloy AZ91D: Insights into coating formation, growth and corrosion resistance. *Surf. Coat. Technol.* **2013**, *217*, 147–155. [CrossRef]
32. Yun, X.; Zhou, Q.Y.; Xiong, J.P. The study of a phosphate conversion coating on magnesium alloy AZ91D: I. Formation, morphology and composition. *Int. J. Electrochem. Sci.* **2015**, *10*, 8454.
33. Meng, X.L.; Liang, J.L.; Yi, L. Influence of sodium molybdate on corrosion resistance of phosphating film on AZ31B magnesium alloy. *Plat. Finish.* **2022**, *44*, 1.
34. Li, J.Z.; Guo, R.G.; Tang, C.B. Modification of OP-10 for corrosion resistance of vanadate conversion coating on Mg alloy. *Mater. Protec.* **2017**, *50*, 52.
35. Zhang, C.Y.; Zhang, J.S.; Zhang, Y. Comparison of calcium phosphate coatings on AZ31 and fluoride-treated AZ31 alloy prepared by hydrothermal method and their electrochemical corrosion behaviour. *Mater. Chem. Phys.* **2018**, *220*, 395–401. [CrossRef]

MDPI
St. Alban-Anlage 66
4052 Basel
Switzerland
www.mdpi.com

Coatings Editorial Office
E-mail: coatings@mdpi.com
www.mdpi.com/journal/coatings

Academic Open
Access Publishing

mdpi.com

ISBN 978-3-7258-1028-4